UNIVERSIDAD DE CHILE
FACULTAD DE CIENCIAS FÍSICAS Y MATEMÁTICAS
DEPARTAMENTO DE GEOLOGÍA

TECTONIC EVOLUTION OF THE CENTRAL ANDES OF NORTHERN CHILE AND ITS RECORD WITHIN THE SALAR DE ATACAMA BASIN (22°30'-24°S)

TESIS PARA OPTAR AL GRADO DE DOCTOR EN CIENCIAS, MENCIÓN GEOLOGÍA

SEBASTIÁN ANDRÉS BASCUÑÁN HUGHES

PROFESOR GUÍA:
DR. MARCELO FARÍAS THIERS

PROFESOR CO-GUÍA:
DR. ANDREI MAKSYMOWICZ JERIA

MIEMBROS DE LA COMISIÓN:
DRA. KATJA DECKART
DR. REYNALDO CHARRIER GONZÁLEZ
DR. ANDRÉS FOLGUERA TELICHEVSKY

SANTIAGO DE CHILE
2022

RESUMEN DE LA TESIS PARA OPTAR AL GRADO DE: Doctor en Ciencias, Mención Geología.

POR: Sebastián Andrés Bascuñán Hughes.

FECHA: 07/03/2022

PROFESOR GUÍA: Dr. Marcelo Farías Thiers

TECTONIC EVOLUTION OF THE CENTRAL ANDES OF NORTHERN CHILE AND ITS RECORD WITHIN THE SALAR DE ATACAMA BASIN (22°30'-24°S)

La Cuenca del Salar de Atacama corresponde a una zona esencial para estudiar los Andes Centrales, y mejorar la comprensión de la construcción del orógeno. Distintos esquemas tectono-estratigráficos, a veces contradictorios, han sido propuestos para su evolución. Para realizar una evaluación de los eventos tectónicos en la cuenca, se hizo un estudio gravimétrico de tres perfiles este-oeste cruzando Cordillera de Domeyko-Salar de Atacama (214 estaciones). Esto fue complementado con perfiles de reflexión sísmica, velocidad de intervalo, registros de perforaciones y estudios magnéticos. Diez muestras para geocronología U-Pb en circón detrítico fueron tomadas para constreñir la deposición de las unidades Cretácico medio-Paleógeno. Los perfiles muestran el contraste entre unidades de alta densidad del basamento paleozoico-triásico de Cordillera de Domeyko, unidades de baja densidad tales como el Grupo Purilactis (Cretácico-Paleogeno) y posiblemente formaciones Naranja y Loma Amarilla, y unidades de menor densidad evaporíticas y finas correspondientes a Formación San Pedro (Oligoceno-Mioceno). La interpretación en conjunto muestra que el basamento se encuentra deformando y empujando las unidades Paleógeno-Cretácico, formando una serie de pliegues de vergencia este que se encuentran cubiertos en discordancia angular por depósitos oligocenos-recientes. Éstos muestran estratos de crecimiento que crecen hacia el este desde el límite occidental de la cuenca, los que encuentran deformados en el área de Cordillera de la Sal. Las edades confirman la ubicación Cretácico medio de la Formación Tonel, que presenta variaciones norte-sur en su patrón de circones detríticos, posiblemente debido a una paleotopografía irregular. Las edades de Formación Purilactis muestran que la deposición continuó durante el Maastrichtiano-Daniano, extendiéndose al Paleógeno. La Formación Naranja presenta edades máximas de deposición en el Maastrichtiano, por lo que se puede considerar un equivalente de la parte superior del Grupo Purilactis. Las unidades muestran el levantamiento temprano y adición de Cordillera de la Costa durante el Cretácico medio-Tardío y el comienzo de la cuenca de antepaís. La adición progresiva de los arcos magmáticos Cretácico Tardío-Paleógeno y el basamento de Cordillera de Domeyko reflejan la evolución de un sistema de antepaís en el Salar de Atacama, desde un *distal foredeep* hasta un *wedge top* en el Eoceno tardío-Oligoceno, donde se incorpora al antearco y el *hinterland.* Los depósitos neógenos evidencian compresión/pos-tectonismo, y el análisis no muestra evidencia de extensión durante el Oligoceno-Mioceno. La evolución de la cuenca se correlaciona con eventos mayores que afectaron el margen desde la 'Fase Peruana', con compresión a lo largo del orógeno, exhumación de segmentos progresivamente al este, erosión por subducción del margen y migración del arco magmático-antepaís a su ubicación actual. La historia tectónica no es compatible con modelos cíclicos para la formación del orógeno, pero es consistente con el registro presente en áreas cercanas de los Andes Centrales.

Abstract

The Salar de Atacama Basin constitutes one of the quintessential study areas in the Central Andes, where several works have been performed aiming to improve the understanding of the building of the orogen. Several stratigraphic and tectonic schemes have been proposed, at times establishing contradictory claims to its evolution.In order to make a better assessment of the tectonic events present in the basin, a gravimetric survey was performed consisting in 214 stations crossing the Cordillera de Domeyko-Salar de Atacama Basin in three east-west profiles, which were complemented with additional geophysical data such as seismic reflection profiles, interval velocities, well logs and magnetic surveys. Ten U-Pb detrital zircon geochronology samples were taken to further constrain the timing of the deposition of the mid-Cretaceous to Paleogene units, allowing for an improved analysis of standing chronostratigraphic issues.

The surveyed profiles show the contrast between high density units, belonging to the crystalline, Paleozoic basement in Cordillera de Domeyko, along with Permo-Triassic deposits, low density units, such as the clastic Cretaceous-Paleogene Purilactis Group, possibly the Naranja and Loma Amarilla formations, and the lowest density units, which comprise the clastic-evaporitic units of the Oligocene-Miocene San Pedro Formation and recent deposits. The interpretation of these contrasts, along with the other geophysical-geological data, show that the basement is thrust eastwards over the Upper Cretaceous-Paleogene units, deforming the latter into a series of mostly east-verging folds, which are overlain in angular unconformity by Oligocene-recent deposits. The latter present growth strata increasing eastwards from the western basin margin and are heavily deformed in the Cordillera de la Sal area. The geochronological analyses confirm the mid-Cretaceous age of the Tonel Formation, which has relevant north-south variations in its detrital zircon patterns, possibly due to an irregular basin paleotopography and its connection to western and southern sources. The ages from the Purilactis Formation show that deposition was ongoing during the Maastrichtian-Danian, thus pushing the top of the formation further into the Paleogene. The samples of the Naranja Formation present maximum depositional ages in the Maastrichtian, and can be considered a southern equivalent of the upper Purilactis Group.

The units analyzed in this study show the early uplift and addition of the Coastal Cordillera as a zircon source during the mid- to Late Cretaceous, which signals the inception of the foreland basin. The progressive addition of various Late Cretaceous-Paleogene magmatic arcs, and the crystalline Cordillera de Domeyko, mark the evolution of this system, which is reflected in the position of the basin, changing progressively from a distal foredeep to a wedge top around the late Eocene-Oligocene, after which it becomes part of the hinterland and the forearc. The Neogene deposits show evidence reminiscent of a compressive or post-tectonic stage, with no clear evidence for extension during the Oligocene-Miocene. It is proposed that this progression might be found in other basins in the Preandean Depression.

This evolution of the basin can be correlated with the major events that affected the South American margin since the ‘Peruvian Phase’, which have led to orogen-wide compression, eastward-driven exhumation of different segments, subduction erosion of the margin and migration of the volcanic arc-foreland basin system to its present-day location. This tectonic history of the basin is hard to reconcile with models invoking cyclic events for the orogen, but consistent with the geological record of neighboring areas within the Central Andes.

Agradecimientos

Quiero agradecer a los miembros de mi Comisión Doctoral: al Profesor Dr. Reynaldo Charrier, quien ha mostrado desde mi pregrado, pasando por los cursos de magíster, y las tesis de magister y doctorado, un gran apoyo e interés en mi investigación. A la Profesora Dra. Katja Deckart, por su inmensa ayuda durante el mismo tiempo, y el apoyo constante para sacarlo adelante. Al Dr. Andrés Folguera, por sus comentarios, participación e invaluable opinión científica. Quiero agradecer al Dr. Marcelo Farías, por las amplias conversaciones científicas, el haber confiado en mi trabajo, pero por sobre todo haberme dado a mí y a muchos de mis compañeros de laboratorio el apoyo en tiempos muy difíciles. Me será imposible olvidarlo.

También debo agradecer especialmente al Dr. Andrei Maksymowicz. Esta tesis no habría salido adelante sin tu constante empuje, apoyo moral, ánimo, además de tu impresionante conocimiento científico, la asistencia en terrenos, recursos, etc… Gracias por todo el aprendizaje y tu paciencia.

Debo además agradecer al Dr. Fernando Martínez por su gran contribución y ayuda durante esta tesis, particularmente el apoyo en la interpretación sísmica y en las discusiones de mi trabajo. Gracias Pana! Agradezco además a los funcionarios del Departamento de Geología (Maritza Acuña, Vero Carrasco, Blanca Baccola, Quilo, Rosita), y a todos los académicos que me formaron científicamente. Un especial saludo a Dr. Jacobus Le Roux.

Muchas gracias a mis amigos y compañeros de U, en particular a los insignes miembros del RAP: Sres. JA, SH, IG, PGMC, MP, IJP, JFR. Hay luz al final del túnel. También a Pelado, Yerkus, Moyra, Feña Soto con Andrew y Mark, Vale Z., Galle, Quiroga, Chino, Pablo S., Tommy, Vale F., Mari C., Ruso... A mis grandes amigos del Lab: Ataxia, Johnny, Kathy, Blitz. Gracias además a Sergio 'Warrior' Villagrán, Luis Acevedo y Marco Vaccaris, por toda la ayuda logística y la ayuda en esos intensos días en el desierto. Gracias a María José Hernández por tu contribución científica a este trabajo, y por la invitación a ser parte de tu comisión de tesis.

A mis amigos del colegio: Andy, Camilo, Daniel, Emilio, Javier, Juanjo, Juani, Lupe y Maurice. También a Pacita, Sofía, Patty, Camila, Vale y Cachi. Gracias totales a Fran y Nacha! Y gracias a Musta, Vane, Pauli y Fernando!

Agradezco además a mi familia, a quienes les dedico esta tesis: mis hermanos Alex y Jose junto con Marilú, Sofía y Lucas; Mom y Papá, mis tíos Isa, Jota, James, Patty y Pato. Mis primos Gigio, Pato, Caro (gracias Benja!), Ignatius, Flo, Santi, Alan, Andrés, Gabriel y Diego. Muchas gracias Pedro! Y gracias a Babo, María y los chicos por recibirme en D.C. más de una vez! Gracias a los Kausel, Gudi, Christian y familia por su infinito cariño y ánimo estos años.

No puedo olvidar a quienes ya no están. Mis abuelas Rina y Ellen, mi Tía Cheka, mi suegro Teo, mi tía Doris. Son pocos los días en que no pienso en ustedes.

Dedico este trabajo además a Leonie y Clara. Gracias por hacerme la persona más feliz del mundo todos los días. No podría haber sacado esto sin ti, mi amor. Gracias por tu luz! And thank you my cheeky little baby, for lighting up the whole world with your smile every day.

Finalmente, esta tesis está dedicada al Dr. César Arriagada. No estaría acá sin tu confianza en mí, sin tus enseñanzas, ni esa manera de ver la geología que nos enseñaste. Cada vez que vea un cerro me acordaré de tu fuerte risa, y de la pasión que sientes por la geología, la ciencia y el metal.

Esta tesis fue financiada en el marco de la Beca Doctoral CONICYT N°21150380. La Beca Asistencia a Eventos 2016 fue utilizada para asistir al congreso de la American Geophysical Union en 2016. Además, el trabajo fue apoyado por los FONDECYT 11170098, 1161806 y 3150160, y por el proyecto PIA/Anillo ACT172002.

Chapter 1 Contents

Figure Index

Table Index

Chapter 1 : Mountain building processes in the Central Andes, and their record within the Preandean Depression.

1.1.-General Background

The Andean Cordillera corresponds to the prime example of a non-collisional, accretionary orogen (Isacks, 1988; Cawood et al., 2009), and is the most relevant morphotectonic feature of the western margin of South America. The building of the orogen is intimately related to the subduction of an oceanic plate underneath the continent at least since the late Early Jurassic (Charrier et al., 2007; Ramos, 2009, 2010), although recent studies have shown that subduction could have been present along the margin as early as the Late Carboniferous (del Rey et al., 2016; Oliveros et al., 2020; Creixell et al., 2021). The kinematics and buoyance properties of this interaction have been linked to the occurrence of a series of compressional and extensional episodes along the margin (Charrier et al., 2009, 2007; Cobbold et al., 2007; Kay et al., 2005; Megard, 1984; Oliveros et al., 2006; Ramos, 2010, 2009, etc…) This variation in structural style has usually been ascribed to changes both in convergence velocity and convergence angle between both plates, and also their degree of coupling (Pardo-Casas and Molnar, 1987; Scheuber et al., 1994; Somoza and Ghidella, 2005; Seton et al., 2012; Bello-González et al., 2018; Horton, 2018). These conditions are thought to be enhanced by both the subduction of different anomalies present in the oceanic crust and the dip angle of the subducting slab, leading to flat-slab episodes, which have been suggested for different sections of the present-day margin (Gutscher, 2002; Ramos and Folguera, 2009; Ramos, 2010). These episodes have been identified in the geological record by the absence of volcanism and/or the migration and expansion of the magmatic arc, and the ubiquity of important crustal shortening due to strong plate coupling, as exemplified by the occurrence of broken forelands, basement-involved tectonics and basin inversion (James and Sacks, 1999; Ramos, 2009; Ramos and Folguera, 2009; Carrapa et al., 2010; Martínez et al., 2012, 2013, 2015, 2017b; Safipour et al., 2015). The interplay of these factors has been proposed as the main reason for the strong north-to-south variation in structural style and deformation seen in the Andean Orogen (Kley and Monaldi, 1998; James and Sacks, 1999; Ramos et al., 2004; Arriagada et al., 2008; Ramos, 2009, 2010).

Even though this general setting for the history of the orogen has been accepted and refined over the years, many doubts persist regarding the nature and duration of the different tectonic stages involved, and their contribution to the current orogen. Particularly, the contribution of pre-Neogene tectonics to the actual structure of the Andes is still a matter of debate (Garzione et al., 2008; Hoke and Garzione, 2008; Barnes and Ehlers, 2009), owing to multiple issues such as the scarcity and scatter of deposits belonging to some of these periods, the lack of detailed geochronology of the same units, and, also, the absence of high-detail studies regarding their stratigraphy and sedimentology. In essence, these issues, among others, preclude the establishing of a robust evolutionary scheme for the Andean Cordillera.

Part of the debate centers on the idea of a mainly Neogene building of the Andes, as observed in the Sub-Andean Zone and the Eastern Cordillera of Bolivia and Argentina (Isacks, 1988; Allmendinger et al., 1997; Kley, 1999; Garzione et al., 2008; Hoke and Garzione, 2008), against a more prolonged

state of compression, shortening and uplift, which would have started at ca. 100 Ma (Steinmann, 1929; Megard, 1984; Jaillard, 1992, 1993; Arriagada et al., 2006a; Cobbold et al., 2007; Amilibia et al., 2008; Tunik et al., 2010; Merino et al., 2013; Bascuñán et al., 2016; Boyce et al., 2020). This latter scenario would also show the presence of extensional events between compressive stages along the margin (Jordan et al., 2001; Charrier et al., 2002, 2007; Nyström et al., 2003; Muñoz et al., 2018a). A more precise analysis of the mid-Cretaceous to Oligocene history of the Andes is required in order to properly weigh the importance of the events affecting the margin, without neglecting the strong contrary effect produced by erosion.

Recent studies have shown that compressive conditions were predominant for most of the South American margin during the mid- to Late Cretaceous (Megard, 1984; McQuarrie et al., 2005b; Jaimes and de Freitas, 2006; Arriagada et al., 2006a; Cobbold et al., 2007; Tunik et al., 2010; Bascuñán et al., 2016; Boyce et al., 2020). The effects of this 'Peruvian Phase' (Steinmann, 1929) had been identified in various parts of the margin, but the analysis of U-Pb detrital zircon ages from synorogenic deposits has been instrumental in establishing a narrower timeframe for its evolution, as seen in the Neuquén and Salar de Atacama basins. The provenance and sedimentological studies performed in these basins also show that the sediments record the progressive, eastward migration of a foreland basin system (*sensu* DeCelles and Giles, 1996), where different parts of the margin where exhumed, eroded, and subsequently involved as components in the depositional systems.

This Peruvian Phase would in turn be superseded by the 'K-T' event (Cornejo et al., 1997, 2003; Somoza et al., 2012), which would have been responsible for the inversion of previous extensional, Jurassic and Early Cretaceous basins found in the Atacama region of northern Chile, such as the Lautaro and Chañarcillo basins (Martínez et al., 2012, 2013). Here, the published studies show the predominance of inversion tectonics related to previous normal faults (such as harpoon structures), highlighting the importance of structural inheritance in the area. The 'K-T' event has also been identified in the Cerros de Montecristo area, northwest of the city of Calama, based on paleomagnetic data by Somoza et al. (2012). This study shows that the Late Cretaceous rocks of the area were deformed prior to their intrusion by Paleocene rocks; the event was ascribed to the subduction of an oceanic ridge (Farallón-Phoenix boundary) based on plate reconstructions, or typical Andean compression.

The 'K-T' event would have been a short-lived event, after which the dominant condition would have been transtension (Charrier et al., 2009), which would have ended around the middle Eocene with the Incaic Orogeny. This stage shows widespread deformation, uplift and tectonic rotations along the Cordillera de Domeyko, leading to the development of the Incaic Cordillera (Charrier et al., 2009, 2013) and the beginning of uplift of the Puna-Altiplano Plateau (Maksaev and Zentilli, 1999; McQuarrie et al., 2005b; Scheuber et al., 2006). More significantly, this orogeny has been associated with the formation of the Bolivian Orocline, a first-order, subcontinental-scale feature, which is characterized by counter-clockwise and clockwise block rotations north and south of the Arica Bend (ca. 20°S) respectively, and major crustal shortening in the Eastern Cordillera (Arriagada et al., 2008, 2003; McQuarrie, 2002; Roperch et al., 2011, and references therein).

The Incaic Orogeny has been linked to an episode of flat-slab subduction in northern Chile and southern Peru (15-25°S), between 35-25 Ma (James and Sacks, 1999; O'Driscoll et al., 2012), which would be caused by a combination of cratonic root-suction mechanisms and the subduction of an oceanic plateau (a conjugate of the Manihiki Plateau). The north-to-south flattening of the slab would have led to the eastward displacement of the volcanic arc and a magmatic lull in the area over the flat slab, which would have been reinstated during its steepening in the Oligocene (James and Sacks, 1999; Mamani et al., 2010; O'Driscoll et al., 2012). This flat-slab period is also associated with a significant decrease in convergence velocities, and a progressive clockwise rotation of the convergence angle (Somoza and Ghidella, 2005; Barnes and Ehlers, 2009).

According to different margin reconstructions, the characteristic geometry of the Arica Bend seen nowadays was practically finished by the end of the flat-slab episode (McQuarrie, 2002a; Arriagada et al., 2008; Barnes and Ehlers, 2009; O'Driscoll et al., 2012). The end of the event also coincides with the acceleration of convergence rate to its highest values (around 12-13,9 cm/y) during the Cenozoic (Somoza and Ghidella, 2005). However, most of the bend was formed prior to 35 Ma, and in that regard, the timing between the flat slab subduction process and the forming of the bend seems inconsistent.

During the Eocene-Oligocene, the evidence collected so far along the subcontinent shows the occurrence of different, and at times contrasting processes, which vary drastically along the latitude of the margin. Most of the documented evidence for south-central Chile point to extensional processes which led to the formation of the Abanico Basin, an intra-arc basin showing the deposition of more than 3000 m of volcanic and volcano-sedimentary rocks (Charrier et al., 2002, 2007; Nyström et al., 2003; Fock et al., 2005). A similar setting has been proposed for the Cura-Mallín Basin and the Loncopué Trough in south-central Chile and Argentina (Folguera et al., 2010; Radic, 2010; Rojas Vera et al., 2014). More evidence for an extensional setting has been collected from some of the basins along the Cordillera de Domeyko in northern Chile, in the Antofagasta Region (see below). These episodes would have been triggered by an increase in convergence rates along the margin, along with a more orthogonal convergence (Jordan et al., 2001). The events described would have come to an end during the Miocene, due to the Pehuenche-Quechua Orogenies (Salfity et al., 1984; Yrigoyen, 1993; Charrier et al., 2007), showing the inversion of previous basins and establishing the structural configuration of the margin for the Neogene (Giambiagi et al., 2001; Farías et al., 2005, 2008, 2010; Vicente, 2005; Charrier et al., 2009; Ramos, 2009; Rojas Vera et al., 2014; Tapia et al., 2015; Becerra et al., 2017).

However, several key studies in areas northeast of the Antofagasta Region point to an opposite structural setting for the Oligocene-early Miocene. In the Eastern Cordillera of southern Bolivia, the Oligocene-upper Miocene deposits belonging to the Tupiza Basin show that they were deposited on top of a wedge-top zone belonging to an eastward-migrating foreland basin system (Horton, 1998). Elger et al. (2005), based on the analysis of seismic, gravimetric and geochronological data show the presence of an extensional event during the Eocene/earliest Oligocene in the southern Altiplano, which would have been inverted during the Oligocene-late Miocene. The authors argue for a self-organized style of deformation, in contrast to a more continuous migration of the deformation front, as that observed in the Eastern Cordillera of northwestern Argentina (Decelles et al., 2011; Siks and

Horton, 2011; Carrapa et al., 2012; Carrapa and DeCelles, 2015), which was stated based on U-Pb detrital zircon ages, provenance and sedimentological analyses. Independently, Scheuber et al (2006) proposed synchronous extension and compression between 32-19 Ma in the Altiplano and Eastern Cordillera, respectively, probably influenced by hydration of the lithospheric mantle in the upper plate, which would lead to variations in the degree of plate coupling. Regardless of the mechanism involved, an argument can be made for substantial deformation of the margin and eastward propagation of this deformational front at these latitudes.

Further evidence for compressive events around the area can be found in northernmost Chile, where Charrier et al. (2013) showed that there is no significant extensional event for the Precordillera and western Altiplano between 18°-19°S. Instead, the tectonostratigraphic evolution of the area is more consistent with the development of a retroarc foreland basin in the Altiplano area during the late Eocene-Oligocene, and the development of the West- and East-verging Thrust Systems during the late Oligocene-early Miocene. The first system generated a significant amount of uplift (0.1 mm/yr) at the western side of the Altiplano, between 26-8 Ma (Farías et al., 2005; Nester and Jordan, 2012). The Andean Plateau in Peru also presents evidence of contractional faults affecting late Oligocene and early Miocene sediments of the Moquegua Group, which underwent extensional deformation later (Schildgen et al., 2009).

It can be seen from the summary above that the Andean Margin presents important vacuums in its evolutionary history, which have led to contrasting interpretations of its evolution. In this regard, the analysis of long-lived basins can be paramount to unraveling a more continuous and valid interpretation of the different events affecting western South America. It is proposed here that one of these places can be found in the Preandean Depression of northern Chile, specifically in the Salar de Atacama Basin, given its long-lived record of sedimentation and deformation.

1.2.-Tectonics and structure of the Preandean Depression between 22°-24°S

A key place to study the aforementioned tectonic events is the Salar de Atacama Basin, the northernmost and largest basin of the Preandean Depression in the Antofagasta Region of northern Chile (Figure 1.1). Here, the oldest successions found correspond to Paleozoic-Triassic units cropping out around the borders of the basin, displaying some of the oldest rocks found in northern Chile (Raczynski, 1963; Ramírez and Gardeweg, 1982; Marinovic and Lahsen, 1984; Niemeyer, 1989, 2013; Zimmermann et al., 2009; Basso and Mpodozis, 2012; Becerra et al., 2014; Henríquez et al., 2014; Narea et al., 2015). The absence of Jurassic outcrops points to an important gap in the sedimentary record, which continues with the deposits of the Purilactis Group (*sensu* Mpodozis et al., 2005). This group shows the deposition of ca. 6 km of terrigenous, continental deposits, ascribed mainly to braided rivers and ephemeral sheet floods, combined with minor lacustrine, evaporitic and aeolian deposits (Hartley et al., 1988, 1992; Charrier and Reutter, 1990, 1994; Flint et al., 1993; Arriagada, 1999; Mpodozis et al., 2005; Bascuñán et al., 2016). Although many different interpretations have been proposed regarding its age and the tectonic conditions dominant during its deposition, recent studies have established that the Purilactis Group was deposited in the foredeep zone of a foreland basin (*sensu* DeCelles and Giles, 1996), developed during the Late Cretaceous-Paleogene (Arriagada et al., 2006a; Bascuñán et al., 2016).

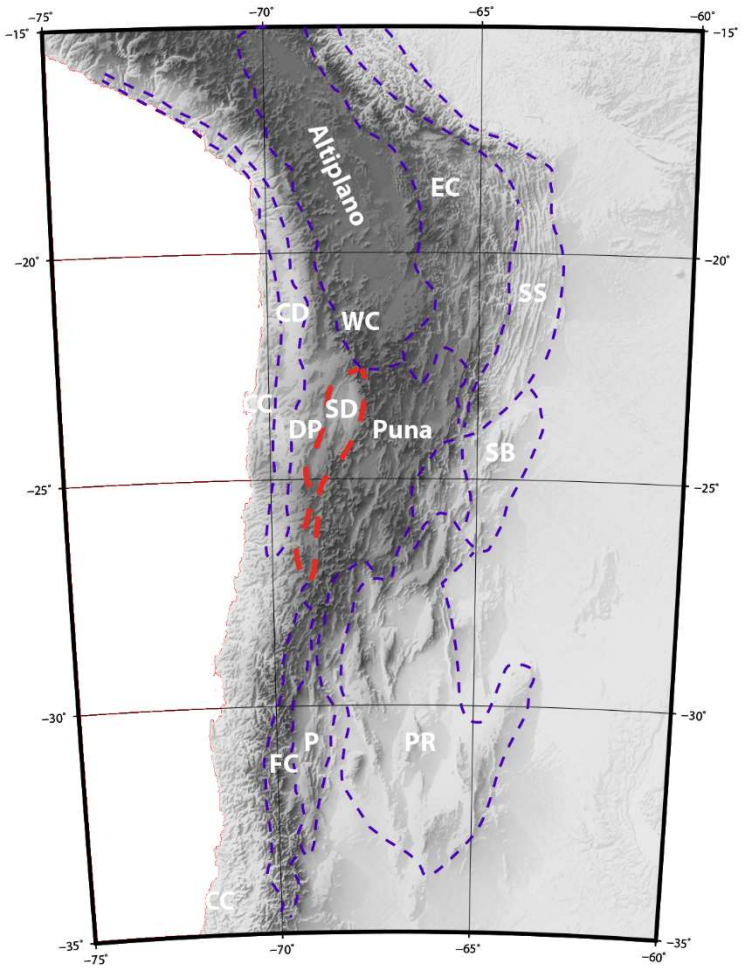

Figure 1.1: Digital Elevation Model (DEM) of the Central Andes between 16°-35°S, showing the main morphostructural features of the orogen. Red dashed line indicates the Preandean Depression (SD). Other abbreviations correspond to: PR, Pampean Ranges; FC, Frontal Cordillera; P, Precordillera in Argentina; CC, Coastal Cordillera; DR, Domeyko Range; SB, Santa Barbara System; SS, Subandean System; EC, Eastern Cordillera; FP, Forearc Precordillera; CD, Central Depression. Modified from Charrier et al. (2007).

The sediments of this group record the progressive exhumation and erosion of different components of the South American margin, due to the eastward migration of the deformation front during the Peruvian Phase (Figure 1.2a, b). The provenance analysis of these deposits shows an increasing presence upwards of crystalline, granitoid clasts, associated with deep exhumation of basement units found in the Cordillera de Domeyko, and an overall trend towards younger maximum depositional ages as recorded in the detrital zircon analysis. These age populations were correlated with two stages in the Peruvian Phase: an "early" phase, starting at ca. 107 Ma, and a "late" phase, starting at ca. 79 Ma, which would have lasted until the K-T boundary. However, new U-Pb detrital zircon ages show that some of the formations previously thought to be Late Cretaceous in age were younger (post 65 Ma). This implies that these units overlap temporally with younger volcanic and clastic deposits assigned to the Cerro Totola and Naranja formations, which are thought to have been deposited as a result of the 'K-T' event (Mpodozis et al., 2005), thus further blurring the

stratigraphic record and extending the time window in which sedimentation of the units belonging to the Purilactis Group took place.

Also, though Somoza et al. (2012) found evidence of the 'K-T' event west of the Salar de Atacama Basin, its identification in the basin itself is based on the correlation of a regional unconformity and the Naranja Formation, which lies above it, with dated units (K-Ar whole rock) found 70 km south of the basin (Gardeweg et al., 1994; Mpodozis et al., 2005). This raises questions about the longitudinal validity of this correlation, as well as about the relation of the Naranja Formation with the formations comprising the Purilactis Group. What is, then, the factual impact of the 'K-T' event on the Salar de Atacama Basin?

Regarding the basal units of the Purilactis Group, the samples obtained from the Tonel Formation, which are thought to signal the inception of the Peruvian Phase, actually belong to units situated west of the basin (see Figure 2 *in* Bascuñán et al., 2016), which show maximum depositional ages in the Late Jurassic; it is possible that the sedimentary dynamics of these deposits had no relation to the units found inside the basin, thus rendering the correlation questionable.

More direct evidence for widespread deformation in the basin can be found for the Eocene, during the Incaic Event (Figure 1.2c), which was also responsible for clockwise rotations of pre-Eocene units and the deposition of the synorogenic Loma Amarilla Formation, dated by Ar-Ar dating at 43,8±0,5 Ma and 42,2±0,9 Ma (Hammerschmidt et al., 1992; Arriagada et al., 2000, 2006a, 2006b, 2008; Mpodozis et al., 2005; Basso and Mpodozis, 2012). These strong effects, along with important uplift along the Cordillera de Domeyko area (Maksaev and Zentilli, 1999; Sánchez et al., 2018; Henríquez et al., 2019), point to a possible migration of the wedge-top area to this zone, but more precise data is needed to constrain it both temporally and locally. A closer inspection of the deformation within the basin and its effects may help to clarify its origin and its relation to the evolution of the Cordillera de Domeyko area.

It is thus relevant to inquire about the beginning, duration and ending of the events that formed the foreland basin, its evolution and migration during the Paleogene, and the episodic or continuous nature of the compressional event(s).

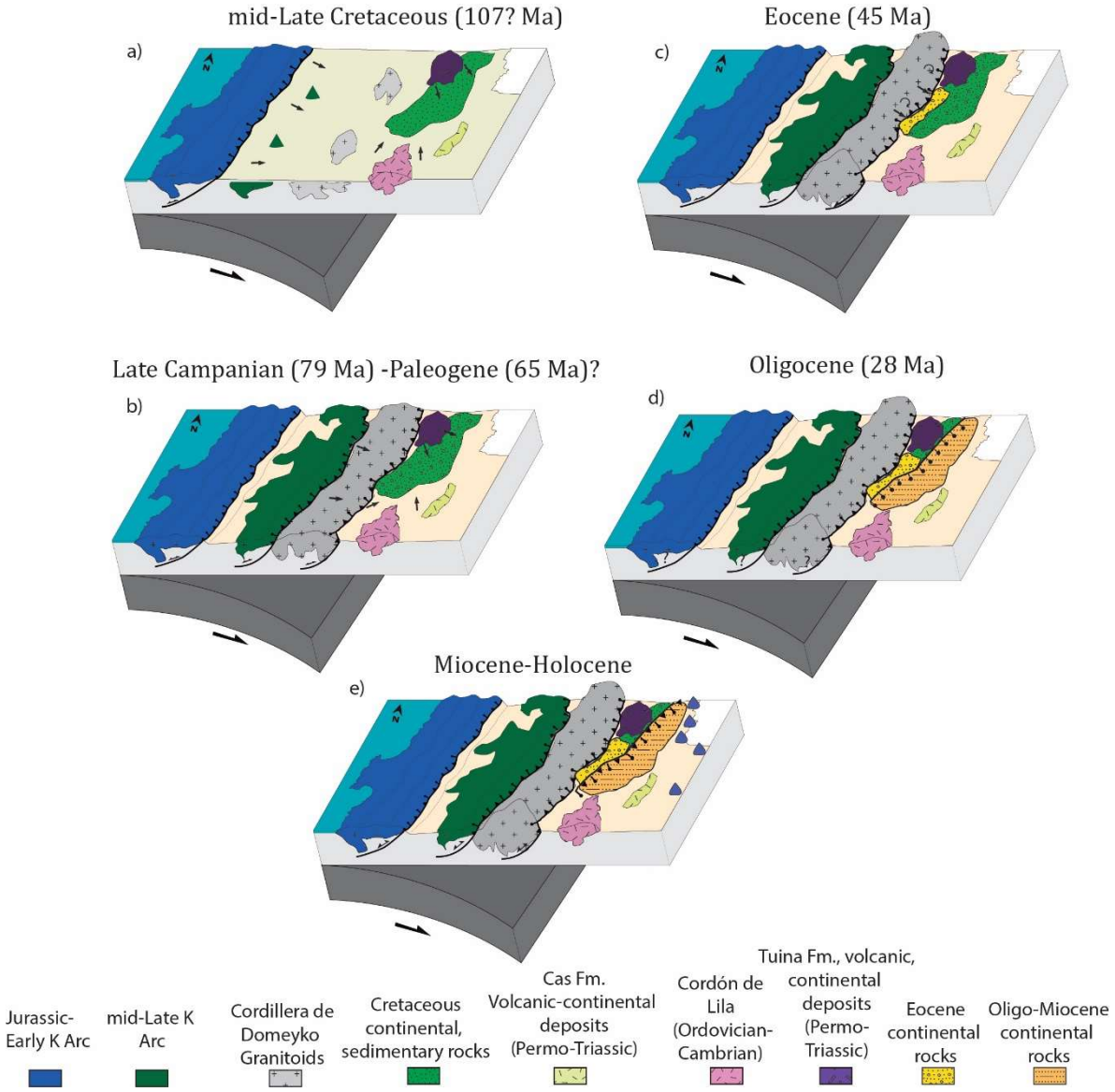

Figure 1.2: Schematic paleogeographic evolution of the Central Andes in northern Chile between 22°-24°S. Coastline corresponds to its present-day outline. Modified from Bascuñán et al. (2016), Pananont et al. (2004), Jordan et al. (2007) and Rubilar et al. (2017).

The Salar de Atacama Basin also holds Oligocene-Miocene continental deposits, such as the Tambores and San Pedro Formations (Figure 1.2d), which are grouped within the Paciencia Group (Brüggen, 1934, 1942, 1950; Travisany, 1978; Flint, 1985; Wilkes and Görler, 1994). According to U-Pb datings performed by Becerra et al. (2014) and Henríquez et al. (2014), together with K-Ar datings (biotite) by Mpodozis et al. (2000) and extensive regional mapping by the same authors, the San Pedro Formation is essentially late Oligocene-early Miocene in age (between 26,8 and 17 Ma). These terrigenous and evaporitic, units, which have been attributed to both compressional and extensional events owing to varying interpretations of seismic sections (Wilkes and Görler, 1994; Pananont et al., 2004; Arriagada et al., 2006a; Jordan et al., 2007; Rubilar, 2015; Rubilar et al., 2017), can be found extensively both along the basin and its subsurface, showing strong evidence

for their deformation possibly during the late Miocene. Similar deposits (regarding depositional age and sedimentology) have been found northwest of the Salar de Atacama in the Calama Basin, where they would have been deposited in an extensional event with some degree of transtensional deformation (El Loa Group; Blanco, 2008). Another basin nearby with a similar transtensional setting is the Papajoy Basin (Tomlinson et al., 2001; Jordan et al., 2007), found farther north. However, this situation contrasts with the setting proposed for the Pampa del Tamarugal Basin and the western side of the Altiplano (see above), between 18-22°S (Farías et al., 2005; Nester and Jordan, 2012), or the neighboring Salar de Punta Negra Basin (Martínez et al., 2017a, 2018).

Considering the different lines of evidence that point to the existence of a north-south variation in tectonic settings along the South American margin, or at least inconsistencies regarding its evolution, what are the defining characteristics of the units deposited during that time in the Cordillera de Domeyko area of northern Chile? How can these deposits be reconciled with the plate geodynamics during the Oligocene-early Miocene? And, also, do these processes have any link to the previous orogeny?

Due to its characteristic location, the Salar de Atacama Basin has been the subject of a wide variety of geophysical studies, starting with seismic prospection by the Empresa Nacional del Petróleo (ENAP) during the 1980's and early 1990's, along with the drilling of a 5400 m-deep exploratory well, named Toconao-1. These seismic lines have been used extensively in the last 30 years, leading to different interpretations regarding the stratigraphy and structural interpretation of the subsurface of the basin (e.g.,Arriagada et al., 2006a; Jordan et al., 2007; Macellari et al., 1991; Muñoz et al., 2002; Pananont et al., 2004; Reutter et al., 2006; Rubilar et al., 2017). These multiple explanations have arisen mainly due to different interpretations of the stratigraphy of the Toconao-1 well, which has no definite constraints regarding the age of its sequences, save for an Apatite Fission Track analysis by Muñoz et al. (2002). This uncertainty regarding its chronostratigraphy may be the foremost hindrance to the correlation of the well with the units cropping out along the El Bordo Escarpment and elsewhere in the basin.

During seismic prospection, ENAP also took gravity measurements which were then compiled and analyzed by Götze & Krause (2002). The isostatic residual gravity field shows that the Salar de Atacama Basin overlies an approximately NW-trending gravity high called the Central Andean Gravity High (CAGH), which would occupy the same position as the Cambrian-Ordovician magmatic arc and would be found at depths of ca. 10-38 km. These dense rocks, along with their possibly ultrabasic roots, would have influenced the later structural evolution of the area. Independently, Yuan et al.(2002) reached to the conclusion that the lithosphere under the basin was cold and dynamically subsided, thus explaining the relation between the topographic low (which is 1 km below isostatic equilibrium) and the thickened crust (ca. 67 km). Schurr and Rietbrock (2004), after analyzing seismic tomography data, also show the presence of a cold, rheologically strong block that can be detected down to depths of 85 km. The cold block would also have a role in keeping the flow of the asthenosphere to the east of the basin, resulting in the displacement of the magmatic arc. Additionally, they posit that the lithospheric and seismic properties of the basin are at odds with significant extensional episodes, instead arguing for both compressional deformation focused on the edges of the basin and coupling of the root with the basin to explain the overall

subsidence of the basin. Reutter et al. (2006), contrasting with previous authors, proposed that this anomaly was formed due to rift tectonics associated with the Salta Rift System, where basic material derived from the mantle rose upwards and was added at different crustal levels, from the Cretaceous up until the Eocene. Important cooling of this block would have only started after the ending of the flat-slab event.

Although the anomaly underneath the Salar de Atacama Basin, whatever its nature and origin, has been emphasized as the reason behind the subsidence of the basin and the displacement of the magmatic arc, its relation to the tectonic history of the basin is still not clear. More so, the existence of this block does not readily explain the N-S disposition of the saltpans found in the Preandean Depression (SERNAGEOMIN, 2003), nor does it fully account for the possible extensional episode proposed for the Oligocene.

1.3.-Work Hypotheses

Both the regional and local geology around the Salar de Atacama Basin presented above show that the margin has significant gaps regarding its tectonic history. Even if a broad tectonic evolution can indeed be sketched from the present data (Figure 1.2 & Figure 1.3), the effective "steps" or transition from one stage to another, and the mechanisms behind these changes, remain elusive. Also, though the current understanding of the tectonic evolution of western South America usually adheres to a step-wise history of the orogen, partly due to gaps in the geological record, an argument can also be made for a more continuous progression, as posited by Noblet et al. (1996), and shown by other authors as the migration of a flexural wave eastwards (Figure 1.3; Carrapa and DeCelles, 2015; DeCelles et al., 2015). The testing of these different hypotheses may shed more light on the evolution of the margin.

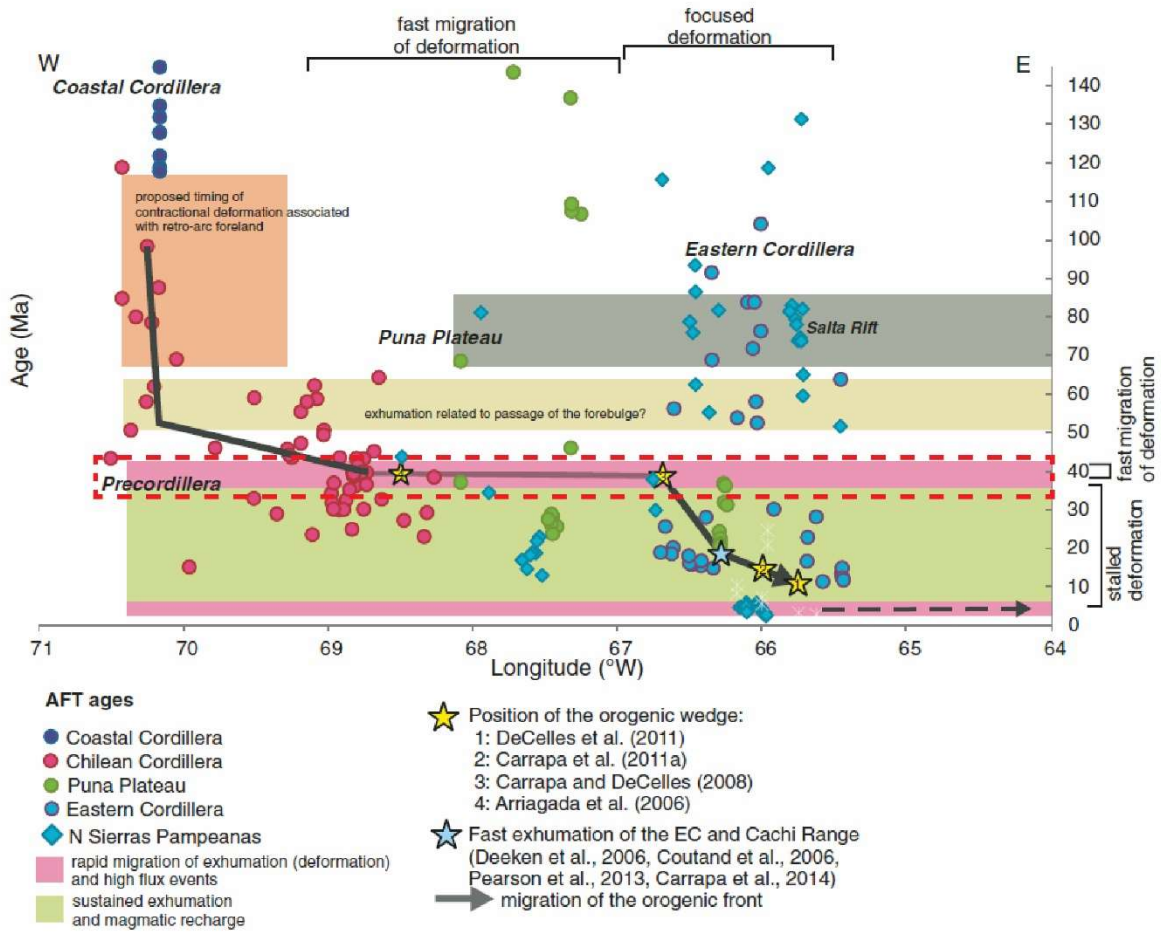

Figure 1.3: Evolution of exhumation based on apatite fission track data. Yellow star indicates the position of the orogenic wedge in northern Chile until the Incaic Event, and its fast migration towards the Eastern Cordillera. Red dashed line also indicates the event in the chart. Modified from Carrapa & DeCelles (2015).

Although the identification of the Salar de Atacama Basin as a foreland basin system during the mid- to Late Cretaceous is congruent with the tectonic history of the Central Andes, the studies so far have not been conclusive regarding its migration and/or termination during the Cenozoic, and its incorporation into the hinterland and forearc. The basin could have either evolved as some of the foreland basin systems seen in Argentina due west (see above), or it could have terminated abruptly, possibly due to "breaking" of the basin (e.g., Montero-López et al., 2018). Clearing this issue will give new insights into the evolution of foreland basin systems, which may be used for studying other recently identified foreland deposits (i.e., Boyce et al., 2020; Merino et al., 2013).

As shown above, most of the tectonic history of the Central Andes has been explained in terms of varying phases of compression and extension, which are correlated with changes in plate dynamics and local characteristics of the subducting plate. Given the demonstrably long-lasting geological record within the Salar de Atacama Basin, it stands to reason that these phases should be more or less present within the basin. Identifying these 'events', ascribing them an age and comparing them

with the history of the Andean Orogen might shed light on the processes behind their occurrence, and to evaluate the different mechanisms proposed for their building (e.g., DeCelles et al., 2015; Gianni et al., 2015; Horton, 2018; Ramos, 2010; Ramos and Folguera, 2009)

All things considered, the main hypothesis behind this thesis is that the Salar de Atacama Basin holds an almost complete record of the tectonic events that have affected the margin since the mid-Late Cretaceous, linked to the eastward migration of a foreland basin system, until the incorporation of the area to the orogenic wedge during the late Eocene-early Oligocene. This system, at first in a back-arc position, shows the progressive addition of different geological units of the actual forearc (Coastal Cordillera, western and eastern Precordillera, corresponding magmatic arcs, Figure 1.1 & Figure 1.2) until the incorporation of the basin within the forearc. The later stages of this hinterland basin (late Oligocene onwards) show the deposition in slightly compressive-quiescent conditions, until another stage of deformation during the late Miocene (Figure 1.2e), which would lead to the final structure of the basin.

A secondary, related hypothesis is that the Salar de Atacama Basin constitutes a natural laboratory (see Jordan et al., 1982), in which the different tectonic events and geodynamic changes proposed for the Central Andes can be studied, in order to assess their feasibility and compatibility with the geological record.

1.4.-Objectives

The general goal of this thesis is to understand the link between the tectonic processes that occurred in the Central Andes of northern Chile during the late Mesozoic-Cenozoic, and their contribution to the building of the Andean Orogen.

The specific goals of this thesis are to:

- Determine the characteristics and chronology of the events that affected the South American margin present in the Salar de Atacama Basin.
- Relate the processes recorded in the basin with those occurring in nearby basins and the Preandean Depression
- Understand the link between the formation of the Preandean Depression and that of the Central Andes of northern Chile.

1.5.-Chapter Description

Chapter 2 presents the analysis of a cross section between the Cerros de Tuina area and the western limit of the Western Cordillera, which includes gravimetric stations, 2-D velocity data, seismic reflection profiles and U-Pb data, thus allowing for the understanding of the structural evolution of the area and its subsurface configuration. An update on the chronostratigraphy of the Upper Cretaceous-Paleogene units is also shown.

Chapter 3 presents an analysis of two gravimetric surveys encompassing the eastern border of Cordillera de Domeyko and the Salar de Atacama Basin. These surveys are also complemented with seismic reflection data and the results of a magnetic survey performed by the INSUD Group of the Departamento de Geofísica of the Universidad de Chile. The integration of the data reveals the often-overlooked interaction of the crystalline, Paleozoic and Paleogene units within the Cordillera de Domeyko and the continental, mainly sedimentary units within the basin.

Chapter 4 shows the results of the analysis of six additional U-Pb detrital zircon samples, taken from units belonging to the Upper Cretaceous-Paleogene successions of the basin, which have been historically classified within the Purilactis Group and Naranja Formations.

Chapter 5 presents a discussion of the main findings within this doctoral thesis, together with an analysis of the various stages proposed for the evolution of the basin and the Central Andes.

Finally, Chapter 6 presents the conclusions and suggested future work for the area.

Chapter 2 : Geometry and late Mesozoic-Cenozoic evolution of the Salar de Atacama Basin (22°30'-24°30'S) in the northern Central Andes: New constraints from geophysical, geochronological and field data.

Published in: *Bascuñán S., Maksymowicz, A., Martínez, F., Becerra, J., Arriagada, C., & Deckart, K. 2019. Geometry and late Mesozoic-Cenozoic evolution of the Salar de Atacama Basin (22°30'-24°30'S) in the northern Central Andes: New constraints from geophysical, geochronological and field data. Tectonophysics 759, 58-78.*

Tectonophysics 759 (2019) 58–78

Contents lists available at ScienceDirect

Tectonophysics

journal homepage: www.elsevier.com/locate/tecto

Geometry and late Mesozoic-Cenozoic evolution of the Salar de Atacama Basin (22°30′-24°30′S) in the northern Central Andes: New constraints from geophysical, geochronological and field data

Sebastián Bascuñán[a,*], Andrei Maksymowicz[b], Fernando Martínez[c], Juan Becerra[d], César Arriagada, Katja Deckart[a,e]

[a] Departamento de Geología, Facultad de Ciencias Físicas y Matemáticas, Universidad de Chile, Plaza Ercilla 803, Santiago, Chile
[b] Departamento de Geofísica, Facultad de Ciencias Físicas y Matemáticas, Universidad de Chile, Blanco Encalada 2002, Santiago, Chile
[c] Departamento de Geología, Universidad Católica del Norte, Angamos 0610, Antofagasta, Chile
[d] SQM Salar S.A., El Trovador 4285, Las Condes, Santiago, Chile
[e] Advanced Mining Technology Center, FCFM, Universidad de Chile, Av. Tupper 2007, Santiago, Chile

ARTICLE INFO

Keywords:
Gravimetry
Seismic profiles
Geochronology
Compression
Andes
Salar de Atacama

ABSTRACT

The late Mesozoic-Cenozoic evolution of the Central Andes of northern Chile consists of a series of events related to changing conditions along the plate margin, leading to different episodes of compression and extension. A long-lasting basin which records these changes corresponds to the Salar de Atacama Basin. Its tectonic history has been blurred by several interpretations of seismic reflection lines and multiple chronostratigraphic correlations between subsurface-surface units. As such, many aspects of its tectonic evolution are still unclear. In this study, we performed an E-W gravimetric profile across the Barros Arana Syncline and the basin. We analyzed interval velocities obtained from seismic reflection studies and reviewed the profiles closest to the gravity survey. Four U-Pb samples for detrital zircon analysis were obtained from Late Cretaceous-Paleogene units. Geophysical data show a segmentation of physical properties within the basin, with denser units and faster interval velocities around the late Mesozoic-early Cenozoic units, and lighter, slower units in the actual salt pan. The main contrast in physical properties is observed in the evaporitic and fine-grained continental deposits of the San Pedro Formation. Geophysical and geological constraints show that its thickness varies between 800 and 1200 m, and that it was deformed during later events. The U-Pb data show that the rocks within the Barros Arana Syncline reach well into the Paleogene, and that they were mainly deformed during the late Eocene Incaic Event, where an east-verging thrust system also involving Permo-Triassic units was developed, establishing the actual structural configuration. The late Oligocene-early Miocene units were then deposited in a post-orogenic setting, with minor compression. A stronger phase around the late Miocene reactivated previous structures and folded these deposits. This continuous, compressive history of the basin, which is mostly a result of the Incaic Event, is in agreement with the regional evolution of the Central Andes.

1. Introduction

The Central Andes of northern Chile (Fig. 1; Gansser, 1973; Ramos, 2010, 2009) constitute a prime interest zone for the understanding of the building of the Andean Cordillera. Its evolution has been marked by different stages of arc-parallel extension and compression related to subduction dynamics, of which some have been identified independently along different areas of the Central Andes (e.g., Charrier et al., 2009, 2007; Cobbold et al., 2007; Kay et al., 2005; Martínez et al., 2013, 2012; Megard, 1984; Noblet et al., 1996; Ramos, 2010, 2009; Sempere, 1995). The understanding of these events and their relation to one another is crucial to unraveling the tectonic history of the South American margin.

A key location for studying the evolution and configuration of the Andean Orogen is the Salar de Atacama Basin, in the Preandean Depression (Fig. 1). The basin presents a remarkable exposition of Paleozoic to Cenozoic outcrops recording much of the geological history of northern Chile (Figs. 2 & 3), along with multiple seismic lines and a 5425-m deep well (Toconao-1) obtained by the Empresa Nacional del Petroleo (ENAP), which has led to many studies regarding its structure,

* Corresponding author.
E-mail address: sebascun@ing.uchile.cl (S. Bascuñán).

https://doi.org/10.1016/j.tecto.2019.04.008
Received 31 July 2018; Received in revised form 7 March 2019; Accepted 7 April 2019
Available online 12 April 2019
0040-1951/

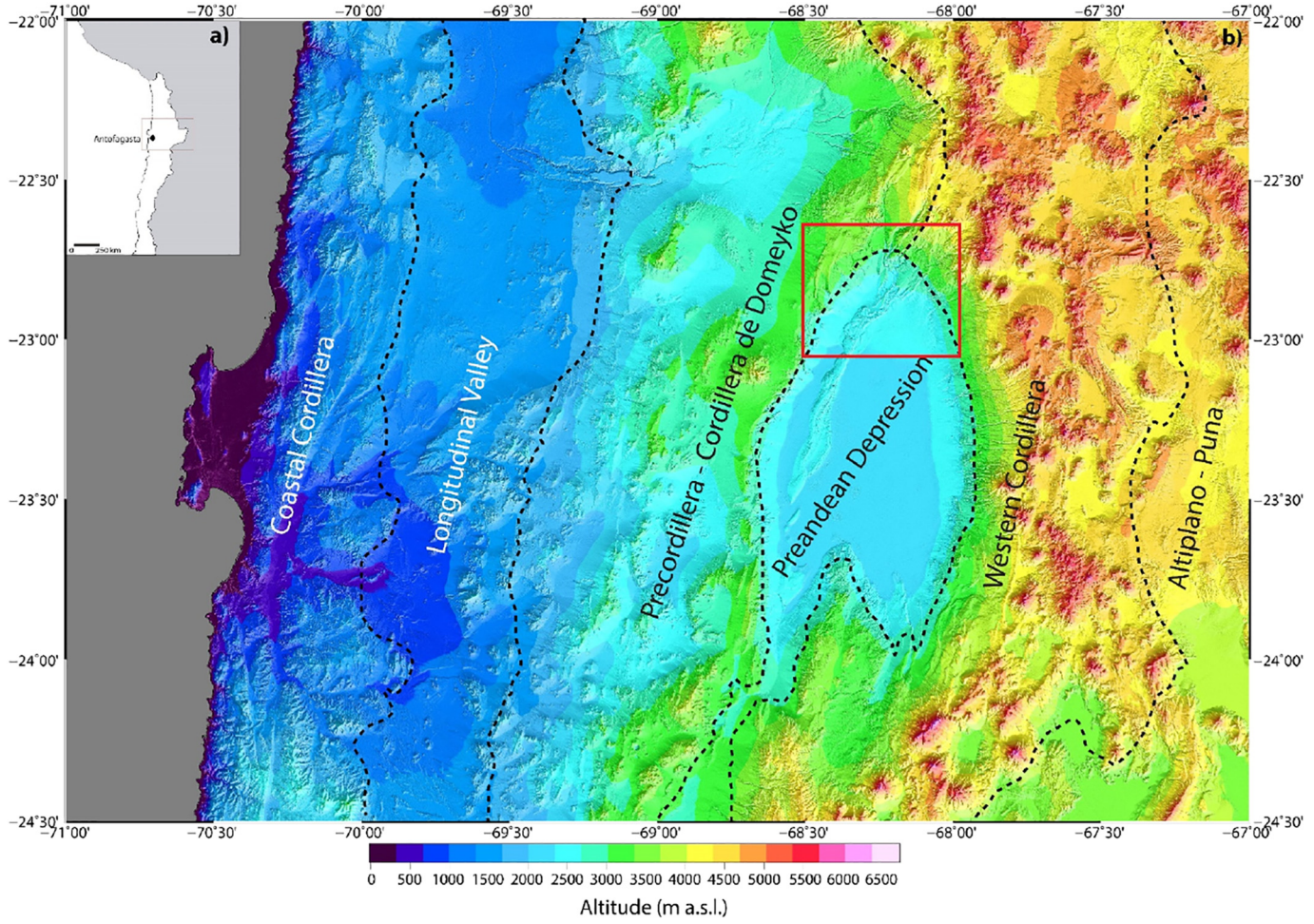

Fig. 1. a) Inset showing the location of the study area in northern Chile. b) Morphostructural segmentation of the Central Andes between 22°-24°30'S, following Amilibia et al. (2008) and Charrier et al. (2013). Red rectangle corresponds to the study area. (For interpretation of the references to colour in this figure legend, the reader is referred to the web version of this article.)

geochronology and stratigraphy (e.g., Arriagada et al., 2006a; Bascuñán et al., 2016; Brüggen, 1950, 1942, 1934; Charrier and Muñoz, 1994; Charrier and Reutter, 1994, 1990; Dingman, 1967, 1963; Flint et al., 1993; Hartley et al., 1992a, 1988; Jordan et al., 2007, 2002; Macellari et al., 1991; Mpodozis et al., 2005; Naranjo et al., 1994; Pananont et al., 2004; Reutter et al., 2006; Rubilar et al., 2017). However, in spite of the growing amount of knowledge obtained over the last 30 years, many questions remain regarding the tectonic conditions during the late Mesozoic-Cenozoic, and the transition between different compressive deformation events, such as the Peruvian Phase (around 100–70 Ma; Cobbold et al., 2007; Fildani et al., 2003; Jaillard, 1993, 1992; Jaimes and de Freitas, 2006; Steinmann, 1929), the KT Event (around 65 Ma; Cornejo et al., 2003, 1993; Somoza et al., 2012) and the Incaic Event (ca. 45–32 Ma; Arriagada et al., 2008; Bosio et al., 2009; Payrola et al., 2009; Charrier et al., 2009; Del Papa et al., 2013; Hongn et al., 2007; Montero-López et al., 2018; O'Driscoll et al., 2012; Steinmann, 1929). Some authors have argued for an evolution under mostly compressive conditions since ca. 90 Ma (Arriagada et al., 2006a), while others suggest an important post-orogenic extensional event for the late Oligocene-early Miocene interval, which provoked localized mechanical subsidence of the basin (Fig. 4; Flint et al., 1993; Jordan et al., 2007; Pananont et al., 2004; Rubilar et al., 2017). Part of this discrepancy arises from opposite interpretations of seismic lines, the complex stratigraphy of the Toconao-1 well, and the multiple chronostratigraphic proposals for the units cropping out in the El Bordo Escarpment (Fig. 2). The lack of additional independent constraints has been thus detrimental to the final evaluation of the seismic lines, the understanding of basin geometry, and to the establishment of a clear regional evolution.

In this work, we performed a gravimetry survey along an E-W profile involving the actual salt pan and the late Mesozoic-Cenozoic synorogenic deposits, together with an analysis of interval velocities and a reexamination of previous seismic reflection profiles (Fig. 2). We also analyze four U/Pb detrital zircon samples in order to provide a more concise time frame for the structural evolution of the basin. This combination of data allows us to clarify the tectonic setting since the Late Cretaceous, and to propose a congruent model involving the events found both in the basin and around the northern Central Andes.

2. Geological setting

The Salar de Atacama Basin is an intramontane basin located between 22°30′-24°30′S, west of the magmatic arc and east of the Cordillera de Domeyko (Figs. 1 & 2), which consists of Paleozoic to Mesozoic rocks bounded by doubly verging, high-angle reverse faults (Amilibia et al., 2008; Breitkreuz and Van Schmus, 1996). The Cordillera de Domeyko is interpreted to have been a prominent part of the Andean orogenic front between the Late Cretaceous and the Eocene (Arriagada et al., 2006a; Bascuñán et al., 2016; Charrier et al., 2009; Maksaev and Zentilli, 1999). An abrupt topographic change towards the east of this range (El Bordo Escarpment) delineates the border between the Salar de Atacama Basin and the Cordillera de Domeyko (Fig. 2). The

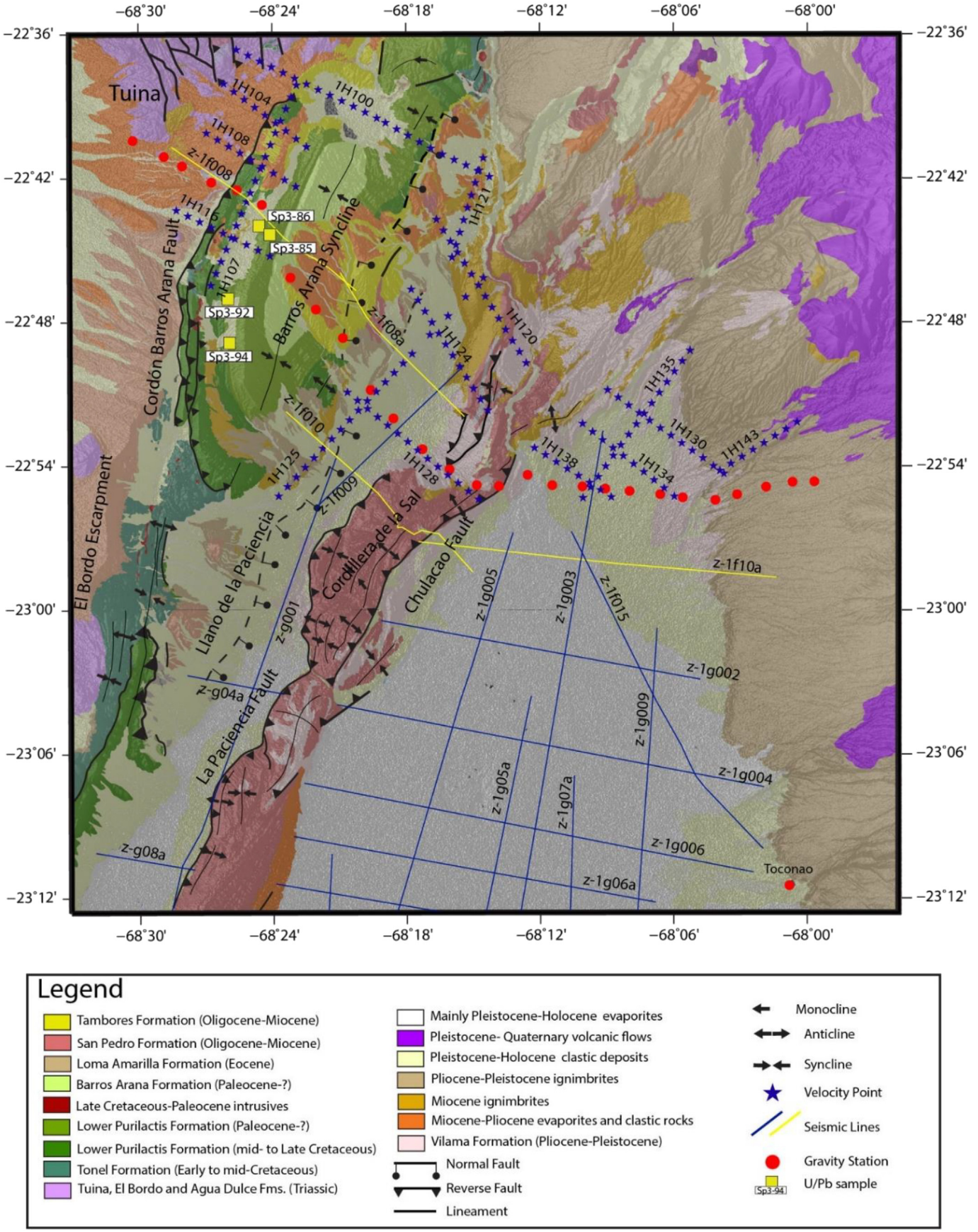

Fig. 2. Geological map, modified from Ramírez and Gardeweg (1982), Marinovic and Lahsen (1984), Basso and Mpodozis (2012), Becerra et al. (2014), Henríquez et al. (2014). Yellow seismic lines correspond to those reviewed in this study. (For interpretation of the references to colour in this figure legend, the reader is referred to the web version of this article.)

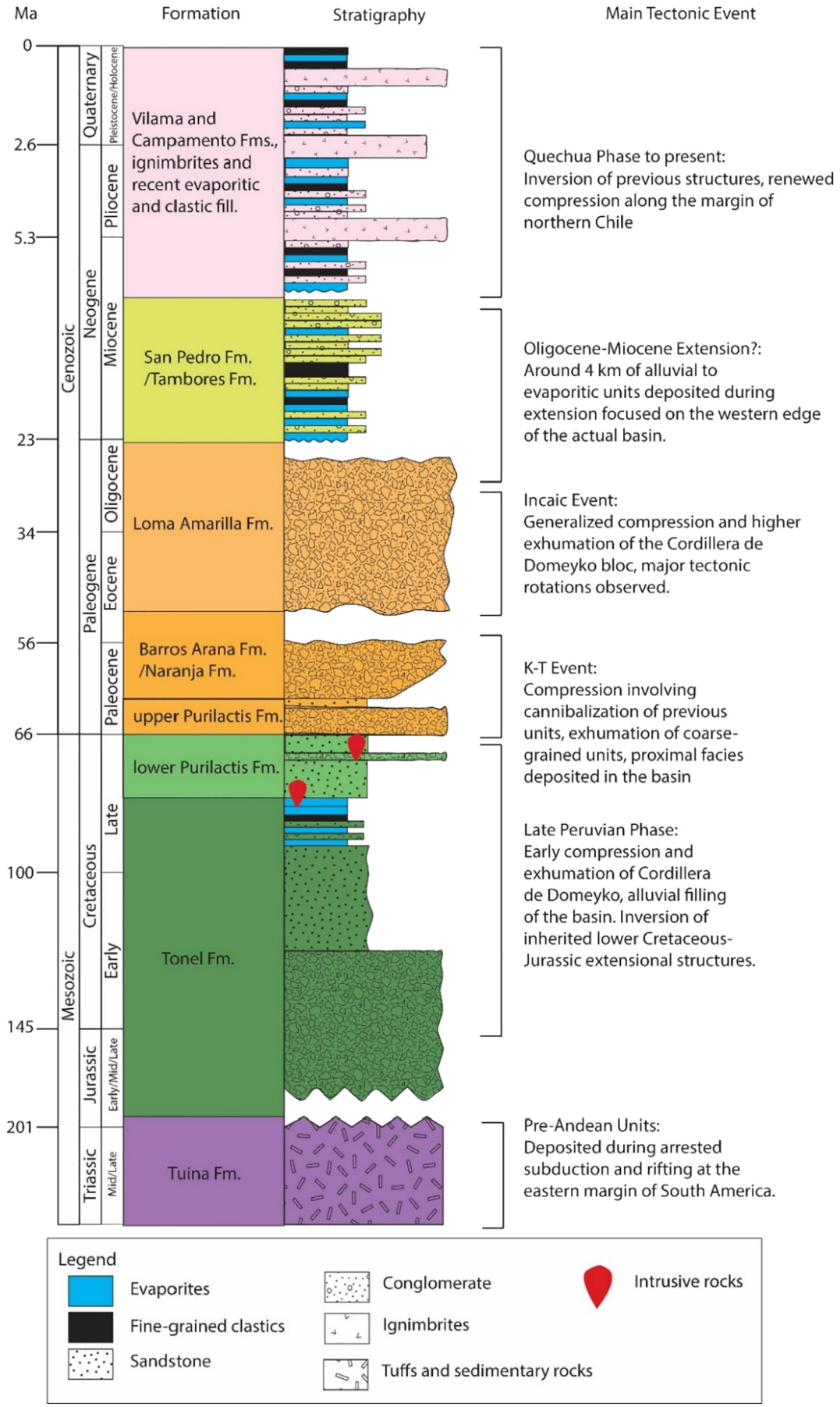

Fig. 3. Simplified tectonostratigraphy of the Salar de Atacama Basin, showing main stratigraphic units and tectonic events. Ages for the units follow the works by Ramírez and Gardeweg (1982), Marinovic and Lahsen (1984), Hammerschmidt et al. (1992), Henríquez et al. (2014), Bascuñán et al. (2016) and Narea et al. (2015).

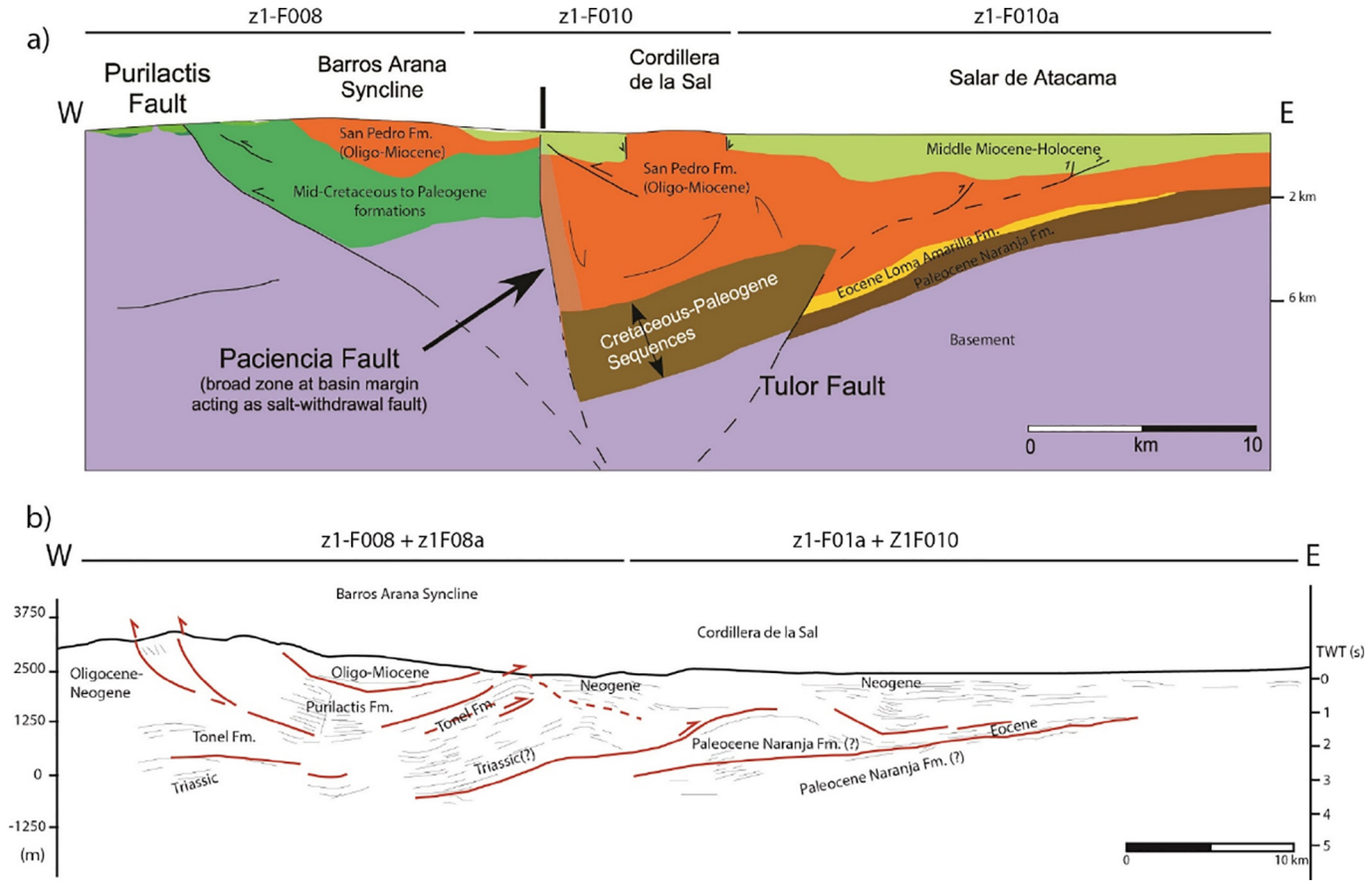

Fig. 4. Alternatives for the structure of the Salar de Atacama Basin. Both cross-sections have been slightly modified from their original sources. A) Cross-section by Pananont et al. (2004). b) Cross-section by Arriagada et al. (2006a).

topographic relief in this area can reach up to 900 m, where mainly Paleozoic to Tertiary rocks are exposed (Arriagada, 1999; Arriagada et al., 2006a; Basso and Mpodozis, 2012; Hammerschmidt et al., 1992). The southern end of the basin is composed of igneous and sedimentary rocks of Ordovician-Carboniferous age exposed along the Cordón de Lila (Coira et al., 2009; Niemeyer, 2013, 1989; Zimmermann et al., 2009). Northwards, the basin abuts against Pliocene-Miocene ignimbrites and other volcanic deposits, which are also found east, as the basin slope gradually rises towards the current magmatic arc (Becerra et al., 2014; Henríquez et al., 2014; Marinovic and Lahsen, 1984; Ramírez and Gardeweg, 1982).

Several distinct structural features can be recognized within the basin. From west to east, these are the Barros Arana Syncline, the Llano de la Paciencia, the Cordillera de la Sal and the current saltpan (Fig. 2). The Barros Arana Syncline is an 80-km long and 16-km wide, NE-SW-oriented syncline, comprised of Upper Cretaceous-Paleogene synorogenic volcanic and sedimentary rocks belonging to the Tonel, Purilactis and Barros Arana Formations (Figs. 2, 3 & 4; Arriagada, 1999; Arriagada et al., 2006a; Bascuñán et al., 2016; Charrier and Reutter, 1994; Hartley et al., 1992a, 1988, Mpodozis et al., 2005, 1999; Reutter et al., 2006). An unconformity separates these rocks from the Oligocene-Miocene Tambores Formation, and other Miocene to Pliocene clastic deposits (Henríquez et al., 2014; Marinovic and Lahsen, 1984).

Recent provenance and geochronological studies have shown that the constituents of these sediments came from an uplifted source to the west, whose location changed progressively from the Coastal Cordillera (Fig. 1) to the Cordillera de Domeyko, between 107 Ma–73 Ma, associated with the eastward migration of the Late Cretaceous contractional deformation front in this part of northern Chile (Bascuñán et al., 2016). The migration of the foreland has been associated with the mid-Cretaceous Peruvian Tectonic Phase (Steinmann, 1929), a compressional event which has been recorded in different parts of the South American margin, albeit with slightly different timings between 100 and 75 Ma (Cobbold and Rossello, 2003; Gianni et al., 2015; Jaillard, 1993, 1992; Jaimes and de Freitas, 2006; Megard, 1984; Merino et al., 2013; Tunik et al., 2010).

The Llano de la Paciencia lies east of the El Bordo Escarpment/Barros Arana Syncline, and west of the Cordillera de la Sal (Fig. 2). It is an 80-km long and 8-km wide sub-basin filled mostly by Quaternary alluvial deposits (Jolley et al., 1990; Marinovic and Lahsen, 1984; Mpodozis et al., 2005). A relevant increase eastward in the slope of the salar marks the beginning of the Cordillera de la Sal, an elongated, SSW-NNE-oriented thin-skin fold belt with a topographic relief of 200 m compared with the basin floor (2300 m a.s.l) (Becerra et al., 2014; Wilkes and Görler, 1994). It is comprised of Oligocene-Miocene evaporites and terrigenous deposits belonging to the San Pedro Formation (part of the Paciencia Group sensu Flint, 1985; see Table 1 for ages), and Pliocene to recent evaporites, lacustrine and fluvial deposits (Vilama and Campamento Fms; Arriagada et al., 2006a; Flint et al., 1993; Jordan et al., 2002; Rubilar et al., 2017). The deposits of the San Pedro Formation show a maximum estimated thickness of 3000–3200 m in some parts of the Cordillera de la Sal (Fig. 5), and its origin is related to the erosion of the units exposed along the El Bordo Escarpment (Figs. 3 & 4; Arriagada et al., 2006a; Becerra et al., 2014; Henríquez et al., 2014; Jordan et al., 2007; Mpodozis et al., 2000; Pananont et al., 2004; Wilkes and Görler, 1994). Regarding the modern-day saltpan, its infill has been identified as alluvial and evaporitic deposits of Quaternary and older age, overlying a complexly deformed substrate (Arriagada et al., 2006a; Flint et al., 1989; Jordan et al., 2007; Macellari et al., 1991; Muñoz et al., 2002; Pananont et al., 2004; Reutter et al., 2006).

Table 1
Compilation of ages relevant for the column in Fig. 3 and the units discussed within this study.

Sample	Unit	Latitude	Longitude	Age	Method	Source
SP3-85	Purilactis Fm.(Seilao Mb)	−22.74844	−68.40390	69.1 ± 1.0	Detrital Zircon U-Pb	This work
SP3-86	Purilactis Fm.(Vizcachita Mb)	−22.73734	−68.40840	66.7 ± 07	Detrital Zircon U-Pb	This work
SP3-94	Purilactis Fm.(Vizcachita Mb)	−22.81586	−68.42898	65.2 ± 0.8	Detrital Zircon U-Pb	This work
SP3-92	Purilactis Fm.(Pajarito Mb)	−22.78433	−68.43210	69.3 ± 0.8	Detrital Zircon U-Pb	This work
SP1-15	Tonel Fm.(Agua Salada)	−22.57265	−68.48394	148.9 ± 2.6	Detrital Zircon U-Pb	Bascuñán et al. (2016)
K-4	Tonel Fm. (La Escalera Mb)	−22.57035	−68.48541	107.6 ± 1.8	Detrital Zircon U-Pb	Bascuñán et al. (2016)
K-18	Tonel Fm. (Arcoiris Mb)	−22.51823	−68.45206	141.6 ± 2.1	Detrital Zircon U-Pb	Bascuñán et al. (2016)
SP3-90	Purilactis Fm. (Limón Verde Mb)	−22.70863	−68.42917	79.0 ± 0.6	Detrital Zircon U-Pb	Bascuñán et al. (2016)
SP3-91	Purilactis Fm. (Limón Verde Mb)	−22.71118	−68.42526	80.3 ± 0.9	Detrital Zircon U-Pb	Bascuñán et al. (2016)
SP3-89	Purilactis Fm. (Licán Mb)	−22.70835	−68.40680	75.4 ± 1.9	Detrital Zircon U-Pb	Bascuñán et al. (2016)
SP3-87	Purilactis Fm.(Río Grande Mb)	−22.74774	−68.39588	73.0 ± 4.0	Detrital Zircon U-Pb	Bascuñán et al. (2016)
SP3-88	Barros Arana Fm.	−22.76087	−68.39001	78.3 ± 1.4	Detrital Zircon U-Pb	Bascuñán et al. (2016)
*	Naranja Fm.	−24.00423	−68.6469	57.9 ± 1.9	K-Ar whole rock	Gardeweg et al. (1994)
*	Naranja Fm.	−24.19869	−68.6428	58.0 ± 3	K-Ar whole rock	Gardeweg et al. (1994)
Pu-1	Loma Amarilla Fm.	−23.59083	−68.6342	43.8 ± 0.5	Ar-Ar biotite	Hammerschmidt et al. (1992)
Pu-13	Loma Amarilla Fm.	−23.33583	−68.6422	44.2 ± 0.9	Ar-Ar biotite	Hammerschmidt et al. (1992)
KP3L	Purilactis Fm. (Vizcachita Mb)	*	*	64 ± 10	Ar-Ar Pyroxene	Flint et al. (1989)
To-432	Loma Amarilla Fm.	−23.52787	−68.6522	39.9 ± 3.0	K-Ar Plagioclase	Ramírez and Gardeweg (1982)
PC-26	Totola Fm.	−23.25453	−68.6082	65.0 ± 2.0	K-Ar whole rock	Mpodozis et al. (2005)
PC-27	Totola Fm.	−23.24877	−68.649	66.0 ± 2.0	K-Ar whole rock	Mpodozis et al. (2005)
PC-28	Totola Fm.	−23.37897	−68.6519	61.0 ± 2.0	K-Ar whole rock	Mpodozis et al. (2005)
PC-13	Loma Amarilla Fm.	−23.5189	−68.654	33.9 ± 1.5	K-Ar Amphibole	Mpodozis et al. (2005)
MM54	San Pedro Fm.	−22.61723	−68.3345	26.6 ± 0.8	K-Ar biotite	Mpodozis et al. (2000)
MM54′	San Pedro Fm.	−22.61723	−68.3345	26.8 ± 1.4	K-Ar biotite	Mpodozis et al. (2000)
SB-T	San Pedro Fm.	−22.79529	−68.2166	28 ± 0.8	K-Ar biotite	Travisany (1978)
MC-777	San Pedro Fm.	−22.903335	−68.2217	24.9 ± 1	K-Ar biotite	Naranjo et al. (1994)
*	San Pedro Fm.	−22.90363	−68.2216	24.9 ± 6	K-Ar biotite	Marinovic and Lahsen (1984)
SP5-197	Vilama Fm.	−22.907	−68.2477	2.94 ± 0.03	U-Pb zircon	Henríquez et al. (2014)
NP-90	Vilama Fm.	−22.89854	−68.2146	2 ± 0.9	K-Ar biotite	Naranjo et al. (1994)
84081	Vilama Fm.	−22.851071	−68.1083	4.14 ± 0.24	K-Ar biotite	de Silva (1989)
83036	Vilama Fm.	−22.736536	−68.1674	4.35 ± 0.19	K-Ar biotite	de Silva (1989)
MM101	Vilama Fm.	−22.82666	−68.2028	5.8 ± 0.5	K-Ar biotite	Mpodozis et al. (2000)
MM35	Vilama Fm.	−22.891593	−68.2147	4.5 ± 0.4	K-Ar biotite	Mpodozis et al. (2000)
MM40	Vilama Fm.	−22.917057	−68.2351	5.3 ± 0.5	K-Ar biotite	Mpodozis et al. (2000)
MM48	Vilama Fm.	−22.902487	−68.2166	3.7 ± 1	K-Ar biotite	Mpodozis et al. (2000)
SP3-77	San Pedro Fm.	−22.965136	−68.3321	18.9 ± 0.2	U-Pb detrital zircon	Henríquez et al. (2014)
09KMAD06	Loma Amarilla Fm.	−23.6904	−68.6248	95–227	U-Pb single zircon grains	Reiners et al. (2015)
09KMAD13	Loma Amarilla Fm.	−23.6969	−68.6336	55–241	U-Pb single zircon grains	Reiners et al. (2015)
09KMAD11	Loma Amarilla Fm.	−23.6976	−68.6424	65–265	U-Pb single zircon grains	Reiners et al. (2015)
09KMAD09	Loma Amarilla Fm.	−23.6988	−68.6503	258–272	U-Pb single zircon grains	Reiners et al. (2015)
09KMAD08	Loma Amarilla Fm.	−23.6989	−68.6714	256–308	U-Pb single zircon grains	Reiners et al. (2015)
09KMAD14	Naranja Fm.	−23.6023	−68.6252	72–81	U-Pb single zircon grains	Reiners et al. (2015)
MS160110-1D	Quebrada de Pajonales Fm.	−24.36785	−68.5738	76.0 ± 9.0	U-Pb detrital zircon	Solari et al. (2017)
BB-160409-1D	Quebrada de Pajonales Fm.	−24.36671	−68.6048	64.5 ± 6.8	U-Pb detrital zircon	Solari et al. (2017)
IME-074D	Quebrada de Pajonales Fm.	−24.164909	−68.6054	64.3 ± 4.4	U-Pb detrital zircon	Solari et al. (2017)
IM260915-1D	Naranja Fm.	−24.048495	−68.6459	230.1 ± 2.9	U-Pb detrital zircon	Solari et al. (2017)
IM300915-3D	Naranja Fm.	−24.009444	−68.6476	57.4 ± 0.3	U-Pb detrital zircon	Solari et al. (2017)
MS151203-1D	Loma Amarilla Fm.	−23.987721	−68.6434	40.1 ± 1.1	U-Pb detrital zircon	Solari et al. (2017)
IME050a	Loma Amarilla Fm.	−24.02325	−68.6829	237.1 ± 3.1	U-Pb detrital zircon	Solari et al. (2017)
IME050b	Loma Amarilla Fm.	−24.02325	−68.6829	231.6 ± 1.9	U-Pb detrital zircon	Solari et al. (2017)
BB-160330-1D	Tambores Fm.	−24.009325	−68.6795	28.6 ± 0.6	U-Pb detrital zircon	Solari et al. (2017)
*	Loma Amarilla Fm.	−23.360023	−68.6318	59.1 ± 2.0	K-Ar whole rock	Basso and Mpodozis (2012)
*	Cerro Totola Fm.	−23.360725	−68.6295	64.0 ± 2.0	K-Ar whole rock	Basso and Mpodozis (2012)

A variety of geophysical studies have been carried out both within and around the Salar de Atacama Basin, mainly focusing on its mid to upper crustal structure and composition. These include seismic reflection profiles carried out by ENAP (Empresa Nacional del Petróleo), gravity surveys (Götze et al., 1994; Götze and Krause, 2002) and seismic studies (Schmitz et al., 1999; Schurr and Rietbrock, 2004; Yuan et al., 2002). These studies show that a distinct gravity high can be found beneath the basin, which would correspond to a high-density body found 10 to 38 km beneath the saltpan, possibly consisting in a mix of gneisses and metabasites with moderate Vp/Vs ratios, rheologically strong and thermally cold. Also, the Moho depth (ca. 67 km) seems to be anomalously high for the current altitude of the basin, which, together with previous data, suggests that the block is mechanically coupled to the Nazca plate, thus apparently explaining local elevation (Yuan et al., 2002).

The interpretations of the subsurface of the basin have varied importantly over the last 25 years, showing at times contrasting results. Flint et al. (1993) argued for extensional (and later strike-slip) conditions dominating most of the basin history from the Permo-Triassic up to the Miocene, based on their analysis of five sequences. Muñoz et al. (2002) analyzed the Toconao-1 well results and the seismic line that intersects it, and obtained six (seven including the basement) stratigraphic sequences ranging from the mid-Cretaceous (Cenomanian-Maastrichtian) to the Holocene. They concluded that the basin had experienced moderate extension during the Late Cretaceous, followed by strong inversion during the early Paleocene, and basement-involved tectonics during the Eocene. This deformation would have later transferred in sequence to younger layers, thus establishing a mainly compressive history for the basin. This tectonic frame was then brought into question by Pananont et al. (2004), who reinterpreted the seismic section associated with the well, obtaining six sequences which were then extended northwards in order to interpret some of the

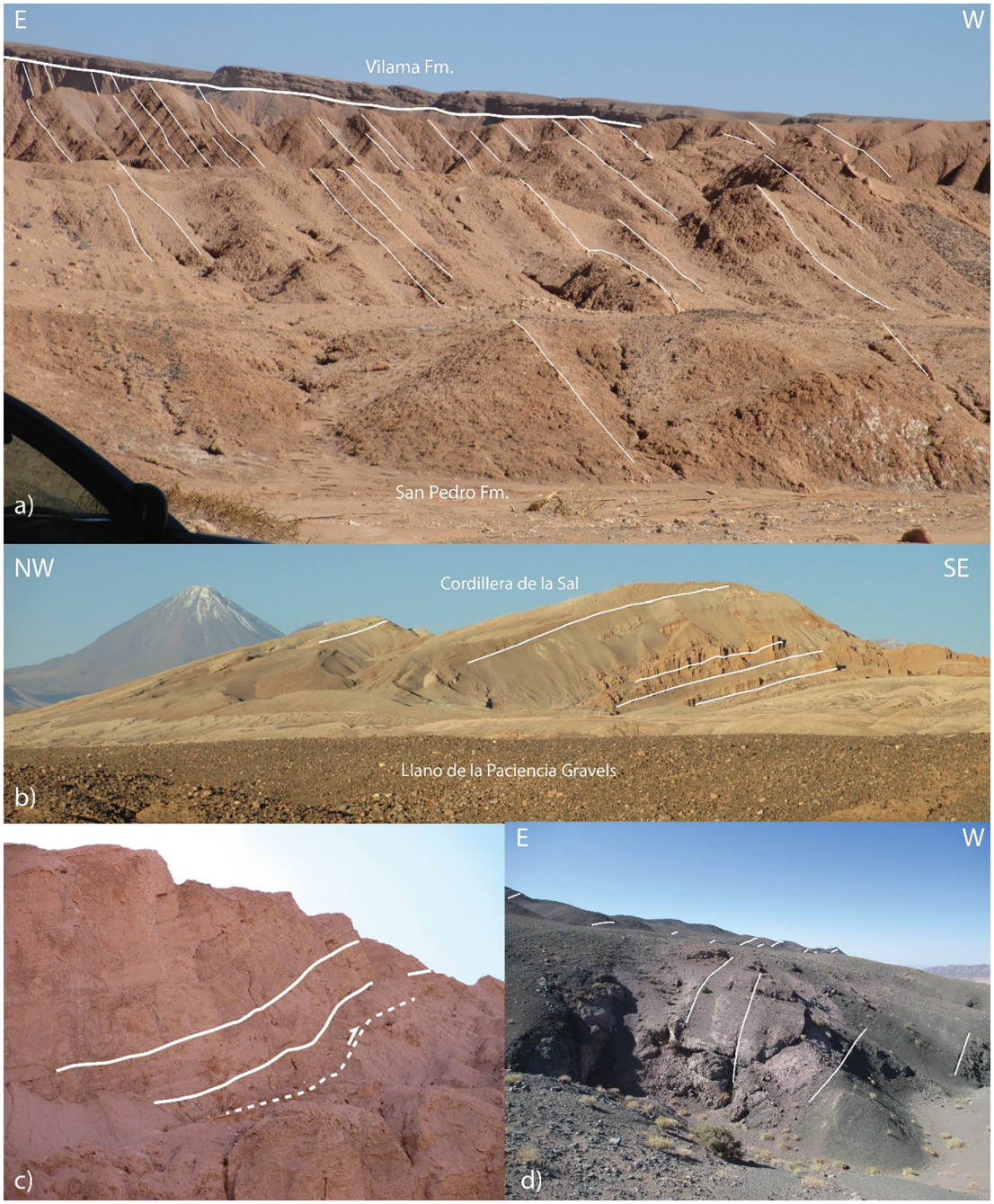

Fig. 5. Examples of structural and geological features within the study area. a) Unconformity between the San Pedro Fm (late Oligocene-early Miocene) and the Vilama Fm. (late Miocene-Pliocene). b) Folded San Pedro Fm., known as the Cordillera de la Sal. c) Compressive features within the San Pedro Fm. d) Deposits of the Vizcachita Member of the Purilactis Fm., where some of the U/Pb samples were taken.

northernmost seismic lines (Figs. 2 & 4a). They also used the results from Jordan et al. (2002), who analyzed some of the southernmost lines and studied the shallow evaporitic units (down to 900 m in depth approximately) of the salt pan. Under their new proposal, the mid-Cretaceous to Paleocene-Eocene sequences would represent deposition under mostly compressive conditions, with the latter representing the deposits associated with the Incaic Orogeny. Afterwards, east-west extension, combined with some degree of transtension, would have generated a large normal fault, which led to the deposition of Oligo-Miocene deposits (Fig. 4a). A similar view was held by Jordan et al. (2007), who reviewed most of the seismic sections and elaborated thickness maps for the different sequences. Both Pananont et al. (2004) and Jordan et al. (2007) argue for a return to compressive conditions at the end of the early Miocene. On the other hand, Arriagada et al. (2006a), based on their interpretation of the seismic sections and the Toconao-1 well, along with multiple field observations, suggest the presence of at least six sequences within the basin, which are associated with the outcrops along the El Bordo Escarpment, following the chronostratigraphy developed by Mpodozis et al. (2005). The Salar de Atacama Basin would mostly record compressive conditions since 90 Ma, with no evidence for large extensional processes (Fig. 4b).

More recently, Rubilar et al. (2017) performed a structural reconstruction of several cross-sections perpendicular to the Cordillera de la Sal, which were based on their interpretation of seismic sections belonging mostly to the central and southern parts of the basin. Their results show the wide presence of inversion tectonics during the

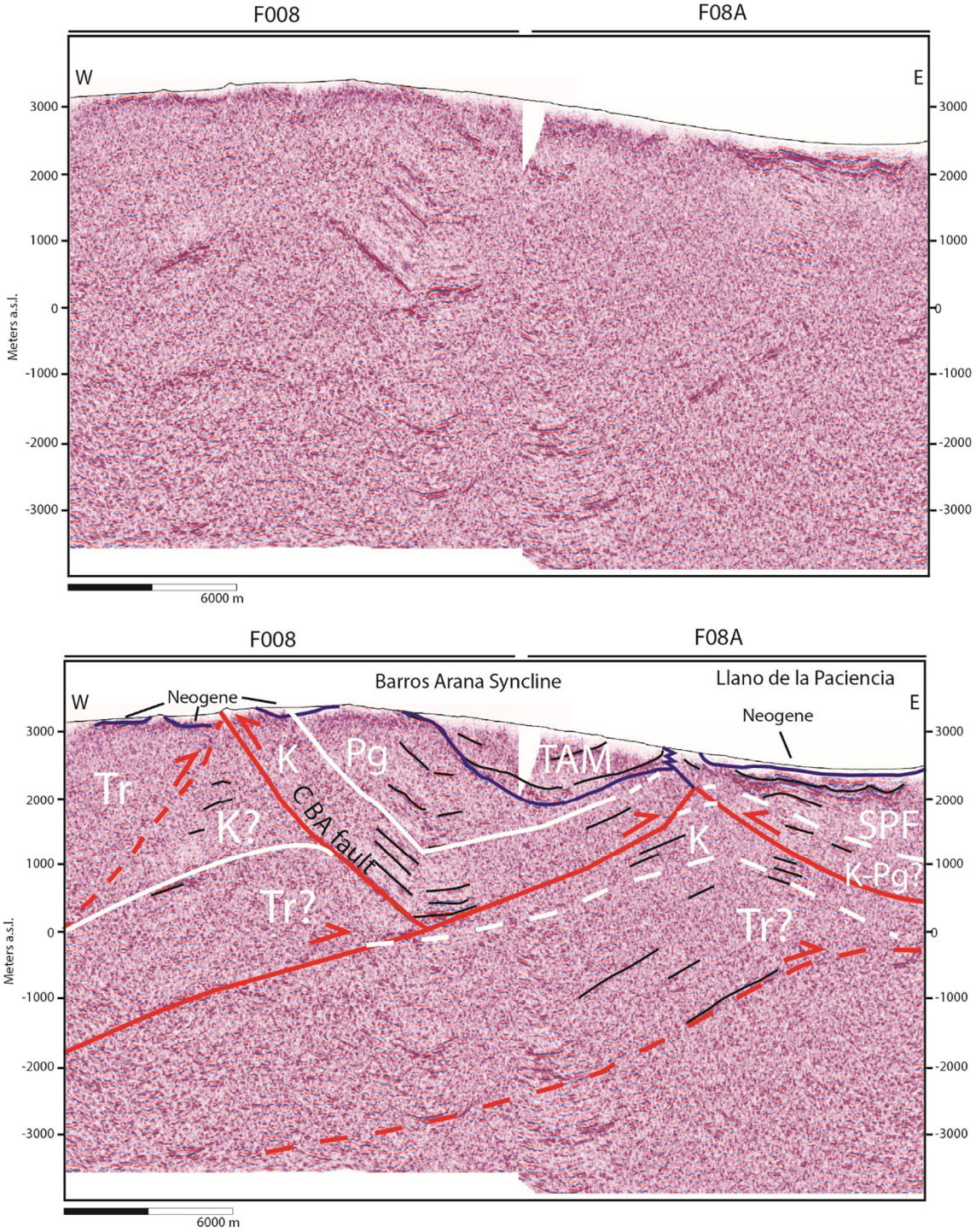

Fig. 6. Uninterpreted (above) and interpreted (below) profiles F008-F08A. Letters correspond to: Tr, Triassic (Tuina Formation); K, Tonel to lower Purilactis Formation; Pg, upper Purilactis and Barros Arana Formation; TAM, Tambores Formation; SPF, San Pedro Formation; CBA, Cordón Barros Arana Fault. Blue lines indicate unconformities seen at the surface. (For interpretation of the references to colour in this figure legend, the reader is referred to the web version of this article.)

Neogene, which would have been facilitated by the presence of Oligocene synextensional evaporites. These evaporites act as a detachment level and show a south-to-north deepening; these levels are associated with the extensional episode posited by some of the authors mentioned above.

3. Methodology

3.1. Seismic reflection profiles

A subset of the seismic reflection profiles provided by ENAP has been used in this study (Fig. 2), covering roughly the northernmost parts of the basin, comprising around 77 km of sections acquired with a Vibroseis source. These lines correspond to 1F008-1F008A (Fig. 6) and

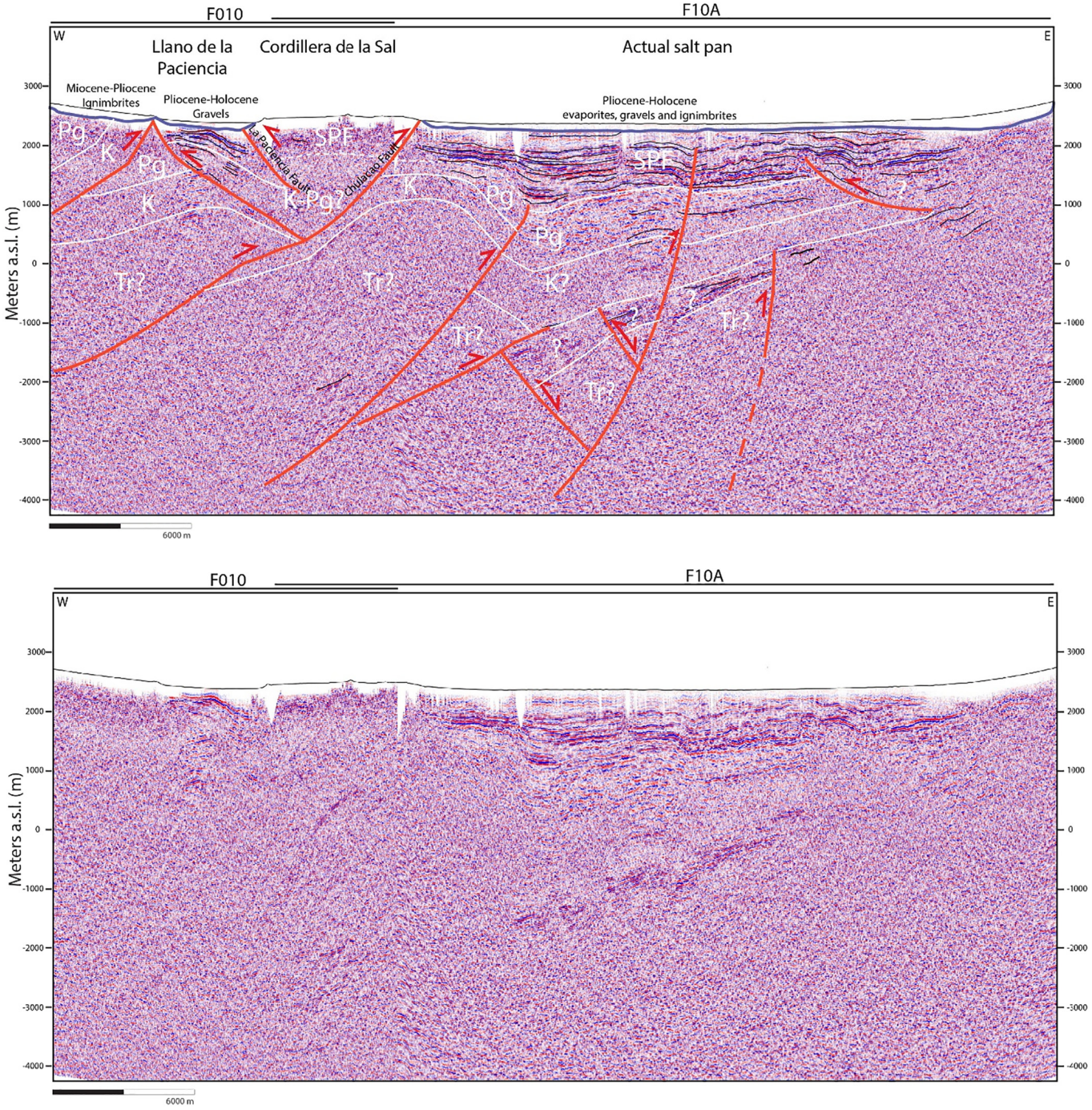

Fig. 7. Uninterpreted (above) and interpreted (below) seismic profiles F010-F10A. Acronyms are the same as in Fig. 6.

1F010-1F010A (Fig. 7), some of which have been previously studied with varying interpretations (Fig. 4). The seismic lines, whose static corrections followed a sloping datum, were adjusted to the SRTM DEM topography by modifying trace position. The highest value becomes fixed at 0 s TWT, and each trace at a lower altitude is shifted in the time domain using a replacement velocity of 3500 m/s. This process was performed with Seismic Unix and Python tools. The seismic profiles were depth-converted using Move 2017.1 by Midland Valley Ltd., following Eq. (1), which is itself a derivation of a linear equation relating instantaneous velocity to depth (e.g., Al-Chalabi and Rosenkranz, 2002)

$$Z\,(m) = V_0 * (e^{kt} - 1)/k). \quad (1)$$

where Z is the thickness of the top layer in meters, V_0 is the velocity at the top of the layer in m/s, k is the rate at which velocity changes with depth and t is the one-way travel time for layer thickness, in seconds.

Assuming a fixed velocity of V_o = 3500 m/s (within the velocity range from the CDP velocity data, see below), k equals 0, and accounting for two-way travel time, Eq. (1) becomes:

$$Z\,(m) = V_0 t/2 \quad (2)$$

The seismic profiles were then interpreted following standard seismic reflection techniques, such as identifying tectonic and/or stratigraphic reflector truncations, grouping the sequences according to the nature of their reflectors (continuity, spacing and amplitude), and identifying seismic surfaces and sequence boundaries (Catuneanu et al., 2011; Cross and Lessenger, 1988). The grouping of the different

sequences follows closely those proposed by earlier authors (Arriagada et al., 2006a; Jordan et al., 2007; Pananont et al., 2004), and the geological maps by Becerra et al. (2014) and Henríquez et al. (2014).

3.2. CDP Velocity

Another way to estimate the depth at which physical properties change in the seismic sections is by analyzing the Common Depth Point (CDP) interval velocity, generated through NMO processing. These were found in some of the paper versions of the seismic lines provided by ENAP (seismic lines 1H100, 1H104, 1H107, 1H108, 1H116, 1H120, 1H121, 1H124, 1H125, 1H128, 1H130, 1H134, 1H135, 1H138 AND 1H143), showing root mean square 1D velocities at certain TWT depths for points spaced on horizontal axis between 2 and 2.5 km. This data was digitized and converted to interval velocities following the relation described by Dix (1955):

$$V_{int} = \left[\frac{t_2 * {V_{RMS2}}^2 - t_1 * {V_{RMS1}}^2}{t_2 - t_1} \right]^{1/2} \quad (3)$$

The resulting values were lineally interpolated and gridded using a combination of GMT and Python, thus producing different map view velocity slices spaced 250 m a. s. l. (Fig. 8). For simplicity, and to start with an elevation common to all lines, the slices started at 2000 m a.s.l., although some sections, particularly those to the west, reach higher altitudes (around 3300 m a.s.l.). A velocity cross-section following the trace of the gravimetric survey was also obtained, together with a combination of lines 1H100 and 1H120 (Fig. 9).

3.3. Gravity data

An E-W gravity profile was carried out within the Salar de Atacama Basin in order to test current structural models regarding its internal architecture (Fig. 4). The profile consists of 29 stations, spaced every 1 km (Fig. 2). Its strike was semi orthogonal to regional structures such as the Cordillera de la Sal and the Barros Arana Syncline. The objective of the profile was to check and identify any matches between the much-discussed seismic reflection profiles and the gravity response of the different bodies suspected to lie beneath the surface of the actual basin and along its edges. Measurement was taken both on- and off-road, trying to match as closely as possible the surficial traces of the seismic profiles taken during the 1980's. A CG-3 Scintrex Autograv gravity meter, with a 0.005 mGal resolution, was used for all measurements. Coordinates and elevations were acquired with a Topcon-Hiper V D-GPS system. Gravity reduction was done according to standard procedures, such as those described by Blakely (1996). These involve Earth tide correction following the algorithm of Longman (1959), correcting for instrumental drift by performing a time linear interpolation between the daily measurements taken at the gravity base station (0.02–0.2 mGal h^{-1}), removing the normal gravity trend associated with the WGS84 ellipsoid, and applying both free-air and simple Bouguer anomaly corrections with the D-GPS elevation and a background density of 2.67 g/cm^{-3}. Afterwards, the complete Bouguer anomaly was obtained by performing a terrain correction using a 50 × 50 km, high-resolution (92 × 92 m) SRTM digital elevation model (DEM). The data was modeled using ModelVision 13.0 (Fig. 10). The measurements can be found in Supplementary Material A.

3.4. U-Pb detrital zircon geochronology

Another useful tool to understand the geological evolution of a given area, particularly those with few igneous outcrops, corresponds to U-Pb detrital zircon geochronology. Although previous studies have aided in establishing the timeframe of the tectonic evolution of the basin (Bascuñán et al., 2016; Mpodozis et al., 2005), four additional samples belonging to the Purilactis Formation were analyzed (Figs. 2 & 5d), in order to evaluate and enhance previous interpretations. The samples correspond to medium- to coarse-grained sandstones belonging to the Pajarito Member (SP3-92), the Vizcachita Member (SP3-86, SP3-84), and the Seilao Member (SP3-85) (Fig. 11). Table 1 summarizes the ages of the data presented here and other relevant ages found both within the study area and in neighboring areas around Cordillera de Domeyko, compiled from several sources (Bascuñán et al., 2016; Basso and Mpodozis, 2012; Becerra et al., 2014; de Silva, 1989; Flint et al., 1989; Gardeweg et al., 1994; Hammerschmidt et al., 1992; Henríquez et al., 2014; Marinovic and Lahsen, 1984; Mpodozis et al., 2000, 2005; Naranjo et al., 1994; Ramírez and Gardeweg, 1982; Reiners et al., 2015; Solari et al., 2017; Travisany, 1978).

The samples were processed at the Sample Preparation Laboratory of the Geology Department of the Universidad de Chile, using Gemeni Table, Frantz magnetic separator and heavy liquid procedures. The zircons were separated manually operating a binocular microscope and were then sent to the Laboratorio de Estudios Isotópicos (LEI) of the Geoscience Center of the Universidad Nacional Autónoma de México (UNAM). Around 100 random grains were analyzed with a *Resonetics Resolution M50* 193 nm laser *Excimer* connected to a *Thermo Xii Series Quadrupole Mass Spectrometer*, utilizing a 23 µm laser diameter for ablation. Additional technical details are described in Solari et al. (2010). All unit ages and designations follow those of the International Stratigraphic Chart (Cohen et al., 2013).

The best age for each zircon was defined using the same criteria as in Bascuñán et al. (2016), and sample age was calculated using *Isoplot v.3.7.* (Ludwig, 2008), obtaining averages for the youngest populations with more than three zircons. Relevant peaks and populations were also analyzed using the spreadsheet Age Pick developed by the LaserChron Center at the University of Arizona. The resulting data tables can be found in Supplementary Material B.

4. Results

4.1. Seismic profiles and main structural components

The interpretation of the seismic sections follows some of the basic observations made from previous works, such as those of Pananont et al. (2004), Arriagada et al. (2006a) and Jordan et al. (2007). The geometries and limits of the different sequences were compared and evaluated, observing a general conformity among the authors in the area of the Barros Arana Syncline (Figs. 4 & 6). The areas to the east show some divergences, particularly regarding the age of the sequences, which are presented below. Six major sequences were interpreted and correlated with the rocks cropping out around the edges of the Salar de Atacama Basin and its interior (Fig. 2). The interpretations are presented in Figs. 6 & 7.

Sections F008 and F08A, which are nearly perpendicular to the strike of the Barros Arana Syncline (Figs. 2 & 6), show clearly the geometry of this structure, which corresponds to an asymmetric, east-verging syncline, mainly involving Upper Cretaceous and Paleocene synorogenic deposits of the Purilactis Group (K-Pg). Its limbs loose lateral continuity, and are cut by shallow, high-amplitude reflectors. These have been associated with east- and west- verging reverse faults, some of which can be seen on the surface (Fig. 2). The upper section of the fold is unconformably covered by slightly folded, shallow seismic reflectors related to the Oligocene-Miocene deposits of the Tambores Formation (TAM) (Figs. 2 & 6). West of the syncline, a series of chaotic reflection patterns have been correlated to Triassic volcano-sedimentary rocks, which have been considered part of the basement of the basin (Tuina Fm, Tr; Henríquez et al., 2014; Narea et al., 2015; Raczynski, 1963). Based on this seismic and structural relation, a basement wedge associated with an east-verging thrust ramp is interpreted to lie underneath the Barros Arana Syncline. This structural style is commonly created from the movement of a basement block detached along the contact between basement and cover rocks. Underlying this

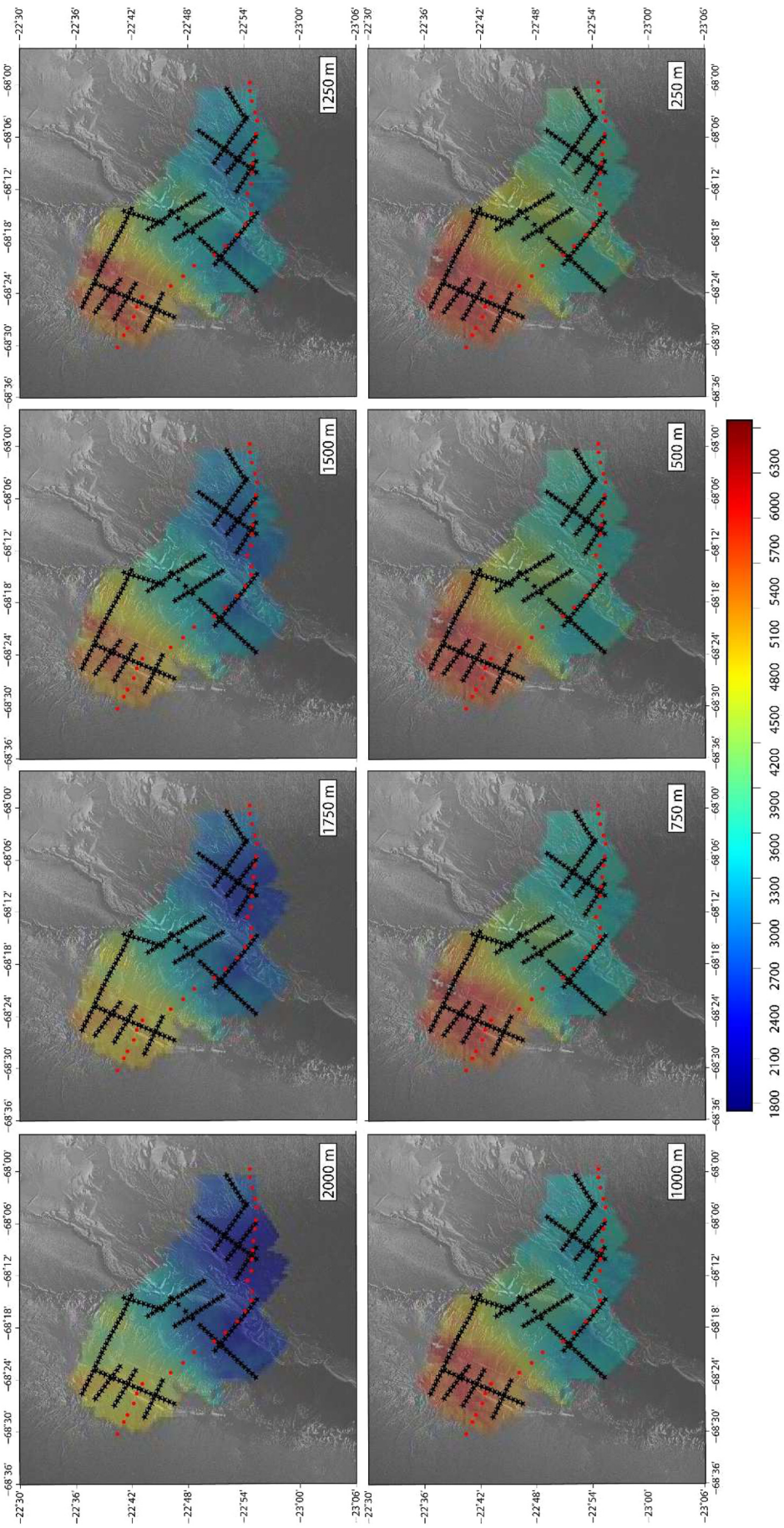

Fig. 8. Interval velocity slices, draped over the digital elevation model (DEM). Meters above sea level are given in the white box in the lower right corner of each slice. Red dots correspond to gravity stations, and black stars to CDP velocity points. (For interpretation of the references to colour in this figure legend, the reader is referred to the web version of this article.)

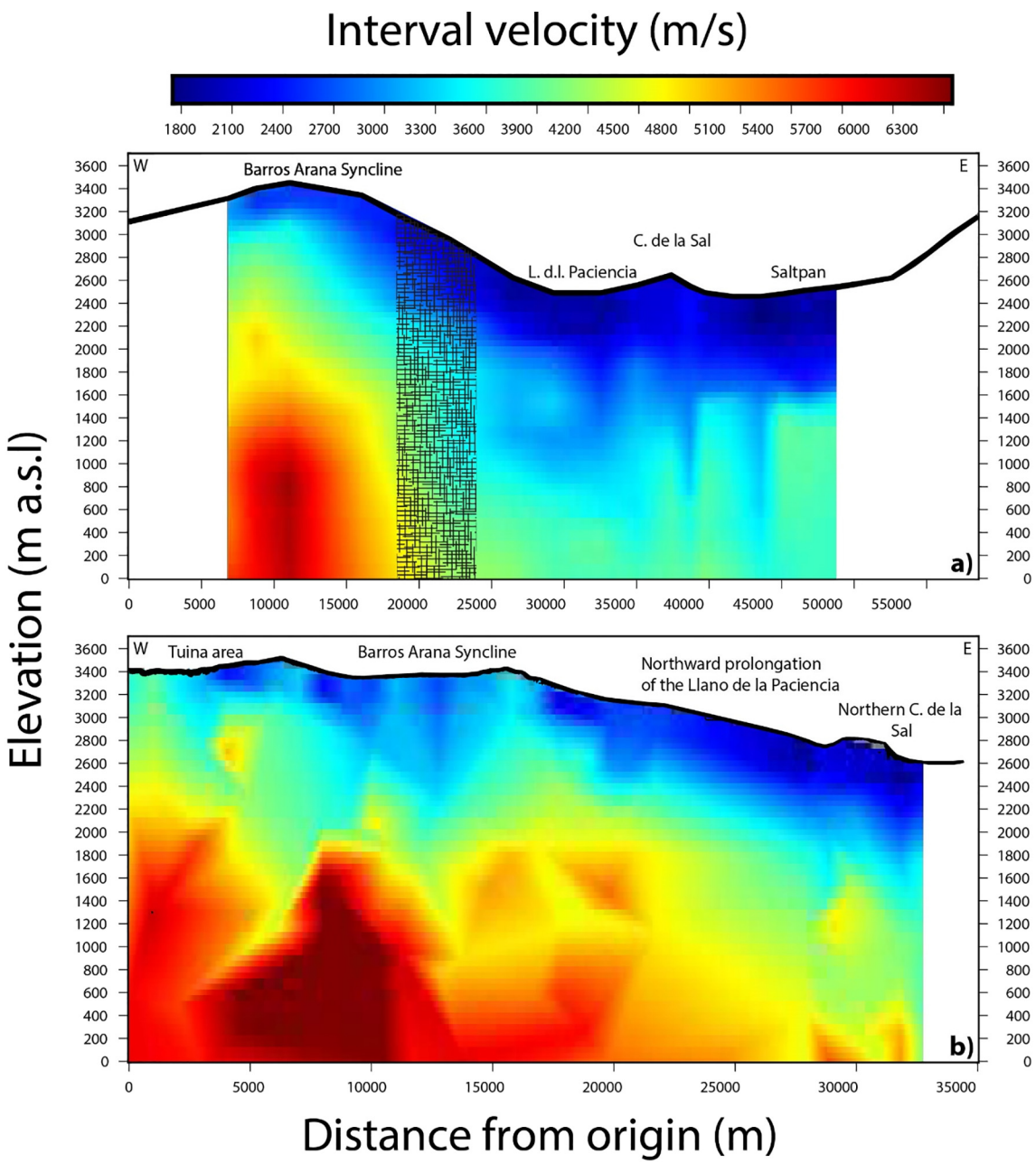

Fig. 9. a) Interval velocity cross-section along the gravimetry profile. Crisscrossed rectangle represents area with no CDP data. b) Composite cross-section, made up from lines 1H100 and 1H120. Line location in Fig. 2, and data interpolated from Fig. 8.

zone, some of the most relevant folded seismic reflectors have been identified as part of an east-verging, basement-involved fold, related to east-verging reverse faults. These faults also detach part of the syncline, placing its eastern flank on top of units higher in the stratigraphic column.

East of the Barros Arana Syncline, in the Llano de la Paciencia area, a series of high-amplitude seismic reflectors associated with the Oligocene-Miocene San Pedro Formation (SPF) have been identified (Arriagada et al., 2006a; Becerra et al., 2014; Henríquez et al., 2014; Pananont et al., 2004). These are frequently folded, and show some geometries related to growth strata and wedge shapes similar to those reported for synorogenic deposits. Laterally, these are cut by west- and east-verging, subsidiary thin-skinned thrust faults (Figs. 6 & 7). These Cenozoic units show more deformation with closer proximity to the Cordillera de la Sal, and an increase in dip downwards. On the other hand, the Oligo-Miocene units unconformably overlie rocks with low-amplitude, discontinuous reflectors, interpreted here to be part of the same rocks that comprise the Barros Arana Syncline (K-Pg).

The easternmost part of Fig. 6 overlaps with sections F010 and F010A (Fig. 7), particularly the area between the Llano de la Paciencia and the Cordillera la Sal, although their traces are located 9.5 km to the south (Fig. 2). These seismic profile sections clearly show an abrupt angular unconformity between the sub horizontal to east-dipping Oligo-Miocene (SPF) and Late Cretaceous-Paleogene (K-Pg) units and the west-dipping Triassic (Tr?) units beneath them. Here, the Cordillera de la Sal appears as a doubly verging, reverse-fault bound, nearly symmetrical structure (Fig. 2). This fault is associated with other deep, high-amplitude reflectors, forming part of an east-verging fault system, in continuation with the structural style seen in the previous sections. East of the Cordillera de la Sal, the Oligo-Miocene units (SPF), which usually display continuous and relatively high-amplitude reflectors, are seen forming broad folds which become tighter closer to the eastern

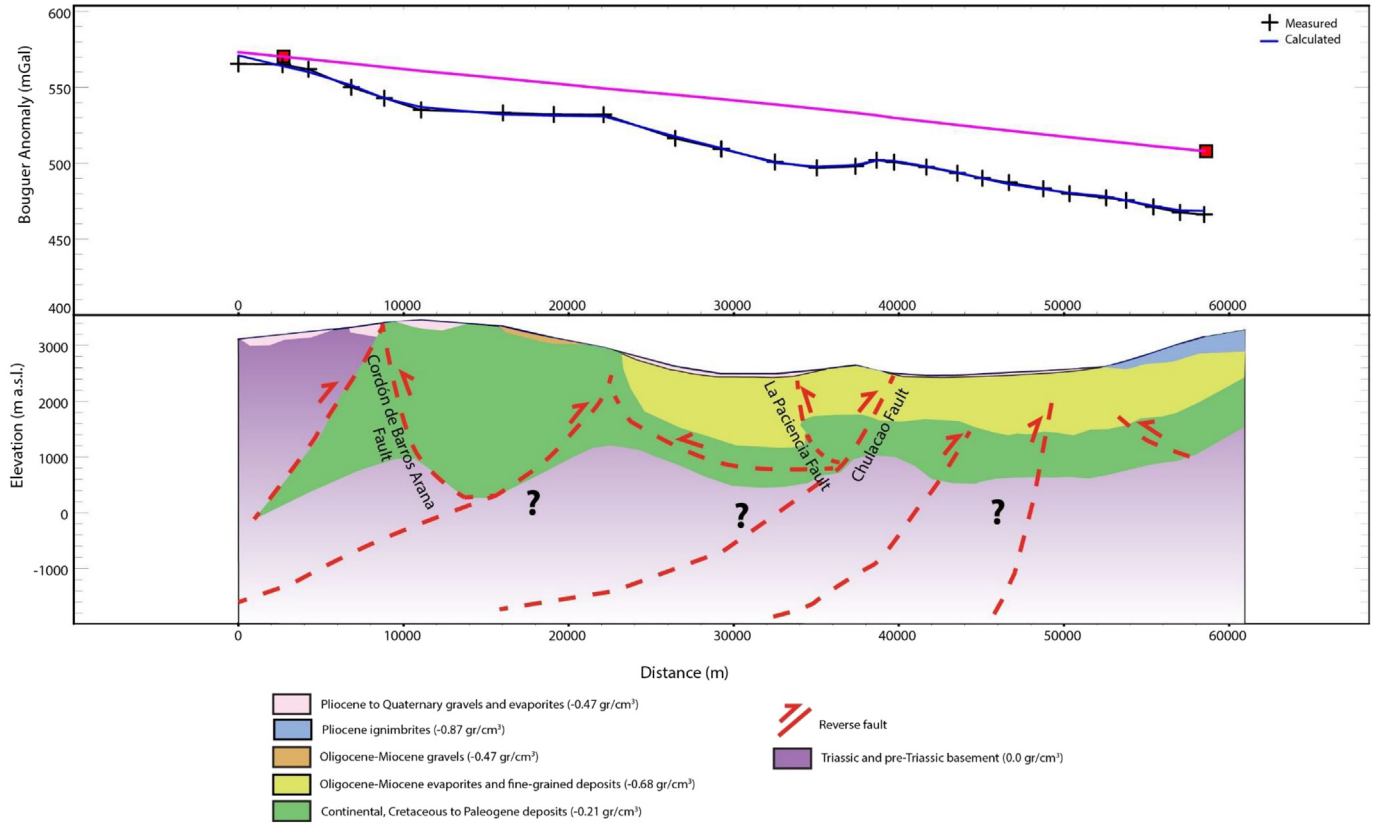

Fig. 10. Gravimetry results, showing the Complete Bouguer anomaly (above) and the modeled bodies and densities assigned (below). Location of the profile in Fig. 2.

border of the saltpan. The variations in SPF strata thickness follow closely the deformation of the previous strata.

The first-order structural style along these seismic profiles is represented by a set of east-verging reverse faults that appear to affect the basement of the basin. The hanging wall of these faults are composed of asymmetrical anticlines, and the footwall shows footwall syncline folds (Figs. 6 & 7). Although the quality of the seismic sections is relatively poor below 1000 m a.s.l., several high-amplitude reflectors delineate a west-dipping surface, which is interpreted as the top of the Triassic-Mesozoic (?) units, based partly on previous interpretations (Fig. 4) and the presence of units with a similar age and structural disposition southeast of the study area (Becerra et al., 2014; Niemeyer, 2013). Under the central part, some small-scale features resembling growth strata are also preserved in this surface, which can only be loosely assigned to the Early Cretaceous-Triassic (?) interval. These usually show some variation of thickness, and appear to be accumulated at the hanging wall block of previous normal faults (Fig. 7). These units are asymmetrically folded, and have structural geometries associated with tectonic inversion, suggesting thus that previous normal faults were partially reactivated.

The western end of the surface limiting the Triassic and Cretaceous (Tr? K?) sequences is folded into a syncline, which also encompasses some of the units above it (Fig. 7). The decrease in dip upwards also highlights the presence of an unconformity between the SPF and older units (Pg, K?), both of which are affected by more recent, reverse faulting. The units between the SPF and the west-dipping reflector show a progressive decrease in thickness eastwards, from around 2000 m in the center of the seismic section (near the syncline axis) to around 1000 m near the eastern limit. These rocks are assigned to the Late Cretaceous-Paleogene interval, based on previous studies (Fig. 4) and regional geology (Fig. 2).

4.2. Velocity analysis

The interpolation of the 1D CDP velocity data (Figs. 8 & 9) yields relevant data that serves as an independent constraint for the density and structural modeling. Fig. 8 shows the velocity map at different altitudes, highlighting the general decrease in velocity from west to east, which is generally more pronounced between 2000 and 1250 m a.s.l. There are overall high velocity values (3800 m/s and higher) around the western Barros Arana Syncline and close to the Triassic outcrops (Fig. 2), which decrease steadily towards its eastern border and the Llano de la Paciencia. The area east of the syncline axis shows lower velocities than its western counterpart, and the pattern becomes more complex with increasing depth. The slices between 1750 and 1250 m a.s.l. reveal that the area can be separated into several domains, with an overall low velocity zone underneath the Llano de la Paciencia and the western border of the Cordillera de la Sal (with velocities increasing in depth from 2600 m/s to 3300 m/s), another narrow area with higher average velocities underneath the Cordillera de la Sal (starting from 2900 m/s and increasing more rapidly with depth), and another low-velocity area towards the east (velocities around 2600 m/s, shifting rapidly to 3400–3500 m/s between 1250 and 1500 m a.s.l.). Deeper slices (1000 m a.s.l. and below) show a similar pattern, with higher velocities below the Cordillera de la Sal area. Another trend seen in deeper slices is a relative increase in velocity north of the gravimetric profile (red dots in Figs. 2 & 8), between the Cordillera de la Sal and the Barros Arana Syncline, with velocity values over 4000 m/s, much faster than both the Cordillera de la Sal and the low-velocity domains.

The velocity cross-section illustrates the features discussed above, but presents a clearer view of the data underlying the gravimetric section (Fig. 9a). The high-velocity zone, corresponding to Triassic-Cretaceous units is clearly visible, showing a steady decrease in velocity towards the Llano de la Paciencia. This area displays velocities around 3200–3800 m/s, between 350 and 1150 m a.s.l. This effectively

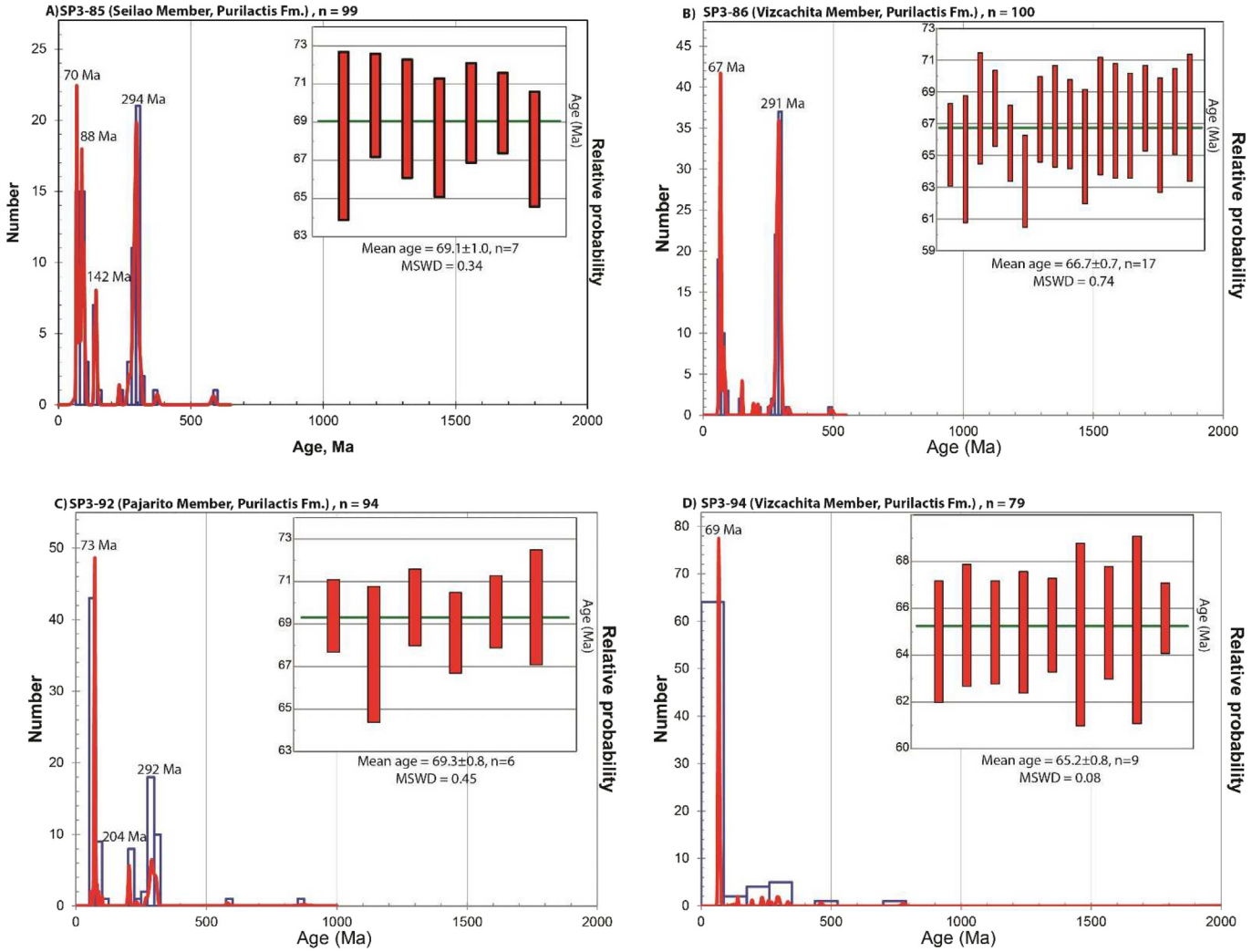

Fig. 11. U/Pb detrital zircon ages. Sample locations in Fig. 2.

accounts for lower velocities in this area in comparison to its immediate surroundings, related to the low velocities seen in map view. An abrupt change in velocity is recorded in the units east of the Cordillera de la Sal, where a nearly flat surface at ca. 1600 m a.s.l. separates units with velocities below 2800 m/s above the surface, and units with velocities over 3600 m/s beneath it. This "flat" surface displays some asperities, which may be related to the small-scale folds and structures seen in seismic section F10A (Fig. 7), and the intense deformation seen in the Cordillera de la Sal. Fig. 9b shows the transition from the Tuina Area to the northern Cordillera de la Sal (Fig. 2). A prevalence of high velocities around the Tuina-Barros Arana Syncline is also noticeable, with a slight drop in velocity and a "V"-shape geometry for the velocity in the latter part. The area shows a large number of artifacts below 2700 m a.s.l., and abrupt lateral changes in velocity, which become smoother eastwards. East of the syncline, the velocity bands between 2800 and 4000 m/s adopt a nearly parallel disposition, mimicking the topographic drop eastwards (from 3300 to 2600 m a.s.l.). This 'subparallel' trend is visible up to 4400 m/s, above which the data is more irregular.

4.3. Gravity survey and density structure

The density modeling was carried out using several constraints to define the geometries of the modeled bodies; a primary source of information was the geological maps by Becerra et al. (2014) and Henríquez et al. (2014). It was assumed that long-wavelength gravity anomalies were a response to density contrasts between the upper Mesozoic-Cenozoic outcrops and the basement, defined as older units belonging especially to the Triassic (such as the Tuina Fm., Fig. 2). The latter are found cropping out at the western edge of the profile, thus allowing to define one of the endpoints of the regional gravity trend.

Since the only basement outcrops at the eastern border of the Salar de Atacama are found ca. 38 km south of the eastern end of the profile, it was necessary to use the velocity data (Figs. 8 & 9), and the interpretations of the seismic sections (Figs. 6 & 7) to constrain the gravity trend. In this way the chosen regional trend is in agreement with more than one independent set of data. More importantly, the overall geometry of the modeled bodies does not undergo significant changes with slight variations of this fix. The dataset mentioned above was also crucial in understanding subsurface structural styles, and both the folding and faulting variations along the section. The bodies were modeled as contrasts relative to a background of density 0 g/cc^3, represented by the pre-Jurassic formations (Figs. 2 & 3). The contrasts for the sedimentary units were chosen after several iterations of the modeling, following the shape of the bodies seen in the seismic sections, the velocity data and the regional geology (see Table 2).

Fig. 10 shows the complete Bouguer Anomaly, with multiple short-wavelength deviations from the regional tendency. Following both the seismic sections and the velocity data (Figs. 6, 7, 8 & 9), the gravity highs have been linked to the presence near the surface of Triassic rocks and/or structural highs; conversely, the gravity lows have been

Table 2
Density contrasts used in the gravity modeling (Fig. 10).

Geological unit	Density contrast (gr/cm3)
Pliocene to Quaternary gravels and evaporites	−0.47
Pliocene Ignimbrites	−0.87
Oligocene-Miocene gravels	−0.47
Oligocene-Miocene evaporites and fine-grained clastics	−0.68
Continental, Cretaceous to Paleogene deposits	−0.21
Triassic and pre-Triassic basement	0

interpreted as depocenters involving Cretaceous to Paleogene, coarse continental deposits, Oligocene-Miocene evaporites associated with fine-grained clastics, and the Pliocene to recent cover of the saltpan. From west to east, the first gravity low is associated with exposed, folded rocks belonging to the Purilactis and Barros Arana Formations, which comprise the Barros Arana Syncline (Fig. 2). The gravity model shows this structure, though it also requires that some of its lower members be present underneath the basement towards the west. The best fit to the data requires an average density of -0.21 g/cm^3 for the units of the Barros Arana Syncline. It is relevant to note that the hinge of the Barros Arana Syncline does not coincide with the minimum of the local low gravity anomaly observed in the zone (Fig. 6), which requires the inclusion of a body with the same density associated to the syncline to the west, and the modeling of thin surficial gravels (-0.47 g/cm^3) belonging to recent deposits and the southern fringes of the outcrops belonging to the Oligocene-Miocene Tambores Formation, which have a reduced thickness in this area (Figs. 2 & 6).

Immediately east of the syncline, the following low gravity anomaly shows an east-dipping gradient forming a scoop-shaped geometry (Fig. 10). The gravity high separating both lows has been interpreted as a result of the proximity to the surface of basement rocks, which are not seen cropping out (Figs. 2, 6 & 7). This area involves the transition from the El Bordo Escarpment-Barros Arana Syncline towards the Llano de la Paciencia-Cordillera de la Sal, with a continuous drop in topography interrupted by a sudden raise in surface topography (up to 200 m). Here, the units observed at the surface involve mainly a recent cover of gravels, which are found unconformably overlying folded deposits belonging to Oligocene-Miocene units towards the east (Fig. 5a, b, c). The wedge-shaped geometries seen in Fig. 7 are linked to the San Pedro Formation, showing a much lower density than its surrounding counterparts (-0.68 g/cm^3), and some units of the Late Cretaceous-Paleogene. The eastern side of this gravity anomaly roughly coincides at the surface with the eastern limit of the reverse fault-bound Cordillera de la Sal (Figs. 2 & 7). It is worth mentioning that the depth of the San Pedro Formation in the profile is deeper than seen in Fig. 7, owing to the increase in depth of this limit northwards (around 1200–1300 m in Fig. 6). For simplicity, the deposits of the Vilama Formation have been included within the Oligocene-Miocene deposits for the gravimetric modeling, owing to their reduced thickness in the area (Fig. 2; Blanco et al., 2000; Henríquez et al., 2014).

The area east of the Cordillera de la Sal shows both a progressive increase in topography towards the Western Cordillera, and a relatively flat, east-dipping gravity signal (Fig. 10). The area presents a recent cover involving gravels and recent evaporites, along with Pliocene ignimbrites towards the east (Fig. 2). The density used to model the latter is -0.87 g/cm^3, which is within the range used for modeling similar ignimbrites in the Pacana Caldera, east of the study area (Delgado and Pavez, 2015). This "flat" gravity signal follows both the reflectors seen in the seismic sections (Fig. 7) and a prominent change in velocity (Fig. 9), separating the evaporitic and fine-grained clastic deposits from the older, denser Cretaceous to Paleogene units. The units show a progressive tapering towards the east, and the basement in the area adopts a west-dipping disposition, as seen in outcrops along the southeastern border of the basin (Fig. 7; Becerra et al., 2014).

4.4. -Maximum depositional ages and relevant populations

4.4.1. Sample SP3-85 (Seilao Member, Purilactis Fm.)

The maximum depositional age obtained for the sample belonging to the Seilao Member is 69.1 ± 1.0 Ma (Fig. 11a). The major populations are clustered around 294 Ma (n = 24, Permo-Carboniferous), followed by Upper Cretaceous populations (n = 11 and 10 at 70 and 88 Ma, respectively). Other sizeable populations occur between 93 and 96 Ma (n = 17, mid-Cretaceous), between 78 and 82 (n = 9, Late Cretaceous) and at 142 Ma (n = 6, Early Cretaceous). The major relative probability peaks are found at 70 (Maastrichtian) and 294 Ma (Sakmarian), followed by peaks at 88 and 142 Ma (Coniacian and Berriasian, respectively).

4.4.2. Sample SP3-86 (Vizcachita Member, Purilactis Fm.)

The first of two samples of the Vizcachita Member (Fig. 11b), obtained close to the contact with the Seilao Member, has a maximum depositional age of 66.8 ± 0.7 Ma, with large populations around this same age (n = 23) and 291 Ma (n = 45). The relative probability plot shows high peaks at 67 Ma (Maastrichtian) and 291 Ma (Sakmarian).

4.4.3. Sample SP3-92 (Pajarito Member, Purilactis Fm.)

The maximum depositional age obtained for this sample is 69.3 ± 0.8 Ma (Fig. 11c), with large populations at 73 Ma (n = 37, Late Cretaceous), 292 Ma (n = 15, Early Permian), 304 Ma (n = 12, Late Carboniferous), and 204 Ma (n = 8, Late Triassic). Its highest relative probability peaks are found at 73 Ma (Campanian), 204 Ma (Rhetian) and 292 Ma (Sakmarian).

4.4.4. Sample SP3-94 (Vizcachita Member, Purilactis Fm.)

The second sample of the Vizcachita Member, found towards its base, shows some noteworthy differences (Fig. 11d). The maximum depositional age for this sample is 65.2 ± 0.7 Ma, around which it has its largest population (n = 47 for 69 Ma, Late Cretaceous). A smaller population is also found at 76 Ma (n = 7), and only n = 3 zircons at 297 Ma (Early Permian). As with its composition, its relative probability plot differs from that of sample SP3-86, although it shares a peak at 69 Ma (Maastrichtian).

4.4.5. Population provenance

Many of the populations found in these samples have already been linked to their possible geological sources by Bascuñán et al. (2016). A summary of each identified source is shown below.

The oldest and most recurring population belongs to the 291–304 Ma range (early Permian-late Carboniferous), which has been ascribed to the upper Carboniferous-Permian units cropping out along the Cordillera de Domeyko, such as the Complejo Intrusivo Sierra de Limón Verde (Marinovic and Lahsen, 1984), the Agua Dulce Formation, and other granitoids and related intrusives (Basso and Mpodozis, 2012; Breitkreuz et al., 1992; Ramírez and Gardeweg, 1982). Only one of the samples shows a sizeable population belonging to the Late Triassic (204 Ma), whose provenance might be one of several Triassic outcrops, such as the Las Lomas and El Bordo beds (Fig. 2, Basso and Mpodozis, 2012), or the uppermost Tuina Formation (Henríquez et al., 2014; Narea et al., 2015). The detrital zircons associated with the Late Jurassic-Early Cretaceous (142 Ma) derive from the erosion of andesites and intrusives within the age range located farther to the west, around the Coastal Cordillera (Oliveros et al., 2006; Pichowiak et al., 1990). The basal units of the Tonel Formation could also be a source of recycled zircons (Bascuñán et al., 2016).

The populations within the Late Cretaceous show different clusters, of which some are closer to the early Late Cretaceous (for example, Sample SP3-85). These may come either from formations representing the volcanic arc of that time in the Central Valley (Quebrada Mala and Paradero del Desierto formations; Cortés, 2000; Marinovic and García, 1999). Basso and Mpodozis (2012) also report intrusives with ages

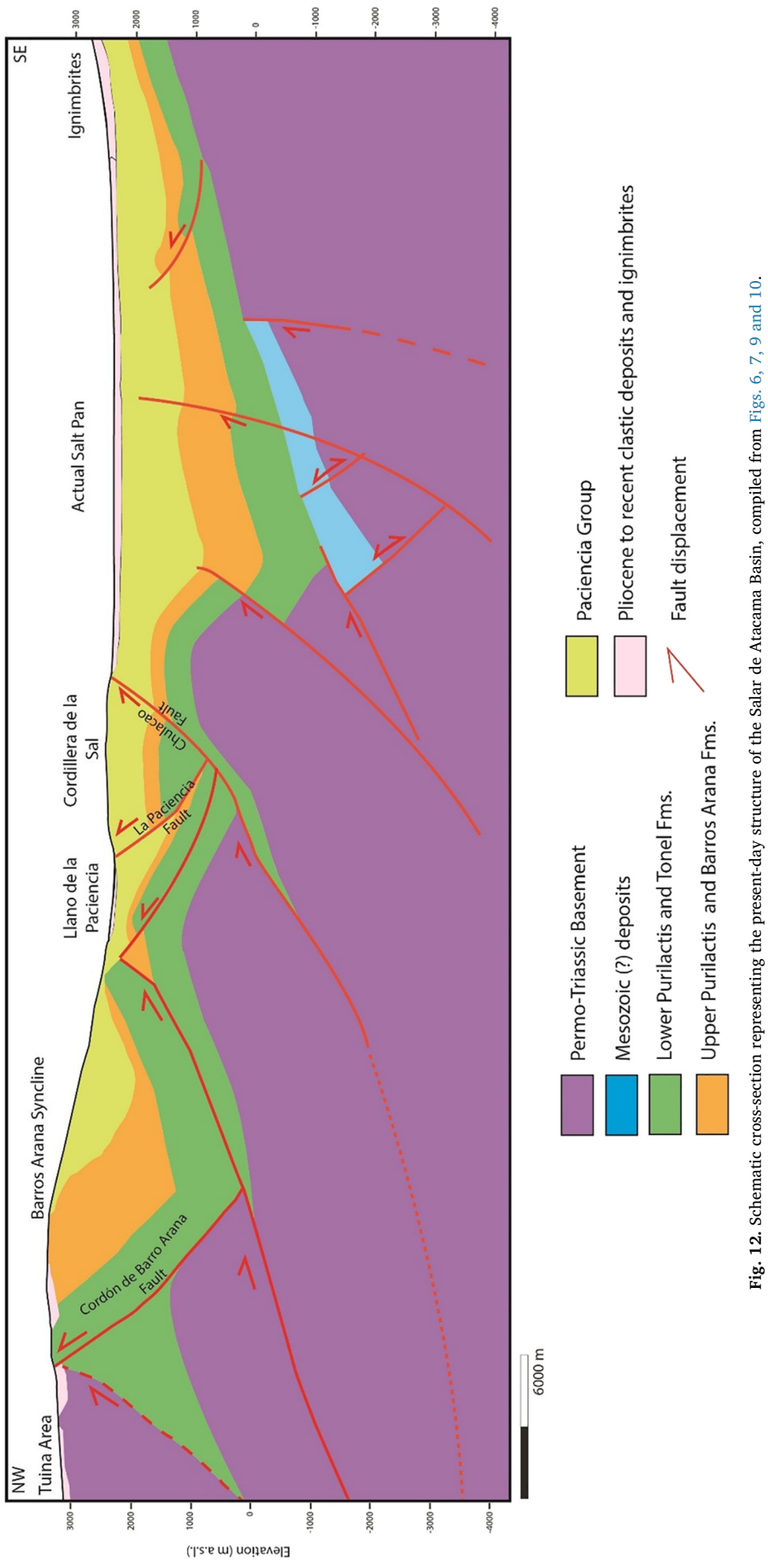

Fig. 12. Schematic cross-section representing the present-day structure of the Salar de Atacama Basin, compiled from Figs. 6, 7, 9 and 10.

between 76 and 99 Ma intruding the Caracoles Group at the Cerro de Caracoles area. The latest Upper Cretaceous-Paleocene zircons, which reach into the Danian, may come from the erosion of various intrusives of Late Cretaceous-Paleocene age west of the study area, of which the closest outcrops can be found around Cerro Quimal, southwest of the study area (Basso and Mpodozis, 2012; Mpodozis et al., 2005).

5. Discussion

The results obtained above and their integration (Fig. 12) aid in understanding the evolution of the Salar de Atacama Basin, and of the Pre Andean Depression. The gravimetric modeling of the Barros Arana Syncline coincides with the interpretation of the syncline as obtained from seismic sections (Figs. 4 & 6), although, and in contrast with previous interpretations, the presence of Late Cretaceous-Paleogene units has been identified both to the west and east of the syncline. To the west, these units are part of the first gravimetric low, and are overlain by the outcropping Tuina Formation (Fig. 2). This area, comprising most of the western flank of the syncline, consistently shows the highest interval velocities within the study area regardless of depth, also showing large vertical gradients when compared with areas farther to the east (Figs. 8 & 9). The reason for this segmentation of the velocity properties within the study area can be ascribed to the presence beneath the surface of both the Tuina Formation and the formations comprising the syncline, which are expected to possess higher velocities than their more recent counterparts, based on lithology alone. The presence of Late Cretaceous-Paleocene intrusives (Fig. 2) may also affect the velocity around this area, but their outcrops are scarce and widely spaced, and, as such, their effect on the measurements may be only local; the same argument can be made for the gravity modeling. The decrease in velocity seen in the eastern flank of the syncline/western side of the basin, at all depth slices (Fig. 8), must take into consideration the lack of velocity data around this area, with a gap in velocity points roughly between the syncline axis and the western border of the Llano de la Paciencia. An analysis of the points north of this area (Figs. 2, 8 & 9b) shows that the transition from the syncline towards the basin might be smoother than seen in the velocity cross-section (Fig. 9a), with a steady drop in velocity and a trend semi parallel to the topography. This transition agrees with the structural continuity seen in the seismic sections due south (Figs. 6 & 7), where the basement is progressively found at an increasing depth towards the east. Some variations may occur due to the position of the Oligo-Miocene Tambores Formation, which have been modeled in the gravity section as less dense than their older counterparts, and whose thickest deposits are found near the center of the eastern flank of the syncline (Fig. 2). However, the gravimetric/velocity sections are located on the southern, thinner parts of this formation, which should only affect measurements mildly (see above).

The velocity and gravity models do not allow for the differentiation between the members belonging to the Tonel, Purilactis and Barros Arana Formations (Purilactis Group sensu Mpodozis et al., 2005), but they can be clearly distinguished from the outcropping Oligo-Miocene or recent strata (Fig. 5b), which is relevant to infer the presence of the former units beneath the surface to the east. In particular, the low-density San Pedro Formation, which comprises most of the Cordillera de la Sal, is the most sensitive to variations in thickness and shape regarding the gravimetric model, and thus delimits the late Paleogene-Neogene geometry of the basin. Regarding its shape, the gravimetric model shows a steady drop in gravity from the syncline border towards the Cordillera de la Sal, where the gravity signal suggests a depocenter with a higher slope on its west-tilted eastern edge (Fig. 10). This feature may be due to the proximity to the surface of Triassic units, which is obtained both from the modeling and the analysis of seismic sections, and also because of the pop-up like deformation of the Late Cretaceous-Paleocene rocks assumed to underlie the San Pedro Formation (Figs. 7 & 10). The bottom, scoop-shaped surface of the San Pedro Formation shows an increasing depth northward, from around 800 m in Fig. 7 to 1200–1300 m in Fig. 6, which is consistent with the gravity modeling. As for the velocities within this depocenter, they are on average lower than those found, at the same altitude in the syncline area, and the slices between 1500 and 1250 m a.s.l. show a local, roughly NNE, high-velocity zone beneath the Cordillera de la Sal, which might be related to the proximity of Triassic and Upper Cretaceous-Paleocene units, albeit not conclusively (Fig. 8). The cross section in this area presents artifacts or noise possibly arising from the intense deformation of the Cordillera de la Sal, which also includes salt diapirs and other complex structures arising from salt tectonics (Fig. 2; Rubilar et al., 2017; Wilkes and Görler, 1994). A different situation can be observed east of the Cordillera de la Sal, where the velocity cross-section shows a prominent, near-horizontal contrast between low-velocity units above (up to 2600–2800 m/s), and high-velocity units below (Figs. 8 and 9). This abrupt transition is at an altitude between 1400 and 1600 m a.s.l., which is consistent with the limit between the San Pedro Formation and older Upper Cretaceous-Paleogene units as interpreted from the seismic sections (Fig. 7). Accordingly, this limit was used to constrain the gravimetric modeling of the low-density deposits, underscoring again the contrast between the San Pedro Formation and the pre-Oligocene units, as described to the west.

The addition of new U-Pb detrital zircon age data is relevant to further unravel the development of the Salar de Atacama Basin. The obtained age populations are in general agreement with those previously published by several authors (see Table 1), with minor differences. As such, the populations identified in these rocks indicate the erosion of a source composed mainly of Late Cretaceous and Permian-Carboniferous rocks, with minor additions of Late Jurassic-Early Cretaceous and Late Triassic zircons. The sources of these zircon populations have been shown to lie west of the study area, which is also supported by previous paleocurrent studies (Bascuñán et al., 2016; Hartley et al., 1992a, 1988). This western, exhumed source might range from the Cordillera de Domeyko to sources even farther to the west, such as the Late Cretaceous rocks of the Central Valley and the Late Jurassic-Early Cretaceous arc of the actual Coastal Cordillera, in successive steps (Bascuñán et al., 2016).

What is strikingly different from previous data is the recognition of younger zircon populations in the Purilactis Formation reaching the Danian (earliest Paleocene) (Fig. 11b, d). They are particularly evident in the Vizcachita Member, whose maximum depositional ages are clearly from the K-T interval, thus redefining the age of the Purilactis and Barros Arana Formations, which were previously assigned to the Late Cretaceous-KT range (107–65 Ma, e.g., Arriagada et al., 2006a; Bascuñán et al., 2016; Jordan et al., 2007), and whose cap was presumed to be the volcanic Cerro Totola Formation found south of the study area, with ages between 61 and 70 Ma (Table 1; Basso and Mpodozis, 2012; Mpodozis et al., 2005). Also, the age of the Vizcachita Member is in partial agreement with the Ar-Ar age of an altered lava flow within the same member obtained by Flint et al. (1989), dated at 63.8 ± 1.9 Ma. As such, the Vizcachita Member is a time equivalent of the Cerro Totola Formation, which is seen overlying lower members of the Purilactis Formation to the south, and which has numerous age-related intrusives around Cerro Quimal and within the Tonel-lower Purilactis Formation (Andriessen and Reutter, 1994; Arriagada, 1999; Basso and Mpodozis, 2012; Mpodozis et al., 2005).

The question of the age of the remaining units within the Barros Arana Syncline is relevant to address the tectonic history of the basin. The only visible geological relation between the Barros Arana Formation and younger units is its angular unconformity with the Oligo-Miocene Tambores Formation (Figs. 2 & 6), which could make these units fit a time range similar as that proposed by Charrier and Reutter (1994), reaching well into the Paleogene. This also brings into discussion the temporal relationship between these units and the Loma Amarilla and Naranja Formations, the latter of which is found south of the study area, but which has been considered part of the Paleocene

evolution of the basin (Figs. 2, 3 & 4; Arriagada et al., 2006a; Jordan et al., 2007; Mpodozis et al., 2005; Pananont et al., 2004). Reiners et al. (2015), based on U-Pb and (U-Th/He) dating of single zircon crystals, obtained ages ranging from 49 to 308 Ma for the Loma Amarilla Formation and 72–81 Ma for the Naranja Formation (Table 1), making their youngest zircons older than previously published depositional ages (between 35 and 45 Ma and 58–45 Ma, respectively, following Hammerschmidt et al. (1992) and Mpodozis et al. (2005)). It must be noted that the maximum depositional ages for the Naranja Formation were obtained 70 km south of Cerro Quimal (Gardeweg et al., 1994; Solari et al., 2017), and as such, the ages of Reiners et al. (2015) are the closest ones for this formation within the study area. For this study, it has been considered that the upper Purilactis-Barros Arana Formations may be partial equivalents to the Naranja Formation (Fig. 4), which raises questions regarding both the angular unconformities described to the south along the El Bordo Escarpment, and those assumed for the units within the basin as correlated with seismic sections (Arriagada, 1999; Arriagada et al., 2006a; Jordan et al., 2007; Mpodozis et al., 2005; Muñoz et al., 2002; Pananont et al., 2004). Another option, which is in partial agreement with previous stratigraphic models, is to place these units within a narrow time range (65–58 Ma). This issue may be resolved with the addition of geochronological data from scarcely dated units, but, in any case, the units belonging to the syncline were deposited under compressive conditions associated with the development of a foreland basin during the Late Cretaceous (Arriagada et al., 2006a; Bascuñán et al., 2016), which continued during the Paleogene (including the K-T Event described by Cornejo et al. (2003, 1993)). These deposits would have been then folded and deformed during the Eocene-Oligocene Incaic Event, a widespread deformation event with high exhumation rates around the Cordillera de Domeyko, clockwise tectonic rotations south of the Arica Bend and the formation of the Bolivian Orocline (Arriagada et al., 2008, 2006a, 2006b; del Papa et al., 2010; Maksaev and Zentilli, 1999; McQuarrie, 2002; Narea et al., 2015; O'Driscoll et al., 2012). Regarding the presence of the Loma Amarilla Formation within the basin, it cannot be either confirmed or overruled with the data presented; it may well form thin intervals, as proposed by Pananont et al. (2004), owing to the strong exhumation and deformation during the time of their deposition, or they may have been cannibalized shortly after their deposition. Both alternatives are in agreement with the deposition of the Loma Amarilla in a wedge-top depozone (DeCelles and Giles, 1996).

After the Incaic Event, extensional conditions, together with strike-slip tectonics, have been inferred for the late Oligocene-early Miocene within the basin (Jordan et al., 2007; Pananont et al., 2004; Rubilar et al., 2017). One of the structures attributed to have generated extension during this stage corresponds to the Paciencia Fault (sensu Pananont et al. (2004)). This fault, found at the eastern flank of the Barros Arana Syncline, would have generated around 6 ± 1 km of vertical displacement, effectively controlling the deposition of the Tambores and San Pedro formations. Arriagada et al. (2006a) found no conclusive evidence for this fault at the surface, but Jordan et al. (2007) and Henríquez et al. (2014) document small normal faults affecting Oligocene-Miocene gravels around the Llano de la Paciencia Area (Fig. 2). Also, Martínez et al. (2017) reported mainly inverted and contractional structures in the Salar de Punta Negra Basin, which corresponds to the southward prolongation of the Salar de Atacama.

The geophysical and seismic data compiled and analyzed in this study agree more closely with a contractional setting for most of the basin history (Fig. 12). Under this scheme, sedimentation in the basin would have started during the Peruvian Phase (Bascuñán et al., 2016), and continued throughout the Paleocene. The actual structural configuration of the basin would have been established mainly during the Incaic Event, with the folding and clockwise rotation of Mesozoic-Cenozoic deposits, and the establishment of a thick-skin, east-verging reverse fault system. Some of these faults would have then been reactivated during the late Miocene (Quechua-Pehuenche events; Charrier et al., 2007; Salfity and Marquillas, 1994; Yrigoyen, 1993), leading to the present structure of the basin, especially around the Cordillera de la Sal area and the western flank of the Barros Arana Syncline. The contribution of strike-slip tectonics cannot be assessed with the methods provided in this contribution.

A compressive, though somewhat stalled setting for the Oligocene-early Miocene is consistent with diverse findings in the Central Andes of NW Argentina and southern Bolivia (Allmendinger et al., 1997; Carrapa et al., 2012; Carrapa and DeCelles, 2008, 2015; Decelles et al., 2011; DeCelles et al., 2015; Del Papa et al., 2013; Horton, 1998; McQuarrie, 2002; Quade et al., 2015; Siks and Horton, 2011), showing a gradual shift of the migration front within the Eastern Cordillera and the rising of the eastern margin of the Puna Plateau. Compressive conditions have also been documented north of the study area in Chile, where Charrier et al. (2013) show no significant extensional event for the Precordillera and Western Altiplano between 18°-19°S. Instead, the tectonostratigraphic evolution of the area is more consistent with the development of a retroarc foreland basin in the Altiplano area during the late Eocene-Oligocene, and the development of the West- and East-verging Thrust Systems during the late Oligocene-early Miocene. The first system generated a significant amount of uplift (0.1 mm/yr) at the western side of the Altiplano, between 26 and 8 Ma (Farías et al., 2005; Nester and Jordan, 2012). Also, Martínez et al. (2017) proposed a synorogenic character for the Pampas de Mula Formation in the Salar de Punta Negra Basin, immediately south of the Salar de Atacama.

Finally, the analysis above suggests that the Salar de Atacama Basin was receiving sediments from western sources related to the progressive shift eastwards of the migration front from the Late Cretaceous onwards, which continued well beyond the Paleocene (Vizcachita Member-Barros Arana Formation). After the rapid shift of the deformation front away from the basin into the Eastern Cordillera (Carrapa and DeCelles, 2015), the basin, now in a hinterland position, would have started accumulating deposits of the Paciencia Group, with coarser units closer to more elevated areas (Tambores Formation), and around 800–1200 m of finer units within the actual basin (San Pedro Formation). After the Oligocene magmatic lull, several large ignimbrites were deposited around the basin, and the current magmatic arc was established shortly afterwards (Charrier et al., 2009; Kay and Coira, 2009). Further compression, rotation and reactivation of previous structures would have then occurred within the basin (Cordillera de la Sal), and at the flanks of the Barros Arana Syncline (Fig. 2; Arriagada et al., 2006a; Hartley et al., 1992b; Mpodozis et al., 2005; Rubilar et al., 2017).

6. Summary and Conclusions

A review of the geology of the Salar de Atacama area, and the addition of independent geophysical and geochronological constraints, leads to a deeper understanding of the geological evolution of the basin during the late Mesozoic-Cenozoic. Seismic velocities within and around the basin show a segmentation of its physical properties, roughly corresponding to the boundaries of different geological units. The seismic reflection profiles show that the structure at this latitude consists of an east-verging thrust system, mainly involving Permo-Triassic, Upper Cretaceous and Paleogene (?) units. The gravimetric survey shows that the main density contrast corresponds to the limit between the evaporitic and clastic units of the San Pedro Formation, the deposits of the Purilactis Group and the presence of Triassic outcrops. The San Pedro Formation shows a stratigraphic wedge whose thickness increases eastwards, and clear angular unconformities separate it from previous units. The U-Pb data show populations in general agreement with previous studies, although a prominent late Campanian-early Maastrichtian signal appears. The stratigraphic continuity of the units within the syncline, and their strongly unconformable relation to the overlying Oligocene deposits, show that the structural configuration of the area was primarily formed during the late Eocene-early Oligocene

Incaic Event. The late Oligocene deposits would represent a post-orogenic infill after the eastward migration of the orogenic front, with varying amounts of compression. This compression would have been more relevant during the late Miocene, which shows a reactivation of previous reverse faults and the generation of the Cordillera de la Sal. This relatively continuous, compressive history of the basin throughout the Cenozoic is in general agreement with regional studies both in Chile and in other neighboring areas of the Central Andes.

Acknowledgements

We would like to thank Empresa Nacional del Petróleo (ENAP) for the access to the seismic sections of the Basin. We are also deeply grateful to Alvaro Henríquez and Andrés Fock of Sociedad Química y Minera de Chile S.A. (SQM) for their logistic support and access to the Toconao camp. We thank the IRD-GET for providing the CG-3 Scintrex gravimeter and Midland Valley Ltd., for the license for MOVE 2017. S.B. acknowledges the support of CONICYT-Chile (Grant 21150380). A.M. acknowledges the support of CONICYT-Chile, under the grants FONDECYT N° 3150160 and PIA/Anillo ACT17202. We also appreciate the suggestions and corrections by two anonymous reviewers, which improved this contribution. Sergio Villagrán, Marco Vaccaris and Luis Acevedo are deeply thanked as well for their invaluable field support and software assistance.

Appendix A. Supplementary data

Supplementary data to this article can be found online at https://doi.org/10.1016/j.tecto.2019.04.008.

References

Al-Chalabi, M., Rosenkranz, P.L., 2002. Velocity-depth and time-depth relationships for a decompacted uplifted unit. Geophys. Prospect. 50, 661–664. https://doi.org/10.1046/j.1365-2478.2002.00345.x.

Allmendinger, R.W., Jordan, T.E., Kay, S.M., Isacks, B.L., 1997. The Evolution of the Altiplano-Puna Plateau of the Central Andes. Annu. Rev. Earth Planet. Sci. 25, 139–174. https://doi.org/10.1146/annurev.earth.25.1.139.

Amilibia, M., Sàbat, F., McClay, K.R., Muñoz, J.A., Roca, E., Chong, G., 2008. The role of inherited tectono-sedimentary architecture in the development of the central Andean mountain belt: insights from the Cordillera de Domeyko. J. Struct. Geol. 30, 1520–1539. https://doi.org/10.1016/j.jsg.2008.08.005.

Andriessen, P.A.M., Reutter, K.-J., 1994. K-Ar and fission track mineral age determination of igneous rocks related to multiple magmatic arc systems along the 23°S latitude of Chile and NW Argentina. In: Reutter, K.-J., Scheuber, E., Wigger, P. (Eds.), Tectonics of the Southern Central Andes: Structure and Evolution of an Active Continental Margin. Springer, New York, pp. 141–154.

Arriagada, C., 1999. Geología y Paleomagnetismo del Borde Oriental de la Cordillera de Domeyko entre los 22°45′ y 23°30′ latitud Sur. II Región, Chile. Universidad de Chile.

Arriagada, C., Cobbold, P.R., Roperch, P., 2006a. Salar de Atacama basin: a record of compressional tectonics in the central Andes since the mid-Cretaceous. Tectonics 25https://doi.org/10.1029/2004TC001770. n/a-n/a.

Arriagada, C., Roperch, P., Mpodozis, C., Fernandez, R., 2006b. Paleomagnetism and tectonics of the southern Atacama Desert (25–28°S), northern Chile. Tectonics 25. https://doi.org/10.1029/2005TC001923.

Arriagada, C., Roperch, P., Mpodozis, C., Cobbold, P.R., 2008. Paleogene building of the Bolivian Orocline: tectonic restoration of the central Andes in 2-D map view. Tectonics 27https://doi.org/10.1029/2008TC002269. n/a-n/a.

Bascuñán, S., Arriagada, C., Le Roux, J., Deckart, K., 2016. Unraveling the Peruvian Phase of the Central Andes: Stratigraphy, sedimentology and geochronology of the Salar de Atacama Basin (22°30-23°S), northern Chile. Basin Res. 28, 365–392. https://doi.org/10.1111/bre.12114.

Basso, M., Mpodozis, C., 2012. Carta Cerro Quimal, Región de Antofagasta. Servicio Nacional de Geología y Minería, Carta Geológica de Chile, Serie Geología Básica 143: 46 p. 1 mapa escala 1:100.000. Santiago, Chile.

Becerra, J., Henríquez, S., Arriagada, C., 2014. Geología del Área de Salar de Atacama, Región de Antofagasta. Carta Geológica de Chile. Serie Geología Básica 166. 1 mapa escala 1:100.000. Santiago, Chile.

Blakely, R.J., 1996. Potential Theory in Gravity and Magnetic Applications. Cambridge University Press, New York. https://doi.org/10.1017/CBO9780511549816.

Blanco, N., Mpodozis, C., Gardeweg, M., Jordan, T.E., 2000. Sedimentación del Mioceno Superior-Plioceno en la Cuenca del Salar de Atacama: Estratigrafía de la Formación Vilama, II Región de Antofagasta. In: IX Congreso Geológico Chileno, Actas 1. Puerto Varas, Chile, pp. 446–450.

Bosio, P.P., Powell, J., del Papa, C., Hongn, F., 2009. Middle Eocene deformation–sedimentation in the Luracatao Valley: Tracking the beginning of the foreland basin of northwestern Argentina. J. South Am. Earth Sci. 28, 142–154. https://doi.org/10.1016/j.jsames.2009.06.002.

Breitkreuz, C., Van Schmus, W.R., 1996. U/Pb geochronology and significance of Late Permian ignimbrites in Northern Chile. J. S. Am. Earth Sci. 9, 281–293.

Breitkreuz, C., Helmdach, F.F., Kohring, R., Mosbrugger, V., 1992. Late Carboniferous Intra-arc sediments in the north Chilean Andes: stratrigraphy, paleogeograhpy and paleoclimate. Facies 26, 67–80.

Brüggen, J., 1934. Las Formaciones de Sal y Petróleo de la Puna de Atacama. Boletín Minas y Petróleo 32, 105–122.

Brüggen, J., 1942. Geología de la Puna de San Pedro de Atacama y sus formaciones areniscas y arcillas rojas. In: Congreso Panamericano de Ingeniería de Minas y Geológica, Actas 2, pp. 342–467.

Brüggen, J., 1950. Fundamentos de la Geología de Chile. Instituto Geográfico Militar, Santiago, Chile.

Carrapa, B., DeCelles, P.G., 2008. Eocene exhumation and basin development in the Puna of northwestern Argentina. Tectonics 27. https://doi.org/10.1029/2007TC002127.

Carrapa, B., DeCelles, P.G., 2015. Regional exhumation and kinematic history of the central Andes in response to cyclical orogenic processes. In: DeCelles, P.G., Ducea, M.N., Carrapa, B., Kapp, P.A. (Eds.), Geodynamics of a Cordilleran Orogenic System: The Central Andes of Argentina and Northern Chile. Geological Society of America Memoir 212. The Geological Society of America, pp. 201–213. https://doi.org/10.1130/2015.1212(11).

Carrapa, B., Bywater-Reyes, S.B., Decelles, P.G., Mortimer, E.C., Gehrels, G.E., 2012. Late Eocene-Pliocene basin evolution in the Eastern Cordillera of northwestern Argentina (25°–26°S): regional implications for Andean orogenic wedge development. Basin Res. 24, 249–268. https://doi.org/10.1111/j.1365-2117.2011.00519.x.

Catuneanu, O., Galloway, W.E., Kendall, C.G.S.C., Miall, A.D., Posamentier, H.W., Strasser, A., Tucker, M.E., 2011. Sequence stratigraphy: methodology and nomenclature Gebrüder Borntraeger·Stuttgart 2011. Newsletters Stratigr. 44 (3), 173–245.

Charrier, R., Muñoz, N., 1994. Jurassic-Cretaceous Paleogeographic evolution of the Chilean Andes at 23°-24°S.L. and 34°-35°S.L.: a comparative analysis. In: Reutter, K., Scheuber, E., Wigger, P. (Eds.), Tectonics of the Southern Central Andes: Structure and Evolution of an Active Continental Margin. Springer, New York, pp. 233–242.

Charrier, R., Reutter, K., 1990. The Purilactis Group of Northern Chile: link between arc and backarc during Late Cretaceous and Paleogene. In: Proceedings I ORSTOM-ISAG, pp. 249–252 Grenoble.

Charrier, R., Reutter, K., 1994. The Purilactis group of northern Chile: BOUNDARY between arc and backarc from Late Cretaceous to Eocene. In: Reutter, K., Scheuber, E., Wigger, P. (Eds.), Tectonics of the Southern Central Andes: Structure and Evolution of an Active Continental Margin. Springer, New York, pp. 189–202.

Charrier, R., Pinto, L., Rodriguez, M.P., 2007. Tectonostratigraphic evolution of the Andean Orogen in Chile. In: Geology of Chile, pp. 21–114. https://doi.org/10.1144/GOCH.3.

Charrier, R., Farías, M., Maksaev, V., 2009. Evolución Tectónica, Paleogeográfica y Metalogénica durante el Cenozoico en los Andes de Chile norte y central e implicaciones para las regiones adyacentes de Bolivia y Argentina. Rev. la Asoc. Geológica Argentina 65, 5–35.

Charrier, R., Hérail, G., Pinto, L., García, M., Riquelme, R., Farías, M., Muñoz, N., 2013. Cenozoic tectonic evolution in the Central Andes in northern Chile and west central Bolivia: Implications for paleogeographic, magmatic and mountain building evolution. Int. J. Earth Sci. 102, 235–264. https://doi.org/10.1007/s00531-012-0801-4.

Cobbold, P.R., Rossello, E., 2003. Aptian to recent compressional deformation, foothills of the Neuquén Basin, Argentina. Mar. Pet. Geol. 20, 429–443. https://doi.org/10.1016/S0264-8172(03)00077-1.

Cobbold, P.R., Rossello, E.A., Roperch, P., Arriagada, C., Gomez, L.A., Lima, C., 2007. Distribution, Timing, and Causes of Andean Deformation across South America. vol. 272. London Geol. Soc., pp. 321–343. https://doi.org/10.1144/GSL.SP.2007.272.01.17.

Cohen, K., Harper, D.A.T., Gibbard, P.L., 2013. The ICS International Chronostratigraphic Chart.

Coira, B., Koukharsky, M., Guevara, S.R., Cisterna, C.E., 2009. Puna (Argentina) and northern Chile Ordovician basic magmatism: a contribution to the tectonic setting. J. S. Am. Earth Sci. 27, 24–35. https://doi.org/10.1016/j.jsames.2008.10.002.

Cornejo, P., Mpodozis, C., Ramirez, C.F., Tomlinson, A.J., 1993. Estudio Geológico de la Región de El Salvador y Potrerillos. Servicio Nacional de Geología y Minería, Informe Registrado IR-93-1. Santiago, Chile.

Cornejo, P., Matthews, S., Perez de Arce, C., 2003. The 'K-T' compressive deformation event in northern Chile (24-27°S). X Congr. Geol. Chil. CD-Rom 1–13.

Cortés, J., 2000. Hoja Palestina, Región de Antofagasta. Servicio Nacional de Geología y Minería, Mapas Geológicos 19. 1 mapa escala 1:100.000. Santiago, Chile.

Cross, T.A., Lessenger, M.A., 1988. Seismic stratigraphy. Annu. Rev. Earth Planet. Sci. 16, 319–354.

DeCelles, P.G., Giles, K.A., 1996. Foreland basin systems - reply. Basin Res. 9, 172–176.

Decelles, P.G., Carrapa, B., Horton, B.K., Gehrels, G.E., 2011. Cenozoic foreland basin system in the central Andes of northwestern Argentina: implications for Andean geodynamics and modes of deformation. Tectonics 30, 1–30. https://doi.org/10.1029/2011TC002948.

DeCelles, P.G., Zandt, G., Beck, S.L., Currie, C.A., Ducea, M.N., Kapp, P., Gehrels, G.E., Carrapa, B., Quade, J., Schoenbohm, L.M., 2015. Cyclical orogenic processes in the Cenozoic central Andes. In: Decelles, P.G., Ducea, M.N., Carrapa, B., Kapp, P.A. (Eds.), Geodynamics of a Cordilleran Orogenic System: The Central Andes of Argentina and Northern Chile. Geological Society of America Memoir 212. The Geological Society of America, pp. 459–490. https://doi.org/10.1130/2015.1212(22).

Del Papa, C., Hongn, F., Powell, J., Payrola, P., Do Campo, M., Strecker, M.R., Petrinovic, I., Schmitt, A.K., Pereyra, R., 2013. Middle Eocene-Oligocene broken-foreland

evolution in the Andean Calchaqui Valley, NW Argentina: insights from stratigraphic, structural and provenance studies. Basin Res. 25, 574–593. https://doi.org/10.1111/bre.12018.
Delgado, F., Pavez, A., 2015. New insights into La Pacana caldera inner structure based on a gravimetric study (central Andes, Chile). Andean Geol. 42, 313–328. https://doi.org/10.5027/andgeoV42n3-a02.
Dingman, R.J., 1963. Cuadrángulo Tulor. Instituto de Investigaciones Geológicas, Carta geológica de Chile 11:1–35. 1 mapa escala 1:50.000.
Dingman, R.J., 1967. Geology and Groundwater Resources of the Northern part of the Salar de Atacama, Antofagasta Province, Chile. U.S. Geol. Surv. Bull 1249, 1–49.
Dix, C.H., 1955. Seismic velocities from surface measurements. Geophysics 20, 68–86.
Farías, M., Charrier, R., Comte, D., Martinod, J., Hérail, G., 2005. Late Cenozoic deformation and uplift of the western flank of the Altiplano: evidence from the depositional, tectonic, and geomorphologic evolution and shallow seismic activity (northern Chile at 19°30′S). Tectonics 24, 1–27. https://doi.org/10.1029/2004TC001667.
Fildani, A., Cope, T.D., Graham, S.A., Wooden, J.L., 2003. Initiation of the Magallanes foreland basin: timing of the southernmost Patagonian Andes orogeny revised by detrital zircon provenance analysis. Geology 31, 1081–1084. https://doi.org/10.1130/G20016.1.
Flint, S., 1985. Alluvial fan and playa sedimentation in an Andean arid, closed basin: the Paciencia Group (mid Tertiary), Antofagasta Province, Chile. J. Geol. Soc. Lond. 141, 533–546.
Flint, S., Hartley, A.J., Rex, D.C., Guise, P., Turner, P., 1989. Geochronologv of the purilactis formation, northern Chile: an insight into late cretaceous/earlv tertiarv basin dvnamics of the central Andes. Rev. Geológica Chile 16, 241–246.
Flint, S., Turner, P., Jolley, E.J., Hartley, A.J., 1993. Extensional Tectonics in Convergent Margin Basins - an example from the Salar-De-Atacama. Chilean Andes. Geol. Soc. Am. Bull. 105, 603–617. https://doi.org/10.1130/0016-7606(1993)105<0603.
Gansser, A., 1973. Facts and theories on the Andes: Twenty-sixth William Smith Lecture. J. Geol. Soc. Lond. 129, 93–131. https://doi.org/10.1144/gsjgs.129.2.0093.
Gardeweg, M., Pino, H., Ramírez, C.F., Davidson, J., 1994. Mapa Geológico del área de Imilac y Sierra Almeida, Región de Antofagasta. Servicio Nacional de Geología y Minería. Documento de Trabajo 7. 1 mapa escala 1:100.000. Santiago, Chile.
Gianni, G.M., Navarrete, C.G., Folguera, A., 2015. Synorogenic foreland rifts and transtensional basins: a review of Andean imprints on the evolution of the San Jorge Gulf, Salta Group and Taubaté Basins. J. S. Am. Earth Sci. 64, 288–306. https://doi.org/10.1016/j.jsames.2015.08.004.
Götze, H.-J., Krause, S., 2002. The Central Andean gravity high, a relic of an old subduction complex? J. S. Am. Earth Sci. 14, 799–811. https://doi.org/10.1016/S0895-9811(01)00077-3.
Götze, H.-J., Lahmeyer, B., Schmidt, S., Strunk, S., 1994. The Lithospheric Structure of the Central Andes (20°-26°S) as Inferred from Interpretation of Regional Gravity. In: Reutter, K., Scheuber, E., Wigger, P. (Eds.), Tectonics of the Southern Central Andes: Structure and Evolution of an Active Continental Margin. Springer, New York, pp. 7–21.
Hammerschmidt, K., Döbel, R., Friedrichsen, H., 1992. Implications of 40Ar/39Ar dating of Tertiary volcanic rocks from the north-Chilean Precordillera. Tectonophysics 202, 55–81.
Hartley, A.J., Flint, S., Turner, P., 1988. A proposed lithostratigraphy for the Cretaceous Purilactis Formation, Antofagasta Province, northern Chile. In: Congreso Geológico Chileno, No. 5, Actas 3. Santiago, Chile, pp. H83–H99.
Hartley, A.J., Flint, S., Turner, P., Jolley, E.J., 1992a. Tectonic controls on the development of a semi-arid alluvial basin as reflected in the stratigraphy of the Purilactis Group (upper cretaceous-eocene), northern Chile. J. S. Am. Earth Sci. 5, 275–296. https://doi.org/10.1016/0895-9811(92)90026-U.
Hartley, A.J., Jolley, E.J., Turner, P., 1992b. Paleomagnetic evidence for rotation in the Precordillera of northern Chile: structural constraints and implications for the evolution of the Andean forearc. Tectonophysics 205, 49–64. https://doi.org/10.1016/0040-1951(92)90417-5.
Henríquez, S., Becerra, J., Arriagada, C., 2014. Geología del área San Pedro de Atacama, Región de Antofagasta. Servicio Nacional de Geología y Minería. Carta Geológica de Chile Serie Geología Básica 171. 1 Mapa escala 1:100,000. Santiago, Chile.
Hongn, F., del Papa, C., Powell, J., Petrinovic, I., Mon, R., Deraco, V., 2007. Middle Eocene deformation and sedimentation in the Puna-Eastern Cordillera transition (23°-26°S): Control by preexisting heterogeneities on the pattern of initial Andean shortening. Geology 35, 271–274. https://doi.org/10.1130/G23189A.1.
Horton, B.K., 1998. Sediment accumulation on top of the Andean orogenic wedge: Oligocene to late Miocene basins of the Eastern Cordillera, southern Bolivia. Bull. Geol. Soc. Am. 110, 1174–1192. https://doi.org/10.1130/0016-7606(1998)110<1174:SAOTOT>2.3.CO;2.
Jaillard, E., 1992. La Fase Peruana (Cretáceo Superior) en la Margen Peruana. Boletín la Soc. Geológica del Perú 83, 81–87.
Jaillard, E., 1993. L'évolution tectonique de la marge péruvienne au Sénonien et Paléocene et ses relations avec la géodynamique. 164. Bull. la Société Géologique Fr, pp. 819–830.
Jaimes, E., de Freitas, M., 2006. An Albian-Cenomanian unconformity in the northern Andes: evidence and tectonic significance. J. S. Am. Earth Sci. 21, 466–492. https://doi.org/10.1016/j.jsames.2006.07.011.
Jolley, E.J., Turner, P., Williams, G.D., Hartley, A.J., Flint, S., 1990. Sedimentological response of an alluvial system to Neogene thrust tectonics, Atacama Desert, northern Chile. J. Geol. Soc. Lond. 147, 769–784. https://doi.org/10.1144/gsjgs.147.5.0769.
Jordan, T.E., Muñoz, N., Hein, M., Lowenstein, T., Godfrey, L., Yu, J., 2002. Active faulting and folding without topographic expression in an evaporite basin. Chile. https://doi.org/10.1130/0016-7606(2002)114<1406.
Jordan, T.E., Mpodozis, C., Muñoz, N., Blanco, N., Pananont, P., Gardeweg, M., 2007. Cenozoic subsurface stratigraphy and structure of the Salar de Atacama Basin, northern Chile. J. S. Am. Earth Sci. 23, 122–146. https://doi.org/10.1016/j.jsames.2006.09.024.
Kay, S.M., Coira, B.L., 2009. Lithospheric loss, magmatism, and crustal flow under the central Andean Altiplano-Puna Plateau. Geol. Soc. Am. Mem. 204 (11), 1–32. https://doi.org/10.1130/2009.1204.
Kay, S.M., Godoy, E., Kurtz, A., 2005. Episodic arc migration, crustal thickening, subduction erosion, and magmatism in the south-central Andes. Bull. Geol. Soc. Am. 117, 67–88. https://doi.org/10.1130/B25431.1.
del Papa, C., Kirschbaum, A., Powell, J., Brod, A., Hongn, F., Pimentel, M., 2010. Sedimentological, geochemical and paleontological insights applied to continental omission surfaces: a new approach for reconstructing an eocene foreland basin in NW Argentina. J. S. Am. Earth Sci. 29, 327–345. https://doi.org/10.1016/j.jsames.2009.06.004.
Longman, I.M., 1959. Formulas for computing the tidal acceleration due to the Moon and Sun. J. Geophys. Res. 64, 2351–2355.
Ludwig, K.R., 2008. Isoplot 3.6. Berkeley Geochronology Center Special Publication 4.
Macellari, C.E., Su, M.J., Townsend, F., 1991. Structure and seismic stratigraphy of the Atacama Basin (northern Chile). In: Congreso Geológico Chileno, No. 6, Actas 1, pp. 133–137.
Maksaev, V., Zentilli, M., 1999. Fission track thermochronology of the Domeyko Cordillera, northern Chile: Implications for Andean tectonics and porphyry copper metallogenesis. Explor. Min. Geol. 8, 65–89.
Marinovic, N., García, M., 1999. Hoja Pampa Unión. Región de Antofagasta. Servicio Nacional de Geología Y Minería, Mapas Geológicos 9. 1 mapa escala 1:100.000. Santiago, Chile.
Marinovic, N., Lahsen, A., 1984. Hoja Calama. Servicio Nacional de Geología Y Mineria, Carta Geológica de Chile 58. 1 mapa escala 1:250.000. Santiago, Chile.
Martínez, F., Arriagada, C., Mpodozis, C., Peña, M., 2012. The Lautaro Basin: A Record of Inversion Tectonics in Northern Chile. vol. 39.
Martínez, F., Arriagada, C., Peña, M., Del Real, I., Deckart, K., 2013. The structure of the Chañarcillo Basin: an example of tectonic inversion in the Atacama region, northern Chile. J. S. Am. Earth Sci. 42, 1–16. https://doi.org/10.1016/j.jsames.2012.07.001.
Martínez, F., Gonzalez, R., Bascuñan, S., Arriagada, C., 2017. Structural styles of the Salar de Punta Negra Basin in the Preandean Depression (24°-25°S) of the Central Andes. J. S. Am. Earth Sci. 1–12. https://doi.org/10.1016/j.jsames.2017.08.004.
McQuarrie, N., 2002. The kinematic history of the central Andean fold-thrust belt, Bolivia: Implications for building a high plateau. Bull. Geol. Soc. Am. 114, 950–963. https://doi.org/10.1130/0016-7606(2002)114<0950:TKHOTC>2.0.CO;2.
Megard, F., 1984. The Andean orogenic period and its major structures in central and northern Peru. J. Geol. Soc. Lond. 141, 893–900. https://doi.org/10.1144/gsjgs.141.5.0893.
Merino, R., Salazar, E., Mora-Franco, C., Creixell, C., Coloma, F., Oliveros, V., 2013. Fluvial deposition and retro-arc volcanism in a Late Cretaceous foreland basin and the unroofing of the Early Cretaceous arc in the chilean Frontal Cordillera at 28°30′S, Atacama Region. Bolletino di Geofis. Teor. ed Appl. 54, 237–238.
Montero-López, C., del Papa, C., Hongn, F., Strecker, M.R., Aramayo, A., 2018. Synsedimentary broken-foreland tectonics during the Paleogene in the Andes of NW Argentine: new evidence from regional to centimetre-scale deformation features. Basin Res. 30, 142–159. https://doi.org/10.1111/bre.12212.
Mpodozis, C., Arriagada, C., Roperch, P., 1999. Cretaceous to Paleogene Geology of the Salar de Atcama Basin, northern Chile: A reappraisal of the Purilactis Group Stratigraphy. In: Proceedings IV IRD-ISAG, pp. 523–526 IRD Editions, Goettingen, Germany.
Mpodozis, C., Blanco, N., Jordan, T.E., Gardeweg, M., 2000. Estratigrafía y Deformación del Cenozoico Tardío en la Región norte de la Cuenca del Salar de Atacama: La zona de Vilama-Pampa Vizcachitas. In: Congreso Geológico Chileno No. 9 Actas, 2. Puerto Varas, Chile, pp. 598–603.
Mpodozis, C., Arriagada, C., Basso, M., Roperch, P., Cobbold, P., Reich, M., 2005. Late Mesozoic to Paleogene stratigraphy of the Salar de Atacama Basin, Antofagasta, Northern Chile: implications for the tectonic evolution of the Central Andes. Tectonophysics 399, 125–154. https://doi.org/10.1016/j.tecto.2004.12.019.
Muñoz, N., Charrier, R., Jordan, T., 2002. Interactions between basement and cover during the evolution of the Salar de Atacama Basin, northern Chile. Rev. geológica Chile 29, 3–29. https://doi.org/10.4067/S0716-02082002000100004.
Naranjo, J.A., Ramirez, C.F., Pankoff, R., 1994. Morphostratigraphic evolution of the northwestern margin of the Salar de Atacama basin (23°S-68°W). Andean Geol. 21, 91–103. https://doi.org/10.5027/andgeov21n1-a05.
Narea, K., Peña, M., Bascuñán, S., Becerra, J., Gómez, I., Deckart, K., Munizaga, F., Maksaev, V., Arriagada, C., Roperch, P., 2015. Paleomagnetism of Permo-Triassic and Cretaceous rocks from the Antofagasta region, northern Chile. J. S. Am. Earth Sci. 64, 261–272. https://doi.org/10.1016/j.jsames.2015.09.008.
Nester, P., Jordan, T., 2012. The Pampa del Tamarugal Forearc Basin in Northern Chile: the interaction of tectonics and climate. Tectonics Sediment. Basins Recent Adv 369–381. https://doi.org/10.1002/9781444347166.ch18.
Niemeyer, H., 1989. El Complejo Ígneo-Sedimentario del Cordón de Lila, Región de Antofagasta: significado tectónico. Rev. Geológica Chile 16, 163–181.
Niemeyer, H., 2013. Geología del área Cerro Lila-Peine, Región de Antofagasta. In: Servicio Nacional de Geología y Mineria. Carta Geológica de Chile, Serie Geología Básica 147. 1 mapa escala 1:100.000. Santiago, Chile.
Noblet, C., Lavenu, A., Marocco, R., 1996. Concept of continuum as opposed to periodic tectonism in the Andes. Tectonophysics 255, 65–78. https://doi.org/10.1016/0040-1951(95)00081-X.
O'Driscoll, L.J., Richards, M.A., Humphreys, E.D., 2012. Nazca-South America interactions and the late Eocene-late Oligocene flat-slab episode in the central Andes. Tectonics 31, 1–16. https://doi.org/10.1029/2011TC003036.

Oliveros, V., Féraud, G., Aguirre, L., Fornari, M., Morata, D., 2006. The Early Andean Magmatic Province (EAMP): 40Ar/39Ar dating on Mesozoic volcanic and plutonic rocks from the Coastal Cordillera, northern Chile. J. Volcanol. Geotherm. Res. 157, 311–330. https://doi.org/10.1016/j.jvolgeores.2006.04.007.

Pananont, P., Mpodozis, C., Blanco, N., Jordan, T.E., Brown, L.D., 2004. Cenozoic evolution of the northwestern Salar de Atacama Basin, northern Chile. Tectonics 23, 1–19. https://doi.org/10.1029/2003TC001595.

Payrola, P., Powell, J., Papa, C. del, Hongn, F., 2009. Middle Eocene deformation-sedimentation in the Luracatao Valley: Tracking the beginning of the foreland basin of northwestern Argentina. J. S. Am. Earth Sci. 28, 142–154. https://doi.org/10.1016/j.jsames.2009.06.002.

Pichowiak, S., Buchelt, M., Damm, K.-W., 1990. Magmatic Activity and Tectonic Setting of the Early Stages of the Andean Cycle in Northern Chile. pp. 127–144. https://doi.org/10.1130/SPE241-p127.

Quade, J., Dettinger, M.P., Carrapa, B., DeCelles, P., Murray, K.E., Huntington, K.W., Cartwright, A., Canavan, R.R., Gehrels, G., Clementz, M., 2015. The growth of the central Andes, 22°S–26°S. In: Decelles, P.G., Ducea, M.N., Carrapa, B., Kapp, P.A. (Eds.), Geodynamics of a Cordilleran Orogenic System: The Central Andes of Argentina and Northern Chile: Geological Society of America Memoir 212. The Geological Society of America, pp. 277–308. https://doi.org/10.1130/2015.1212(15).

Raczynski, A., 1963. Geología del distrito minero de Tuina. (BSc Thesis).

Ramírez, C.F., Gardeweg, M., 1982. Hoja Toconao. Carta Geológica de Chile 54. 1 mapa escala 1:250.000. Santiago, Chile.

Ramos, V.A., 2009. Anatomy and global context of the Andes: Main geologic features and the Andean orogenic cycle. Geol. Soc. Am. Mem. 204, 31–65. https://doi.org/10.1130/2009.1204(02.

Ramos, V.A., 2010. The Tectonic Regime along the Andes: Present-Day and Mesozoic Regimes. 25. pp. 2–25. https://doi.org/10.1002/gj.

Reiners, P.W., Thomson, S.N., Vernon, A., Willett, S.D., Zattin, M., Einhorn, J., Gehrels, G., Quade, J., Pearson, D., Murray, K.E., Cavazza, W., 2015. Low-temperature thermochronologic trends across the central Andes, 21°S-28°S. In: DeCelles, P.G., Ducea, M.N., Carrapa, B., Kapp, P.A. (Eds.), Memoir of the Geological Society of America. The Geological Society of America, pp. 215–249. https://doi.org/10.1130/2015.1212(12).

Reutter, K.J., Charrier, R., Gotze, H.J., Schurr, B., Wigger, P., Scheuber, E., Giese, P., Reuther, C.D., Schmidt, S., Rietbrock, A., Chong, G., Belmonte-Pool, A., 2006. The Salar de Atacama Basin: a Subsiding Block within the Western Edge of the Altiplano-Puna Plateau. Andes Act. Subduction Orogeny 303–325. https://doi.org/10.1007/978-3-540-48684-8_14.

Rubilar, J., Martínez, F., Arriagada, C., Becerra, J., Bascuñán, S., 2017. Structure of the Cordillera de la Sal: a key tectonic element for the Oligocene-Neogene evolution of the Salar de Atacama basin, Central Andes, northern Chile. J. S. Am. Earth Sci. https://doi.org/10.1016/j.jsames.2017.11.013.

Salfity, J.A., Marquillas, R.A., 1994. Tectonic and Sedimentary Evolution of the Cretaceous-Eocene Salta Group Basin, Argentina. Cretaceous Tectonics of the Andes, Evolution Sciences Monograph Series Friedr, Vieweg & Sohn, Braunschweig/Wiesbaden, pp. 266–315.

Schmitz, M., Lessel, K., Giese, P., Wigger, P., Araneda, M., Bribach, J., Graeber, F., Grunewald, S., Haberland, C., Lüth, S., Röwer, P., Ryberg, T., Schulze, A., 1999. The crustal structure beneath the Central Andean forearc and magmatic arc as derived from seismic studies - the PISCO 94 experiment in northern Chile (21°-23°S). J. S. Am. Earth Sci. 12, 237–260. https://doi.org/10.1016/S0895-9811(99)00017-6.

Schurr, B., Rietbrock, A., 2004. Deep seismic structure of the Atacama basin, northern Chile. Geophys. Res. Lett. 31, 10–13. https://doi.org/10.1029/2004GL019796.

Sempere, T., 1995. Phanerozoic evolution of Bolivia and adjacent regions. Pet. basins South Am. 62, 207–230.

Siks, B.C., Horton, B.K., 2011. Growth and fragmentation of the Andean foreland basin during eastward advance of fold-thrust deformation, Puna plateau and Eastern Cordillera, northern Argentina. Tectonics 30, 1–27. https://doi.org/10.1029/2011TC002944.

de Silva, S.L., 1989. Geochronology and stratigraphy of the ignimbrites from the 21°30′S to 23°30′S portion of the Central Andes of Northern Chile. J. Volcanol. Geotherm. Res. 27, 93–131.

Solari, L.A., Gómez-Tuena, A., Bernal, J.P., Pérez-Arvizu, O., Tanner, M., 2010. U-Pb zircon geochronology with an integrated la-icp-ms microanalytical workstation: Achievements in precision and accuracy. Geostand. Geoanalytical Res. 34, 5–18. https://doi.org/10.1111/j.1751-908X.2009.00027.x.

Solari, M., Venegas, C., Montecino, D., Astudillo, N., Cortés, J., Bahamondes, B., Espinoza, F., 2017. Geología del área Imilac-Quebrada Guanaqueros, Región de Antofagasta. Carta Geológica de Chile, Serie Básica, No.191. 1 mapa escala 1:100.000. Santiago, Chile.

Somoza, R., Tomlinson, A.J., Caffe, P.J., Vilas, J.F., 2012. Paleomagnetic evidence of earliest Paleocene deformation in Calama (~22°S), northern Chile: Andean-type or ridge-collision tectonics? J. S. Am. Earth Sci. 37, 208–213. https://doi.org/10.1016/j.jsames.2012.04.001.

Steinmann, G., 1929. Geologie von Peru. Carl Winters Universitats-Buchhandlung.

Travisany, V., 1978. Mineralización cuprífera en areniscas de la Formación San Pedro en el distrito San Bartolo. Memoria de Título. Universidad de Chile.

Tunik, M., Folguera, A., Naipauer, M., Pimentel, M., Ramos, V.A., 2010. Early uplift and orogenic deformation in the Neuquén Basin: Constraints on the Andean uplift from U-Pb and Hf isotopic data of detrital zircons. Tectonophysics 489, 258–273. https://doi.org/10.1016/j.tecto.2010.04.017.

Wilkes, E., Görler, K., 1994. Sedimentary and Structural Evolution of the Salar de Atacama Depression. In: Reutter, K., Scheuber, E., Wigger, P. (Eds.), Tectonics of the Southern Central Andes: Structure and Evolution of an Active Continental Margin. Springer, New York, pp. 171–188.

Yrigoyen, M., 1993. Los depósitos sinorogénicos terciarios. In: Ramos, V.A. (Ed.), Geología y Recursos Naturales de Mendoza, 12° Congreso Geológico Argentino y 2° Congreso de Exploración de Exploración de Hidrocarburos (Mendoza), Relatorio 1. Mendoza, pp. 123–148.

Yuan, X., Sobolev, S., Kind, R., 2002. Moho topography in the central Andes and its geodynamic implications. Earth Planet. Sci. Lett. 199, 389–402. https://doi.org/10.1016/S0012-821X(02)00589-7.

Zimmermann, U., Niemeyer, H., Meffre, S., 2009. Revealing the continental margin of Gondwana: the Ordovician arc of the Cordón de Lila (northern Chile). Int. J. Earth Sci. 99, 39–56. https://doi.org/10.1007/s00531-009-0483-8.

Chapter 3 : Multi-proxy insights into the structure and geometry of the tectonic boundary at the Cordillera de Domeyko-Salar de Atacama border: An example of the interplay between basement and foreland basins.

Published in: *Bascuñán, S., Maksymowicz, A., Martínez, F., Hernández, M.J., Becerra, J., Arriagada, C. 2021. Multi-proxy insights into the structure and geometry of the tectonic boundary at the Cordillera de Domeyko-Salar de Atacama border: An example of the interplay between basement and foreland basins. Tectonophysics 807: 228818.*

Tectonophysics 807 (2021) 228818

Contents lists available at ScienceDirect

Tectonophysics

journal homepage: www.elsevier.com/locate/tecto

Multi-proxy insights into the structure and geometry of the tectonic boundary at the Cordillera de Domeyko-Salar de Atacama border: An example of the interplay between basement and foreland basins

Sebastián Bascuñán [a,*], Andrei Maksymowicz [b], Fernando Martínez [c], María José Hernández [b], Juan Becerra [d], César Arriagada

[a] Departamento de Geología, Facultad de Ciencias Físicas y Matemáticas, Universidad de Chile, Plaza Ercilla 803, Santiago, Chile
[b] Departamento de Geofísica, Facultad de Ciencias Físicas y Matemáticas, Universidad de Chile, Blanco Encalada 2002, Santiago, Chile
[c] Departamento de Geología, Universidad Católica del Norte, Angamos 0610, Antofagasta, Chile
[d] SQM Salar S.A., El Trovador 4285, Las Condes, Santiago, Chile

ARTICLE INFO

Keywords:
Gravimetry
Seismic profiles
Magnetism
Andes
Salar de Atacama

ABSTRACT

The study of the Cordillera de Domeyko and the Salar de Atacama Basin in northern Chile has been critical to understand the generation of the Andean Cordillera and the migration of the deformation front eastwards. However, the relation between the uplift of the range, its temporal pattern, and the formation of the Preandean Depression have not been fully understood. In this article, we forward modeled two gravimetry surveys, consisting in 185 stations crossing the boundary between the Salar de Atacama Basin and Cordillera de Domeyko, with the goal of understanding the physical traits of each domain and the variations in basin geometry. We interpreted two seismic reflection profiles, along with log data from one well in the basin center, and additionally, we analyzed an inversion of the magnetic anomaly for both lines. The results of the analysis show the segmentation of physical properties into two domains. The first is interpreted as basement (Triassic-older) units, while the other shows the presence of gravity lows correlated with late Mesozoic-Cenozoic units cropping out along the western edge of the basin. The magnetic anomalies identified were correlated with variations within the basement and outcrops of crystalline intrusives. Within the sedimentary units, the Late Cretaceous-Paleogene Purilactis Group and Paleogene-Eocene formations were distinguished from the evaporite-rich Oligocene-Miocene Paciencia Group. The latter was deposited after a compressive event (Incaic Event) which thrusted basement units eastwards, inverted Mesozoic extensional faults, and generated the accommodation space required for its deposition. The basin then experienced renewed compression during the Miocene. This interplay between basement uplift and thrusting, along with fault inversion and basin generation, is a characteristic found in other parts of the Salar de Atacama Basin and the orogen, suggesting that this tectonic style might be prevalent in other basins comprising the Preandean Depression and along the Central Andes.

1. Introduction

The Central Andes has been a major research focus as it is an example of a non-collisional, accretionary orogen (Cawood et al., 2009; Dewey and Bird, 1970; Ramos, 2009). Understanding how it evolved, the involved geodynamic/tectonic variables (e.g, Heuret and Lallemand, 2005; Ramos, 2009; Schellart, 2008), and its similarities and/or differences from orogens worldwide (Cawood et al., 2009; DeCelles et al., 2015; Vanderhaeghe, 2012) can give us insight into past orogens. In this regard, the last decades have seen many different tectonic models arise for the Andean orogen, where different geodynamic variables are treated with varying degrees of importance relative to their contribution to the building of the orogen. These include: variations of plate kinematics (Heuret and Lallemand, 2005; Scheuber et al., 1994); the pre-orogenic configuration of the continental margin (López et al., 2020; Martínez et al., 2018, 2020); the migration of the volcanic arcs (Charrier et al., 2009; Kay et al., 2005; Kay and Coira, 2009); the subduction of aseismic oceanic ridges (Somoza et al., 2012; Yáñez et al., 2001); along-strike differential shortening (Arriagada et al., 2008; McQuarrie, 2002a), among others. It is then necessary to study and understand the

* Corresponding author.
E-mail address: sebascun@ing.uchile.cl (S. Bascuñán).

https://doi.org/10.1016/j.tecto.2021.228818
Received 23 August 2020; Received in revised form 21 February 2021; Accepted 8 March 2021
Available online 14 March 2021

various heterogeneous segments of the Central Andes in order to reach a more comprehensive model of its formation.

The Salar de Atacama Basin in the Central Andes of northern Chile is the major saltpan within the Preandean Depression, nestled between the Precordillera and the Western Cordillera (Figs. 1 and 2). It stands out as a natural laboratory with excellent exposures of stratigraphic and structural relationships that record most of the Mesozoic geological history of the area (Amilibia et al., 2008; Bascuñán et al., 2016; Charrier and Reutter, 1994; Mpodozis et al., 2005) These attributes make it an interesting type area for understanding the evolution of the orogen at these latitudes; however, regional studies of the aforementioned features have usually led to contrasting interpretations of the evolution of the basin, particularly during the Paleogene-Neogene, where extensional (Flint et al., 1993; Hartley et al., 1992; Jordan et al., 2007; Pananont et al., 2004; Rubilar et al., 2017) and compressional (Arriagada et al., 2006a; Bascuñán et al., 2019; Wilkes and Görler, 1994) settings have been invoked to explain its tectonic evolution. These units would have been deposited after mostly compression during the Late Cretaceous-Early Paleogene ('Peruvian Phase', Steinmann, 1929). The main question that follows then is what are the factual steps of the formation of the Cordillera de los Andes recorded in the Salar de Atacama Basin? And is this evolution coherent with that proposed for neighboring areas?

A relevant issue around these questions is the uncertain association of the units within the actual salt pan with those cropping out along the basin, which have seen numerous changes in their chronostratigraphy over the last few years (Bascuñán et al., 2016, 2019; Becerra et al., 2014; Charrier and Muñoz, 1994; Charrier and Reutter, 1990, 1994; Flint et al., 1989; Hartley et al., 1992; Henríquez et al., 2014; Mpodozis et al., 1999). Since the link between the formations found surrounding the basin, seismic sequences and exploratory wells in the middle of the basin (Fig. 2a) can only provide insights over certain areas, its extrapolation to the rest of the seismic sections has proven to be difficult and leading to opposing interpretations (e.g., Arriagada et al., 2006a; Bascuñán et al., 2019; Jordan et al., 2007; Pananont et al., 2004; Rubilar et al., 2017).

In order to study the geometry of the Salar de Atacama Basin and the link between deformation events and sedimentation, we have performed gravimetry surveys comprising two *E*-W oriented transects across the Precordillera and the Salar de Atacama Basin. A reexamination of some of the 2-D seismic reflection profiles and well-log data (gamma ray log, velocity surveys) obtained from the Toconao-1 well was also performed, which were then used as an input for the gravimetric forward modeling. The interpretation of the gravimetry profiles also incorporated the magnetic anomaly data acquired by the scientific project "The Interplay between Subduction Processes and Natural Disasters in Chile" (INSUD) in northern Chile in 2019. The data gathered here allows to interpret that the Salar de Atacama Basin was formed mainly in a compressional setting from the Late Cretaceous onwards, directly linked to the thrusting of the Precordillera eastwards. A latitudinal segmentation of deformation is also found, which involves the inversion of previous structures, as well as the reactivation of reverse faults later on in its history. This work also sheds light on the relation between the formation

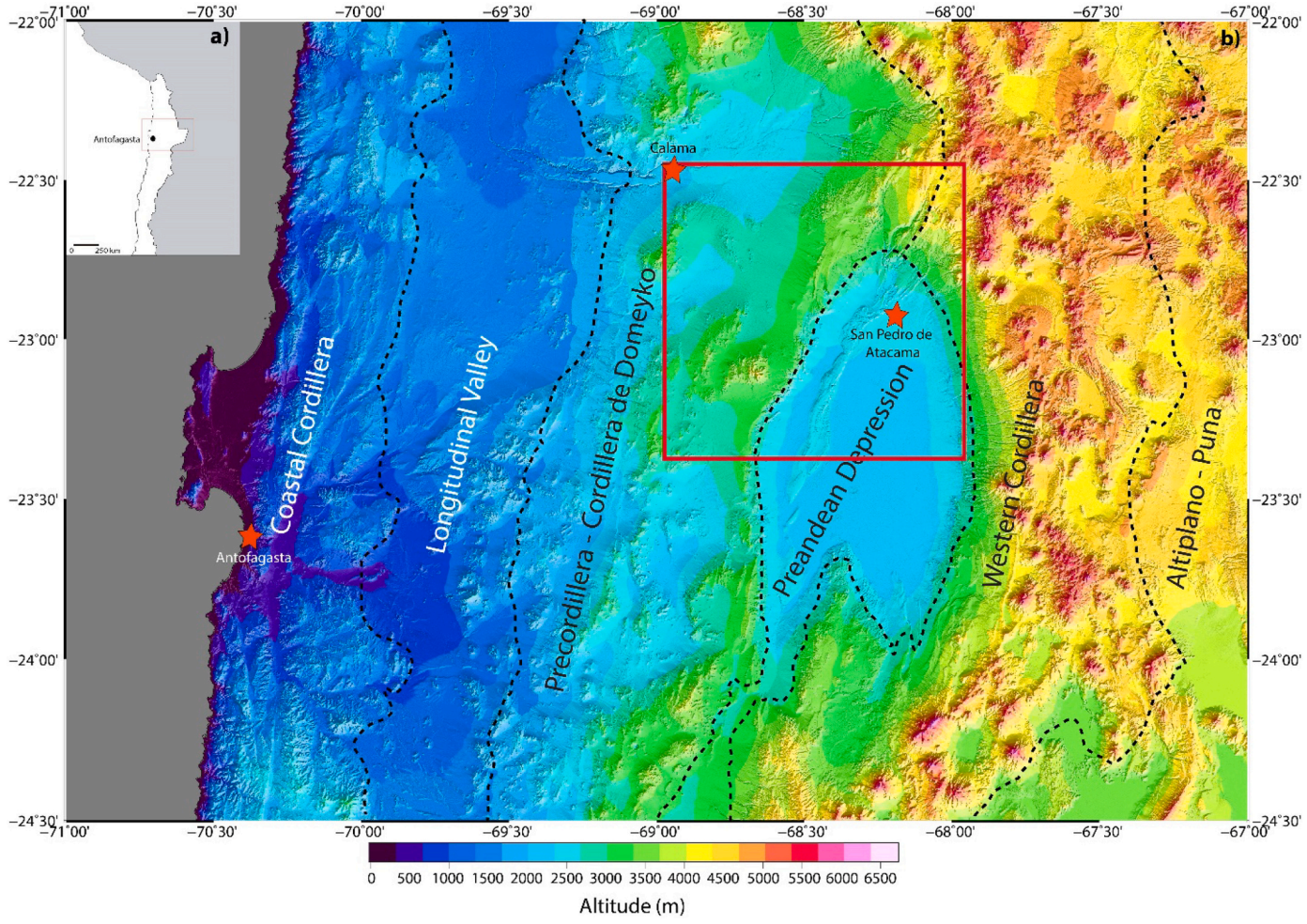

Fig. 1. a) Study location in northern Chile. b) Morphostructural domains of the Central Andes between 22° and 24°30'S. Red stars show major cities in the region, while the red box shows the study region. Modified from Bascuñán et al. (2019). (For interpretation of the references to colour in this figure legend, the reader is referred to the web version of this article.)

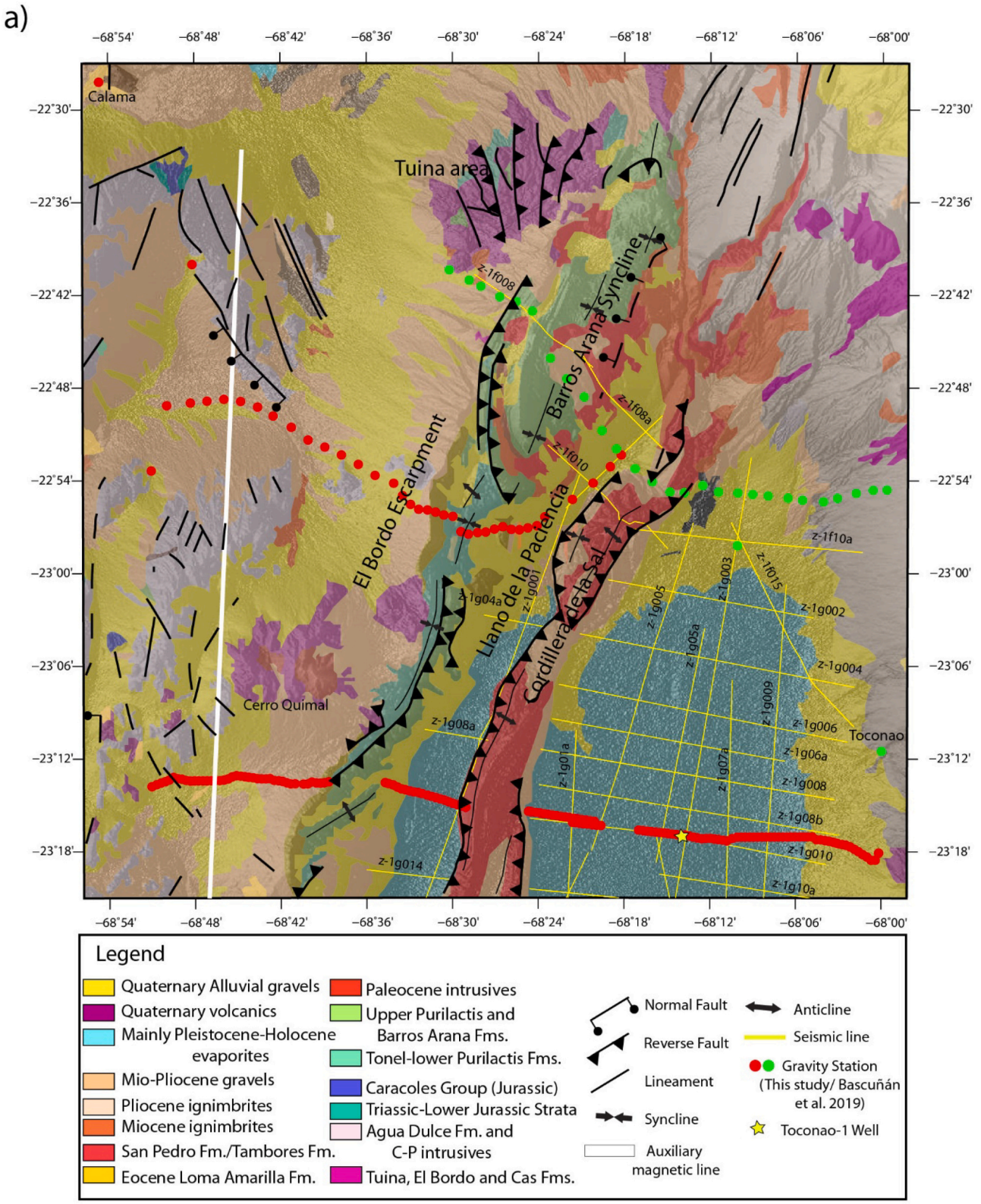

Fig. 2. a) Geological map of the study area draped over the SRTM digital elevation model (DEM), following SERNAGEOMIN (2003), Ramírez and Gardeweg (1982), Marinovic and Lahsen (1984), Basso and Mpodozis (2012), Henríquez et al. (2014) and Becerra et al. (2014). b) Total Field Anomaly, with a Reduced to the Pole (RTP) filter, following the Earth's magnetic field of 1985 by Hernández (2019). Greyscale background image also corresponds to the SRTM DEM of the study area, while white lines correspond to the magnetic lines modeled in this study, and yellow star shows the position of the Toconao-1 well. (For interpretation of the references to colour in this figure legend, the reader is referred to the web version of this article.)

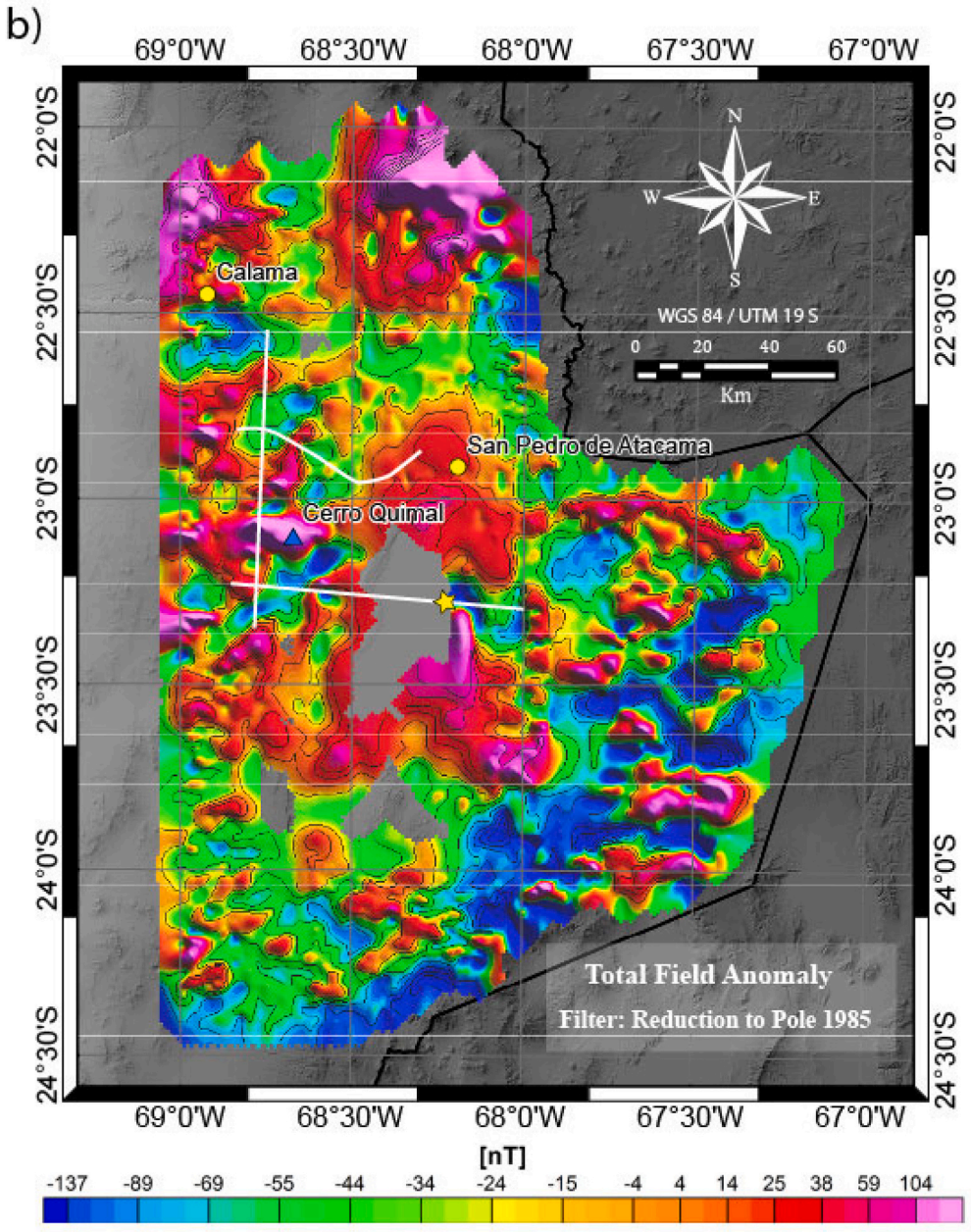

Fig. 2. (*continued*).

of the Preandean Depression and that of the Precordillera, and how the evolution of the latter is recorded within the former.

2. Geological setting

The Central Andes in northern Chile displays several morphostructural units, which are intimately related both to current and past geological conditions along the Nazca-South America margin (Allmendinger et al., 1997; Charrier et al., 2007; Isacks, 1988; Somoza, 1998). The study area covers three of these geomorphological units (Figs. 1 and 2), corresponding to the Precordillera, locally known as the Cordillera de Domeyko, the Preandean Depression, mainly involving the Salar de Atacama, and part of the westernmost expression of the Western Cordillera, which is the current magmatic arc (Charrier et al., 2007; Kay and Coira, 2009; Mpodozis et al., 2005). A brief description of these geomorphological units is presented below.

The Cordillera de Domeyko extends from 20° to 28°S, reaching altitudes between 3000 and 5000 m a.s.l. (Allmendinger et al., 1997; Charrier et al., 2007; Maksaev and Zentilli, 1999). It is composed of Paleozoic to Mesozoic crystalline basement, volcanic and sedimentary rocks, overlain by marine and continental successions reaching Cenozoic ages (Breitkreuz and Van Schmus, 1996; Charrier et al., 2007, 2009; Cornejo et al., 1993; Cortés, 2000; Maksaev and Zentilli, 1999; Marinovic and García, 1999; Marinovic and Lahsen, 1984; Ramírez and Gardeweg, 1982). The area occupied an arc setting during the Late Cretaceous-Eocene, as suggested by its volcanic successions and related intrusives (Fig. 3a; Arriagada et al., 2003; Basso and Mpodozis, 2012; Charrier et al., 2007; Marinovic and Lahsen, 1984; Somoza et al., 2012), and recent sedimentological, geochronological and structural data in the region point to an early period of uplift during the Late Cretaceous (Amilibia et al., 2008; Arriagada et al., 2006a; Bascuñán et al., 2016; Martínez et al., 2018, 2020). The Cordillera de Domeyko later experienced intense uplift, deformation and clockwise tectonic rotations during the Late Eocene-Early Oligocene Incaic event, which formed the

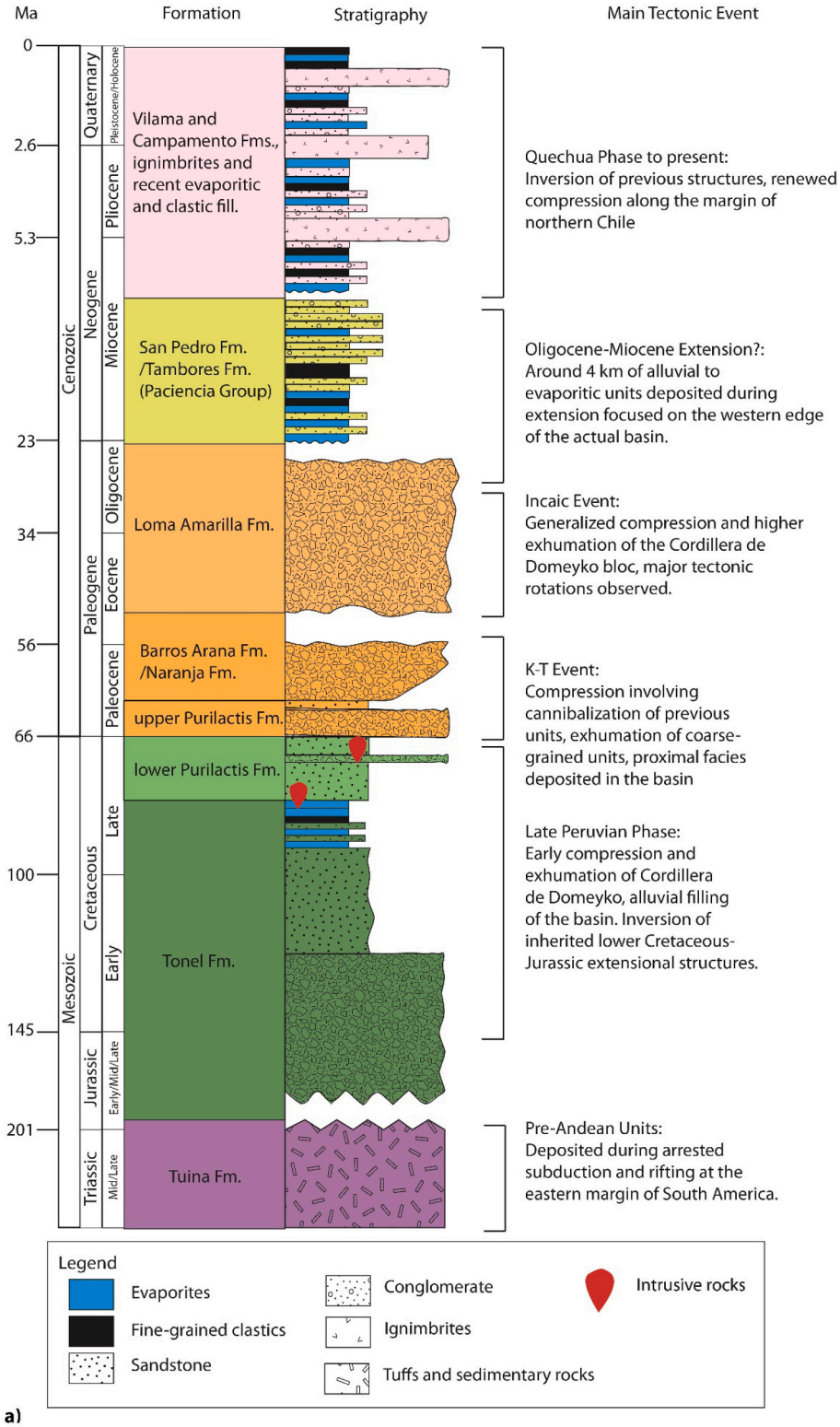

Fig. 3. a) Simplified tectonostratigraphy of the Salar de Atacama Basin, modified from Bascuñán et al. (2019). b) Stratigraphy of the Toconao-1 well, and its interpretations. See Fig. 2 for location of the well.

Arica Bend and established most of the actual margin configuration (Arriagada et al., 2000, 2006b, 2008; Barnes and Ehlers, 2009; Charrier et al., 2009; Maksaev and Zentilli, 1999; McQuarrie, 2002a; Narea et al., 2015; O'Driscoll et al., 2012). Regarding its actual structure, the surficial evidence shows that Paleozoic to Mesozoic units are bounded by N-S striking and doubly verging high-angle reverse faults (Amilibia et al., 2008; Basso and Mpodozis, 2012; López et al., 2019; Maksaev and Zentilli, 1999; Martínez et al., 2017).

The eastern border of the Cordillera de Domeyko limits along the Salar de Atacama Basin (Figs. 1 and 2). The border between these

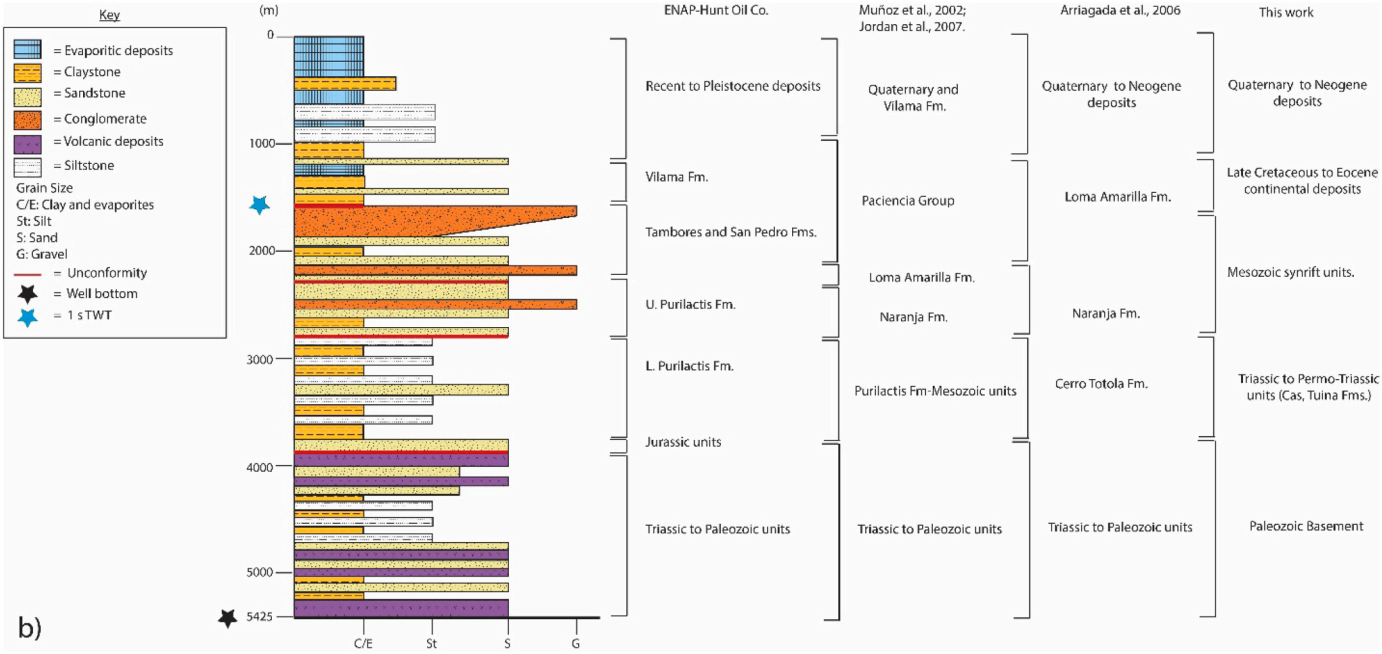

Fig. 3. (*continued*).

morphostructural units is an abrupt boundary which shows a marked decrease in topographic height. This limit, known as El Bordo Escarpment (Fig. 2a), exhibits a topographic difference of up to 900 m between the saltpan base level (ca. 2300 m a.s.l.) and the top of the escarpment. It also presents an almost continuous exposition of asymmetrically folded Upper Cretaceous-Paleogene continental clastic and volcanic successions belonging to the Purilactis Group, interspersed with Triassic volcanics and sedimentary units, and Cenozoic continental successions (Arriagada et al., 2000, 2006a; Bascuñán et al., 2016; Becerra et al., 2014; Charrier and Reutter, 1990, 1994; Flint et al., 1993; Hartley et al., 1992; Henríquez et al., 2014; Marinovic and Lahsen, 1984; Mpodozis et al., 1999, 2005; Ramírez and Gardeweg, 1982; Wilkes and Görler, 1994).

Three geomorphological subregions have been identified within the basin, corresponding to the Llano de la Paciencia, the Cordillera de la Sal, and the actual salt pan (Fig. 2). The first corresponds to the domain between the escarpment and the Cordillera de la Sal, covered mostly by recent alluvial gravels (Becerra et al., 2014; Henríquez et al., 2014; Jolley et al., 1990). The Cordillera de la Sal separates this feature from the actual salt pan, rising ca. 200 m above its surroundings, where it displays intense folding of evaporitic and fine-grained clastic deposits belonging to the Oligocene-Miocene San Pedro and Pliocene-Pleistocene Vilama formations (Becerra et al., 2014; Henríquez et al., 2014; Mpodozis et al., 2000; Wilkes and Görler, 1994).

The actual saltpan is flanked on its eastern and northern sides by extensive ignimbritic covers that make up the westernmost part of the Western Cordillera in the area (Figs. 1 and 2), that range in age from Miocene to Pleistocene. Scarce outcrops of welded, crystalline tuffs and andesitic lavas of Triassic age belonging to the Cas Formation are also found southeast of the study area (Becerra et al., 2014; Henríquez et al., 2014; Kay and Coira, 2009; Marinovic and Lahsen, 1984; Ramírez and Gardeweg, 1982; Salisbury et al., 2011).

2.1. Stratigraphy of the Toconao-1 well and correlation with surface outcrops

The Toconao-1 well (Figs. 2 and 3), shows the presence of 980 m of evaporites, such as halite and anhydrite, interbedded with brown claystones and scarce shale, followed by red-brown claystones, sandstone and anhydrite beds until 1590 m in depth. The well (Fig. 3b) then shows a change to a downward-fining, reddish, volcanic conglomerate transitioning into sandstones and claystones, with an abundance of lithic grains that proceed up to 2813 m. Past this mark, the lithologies correspond to reddish siltstones interbedded with claystones, and minor sandstone, with small intervals showing glauconite grains and thin limestone beds. Coarser units are found past 3734 m, where sandstones, and then more volcanoclastic units, become the main lithologies until 4315 m. Afterwards, grey claystones and shales become prominent, interbedded with thin limestone beds and, towards the base (4934 m), sandstones and volcanic units. The rest of the well is predominantly volcanoclastic, with rocks such as lithic sandstones, tuffs and tuffaceous claystones.

Fig. 3b summarizes the different interpretations given to the stratigraphy of the Toconao-1 well over the last 30 years. These have arisen mostly from the weight given by the authors to the evidence present at the time of the correlation, which includes apatite fission track data, the presence of scarce glauconite grains, the interpretation of the seismic data, and the knowledge of the formations surrounding the basin and in neighboring regions.

3. Methods

3.1. Density log and velocity survey

The density and velocity survey acquired from the Toconao-1 well by ENAP (Empresa Nacional del Petróleo) were reviewed to characterize the interval velocity of the strata encountered in the well and the density of the formations. This information is necessary to a) generate time-to-depth conversions of the seismic sections interpreted in this study that are adjusted to the velocities encountered in the well, b) model the gravity anomalies using density values that correspond to those found in the basin, and c) analyze whether the changes in physical properties found downhole can be correlated with formation boundaries and/or lithological variations.

The Vp (P-wave) depth velocity profile data corresponds to an uphole velocity survey acquired from the Toconao-1 well (Figs. 2, 3b and 4). This survey gives an approach to the bulk Vp velocity of the sedimentary sequences as compared with the velocity data obtained

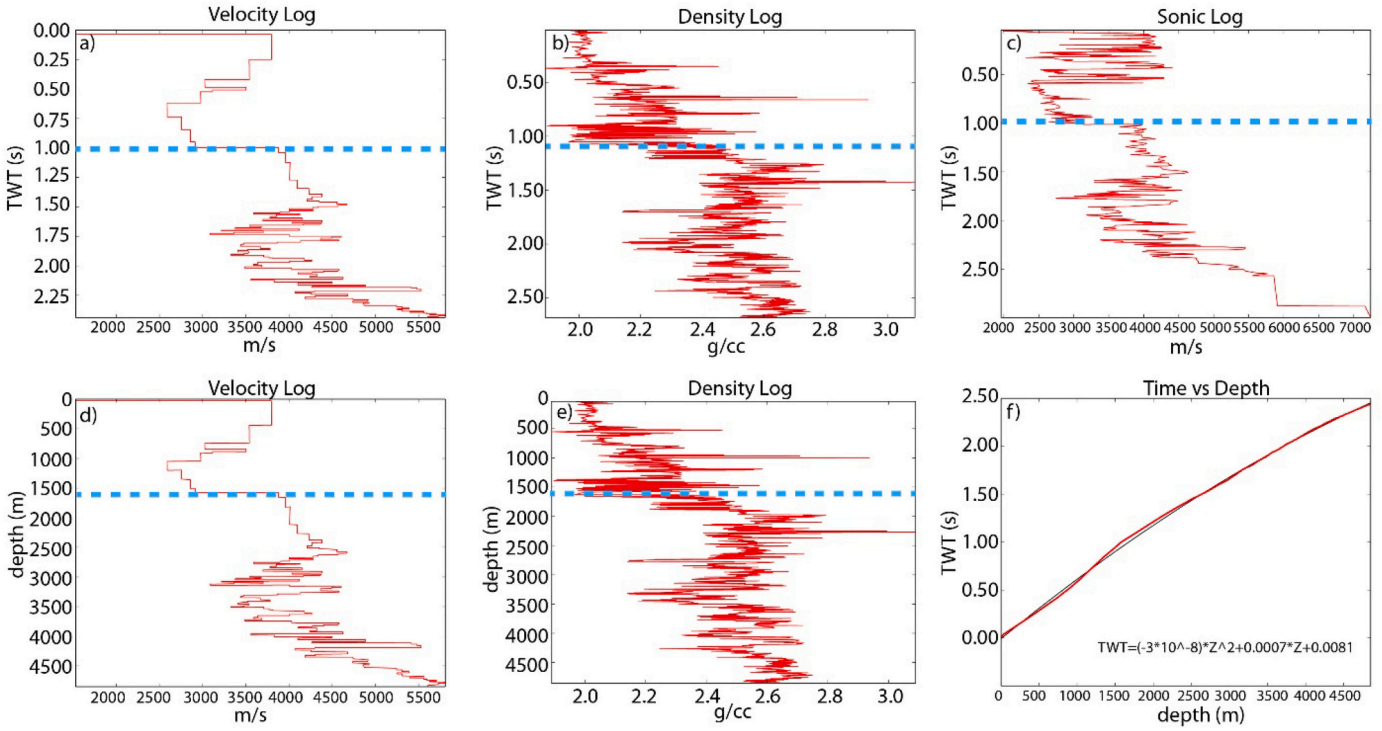

Fig. 4. Geophysical data from the Toconao-1 well, provided by ENAP. a) Interval velocity obtained from a vertical seismic profile (VSP). b) Density log. c) Velocity log obtained from direct borehole measurements (Sonic log). d) VSP log converted to two-way travel time (TWT). e) Density log converted to TWT, following the polynomial approximation seen in f). Blue dashed line corresponds to 1 s (TWT), which marks a relevant change in physical properties discussed in the text. (For interpretation of the references to colour in this figure legend, the reader is referred to the web version of this article.)

from the sonic log, which yields a local velocity from the wall of the hole (Fig. 4a, c and d; Muñoz et al., 2002); both sets were reviewed nonetheless in order to identify geophysical/geological boundaries. The density data (Fig. 4b, e) was obtained from the bulk density log performed on the same well.

Since both surveys consisted of data vs. depth in meters, it was necessary to transform the depth scale into two-way travel time (TWT) in order to jointly interpret them with the seismic sections. Following the procedures set forth by Yilmaz (2001), the conversion was done using the interval velocities of each layer, by dividing the length of a layer by its interval velocity thus obtaining a time amount. The cumulative sum of these amounts yields the one-way travel time at which the interval velocities change. The different sums were multiplied by two to obtain the two-way travel time (TWT), thus enabling the plotting of interval velocities vs. time (Fig. 4a), and time vs. depth (Fig. 4d). The latter was used for plotting other data (such as density, Fig. 4b) vs. time by obtaining a mathematical expression for the increase in time vs. depth. Eq. (1) shows the polynomial best fit for the red curve in Fig. 4f:

$$TWT = -3*10^{-8}*Z^2 + 0.0007Z + 0.0081 \quad (1)$$

Where TWT is in seconds, and variable Z is in meters.

3.2. Seismic reflection profiles

Seismic reflection surveys have played a critical role worldwide in the oil industry, and are a staple procedure when prospecting reservoirs (e.g., Burg, 2018; Howell et al., 2005; Jia et al., 1998; Wang et al., 2018; Yilmaz, 2001). In this study, the seismic sections obtained by ENAP were studied to identify first-order tectonic features and depositional styles within the salar.

The seismic reflection profiles correspond to lines acquired through a combination of Vibroseis and explosive sources that cover the central part of the basin (Fig. 2, ca. 84 km). The Toconao-1 well was drilled following the analysis of z-1G010, and, as such, it is one of the few lines with which a correlation with surface stratigraphy can be proposed. The chosen two-way travel time profiles (z-1G08a, z-1G008 and z-1G010) were converted to depth using software Move 2017.1 by Midland Valley Ltd., following the methodology employed by Bascuñán et al. (2019), where a constant velocity of 3500 m/s was used. The quality of the seismic data is poor to moderate (Figs. 5 and 6), with generally mildly chaotic to chaotic reflectors below 1.6–2 s (TWT) or ca. 2500–3200 m, and the first 0.3 s (TWT) or 500 m, depending on the seismic section. However, they can nonetheless be used to identify major unconformities and boundaries between regional units, although the precise identification of the geological successions is hard to achieve without a better geological control (e.g., additional wells). The continuity of seismic reflectors within this range can also be usually followed and highlighted.

The physical properties of the seismic reflectors were studied, allowing for their characterization and grouping into seismic sequences following the classification of reflector terminations and patterns by Catuneanu et al. (2011), Cross and Lessenger (1988), among others. The age of the different units was assigned based on several criteria, such as: a) the review of previous seismic studies (Arriagada et al., 2006a; Bascuñán et al., 2019; Jordan et al., 2007; Martínez et al., 2018; Muñoz et al., 2002; Reutter et al., 2006), b) the analysis of the Toconao-1 well (Fig. 3), c) the existing geochronological data (Bascuñán et al., 2016, 2019; Mpodozis et al., 2000, 2005), and d) the latest geological maps of the area (Becerra et al., 2014; Henríquez et al., 2014).

3.3. Gravimetry data

The gravimetry survey presented in this study was made for two main objectives: first, to describe the general geometry of the basement of the basin, which also includes the definition of the geometry of the sedimentary successions within, and second, to help understand the interaction between the basement of the Cordillera de Domeyko and the units within the Salar. Interaction is here understood as the tectonic

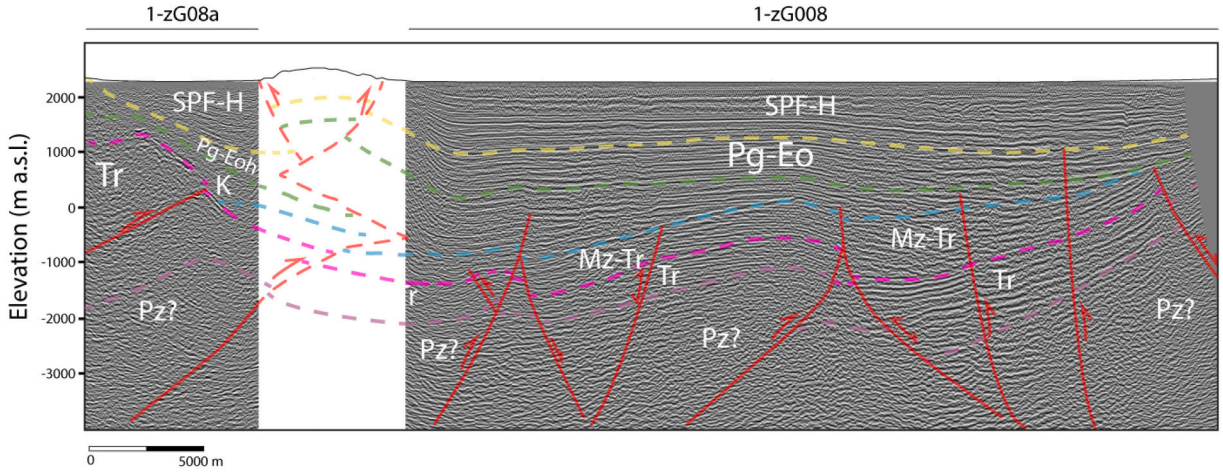

Fig. 5. Interpretation of lines 1-zG08a and 1-zG008. Lines have been dashed and made transparent to allow for the comparison of the uninterpreted and interpreted sections. Location in Fig. 2. Letters correspond to: Pz?: Paleozoic basement. Tr: Triassic to Permo-Triassic units (Tuina and Cas formations, El Bordo Strata). Mz-Tr: Mesozoic successions. K: Tonel, Purilactis and Cerro Totola formations. Pg-Eo: Naranja and Loma Amarilla formations. SPF-H: Paciencia Group and recent deposits.

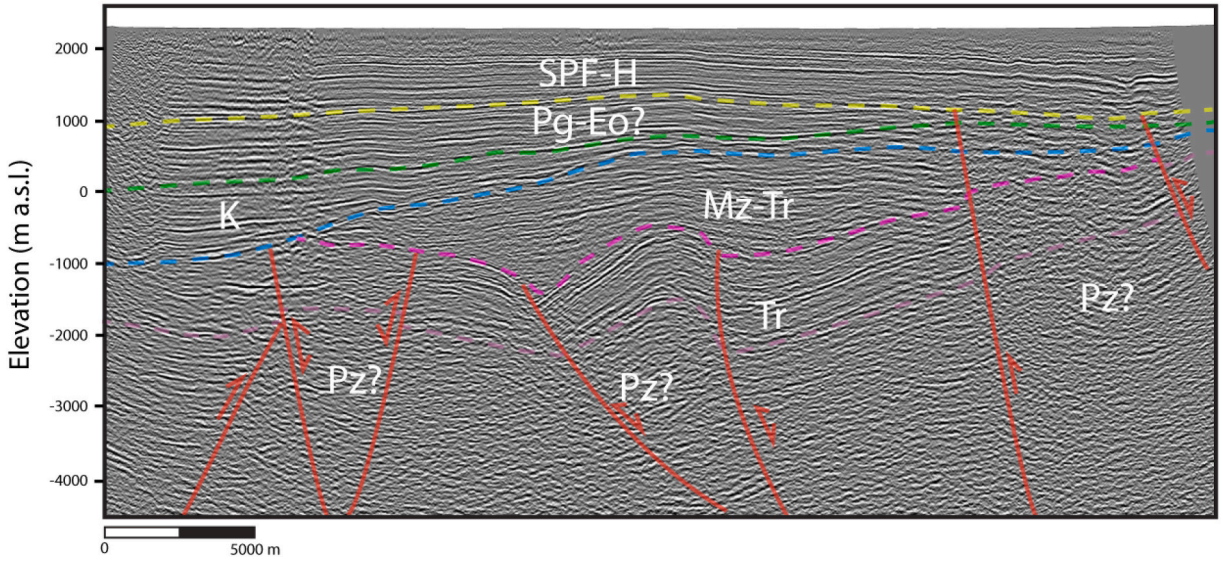

Fig. 6. Interpretation of Line z-1G010. Lines have been dashed and made transparent to allow for the comparison of the uninterpreted and interpreted sections. Location in Fig. 2. Acronyms are the same as in Fig. 5.

configuration between both morphostructural domains. The profiles surveyed here, along with those of Bascuñán et al. (2019), correspond to some of the few detailed gravimetric surveys crossing the western limit of the basin (El Bordo Escarpment) towards the basin, although broader regional surveys have been performed (e.g., Götze et al., 1994; Götze and Krause, 2002).

The gravimetry field measurements used in this study amount to 185 stations, acquired along *E*-W profiles (Fig. 2). These gravimetry stations were spaced between 500 m for the southern profile, and 1–2 km for the northern profile. Two base stations, required for estimating the diurnal instrumental drift, were placed in Calama and Toconao (Figs. 1 and 2). The equipment used in this study correspond to a CG-3 Scintrex Autograv gravimetry meter (0.005 mGal resolution) for the gravimetry stations, and a Topcon-Hiper V differential GPS system for all position and elevation measurements. In order to tie the regional gravimetric response to the basements units, which is a basic experimental design requirement needed to model the basin fill properly, the northern survey was tied to the survey performed by Bascuñán et al. (2019), while the southern profile was tied to basement outcrops on both ends (see below for additional details). One section matches seismic line z-1G010 as close as possible, thus adding an additional independent variable to the seismic section analysis within the basin.

The gravimetry data was then reduced following the procedures and techniques described in Blakely (1996), which include Earth tide correction (Longman, 1959), instrumental drift correction accounting for the variations in daily measurements taken at the gravity base station (0.02–0.2 mGal h^{-1}), and removal of the ellipsoid normal gravity. Free-air and simple Bouguer anomalies were calculated using measured D-GPS elevations and a reference density of 2.67 g/cm^{-3}. The high resolution (92 × 92 m) SRTM DEM covering the study area was used for the calculation of the terrain correction and its reduction from the simple Bouguer anomaly into the complete Bouguer anomaly. The terrain correction was calculated following a combination of the algorithms proposed by Nagy (1966) and Kane (1962).

The data was then forward modeled using software ENCOM-ModelVision 13.0 (Figs. 7 and 8), where variables such as the difference in density between the units and the basement, the interpretation of the seismic profiles, the density reported from the Toconao-1 well,

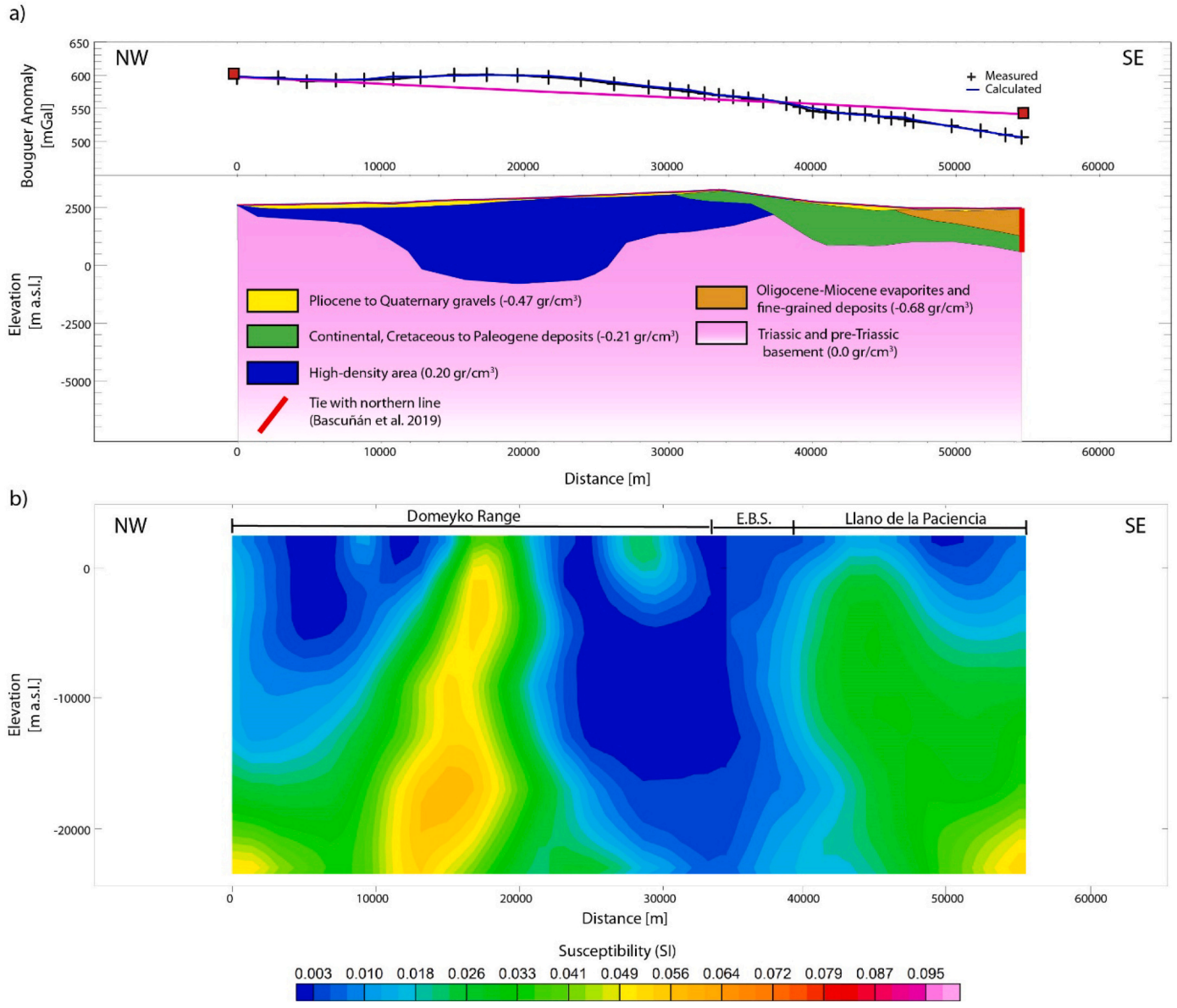

Fig. 7. a) Gravimetry results and b) magnetic modeling of the northern profile (Location in Fig. 2).

and the thicknesses of the units cropping out along the El Bordo Escarpment were used and scrutinized to reach the final models. The forward modeling of the gravimetry anomaly must first identify the trend for the regional gravity, which is independent for each profile considering the data available in each case. For the northern profile, the regional gravity trend was fixed on its eastern side following the regional trend utilized in the modeling of the Barros Arana Syncline done by Bascuñán et al. (2019). The western point was fixed by utilizing an auxiliary, NNE-SSW line with two points measured on outcrops of Carboniferous-Permian granitoids (Fig. 2a). In the case of the southern profile, the eastern point of the gravity low was measured on outcrops of the Triassic Cas Formation (Becerra et al., 2014). The western point was measured on tuffs and volcanic deposits of the Agua Dulce Formation (Basso and Mpodozis, 2012). The density bodies were then modeled as contrasts relative to a background density (Table 1), and utilizing both the contrasts obtained by Bascuñán et al. (2019), and the values found within the Toconao-1 exploration well. The latter data represent only local values of density measured within a borehole, and, as such, must be taken with caution; in this regard, the density change interphase was more relevant to the modeling than the high-frequency changes observed in the well (Fig. 4). The gravimetry station data are found in Supplementary Material A.

3.4. Magnetic data

This study was complemented with available aeromagnetic data and the magnetic survey carried out by INSUD in 2019. This information was used to identify and describe the magnetic response of the crystalline and/or volcanic units found in the study area, and to integrate said data with that of the preceding sections (Fig. 2b).

The first database consists in the aeromagnetic surveys of the area obtained by SERNAGEOMIN (1984, 1986), which were spaced every 2.5 km and obtained at an altitude of 600 m above the surface. This was complemented with 491 ground station magnetic field intensity measurements in the Precordillera and Salar de Atacama Basin with a spacing of 2 km, utilizing an Overhauser GSM-19 magnetometer with a 0.01 nT resolution and an integrated GPS. A G-856 proton precession magnetometer was used as a base for the ground study, set at a sampling frequency of 1 measurement every 30 s and installed close to the study area at a fixed location. This allowed for the application of a diurnal

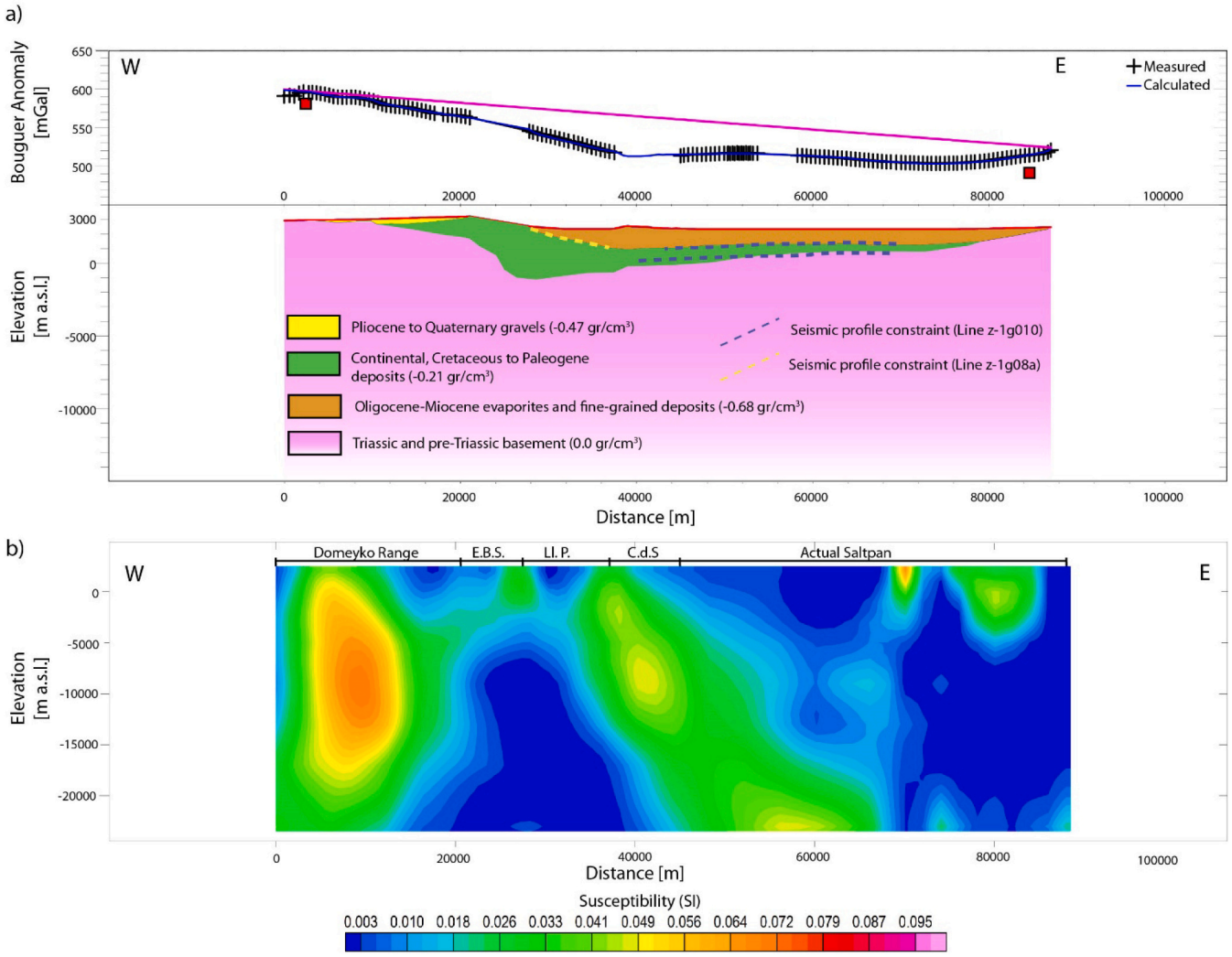

Fig. 8. a) Gravimetry results and b) magnetic modeling of the southern profile (Location in Fig. 2). Seismic constraints refer to the interpreted boundaries from other studies (see Fig. 5).

Table 1
Density contrasts used in the gravity modeling (Figs. 7 and 8).

Geological unit	Density contrast (gr/cm^3)
Pliocene to Quaternary gravels and evaporites	−0.47
High-density body	−0.2
Oligocene-Miocene evaporites and fine-grained clastics	−0.68
Continental, Cretaceous to Paleogene deposits	−0.21
Pre-Cretaceous basement	0

correction to the dataset. The total field anomaly is then obtained after the application of the standard corrections described in Blakely (1996) and Luyendyk (1997). These involve the cleaning of spikes and noise, diurnal corrections, line leveling and the removal of the International Geomagnetic Reference Field (IGRF). The aeromagnetic survey was processed with the IGRF of 1985, while the ground survey was processed with the IGRF of 2015.

In order to merge the aeromagnetic data (acquired at 600 m above the topography) with the ground measurements, we applied the vertical analytic continuation filter (see Blakely (1996) for a complete theoretical derivation and additional references). As the upward and downward continuations are low-pass and high-pass filters respectively, this procedure incurs in a trade-off between the reduction in amplitude of small anomalies observed at lower levels (in this case, the surface) and the amplification of high frequency noise in survey data acquired at higher altitudes (Nabighian et al., 2005). After several preliminary experiments, we observed that the downward continuation at 100 m of the aeromagnetic data did not increase the signal noise significantly (see Supplementary Material B). Accordingly, we moved the ground surface data 500 m upwards, positioning both datasets at the same level (500 m). This procedure has been broadly used to make joint interpretations of surveys taken at different elevations (e.g., Ontario Geological Survey, 2017; Patibandla and Dadhwal, 2020; Roberts and Jachens, 1999).

Hernández (2019) performed an inversion of the total field anomaly dataset (8710 datapoints) to obtain a 3D susceptibility model, following the MAG3D method developed by Li and Oldenburg (1993). The algorithm assumes that the measured magnetic field consists only in induced magnetization, and the solution is obtained by finding a model which both reproduces the data and minimizes an objective function. This function considers the structural complexity of the model, how close the model is to the reference model, and the smoothing coefficients in each spatial direction. A background susceptibility of 0.001 (SI) was used as a reference model, and the external magnetic field was set to the IGRF of 1985 (Inclination: −17.6, Declination: 0.1, Intensity: 24540 nT). Smoothing coefficients were set to their recommended value and later varied, although this had only a minor influence on the result. The final model had an RMS value of 5.66. A more thorough description of the process can be found in Supplementary Material B.

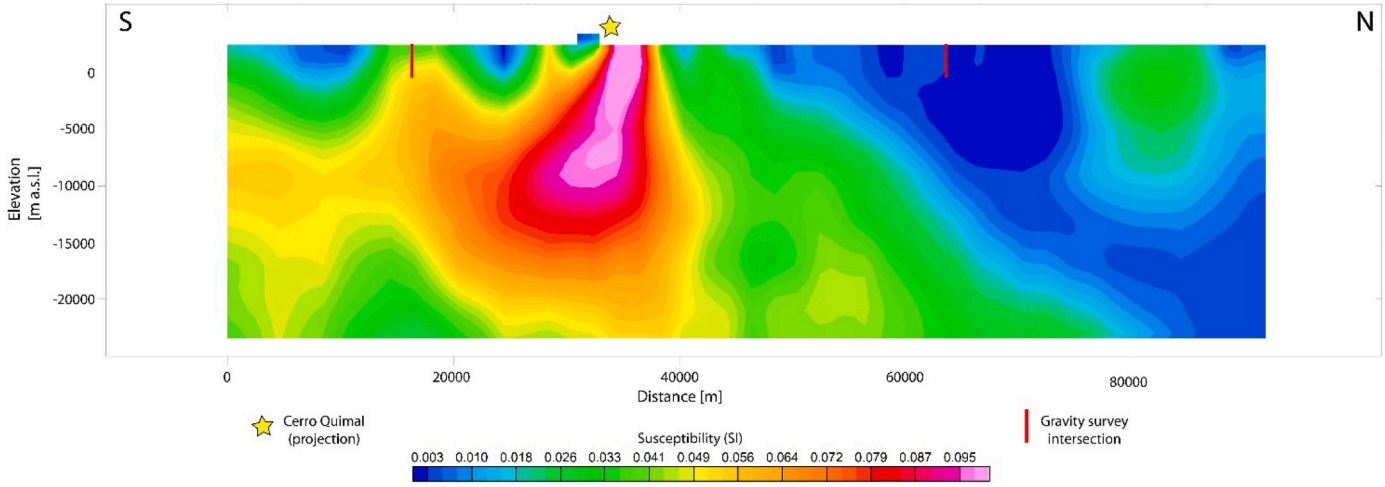

Fig. 9. Magnetic modeling of the auxiliary profile (Location in Fig. 2).

Cross sections of the susceptibility model along the gravity survey (Figs. 7 and 8), and a N-S line through Cordillera de Domeyko which links both profiles (Fig. 9), were generated and analyzed together with the gravimetry sections for the purpose of this work.

4. Results

4.1. Log analysis

The velocity logs (Fig. 4a, c and d) show, at first, wide intervals (0.05–0.2 s) with a decreasing velocity pattern from 3900 m/s to around 2600 m/s at 0.61 s TWT or 1044 m. The interval between 0.61 and 1 s TWT shows constant, low velocities of 2600–2900 m/s. A major change is registered at 1 s TWT (1580–1650 m), showing an increase from 2900 m/s to 3880 m/s (Fig. 3b). The log shows a slow but steady increase between the latter value and 4200 m/s until around 1.44 s TWT (2475 m), where a progressive decrease in velocity is seen until 1.73 s TWT (3120 m), correlated with a downward-fining trend in the exploratory well. Though the tendency of the values at this point clearly shows a decrease in velocity, the intervals are smaller and vary more frequently. This "high-frequency" change in velocity is constant down to the bottom of the well (around 2.44 s TWT, or 4852 m), though showing an increase in velocity up to values of 5600 m/s.

On the other hand, the density log data (Figs. 4b and e) show mainly low-density values (1.9–2.0 g/cc) between 0 and 0.52 s TWT (0–780 m), associated with the presence of fine-grained clastic deposits and evaporites in the Toconao-1 well. Afterwards, the values rise steadily, albeit with a more noticeable, high-frequency variation of the measurements, up until around 0.87 s TWT (1350 m). The values for this interval go from 2.1 to 2.3 g/cc, after which the data is more scattered, particularly between 0.87 and 1.1 s TWT (1633 m), with an average of 2.15 g/cc. Past this mark, density increases more steeply between 1.1 and 1.43 s TWT (2268 m), ranging around 2.2–2.9 g/cc and averaging 2.53 g/cc. Afterwards, the log shows an average density of 2.52 g/cc, with high frequency variations along an approximate trend line of 2.5 g/cc.

4.2. Seismic profiles and main structural components

Figs. 5 and 6 show the interpretation of the depth-converted seismic sections, and the sequences identified within them. West of lines z-1G010 and z-1G008, the main structure observed from field observations and satellite imagery corresponds to the southward continuation of the Barros Arana Syncline (Fig. 2a), involving the Tonel Formation, the lower Purilactis Formation, and the Cerro Totola Formation (Unit K). It apparently forms a southwest-plunging, tight syncline west of z-1G010, and its eastern flank is not seen west of z-1G08A. The whole structure cannot be observed in the subsurface of the latter line, but its eastern flank and a broad anticline, likely representing the folding of the same units, can be discerned (Fig. 5). These units are placed over a basement-cored anticline (Tr), and they show an increase in thickness eastwards to line z-1G008. They most likely incorporate units belonging to the Paleogene-Eocene (Pg-Eo), which are seen southwards of the study area, and which are deformed in a similar style to the Upper Cretaceous units (Arriagada et al., 2006a; Basso and Mpodozis, 2012; Henríquez et al., 2014). Paleogene units showing the same deformation style are also observed northwards (Bascuñán et al., 2019). These units lie below low-amplitude reflectors with good lateral continuity (Units SPF-H), that show a systematic decrease in dip upwards, and geometries resembling growth strata in synorogenic settings, with an increase in thickness eastwards (e.g., Carrera and Muñoz, 2008; Fennell et al., 2017; Martínez et al., 2017). The lower parts of section z-1G08A (below 0 m a.s.l.) show the reflectors resembling an antiformal stack and thrust faults verging to the east, the latter of which can also be seen at the surface around Cerro Quimal (Fig. 2). The extent to which these faults affect the Cordillera de la Sal cannot be discerned with this section, but several authors have argued for deep-seated faults and structures which, along with diapirism, would have generated this relief (e.g., Rubilar et al., 2017; Wilkes and Görler, 1994).

The synorogenic sequences to the east (between the surface and ca. 1000 m b.s.l.) show west-dipping to semi horizontal reflectors, overlying steeper, west-dipping units belonging to the pre-Cretaceous successions (Mz-Tr, Tr, Pz?) in the eastern half of lines z-1G010 and z-1G08, separated by an angular unconformity; the most recent deposits show an essentially semi horizontal character (Figs. 5 and 6). The Upper Cretaceous and Eocene-Paleogene successions (K and Pg-Eo) show onlap terminations against a west-dipping surface (blue reflector) between 250 m a.s.l and 1000 m b.s.l. Several near-vertical structures, interpreted as normal and inverted faults, exist below this reflector, which accommodated Mesozoic (Mz-Tr) successions that show strong *E*-W and N-S variations in thickness when moving away from the controlling fault, and onlap terminations against them. Subsequent compressive reactivation of these structures is observed in these lines and in other parts of the basin, as shown by Martínez et al. (2018), which may also affect the most recent cover of the saltpan. The eastern part of line z-1G008 clearly shows the angular unconformity between the west-dipping underlying pre-Cretaceous successions and the Cenozoic strata; the former crop out ca. 6 km east of the end of line z-1G010, showing a similar structural disposition (Cas Formation; Becerra et al., 2014). Units K and Pg-Eo both pinch out at the eastern end of the seismic lines.

4.3. Gravity survey and density structure

The complete Bouguer anomaly for the northern and southern profiles can be found in Figs. 7 and 8, respectively. The short-wavelength gravity lows have been interpreted as depocenters and/or deposits belonging to the Cretaceous-Eocene (Purilactis Group to Loma Amarilla Formation), and the Oligo-Miocene to recent evaporites and fine-grained deposits. The gravity highs, on the other hand, have been linked to the presence of either Paleogene intrusives and/or Triassic to Upper Paleozoic deposits. The modeled contrast densities can be found in Table 1.

The northern profile (Fig. 7) shows the presence of a wide, distinct gravity high encompassing much of the measured profile, which shows a decrease towards its eastern end. This high has been attributed to the different Permian-Carboniferous and Triassic units present at this border of the Cordillera de Domeyko (Fig. 2a), which comprises crystalline tuffs, andesitic lavas and granitoids (Basso and Mpodozis, 2012). Also, the presence of a Paleogene intrusive cannot be ruled out, as the magnetic anomalies show the presence of a magnetized body (see below), which could be the northward prolongation of those intrusives and related found in Cerro Quimal (Andriessen and Reutter, 1994; Basso and Mpodozis, 2012). Eastwards, and starting around the escarpment, the gravity low is represented by the evaporites and fine-grained clastics of the Oligocene-Miocene San Pedro Formation (-0.68 g/cc^3), and the successions of the Tonel and Purilactis Formations (-0.21 g/cc^3). Considering that the thickness of the units at the northeastern limit should coincide with those reported by Bascuñán et al. (2019), the gravimetry survey shows the continuity towards the escarpment of the low-density units, where the geometry of the Purilactis-Tonel body shows that its deposits are found west of the escarpment and buried beneath Miocene to recent gravels (-0.47 g/cc^3). The presence of units belonging to the Tonel Formation over the basement west of the El Bordo Escarpment has been documented previously by several authors (Bascuñán et al., 2016; Basso and Mpodozis, 2012; Henríquez et al., 2014; Narea et al., 2015).

The southern profile (Fig. 8) shows, from west to east, slight deviations from the regional trend during its first 8 km, owing to the presence of Miocene to recent gravels (-0.47 g/cc^3) covering the same Permian-Carboniferous volcanic successions and intrusives as those found northwards, belonging to the Agua Dulce Formation (Basso and Mpodozis, 2012). The deviation increases when approaching the El Bordo Escarpment, where outcrops of the Tonel, Purilactis and Cerro Totola Formations are found (-0.21 g/cc^3), and where the topography abruptly drops from around 3200 m a.s.l to 2370 m a.s.l. These units form a wedge underneath the gravel cover, which increases in depth eastwards towards the basin center, showing its maximum depth beneath the Llano de la Paciencia area, west of the Cordillera de la Sal. The evaporites and fine-grained deposits belonging to the San Pedro Formation and Pliocene-recent evaporites are incorporated from this point onwards, forming a wedge underlain by deposits belonging to the Purilactis Group and Paleocene to Eocene (?) continental deposits with similar densities as those found around the escarpment to the west (-0.21 g/cc^3). These low-density units follow the sub horizontal reflectors seen in Fig. 6, with only minor changes in thickness, the most relevant of which is found beneath the Cordillera de la Sal. The evaporites thin out at the basin edge, while the underlying clastic sequence mimics the west-dipping reflector found in Figs. 5 and 6, and also pinches out to the east, where both successions overlap the Mesozoic basement that crops out in this area (Fig. 2; Becerra et al., 2014; Niemeyer, 2013). The high-density unit modeled in Fig. 7 was not required here, though it may continue west of the western end of the profile.

4.4. Magnetic modeling

The distinct, high-gravity anomaly found in the northern profile (Fig. 7), and the proximity of the gravity profiles to large igneous intrusions such as Cerro Quimal (Fig. 2), raised the issue that there could be bodies with a higher density than the background, and that they could be recognized in a magnetic survey. A review of the total field anomaly obtained by Hernández (2019) (Fig. 2b) reveals the presence of several long- and short-wavelength magnetic anomalies within the study area, with a large anomaly present underneath the Salar de Atacama Basin (with a length of ca. 110 km and a width of ca. 60 km), and a north-south succession of highs and lows within Cordillera de Domeyko, with a pronounced peak in the Cerro Quimal area.

The analysis of the northern susceptibility model profile (Fig. 7) shows, from west to northeast, distinct mid- to short-wavelength anomalies, the most noticeable of which reaches susceptibility values over 0.055 (SI), while the rest are usually lower than 0.04 (SI). An anomaly is prominent and close to the surface west of El Bordo Escarpment, where it is around 8 km wide; its width increases with increasing depth, and its western side shows a west-dipping surface which reaches depths of ca. 15 km b.s.l. The eastern side of the anomaly shows a sub vertical, irregular shape, which on the surface would be located around 10 km NW of the escarpment (Figs. 2b and 7).

The northeastern part of the profile shows a short-wavelength anomaly ca.5 km wide, located between the surface and 4400 m b.s.l., a magnetic susceptibility of 0.026 (SI), and surrounded by low susceptibilities. The eastern end of the anomaly coincides with the El Bordo Escarpment. The large anomaly seen to the NE starts in the middle of the Llano de la Paciencia (Figs. 2 and 7), and presents sides dipping in opposite directions close to the surface, which become steeper with increasing depth. The width of the anomaly at 0 m a.s.l. is of ca. 5 km, and it also widens with depth, especially towards the NE side. The susceptibilities within the anomaly are mostly uniform, with values around 0.026–0.033 (SI). Regarding the position of the anomalies with respect to the modeled geological units, the magnetic anomalies in the middle of the section, found immediately west of the escarpment, overlap in some areas with the high-density body obtained from the gravimetric analysis.

At least three origins for this anomaly are possible: a) the anomaly might represent variations within the Agua Dulce Fm. and associated Carboniferous-Permian intrusives, similar to what happens in the southern profile (see below), b) the anomaly could be an equivalent to the Cerro Quimal intrusives and related units, which are found south of the profile and also intruding the Late Cretaceous units (Fig. 2 and c) it could represent an uneven mixture of both sources. The latter option appears the most coherent with the geophysical and geological data collected here, but an assessment of the contribution of each source cannot be performed with the available data.

The southern susceptibility model cross section (Fig. 8) shows that its western border, involving much of the El Bordo Escarpment, displays a large magnetic anomaly that crops out on the surface, along with some low-scale variations of the susceptibility around the continuation of the Barros Arana Syncline. The major anomaly to the west has susceptibilities ranging between 0.026 and 0.07 (SI), with a high susceptibility zone ca. 15 km tall and 8 km wide, between 0 m and 15 km b.s.l. The susceptibility around the Barros Arana Syncline is in the lower end of the aforementioned range. These susceptibilities are similar to those expected for basaltic to dacitic intrusions or deposits, according to several authors (e.g., Alatorre-Zamora et al., 2015; García-Abdeslem, 2014; Hunt et al., 1995), which are known to crop out along the El Bordo Escarpment (Arriagada et al., 2006a; Basso and Mpodozis, 2012; Henríquez et al., 2014; Mpodozis et al., 1999). This area (or conversely, these anomalies) cannot be directly correlated with the geological units interpreted from the gravity profile, but its eastern part does show an overlap with the Cretaceous-Paleogene units, possibly those of the Cerro Totola Formation.

The section shows a broad anomaly eastwards, whose sides dip to the east, and with susceptibilities ranging between 0.026 and 0.049 (SI). At the surface, the anomaly encompasses part of the Cordillera de la Sal (Fig. 2), forming a narrow anomaly ca. 5 km long surrounded by lower

susceptibility zones, one of which is especially wide towards the east. The high susceptibility area does widen with depth (up to ca. 20 km wide at 5 km b.s.l.), overall maintaining the eastwards dip of its sides. Small anomalies, though at times showing high susceptibilities (over 0.064 (SI)) can be found to the east, in an area within the actual salt pan and before the alluvial deposits on the eastern side of the basin (Fig. 2). They are ca. 5–10 km wide, and can reach depths of 5 km b.s.l. In a manner similar to the western part, the anomalies do not always overlap with the modeled gravity bodies, which were correlated with Cretaceous to recent deposits. They appear to be a response of part of the basement of the basin, which crops out close to the eastern end of the section (Becerra et al., 2014). The wide range of the susceptibilities could also be due to basic intrusions within the basement (Alatorre-Zamora et al., 2015; García-Abdeslem, 2014; Hunt et al., 1995).

The addition of a N-S line (Figs. 2 and 9) was carried out to link and test the magnetic anomalies found in both profiles, and also to obtain insight into the origin of said anomalies. It can be divided into two zones, with Cerro Quimal serving as the transition area. From south to north, the line shows a large, high susceptibility zone (> 0.026 (SI)), with small-scale areas with lower susceptibilities, and a wide, irregular area (ca. 25 km) with very high susceptibilities, even reaching peaks of over 0.095 (SI) close to the surface around the latitude as Cerro Quimal (Fig. 2). Towards the north, a north-dipping limit separates these anomalies from a wide area with overall low susceptibilities, with the exception of a ca. 10 km wide and 12 km deep zone close to the end of the line. The susceptibility in this area reaches around 0.026 (SI). Overall, the magnetic anomalies in this profile can be linked to the presence at the surface of the Upper Cretaceous-Paleogene intrusive rocks related to Cerro Quimal (Fig. 2), along with the Permian-Carboniferous granitoids and deposits documented in the area, and some minor basic intrusions (Basso and Mpodozis, 2012; Henríquez et al., 2014; Marinovic and Lahsen, 1984; Ramírez and Gardeweg, 1982).

5. Discussion

The integration of the field and geophysical data produced in this study leads to a better understanding of the structure of the Salar de Atacama Basin, its interaction with Cordillera de Domeyko, and its present-day configuration (Fig. 10). The northern gravimetry profile (Fig. 7) shows a western domain associated with units whose densities are either the same as or higher than the basement, covered by a thin sedimentary layer. On the other hand, the eastern domain is comprised mostly of units with lower densities than the background, marking a distinct gravity low. The interphase between both corresponds roughly with the El Bordo Escarpment, where the lower units of the Purilactis Group (Tonel and Purilactis Fms.) are exposed in a series of complex folds involving continental successions and evaporitic layers, whose axes follow the trend of the larger Barros Arana Syncline due ca. 6 km north (Fig. 2; Arriagada et al., 2006a; Bascuñán et al., 2016; Mpodozis et al., 2005). Although the gravity survey cannot distinguish between the individual folds, it reveals at least three characteristics regarding the Upper Cretaceous units; first, as shown above, that these units extend eastward into the basin; second, that its largest thickness is found directly south of the syncline; and third, that the units display a structure resembling a structural lid (e.g. towards the west, where a thin wedge overlies the basement/high-density unit. A similar disposition can be observed in the southern gravity profile (Fig. 8), located ca. 30 km south, where the profile also shows the increase in Upper Cretaceous-Paleogene deposits eastwards, and their thinning towards the eastern end of the basin. This disposition was not identified in the analysis done by Bascuñán et al. (2019), where the basement units belonging to the Triassic Tuina Formation are structurally placed over a wedge of Upper Cretaceous units. This is possibly related to the style and amount of exhumation of the different units comprising the basement of Cordillera de Domeyko. As such, the Cenozoic configuration of the basin is directly related to the thrusting eastwards of Cordillera de Domeyko which both deforms the pre-Oligocene successions and generates, at least partly, the accommodation space required for younger units.

This contrast between the basement (which comprises the pre-Upper Cretaceous, volcanosedimentary and crystalline units) and the sedimentary successions can also be derived from the modeling of the magnetic lines (Figs. 7, 8 and 9). The N-S magnetic line measured exclusively west of the El Bordo Escarpment (Figs. 2b and 9) displays a wide magnetic anomaly with internal variations that reaches the surface in the area around Cerro Quimal. In the case of the other *E*-W lines, the magnetic anomalies mostly overlap with areas modeled as basement in the gravity modeling. In some cases, a minor overlap can be seen with Upper Cretaceous-Paleogene units (Figs. 7 and 8), and Mesozoic-Oligocene units (Fig. 8). As stated above, the anomalies within the Cordillera de Domeyko might come from multiple sources, although two are clear at the surface: first, the intrusion of Upper Cretaceous to

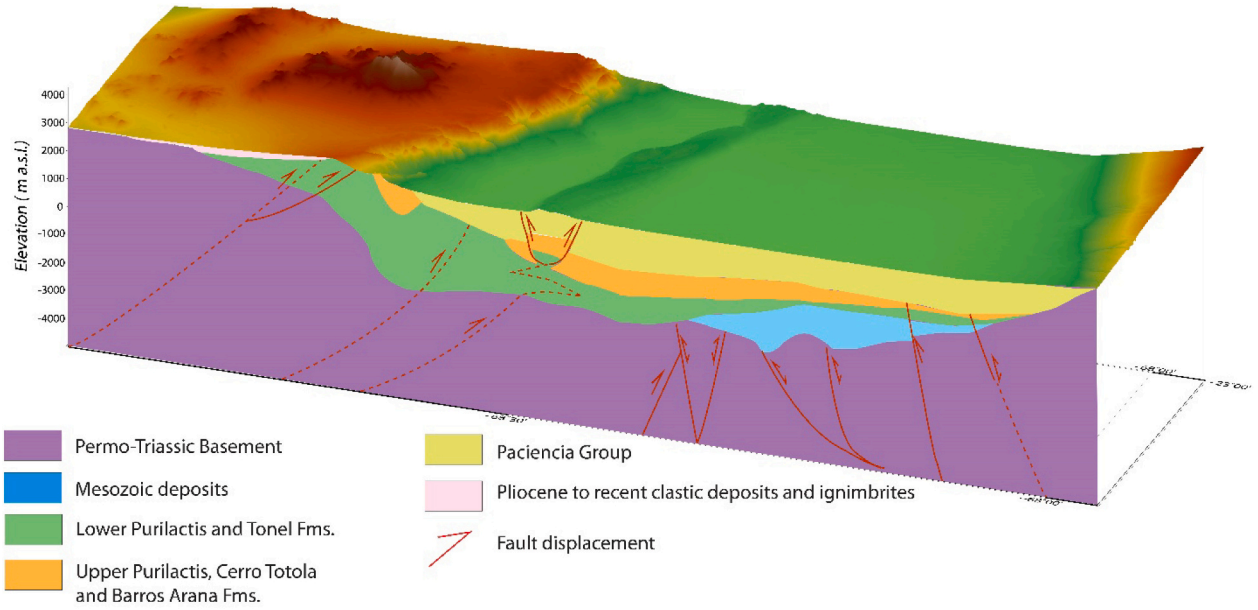

Fig. 10. 3D view of the integration of the analyzed data, following the strike of the southern profile and line 1-zG010, and its DEM topography.

Paleogene rocks, and second, the crystalline components of the basement (Basso and Mpodozis, 2012; Marinovic and Lahsen, 1984), which are seen thrusted over younger units in the Cerro Quimal and Cerro Negro areas farther south, and in other areas of Cordillera de Domeyko (Amilibia et al., 2008; Arriagada et al., 2006a; Henríquez, 2012; Mpodozis et al., 1999). This is in agreement with field observations that show that only the lower part of the Purilactis Group presents sparse Upper Cretaceous-Lower Paleogene intrusions, and that volcanic and/or crystalline units are largely absent from subsequent formations, save for thin lava layers within the Naranja Formation and the upper Purilactis Formation, the Cerro Totola Formation, and tuff layers within the San Pedro Formation (Becerra et al., 2014; Charrier and Reutter, 1994; Flint et al., 1989; Gardeweg et al., 1994; Hammerschmidt et al., 1992; Hartley et al., 1992; Henríquez et al., 2014; Mpodozis et al., 2005; Solari et al., 2017).

The density contrasts used for modeling (Table 1) differ from those that may be calculated from the Toconao-1 well (Fig. 4b, e), where a larger density contrast could have been expected for the Purilactis Group-Paleogene continental clastics (−0.3 vs −0.21 g/cc^3), and a smaller one for the evaporitic successions (−0.42 vs −0.68 g/cc^3). At least two reasons explain this discrepancy; the first one involves the state of the rock after its boring, which inevitably damages the walls of the well, leading thus to values that are only representative of the local state of the rocks. The second explanation is that the well cannot account for the lateral and vertical variations in density bound to occur in any rock unit, and as such should not be given regional significance.

The density log is useful though for making a comparison with the other logs (Fig. 4), showing that changes in density roughly coincide with areas where other physical changes occur. As such, the modeling does respect the depths of the well identified as major physical boundaries, which also coincide with major reflections within the seismic sections (Figs. 5 and 6). In this regard, the blue reflector (ca. 1 s TWT) seen in the VSP log (Fig. 4a), roughly equivalent to 1580–1650 m depth, corresponds to the main limit observed, which has been interpreted as the boundary between the Purilactis Group and the Mesozoic units represented by a prominent west-dipping reflector seen in the seismic sections (Figs. 5 and 6). It is worth noting that the gravity survey does not match exactly with the blue reflector in the westernmost end of line z-G010 (Fig. 6), but with some of the reflectors approximately 0.5 s TWT above, a discrepancy possibly due to the increase in compaction with depth, or lithological variations within the unit (Fig. 8). Though previous authors have considered the deformed units below the blue reflector as part of the Purilactis Group (Jordan et al., 2007; Muñoz et al., 2002; Pananont et al., 2004; Rubilar et al., 2017), or the Naranja Formation (Arriagada et al., 2006a), the interpretation here is closer to that of Martínez et al. (2018), where several extensional features led them to conclude that those sequences belonged to Lower Cretaceous or earlier successions. These features are also observed in the northern parts of the basin (Bascuñán et al., 2019), and in the southern Salar de Punta Negra Basin (Martínez et al., 2017).

The gravity and seismic profiles and analysis performed in this study show the close relation between deformation at the eastern edge of the Cordillera de Domeyko, the formation of the Barros Arana Syncline and the modern Salar de Atacama Basin, and are in agreement with the studies performed by Martínez et al. (2018, 2019, 2020) and Bascuñán et al. (2019). Although the Cordillera de la Sal domain is not imaged in seismic reflection profiles at this latitude, a link between its formation and the structures found in the profiles has been studied by various authors, with explanations ranging from diapiric flow, inversion and transpression following an extensional episode (Jordan et al., 2007; Pananont et al., 2004; Rubilar et al., 2017), to a surficial expression of the faults involving the Purilactis Group (Arriagada et al., 2006a; Reutter et al., 2006; Wilkes and Görler, 1994). As shown here, the low-density body, associated with the San Pedro Formation and recent evaporites, presents an overall increase in thickness eastwards from the El Bordo Escarpment, and growth-strata geometries that suggest its compressive origin, such as those observed in the seismic profiles and gravity analysis due north, close to the San Pedro de Atacama area and the Barros Arana Syncline (Bascuñán et al., 2019).

One pressing issue in the area resides within the units ascribed to the Paleogene, mainly regarding their chronostratigraphy and their presence within the basin, as well as their variations in lithofacies and their tectonic background. To the north, they are represented by aeolian deposits and alluvial/fluvial units belonging to the upper Purilactis and Barros Arana Formations (Bascuñán et al., 2016; Charrier and Reutter, 1994; Hartley et al., 1992; Mpodozis et al., 2005), which are not seen towards the south, but are thought to be possible time-equivalents of the Naranja Formation (Bascuñán et al., 2019). Given the U—Pb detrital zircon ages published by Bascuñán et al. (2019), and the lack of prominent unconformities between the Upper Cretaceous-Paleogene units, the authors argued that there was no visible deformation event between both units, and that the configuration of the syncline was mainly achieved during the Incaic Event, between the Eocene-Oligocene (Arriagada et al., 2006a, 2006b, 2008; Maksaev and Zentilli, 1999; Narea et al., 2015; O'Driscoll et al., 2012). This unconformity cannot be identified through the gravimetric method due to the similarity in density contrasts between both units, but some reflector terminations do point out to a slight unconformity towards the basin center (Figs. 5 and 6; Martínez et al., 2018), reflecting that the so-called K-T Event (Cornejo et al., 2003, 1993) may have been present in the area, showing N-S variations in its expression, but would have been tectonically less relevant than the Incaic Event.

Regarding the timing of the deformation events affecting Cordillera de Domeyko, Maksaev and Zentilli (1999) presented apatite fission track data showing the erosion of 4–5 km of rocks between ca. 40–30 Ma and as early as 50 Ma, coinciding with the emplacement of some of the major porphyry copper deposits in northern Chile. Sanchez et al. (2018) studied the Centinela District west of the Salar de Atacama Basin, and obtained similar results showing that the Incaic Event was protracted in time, instead of a short event. They also found evidence for an earlier exhumation event during the KT and show that there was only minor exhumation from the Early Oligocene to the present day. Closer to the basin, Andriessen and Reutter (1994) obtained a mean cooling age of 62 ± 6 Ma from the Paleogene intrusive associated with Cerro Quimal, which would have quickly ascended after its cooling. Henriquez et al. (2019) obtained AFT and AHe samples from the El Bordo Escarpment and Cerro Quimal, and concluded that there were three exhumation stages, with ca. 2.5 km of erosion between 86 and 65 Ma, another event between 65 and 50 Ma involving the migration of the orogenic front to the basin and wedge-top deposition, and finally another stage between 50 and 28 Ma, with the erosion of ca. 1.6–3.3 km of rocks between 50 and 40 Ma and no more than 1.7 km between 40 and 28 Ma. They also argued for limited erosion and exhumation from the Oligocene onwards, which was also confirmed by Reiners et al. (2015), who analyzed several AFT and apatite-zircon He systems and (U—He)/Th from single zircon crystals belonging to the Loma Amarilla Formation, showing partial resetting of this formation and a maximum date of exhumation of its base at ca. 20–22 Ma (with no more than 2–3 km of erosion). Also, Sanchez (2017) recognized an exhumation event within samples belonging to the Cerro Quimal intrusive, where a surface uplift of between 1 and 2 km would have occurred after 10 Ma.

The exhumation data above, and that of the works performed both in and around Cordillera de Domeyko and its sedimentary basins (see above), suggest that, notwithstanding the N-S variation in second-order deformation patterns, the Salar de Atacama basin records a large part of the deformation generating the Central Andes, starting with the exhumation and deformation of sources west of the basin, which are diachronically incorporated into the sediments shed into the basin during the Late Cretaceous-Paleogene, as part of the foredeep fill (Bascuñán et al., 2019, 2016; Hartley et al., 1992; Henriquez et al., 2019; Merino et al., 2013). A migration of the orogenic wedge, or its incorporation of the western border of the basin, is evidenced by the scattered amount of Eocene-Lower Oligocene deposits of the Loma

Amarilla Formation, the inversion of Mesozoic and/or Permo-Triassic normal faults associated with *syn*-rift deposits (Figs. 5 and 6; Martínez et al., 2018), and the thrusting eastwards of basement units and crystalline intrusives, such as those around Cerro Negro and Cerro Quimal (Amilibia et al., 2008; Arriagada et al., 2006a; Bascuñán et al., 2019; Mpodozis et al., 2005). This event thus generates the accommodation space necessary for the deposition of the Oligocene-Miocene successions in a hinterland position, which are directly derived from the units exposed to the west (Becerra et al., 2014; Henríquez et al., 2014; Wilkes and Görler, 1994) and the deposition of evaporitic horizons under arid to hyper-arid conditions (Rech et al., 2019). Deformation during the Late Miocene (Jordan et al., 2010) then generated the Cordillera de la Sal, which might have been formed through the reactivation of reverse faults rooted in the basement, leading to a 'wedge thrust' (Figs. 5 and 10; Bascuñán et al., 2019; Medwedeff, 1990; Muñoz et al., 2002; Reutter et al., 2006), or as part of a detachment between the Paciencia Group and Late Cretaceous-Eocene deposits (Rubilar et al., 2017).

Although the Salar de Atacama Basin has been widely recognized as a relevant topographic anomaly within the Central Andes (Isacks, 1988), its formation is probably also linked to that of the other basins within the Pre-Andean Depression (Charrier et al., 2007), which can be seen as a by-product of the uplift of the Cordillera de Domeyko Range, or the fossilized evidence of its foredeep stage (Amilibia et al., 2008; Bascuñán et al., 2016). In this regard, the evolution of the basin is similar to that proposed by Martínez et al. (2017, 2018, 2019, 2020) for the Salar de Punta Negra Basin, where its formation is dominated by, first, the generation of Mesozoic extensional structures, followed by their positive reactivation (inversion), and finally the formation of basement-involved reverse faults, which can decapitate older structures and place the Paleozoic basement over younger strata. In this regard, contraction appears as the main mechanism for basin subsidence. Moreover, the history revealed in the basin can be compared with other parts of the orogen, such as the Central Depression-western Cordillera de Domeyko limit west of Calama (López et al., 2019), or the same boundary in the Pampa de Tamarugal, further north (Fuentes et al., 2018), where a similar timeline for the evolution of said segments of the orogen has been proposed, with a strong emphasis on the inversion of previous Mesozoic extensional features. Further studies of the basins composing the depression, along with the analysis of its stratigraphy and structure, will aid in establishing a general framework not only for its formation but also for the uplift of the Cordillera de Domeyko and its contribution to the orogen.

Finally, the style of deformation and interplay observed can also be compared with that seen in other basins worldwide, such as the Junggar Basin (Guan et al., 2016; Tang et al., 2015) and the Tarim Basin (Chen et al., 2004; Jia et al., 1998), where Jurassic rifting of the basin is later inverted during the Late Jurassic-Early Cretaceous, with the basement range impinging on the area from the Cretaceous onwards. Future works in the study area could be developed to gauge the influence of inversion and basement-involved reverse faulting in the area, developing similar strategies as studies in other parts of the Andes (Carrera et al., 2006; Carrera and Muñoz, 2008; Giambiagi et al., 2003; McQuarrie, 2002b) the Alpine-Apennine system (Butler et al., 2006), the Kirthar Fold Belt of Pakistan (Hinsch et al., 2019), among others, all of which experienced varying degrees of fault inversion and basement-involved reverse faulting under various regional tectonic conditions.

6. Conclusions

This work consisted in the geophysical and geological analysis of the boundary between the Precordillera and the Preandean Depression in northern Chile, specifically in two transects crossing the El Bordo Escarpment, next to the Salar de Atacama Basin. The gravimetry surveys reveal the prevalence of basement, understood as Triassic (Jurassic?) to earlier deposits, and crystalline intrusive units within the eastern border of Cordillera de Domeyko, with a minor gravel cover. The domain involving the escarpment and the basin shows the prevalence of low-density units, consisting in Upper Cretaceous to Eocene continental deposits and scarce volcanic beds (Tonel, Purilactis, Barros Arana, Cerro Totola, Naranja, and Loma Amarilla Formations), and Oligocene to recent fine-grained clastic deposits and evaporites (San Pedro Formation upwards). The modeling of the magnetic anomaly along these lines confirms the general segmentation of the domains, and the association of magnetic units with either volcanic deposits or igneous intrusives within the basement. The interpretation of seismic reflection profiles, velocity surveys and log data within the basin shows overlaps with the other surveys, particularly regarding the change between the evaporite-rich deposits and the continental, clastic units. The results show that the main deformation stage involved the Late Cretaceous-Paleogene units, which occupied mostly a foredeep position in the basin, until its incorporation into the orogenic wedge during the Incaic Event. Here, thrusting of the basement and crystalline units of the Cordillera de Domeyko, along with the inversion of previous Mesozoic structures, led to most of the structural configuration seen today, and to the generation of accommodation space for the Paciencia Group and more recent deposits. The latter are known to have been deformed mostly during the Late Miocene, as evidenced in the Cordillera de la Sal and key locations within Cordillera de Domeyko, such as Cerro Quimal. The evolution of this part of the basin, and of the eastern flank of Cordillera de Domeyko, is consistent with the findings at other latitudes within the Preandean Depression, showing the close interplay between basement thrusting, exhumation, structural inversion and the generation of foreland basins in northern Chile, and consequently are a prominent feature of the formation of the Central Andes.

Declaration of Competing Interest

The authors declare that they have no known competing financial interests or personal relationships that could have appeared to influence the work reported in this paper.

Acknowledgements

We are deeply grateful for the access granted by Empresa Nacional del Petróleo (ENAP) to their seismic lines and compilation of the different surveys performed in the Salar de Atacama. We also want to thank Alvaro Henríquez and Andrés Fock of Sociedad Química y Minera de Chile S.A. (SQM, now at WSP Chile) for the access to the Toconao Camp and their support. We are also thankful to Midland Valley Ltd., and IRD-GET for providing the license for MOVE 2017 and the CG-3 Scintrex gravimeter, respectively. A.M. acknowledges the support of CONICYT-Chile, under the Chilean Fondo Nacional de Desarrollo Científico y Tecnológico (FONDECYT), Grant 3150160 and PIA/Anillo ACT172002. S.B. acknowledges the support of CONICYT-Chile, Grant 21150380. F.M. acknowledges the support of CONICYT-Chile, under the Chilean Fondo Nacional de Desarrollo Científico y Tecnológico (FONDECYT), Grant 11170098. Finally, we want to thank the invaluable support provided by Sergio Villagrán, Marco Vaccaris and Luis Acevedo.

Appendix A. Supplementary data

Supplementary data to this article can be found online at https://doi.org/10.1016/j.tecto.2021.228818.

References

Alatorre-Zamora, M.A., Campos-Enríquez, J.O., Rosas-Elguera, J.G., Peña-García, L., Maciel-Flores, R., Fregoso-Becerra, E., 2015. Chapala half-graben structure inferred. A magnetometric study. Geofis. Int. 54, 323–342.

Allmendinger, R.W., Jordan, T.E., Kay, S.M., Isacks, B.L., 1997. The evolution of the Altiplano-Puna Plateau of the Central Andes. Annu. Rev. Earth Planet. Sci. 25, 139–174. https://doi.org/10.1146/annurev.earth.25.1.139.

Amilibia, M., Sàbat, F., McClay, K.R., Muñoz, J.A., Roca, E., Chong, G., 2008. The role of inherited tectono-sedimentary architecture in the development of the central Andean mountain belt: insights from the Cordillera de Domeyko. J. Struct. Geol. 30, 1520–1539. https://doi.org/10.1016/j.jsg.2008.08.005.

Andriessen, P.A.M., Reutter, K.-J., 1994. K-Ar and fission track mineral age determination of igneous rocks related to multiple magmatic arc systems along the 23°S latitude of Chile and NW Argentina. In: Reutter, K.-J., Scheuber, E., Wigger, P. (Eds.), Tectonics of the Southern Central Andes: Structure and Evolution of an Active Continental Margin. Springer, New York, pp. 141–154.

Arriagada, C., Roperch, P., Mpodozis, C., 2000. Clockwise block rotations along the eastern border of the Cordillera de Domeyko, Northern Chile (22°45′–23°30′S). Tectonophysics 326, 153–171. https://doi.org/10.1016/S0040-1951(00)00151-7.

Arriagada, C., Roperch, P., Mpodozis, C., Dupont-Nivet, G., Cobbold, P.R., Chauvin, A., Cortés, J., 2003. Paleogene clockwise tectonic rotations in the forearc of Central Andes, Antofagasta region, northern Chile. J. Geophys. Res. Solid Earth 108. https://doi.org/10.1029/2001JB001598.

Arriagada, C., Cobbold, P.R., Roperch, P., 2006a. Salar de Atacama basin: a record of compressional tectonics in the Central Andes since the mid-Cretaceous. Tectonics 25. https://doi.org/10.1029/2004TC001770.

Arriagada, C., Roperch, P., Mpodozis, C., Fernandez, R., 2006b. Paleomagnetism and tectonics of the southern Atacama Desert (25-28°S), northern Chilea. Tectonics 25. https://doi.org/10.1029/2005TC001923.

Arriagada, C., Roperch, P., Mpodozis, C., Cobbold, P.R., 2008. Paleogene building of the Bolivian Orocline: Tectonic restoration of the Central Andes in 2-D map view. Tectonics 27. https://doi.org/10.1029/2008TC002269.

Barnes, J.B., Ehlers, T.A., 2009. End member models for Andean Plateau uplift. Earth-Sci. Rev. 97, 105–132. https://doi.org/10.1016/j.earscirev.2009.08.003.

Bascuñán, S., Arriagada, C., Le Roux, J., Deckart, K., 2016. Unraveling the Peruvian Phase of the Central Andes: stratigraphy, sedimentology and geochronology of the Salar de Atacama Basin (22°30-23°S), northern Chile. Basin Res. 28, 365–392. https://doi.org/10.1111/bre.12114.

Bascuñán, S., Maksymowicz, A., Martínez, F., Becerra, J., Arriagada, C., Deckart, K., 2019. Geometry and late Mesozoic-Cenozoic evolution of the Salar de Atacama Basin (22° 30′ -24° 30′ S) in the northern Central Andes: new constraints from geophysical, geochronological and field data. Tectonophysics 759, 58–78. https://doi.org/10.1016/j.tecto.2019.04.008.

Basso, M., Mpodozis, C., 2012. Carta Cerro Quimal, Región de Antofagasta. In: Servicio Nacional de Geología y Minería, Carta Geológica de Chile, Serie Geología Básica 143, 46 p. 1 mapa escala 1:100.000. Santiago, Chile.

Becerra, J., Henríquez, S., Arriagada, C., 2014. Geología del Área de Salar de Atacama, Región de Antofagasta. In: Carta Geológica de Chile, Serie Geología Básica 166. 1 mapa escala 1:100.000. Santiago, Chile.

Blakely, R.J., 1996. Potential Theory in Gravity and Magnetic Applications. Cambridge University Press, New York. https://doi.org/10.1017/CBO9780511549816.

Breitkreuz, C., Van Schmus, W.R., 1996. U/Pb geochronology and significance of Late Permian ignimbrites in Northern Chile. J. S. Am. Earth Sci. 9, 281–293.

Burg, J.P., 2018. Geology of the onshore Makran accretionary wedge: synthesis and tectonic interpretation. Earth-Sci. Rev. 185, 1210–1231. https://doi.org/10.1016/j.earscirev.2018.09.011.

Butler, R.W.H., Tavarnelli, E., Grasso, M., 2006. Structural inheritance in mountain belts: an Alpine-Apennine perspective. J. Struct. Geol. 28, 1893–1908. https://doi.org/10.1016/j.jsg.2006.09.006.

Carrera, N., Muñoz, J.A., 2008. Thrusting evolution in the southern Cordillera Oriental (northern Argentine Andes): constraints from growth strata. Tectonophysics 459, 107–122. https://doi.org/10.1016/j.tecto.2007.11.068.

Carrera, N., Muñoz, J.a., Sàbat, F., Mon, R., Roca, E., 2006. The role of inversion tectonics in the structure of the Cordillera Oriental (NW Argentinean Andes). J. Struct. Geol. 28, 1921–1932. https://doi.org/10.1016/j.jsg.2006.07.006.

Catuneanu, O., Galloway, W.E., Kendall, C.G.S.C., Miall, A.D., Posamentier, H.W., Strasser, A., Tucker, M.E., 2011. Sequence stratigraphy: methodology and nomenclature Gebrüder Borntraeger · Stuttgart 2011. Newsl. Stratigr. 44 (3), 173–245.

Cawood, P.A., Kröner, A., Collins, W.J., Kusky, T.M., Mooney, W.D., Windley, B.F., 2009. Accretionary orogens through Earth history. Geol. Soc. London Spec. Publ. 318, 1–36. https://doi.org/10.1144/SP318.1.

Charrier, R., Muñoz, N., 1994. Jurassic-Cretaceous Paleogeographic evolution of the Chilean Andes at 23°-24°S.L. and 34°-35°S.L.: a comparative analysis. In: Reutter, K., Scheuber, E., Wigger, P. (Eds.), Tectonics of the Southern Central Andes: Structure and Evolution of an Active Continental Margin. Springer, New York, pp. 233–242.

Charrier, R., Reutter, K., 1990. The Purilactis Group of Northern Chile: link between arc and backarc during Late Cretaceous and Paleogene. In: Proceedings I ORSTOM-ISAG, Grenoble, pp. 249–252.

Charrier, R., Reutter, K., 1994. The Purilactis group of northern Chile: boundary between arc and backarc from Late Cretaceous to Eocene. In: Reutter, K., Scheuber, E., Wigger, P. (Eds.), Tectonics of the Southern Central Andes: Structure and Evolution of an Active Continental Margin. Springer, New York, pp. 189–202.

Charrier, R., Pinto, L., Rodriguez, M.P., 2007. Tectonostratigraphic evolution of the Andean Orogen in Chile. In: Geology of Chile, pp. 21–114. https://doi.org/10.1144/GOCH.3.

Charrier, R., Farías, M., Maksaev, V., 2009. Evolución Tectónica, Paleogeográfica y Metalogénica durante el Cenozoico en los Andes de Chile norte y central e implicaciones para las regiones adyacentes de Bolivia y Argentina. Rev. Asoc. Geol. Argent. 65, 5–35.

Chen, S., Tang, L., Jin, Z., Jia, C., Pi, X., 2004. Thrust and fold tectonics and the role of evaporites in deformation in the Western Kuqa Foreland of Tarim Basin, Northwest China. Mar. Pet. Geol. 21, 1027–1042. https://doi.org/10.1016/j.marpetgeo.2004.01.008.

Cornejo, P., Mpodozis, C., Ramirez, C.F., Tomlinson, A.J., 1993. Estudio Geológico de la Región de El Salvador y Potrerillos. Servicio Nacional de Geología y Minería, Informe Registrado IR-93-1, Santiago, Chile.

Cornejo, P., Matthews, S., Perez de Arce, C., 2003. The 'K-T' compressive deformation event in northern Chile (24-27°S). X Congr. Geol. Chil. CD-Rom 1–13.

Cortés, J., 2000. Hoja Palestina, Región de Antofagasta. Servicio Nacional de Geología y Minería. In: Mapas Geológicos 19. 1 mapa escala 1:100.000. Santiago, Chile.

Cross, T.A., Lessenger, M.A., 1988. Seismic stratigraphy. Annu. Rev. Earth Planet. Sci. 16, 319–354.

DeCelles, P.G., Zandt, G., Beck, S.L., Currie, C.A., Ducea, M.N., Kapp, P., Gehrels, G.E., Carrapa, B., Quade, J., Schoenbohm, L.M., 2015. Cyclical orogenic processes in the Cenozoic central Andes. In: Decelles, P.G., Ducea, M.N., Carrapa, Barbara, Kapp, P.A. (Eds.), Geodynamics of a Cordilleran Orogenic System: The Central Andes of Argentina and Northern Chile, Geological Society of America Memoir, Vol. 212. The Geological Society of America, pp. 459–490. https://doi.org/10.1130/2015.1212(22.

Dewey, J.F., Bird, J.M., 1970. Mountain belts and the new global tectonics. J. Geophys. Res. 75, 2625–2647.

Fennell, L.M., Folguera, A., Naipauer, M., Gianni, G., Rojas Vera, E.A., Bottesi, G., Ramos, V.A., 2017. Cretaceous deformation of the southern Central Andes: synorogenic growth strata in the Neuquén Group (35° 30′-37° S). Basin Res. 29, 51–72. https://doi.org/10.1111/bre.12135.

Flint, S., Hartley, A.J., Rex, D.C., Guise, P., Turner, P., 1989. Geochronologv of the purilactis formation, northern Chile: an insight into late cretaceous/earlv tertiarv basin dvnamics of the Central Andes. Rev. Geol. Chile 16, 241–246.

Flint, S., Turner, P., Jolley, E.J., Hartley, A.J., 1993. Extensional Tectonics in Convergent Margin Basins – an example from the Salar-De-Atacama, Chilean Andes. Geol. Soc. Am. Bull. 105, 603–617. https://doi.org/10.1130/0016-7606(1993)105<0603.

Fuentes, G., Martínez, F., Bascuñan, S., Arriagada, C., Muñoz, R., 2018. Tectonic architecture of the Tarapacá Basin in the northern Central Andes: new constraints from field and 2D seismic data. Geosphere 14, 2430–2446. https://doi.org/10.1130/GES01697.1.

García-Abdeslem, J., 2014. On the significance of magnetic anomalies from the Baja California Peninsula: its relationship with IOCG deposits and the deep crustal magnetic layer. Rev. Mex. Cienc. Geol. 31, 270–279.

Gardeweg, M., Pino, H., Ramírez, C.F., Davidson, J., 1994. Mapa Geológico del área de Imilac y Sierra Almeida, Región de Antofagasta. In: Servicio Nacional de Geología y Minería. Documento de Trabajo 7. 1 mapa escala 1:100.000. Santiago, Chile.

Giambiagi, L.B., Alvarez, P.P., Godoy, E., Ramos, V.A., 2003. The control of pre-existing extensional structures on the evolution of the southern sector of the Aconcagua fold and thrust belt, southern Andes. Tectonophysics 369, 1–19. https://doi.org/10.1016/S0040-1951(03)00171-9.

Götze, H.-J., Krause, S., 2002. The Central Andean gravity high, a relic of an old subduction complex? J. S. Am. Earth Sci. 14, 799–811. https://doi.org/10.1016/S0895-9811(01)00077-3.

Götze, H.-J., Lahmeyer, B., Schmidt, S., Strunk, S., 1994. The Lithospheric Structure of the Central Andes (20°–26°S) as Inferred from Interpretation of Regional Gravity. In: Reutter, K., Scheuber, E., Wigger, P. (Eds.), Tectonics of the Southern Central Andes: Structure and Evolution of an Active Continental Margin. Springer, New York, pp. 7–21.

Guan, S., Stockmeyer, J.M., Shaw, J.H., Plesch, A., Zhang, J., 2016. Structural inversion, imbricate wedging, and out-of-sequence thrusting in the southern Junggar fold-and-thrust belt, northern Tian Shan, China. Am. Assoc. Pet. Geol. Bull. 100, 1443–1468. https://doi.org/10.1306/04041615023.

Hammerschmidt, K., Döbel, R., Friedrichsen, H., 1992. Implications of 40Ar/39Ar dating of Tertiary volcanic rocks from the north-Chilean Precordillera. Tectonophysics 202, 55–81.

Hartley, A.J., Flint, S., Turner, P., Jolley, E.J., 1992. Tectonic controls on the development of a semi-arid alluvial basin as reflected in the stratigraphy of the Purilactis Group (upper cretaceous-eocene), northern Chile. J. S. Am. Earth Sci. 5, 275–296. https://doi.org/10.1016/0895-9811(92)90026-U.

Henríquez, S., 2012. Estructura del Salar de Atacama: Implicancias en la estructura cortical de los Andes Centrales. Universidad de Chile.

Henríquez, S., Becerra, J., Arriagada, C., 2014. Geología del área San Pedro de Atacama, Región de Antofagasta. In: Servicio Nacional de Geología y Minería. Carta Geológica de Chile Serie Geología Básica 171. 1 Mapa escala 1:100,000. Santiago, Chile.

Henriquez, S., DeCelles, P.G., Carrapa, B., 2019. Cretaceous to Middle Cenozoic exhumation history of the Cordillera de Domeyko and Salar de Atacama Basin, Northern Chile. Tectonics. https://doi.org/10.1029/2018TC005203.

Hernández, M.J., 2019. Distribución Tridimensional de Cuerpos Magnetizados Profundos y Estructura de la Corteza Continental en el Norte de Chile, Región de Antofagasta (22°-24°S). Universidad de Chile.

Heuret, A., Lallemand, S., 2005. Plate motions, slab dynamics and back-arc deformation. Phys. Earth Planet. Inter. 149, 31–51. https://doi.org/10.1016/j.pepi.2004.08.022.

Hinsch, R., Asmar, C., Nasim, M., Asif Abbas, M., Sultan, S., 2019. Linked thick-to thin-skinned inversion in the central Kirthar Fold Belt of Pakistan. Solid Earth 10, 425–446. https://doi.org/10.5194/se-10-425-2019.

Howell, J.a., Schwarz, E., Spalletti, L.a., Veiga, G.D., 2005. The Neuquen Basin: an overview. Geol. Soc. Lond. Spec. Publ. 252, 1–14. https://doi.org/10.1144/GSL.SP.2005.252.01.01.

Hunt, C., Moskowitz, B., Banerjee, S., 1995. Magnetic properties of rocks and minerals. In: Rock Physics and Phase Relations: A Handbook of Physical Constants, pp. 189–203. https://doi.org/10.1016/b978-044452748-6/00049-3.

Isacks, B.L., 1988. Uplift of the Central Andean Plateau and bending of the Bolivian Orocline. J. Geophys. Res. 93, 3211. https://doi.org/10.1029/JB093iB04p03211.
Jia, D., Lu, H., Cai, D., Wu, S., Shi, Y., Chen, C., 1998. Structural features of northern Tarim Basin: implications for regional tectonics and petroleum traps. Am. Assoc. Pet. Geol. Bull. 82, 147–159.
Jolley, E.J., Turner, P., Williams, G.D., Hartley, A.J., Flint, S., 1990. Sedimentological response of an alluvial system to Neogene thrust tectonics, Atacama Desert, northern Chile. J. Geol. Soc. Lond. 147, 769–784. https://doi.org/10.1144/gsjgs.147.5.0769.
Jordan, T.E., Mpodozis, C., Muñoz, N., Blanco, N., Pananont, P., Gardeweg, M., 2007. Cenozoic subsurface stratigraphy and structure of the Salar de Atacama Basin, northern Chile. J. S. Am. Earth Sci. 23, 122–146. https://doi.org/10.1016/j.jsames.2006.09.024.
Jordan, T.E., Nester, P.L., Blanco, N., Hoke, G.D., Dávila, F., Tomlinson, A.J., 2010. Uplift of the Altiplano-Puna plateau: a view from the west. Tectonics 29. https://doi.org/10.1029/2010TC002661.
Kane, M.F., 1962. A comprehensive system of terrain corrections using a digital computer. Geophysics XXVII, 455–462.
Kay, S.M., Coira, B.L., 2009. Lithospheric loss, magmatism, and crustal fl ow under the central Andean Altiplano-Puna Plateau. Geol. Soc. Am. Mem. 204, 1–32. https://doi.org/10.1130/2009.1204(11).
Kay, S.M., Godoy, E., Kurtz, A., 2005. Episodic arc migration, crustal thickening, subduction erosion, and magmatism in the south-Central Andes. Bull. Geol. Soc. Am. 117, 67–88. https://doi.org/10.1130/B25431.1.
Li, Y., Oldenburg, D.W., 1993. 3-D inversion of magnetic data. In: 1993 SEG Annu. Meet. 61, pp. 400–402. https://doi.org/10.1190/1.1822498.
Longman, I.M., 1959. Formulas for computing the tidal acceleration due to the Moon and Sun. J. Geophys. Res. 64, 2351–2355.
López, C., Martínez, F., Maksymowicz, A., Giambiagi, L., Riquelme, R., 2019. What is the structure of the forearc region in the Central Andes of northern Chile? An approach from field data and 2-D reflection seismic data. Tectonophysics 769, 228187. https://doi.org/10.1016/j.tecto.2019.228187.
López, C., Martínez, F., Del Ventisette, C., Bonini, M., Montanari, D., Muñoz, B., Riquelme, R., 2020. East-vergent thrusts and inversion structures: an updated tectonic model to understand the Domeyko Cordillera and the Salar de Atacama Basin transition in the western Central Andes. J. S. Am. Earth Sci. 103, 102741. https://doi.org/10.1016/j.jsames.2020.102741.
Luyendyk, A.P.J., 1997. Processing of airborne magnetic data. AGSO J. Aust. Geol. Goephys. 17, 31–38.
Maksaev, V., Zentilli, M., 1999. Fission track thermochronology of the Domeyko Cordillera, northern Chile: Implications for Andean tectonics and porphyry copper metallogenesis. Explor. Min. Geol. 8, 65–89.
Marinovic, N., García, M., 1999. Hoja Pampa Unión. Región de Antofagasta. In: Servicio Nacional de Geología y Minería, Mapas Geológicos 9. 1 mapa escala 1:100.000. Santiago, Chile.
Marinovic, N., Lahsen, A., 1984. Hoja Calama. In: Servicio Nacional de Geología y Mineria, Carta Geológica de Chile 58. 1 mapa escala 1:250.000. Santiago, Chile.
Martínez, F., Gonzalez, R., Bascuñan, S., Arriagada, C., 2017. Structural styles of the Salar de Punta Negra Basin in the Preandean Depression (24°-25°S) of the Central Andes. J. S. Am. Earth Sci. 1–12. https://doi.org/10.1016/j.jsames.2017.08.004.
Martínez, F., López, C., Bascuñan, S., Arriagada, C., 2018. Tectonic interaction between Mesozoic to Cenozoic extensional and contractional structures in the Preandean Depression (23°–25°S): geologic implications for the Central Andes. Tectonophysics 744, 333–349. https://doi.org/10.1016/j.tecto.2018.07.016.
Martínez, F., López, C., Parra, M., Espinoza, D., 2019. Testing the occurrence of thick-skinned triangle zones in the Central Andes forearc: example from the Salar de Punta Negra Basin in northern Chile. J. Struct. Geol. 120, 14–28. https://doi.org/10.1016/j.jsg.2018.12.009.
Martínez, F., López, C., Parra, M., 2020. Effects of pre-orogenic tectonic structures on the Cenozoic evolution of Andean deformed belts: evidence from the Salar de Punta Negra Basin in the Central Andes of Northern Chile. Basin Res. 1–22. https://doi.org/10.1111/bre.12436.
McQuarrie, N., 2002a. Initial plate geometry, shortening variations, and evolution of the Bolivian orocline. Geology 30, 867–870. https://doi.org/10.1130/0091-7613(2002)030<0867:IPGSVA>2.0.CO;2.
McQuarrie, N., 2002b. The kinematic history of the central Andean fold-thrust belt, Bolivia: implications for building a high plateau. Bull. Geol. Soc. Am. 114, 950–963. https://doi.org/10.1130/0016-7606(2002)114<0950:TKHOTC>2.0.CO;2.
Medwedeff, D.A., 1990. Geometry and kinematics of an active, laterally propagating wedge-thrust, wheeler ridge, California: ABSTRACT. Am. Assoc. Pet. Geol. Bull. 74 https://doi.org/10.1306/44b4b61c-170a-11d7-8645000102c1865d.
Merino, R., Salazar, E., Mora-Franco, C., Creixell, C., Coloma, F., Oliveros, V., 2013. Fluvial deposition and retro-arc volcanism in a Late Cretaceous foreland basin and the unroofing of the Early Cretaceous arc in the chilean Frontal Cordillera at 28°30'S, Atacama Region. Boll. Geof. Teor. Appl. 54, 237–238.
Mpodozis, C., Arriagada, C., Roperch, P., 1999. Cretaceous to Paleogene Geology of the Salar de Atcama Basin, northern Chile: a reappraisal of the Purilactis Group Stratigraphy. In: Proceedings IV IRD-ISAG. IRD Editions, Goettingen, Germany, pp. 523–526.
Mpodozis, C., Blanco, N., Jordan, T.E., Gardeweg, M., 2000. Estratigrafía y Deformación del Cenozoico Tardío en la Región norte de la Cuenca del Salar de Atacama: La zona de Vilama-Pampa Vizcachitas. In: Congreso Geológico Chileno No. 9 Actas, 2. Puerto Varas, Chile, pp. 598–603.
Mpodozis, C., Arriagada, C., Basso, M., Roperch, P., Cobbold, P., Reich, M., 2005. Late Mesozoic to Paleogene stratigraphy of the Salar de Atacama Basin, Antofagasta, Northern Chile: implications for the tectonic evolution of the Central Andes. Tectonophysics 399, 125–154. https://doi.org/10.1016/j.tecto.2004.12.019.
Muñoz, N., Charrier, R., Jordan, T., 2002. Interactions between basement and cover during the evolution of the Salar de Atacama Basin, northern Chile. Rev. Geol. Chile 29, 3–29. https://doi.org/10.4067/S0716-02082002000100004.
Nabighian, M.N., Grauch, V.J.S., Hansen, R.O., LaFehr, T.R., Li, Y., Peirce, J.W., Phillips, J.D., Ruder, M.E., 2005. The historical development of the magnetic method in exploration. Geophysics 70, 33ND–61ND. https://doi.org/10.1190/1.2133784.
Nagy, D., 1966. The prism method for terrain corrections using digital computers. Pure Appl. Geophys. 63, 31–39. https://doi.org/10.1007/BF00875156.
Narea, K., Peña, M., Bascuñán, S., Becerra, J., Gómez, I., Deckart, K., Munizaga, F., Maksaev, V., Arriagada, C., Roperch, P., 2015. Paleomagnetism of Permo-Triassic and Cretaceous rocks from the Antofagasta region, northern Chile. J. S. Am. Earth Sci. 64, 261–272. https://doi.org/10.1016/j.jsames.2015.09.008.
Niemeyer, H., 2013. Geología del área Cerro Lila-Peine, Región de Antofagasta. In: Servicio Nacional de Geología y Mineria. Carta Geológica de Chile, Serie Geología Básica 147. 1 mapa escala 1:100.000. Santiago, Chile.
O'Driscoll, L.J., Richards, M.A., Humphreys, E.D., 2012. Nazca-South America interactions and the late Eocene-late Oligocene flat-slab episode in the Central Andes. Tectonics 31, 1–16. https://doi.org/10.1029/2011TC003036.
Ontario Geological Survey, 2017. Geophysical Data Set 1037, Revised - Ontario Airborne Geophysical Surveys, Magnetic Data. Ontario Geol. Surv.
Pananont, P., Mpodozis, C., Blanco, N., Jordan, T.E., Brown, L.D., 2004. Cenozoic evolution of the northwestern Salar de Atacama Basin, northern Chile. Tectonics 23, 1–19. https://doi.org/10.1029/2003TC001595.
Patibandla, C., Dadhwal, V.K., 2020. Aeromagnetic anomaly map for India: the scientific need. Arab. J. Geosci. 13 https://doi.org/10.1007/s12517-020-05453-0.
Ramírez, C.F., Gardeweg, M., 1982. Hoja Toconao. In: Carta Geológica de Chile 54. 1 mapa escala 1:250.000. Santiago, Chile.
Ramos, V.A., 2009. Anatomy and global context of the Andes: main geologic features and the Andean orogenic cycle. Geol. Soc. Am. Mem. 204, 31–65. https://doi.org/10.1130/2009.1204(02).
Rech, J.A., Currie, B.S., Jordan, T.E., Riquelme, R., Lehmann, S.B., Kirk-Lawlor, N.E., Li, S., Gooley, J.T., 2019. Massive middle Miocene gypsic paleosols in the Atacama Desert and the formation of the Central Andean rain-shadow. Earth Planet. Sci. Lett. 506, 184–194. https://doi.org/10.1016/j.epsl.2018.10.040.
Reiners, P.W., Thomson, S.N., Vernon, A., Willett, S.D., Zattin, M., Einhorn, J., Gehrels, G., Quade, J., Pearson, D., Murray, K.E., Cavazza, W., 2015. Low-temperature thermochronologic trends across the Central Andes, 21°S-28°S. In: DeCelles, P.G., Ducea, M.N., Carrapa, B., Kapp, P.A. (Eds.), Memoir of the Geological Society of America. The Geological Society of America, pp. 215–249. https://doi.org/10.1130/2015.1212(12).
Reutter, K.J., Charrier, R., Gotze, H.J., Schurr, B., Wigger, P., Scheuber, E., Giese, P., Reuther, C.D., Schmidt, S., Rietbrock, A., Chong, G., Belmonte-Pool, A., 2006. The Salar de Atacama Basin: a subsiding block within the Western Edge of the Altiplano-Puna Plateau. Andes Act. Subduct. Orogeny 303–325. https://doi.org/10.1007/978-3-540-48684-8_14.
Roberts, B.C.W., Jachens, R.C., 1999. Preliminary aeromagnetic anomaly map of California: U.S. Geological Survey Open-File Report 99–440, 14 p., scale 1: 5,600,000, http://geopubs.wr.usgs.gov/open-file/of99-440. U.S. Geological Survey.
Rubilar, J., Martínez, F., Arriagada, C., Becerra, J., Bascuñán, S., 2017. Structure of the Cordillera de la Sal: a key tectonic element for the Oligocene-Neogene evolution of the Salar de Atacama basin, Central Andes, Northern Chile. J. S. Am. Earth Sci. https://doi.org/10.1016/j.jsames.2017.11.013.
Salisbury, M.J., Jicha, B.R., de Silva, S.L., Singer, B.S., Jiménez, N.C., Ort, M.H., 2011. 40Ar/39Ar chronostratigraphy of Altiplano-Puna volcanic complex ignimbrites reveals the development of a major magmatic province. Bull. Geol. Soc. Am. 123, 821–840. https://doi.org/10.1130/B30280.1.
Sanchez, C., 2017. Denudation Evolution and Geomorphic Context of Supergene Copper Mineralization in Centinela District, Atacama Desert, Chile, from Thermochronology and Cosmogenic Nuclides. Université Toulouse 3 Paul Sabatier en co-tutelle avec la Universidad Católica del Norte, Antofagasta, Chile.
Sanchez, C., Brichau, S., Riquelme, R., Carretier, S., Bissig, T., Lopez, C., Mpodozis, C., Campos, E., Regard, V., Hérail, G., Marquardt, C., 2018. Exhumation history and timing of supergene copper mineralisation in an arid climate: new thermochronological data from the Centinela District, Atacama, Chile. Terra Nova 30, 78–85. https://doi.org/10.1111/ter.12311.
Schellart, W.P., 2008. Overriding plate shortening and extension above subduction zones: a parametric study to explain formation of the Andes Mountains. Bull. Geol. Soc. Am. 120, 1441–1454. https://doi.org/10.1130/B26360.1.
Scheuber, E., Bogdanic, T., Jensen, A., Reutter, K.-J., 1994. Tectonic development of the North Chile Andes in relation to Plate convergence and magmatism since the Jurassic. In: Reutter, K.-J., Scheuber, E., Wigger, P. (Eds.), Tectonics of the Southern Central Andes: Structure and Evolution of an Active Continental Margin. Springer, Berlin, p. 332.
SERNAGEOMIN, 1984. Carta Magnética Chile, I Región Oriente. Santiago, Chile.
SERNAGEOMIN, 1986. Carta Magnética Chile, II Región Oriente. Santiago, Chile.
SERNAGEOMIN, 2003. Mapa Geológico de Chile. 1 mapa escala 1:1.000.000. Santiago, Chile.
Solari, M., Venegas, C., Montecino, D., Astudillo, N., Cortés, J., Bahamondes, B., Espinoza, F., 2017. Geología del área Imilac-Quebrada Guanaqueros, Región de Antofagasta. In: Carta Geológica de Chile, Serie Básica, No.191. 1 mapa escala 1: 100.000. Santiago, Chile.
Somoza, R., 1998. Updated Nazca (Farallon)-South America relative motions during the last 40 My: implications for mountain building in the central Andean region. J. S. Am. Earth Sci. 11, 211–215. https://doi.org/10.1016/S0895-9811(98)00012-1.
Somoza, R., Tomlinson, A.J., Caffe, P.J., Vilas, J.F., 2012. Paleomagnetic evidence of earliest Paleocene deformation in Calama (~22°S), northern Chile: Andean-type or

ridge-collision tectonics? J. S. Am. Earth Sci. 37, 208–213. https://doi.org/10.1016/j.jsames.2012.04.001.
Steinmann, G., 1929. Geologie von Peru. Carl Winters Universitats-Buchhandlung.
Tang, J., He, D., Li, D., Ma, D., 2015. Large-scale thrusting at the northern Junggar Basin since Cretaceous and its implications for the rejuvenation of the Central Asian Orogenic Belt. Geosci. Front. 6, 227–246. https://doi.org/10.1016/j.gsf.2014.07.003.
Vanderhaeghe, O., 2012. The thermal-mechanical evolution of crustal orogenic belts at convergent plate boundaries: a reappraisal of the orogenic cycle. J. Geodyn. 56–57, 124–145. https://doi.org/10.1016/j.jog.2011.10.004.
Wang, Y., Jia, D., Pan, J., Wei, D., Tang, Y., Wang, G., Wei, C., Ma, D., 2018. Multiple-phase tectonic superposition and reworking in the Junggar Basin of northwestern China-implications for deepseated petroleum exploration. Am. Assoc. Pet. Geol. Bull. 102, 1489–1521. https://doi.org/10.1306/10181716518.
Wilkes, E., Görler, K., 1994. Sedimentary and structural evolution of the Salar de Atacama Depression. In: Reutter, K., Scheuber, E., Wigger, P. (Eds.), Tectonics of the Southern Central Andes: Structure and Evolution of an Active Continental Margin. Springer, New York, pp. 171–188.
Yáñez, G.A., Ranero, C.R., von Huene, R., Díaz, J., 2001. Magnetic anomaly interpretation across the southern Central Andes (32°-34°S): the role of the Juan Fernández Ridge in the late Tertiary evolution of the margin. J. Geophys. Res. Solid Earth 106, 6325–6345. https://doi.org/10.1029/2000jb900337.
Yilmaz, Ö., 2001. Seismic Data Analysis: Processing, Inversion, and Interpretation of Seismic Data, Investigations in Geophysics. https://doi.org/10.1190/1.9781560801580.

Chapter 4 : Age and provenance of the Mesozoic-Cenozoic sedimentary units within the Salar de Atacama Basin-El Bordo Escarpment

4.1.-Introduction and standing geochronological issues

Since its initial studies by Brüggen (1934, 1942, 1950), the near-absence of fossil remains and lack of datable geological horizons made the age of the geological units within the El Bordo Escarpment and the Salar de Atacama Basin doubtful. Several attempts at identifying the age of the upper Mesozoic-lower Cenozoic to Cenozoic successions were made, with contrasting results owing to the methods used. A brief summary of the main geochronological findings and stratigraphic assignments is presented here; a more detailed review can be found in Bascuñán (2014).

After the works of Brüggen (1934, 1942, 1950), who assigned the Purilactis Formation to the Early Cretaceous based on the presence of reworked Jurassic fossils, Dingman (1963, 1967) assigned the underlying Tonel Formation to the Jurassic, owing to its stratigraphic position below the Purilactis Formation. Later, Ramírez & Gardeweg (1982) included both formations into the Purilactis Formation, assigning it to the Late Jurassic-Cretaceous. This was further narrowed down by Marinovic & Lahsen (1984), who considered that the formation(s) had been mostly deposited during the Cretaceous. Afterwards, Hartley et al. (Hartley et al., 1988, 1992) divided the formation into the original Tonel and Purilactis Formations, and assigned a Late Jurassic and Cretaceous-Paleogene age to each formation respectively, based on the presence of an Ar-Ar age of 64±10 Ma obtained from a lava within the Vizcachita Member (Flint et al., 1989). The maximum depositional age was determined at 39.3 ±3 Ma (K-Ar), which corresponds to a lava bed assigned to the Cinchado Formation according to Ramírez & Gardeweg,(1982), or the Loma Amarilla Formation following Basso & Mpodozis (2012).

On the other hand, Charrier & Reutter (1990, 1994) termed the Purilactis Group, which comprised the Cinchado Formation of Ramírez and Gardeweg (1982), the Tonel Formation and Purilactis Formation, which considered slightly different unit limits than other studies, and the Yesífera Superior Formation. The base of the Purilactis Formation was dated at 44.0±0.9 and 43.8±0.5 Ma (Ar-Ar) from pyroclastic beds obtained from a location close to where Hammerschmidt et al. (1992) would later obtain their samples for the Loma Amarilla Formation, and the authors considered that the K-T age obtained by Flint et al. (1989) was in fact closer to that obtained in their work if the Ar release spectra was reinterpreted.

Further changes in chronostratigraphy were later done by Arriagada (1999), Mpodozis et al. (Mpodozis et al., 1999, 2005) and Arriagada et al. (2000, 2006a), who redefined the stratigraphic limits of the Purilactis Group, obtained new K-Ar ages from the Cerro Totola Formation and related intrusives, and also obtained paleomagnetic measurements from most of the formations. The Tonel and lower Purilactis Formation were assigned to the mid-Cretaceous (119-84 Ma) based on its stratigraphic relations and the presence of normal polarity among all samples of this bracket. The Barros Arana Formation was given a Late Cretaceous age, and was placed beneath the Cerro Totola Formation (Maastrichtian-Danian). The Naranja Formation was placed above the Cerro Totola

Formation based on K-Ar whole rock ages (57.9±1.9 and 58.0±3 Ma) obtained from a lava bed at the top of the formation by Gardeweg et al. (1994).

In the last decade, several advances involving the timing of deposition of these units and their provenance have been made (e.g., Bascuñán et al., 2019, 2016; Henriquez et al., 2019; Henríquez et al., 2014). However, even with this new data, several questions remain, such as the age and correlation of the units supposed to belong to the Tonel Formation west of the Tuina area, with those dated by Bascuñán et al. (2016); the ages and relation of similar units southwards, within the El Bordo Escarpment; and, the age and provenance of the Naranja Formation, whose age was correlated with those of a similar horizon around 50 kms southwards (Gardeweg et al., 1994; Solari et al., 2017), which was also dated by Henríquez et al. (2019).

As explained in Chapter 1, the relevance of addressing these issues is that numerous contributions have relied on the different geochronological frames of the area as an example of the tectonic and sedimentary processes affecting the northern Central Andes and its build-up. It is clear then that a robust framework, regarding structure, stratigraphy and geochronology are key to properly deciphering the construction of this orogen.

4.2.-Methodology

The samples presented in this chapter were taken in August 2017, on the same field trip where the gravimetric survey in Chapter 2 was performed. Their location is found in Figure 4.1.

The rock samples were processed at the Sample Preparation Laboratory of the Geology Department of the Universidad de Chile, using Gemeni Table, Frantz magnetic separator and heavy liquid procedures. The zircons were separated manually operating a binocular microscope and were then sent to the Laboratorio de Estudios Isotópicos (LEI) of the Geoscience Center of the Universidad Nacional Autónoma de México (UNAM). Around 100 random grains were analyzed with a *Resonetics Resolution M50* 193 nm laser *Excimer* connected to a *Thermo Xii Series Quadrupole Mass Spectrometer*, utilizing a 23 μm laser diameter for ablation. Additional technical details are described in Solari et al. (2010). All unit ages and designations follow those of the International Stratigraphic Chart (Cohen et al., 2013).

The best age for each zircon was defined using the same criteria as in Bascuñán et al. (2016), and sample age was calculated using *Isoplot v.3.7.* (Ludwig, 2008), obtaining averages for the youngest populations with more than three zircons. Relevant peaks and populations were also analyzed using the spreadsheet Age Pick developed by the LaserChron Center at the University of Arizona. The resulting data tables can be found in Supplementary Material B.

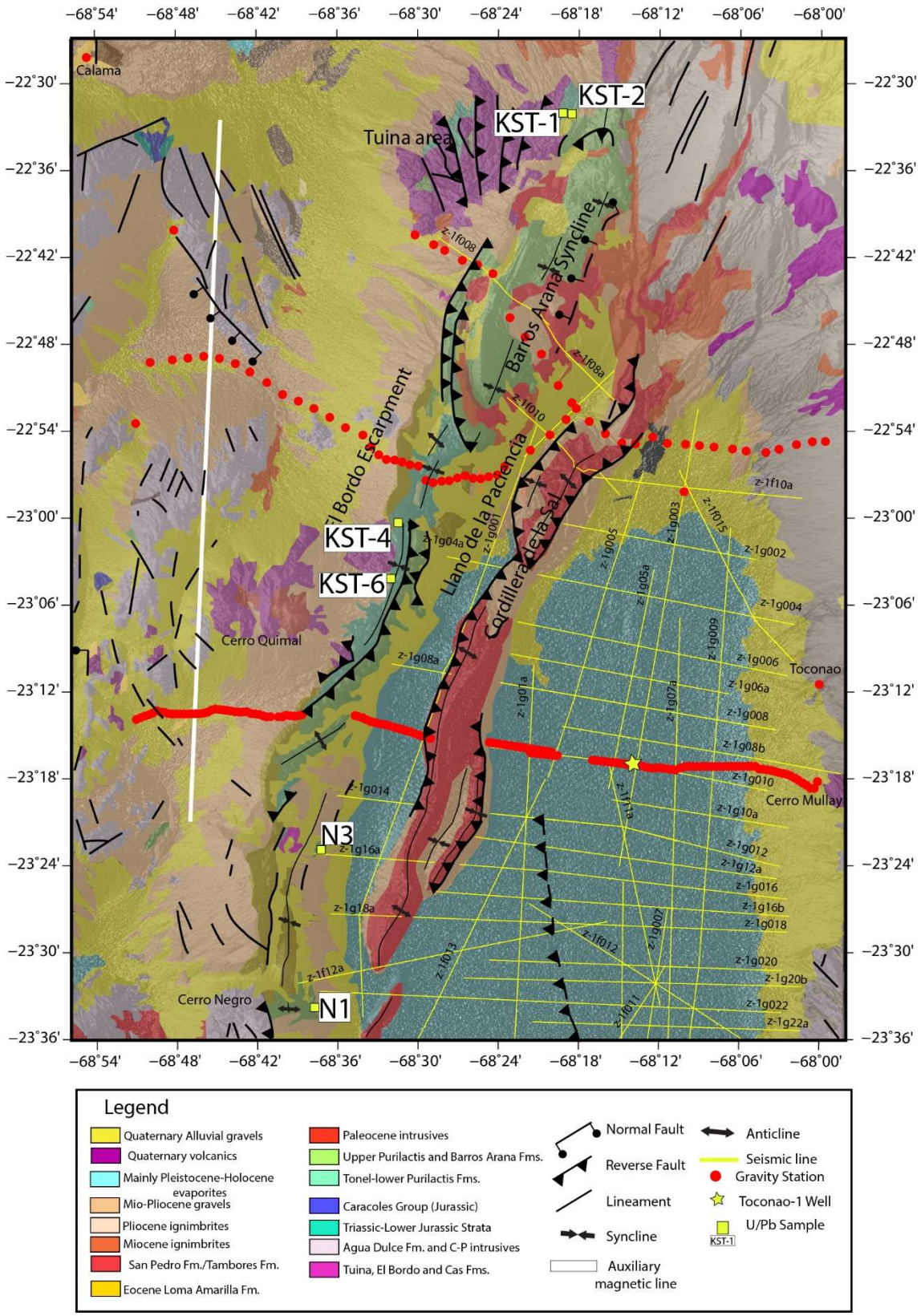

Figure 4.1: Geological map of the study area with sample location.

4.3.-Results

Tonel Formation

Four samples from the Tonel Formation were analyzed in order to narrow the timespan of its deposition. They also comprise some of the first detrital zircon samples obtained for this formation within the basin. The basalmost sample (KST-1, Figure 4.2a) has a large population (n= 89) between 238 and 268 Ma (between Ladininan and Wordian), with a well-defined relative probability peak around 251 Ma (Induan, n=55). Its maximum depositional age has been estimated at 242.4±1.4 Ma. The sample contains younger zircons, but not enough to define a population, with the youngest being 101.2 Ma in age.

Sample KST-2 (Figure 4.2b), located 370 m up-column, has most of its zircons between 234-267 Ma (Carnian-Wordian, n= 90), with relative probability peaks around 238 (Ladinian, n=10), 252 (Changhsingian, n=54) and 248 Ma (Olenekian, n=60). The maximum depositional age is 238±1.3 Ma, and it also possesses one younger zircon aged 102.2 Ma.

The other samples belonging to the Tonel Formation were obtained 61 km southwards, close to the contact with the Agua Dulce Formation (sensu Basso & Mpodozis, 2012). Stratigraphically speaking, they would be below samples KST-1 and KST-2, following the same authors and the regional map by Henríquez et al. (2013). Sample KST-4 (Figure 4.3a) has an heterogenous population distribution, with relative probability distribution peaks around 144 (Berriasian, n=6), 238 (Ladinian, n=10), 244 (Anisian, n=16), and 251 Ma (Induan, n=15). Minor peaks are found at 113 (Albian-Aptian, n=5), 140 (Berriasian, n=5), 151 (Tithonian, n=5), 480 (Tremadocian, n=5), 523 (Cambrian, n=4) and 544 (Ediacaran, n=3). Its maximum depositional age is 112.6±1.6 Ma.

Sample KST-6 (Figure 4.3b) which would be located below the previous sample, and which is found 3.8 km to the southeast, shows relevant peaks around 247 (Anisian-Olenekian, n=6), 253 (Changhsingian, n=8), and 633 Ma (Ediacaran, n=6). Minor peaks are found at 237 (Carnian-Ladinian, n=4), 284 (Artinskian, n=3), 293 (Sakmarian, n=3), 621 (Ediacaran, n=3), 653 (Ediacarann=4), 670 (Ediacaran, n=3), 1064 (Stenian, n=3), 1089 (Stenian, n=5) and 1820 Ma (Orosirian, n=4). The maximum depositional age for this sample is 236.3±5.3, with its youngest zircon at 70.7 Ma.

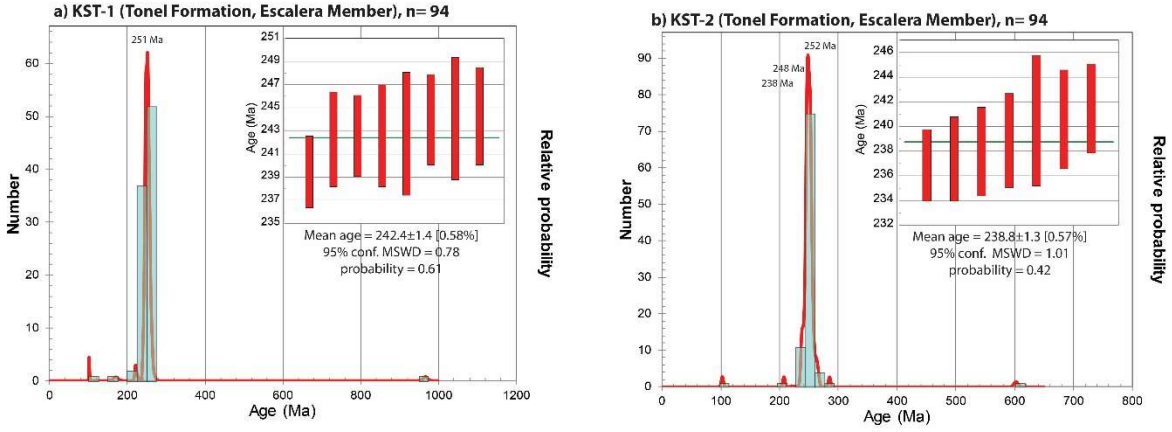

Figure 4.2: U/Pb detrital zircon ages for samples KST-1 and KST-2. Location in Figure 4.1.

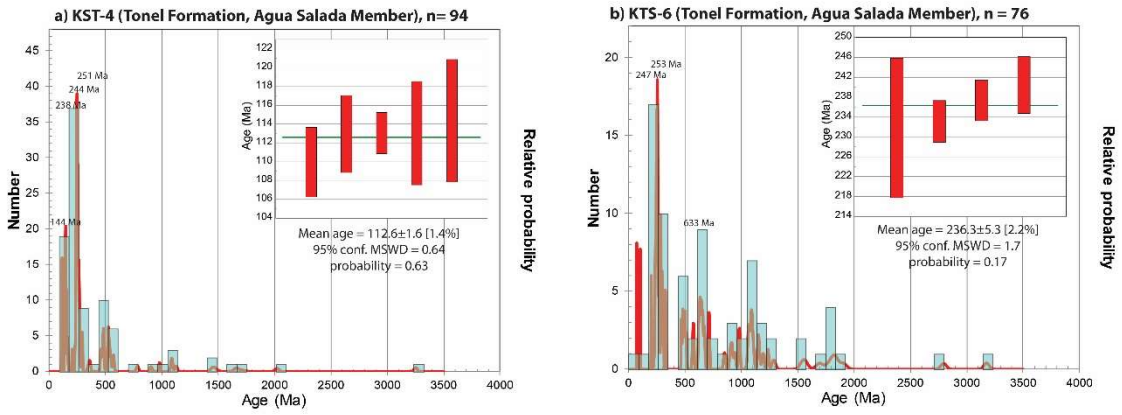

Figure 4.3: U/Pb detrital zircon ages for samples KST-4 and KST-6. Location in Figure 4.1.

Naranja Formation

Two detrital zircon samples were obtained for the Naranja Formation along the El Bordo Escarpment, which can be compared with the sample dated by Henríquez et al. (2019) and one taken by Solari et al. (2017) farther south. The northernmost sample (N-3, Figure 4.4a) shows large relative probability age peaks around 69 (Maastrichtian n=9), 72 (Campanian, n=16), 78 (Campanian, n=14) and 295 Ma (Sakmarian, n=11), and minor peaks at 150 (Tithoniann=3), 170 (Bajocian-Aalenian, n=3), 175 (Toarcian, n=3) and 203 Ma (Rhaetian, n=3). The obtained maximum depositional is 68.95±0.65 Ma.

Finally, sample N-1 (Figure 4.4b), found 18 km to the south, has relative probability age peaks at 74 (Campanian, n=19), 79 (Campanian, n=21) and 302 Ma (Gzhelian, n=9), while minor peaks are found at 68 (Maastrichtian, n=5), 85 (Santonian, n=4), 90 (Turonian, n=5), 140 (Berriasian, n=3), 147 (Tithonian, n=4), 257 (Wuchiapingian, n=3) and 292 Ma (Sakmarian, n=5). The maximum depositional age is 68.4±1.3 Ma.

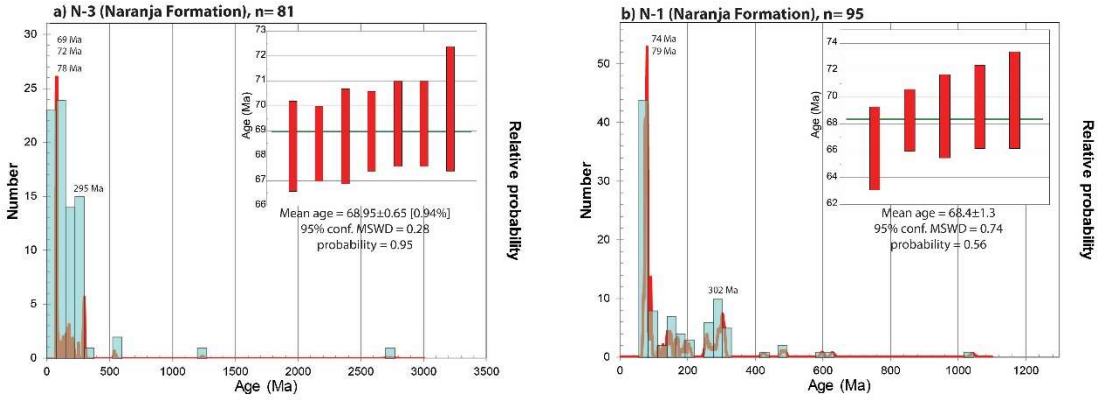

Figure 4.4: U/Pb detrital zircon ages for samples N-3 and N-1. Location in Figure 4.1

The relative probability plot of all samples (including those from Chapter 2) can be seen in Figure 4.5. The same plot for the samples including those published by Bascuñán et al. (2016) can be seen in Figure 4.6.

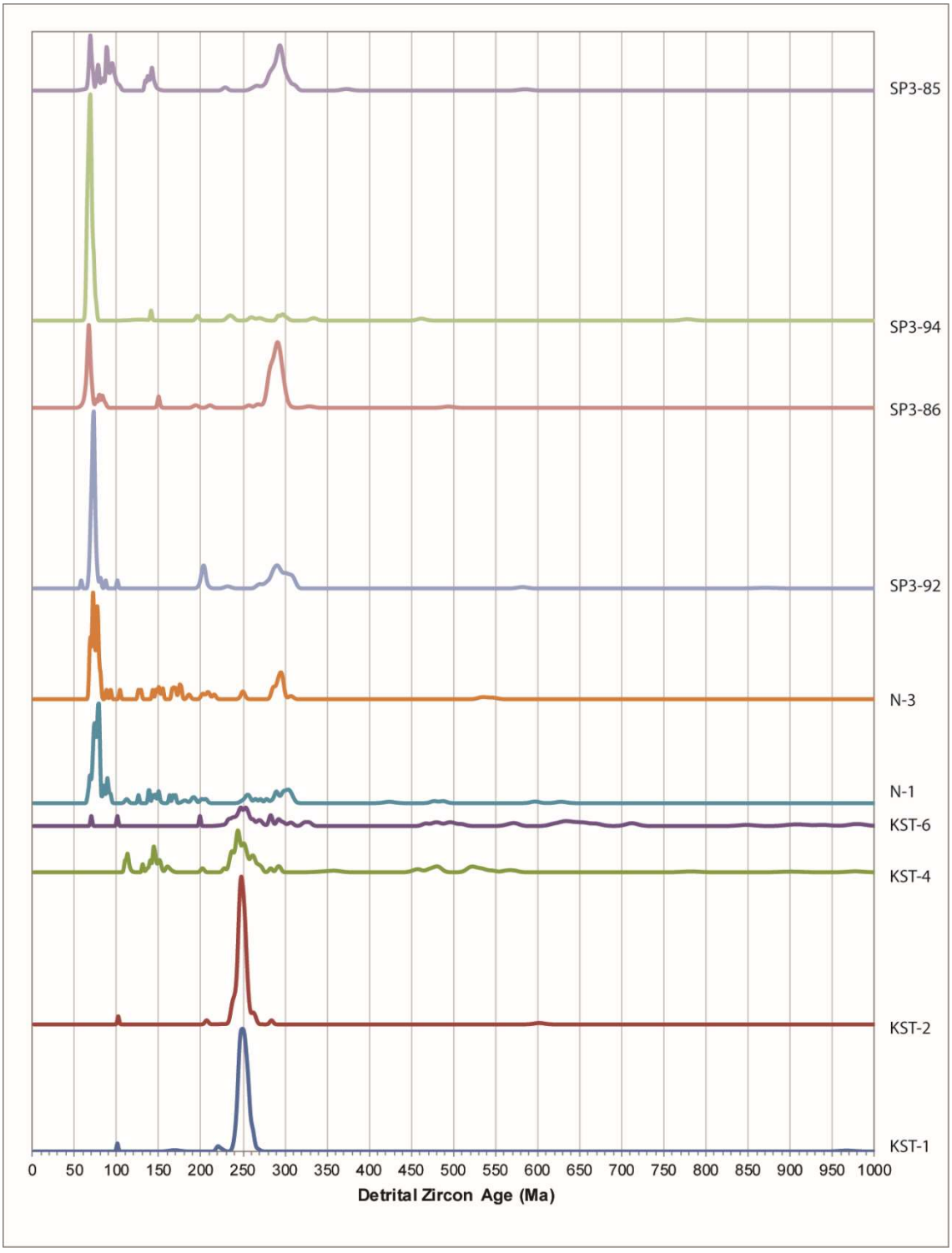

Figure 4.5: Relative probability plot for all the U-Pb samples considered in this study. Sample SP3-92 belongs to the Pajarito Member, samples SP3-86 and SP3-94 to the Vizcachita Member, and SP3-85 to the Seilao Member. The U-Pb detrital zircon patterns and their location can be seen in Chapter 2.

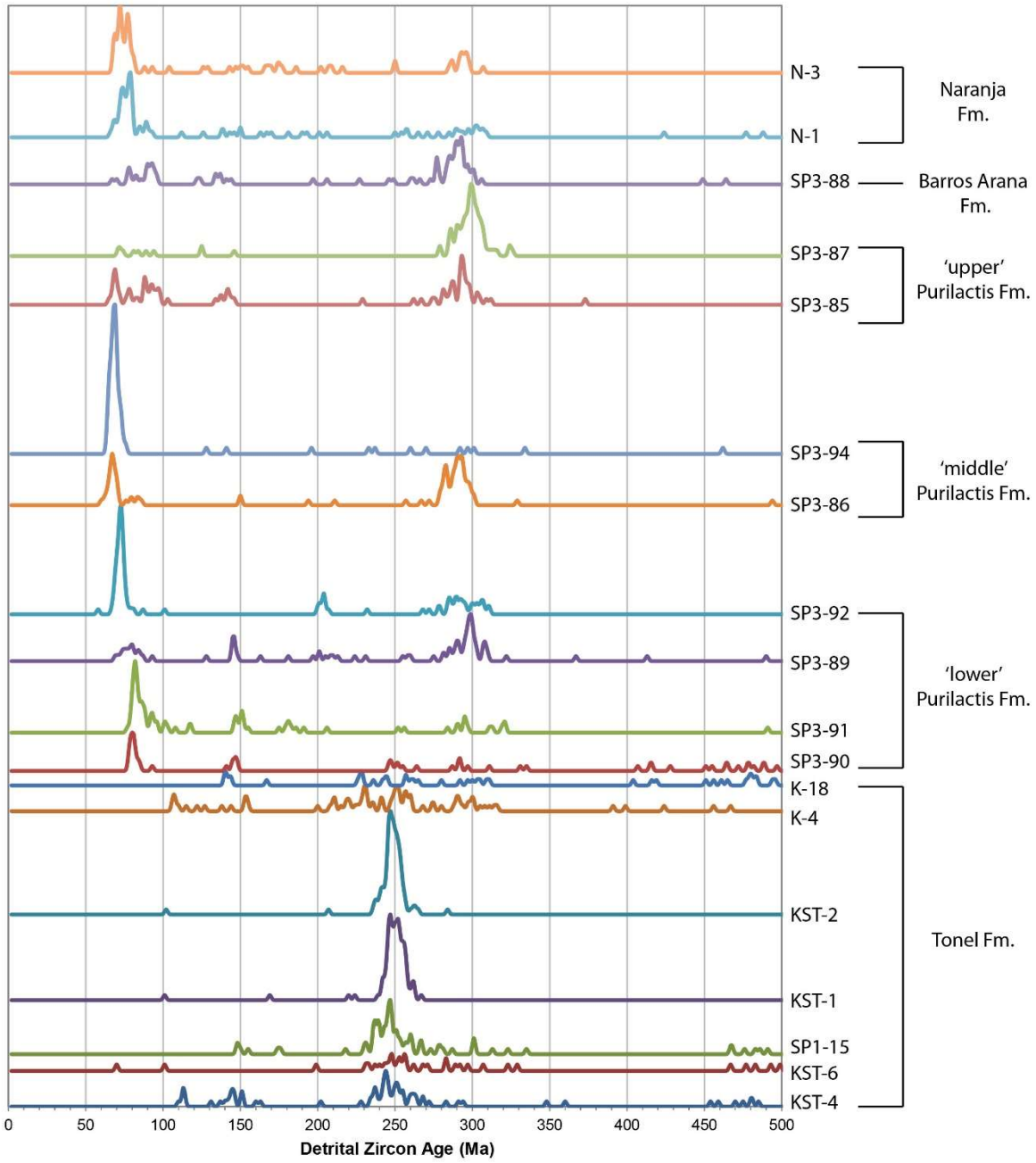

Figure 4.6: Relative probability plot for all samples in this study and those obtained by Bascuñán et al. (2016).

4.4.-Provenance

The rocks analyzed in this study show a wide variety of populations, owing to the ever-changing evolution of the orogenic front and the dynamics of the alluvial systems feeding the basin. The oldest populations found at ca.1820 Ma have only been seen in the Central Andes of northern Chile as minor populations of other U-Pb detrital analyses, such as the Permian Huasco beds at the Chilean coast around 28°30'S (Bahlburg et al., 2009) and the Devonian-Carboniferous Pampa Quenante Strata-Cerro Limón Verde Strata found south of Calama and west of the study area

(Morandé, 2014), which also hold several populations of Neoproterozoic ages similar to those found in samples KST-4 and KST-6. The latter area also shows the presence of diamictites with maximum depositional ages around 1065 Ma (Morandé, 2014), which correspond to some of the oldest rocks identified in the area. The erosion of these units would explain their presence in the rocks belonging to the Tonel Formation.

Sample KST-4, in particular, presents Ordovician and Cambrian populations which are not shared with other samples. These ages, however are more commonly found in northern Chile, with locations such as the Mejillones Peninsula (Casquet et al., 2014), where they correspond to large populations within some samples. The largest population peaks in the strata found the in the Sierra Limón Verde south of Calama are around 471-480, and 532-542 Ma (Morandé, 2014), which have also been identified on the coast of northern Chile in the El Toco Formation between 21°15'-22°15'S (Bahlburg et al., 2009). Ordovician rocks are also commonly found south of the study area at the southern end of the Salar de Atacama in the Cordón de Lila Complex (Niemeyer, 1989, 2013; Zimmermann et al., 2009). Similar ages are also observed in Ordovician granitoids and intrusives (Sola et al., 2013), the Aguada de la Perdiz Formation, close to the international border between Chile and Argentina (Bahlburg and Hervé, 1997), and the Sierra de Moreno Complex, north of Calama (Skarmeta, 1993).

The earliest Permian-Carboniferous peaks found in the Naranja Formation (Samples N1-N3) are probably derived from the Carboniferous-Permian granitoids and intrusives found west within the Cordillera de Domeyko, and volcanic formations such as the Agua Dulce Formation (Ramírez and Gardeweg, 1982; Marinovic and Lahsen, 1984; Basso and Mpodozis, 2012; Morandé, 2014; Solari et al., 2017). Permian units have also been reported in the Cordón de Lila area, though with no definitive age (Cerro Negro Strata, Niemeyer, 2013).

Several populations are found within the Permian-Triassic, notably between 237-268 Ma, though peaking around ca. 250 Ma. They comprise most of the zircons of the northernmost samples of the Tonel Formation (KST-1 and KST-2), owing to its proximity and derivation from the Tuina Formation (Figure 4.2), which has been assigned to the Triassic-Permian (235-254 Ma, Henríquez et al., 2014). Similar ages are also present in the Cas, Peine and Cerros Negros Formations on the southeastern border of the Salar de Atacama Basin, and in Permian intrusives along the Cordón de Lila Area (Niemeyer, 2013; Becerra et al., 2014). These ages are also found in the same granitoids within Cordillera de Domeyko, and in the El Bordo Strata around Cerro Quimal (Ramírez and Gardeweg, 1982; Marinovic and Lahsen, 1984; Basso and Mpodozis, 2012; Solari et al., 2017). Late Triassic peaks are only observed in sample N-3, which could derive from the Las Lomas Strata found in the Cordillera de Domeyko (Basso and Mpodozis, 2012).

Middle Jurassic to Upper Cretaceous populations (between 145-170 Ma) are not common, with the exception of sample KST-4 (Figure 4.3). Units of this age belonging to the Caracoles Group do crop out close the study area, but mostly comprise marine sedimentary units (Ramírez and Gardeweg, 1982; Marinovic and García, 1999; Basso and Mpodozis, 2012). Volcano-sedimentary units of this age are found west of Cordillera de Domeyko, such as the in the Sierra de Fraga and Candeleros Formations (Cornejo et al., 2009). Igneous and volcanic units are also widespread along the Coastal Cordillera, comprising the La Negra Arc (Pichowiak et al., 1990; Basso, 2004; Oliveros et al., 2006). The Albian-Aptian peak, found only in KST-4, is probably derived from similar units.

Finally, the Upper Cretaceous zircons found in samples N-1 and N-3 (Figure 4.4) are likely derived from formations that represent the volcanic arc of that time, such as the Quebrada Mala and Llanta Formations and the Paradero del Desierto Strata, in the actual Central Valley and western border of the Cordillera de Domeyko (Cortés, 2000; Basso, 2004; Marinovic, 2007).

A further analysis and integration of the provenance data into the geological history of the is discussed in Chapter 5.

Chapter 5 : Discussion.

This segment of this thesis will analyze five topics and areas which arise from the examination of prior data and that acquired in this work. These correspond to the chronostratigraphy of the basin, its paleographic evolution and structure of the basin as part of the Preandean Depression, a review of the various events proposed for the Central Andes and their record within the basin, and a brief analysis of the geophysical anomalies found beneath it.

5.1.-Basin chronostratigraphy and pending issues

This thesis produced a total of ten U-Pb detrital zircon ages for the suspected Upper Cretaceous-Paleogene successions cropping out along the El Bordo Escarpment. These must be analyzed together with the eight ages obtained by Bascuñán et al. (2016) in similar units, and those dated by other authors utilizing different methods (e.g., Henriquez et al. (2019), Solari et al. (2017), Blanco et al. (2003), Mpodozis et al. (Mpodozis et al., 2000, 2005), among others). This discussion will be separated according to the three major formations that constitute the Purilactis Group *sensu* Mpodozis et al. (Mpodozis et al., 2005) (Tonel, Purilactis and Barros Arana Formations), and the Naranja Formation. A summary of different chronostratigraphic interpretations can be seen in Figure 5.1.

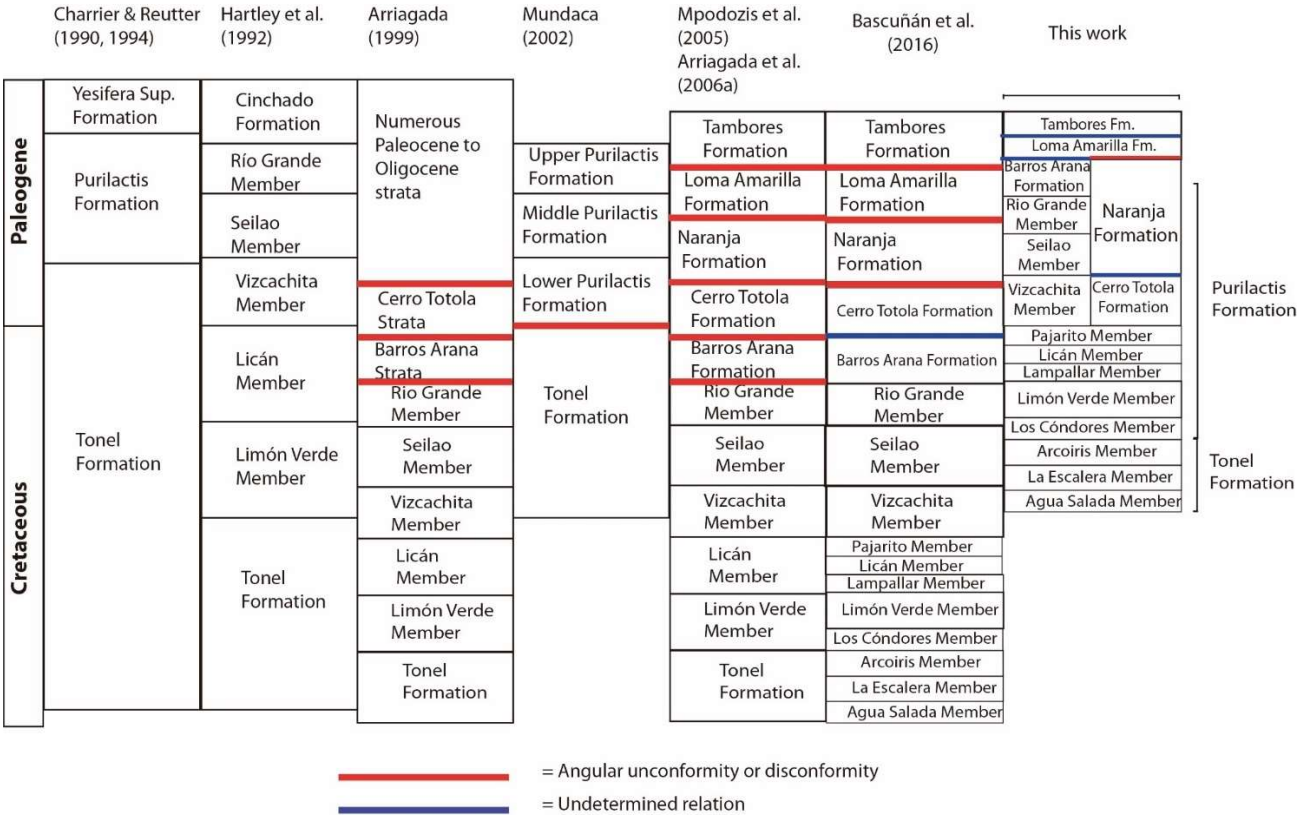

Figure 5.1: Comparison of chronostratigraphic charts and the work presented in this thesis.

Tonel Formation (112-79 Ma)

The age span of the Tonel Formation was not conclusively resolved by Henriquez et al. (2014) nor by Bascuñán et al. (2016). Both studies analyzed three U-Pb detrital zircon samples from rocks assigned to the Tonel Formation which cropped out on the northwestern limit of the Cerros de Tuina area (see Figure 2 in Bascuñán et al., 2016). The correlation of these rocks with those found on the eastern border of the Cordillera de Domeyko was done based mainly on its lithology and supposed age, and further analysis was required to test this relation. The youngest maximum depositional age was found in the middle member of the Tonel Formation (La Escalera Member, ca. 107.6 ± 1.8 Ma), placing it in the Cenomanian-Albian limit. The lower and upper members had maximum depositional ages in the Tithonian (Agua Salada Member, 148.9 ±2.6 Ma) and Berriasian (Arcoiris Member, 141.6 ± 2.1 Ma), respectively.

The new samples presented in this contribution (see Chapter 4) show zircon distributions akin to those found before, where Middle Triassic to Late Triassic-Permian populations correspond to the largest groups found (see Figure 11 *in* Bascuñán et al., 2016). Bascuñán (2014) and Bascuñán et al. (2016) suggest that the Tuina Formation was already above the base level and a source of sediment and zircons for the Tonel Formation. This elevated area would have blocked the arrival of other sources to the northernmost samples obtained here (KST-1 and KST-2). The youngest zircons found in each of these samples (101.2 and 102.2 Ma, respectively) are not statistically relevant, and cannot be considered as maximum depositional ages. However, their similar ages, and their similarity to the age obtained in the middle member of the Tonel Formation farther west suggest that samples with these ages could be found along the El Bordo Escarpment with further testing.

The southern samples (KST-4 and KST-6, Figure 4.3) show heterogenous zircon distributions, implying a wider variety of sources than the northern samples. Although they are found in stratigraphically lower levels (Basso and Mpodozis, 2012), their distribution patterns are more similar to the one obtained for the upper member of the Tonel Formation, particularly KST-6, albeit without the Early Cretaceous populations (Figure 11c in Bascuñán et al., 2016). KST-4 yields the youngest maximum depositional age found so far for the Tonel Formation within the basin (112.6 ± 1.6 Ma), and, as such, confirms its overall stratigraphic position in the transition from the Early to the Late Cretaceous. Since these late Upper Cretaceous zircons come from sources farther to the west (more than 100 km), this suggests that there were variations in the paleotopography and paleodrainage, such as the Cerros de Tuina area, which impeded the transport eastward of certain zircons. The higher presence of evaporites both to the south and east of the Barros Arana Syncline support this irregular topography, and, in the case of the southernmost samples, the heterogeneous sources also show that they were receiving zircons from many sources located in the present Cordillera de Domeyko and in the Cordón de Lila area, which were apparently not transported northwards (see Chapter 4).

If the sample yielding the youngest maximum depositional age is effectively from the basalmost member of the Tonel Formation, then it would be possible to ascertain that sedimentation of the entire succession is in partial agreement with the age suggested by Bascuñán et al. (2016), but this time with a better constraint for the lowest member. Further sampling is needed to find the end of its deposition, which was been posited by those authors at ca. 79 Ma.

Ultimately, the Tonel Formation still presents relevant questions that need to be cleared to further understand its origins. Additional studies emphasized on its stratigraphy, sedimentology and provenance, including U-Pb detrital zircon data and paleocurrent analysis, might better identify zircon sources and their overall contribution, especially in the case of the Cordón de Lila area. As such, the area northeast of Cerro Quimal is of prime interest, as it is located almost in the center of the depocenter at that time.

The work done here and by previous authors cannot exclude the possibility that the Tonel Formation northward, where the northernmost samples were taken, is different from the Tonel Formation found both southward and westward. On the other hand, their lithofacies and zircon population distribution tend to reaffirm their correlation, and it is now possible to positively correlate the units found on the western border of the Cerros de Tuina area with those within the basin.

Purilactis Formation (79 Ma-Paleocene)

The ages found in this work bring into question much of the previously established chronostratigraphy of the Purilactis Formation, and its relation to similar units found in the southern segments of the basin and the eastern border of the Cordillera de Domeyko. According to Bascuñán et al. (2016), the formation would have been deposited between ca. 79 and 73 Ma, with the first age being found in the Limón Verde Member (second member of the formation from bottom to top), approximately 500 m into the column. The second age was found within the Rio Grande Member, which corresponds to the last member of the formation, found at ca. 4000 m of the stratigraphic column. Older ages, ranging between 75-80 Ma, were also found within the column.

The samples belonging to the Vizcachita Member, found between 2200-2400 m into the column, prove that the Purilactis Formation was still being deposited during the Maastrichtian-Danian interval, extending the formation well into the Paleogene (see Chapter 2, Bascuñán et al., 2019). This age is close to that obtained by Flint et al. (1989) from an altered lava found within the Vizcachita Member. Following the compiled stratigraphic column of Bascuñán et al. (2016), at least another 1600 m belonging to the Purilactis Formation, plus the ca. 1200 m of the Barros Arana Formation, were deposited after ca. 65 Ma (see below).

The traditional understanding of the tectonostratigraphy of the basin placed the units belonging to the Purilactis Group (*sensu* Mpodozis et al., 2005) beneath volcanic deposits of the Cerro Totola Formation, dated between 61-70 Ma, found south of the Barros Arana Syncline (Arriagada, 1999; Mpodozis et al., 2005; Arriagada et al., 2006a; Basso and Mpodozis, 2012). This view was held, and modified only in a minor way, by subsequent authors which studied different facets of the basin and the Central Andes, including the studies involving the seismic data (Muñoz et al., 2002; Pananont et al., 2004; Jordan et al., 2007). It can be readily concluded that at least the Vizcachita Member is a time-equivalent of the Cerro Totola Formation and the dykes and small intrusives found within deposits belonging to the Tonel and lower Purilactis Formations (Basso and Mpodozis, 2012; Henríquez et al., 2014). Farther south, it can be correlated with the Pajonales Formation, where similar ages have also been found for its topmost member (Bahamondes, 2017; Solari et al., 2017).

Regarding their zircon populations, the patterns found for the samples in Chapter 2 are consistent with those obtained by Bascuñan et al. (2016), showing an increasing prevalence of Carboniferous-

Permian populations at higher levels in the stratigraphic column, with the exception of one sample belonging to the aeolian Vizcachita Member (sample SP3-94), which presents mostly Danian-Maastrichtian zircons.

In conclusion, the Purilactis Formation can be separated into two distinct time ages: the lower Purilactis Formation, comprising the Los Cóndores and Pajarito members and those in between, would have been deposited between ca. 79 and 65 Ma. The upper Purilactis Formation, including the Vizcachita Member upwards, was then deposited after 65 Ma, with no clear age for the end of its deposition (see below). As such, the sedimentation rate for the lower Purilactis Formation (considering ca. 2200 m, following Bascuñán et al., 2016) is around 157 m/Ma.

Barros Arana Formation (Paleocene-Eocene?)

Although samples from the Barros Arana Formation were not analyzed in this thesis, its depositional age must also be changed following the discussion above. Charrier & Reutter (1990, 1994) and Hartley et al. (1992), had considered the Barros Arana Formation part of the Cinchado Formation found within the Cordillera de Domeyko to the east, and suggested a Paleocene age for its deposition, which is in agreement with the obtained results. The formation is unconformably overlain by upper Oligocene-early Miocene conglomerates belonging to the Tambores Formation (Henríquez et al., 2014), and, as such, its folding must have occurred prior to the deposition of these successions.

Given the noticeable impact of the Incaic Orogeny in this area (Arriagada et al., 2006a, 2006b, 2008; Narea et al., 2015), which led to the folding and clockwise rotation of the pre-Oligocene formations, the conclusion in Chapter 2 was that the Barros Arana Formation must have been deposited at least prior to this epoch, possibly even reaching the early Eocene. A correlation with the Loma Amarilla Formation found farther south cannot be excluded based on its recorded ages (42-44 Ma, Hammerschmidt et al., 1992; Henriquez et al., 2019), and other criteria must be considered, such as their degree of lithification, which is much higher in the case of the Barros Arana Formation. This, however, could also be due to along-strike changes in sedimentary properties, an issue which is also present within the Naranja Formation.

Naranja Formation (68 Ma-57 Ma)

Much of the understanding of the Naranja Formation and its age can be attributed to the work done by Gardeweg et al. (1994), Arriagada (1999) and Mpodozis et al. (Mpodozis et al., 1999, 2005). These authors assigned these fine-grained, red-to-orange, continental deposits to the Paleocene, based on K-Ar whole rock ages found in lava horizons interbedded within the formation around 70 km south of Cerro Quimal. More recently, Bahamondes (2017) and Solari et al. (2017) dated the same lava horizon which caps the Naranja Formation, obtaining a detrital zircon U-Pb age of 57.4 ± 0.3 Ma, in agreement with previous studies. However, their analyses of detrital zircons within the sedimentary part of the formation yielded a maximum depositional age of 229.4 ± 2.6 Ma.

The ages presented here, along with one sampled by Henriquez et al. (2019), correspond to the first U-Pb detrital zircon ages for the Naranja Formation within the Salar de Atacama Basin. Regarding the latter study, the zircon population distribution showed a large cluster around 73.7 Ma (n = 38), followed by minor Permian-Carboniferous and Middle Jurassic populations (n < 12). Its distribution then is close to that observed in Chapter 4, where the largest populations are found in the Late

Cretaceous, although the depositional ages found are younger (Maastrichtian v. Campanian). The maximum depositional ages obtained, and the zircon population pattern, correlate well with one of the samples taken from the lower Purilactis Formation (Pajarito Member, see Chapter 2).

The lava bed studied by Bahamondes (2017) and Solari et al. (2017) does not extend northward into the Salar de Atacama Basin. It is not found in the Cerro Negro Area, where Henríquez (2012) studied the structural geology and stratigraphy of the area, which mainly involves the Loma Amarilla and Naranja Formations. The contact, however, between the Loma Amarilla and Naranja Formation is observed, thus placing the Naranja Formation beneath it, in erosional unconformity according to Bahamondes (2017). On the other hand, Arriagada (1999), and Mpodozis et al. (Mpodozis et al., 1999, 2005) mention a strong angular unconformity between the Tonel and Naranja Formations close to where sample N3 in Chapter 4 was taken, and also between the latter and the Cerro Totola Formation. However, a close inspection of the area, which is heavily deformed, also raises the possibility that the contact between said units is a fault, and in, some cases, might also be conformable (Figure 5.2, Arriagada et al., 2006a).

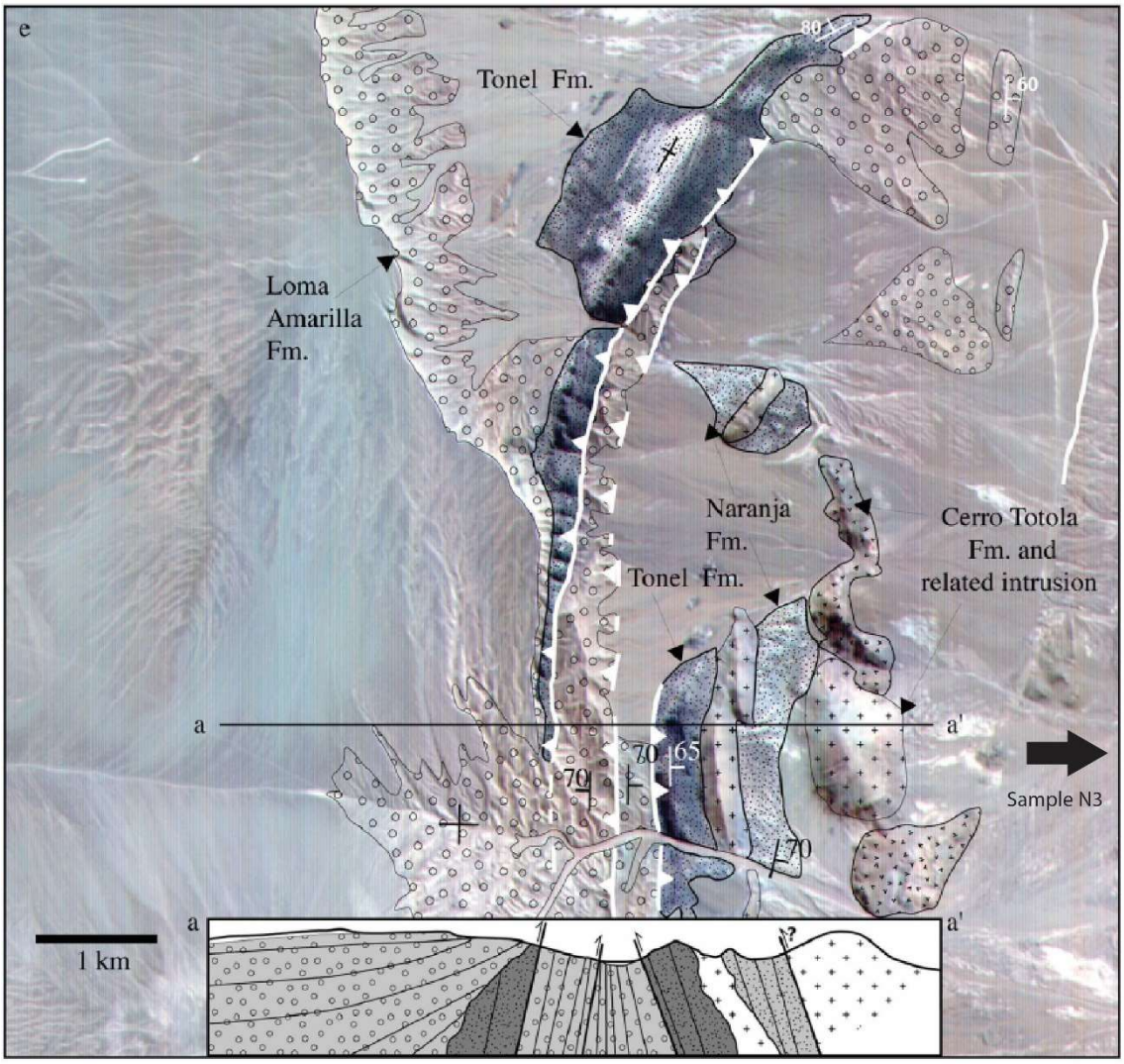

Figure 5.2: LANDSAT image and cross section of the El Bordo Escarpment-Salar de Atacama area, south of Cerro Quimal. Modified from Arriagada et al. (2006). Black arrow indicates the location of sample N3, found approximately 1 km east of the figure.

In summary, the Naranja Formation presents at least three options regarding its chronostratigraphic placement; first, the sedimentary part could be an equivalent of the lower Purilactis Formation (one of the members older than 65 Ma), which would agree with all samples taken so far (even the single crystal dates taken by Reiners et al., 2015), but not with the contact reported by Arriagada (1999) and Mpodozis et al. (Mpodozis et al., 1999, 2005). Second, the formation could be an equivalent either of the upper Purilactis (if the previous contact does not hold) or Barros Arana Formation, both of which are missing in this part of the basin. A third option would be to place it above the Barros Arana Formation, as in Mpodozis et al. (Mpodozis et al., 2005), which would imply sedimentation rates over 400 m/Ma for the Barros Arana Syncline, between 65-58 Ma, following the stratigraphic column by Bascuñán et al. (2016).

Here, the second option was chosen for the chronostratigraphic chart (Figure 5.1), thus making the Naranja Formation a southern equivalent of the upper Purilactis-Barros Arana Formations. It is

clear from the analysis above that more work in the area must be performed to finally solve this issue, of which several options are suggested in Chapter 6.

5.2.-Late Mesozoic-Cenozoic paleogeographic evolution of the Salar de Atacama Basin

One of the direct conclusions from the various geophysical-geological analyses derived from this thesis is the close relation between the Salar de Atacama Basin and the evolution of the Central Andes. In this regard, the Salar de Atacama Basin must be separated into at least two different depocenters: a) one involving the Upper Cretaceous to Paleogene units, b) another involving the Oligocene to recent strata. It is also apparent from the analysis that the basin also accumulated sediments during the Paleozoic, the Triassic and possibly the Jurassic-Early Cretaceous, where it was connected to the backarc basin of northern Chile (Ramírez and Gardeweg, 1982; Marinovic and Lahsen, 1984; Niemeyer, 2013, 1989; Charrier and Reutter, 1990, 1994; Damm et al., 1990; Charrier and Muñoz, 1994; Charrier et al., 2007; Amilibia et al., 2008; Zimmermann et al., 2009; Basso and Mpodozis, 2012; Martínez et al., 2017a). Here, I will focus mainly on its Late Mesozoic to recent paleogeography and evolution.

Figure 5.3 presents a schematic, paleogeographic evolution of the Central Andes between 22°-24°S. The first stage (Figure 5.3a) shows the exhumation of the Coastal Cordillera during the mid-Cretaceous, leading to its erosion and the transport of its zircons eastwards along with late Lower Cretaceous zircons derived from the magmatic arc in the Central Valley. These are mixed with various sources, of which the most prominent within the Tonel Formation is the Triassic (see above). The depocenter of this "Tonel" basin is hard to locate, given that it involves not only the Barros Arana Syncline-El Bordo Escarpment area, as its deposits are also located in the northwestern parts of the Cerros de Tuina area (Narea et al., 2015), and southwest of Cerro Quimal, within Cordillera de Domeyko (Basso and Mpodozis, 2012). The coarse, basalmost deposits however are found mainly east of Cerro Quimal and in the northernmost tip of the Barros Arana Syncline, indicating that these must have been areas with enough accommodation space to show most of the entire column. If these are indeed the only areas with such deposits, the basin axis would have been located ca. 5 km to the west of the Barros Arana Syncline axis. Regarding the timing of exhumation, Juez-Larré et al. (2010) argued for Late Cretaceous (60-80 Ma) and Eocene (40-50 Ma) stages for the Coastal Cordillera. Sanchez (2017) analyzed two samples from the same area, showing a steady cooling from the Early Cretaceous to 90 Ma, which is within the age range assigned for the beginning of sedimentation in the Tonel Formation (Mpodozis et al., 2005; Arriagada et al., 2006a; Bascuñán et al., 2016). This "Peruvian" phase (Steinmann, 1929) has been correlated with similar compressional events found along the western margin of South America (Megard, 1984; Jaillard, 1992, 1993; Cobbold and Rossello, 2003; Parada et al., 2005; Jaimes and de Freitas, 2006; Cobbold et al., 2007; Tunik et al., 2010; Merino et al., 2013; Fennell et al., 2017; Muñoz et al., 2018b; Boyce et al., 2020), highlighting the initiation of the foreland basin in the backarc region, and the change from extensional to compressive conditions.

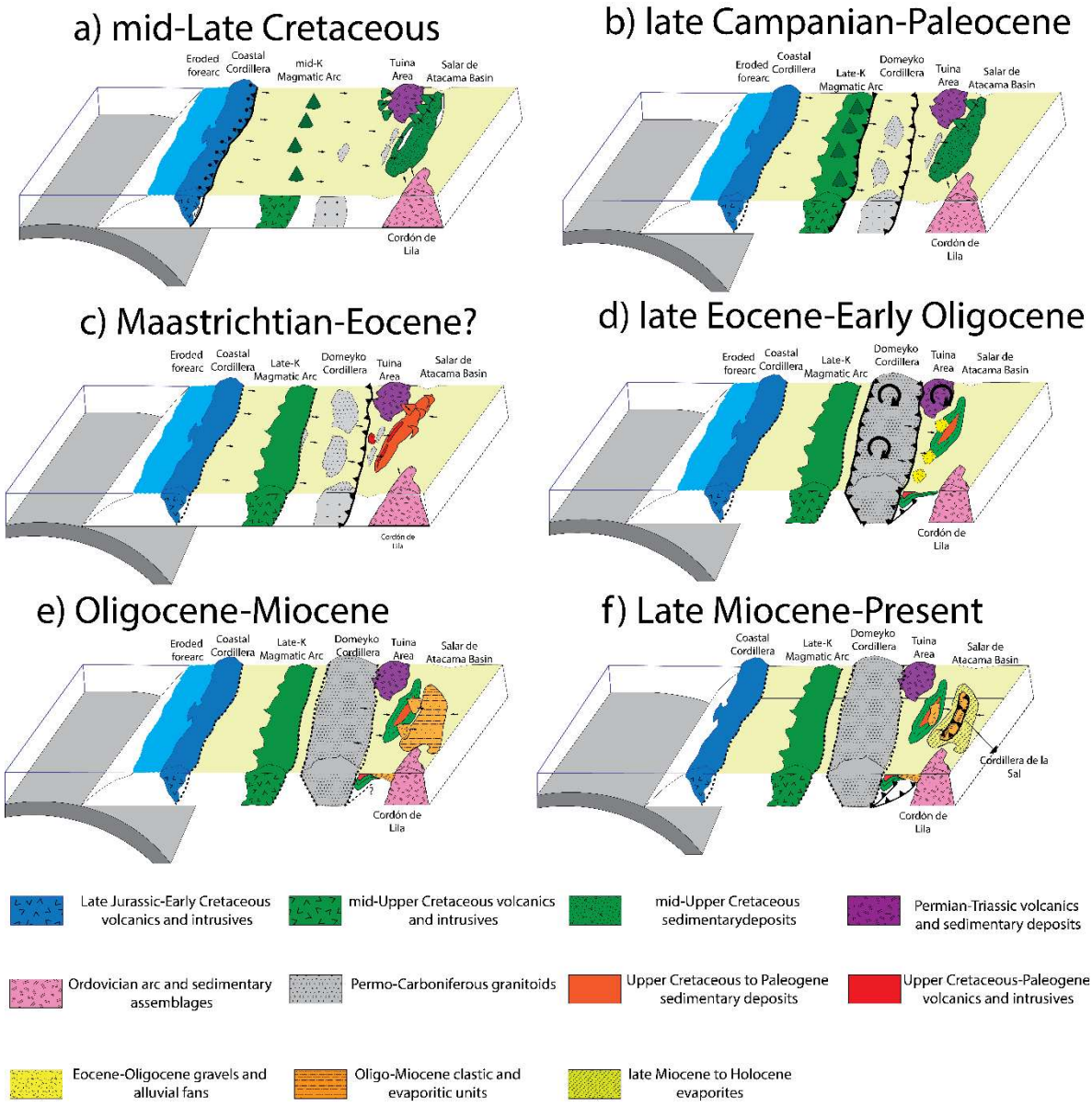

Figure 5.3: Schematic paleogeographic evolution of the Central Andes of northern Chile between ca. 22°-24°S.

The deposition of the upward-fining, continental Tonel Formation is superseded by the Purilactis Formation (Figure 5.3b), whose lower members are mostly dominated by Campanian to Maastrichtian-Danian zircons (between 79-65 Ma), with facies showing distal, sand-bed rivers and mostly shallow, gravel-bed, braided rivers (Hartley et al., 1988, 1992; Bascuñán et al., 2016). Its zircon distribution, clast count and paleocurrent directions indicate that its source region was located to the west, and mainly involved the mid-Cretaceous magmatic arc located in the Central Valley (Marinovic and García, 1999; Cortés, 2000; Tomlinson et al., 2001; Charrier et al., 2007; Marinovic, 2007; Cornejo et al., 2009). An incipient exhumation of the basement within Cordillera de Domeyko might have also occurred, owing to the presence of zircons around ca. 300 Ma within some of these samples, which would not have blocked the arrival of zircons from the mid-

Cretaceous arc, nor from the Coastal Cordillera, whose populations are present but diminished (Bascuñán et al., 2016). The axis of the foredeep would have been mostly the same as the axis of the Barros Arana Syncline, although some variations regarding the location of the depocenter can be seen between members, as examined by Araya (2016), which are more noticeable in the upper members.

A basinwide change in the depositional regime occurs afterwards, leading to the deposition of the mostly aeolian Vizcachita Member in the Barros Arana Syncline area, and the volcanic Cerro Totola Formation to the south, around the Maastrichtian-Danian (KT) limit (Figure 5.3c). Multiple small subvolcanic rocks are also emplaced in the area, mostly intruding the Tonel-lower Purilactis Formations, with ages ranging between 56-68 Ma (Henríquez et al., 2014), and/or 61-70 Ma (Mpodozis et al., 2005; Basso and Mpodozis, 2012), with Cerro Quimal representing the largest one in the area. This igneous activity represents the easternmost reach of the arc at these latitudes during the Late Cretaceous-Paleocene before it became narrower during the Eocene (Haschke et al., 2006; Trumbull et al., 2006). The upper Purilactis (Seilao and Rio Grande Members) and Barros Arana Formations show a return to gravel-bed braided rivers and lacustrine intervals, with the latter formation showing an increase in channel depth and clast size, indicating that the basin foredeep was in a proximal position in regards to the orogen (Bascuñán et al., 2016). These units also show a prominent presence of Carboniferous-Permian zircons and granitoid clasts, which are derived from Cordillera de Domeyko to the west (Hartley et al., 1992; Basso and Mpodozis, 2012; Bascuñán et al., 2016). The axis of the basin would have remained in a similar position, although the depocenter of the Seilao and Río Grande Members appears to have been located in the western flank of the syncline (Araya, 2016). South of the Barros Arana Syncline, the contemporaneous deposits along the El Bordo Escarpment (see above) consist in fine- to medium-grained, highly deformed sandstones, limestones and evaporites of the Naranja Formation, whose deposition ended close to ca. 57 Ma (Gardeweg et al., 1994; Arriagada, 1999; Mpodozis et al., 1999, 2005; Basso and Mpodozis, 2012; Bahamondes, 2017; Solari et al., 2017).

The next step in the geological history of the Salar de Atacama Basin occurs during the late Eocene-early Oligocene "Incaic" event that affected large swaths of the Central Andes, involving the exhumation of most of the basement within Cordillera de Domeyko, clockwise and counterclockwise tectonic rotations south and north of the Arica Bend respectively, leading to the formation of the Bolivian Orocline, uplifting of the Andean Plateau, and extensive crustal shortening along the margin (Maksaev and Zentilli, 1999; Arriagada et al., 2000, 2003, 2006b, 2008; McQuarrie, 2002a; McQuarrie et al., 2005a; Hongn et al., 2007; Charrier et al., 2007, 2009; Cobbold et al., 2007; Barnes et al., 2008; Amilibia et al., 2008; Barnes and Ehlers, 2009; del Papa et al., 2010; Roperch et al., 2011; O'Driscoll et al., 2012; Del Papa et al., 2013; Narea et al., 2015; Sanchez, 2017; Sánchez et al., 2018). As discussed in Chapters 2 and 3, it brought about most of the actual structural configuration seen in the basin, which still occupied a back arc position but now within the wedge top depozone of a foreland basin which was quickly migrating to the Eastern Cordillera in Argentina (Arriagada et al., 2006a; Hongn et al., 2007; del Papa et al., 2010; Carrapa et al., 2012; Reiners et al., 2015; Carrapa and DeCelles, 2015; Montero-López et al., 2018; Henríquez et al., 2019). The poorly consolidated, proximal alluvial facies of the Loma Amarilla Formation (Figure 5.3d; Arriagada, 1999; Henríquez, 2012; Henriquez et al., 2019; Henríquez et al., 2014; Mpodozis et al., 2005, 1999) correspond to the deposits of this stage.

Sedimentary deposits younger than the Loma Amarilla Formation, but older than the Tambores Formation (between ca. 42-27 Ma; Blanco et al., 2000; Hammerschmidt et al., 1992; Henríquez et al., 2014; Mpodozis et al., 2000; Travisany, 1978) are not found within the basin, likely due to the their cannibalization and redistribution during the Incaic Orogeny. Deposition of the Tambores Formation occurs mostly at the center of the Barros Arana Syncline (Figure 5.3e), while its finer grained equivalents of the San Pedro Formation (Flint et al., 1993; Wilkes and Görler, 1994; Mpodozis et al., 2000; Henríquez et al., 2014) were deposited to the east, towards the basin center. Several features within the latter formation point to slightly compressive conditions during its deposition, or a period of tectonic quiescence (see Chapters 2 and 3). The effect of strike-slip deformation cannot be ruled out, and the progressive migration of the basin center must also be considered to account for the variation in thickness between members of the Paciencia Group (Wilkes and Görler, 1994). An extra note must be made about the age of this group; although the Paciencia Group has been classically assigned to the Oligocene-Miocene, only the lowermost members of the San Pedro Formation belong to the Oligocene, as dated in the Cordillera de la Sal area (Marinovic and Lahsen, 1984; Naranjo et al., 1994), while most of the middle-upper members are younger than ca. 19 Ma (Henríquez et al., 2014). The Salar de Atacama Basin is now situated in the hinterland, as part of the forearc (Ramírez, 1979; Wilkes and Görler, 1994; Mpodozis et al., 2000; Reutter et al., 2006; Charrier et al., 2009; Henríquez et al., 2014).

The later stages of basin development (Figure 5.3f) show the reactivation of deformation within the basin, as evidenced by the deformation within the Cordillera de la Sal during the middle-late Miocene, before the deposition of wide ignimbrites covering the area, attributed to the late Miocene-Pliocene (Guest, 1969; Wilkes and Görler, 1994; Mpodozis et al., 2000; Becerra et al., 2014; Henríquez et al., 2014; Rubilar et al., 2017). Additional deformation has also affected younger units (Blanco et al., 2000; Mpodozis et al., 2000; Becerra et al., 2014; Henríquez et al., 2014), and continues to affect the basin in several areas (Jordan et al., 2002; Kuhn, 2002; González et al., 2009).

5.3.-Structure and formation of the Precordillera-Preandean Depression boundary

A combination of the data acquired in this thesis is presented as cross-sections in the northern and southern parts of the basin in Figure 5.4. They correspond to the sections analyzed in Chapters 2 and 3 and highlight the interaction between the Cordillera de Domeyko basement to the west, and the Salar de Atacama Basin; it is likely, however, that most of these observations hold true for other basins within the Preandean Depression.

One of the main characteristics observed latitudinally along the basin is the eastward thrusting of basement, which deforms the late Mesozoic-Cenozoic cover, even affecting recent deposits (Figure 5.4a). This Carboniferous-Triassic basement thrusting is clearer in the southern areas of the basin (Figure 5.4b), a fact which has been well recorded around Cerro Negro and Cerro Quimal (Arriagada, 1999; Mpodozis et al., 2005; Arriagada et al., 2006a; Amilibia et al., 2008; Basso and Mpodozis, 2012; Henríquez, 2012). In the northern parts, around the Cerros de Tuina Area (Figure 5.4b), this deformation is not clear at the surface, but directly inferred from the gravity and seismic profiles. Some of the faults affecting the Neogene cover also seem to be rooted in deeper faults affecting the basement, implying that some of these systems have existed since possibly the Eocene onwards.

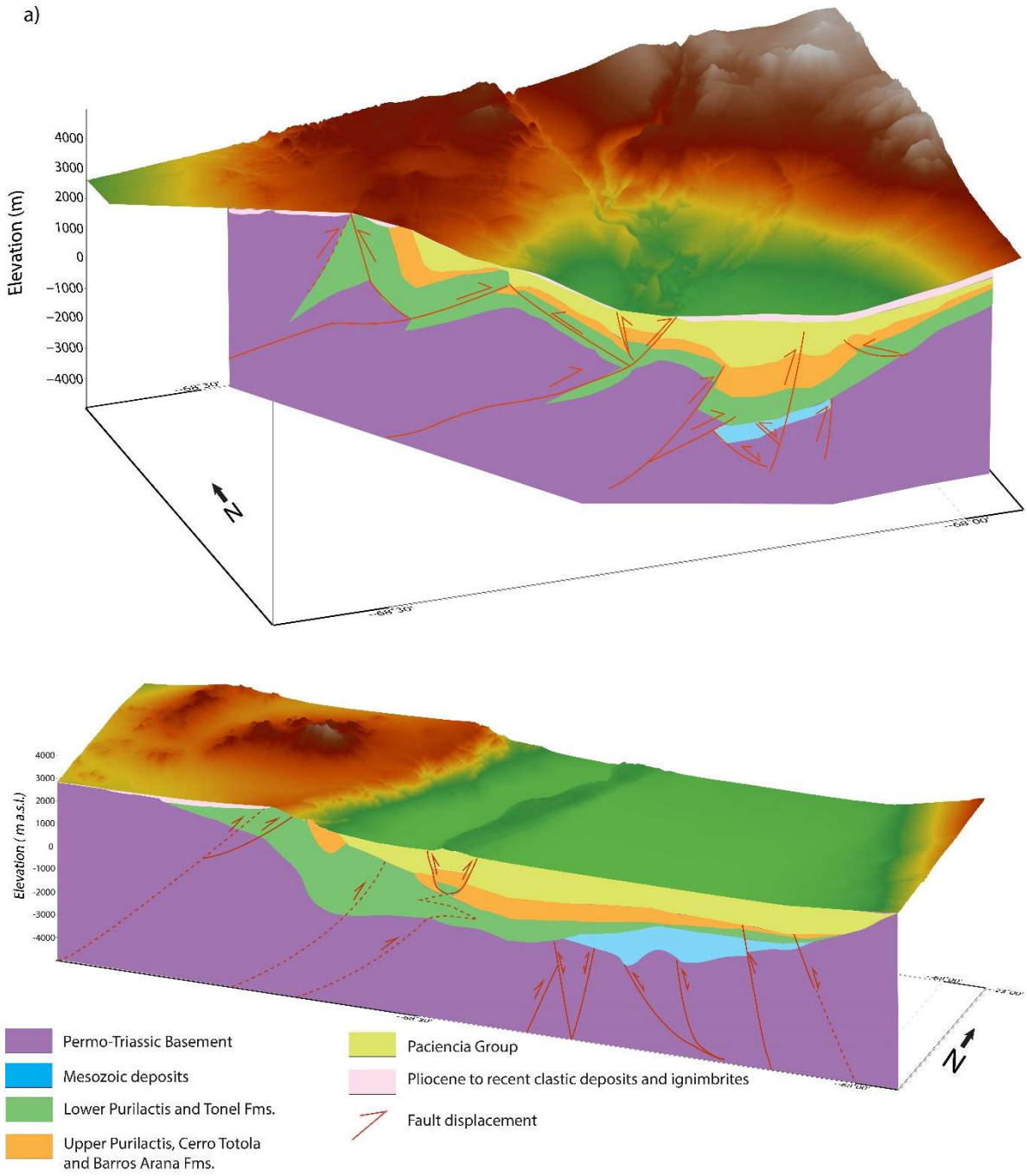

Figure 5.4: Structural interpretation of the surveys crossing a) Cerros de Tuina towards the Western Cordillera (Chapter 2) and b) El Bordo Escarpment south of Cerro Quimal towards the Western Cordillera (Chapter 3)

As discussed in Chapters 2 and 3, some of these features are also observed in other basins of the Preandean Depression, such as the Salar de Punta Negra, where Martinez et al. (Martínez et al., 2017a, 2018) interpreted basement faults reaching the surface and deforming the late Mesozoic-Cenozoic infill, at times decapitating previous structures. They also point out evidence for the inversion of pre-orogenic normal faults (prior to the Late Cretaceous) which might have conditioned the development of the basins within the Preandean Depression. Amilibia et al. (2008)

also argued for the inversion of rift faults that originated during the Triassic and Jurassic-Early Cretaceous, whose interplay would have affected its posterior inversion styles and the formation of Cordillera de Domeyko. This is not immediately evident in the Salar de Atacama area, although the reactivation of smaller normal faults related to Mesozoic rifting does appear to occur (Figure 5.4). Major normal faults, which would have controlled the deposition of the Triassic units have not been documented in the study area, but have been found farther south (e.g., Amilibia et al., 2008; Espinoza et al., 2019; Martínez et al., 2018, 2017a). Regardless, the formation of the actual basins within the depression are a direct consequence of the uplift of the mountain range, and their differences may be ascribed to their pre-Incaic architecture, and how the upper crust responded to its deformation (Arriagada et al., 2000, 2003).

5.4.-Basin response to regional tectonics and plate dynamics

The observations and interpretations laid out in this work above are necessary for the analysis of the tectonic events that led to the development of the Salar de Atacama Basin, to understand how they are registered in its successions and structural setting, and to relate these events with the evolution of the Central Andes. In order to make a more thorough assessment of the tectonic processes involved, special emphasis must also be placed on the plate interphase and the migration of the magmatic arc, which has been shown here to be closely related to the units found in the basin.

Figure 5.5 shows a map of northern Chile indicating the westernmost extent of the various Mesozoic-Cenozoic arcs from the Early Jurassic onwards. Here, the focus of interest is on the migration of the western border of the volcanic arc and the arc-trench distance considering an average arc-trench gap of 300 km (Goss et al., 2013). The volcanic front shows a steady migration eastward, becoming almost stagnant between the Late Cretaceous and the Eocene. The arc presents a noteworthy magmatic lull during the Oligocene, although large-scale ignimbrites can be found in northern Chile, such as the Altos de Pica and Oxaya Formations (Farías et al., 2005; Charrier et al., 2013). The volcanic arc is reinstated during the late early Miocene, where the distinctive bend in the strike of the magmatic arc between ~ 21°-25°S was formed (SERNAGEOMIN, 2003; Stern, 2004; Haschke et al., 2006; Trumbull et al., 2006; Kay and Coira, 2009). The origin of this bend has had multiple interpretations based on the analysis of geophysical data (see Subchapter 5.5).

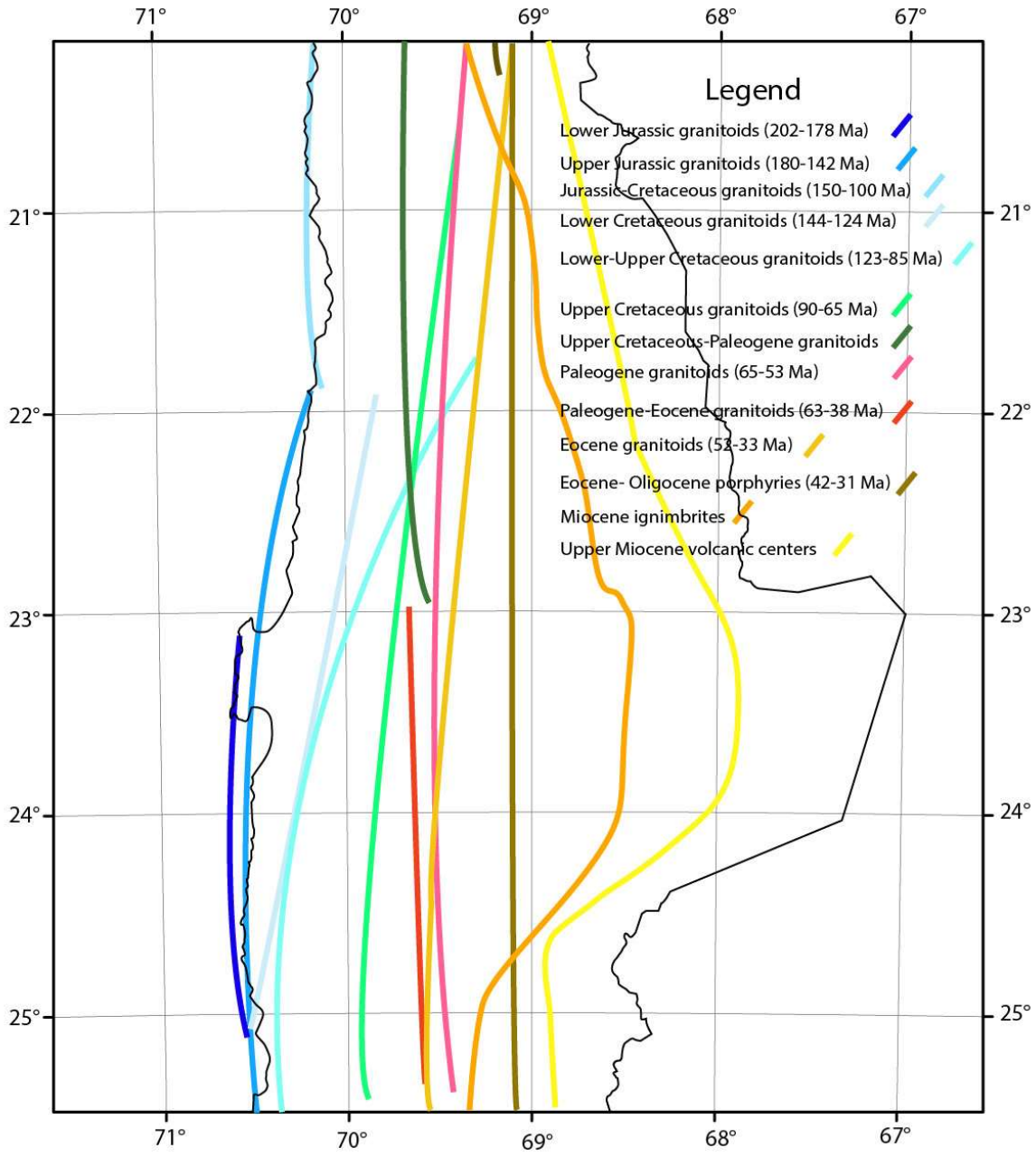

Figure 5.5: Westernmost extent of the different magmatic arcs and their associated deposits. Modified from SERNAGEOMIN (2003, 2013)**, Vásquez & Sepúlveda (2012), Henríquez et al. (2014), Becerra et al. (2014), Basso & Mpodozis (2012).**

Table 5.11 presents the age of the magmatic front and the destruction rates of the forearc margin for the time intervals involved (destroyed plate margin/minimum age), showing values that rarely exceed 2-3 km/Ma; higher values during the Miocene reflect the location of large ignimbrites rather than volcanic bodies, and the degree of their migration must be addressed by other means. These rates are similar to the long-term ($>10^7$ years) trench retreat rates previously calculated for the Central Andes (e.g., Clift and Vannucchi, 2004; Clift and Hartley, 2007; Stern, 2011; von Huene and Ranero, 2003), where it was noted that there are also small-term changes related to plate interaction, trench sedimentation, underplating, among others (e.g., Kukowski and Oncken, 2006).

A link between the active erosion of the forearc margin and eastward migration of the magmatic arc has been recognized by multiple authors (Rutland, 1971; von Huene and Ranero, 2003; Stern, 2004; Haschke et al., 2006; Kukowski and Oncken, 2006; Trumbull et al., 2006; Kay and Coira, 2009; DeCelles et al., 2015b), though the degree of relevance of other factors, such as flat-slab subduction and alternating convergence rates are still a matter of debate. Also, these rates assume that the arc-trench gap (and subduction geometry of the slab) is, on average, constant throughout the geological time, and that the margin has been mostly erosive during this time.

Table 5.1: Volcanic arc, arc-trench gap and long-term destruction rate of the margin.

Volcanic Arc	Minimum Age (Ma)	Maximum Age (Ma)	Minimum Trench-Arc Gap (Km)	Long Term Destruction Rate (Km/Ma)
Early Jurassic	202	178	80.5	1.086633663
Late Jurassic	180	142	87.6	1.18
Jurassic-Cretaceous	150	100	103.2	1.312
Early Cretaceous	144	124	101.1	1.38125
Early to Late Cretaceous	123	85	119.1	1.470731707
Late Cretaceous	90	65	152.6	1.637777778
Paleogene	65	53	188.6	1.713846154
Paleogene-Eocene	63	38	176	1.968253968
Eocene	52	33	185	2.211538462
Miocene	17	5	226	4.352941176

The initiation of compression in the Central Andes during the Late Cretaceous has been classically linked to the opening stages of the South Atlantic Ocean, due to the break-up of western Gondwana, the absolute motion of South America during those stages, and the increase in coupling between the subducting and overriding plates (Zonenshayn et al., 1984; Scheuber et al., 1994; Charrier et al., 2007; Mpodozis and Ramos, 2008; Ramos, 2010; Seton et al., 2012). This 'Peruvian Phase' (Steinmann, 1929) would have started around 75-100 Ma at different parts of the subcontinent, and, as such, constitutes one of the major events registered for the Andean Orogen, although its duration and exact beginning are still unsolved questions (Megard, 1984; Jaillard, 1992, 1993; Cobbold and Rossello, 2003; Howell et al., 2005; Jaimes and de Freitas, 2006; Charrier et al., 2007; Cobbold et al., 2007; Ramos, 2010; Tunik et al., 2010; Merino et al., 2013; Bascuñán et al., 2016; Boyce et al., 2020). From the perspective of the work developed in this thesis, the Late Cretaceous-Paleogene sedimentation in the Salar de Atacama Basin follows closely both the global plate context and the evolution of the forearc margin, with different sedimentary cycles reflecting variations of the orogenic loading west of the basin, and the generation of accommodation space within the basin, of which the most relevant cycle would have occurred at ca. 79 Ma (Bascuñán et al., 2016, 2019). The quasi-stationary nature of the arc-trench gap for the Late Cretaceous-Paleogene (Figure 5.5) also correlates well with the relatively minor migration of the foredeep, which does not show large jumps eastward (see above).

Another deformation event which has been proposed for the Central Andes of northern Chile at ca. 65 Ma is the 'K-T' Event (Cornejo et al., 1997, 2003; Somoza et al., 2012), which has been discussed in previous chapters regarding the observations made from detrital zircon patterns and deformation within the El Bordo Escarpment. Based on palaeomagnetic studies, Somoza et al. (2012) argued for early Paleocene deformation around the Cerros de Montecristo area, northwest of the city of Calama, involving the Upper Cretaceous Quebrada Mala Formation. This deformation could have been either a result of subduction processes along the Andean Margin, or due to the subduction of an oceanic plate boundary (Phoenix-Farallón), which would account for the short-lived nature of the event, and the calc-alkaline to intraplate signature of the volcanism (Cornejo and

Matthews, 2001; Cornejo et al., 2003). However, Somoza et al. (2012) also argued that there was a possibility for a 'southern' interception of this feature with the continental margin (around 33°-33°30'S), which would invalidate this hypothesis for northern Chile.

Following the plate reconstruction provided by Seton et al. (2012), it appears that the 'southern' scenario proposed by Somoza et al. (2012) is more likely than the 'northern' option, and as such the deformation seen in other parts of the margin at this time would have been a product of the migration of the orogenic front eastwards as the forearc margin was being eroded over time. Given that the Salar de Atacama Basin is located eastward of the areas where the 'K-T' event has been reported (e.g., Cornejo et al., 2009, 2003), it is possible that the effect of this 'event' in the area was only the change in lithofacies seen in the aeolian Vizcachita Member of the Purilactis Formation, which also explains the lack of discernible deformation in the area. This encroachment of the orogenic front is also reflected in the upward-coarsening facies seen in the remainder of the upper Purilactis and Barros Arana formations, which supports the notion of an early unroofing of the crystalline basement within Cordillera de Domeyko (Hartley et al., 1988, 1992; Bascuñán et al., 2016; Henríquez et al., 2019). This work cannot account for the change in geochemical signature of the volcanism at that time, which in the case of the Cerro Totola Formation shows an alkaline affinity that has been related to slightly extensional conditions within a crust around 35 km thick (Mpodozis et al., 2005; Haschke et al., 2006). An extensional origin for this formation would have to be reconciled with the 'K-T' event, as its whole rock K-Ar ages range between 64-66 ± 2.0 Ma (Mpodozis et al., 2005), which is close to the age obtained for the Cerro Quimal intrusive, which has been interpreted as being emplaced under compressive conditions (Andriessen and Reutter, 1994; Mpodozis et al., 2005).

The time between the 'K-T' and Incaic events, the latter of which has been usually bracketed between 45-35 Ma (Maksaev and Zentilli, 1999; Mpodozis et al., 2005; Charrier et al., 2007, 2009; Arriagada et al., 2008), also presents questions regarding its tectonic activity. Volcanic, volcano-clastic and intrusive units were certainly being deposited/emplaced west of the Salar de Atacama Basin, comprising successions such as the Augusta Victoria, Icanche, Chile-Alemania, Calama and Cinchado formations, among others (Montaño, 1976; Maksaev, 1978; Ramírez and Gardeweg, 1982; Marinovic and García, 1999; Tomlinson et al., 2010, 2001; Blanco et al., 2003; Tomlinson and Blanco, 2006; Marinovic, 2007; Charrier et al., 2009; Solari et al., 2017), whose deposition occurred within intermontane basins closely associated with the magmatic arc. Charrier et al. (2009) held the view that this deposition occurred mostly under transtensional conditions, similar to what was reported at the latitude of Copiapó farther south (ca. 27°S) (Mpodozis et al., 1995), while other authors such as Amilibia et al. (2008) have argued for mostly compressional conditions for the Chile-Alemania Formation, as part of a syn-inversion succession.

Within the basin, this time interval is represented by both the Naranja, upper Purilactis (Vizcachita Member and above) and the Barros Arana Formations, albeit in different parts of the basin (see above). Mpodozis et al. (Mpodozis et al., 2005) considered that the Naranja Formation had been deposited in a post-tectonic setting after a regional compressive pulse during the early Paleocene, based on its fining upward motif and rapid change from alluvial to evaporite facies, and the angular unconformity separating it from the Tonel Formation, north of the Gaby-Calama road, or the Cerro Totola Formation in the southern El Bordo Escarpment (Mpodozis et al., 1999). On the other hand, the units belonging to the upper Purilactis-Barros Arana Formations have been interpreted as part of

the basin fill originated by the migration eastward of the orogenic front and its activity in Cordillera de Domeyko, showing increasing proportions of granitoid clasts derived from the basement, and upward coarsening motifs (Mpodozis et al., 2005; Arriagada et al., 2006a; Amilibia et al., 2008; Bascuñán et al., 2016, 2019). Regardless of the geometric disposition of these units, the tectonic setting during their deposition is in agreement with mostly compressive conditions, whose relatively continuous deposition ended shortly before the Incaic Event. Further studies of the Naranja/Barros Arana Formations will clarify this relation and/or tectonic setting (see above).

The late Eocene-early Oligocene compressive event experienced throughout large swaths of the Central Andes has been ascribed to several reasons related to changes in the subduction interphase, with the presence of a flat slab or the transition from a normal to sub horizontal subduction as one of the most relevant mechanisms (James and Sacks, 1999; Ramos, 2009; Ramos and Folguera, 2009; Martinod et al., 2010; Horton, 2018). The reasons or variables that led to this flat slab are not clear, but it may have been enhanced by oceanic plate features (e.g., Bello-González et al., 2018; Horton, 2018; James and Sacks, 1999; Martinod et al., 2010; O'Driscoll et al., 2012). Other authors have proposed additional mechanisms for the amount and north-south variation of the shortening, and its rapid jump eastwards at ca. 40 Ma, which are not at odds with this theory. Some of these mechanisms consist in the emplacement eastward of thin basement thrust sheets beneath the Central Andean Plateau, in preexisting weak zones within the crust and mantle due to previous rifting episodes (McQuarrie, 2002b; McQuarrie et al., 2005a), and north-south differential horizontal shortening accounting for the generation of the Central Andean Rotation Pattern (Isacks, 1988; Arriagada et al., 2008; Roperch et al., 2011).

In particular, the flat slab model is invoked to explain the magmatic lull between ca. 52-31 Ma in Southern Perú and between ca. 35-25 Ma in northern Chile (Sandeman et al., 1995; James and Sacks, 1999), and the rapid eastward migration of the deformation front between ca. 45-35 Ma from the Altiplano to the Eastern Cordillera in Bolivia and northern Chile (around 400 km inboard following McQuarrie et al. (2005a)). James & Sacks (1999) propose that deformation actually migrated during the transition from normal to flat subduction, and that the time of the magmatic lull represents diminishing deformation in the area between 14°-24°S. The later transition from flat to normal subduction at ca. 25 Ma would have led to the influx of asthenospheric mantle westwards with the consequent migration trenchward of the magmatic arc, the melting of lithosphere beneath the eastern Altiplano and Eastern Cordillera and their uplift, and the generation of the Bolivian Orocline.

Ramos and Folguera (2009) reviewed the flat slab subduction segments along South America, emphasizing their cyclic nature and reoccurring appearance in the geological record. The normal to flat slab transition would include a migration and expansion of the magmatic arc, the uplift of the Main Andes, the generation of broken foreland basins such as those in the Sierras Pampeanas, and the subsidence of basins in the Subandean region and the Altiplano. The steepening of the slab would conversely lead to a rhyolitic flare-up, such as those evidenced by large ignimbrites in the Altiplano-Puna region and northern Chile (de Silva, 1989; Kay and Coira, 2009; Salisbury et al., 2011), thermal uplift owing to lithospheric removal and subsequent extension by vertical collapse, and migration of deformation to the foreland.

An examination of the proposed flat slab stages in northern Chile and the study area yields the following observations. The Incaic Event shows strong N-S variations in shortening, and the

Chilean side of the margin was heavily involved, with average clockwise rotations of 29° as shown by Arriagada et al. (2000, 2003, 2006b, 2008) and Narea et al. (2015), among others. This rotation and associated shortening, have been bracketed between 40-15 Ma, although likely ending at ca. 24 Ma (Arriagada et al., 2008; O'Driscoll et al., 2012), with thermochronological data showing little to no exhumation in Cordillera de Domeyko after 30 Ma (Maksaev and Zentilli, 1999; Sánchez et al., 2018). Intrusive units with this age (ca. 45-34 Ma) are found along the Precordillera (Figure 5.5), comprising several units at times linked to some of the largest porphyry copper deposits in Chile (e.g., Cornejo et al., 1997; Sillitoe, 2010; Sillitoe and McKee, 1996; Tomlinson et al., 2010; Tosdal and Richards, 2001; Wörner and Hammerschmidt, 2000). Also, a magmatic lull does exist during most of the Oligocene, but the resumption of magmatism shows strong N-S variations in style, width, and position of the magmatic arc, as recognized by Trumbull et al. (2006), who showed that the volcanic arc was broadened between 20°-23°S, but that it became more narrow to the south; they also showed that the volcanic arc south of 23°S presented no widening before ca. 30 Ma, a fact that James and Sacks (1999) attributed to a fast shallowing of the slab. Also, and as seen in Figure 5.5, the western extent of late Miocene volcanism occupies a position close to the previous arc north and south of the Salar de Atacama Basin.

Several contentious points must be addressed regarding the building of the Andes during the late Eocene-middle Oligocene, and the presence of a flat slab event:

1. Although a north-to-south flattening of the slab has been proposed, deformation within the eastern Altiplano, Eastern Cordillera and northern Chile is mostly bracketed within 45-30 Ma (McQuarrie, 2002b; McQuarrie et al., 2005a, 2008; Hoke and Lamb, 2007; Barnes et al., 2008; Barnes and Ehlers, 2009). This deformation event reaches other parts far to the south along Cordillera de Domeyko (Charrier et al., 2009), and the Frontal Cordillera in Chile between 28°-29°S (Martínez et al., 2017b), showing little north-to-south migration, and that it occurs almost simultaneously along the margin.
2. James and Sacks (1999) argued that the shallowing of the slab was 'fast', owing to the absence of eastward expansion of the magmatic arc. Arc products between 45-32 Ma have been found in the Andahuaylas-Anta arc of Perú, showing a N-NE migration of the arc of 200 km, occupying that position until ca. 30 Ma (Perelló et al., 2003; Mamani et al., 2010). This concurs well with the 'normal-to-flat' transition between 50-40 Ma, and the following 'flat-to-normal' transition around ca. 30 Ma (James and Sacks, 1999), but not with the timing of deformation (Point 1). As such, a dichotomy appears where the normal-to-flat slab transition leads to an expansion/migration of the magmatic arc in Perú, but not in Chile-Argentina (Figure 5.5) (Trumbull et al., 2006; Coira and Zappettini, 2008).
3. The trenchward migration of the magmatic arc in Southern Perú (Mamani et al., 2010), which would have resulted during the 'flat-to-normal' transition of the slab does not occur in Chile within the study area (Figure 5.5), although it has been argued that the arc expanded eastwards and was then narrowed for the segment between 20°-23°S during the Oligocene/early Miocene (Trumbull et al., 2006).
4. The 'flat-to-normal' transition stage between 25-15 Ma proposed by James and Sacks (1999) would lead to an episode of intense crustal deformation, uplift of the Altiplano and the generation of the Bolivian Orocline, which have been shown to have started earlier (e.g., Barnes and Ehlers, 2009). The extensional collapse of previously contracted structures proposed by Ramos and Folguera (2009) can also be contested, as extension is not clearly

seen in the actual forearc associated with this stage (Bascuñán et al., 2019; Charrier et al., 2013; this work), and the increase in deformation in the Subandean belt has been shown to occur during the latest Miocene-Pliocene (Carrapa and DeCelles, 2015).

A different scenario for the construction of the Andean Cordillera was proposed by DeCelles et al. (2015b), where the evolution of the orogen is driven by cycles showing rapid advances of the orogenic wedge, high flux events, and the removal of dense roots and lower crust eclogites by foundering of convective instabilities, either by delamination or the "dripping" of Rayleigh-Taylor instabilities. For the Central Andes, the timing of these events would be between ca. 42-36 Ma for a foundering event leading to an increase in shortening and the rapid migration of the deformation front into the eastern Puna. This foundering would have taken place during the final stages of a high-flux volcanic event between ca. 50-40 Ma, and the magmatic lull between ca. 36-26 Ma would represent a recharge interval, where the propagation of the deformation front is slow. High-flux magmatism would have started again at ca. 25 Ma, with a possible removal after ca. 15 Ma signaling the beginning of migration of the deformation front towards the Subandean region.

Haschke et al. (2006) performed a review of the different volcanic arcs of the Central Andes in Chile, analyzing its ages, geochemical features and relation to various plate parameters, which led them to propose the presence of cycles within the activity in the arc, which would be linked to the presence of various flat slabs, thus explaining the presence or absence (and increase) of volcanic activity and the increase in La/Yb ratios along any given cycle of arc activity. A review of the geochemistry of the arc systems in northern Chile surpasses the scope of this work, but the ages of the arc components, and consequentially of the cycle, must be brought into question. The activity of the volcanic arc between 58 Ma and 42-44 Ma (the age of the lavas on top of the Naranja Formation and the age of the tuffs within the Loma Amarilla Formation, respectively, see above) seems to have been minimal, as shown by the scarce presence of said ages in different maps of northern Chile (Maksaev, 1978; Cortés, 2000; Tomlinson et al., 2001, 2010; Blanco et al., 2003; Basso, 2004; Tomlinson and Blanco, 2006; Blanco and Tomlinson, 2009; Basso and Mpodozis, 2012; Solari et al., 2017). It is not the presence of the arc that is disputed, but its significance as a 'high-flux event' *sensu* DeCelles et al. (2015b), who argued for the existence of this event based on detrital zircon ages between 50-40 Ma obtained from samples in Sierra de Moreno; these may indeed represent the erosion of said arc, but do not appear to be prevalent in other units, particularly those on the eastern side of Cordillera de Domeyko or in the Pre-Andean Depression (e.g., this work; Bahamondes, 2017; Bascuñán et al., 2019, 2016; Henriquez et al., 2019; Solari et al., 2017).

Also, even though the work presented in this thesis is in agreement with the proposal of an eastward migration of the deformation front during the late Eocene-early Oligocene, many other studies of the Paleogene basins in northern Argentina reached the conclusion that the dominant setting was that of a 'broken' foreland, where the deformation at that time was occurring synchronously in the Western Cordillera, the Puna, and the Eastern Cordillera between ca. 22°-26°S (Hongn et al., 2007; Payrola et al., 2009; del Papa et al., 2010; Del Papa et al., 2013; Montero-López et al., 2018). The observations and interpretations compiled here may serve as input for future work trying to elucidate the style and magnitude of the deformation within the area and eastwards.

The tectonic conditions after the Incaic Event seem to have been slightly compressive or 'quiescent' during the deposition of the San Pedro and Tambores formations, when the basin was finally incorporated within the forearc (see above), between ca. 28 and 9-17 Ma (Travisany, 1978; Mpodozis et al., 2000; Becerra et al., 2014; Henríquez et al., 2014). An amagmatic flat slab event, associated with the subduction of the Juan Fernandez Ridge, has also been proposed for this part of the Central Andes between ca. 26-17 Ma, with slab steepening occurring between 16-11 Ma and 10-6 Ma, leading to the deposition of the large ignimbrites seen in the Salar de Atacama area (de Silva, 1989; Kay and Coira, 2009). However, it is hard to reconcile this event with the north-south variations in volcanic activity seen by other authors and discussed above, and is particularly problematic when reviewing the proposed path for the subduction of the Juan Fernandez Ridge, which can be even linked to an increase in magmatic activity (Trumbull et al., 2006). DeCelles et al. (2015b) also argued that there is no deformation associated with the uplift of basement blocks, as would be expected from flat slab events (e.g., Ramos, 2009; Ramos and Folguera, 2009). Deformation within the Salar de Atacama Basin is mostly recorded afterwards, during the late Miocene (Blanco et al., 2000; Mpodozis et al., 2000; Jordan et al., 2010; Becerra et al., 2014; Henríquez et al., 2014; Sanchez, 2017; Rubilar et al., 2017; Bascuñán et al., 2019). The westernmost limit of the early-late Miocene magmatic arc roughly coincides with the Eocene limit, though it is curved around the Salar de Atacama area (Figure 5.5). As a side note, the existence of a flat slab at the same time would also preclude the existence of an extensional event on this side of the Central Andes for that time (Pananont et al., 2004; Jordan et al., 2007; Blanco, 2008).

The upper Miocene deformation seen within the Cordillera de la Sal and the San Pedro-Tambores formations has been associated with the 'Quechua' Phase or Event, which has been ascribed to an increase in convergence velocities between Nazca and South America, although they have steadily diminished since ca. 10 Ma (Steinmann, 1929; Megard, 1984; Pardo-Casas and Molnar, 1987; Silver et al., 1998; Somoza, 1998; Somoza and Ghidella, 2005; Charrier et al., 2009). This phase would have led to renewed deformation within the western flank of the Central Andes, the incision of the previous topography, and a generalized episode of westward tilting of the forearc in northern Chile (Farías et al., 2005, 2008; Riquelme et al., 2007; Jordan et al., 2010; Charrier et al., 2013; Fuentes et al., 2018). The effects of said stage can also be readily seen within the basin, with the deformation along the western flank of the Barros Arana Syncline, and the angular unconformity between the Vilama and San Pedro Formations (Blanco et al., 2000; Mpodozis et al., 2000; Arriagada et al., 2006a; Basso and Mpodozis, 2012; Becerra et al., 2014; Henríquez et al., 2014; Bascuñán et al., 2019). Sanchez et al. (2017) obtained a post-10 Ma cooling signal in samples obtained from the intrusive in Cerro Quimal, corresponding to the first records of cooling within that age for the region, and which can be linked to the westward tilting and rotation for the forearc region west of the Pre-Andean Depression, as shown by Jordan et al. (2010). The reasons for this uplift are still under discussion, but may include the underthrusting of the Brazilian shield and ductile flow of the lower crust (Beck and Zandt, 2002; Farías et al., 2005; Tassara, 2005), delamination of eclogitic crust (Kay et al., 1999; Garzione et al., 2008; Hoke and Garzione, 2008; Kay and Coira, 2009), or a combination of processes including crustal thickening, the removal of dense lithospheric roots, and/or the addition of volcanic products to the Andean edifice (Beck et al., 2015; DeCelles et al., 2015a, 2015b; Quade et al., 2015). Theories favoring long-term uplift of the

region are more consistent with the work presented here, as most of the structural configuration of the region appears to have been achieved during the Incaic Event, even though the contribution of upper Miocene deformation is undoubtful (see Chapters 2 and 3). The models involving recent delamination also tend to overlook prior exhumation of the Andes (e.g., Garzione et al., 2008), with recent paleoaltimetry studies showing that parts of the Western Cordillera and Altiplano-Puna (including Cordillera de Domeyko) may have reached high elevations by the late Eocene (Quade et al., 2015).

It is clear from the minor review in this Chapter that much work still has to be done in this area of the Central Andes as in others, in order to elaborate a comprehensive model for the building of the Andean Orogen, which must incorporate not only the issues raised above within the Salar de Atacama Basin, but those that may arise from further studies in the mountain range. As stated by Jordan et al. (1982), the Andes correspond to a natural laboratory in which the different processes leading to deformation of the continental margin can be studied through various means; in this regard, one of the primary conclusions of the work developed in this PhD. Thesis is that the Salar de Atacama Basin indeed is a natural laboratory with which different existing, as well as future models, can be tested against. In particular, the record within the Salar de Atacama Basin leans toward a steady evolution of the margin, where the volcanic and deformation fronts migrate progressively eastwards, where subduction erosion processes are fundamental to the migration of these features. The idea of 'cycles' involving magmatic events and/or flat-normal slab transitions seem incompatible not only with the basin history, but also with that of other latitudes within the Central Andes, as is the link between regional tectonic conditions (compressive or extensional) and convergence velocities as proposed in earlier studies (e.g., Jordan et al., 2007; Somoza and Ghidella, 2005), particularly if the trench normal velocity is over 4 cm/a, following Maloney et al. (2013).

5.5.-Regarding the Salar de Atacama Basin as an anomaly

The Salar de Atacama Basin has been a key location for geological studies within the Andes since at least the times of Brüggen (1934, 1942, 1950), partly because of its almost complete stratigraphic record from the Late Cretaceous onwards, but also due to its anomalous topography, where the magmatic arc has been deflected around ca. 60 km eastwards from the almost N-S regular trend (Figure 5.5, Mpodozis et al., 2005).

This deflection led many researchers to conclude that there were abnormalities or crustal variations beneath the Salar de Atacama Basin, which led to the deflection of the volcanic arc, and its survival as an 'abnormal' feature within the Precordillera-Western Cordillera; some of the key studies and findings are summarized below:

- Based on regional gravimetric studies and residual isostatic modeling performed in the Central Andes in the 1990's, Götze et al. (1994; 2002) and Reutter et al. (2006) identified a NW-SE trending 'Central Andean Gravity High' (CAGH) between 22°-26°S, which encompasses the Calama Basin, the Salar de Atacama Basin, and continues south-eastwards to the Arizaro and the Salar de Pipanaco Basins in Argentina. This anomaly, whose trend differs sharply from the approximately N-S trend seen in Mesozoic-Cenozoic structures and arcs, would be composed of volcanic rocks and

intrusives belonging to the Ordovician 'Faja Eruptiva de la Puna Occidental' (Bahlburg and Hervé, 1997; Charrier et al., 2007; Bahlburg et al., 2009; Zimmermann et al., 2009), along with younger components (Triassic and upwards), although Reutter et al. (2006), argued for a dominant presence of Cretaceous units associated with the Salta Rift. According to Götze & Krause (2002), the density anomaly that generates the CAGH lies between 10-38 km deep, and its dimensions are ca. 400 km in length and 100-140 km in width. Reutter et al. (2006) identified three small-wavelength highs within this forearc gravity high (Quimal-Tuina, Peine and Lila Highs), which lie at shallower depths than the regional high, between 4-6 km in depth.

- Further studies involving similar gravity datasets have been recently published by Yañez & Rivera (2019a), who obtained a residual gravity anomaly of Chile from ca. 45°S northwards, and performed a spectral analysis to estimate the depth of various crustal dense blocks. These where shown to lie between 12-27 km deep, with the block below the Salar de Atacama Basin lying in between 16.5-24.2 km deep. The origin of these blocks is uncertain, but could be the product of either rifting during the Triassic, or due to changes in subduction dynamics (roll-back) before the 'Andean' Cycle *sensu* Charrier et al. (2007). Different types of flows, particularly those associated with the magmatic arc beneath the Salar de Atacama Basin, would be diverted by these blocks around its edges, especially under the presence of a trans-lithospheric fault (TLF), which correspond to large NW-SE lineaments that do not follow the general N-S trend of most of the features of the Central Andes.
- Electromagnetic studies have also been performed in the Salar de Atacama and the forearc-arc-backarc transition; Magnetotelluric measurements presented by Díaz et al. (2012), which included multiple broadband measurements around Lascar volcano, show the electric conductivity distribution of a west-east profile starting from Cordillera de Domeyko towards the northern Puna. The modeling shows mainly highly resistive features around Cordillera de Domeyko, and an increase in conductivity in the Salar de Atacama, related to the presence of water springs and faults through which they could reach the surface, with an increase in depth of the conductive feature towards the western part of the basin, associated with deeper faulting (ca. 5 km). High conductivity areas are seen towards the arc and backarc, particularly beneath the Puna plateau. Ślęzak et al. (2021) performed a similar study in the region, also including the forearc west of Cordillera de Domeyko. Areas with high conductivity zones are found on the western border of Cordillera de Domeyko, which reaches down towards the Nazca slab interface. The Cordillera de Domeyko coincides with a high resistivity zone, while the Salar de Atacama shows north-south contrasts (below the shallow conductors associated with the saltpan), with high resistivities at shallow depths north of the Cordón de Lila, and mildly conductive areas in the northernmost part of the basin. The rest of the crustal areas show in general high resistivities, which were associated with low fluid content and high density within the crust. In essence, these studies agree with the proposed thermal configuration of the crust underneath the basin (based on gravity and seismic methods), and provide more discrimination of the physical characteristics within the basin, which can be usually related to the outcropping geology of the area (basement, basin infill, and volcanic arc).

- Schurr & Rietbrock (2004) derived Vp, Vp/Vs, and attenuation (Qp) values through local earthquake tomography for the area between ca. 21°-25°S, showing that the mid-lower crust beneath the Salar de Atacama Basin (down to 85 km) presents high velocities which mirror the shape of the Pre-Andean Depression. The Vp/Vs data show a crustal segmentation between the arc and the edge of the basin, where ratios are higher in the former than in the latter, similar to what is observed in the mantle. The Qp data, on the other hand, show its highest values beneath the basin in both the lower crust and mantle, and also that it is clearly separated from the magmatic arc and the Cordillera de Domeyko, at least on the crustal level. Based on this dataset, the authors argued that the crust underneath the basin is likely composed of both metabasites and gneisses, and that this lithosphere is cold and rheologically strong. This cold lithospheric block would displace hot isotherms to the east, impede the westward flow of asthenospheric mantle, and deflect the magmatic arc at this latitude. Mechanical coupling of this lithosphere with the subducting plate would also explain the elevation of the basin and the compressive deformation at its edges.
- A similar conclusion was reached independently by Yuan et al. (2002), who studied the continental Moho in the Central Andes through P-to-S wave conversion, showing the presence of a crust around 67 km thick beneath the Salar de Atacama Basin, which would lie 1 km below isostatic equilibrium, and which would be coupled with the Nazca plate. However, the model revealed several blocks with higher elevations than those that would be determined by their crustal thickness, which, when taken together with the Salar de Atacama Block, would reach the average crustal density of the area. The cross sections of the Central Andes structure obtained by Yuan et al. (2000) show an increase in Moho depth along the longitude of the basin in several N-S profiles, which, according to the authors, is not associated with large changes in regional topography. Also, the derivation of the continental Moho boundary by Tassara & Echaurren (2012), as also shown by Metcalf et al. (2015), reveals an overall constant thickness for the Moho along a north-south profile between 20°S-27°S, with little or no variation beneath the Salar de Atacama. The latter study proposes an increase in thickness for the lithosphere-asthenosphere boundary beneath the saltpan, but the review of the modelling done by Tassara & Echaurren (2012) indicates that the Salar de Atacama is only part of a larger anomaly in Moho geometry. As such, it is hard to associate the existence of the Salar de Atacama Basin, or of the Preandean Depression, with a punctual change in the Moho/lithosphere-asthenosphere boundary shape, as the correlation with changes in these features is not straightforward.
- More recently, a 3D seismic wave tomography and hypocenter determination study over the northern part of the magmatic deflection shows that there is an eastward shift in the location of hypocenters of similar depth south of 21°S, which indicates that the dip of the Nazca slab decreases towards the south at 90-110 km in depth (Comte et al., 2016). This could explain the deflection of the volcanic arc seen in the area, which would be a recent feature compared to the formation of the basin, but not its deformational history.

A special note must be made regarding the CAGH. Götze & Krause (2002) noted that the positive anomalies from their isostatic residual gravity model could also be connected with other highs within the Andean region, such as the Coastal Cordillera, the Altiplano-Puna, and the Eastern Cordillera, which would make them part of the normal crustal density of the studied region. Most of the negative anomalies could be explained by the presence of the recent (early Miocene-Holocene) magmatic arc, and the 'normal' crust would be composed of mainly lower Mesozoic-Paleozoic units. The residual gravity anomaly shown by Yañez & Rivera (2019b) effectively shows an area similar to the CAGH within the study region, which could also be connected to parts of the Coastal Cordillera and the northern regions in Chile-Bolivia.

The link between the anomalies (shallow- or deep-seated) with the formation of the basin must be brought into question, as the Preandean Depression (or Salars Depression, following Charrier et al. (2007)) extends to the north and south of the Salar de Atacama Basin (between 21°-27°30'S, Figure 1.1), and can be linked then to the blocks constituting Cordillera de Domeyko, and their uplift (see above). In other words, the trend of the depression does not coincide with that of the NW-SE gravity highs (Götze et al., 1994; Götze and Krause, 2002; Reutter et al., 2006; Yáñez and Rivera, 2019b). In any case, these anomalies have a longer wavelength than that of the profiles measured here, and the structural style observed is independent of the deeper structure of the crust; as such, the hypothetical influence of the anomalies on this thesis can be ruled out, based on a) the consistency between the gravity profiles and surface geology, and b) their match, albeit not perfect, with other independent sets of geophysical data (see Chapters 2 and 3).

The suggested mechanical coupling between the lithosphere underlying the Salar de Atacama Basin and the slab (Yuan et al., 2002; Schurr and Rietbrock, 2004) also raises several issues, the foremost being that of the time and duration of the coupling. Given the geological history of the region and the deflection of the magmatic arc since the early Miocene (Figure 5.5; Allmendinger et al., 1997; de Silva, 1989; Jordan et al., 2007; Kay et al., 1999; Kay and Coira, 2009; Marinovic and Lahsen, 1984; Ramírez and Gardeweg, 1982; Salisbury et al., 2011; SERNAGEOMIN, 2003), the coupled region below the Preandean Depression would then be a current property of the interplate boundary. If the 'coupled' area was formed earlier (Eocene-Oligocene), then a) it would have remained after the successive displacements of the arc, and b) it would have lasted for around 35 My, even given the thermal-tectonic changes in the area. This coupling would not not explain the appearance of other intermontane basins along the Preandean Depression, or the long-lasting existence of the Salar de Atacama Basin as a depositional system and its geological/structural evolution.

It is clear from this summary that the anomalies and related bodies found by previous researchers comprise a wide range of depths, from the upper crust down to the slab interface, which makes it necessary to perform more detailed geophysical and geological studies in the area to understand the nature of the crust-mantle, its thermal-rheological state, its effects on the geology of the upper plate, as well as the geometry of the subducting plate, studies which go beyond the scope of this thesis. Some of these topics have been researched by previous studies, usually in a more regional context, but provide nonetheless a relevant foundation for additional, more localized work (e.g., Beck et al., 2015; Belmonte-Pool, 2002; Contreras-Reyes et al.,

2012; Maksymowicz et al., 2018; McQuarrie et al., 2005b; Metcalf and Kapp, 2015; Schmitz et al., 1999; Tassara, 2005; Tassara et al., 2007; Tassara and Echaurren, 2012).

Chapter 6 : Conclusions and future work.

The geophysical (gravity, seismic velocities, magnetism, well logs) and geological data obtained in this work allow for the characterization and segmentation of the physical properties within the Precordillera-Preandean Depression, and for the association of these properties with known geological units. The profiles surveyed on the northern side of the San Pedro de Atacama Basin show the presence of an east-verging thrust system, where the Permian-Triassic units are thrust over the sedimentary successions of Upper Cretaceous-Paleogene age (Tonel, Purilactis, Barros Arana Formations, possibly including the Naranja-Loma Amarilla Formations), which are deformed into a series of folds which are overlain in angular unconformity by Neogene successions (San Pedro Formation and recent evaporites). The latter display growth strata that whose thickness increase eastwards, and an important amount of deformation within the Cordillera de la Sal area. The most relevant geophysical contrasts when compared to the basement are those of the fine-grained, clastic and evaporitic units of the San Pedro Formation, and, minorly, those of the Upper Cretaceous-Paleogene deposits. The central and southern profiles show a similar configuration, where the Cordillera de Domeyko presents units with higher densities than those within the basin, the former of which are correlated with the widely reported Paleozoic, crystalline and volcanosedimentary units found west of the basin. The El Bordo Escarpment shows the limits between the basement, which is seen thrusting over and deforming the Upper Cretaceous-Paleogene deposits, and the continental, mostly sedimentary successions comprising the Salar de Atacama Basin.

The analysis of ten new U-Pb detrital zircon geochronology samples leads to a refinement and better understanding of the history of the basin during the Cretaceous onwards, along with further questions. The ages obtained for the Tonel Formation lie in the Ladinian-Albian interval, with a maximum depositional age for its oldest member of ca. 112.6±1.6 Ma, close to its proposed mid-Cretaceous age. These samples also evidence the N-S variation in paleotopography and zircon/sediment source for this formation. The samples obtained from the middle of the Purilactis Formation revealed maximum depositional ages of 65.02±0.8 and 66.7±0.7 Ma, corresponding to the ‘K-T’ boundary, thus pushing forward the upper age of the Purilactis and Barros Arana Formations to the Paleogene. Finally, the samples belonging to the Naranja Formation were dated at 68.95±0.65 and 68.4±1.3 Ma, which are close to the ages of the upper Purilactis and Barros Arana Formations. The Naranja Formation is thus assumed to be the southern equivalent of the latter units, although this issue is still open.

The units within the Salar de Atacama Basin record the early uplift of the Coastal Cordillera, around the mid-to-Late Cretaceous, the formation of the related foreland basin, and the addition within the depositional system of units eroded from the Late Cretaceous-Paleogene magmatic arc and the Paleozoic basement of the Cordillera de Domeyko, in successive eastward “steps”, which also show variations in lithofacies and detrital zircon populations. The basin shows the transition from a distal to proximal foredeep (Tonel, Purilactis, Barros Arana and Naranja Formations), the wedge-top (Loma Amarilla Formation), all of them in a context of back-arc sedimentation, and its later, final incorporation into the forearc in a hinterland position. The formation of the basin would have been a direct consequence of the compressive deformation initiated during the ‘Peruvian’ phase of mountain building in the Central Andes, and most of its structural configuration would

have been reached during the 'Incaic' Event occurring during the late Eocene-early Oligocene; the Neogene units usually ascribed to an extensional setting would have been deposited in a post-tectonic, slightly compressive setting, with renewed compression occurring during the late Miocene. This event, together with the establishment of the modern arc, constitute the final stages within the evolution of the basin. The evolution presented here is not exclusive of the Salar de Atacama Basin, with a relatively similar history occurring in other basins within the Preandean Depression, such as the Salar de Punta Negra Basin.

Given its long-lasting existence and almost continuous stratigraphic record since the mid-Cretaceous, the Salar de Atacama Basin presents itself as a natural laboratory in which to test the different theories and models elaborated for the evolution of the South American margin and the building of the orogen. The Late Cretaceous evolution of the basin ('Peruvian' phase) is in agreement with plate reconstructions and the deformation patterns observed along the orogen, and it also concurs with the migration of the magmatic front and the subduction erosion of the forearc. Other 'events' occurring before the late Eocene are not directly observed, or alternatively can be related to the migration of the deformation front close to the study area. The structural styles observed within the basin, the rotation reported for many of its units and the cannibalization of previous deposits, along with the regional exhumation and deformation patterns observed along the margin are consistent with the occurrence of the 'Incaic' Event, but its origin due to a flat slab event, or cyclical processes within the arc-margin are inconsistent with the findings of this work and regional geology. A change to extensional conditions after the late Eocene-early Oligocene also has no support within the geological-geophysical record, which instead show conditions akin to mild compression or post-tectonic quiescence. Finally, the deformation during the late Miocene is also consistent with that observed along the margin around the Central Andes, in a context where uplift, exhumation and deformation have been a long-lasting process. The general agreement with most of the recorded tectonic events along the margin, and the consistency of its geological evolution with areas surrounding it, disprove the notion of the basin as an anomaly, but rather as an integral part and record of the building of the orogen.

Future work must be performed on several key questions, of which only a few are given below:

Which are the basin-wide variations in deposition style within the San Pedro Formation? What information can be extracted from its paleocurrents, and its lateral interfingering with the Tambores Formation? What is the precise timing of its deposition?

Is the Barros Arana Formation an equivalent of the Naranja Formation? Even though it is usually highly folded and deformed: can additional sedimentological data be derived from the latter formation? If so, can it give additional information about the sedimentation within the basin, and its position in a foreland system?

What is the nature of the contact between the Loma Amarilla and Naranja Formations? Are the gravel deposits found in the El Bordo Escarpment part of the Loma Amarilla Formation, or do they belong to younger units? What is the upper age of this formation? Similar questions about its sedimentology as those presented for other formations are also valid.

What are the regional variations in the Late Cretaceous-Paleogene basin topography that can be revealed with a thorough study of the Tonel and Purilactis Formations south and north of the Barros

Arana Syncline? What is the age of the units assigned to the Purilactis Formation south of the syncline?

Does the proposed evolution for the Salar de Atacama Basin match that of the other basins of the Preandean Depression? What is the causal link between the formation of the Precordillera and the depression? In this sense, can a general structural and sedimentary evolution be proposed for the Preandean Depression?

Can additional surface geophysics surveys, such as those utilized in this study, give additional information of the N-S variations of the structure of the Preandean Basins? Would the segmentation observed here be also noticeable in the rest of the basins? What other techniques can give us additional, independent geological constraints?

Can this hypothetical model for the evolution of the Preandean Depression give insights into the formation of the Central Andes that is consistent with the regional context? What are the driving factors that lead to the recorded 'events' and the generation of the orogen?

In other words: What are the main factors involved in mountain building processes?

Chapter 7 : Bibliography

Allmendinger, R.W., Jordan, T.E., Kay, S.M., and Isacks, B.L., 1997, The Evolution of the Altiplano-Puna Plateau of the Central Andes: Annual Review of Earth and Planetary Sciences, v. 25, p. 139–174, doi:10.1146/annurev.earth.25.1.139.

Amilibia, M., Sàbat, F., McClay, K.R., Muñoz, J.A., Roca, E., and Chong, G., 2008, The role of inherited tectono-sedimentary architecture in the development of the central Andean mountain belt: Insights from the Cordillera de Domeyko: Journal of Structural Geology, v. 30, p. 1520–1539, doi:10.1016/j.jsg.2008.08.005.

Andriessen, P.A.M., and Reutter, K.-J., 1994, K-Ar and fission track mineral age determination of igneous rocks related to multiple magmatic arc systems along the 23°S latitude of Chile and NW Argentina., *in* Reutter, K.-J., Scheuber, E., and Wigger, P. eds., Tectonics of the Southern Central Andes: Structure and Evolution of an Active Continental Margin, New York, Springer, p. 141–154.

Araya, J., 2016, Reconstrucción estructural 3D, Sinclinal de Barros Arana, Cuenca del Salar de Atacama (22°30'S-23°S): Universidad de Chile, 58 p.

Arriagada, C., 1999, Geología y Paleomagnetismo del Borde Oriental de la Cordillera de Domeyko entre los 22°45' y 23°30' latitud Sur. II Región, Chile.: Universidad de Chile, 176 p.

Arriagada, C., Cobbold, P.R., and Roperch, P., 2006a, Salar de Atacama basin: A record of compressional tectonics in the central Andes since the mid-Cretaceous: Tectonics, v. 25, p. n/a-n/a, doi:10.1029/2004TC001770.

Arriagada, C., Roperch, P., and Mpodozis, C., 2000, Clockwise block rotations along the eastern border of the Cordillera de Domeyko, Northern Chile (22°45′–23°30′S): Tectonophysics, v. 326, p. 153–171, doi:10.1016/S0040-1951(00)00151-7.

Arriagada, C., Roperch, P., Mpodozis, C., and Cobbold, P.R., 2008, Paleogene building of the Bolivian Orocline: Tectonic restoration of the central Andes in 2-D map view: Tectonics, v. 27, doi:10.1029/2008TC002269.

Arriagada, C., Roperch, P., Mpodozis, C., Dupont-Nivet, G., Cobbold, P.R., Chauvin, A., and Cortés, J., 2003, Paleogene clockwise tectonic rotations in the forearc of central Andes, Antofagasta region, northern Chile: Journal of Geophysical Research: Solid Earth, v. 108, doi:10.1029/2001JB001598.

Arriagada, C., Roperch, P., Mpodozis, C., and Fernandez, R., 2006b, Paleomagnetism and tectonics of the southern Atacama Desert (25-28°S), northern Chile: Tectonics, v. 25, p. n/a-n/a, doi:10.1029/2005TC001923.

Bahamondes, B., 2017, Evolución Sedimentaria, Cretácico Superior a Paleógena, de la cuenca Pre-Andina en los sectores del Salar de Imilac y Sierra de Almeida (24°S-24°30'S): Universidad de Chile, 165 p.

Bahlburg, H., and Hervé, F., 1997, Geodynamic evolution and tectonostratigraphic terranes of northwestern Argentina and northern Chile: Bulletin of the Geological Society of America, v. 109, p. 869–884, doi:10.1130/0016-7606(1997)109<0869:GEATTO>2.3.CO;2.

Bahlburg, H., Vervoort, J.D., Du Frane, S.A., Bock, B., Augustsson, C., and Reimann, C., 2009, Timing of crust formation and recycling in accretionary orogens: Insights learned from the western

margin of South America: Earth-Science Reviews, v. 97, p. 215–241, doi:10.1016/j.earscirev.2009.10.006.

Barnes, J.B., and Ehlers, T.A., 2009, End member models for Andean Plateau uplift: Earth-Science Reviews, v. 97, p. 105–132, doi:10.1016/j.earscirev.2009.08.003.

Barnes, J.B., Ehlers, T.A., McQuarrie, N., O'Sullivan, P.B., and Tawackoli, S., 2008, Thermochronometer record of central Andean Plateau growth, Bolivia (19.5°S): Tectonics, v. 27, p. 1–25, doi:10.1029/2007TC002174.

Bascuñán, S., 2014, Stratigraphy, sedimentology and geochronology of the Tonel, Purilactis and Barros Arana Formationsin the Salar de Atacama Basin (22°30'-23°S), Chile: Universidad de Chile, 138 p.

Bascuñán, S., Arriagada, C., Le Roux, J., and Deckart, K., 2016, Unraveling the Peruvian Phase of the Central Andes: Stratigraphy, sedimentology and geochronology of the Salar de Atacama Basin (22°30-23°S), northern Chile: Basin Research, v. 28, p. 365–392, doi:10.1111/bre.12114.

Bascuñán, S., Maksymowicz, A., Martínez, F., Becerra, J., Arriagada, C., and Deckart, K., 2019, Geometry and late Mesozoic-Cenozoic evolution of the Salar de Atacama Basin (22 ° 30 ′ -24 ° 30 ′ S) in the northern Central Andes : New constraints from geophysical , geochronological and fi eld data: Tectonophysics, v. 759, p. 58–78, doi:10.1016/j.tecto.2019.04.008.

Basso, M., 2004, Carta Baquedano, región de Antofagasta. Carta Geológica de Chile, Serie Geología Básica 82. 26 p. 1 mapa escala 1:100.000.:

Basso, M., and Mpodozis, C., 2012, Carta Cerro Quimal, Región de Antofagasta. Servicio Nacional de Geología y Minería, Carta Geológica de Chile, Serie Geología Básica 143: 46 p. 1 mapa escala 1:100.000.:

Becerra, J., Arriagada, C., Contreras-Reyes, E., Bascuñan, S., De Pascale, G.P., Reichert, C., Díaz-Naveas, J., and Cornejo, N., 2017, Gravitational deformation and inherited structural control on slope morphology in the subduction zone of north-central Chile (ca . 29-33°S): Basin Research, v. 29, p. 798–815, doi:10.1111/bre.12205.

Becerra, J., Henríquez, S., and Arriagada, C., 2014, Geología del Área de Salar de Atacama, Región de Antofagasta. Carta Geológica de Chile, Serie Geología Básica 166. 1 mapa escala 1:100.000.:

Beck, S.L., and Zandt, G., 2002, The nature of orogenic crust in the central Andes: Journal of Geophysical Research: Solid Earth, v. 107, p. ESE 7-1-ESE 7-16, doi:10.1029/2000JB000124.

Beck, S.L., Zandt, G., Ward, K.M., and Scire, A., 2015, Multiple styles and scales of lithospheric foundering beneath the Puna Plateau, central Andes, *in* Geodynamics of a Cordilleran Orogenic System: The Central Andes of Argentina and Northern Chile, Geological Society of America, doi:10.1130/2015.1212(03).

Bello-González, J.P., Contreras-Reyes, E., and Arriagada, C., 2018, Predicted path for hotspot tracks off South America since Paleocene times: Tectonic implications of ridge-trench collision along the Andean margin: Gondwana Research, v. 64, p. 216–234, doi:10.1016/j.gr.2018.07.008.

Belmonte-Pool, A., 2002, Krustale Seismizität, Struktur und Rheologie der Oberplatte zwischen der Präkordillere und dem magmatischen Bogen in Nordchile (22°S-24°S): Freie Universität Berlin.

Blanco, N., 2008, Estratigrafía y Evolución Tectono-sedimentaria de la cuenca Cenozoica de Calama (Chile, 22°S): Universidad de Barcelona, 68 p.

Blanco, N., Mpodozis, C., Gardeweg, M., and Jordan, T.E., 2000, Sedimentación del

Mioceno Superior-Plioceno en la Cuenca del Salar de Atacama: Estratrigrafía de la Formación Vilama, II Región de Antofagasta, *in* IX Congreso Geológico Chileno, Actas 1, Puerto Varas, Chile, p. 446–450.

Blanco, N., and Tomlinson, A.J., 2009, Carta Chiu Chiu, Región de Antofagasta. Nacional de Geología y Minería, Carta Geológica de Chile, Serie Geología Básica 117. 54 p. 1 mapa escala 1:50000.:

Blanco, N., Tomlinson, A.J., Mpodozis, C., Pérez de Arce, C., and Matthews, S., 2003, Formación Calama, Eoceno, II región de Antohagasta (Chile): Estratigrafía e implicancias tectónicas: 10 Congreso Geológico Chileno,.

Boyce, D., 2015, Modelo de evolución tectónica y paleogeográfica del margen andino en Chile Central durante el Cretácico medio a tardío: el registro estructural y sedimentario en la Formación Las Chilcas: Memoria de Titulo (Inédito), Universidad de Chile, Departamento de Geología, p. 296 p. Santiago.

Boyce, D., Charrier, R., and Farías, M., 2020, The first Andean compressive tectonic phase. Sedimentologic and structural analysis of mid-Cretaceous deposits in the Coastal Cordillera, Central Chile (32°50'S): Tectonics, p. 2019TC005825, doi:10.1029/2019TC005825.

Brüggen, J., 1950, Fundamentos de la Geología de Chile: Santiago, Chile, Instituto Geográfico Militar, 374 p.

Brüggen, J., 1942, Geología de la Puna de San Pedro de Atacama y sus formaciones areniscas y arcillas rojas., *in* Congreso Panamericano de Ingeniería de Minas y Geológica, Actas 2, p. 342–467.

Brüggen, J., 1934, Las Formaciones de Sal y Petróleo de la Puna de Atacama: Boletín de Minas y Petróleo, v. 32, p. 105–122.

Carrapa, B., Bywater-Reyes, S.B., Decelles, P.G., Mortimer, E.C., and Gehrels, G.E., 2012, Late Eocene-Pliocene basin evolution in the Eastern Cordillera of northwestern Argentina (25°-26°S): Regional implications for Andean orogenic wedge development: Basin Research, v. 24, p. 249–268, doi:10.1111/j.1365-2117.2011.00519.x.

Carrapa, B., and DeCelles, P.G., 2015, Regional exhumation and kinematic history of the central Andes in response to cyclical orogenic processes, *in* DeCelles, P.G., Ducea, M.N., Carrapa, B., and Kapp, P.A. eds., Geodynamics of a Cordilleran Orogenic System: The Central Andes of Argentina and Northern Chile: Geological Society of America Memoir 212, The Geological Society of America, p. 201–213, doi:10.1130/2015.1212(11).

Carrapa, B., Hauer, J., Schoenbohm, L., Strecker, M.R., Schmitt, A.K., Villanueva, A., and Gómez, J.S., 2010, Dynamics of deformation and sedimentation in the northern Sierras Pampeanas : An integrated study of the Neogene Fiambalá basin , NW Argentina : Reply: Geological Society of America Bulletin, v. 122, p. 950–953, doi:10.1130/B30134.1.

Casquet, C., Hervé, F., Pankhurst, R.J., Baldo, E., Calderón, M., Fanning, C.M., Rapela, C.W., and Dahlquist, J., 2014, The Mejillonia suspect terrane (Northern Chile): Late Triassic fast burial and metamorphism of sediments in a magmatic arc environment extending into the Early Jurassic: Gondwana Research, v. 25, p. 1272–1286, doi:10.1016/j.gr.2013.05.016.

Cawood, P.A., Kröner, A., Collins, W.J., Kusky, T.M., Mooney, W.D., and Windley, B.F., 2009, Accretionary orogens through Earth history: Geological Society, London, Special Publications, v. 318, p. 1–36, doi:10.1144/SP318.1.

Charrier, R., Baeza, O., Elgueta, S., Flynn,

J.J., Gans, P., Kay, S.M., Muñoz, N., Wyss, A.R., and Zurita, E., 2002, Evidence for Cenozoic extensional basin development and tectonic inversion south of the flat-slab segment, southern Central Andes, Chile (33°-36°S.L.): Journal of South American Earth Sciences, v. 15, p. 117–139, doi:10.1016/S0895-9811(02)00009-3.

Charrier, R., Farías, M., and Maksaev, V., 2009, Evolución Tectónica, Paleogeográfica y Metalogénica durante el Cenozoico en los Andes de Chile norte y central e implicaciones para las regiones adyacentes de Bolivia y Argentina: Revista de la Asociación Geológica Argentina, v. 65, p. 5–35.

Charrier, R., Hérail, G., Pinto, L., García, M., Riquelme, R., Farías, M., and Muñoz, N., 2013, Cenozoic tectonic evolution in the Central Andes in northern Chile and west central Bolivia: Implications for paleogeographic, magmatic and mountain building evolution: International Journal of Earth Sciences, v. 102, p. 235–264, doi:10.1007/s00531-012-0801-4.

Charrier, R., and Muñoz, N., 1994, Jurassic-Cretaceous Paleogeographic evolution of the Chilean Andes at 23°-24°S.L. and 34°-35°S.L.: a comparative analysis., *in* Reutter, K., Scheuber, E., and Wigger, P. eds., Tectonics of the Southern Central Andes: Structure and Evolution of an Active Continental Margin, New York, Springer, p. 233–242.

Charrier, R., Pinto, L., and Rodriguez, M.P., 2007, Tectonostratigraphic evolution of the Andean Orogen in Chile, *in* Geology of Chile, v. 1, p. 21–114, doi:10.1144/GOCH.3.

Charrier, R., and Reutter, K., 1990, The Purilactis Group of Northern Chile : Link between arc and backarc during Late Cretaceous and Paleogene., *in* Proceedings I ORSTOM-ISAG, Grenoble, p. 249–252.

Charrier, R., and Reutter, K., 1994, The Purilactis group of northern Chile: Boundary between arc and backarc from Late Cretaceous to Eocene., *in* Reutter, K., Scheuber, E., and Wigger, P. eds., Tectonics of the Southern Central Andes: Structure and Evolution of an Active Continental Margin, New York, Springer, p. 189–202.

Clift, P.D., and Hartley, A.J., 2007, Slow rates of subduction erosion and coastal underplating along the Andean margin of Chile and Peru: Geology, v. 35, p. 503–506, doi:10.1130/G23584A.1.

Clift, P., and Vannucchi, P., 2004, Controls on tectonic accretion versus erosion in subduction zones: Implications for the origin and recycling of the continental crust: Reviews of Geophysics, v. 42, doi:10.1029/2003RG000127.

Cobbold, P.R., and Rossello, E., 2003, Aptian to recent compressional deformation, foothills of the Neuquén Basin, Argentina: Marine and Petroleum Geology, v. 20, p. 429–443, doi:10.1016/S0264-8172(03)00077-1.

Cobbold, P.R., Rossello, E.A., Roperch, P., Arriagada, C., Gómez, L.A., and Lima, C., 2007, Distribution, timing, and causes of Andean deformation across South America: London Geological Society, v. 272, p. 321–343, doi:10.1144/GSL.SP.2007.272.01.17.

Cohen, K.., Harper, D.A.T., and Gibbard, P.L., 2013, The ICS International Chronostratigraphic Chart.:, http://www.stratigraphy.org/ICSchart/ChronostratChart2017-02.pdf.

Coira, B., and Zappettini, E., 2008, Mapa geológico de la provincia de Jujuy:, http://www.mineriajujuy.gob.ar/files_site/relatorio_geologia_2008/mapa_geologico_de_jujuy.pdf.

Comte, D., Carrizo, D., Roecker, S., Ortega-Culaciati, F., and Peyrat, S., 2016, Three-dimensional elastic wave speeds in the northern Chile subduction zone: Variations in hydration in the supraslab mantle: Geophysical Journal

International, v. 207, p. 1080–1105, doi:10.1093/gji/ggw318.

Contreras-Reyes, E., Jara, J., Grevemeyer, I., Ruiz, S., and Carrizo, D., 2012, Abrupt change in the dip of the subducting plate beneath north Chile: Nature Geoscience, v. 5, p. 342–345, doi:10.1038/ngeo1447.

Cornejo, P., and Matthews, S., 2001, Evolution of magmatism from the uppermost Cretaceous to Oligocene and its relationship to changing tectonic regime, *in* 3rd South American Symposium on Isotope Geology, p. 558–561.

Cornejo, P., Matthews, S., and Perez de Arce, C., 2003, The 'K-T' compressive deformation event in northern Chile (24-27ºS): X Congreso Geologico Chileno, v. CD-Rom, p. 1–13.

Cornejo, P., Mpodozis, C., Rivera, O., and Matthews, S.J., 2009, Carta Exploradora, Regiones de Antofagasta y Atacama. Carta Geológica de Chile, Serie Geología Básica 119. 99 p. 1 mapa escala 1:100.000.:

Cornejo, P.C., Tosdal, R.M., Mpodozis, C., Tomlinson, A.J., Rivera, O., and Fanning, C.M., 1997, El Salvador, Chile porphyry copper deposit revisited: geologic and geochronologic framework: International Geology Review, v. 39, p. 22–54.

Cortés, J., 2000, Hoja Palestina, Región de Antofagasta. Servicio Nacional de Geología y Minería, Mapas Geológicos 19. 1 mapa escala 1:100.000.:

Creixell, C., Sepúlveda, F., Álvarez, J., Vásquez, P., and Velásquez, R., 2021, The carboniferous onset of subduction at SW Gondwana revisited: Sedimentation and deformation processes along the late Paleozoic forearc of north Chile (21°–33° S): Journal of South American Earth Sciences, v. 107, doi:10.1016/j.jsames.2020.103149.

Damm, K.-W., Pichowiak, S., Harmon, R.S., Todt, W., Kelley, S., Omarini, R., and Niemeyer, H., 1990, Pre-Mesozoic evolution of the central Andes; The basement revisited: , p. 101–126, doi:10.1130/SPE241-p101.

Decelles, P.G., Carrapa, B., Horton, B.K., and Gehrels, G.E., 2011, Cenozoic foreland basin system in the central Andes of northwestern Argentina: Implications for Andean geodynamics and modes of deformation: Tectonics, v. 30, p. 1–30, doi:10.1029/2011TC002948.

DeCelles, P.G., Carrapa, B., Horton, B.K., McNabb, J., Gehrels, G.E., and Boyd, J., 2015a, The Miocene Arizaro Basin, central Andean hinterland: Response to partial lithosphere removal? Geological Society of America Memoirs , v. 212, p. 359–386, doi:10.1130/2015.1212(18).

DeCelles, P.G., and Giles, K.A., 1996, Foreland basin systems - Reply: Basin Research, v. 9, p. 172–176.

DeCelles, P.G., Zandt, G., Beck, S.L., Currie, C.A., Ducea, M.N., Kapp, P., Gehrels, G.E., Carrapa, B., Quade, J., and Schoenbohm, L.M., 2015b, Cyclical orogenic processes in the Cenozoic central Andes, *in* Decelles, P.G., Ducea, M.N., Carrapa, B., and Kapp, P.A. eds., Geodynamics of a Cordilleran Orogenic System: The Central Andes of Argentina and Northern Chile: Geological Society of America Memoir 212., The Geological Society of America, p. 459–490, doi:10.1130/2015.1212(22).

Díaz, D., Brasse, H., and Ticona, F., 2012, Conductivity distribution beneath Lascar volcano (Northern Chile) and the Puna, inferred from magnetotelluric data: Journal of Volcanology and Geothermal Research, v. 217–218, p. 21–29, doi:10.1016/j.jvolgeores.2011.12.007.

Dingman, R.J., 1963, Cuadrángulo Tulor. Instituto de Investigaciones Geológicas, Carta geológica de Chile 11:1-35. 1 mapa escala 1:50.000:

Dingman, R.J., 1967, Geology and Groundwater Resources of the Northern part of the Salar de Atacama, Antofagasta Province, Chile.: U.S. Geological Survey Bulletin, v. 1249, p. 1–49.

Elger, K., Oncken, O., and Glodny, J., 2005, Plateau-style accumulation of deformation: Southern Altiplano: Tectonics, v. 24, p. 1–19, doi:10.1029/2004TC001675.

Espinoza, M. et al., 2019, The synrift phase of the early Domeyko Basin (Triassic, northern Chile): Sedimentary, volcanic, and tectonic interplay in the evolution of an ancient subduction-related rift basin: Basin Research, v. 31, p. 4–32, doi:10.1111/bre.12305.

Farías, M., Charrier, R., Carretier, S., Martinod, J., Fock, A., Campbell, D., Cáceres, J., and Comte, D., 2008, Late Miocene high and rapid surface uplift and its erosional response in the Andes of central Chile (33° - 35°S): Tectonics, v. 27, doi:10.1029/2006TC002046.

Farías, M., Charrier, R., Comte, D., Martinod, J., and Hérail, G., 2005, Late Cenozoic deformation and uplift of the western flank of the Altiplano: Evidence from the depositional, tectonic, and geomorphologic evolution and shallow seismic activity (northern Chile at 19°30′S): Tectonics, v. 24, p. 1–27, doi:10.1029/2004TC001667.

Farías, M., Comte, D., Charrier, R., Martinod, J., David, C., Tassara, A., Tapia, F., and Fock, A., 2010, Crustal-scale structural architecture in central Chile based on seismicity and surface geology: Implications for Andean mountain building: Tectonics, v. 29, doi:10.1029/2009TC002480.

Fennell, L.M., Folguera, A., Naipauer, M., Gianni, G., Rojas Vera, E.A., Bottesi, G., and Ramos, V.A., 2017, Cretaceous deformation of the southern Central Andes: synorogenic growth strata in the Neuquén Group (35° 30′-37° S): Basin Research, v. 29, p. 51–72, doi:10.1111/bre.12135.

Flint, S., 1985, Alluvial fan and playa sedimentation in an Andean arid, closed basin: the Paciencia Group (mid Tertiary), Antofagasta Province, Chile.: Journal of the Geological Society of London, v. 141, p. 533–546.

Flint, S., Hartley, A.J., Rex, D.C., Guise, P., and Turner, P., 1989, Geochronologv of the purilactis formation, northern chile: an insight into late cretaceous/earlv tertiarv basin dvnamics of the central andes: Revista Geológica de Chile, v. 16, p. 241–246.

Flint, S., Turner, P., Jolley, E.J., and Hartley, A.J., 1993, Extensional Tectonics in Convergent Margin Basins - an Example From the Salar-De-Atacama, Chilean Andes: Geological Society of America Bulletin, v. 105, p. 603–617, doi:10.1130/0016-7606(1993)105<0603.

Fock, A., Charrier, R., Farías, M., Maksaev, V., Fanning, C.M., and Álvarez, P., 2005, Exhumation and uplift of the western main cordillera between 33 ° and 34 ° S, *in* 6th International Symposium on Andean Geodynamics (ISAG 2005, Barcelona), Extended Abstracts, Barcelona, p. 273–276.

Folguera, A., Rojas Vera, E., Bottesi, G., Zamora Valcarce, G., and Ramos, V.A., 2010, The Loncopué Trough: A Cenozoic basin produced by extension in the southern Central Andes: Journal of Geodynamics, v. 49, p. 287–295, doi:10.1016/j.jog.2010.01.009.

Fuentes, G., Martínez, F., Bascuñan, S., Arriagada, C., and Muñoz, R., 2018, Tectonic architecture of the Tarapacá Basin in the northern Central Andes: New constraints from field and 2D seismic data: Geosphere, v. 14, p. 2430–2446, doi:10.1130/GES01697.1.

Gardeweg, M., Pino, H., Ramírez, C.F., and Davidson, J., 1994, Mapa Geológico del área de Imilac y Sierra Almeida, Región

de Antofagasta. Servicio Nacional de Geología y Minería. Documento de Trabajo 7. 1 mapa escala 1:100.000.:

Garzione, C.N., Hoke, G.D., Libarkin, J.C., Withers, S., MacFadden, B., Eiler, J., Ghosh, P., and Mulch, A., 2008, Rise of the Andes: Science, v. 320, p. 1304–1307, doi:10.1126/science.1148615.

Giambiagi, L.B., Tunik, M.A., and Ghiglione, M., 2001, Cenozoic tectonic evolution of the Alto Tunuyán foreland basin above the transition zone between the flat and normal subduction segment (33°30′-34°S), western Argentina: Journal of South American Earth Sciences, v. 14, p. 707–724, doi:10.1016/S0895-9811(01)00059-1.

Gianni, G.M., Navarrete, C.G., and Folguera, A., 2015, Synorogenic foreland rifts and transtensional basins: A review of Andean imprints on the evolution of the San Jorge Gulf, Salta Group and Taubaté Basins: Journal of South American Earth Sciences, v. 64, p. 288–306, doi:10.1016/j.jsames.2015.08.004.

González, G., Cembrano, J., Aron, F., Veloso, E.E., and Shyu, J.B.H., 2009, Coeval compressional deformation and volcanism in the central Andes, case studies from northern Chile (23°S-24°S): Tectonics, v. 28, p. 1–18, doi:10.1029/2009TC002538.

Goss, A.R., Kay, S.M., and Mpodozis, C., 2013, Andean Adakite-like high-Mg Andesites on the Northern Margin of the Chilean-Pampean Flat-slab (27-28.58°S) Associated with Frontal Arc Migration and Fore-arc Subduction Erosion: Journal of Petrology, v. 54, p. 2193–2234, doi:10.1093/petrology/egt044.

Götze, H.-J., and Krause, S., 2002, The Central Andean gravity high, a relic of an old subduction complex? Journal of South American Earth Sciences, v. 14, p. 799–811, doi:10.1016/S0895-9811(01)00077-3.

Götze, H.-J., Lahmeyer, B., Schmidt, S., and Strunk, S., 1994, The Lithospheric Structure of the Central Andes (20°-26°S) as Inferred from Interpretation of Regional Gravity, *in* Reutter, K., Scheuber, E., and Wigger, P. eds., Tectonics of the Southern Central Andes: Structure and Evolution of an Active Continental Margin, New York, Springer, p. 7–21.

Guest, J.E., 1969, Geological Society of America Bulletin Upper Tertiary Ignimbrites in the Andean Cordillera of Part of the Antofagasta Province , Northern Chile:, doi:10.1130/0016-7606(1969)80.

Gutscher, M.A., 2002, Andean subduction styles and their effect on thermal structure and interplate coupling: Journal of South American Earth Sciences, v. 15, p. 3–10, doi:10.1016/S0895-9811(02)00002-0.

Hammerschmidt, K., Döbel, R., and Friedrichsen, H., 1992, Implications of 40Ar/39Ar dating of Tertiary volcanic rocks from the north-Chilean Precordillera: Tectonophysics, v. 202, p. 55–81.

Hartley, A.J., Flint, S., and Turner, P., 1988, A proposed lithostratigraphy for the Cretaceous Purilactis Formation, Antofagasta Province, northern Chile, *in* Congreso Geológico Chileno, No. 5, Actas 3, Santiago, Chile, p. H83–H99.

Hartley, A.J., Flint, S., Turner, P., and Jolley, E.J., 1992, Tectonic controls on the development of a semi-arid alluvial basin as reflected in the stratigraphy of the Purilactis Group (upper cretaceous-eocene), northern Chile: Journal of South American Earth Sciences, v. 5, p. 275–296, doi:10.1016/0895-9811(92)90026-U.

Haschke, M., Günther, A., Melnick, D., Echtler, H., Reutter, K.-J., Scheuber, E., and Oncken, O., 2006, Central and Southern Andean Tectonic Evolution Inferred from Arc Magmatism, *in* The Andes, p. 337–353, doi:10.1007/978-3-

540-48684-8_16.

Henríquez, S., 2012, Estructura del Salar de Atacama: Implicancias en la estructura cortical de los Andes Centrales: Universidad de Chile, 97 p.

Henríquez, S., Becerra, J., and Arriagada, C., 2014, Geología del área San Pedro de Atacama, Región de Antofagasta. Servicio Nacional de Geología y Minería. Carta Geológica de Chile Serie Geología Básica 171. 1 Mapa escala 1:100,000.:

Henríquez, S., DeCelles, P.G., and Carrapa, B., 2019, Cretaceous to Middle Cenozoic Exhumation History of the Cordillera de Domeyko and Salar de Atacama Basin, Northern Chile: Tectonics, doi:10.1029/2018TC005203.

Hoke, G.D., and Garzione, C.N., 2008, Paleosurfaces, paleoelevation, and the mechanisms for the late Miocene topographic development of the Altiplano plateau: Earth and Planetary Science Letters, v. 271, p. 192–201, doi:10.1016/j.epsl.2008.04.008.

Hoke, L., and Lamb, S., 2007, Cenozoic behind-arc volcanism in the Bolivian Andes, South America: Implications for mantle melt generation and lithospheric structure: Journal of the Geological Society, v. 164, p. 795–814, doi:10.1144/0016-76492006-092.

Hongn, F., del Papa, C., Powell, J., Petrinovic, I., Mon, R., and Deraco, V., 2007, Middle Eocene deformation and sedimentation in the Puna-Eastern Cordillera transition (23°-26°S): Control by preexisting heterogeneities on the pattern of initial Andean shortening: Geology, v. 35, p. 271–274, doi:10.1130/G23189A.1.

Horton, B.K., 1998, Sediment accumulation on top of the Andean orogenic wedge: Oligocene to late Miocene basins of the Eastern Cordillera, southern Bolivia: Bulletin of the Geological Society of America, v. 110, p. 1174–1192, doi:10.1130/0016-7606(1998)110<1174:SAOTOT>2.3.CO;2.

Horton, B.K., 2018, Tectonic Regimes of the Central and Southern Andes : Responses to Variations in Plate Coupling During Subduction: Tectonics, v. 37, p. 1–28, doi:10.1002/2017TC004624.

Howell, J.A., Schwarz, E., Spalletti, L.A., and Veiga, G.D., 2005, The Neuquén Basin: an overview: Geological Society, London, Special Publications, v. 252, p. 1–14, doi:10.1144/GSL.SP.2005.252.01.01.

von Huene, R., and Ranero, C.R., 2003, Subduction erosion and basal friction along the sediment-starved convergent margin off Antofagasta, Chile: Journal of Geophysical Research: Solid Earth, v. 108, doi:10.1029/2001jb001569.

Isacks, B.L., 1988, Uplift of the Central Andean Plateau and bending of the Bolivian Orocline: Journal of Geophysical Research, v. 93, p. 3211, doi:10.1029/JB093iB04p03211.

Jaillard, E., 1993, L'évolution tectonique de la marge péruvienne au Sénonien et Paléocene et ses relations avec la géodynamique: Bulletin de la Société Géologique de France, v. 164, p. 819–830.

Jaillard, E., 1992, La Fase Peruana (Cretáceo Superior) en la Margen Peruana.: Boletín de la Sociedad Geológica del Perú, v. 83, p. 81–87, http://isterre.fr/docrestreint.api/2217/dbe0cdccb5952c4c5fcb6d7fe5e561c34ce3f987/pdf/_92_Jaillard_BSGPeru_.pdf.

Jaimes, E., and de Freitas, M., 2006, An Albian-Cenomanian unconformity in the northern Andes: Evidence and tectonic significance: Journal of South American Earth Sciences, v. 21, p. 466–492, doi:10.1016/j.jsames.2006.07.011.

James, D.E., and Sacks, I.S., 1999, Cenozoic Formation of the Central Andes: A Geophysical Perspective, *in* Skinner, B.J. ed., Geology and Ore Deposits of

the Central Andes, Special Publ. No. 7, Society of Economic Geologists, p. 1–25.

Jordan, T.E., Burns, W.M., Veiga, R., Pangaro, F., Copeland, P., and Mpodozis, C., 2001, Extension and basin formation in the southern Andes caused by increased convergence rate.: Tectonics, v. 20, p. 308–424, doi:10.1029/1999TC001181.

Jordan, T.E., Isacks, B.L., Ramos, V.A., and Allmendinger, R.W., 1982, Mountain building in the Central Andes: Episodes, v. 3, p. 20–26.

Jordan, T.E., Mpodozis, C., Muñoz, N., Blanco, N., Pananont, P., and Gardeweg, M., 2007, Cenozoic subsurface stratigraphy and structure of the Salar de Atacama Basin, northern Chile: Journal of South American Earth Sciences, v. 23, p. 122–146, doi:10.1016/j.jsames.2006.09.024.

Jordan, T.E., Muñoz, N., Hein, M., Lowenstein, T., Godfrey, L., and Yu, J., 2002, Active faulting and folding without topographic expression in an evaporite basin , Chile:, doi:10.1130/0016-7606(2002)114<1406.

Jordan, T.E., Nester, P.L., Blanco, N., Hoke, G.D., Dávila, F., and Tomlinson, A.J., 2010, Uplift of the Altiplano-Puna plateau: A view from the west: Tectonics, v. 29, doi:10.1029/2010TC002661.

Juez-Larré, J., Kukowski, N., Dunai, T.J., Hartley, A.J., and Andriessen, P.A.M., 2010, Thermal and exhumation history of the Coastal Cordillera arc of northern Chile revealed by thermochronological dating: Tectonophysics, v. 495, p. 48–66, doi:10.1016/j.tecto.2010.06.018.

Kay, S.M., and Coira, B.L., 2009, lithospheric loss , magmatism , and crustal fl ow under the central Andean Altiplano-Puna Plateau: Geological Society of America Memoir, v. 204, p. 1–32, doi:10.1130/2009.1204(11).

Kay, S.M., Godoy, E., and Kurtz, A., 2005, Episodic arc migration, crustal thickening, subduction erosion, and magmatism in the south-central Andes: Bulletin of the Geological Society of America, v. 117, p. 67–88, doi:10.1130/B25431.1.

Kay, S.M., Mpodozis, C., and Coira, B., 1999, Neogene magmatism, tectonism, and mineral deposits of the Central Andes (22 degrees S to 33 degrees S latitude): Geology and Ore Deposits of the Central Andes, p. 27–59.

Kley, J., 1999, Geologic and geometric constraints on a kinematic model of the Bolivian orocline: Journal of South American Earth Sciences, v. 12, p. 221–235, doi:10.1016/S0895-9811(99)00015-2.

Kley, J., and Monaldi, C.R., 1998, Tectonic shortening and crustal thickness in the Central Andes: How good is the correlation? Geology, v. 26, p. 723–726.

Kuhn, D., 2002, Fold and thrust belt structures and strike-slip faulting at the SE margin of the Salar de Atacama basin , Chilean Andes illera n Cord ster We: v. 21, p. 1–17.

Kukowski, N., and Oncken, O., 2006, Subduction Erosion — the “Normal” Mode of Fore-Arc Material Transfer along the Chilean Margin?, *in* The Andes, p. 217–236, doi:10.1007/978-3-540-48684-8_10.

Ludwig, K.R., 2008, Isoplot 3.6. Berkeley Geochronology Center Special Publication 4.: , p. 77.

Macellari, C.E., Su, M.J., and Townsend, F., 1991, Structure and seismic stratigraphy of the Atacama Basin (northern Chile), *in* Congreso Geológico Chileno, No. 6, Actas 1, p. 133–137.

Maksaev, V., 1978, Cuadrángulo Chitigua y sector occidental del cuadrángulo Cerro Palpana, Región de Antofagasta: 55 p.

Maksaev, V., and Zentilli, M., 1999, Fission track thermochronology of the

Domeyko Cordillera, northern Chile: Implications for Andean tectonics and porphyry copper metallogenesis.: Exploration and Mining Geology, v. 8, p. 65–89.

Maksymowicz, A., Ruiz, J., Vera, E., Contreras-Reyes, E., Ruiz, S., Arriagada, C., Bonvalot, S., and Bascuñán, S., 2018, Heterogeneous structure of the Northern Chile marine forearc and its implications for megathrust earthquakes: Geophysical Journal International, v. 215, p. 1080–1097, doi:10.1093/GJI/GGY325.

Maloney, K.T., Clarke, G.L., Klepeis, K.A., and Quevedo, L., 2013, The Late Jurassic to present evolution of the Andean margin: Drivers and the geological record: Tectonics, v. 32, p. 1049–1065, doi:10.1002/tect.20067.

Mamani, M., Wörner, G., and Sempere, T., 2010, Geochemical variations in igneous rocks of the Central Andean orocline (13°S to 18°S): Tracing crustal thickening and magma generation through time and space: Bulletin of the Geological Society of America, v. 122, p. 162–182, doi:10.1130/B26538.1.

Marinovic, N., 2007, Carta Oficina Domeyko, región de Antofagasta. Carta Geológica de Chile, Serie Geologia Básica 105. 41 p. 1 mapa escala 1:100.000.:

Marinovic, N., and García, M., 1999, Hoja Pampa Unión. Región de Antofagasta. Servicio Nacional de Geología y Minería, Mapas Geológicos 9. 1 mapa escala 1:100.000.:

Marinovic, N., and Lahsen, A., 1984, Hoja Calama. Servicio Nacional de Geología y Mineria, Carta Geológica de Chile 58. 1 mapa escala 1:250.000.:

Martínez, F., Arriagada, C., Mpodozis, C., and Peña, M., 2012, The Lautaro Basin: A record of inversion tectonics in northern Chile: Andean Geology, v. 39, doi:10.5027/andgeoV39n2-a04.

Martínez, F., Arriagada, C., Peña, M., Del Real, I., and Deckart, K., 2013, The structure of the Chañarcillo Basin: An example of tectonic inversion in the Atacama region, northern Chile: Journal of South American Earth Sciences, v. 42, p. 1–16, doi:10.1016/j.jsames.2012.07.001.

Martínez, F., Arriagada, C., Valdivia, R., Deckart, K., and Peña, M., 2015, Geometry and kinematics of the Andean thick-skinned thrust systems: Insights from the Chilean Frontal Cordillera (28°–28.5°S), Central Andes: Journal of South American Earth Sciences, v. 64, p. 307–324, doi:10.1016/j.jsames.2015.05.001.

Martínez, F., González, R., Bascuñán, S., and Arriagada, C., 2017a, Structural styles of the Salar de Punta Negra Basin in the Preandean Depression (24°-25°S) of the Central Andes: Journal of South American Earth Sciences, p. 1–12, doi:10.1016/j.jsames.2017.08.004.

Martínez, F., López, C., Bascuñán, S., and Arriagada, C., 2018, Tectonic interaction between Mesozoic to Cenozoic extensional and contractional structures in the Preandean Depression (23°–25°S): Geologic implications for the Central Andes: Tectonophysics, v. 744, p. 333–349, doi:10.1016/j.tecto.2018.07.016.

Martínez, F., Parra, M., Arriagada, C., Mora, A., Bascuñan, S., and Peña, M., 2017b, Late Cretaceous to Cenozoic deformation and exhumation of the Chilean Frontal Cordillera (28°–29°S), Central Andes: Journal of Geodynamics, v. 111, p. 31–42, doi:10.1016/j.jog.2017.08.004.

Martinod, J., Husson, L., Roperch, P., Guillaume, B., and Espurt, N., 2010, Horizontal subduction zones, convergence velocity and the building of the Andes: Earth and Planetary Science Letters, v. 299, p. 299–309, doi:10.1016/j.epsl.2010.09.010.

McQuarrie, N., 2002a, Initial plate geometry, shortening variations, and evolution of the Bolivian orocline: Geology, v. 30, p. 867–870, doi:10.1130/0091-7613(2002)030<0867:IPGSVA>2.0.CO;2.

McQuarrie, N., 2002b, The kinematic history of the central Andean fold-thrust belt, Bolivia: Implications for building a high plateau: Bulletin of the Geological Society of America, v. 114, p. 950–963, doi:10.1130/0016-7606(2002)114<0950:TKHOTC>2.0.CO;2.

McQuarrie, N., Barnes, J.B., and Ehlers, T.A., 2008, Geometric, kinematic, and erosional history of the central Andean Plateau, Bolivia (15-17°S): Tectonics, v. 27, p. 1–24, doi:10.1029/2006TC002054.

McQuarrie, N., Horton, B.K., Zandt, G., Beck, S., and DeCelles, P.G., 2005a, Lithospheric evolution of the Andean fold-thrust belt, Bolivia, and the origin of the central Andean plateau: Tectonophysics, v. 399, p. 15–37, doi:10.1016/j.tecto.2004.12.013.

McQuarrie, N., Horton, B.K., Zandt, G., Beck, S., and DeCelles, P.G., 2005b, Lithospheric evolution of the Andean fold–thrust belt, Bolivia, and the origin of the central Andean plateau: Tectonophysics, v. 399, p. 15–37, doi:10.1016/j.tecto.2004.12.013.

Megard, F., 1984, The Andean orogenic period and its major structures in central and northern Peru: Journal of the Geological Society, v. 141, p. 893–900, doi:10.1144/gsjgs.141.5.0893.

Merino, R., Salazar, E., Mora-Franco, C., Creixell, C., Coloma, F., and Oliveros, V., 2013, Fluvial deposition and retro-arc volcanism in a Late Cretaceous foreland basin and the unroofing of the Early Cretaceous arc in the chilean Frontal Cordillera at 28°30'S, Atacama Region: Bolletino di Geofisica: teorica ed applicata, v. 54, p. 237–238.

Metcalf, K., and Kapp, P., 2015, modern lithospheric structure of the central Andean forearc: Geodynamics of a Cordilleran Orogenic System: The Central Andes of Argentina and Northern Chile, v. 1212, p. 61–78, doi:10.1130/2015.1212(04).

Montaño, J.M., 1976, Estudio geológico de la zona de Caracoles y áreas vecinas, con énfasis en el Sistema Jurásico, provincia de Antofagasta, II Región, Chile: Universidad de Chile, 169 p. (*) p.

Montero-López, C., del Papa, C., Hongn, F., Strecker, M.R., and Aramayo, A., 2018, Synsedimentary broken-foreland tectonics during the Paleogene in the Andes of NW Argentine: new evidence from regional to centimetre-scale deformation features: Basin Research, v. 30, p. 142–159, doi:10.1111/bre.12212.

Morandé, J., 2014, El Basamento Pre-Mesozoico De La Sierra Limón Verde : Implicancias Para La Evolución Tectónica Del:

Mpodozis, C., Arriagada, C., Basso, M., Roperch, P., Cobbold, P., and Reich, M., 2005, Late Mesozoic to Paleogene stratigraphy of the Salar de Atacama Basin, Antofagasta, Northern Chile: Implications for the tectonic evolution of the Central Andes: Tectonophysics, v. 399, p. 125–154, doi:10.1016/j.tecto.2004.12.019.

Mpodozis, C., Arriagada, C., and Roperch, P., 1999, Cretaceous to Paleogene Geology of the Salar de Atcama Basin, northern Chile: A reappraisal of the Purilactis Group Stratigraphy, *in* Proceedings IV IRD-ISAG, Goettingen, Germany, IRD Editions, p. 523–526.

Mpodozis, C., Blanco, N., Jordan, T.E., and Gardeweg, M., 2000, Estratigrafía y Deformación del Cenozoico Tardío en la Región norte de la Cuenca del Salar de Atacama: La zona de Vilama-Pampa Vizcachitas, *in* Congreso Geológico Chileno No. 9 Actas, 2, Puerto Varas, Chile, p. 598–603.

Mpodozis, C., Cornejo Peláez, P., Kay, S., and Tittler, A., 1995, La Franja de Maricunga: síntesis de la evolución del Frente Volcánico Oligoceno-Mioceno de la zona sur de los Andes Centrales: Revista geológica de Chile: An international journal on andean geology, v. 22, p. 273–313, doi:10.5027/andgeoV22n2-a10.

Mpodozis, C., and Ramos, V.A., 2008, Tectónica Jurásica en Argentina y Chile: Extensión, subducción oblicua, rifting, deriva y colisiones? Revista de la Asociacion Geologica Argentina, v. 63, p. 481–497.

Muñoz, N., Charrier, R., and Jordan, T., 2002, Interactions between basement and cover during the evolution of the Salar de Atacama Basin, northern Chile: Revista geológica de Chile, v. 29, p. 3–29, doi:10.4067/S0716-02082002000100004.

Muñoz, M., Tapia, F., Persico, M., Benoit, M., Charrier, R., Farías, M., and Rojas, A., 2018a, Extensional tectonics during Late Cretaceous evolution of the Southern Central Andes: Evidence from the Chilean main range at ~35°S: Tectonophysics, v. 744, p. 93–117, doi:10.1016/j.tecto.2018.06.009.

Muñoz, M., Tapia, F., Persico, M., Benoit, M., Charrier, R., Farías, M., and Rojas, A., 2018b, Extensional tectonics during Late Cretaceous evolution of the Southern Central Andes: Evidence from the Chilean main range at ~35°S: Tectonophysics, v. 744, p. 93–117, doi:10.1016/j.tecto.2018.06.009.

Naranjo, J.A., Ramírez, C.F., and Pankoff, R., 1994, Morphostratigraphic evolution of the northwestern margin of the Salar de Atacama basin (23°S-68°W): Andean Geology, v. 21, p. 91–103, doi:10.5027/andgeov21n1-a05.

Narea, K., Peña, M., Bascuñán, S., Becerra, J., Gómez, I., Deckart, K., Munizaga, F., Maksaev, V., Arriagada, C., and Roperch, P., 2015, Paleomagnetism of Permo-Triassic and Cretaceous rocks from the Antofagasta region, northern Chile: Journal of South American Earth Sciences, v. 64, p. 261–272, doi:10.1016/j.jsames.2015.09.008.

Nester, P., and Jordan, T., 2012, The Pampa del Tamarugal Forearc Basin in Northern Chile: The Interaction of Tectonics and Climate: Tectonics of Sedimentary Basins: Recent Advances, p. 369–381, doi:10.1002/9781444347166.ch18.

Niemeyer, H., 1989, El Complejo Ígneo-Sedimentario del Cordón de Lila, Región de Antofagasta: significado tectónico.: Revista Geológica de Chile, v. 16, p. 163–181.

Niemeyer, H., 2013, Geología del área Cerro Lila-Peine, Región de Antofagasta. Servicio Nacional de Geología y Mineria. Carta Geológica de Chile, Serie Geología Básica 147. 1 mapa escala 1:100.000.:

Noblet, C., Lavenu, A., and Marocco, R., 1996, Concept of continuum as opposed to periodic tectonism in the Andes: Tectonophysics, v. 255, p. 65–78, doi:10.1016/0040-1951(95)00081-X.

Nyström, J.O., Vergara, M., Morata, D., and Levi, B., 2003, Tertiary volcanism during extension in the Andean foothills of central Chile (33°15′-33°45′S): Bulletin of the Geological Society of America, v. 115, p. 1523–1537, doi:10.1130/B25099.1.

O'Driscoll, L.J., Richards, M.A., and Humphreys, E.D., 2012, Nazca-South America interactions and the late Eocene-late Oligocene flat-slab episode in the central Andes: Tectonics, v. 31, p. 1–16, doi:10.1029/2011TC003036.

Oliveros, V. et al., 2020, Lithospheric evolution of the Pre- and Early Andean convergent margin, Chile: Gondwana Research, v. 80, p. 202–227, doi:10.1016/j.gr.2019.11.002.

Oliveros, V., Féraud, G., Aguirre, L., Fornari,

M., and Morata, D., 2006, The Early Andean Magmatic Province (EAMP): 40Ar/39Ar dating on Mesozoic volcanic and plutonic rocks from the Coastal Cordillera, northern Chile: Journal of Volcanology and Geothermal Research, v. 157, p. 311–330, doi:10.1016/j.jvolgeores.2006.04.007.

Pananont, P., Mpodozis, C., Blanco, N., Jordan, T.E., and Brown, L.D., 2004, Cenozoic evolution of the northwestern Salar de Atacama Basin, northern Chile: Tectonics, v. 23, p. 1–19, doi:10.1029/2003TC001595.

Del Papa, C., Hongn, F., Powell, J., Payrola, P., Do Campo, M., Strecker, M.R., Petrinovic, I., Schmitt, A.K., and Pereyra, R., 2013, Middle Eocene-Oligocene broken-foreland evolution in the Andean Calchaqui Valley, NW Argentina: Insights from stratigraphic, structural and provenance studies: Basin Research, v. 25, p. 574–593, doi:10.1111/bre.12018.

del Papa, C., Kirschbaum, A., Powell, J., Brod, A., Hongn, F., and Pimentel, M., 2010, Sedimentological, geochemical and paleontological insights applied to continental omission surfaces: A new approach for reconstructing an eocene foreland basin in NW Argentina: Journal of South American Earth Sciences, v. 29, p. 327–345, doi:10.1016/j.jsames.2009.06.004.

Parada, M.A., Feraud, G., Fuentes, F., Aguirre, L., Morata, D., and Larrondo, P., 2005, Ages and cooling history of the Early Cretaceous Caleu pluton: testimony of a switch from a rifted to a compressional continental margin in central Chile: Journal of the Geological Society, v. 162, p. 273–287, doi:10.1144/0016-764903-173.

Pardo-Casas, F., and Molnar, P., 1987, Relative motion of the Nazca (Farallon) and South American Plates since Late Cretaceous time: Tectonics, v. 6, p. 233–248, doi:10.1029/TC006i003p00233.

Payrola, P., Powell, J., Papa, C. del, and Hongn, F., 2009, Middle Eocene deformation-sedimentation in the Luracatao Valley: Tracking the beginning of the foreland basin of northwestern Argentina: Journal of South American Earth Sciences, v. 28, p. 142–154, doi:10.1016/j.jsames.2009.06.002.

Perelló, J., Zárate, A., Ramos, P., Posso, H., Neyra, C., Caballero, A., Fuster, N., and Muhr, R., 2003, Porphyry-Style Alteration and Mineralization of the Middle Eocene to Early Oligocene Andahuaylas-Yauri Belt, Cuzco Region, Peru: Economic Geology, v. 98, p. 1575–1605.

Pichowiak, S., Buchelt, M., and Damm, K.-W., 1990, Magmatic activity and tectonic setting of the early stages of the Andean cycle in northern Chile: , p. 127–144, doi:10.1130/SPE241-p127.

Quade, J., Dettinger, M.P., Carrapa, B., DeCelles, P., Murray, K.E., Huntington, K.W., Cartwright, A., Canavan, R.R., Gehrels, G., and Clementz, M., 2015, The growth of the central Andes, 22°S–26°S, *in* Decelles, P.G., Ducea, M.N., Carrapa, B., and Kapp, P.A. eds., Geodynamics of a Cordilleran Orogenic System: The Central Andes of Argentina and Northern Chile: Geological Society of America Memoir 212., The Geological Society of America, p. 277–308, doi:10.1130/2015.1212(15).

Raczynski, A., 1963, Geología del distrito minero de Tuina. BSc Thesis.: 117 p.

Radic, J.P., 2010, Las cuencas cenozoicas y su control en el volcanismo de los Complejos Nevados de Chillán y Copahue-Callaqui (Andes del sur, 36-39°S): Andean Geology, v. 37, p. 220–246, doi:10.4067/S0718-71062010000100009.

Ramírez, C.F., 1979, Geología del Cuadrángulo Río Grande y sector suroriental del Cuadrángulo Barros

Arana, Provincia El Loa, XI Región: Universidad de Chile, 139 p.

Ramírez, C.F., and Gardeweg, M., 1982, Hoja Toconao. Carta Geológica de Chile 54. 1 mapa escala 1:250.000.:

Ramos, V.A., 2009, Anatomy and global context of the Andes: Main geologic features and the Andean orogenic cycle: Geological Society of America Memoirs, v. 204, p. 31–65, doi:10.1130/2009.1204(02).

Ramos, V.A., 2010, The tectonic regime along the Andes : Present-day and Mesozoic regimes: v. 25, p. 2–25, doi:10.1002/gj.

Ramos, V. a, Cristallini, E., and Introcaso, A., 2004, The Andean Thrust System—Latitudinal Variations in Structural Styles and Orogenic Shortening: Aapg Memoir, v. 82, p. 30–50, http://sites.google.com/site/ecristallini/Ramos_et_al_2004_latitudinal_variati.pdf.

Ramos, V.A., and Folguera, A., 2009, Andean flat-slab subduction through time: Geological Society Special Publication, v. 327, p. 31–54, doi:10.1144/SP327.3.

Reiners, P.W. et al., 2015, Low-temperature thermochronologic trends across the central Andes, 21°S-28°S, *in* DeCelles, P.G., Ducea, M.N., Carrapa, B., and Kapp, P.A. eds., Memoir of the Geological Society of America, The Geological Society of America, v. 212, p. 215–249, doi:10.1130/2015.1212(12).

Reutter, K.J. et al., 2006, The Salar de Atacama Basin: a Subsiding Block within the Western Edge of the Altiplano-Puna Plateau: Andes: Active Subduction Orogeny, p. 303–325, doi:10.1007/978-3-540-48684-8_14.

del Rey, A., Deckart, K., Arriagada, C., and Martínez, F., 2016, Resolving the paradigm of the late Paleozoic–Triassic Chilean magmatism: Isotopic approach: Gondwana Research, v. 37, p. 172–181, doi:10.1016/j.gr.2016.06.008.

Riquelme, R., Hérail, G., Martinod, J., Charrier, R., and Darrozes, J., 2007, Late Cenozoic geomorphologic signal of Andean forearc deformation and tilting associated with the uplift and climate changes of the Southern Atacama Desert (26°S-28°S): Geomorphology, v. 86, p. 283–306, doi:10.1016/j.geomorph.2006.09.004.

Rojas Vera, E.A., Folguera, A., Zamora Valcarce, G., Bottesi, G., and Ramos, V.A., 2014, Structure and development of the Andean system between 36° and 39°S: Journal of Geodynamics, v. 73, p. 34–52, doi:10.1016/j.jog.2013.09.001.

Roperch, P., Carlotto, V., Ruffet, G., and Fornari, M., 2011, Tectonic rotations and transcurrent deformation south of the Abancay deflection in the Andes of southern Peru: Tectonics, v. 30, doi:10.1029/2010TC002725.

Rubilar, J., 2015, Arquitectura interna y desarrollo oligoceno-neogeno de la cuenca del salar de atacama, andes centrales del norte de chile: , p. 1–75.

Rubilar, J., Martínez, F., Arriagada, C., Becerra, J., and Bascuñán, S., 2017, Structure of the Cordillera de la Sal: A key tectonic element for the Oligocene-Neogene evolution of the Salar de Atacama basin, Central Andes, northern Chile: Journal of South American Earth Sciences, doi:10.1016/j.jsames.2017.11.013.

Rutland, R.W.R., 1971, Andean orogeny and ocean floor spreading: Nature, v. 233, p. 252–255, doi:10.1038/233252a0.

Safipour, R., Carrapa, B., Decelles, P.G., and Thomson, S.N., 2015, Exhumation of the Precordillera and northern Sierras Pampeanas and along-strike correlation of the Andean orogenic front, northwestern Argentina, *in* Decelles, P.G., Ducea, M.N., Carrapa, B., and Kapp, P.A. eds., Geodynamics of a Cordilleran Orogenic System: The Central Andes of Argentina and

Northern Chile: Geological Society of America Memoir 212., v. 212, p. 181–199, doi:10.1130/2015.1212(10).

Salfity, J.A., Gorustovich, S., Moya, M.C., and Amengual, R., 1984, Marco tectónico de la sedimentación y efusividad cenozoica de la Puna, *in* 9º Congreso Geológico Argentino, Actas 1, p. 539–554.

Salisbury, M.J., Jicha, B.R., de Silva, S.L., Singer, B.S., Jiménez, N.C., and Ort, M.H., 2011, 40Ar/39Ar chronostratigraphy of Altiplano-Puna volcanic complex ignimbrites reveals the development of a major magmatic province: Bulletin of the Geological Society of America, v. 123, p. 821–840, doi:10.1130/B30280.1.

Sanchez, C., 2017, Denudation evolution and geomorphic context of supergene copper mineralization in Centinela District, Atacama Desert, Chile, from thermochronology and cosmogenic nuclides: Université Toulouse 3 Paul Sabatier en co-tutelle avec la Universidad Católica del Norte, Antofagasta, Chile, 269 p.

Sánchez, C. et al., 2018, Exhumation history and timing of supergene copper mineralisation in an arid climate: New thermochronological data from the Centinela District, Atacama, Chile: Terra Nova, v. 30, p. 78–85, doi:10.1111/ter.12311.

Sandeman, H.A., Clark, A.H., and Farrar, E., 1995, An Integrated Tectono-Magmatic Model for the Evolution of the Southern Peruvian Andes (13–20°S) since 55 Ma: International Geology Review, v. 37, p. 1039–1073, doi:10.1080/00206819509465439.

Scheuber, E., Bogdanic, T., Jensen, A., and Reutter, K.-J., 1994, Tectonic Development of the North Chile Andes in relation to Plate Convergence and Magmatism since the Jurassic, *in* Reutter, K.-J., Scheuber, E., and Wigger, P. eds., Tectonics of the Southern Central Andes: Structure and Evolution of an Active Continental Margin, Berlin, Springer, p. 332.

Scheuber, E., Mertmann, D., Ege, H., Silva-González, P., Heubeck, C., Reutter, K.-J., and Jacobshagen, V., 2006, Exhumation and basin development related to formation of the central Andean plateau, 21°S: The Andes: Active Subduction Orogeny, v. 1, p. 285–301.

Schildgen, T.F., Hodges, K. V., Whipple, K.X., Pringle, M.S., Van Soest, M., and Cornell, K., 2009, Late cenozoic structural and tectonic development of the western margin of the central andean plateau in southwest Peru: Tectonics, v. 28, p. 1–21, doi:10.1029/2008TC002403.

Schmitz, M. et al., 1999, The crustal structure beneath the Central Andean forearc and magmatic arc as derived from seismic studies - the PISCO 94 experiment in northern Chile (21°-23°S): Journal of South American Earth Sciences, v. 12, p. 237–260, doi:10.1016/S0895-9811(99)00017-6.

Schurr, B., and Rietbrock, A., 2004, Deep seismic structure of the Atacama basin, northern Chile: Geophysical Research Letters, v. 31, p. 10–13, doi:10.1029/2004GL019796.

SERNAGEOMIN, 2013, Geología para el Ordenamiento Territorial y la Gestión Ambiental en el área de Iquique-Alto Hospicio. Servicio Nacional de Geología y Minería, Informe Registrado IR-13-53, 41 p., 5 mapas diferentes escalas.:

SERNAGEOMIN, 2003, Mapa Geológico de Chile. 1 mapa escala 1:1.000.000.:

Seton, M. et al., 2012, Global continental and ocean basin reconstructions since 200 Ma: Earth Science Reviews, v. 113, p. 212–270, doi:10.1016/j.earscirev.2012.03.002.

Siks, B.C., and Horton, B.K., 2011, Growth

and fragmentation of the Andean foreland basin during eastward advance of fold-thrust deformation, Puna plateau and Eastern Cordillera, northern Argentina: Tectonics, v. 30, p. 1–27, doi:10.1029/2011TC002944.

Sillitoe, R.H., 2010, Porphyry copper systems: Economic Geology, v. 105, p. 3–41, doi:10.2113/gsecongeo.105.1.3.

Sillitoe, R.H., and McKee, E., 1996, Age of Supergene Oxidation and Enrichment in the Chilean Porphyri Copper Province: Economic Geology, v. 91, p. 164–179.

de Silva, S.L., 1989, Geochronology and Stratigraphy of the Ignimbrites From the 21°30'S To 23°30'S Portion of the Central Andes of Northern Chile: Journal of Volcanology and Geothermal Research, v. 37, p. 93–131.

Silver, P.G., Russo, R.M., and Lithgow-Bertelloni, C., 1998, Coupling of South American and African Plate motion and plate deformation: Science, v. 279, p. 60–63, doi:10.1126/science.279.5347.60.

Skarmeta, J., 1993, Mecanismos de emplazamiento , deformación y transición de diques a filones manto en sedimentos jurásicos y cretácicos del norte de Chile: Revista Geológica de Chile, v. 20, p. 207–227.

Ślęzak, K., Díaz, D., Vargas, J.A., Cordell, D., Reyes-Cordova, F., and Segovia, M.J., 2021, Magnetotelluric image of the Chilean subduction zone in the Salar de Atacama region (23°-24°S): Insights into factors controlling the distribution of volcanic arc magmatism.: Physics of the Earth and Planetary Interiors, v. 318, doi:10.1016/j.pepi.2021.106765.

Sola, A.M., Becchio, R.A., and Pimentel, M.M., 2013, Petrogenesis of migmatites and leucogranites from Sierra de Molinos, Salta, Northwest Argentina: A petrologic and geochemical study: Lithos, v. 177, p. 470–491, doi:10.1016/j.lithos.2013.07.025.

Solari, L.A., Gómez-Tuena, A., Bernal, J.P., Pérez-Arvizu, O., and Tanner, M., 2010, U-Pb zircon geochronology with an integrated la-icp-ms microanalytical workstation: Achievements in precision and accuracy: Geostandards and Geoanalytical Research, v. 34, p. 5–18, doi:10.1111/j.1751-908X.2009.00027.x.

Solari, M., Venegas, C., Montecino, D., Astudillo, N., Cortés, J., Bahamondes, B., and Espinoza, F., 2017, Geología del área Imilac-Quebrada Guanaqueros, Región de Antofagasta. Carta Geológica de Chile, Serie Básica, No.191. 1 mapa escala 1:100.000.:

Somoza, R., 1998, Updated Nazca (Farallon)-South America relative motions during the last 40 My: Implications for mountain building in the central Andean region: Journal of South American Earth Sciences, v. 11, p. 211–215, doi:10.1016/S0895-9811(98)00012-1.

Somoza, R., and Ghidella, M.E., 2005, Convergencia en el margen occidental de América del Sur durante el Cenozoico: subducción de las placas de Nazca, Farallón y Aluk: Revista de la Asociación Geológica Argentina, v. 60, p. 797–809, doi:10.3989/scimar.2002.66n4433.

Somoza, R., Tomlinson, A.J., Caffe, P.J., and Vilas, J.F., 2012, Paleomagnetic evidence of earliest Paleocene deformation in Calama (∼22°S), northern Chile: Andean-type or ridge-collision tectonics? Journal of South American Earth Sciences, v. 37, p. 208–213, doi:10.1016/j.jsames.2012.04.001.

Steinmann, G., 1929, Geologie von Peru: Carl Winters Universitats-Buchhandlung, 448 p.

Stern, C.R., 2004, Active Andean volcanism: Its geologic and tectonic setting: Revista Geologica de Chile, v. 31, p. 161–206, doi:10.4067/S0716-02082004000200001.

Stern, C.R., 2011, Subduction erosion: Rates, mechanisms, and its role in arc

magmatism and the evolution of the continental crust and mantle: Gondwana Research, v. 20, p. 284–308, doi:10.1016/j.gr.2011.03.006.

Tapia, F., Farías, M., Naipauer, M., and Puratich, J., 2015, Late Cenozoic contractional evolution of the current arc-volcanic region along the southern Central Andes (35°20'S): Journal of Geodynamics, v. 88, p. 36–51, doi:10.1016/j.jog.2015.01.001.

Tassara, A., 2005, Interaction between the Nazca and South American plates and formation of the Altiplano-Puna plateau: Review of a flexural analysis along the Andean margin (15°-34°S): Tectonophysics, v. 399, p. 39–57, doi:10.1016/j.tecto.2004.12.014.

Tassara, A., and Echaurren, A., 2012, Anatomy of the Andean subduction zone: Three-dimensional density model upgraded and compared against global-scale models: Geophysical Journal International, v. 189, p. 161–168, doi:10.1111/j.1365-246X.2012.05397.x.

Tassara, A., Swain, C., Hackney, R., and Kirby, J., 2007, Elastic thickness structure of South America estimated using wavelets and satellite-derived gravity data: Earth and Planetary Science Letters, v. 253, p. 17–36, doi:10.1016/j.epsl.2006.10.008.

Tomlinson, A.J., and Blanco, N., 2006, Carta Cerro Jaspe. Geologia de la franja El Abra-Chuquicamata, II región [21º45'-22º30'S]. 196 p. 5 mapas escala 1:50.000:

Tomlinson, A.J., Blanco, N., and Dilles, J.H., 2010, Carta Calama, Región de Antofagasta. Carta Geológica de Chile, Serie Preliminar 8. 1 mapa escala 1:100.000.:

Tomlinson, A.J., Blanco, N., Maksaev, V., Dilles, J., Grunder, A.L., and Ladino, M., 2001, Geología de la Precordillera Andina de Quebrada Blanca-Chuquicamata, Regiones I y II (20°30'-22°30'S):

Tosdal, R.M., and Richards, J.P., 2001, Magmatic and Structural controls on the Development of Porphyry Cu±Mo±Au Deposits: Society of Economic Geologists Reviews, v. 14, p. 157–181.

Travisany, V., 1978, Mineralización cuprífera en areniscas de la Formación San Pedro en el distrito San Bartolo. Memoria de Título.: Universidad de Chile, 70 p.

Trumbull, R.B., Riller, U., Oncken, O., Scheuber, E., Munier, K., and Hongn, F., 2006, The Time-Space Distribution of Cenozoic Volcanism in the South-Central Andes: a New Data Compilation and Some Tectonic Implications, *in* Oncken, O., Chong, G., Franz, G., Giese, P., Gotze, H.J., Ramos, V.A., Strecker, M.R., and Wigger, P. eds., The Andes: Active Subduction Orogeny, Berlin, Springer, p. 29–43.

Tunik, M., Folguera, A., Naipauer, M., Pimentel, M., and Ramos, V.A., 2010, Early uplift and orogenic deformation in the Neuquén Basin: Constraints on the Andean uplift from U-Pb and Hf isotopic data of detrital zircons: Tectonophysics, v. 489, p. 258–273, doi:10.1016/j.tecto.2010.04.017.

Vásquez, P., and Sepúlveda, F., 2012, Cartas Iquique y Pozo Almonte, Región de Tarapacá. Servicio Nacional de Geología y Minería, Carta Geológica de Chile, Serie Geología Básica 162-163: 114 p., 1 mapa escala 1:100.000.:

Vicente, J.C., 2005, La fase primordial de estructuración de la faja plegada y corrida del Aconcagua: Importancia de la fase pehuenche del Mioceno inferior: Revista de la Asociacion Geologica Argentina, v. 60, p. 672–684.

Wilkes, E., and Görler, K., 1994, Sedimentary and Structural Evolution of the Salar de Atacama Depression., *in* Reutter, K., Scheuber, E., and Wigger, P. eds., Tectonics of the Southern Central Andes: Structure and Evolution of an Active Continental Margin, New York, Springer, p. 171–188.

Wörner, G., and Hammerschmidt, K., 2000, Geochronology (40Ar/39Ar, K-Ar and He-exposure ages) of Cenozoic magmatic rocks from northern Chile (18-22 S): implications for magmatism and tectonic: Revista geológica de, http://www.scielo.cl/scielo.php?script=sci_arttext&pid=S0716-02082000000200004.

Yáñez, G., and Rivera, O., 2019a, Crustal dense blocks in the fore-arc and arc region of Chilean ranges and their role in the magma ascent and composition: Breaking paradigms in the Andean metallogeny: Journal of South American Earth Sciences, v. 93, p. 51–66, doi:10.1016/j.jsames.2019.04.006.

Yáñez, G., and Rivera, O., 2019b, Crustal dense blocks in the fore-arc and arc region of Chilean ranges and their role in the magma ascent and composition: Breaking paradigms in the Andean metallogeny: Journal of South American Earth Sciences, v. 93, p. 51–66, doi:10.1016/j.jsames.2019.04.006.

Yrigoyen, M., 1993, Los depósitos sinorogénicos terciarios, *in* Ramos, V.A. ed., Geología y Recursos Naturales de Mendoza, 12º Congreso Geológico Argentino y 2º Congreso de Exploración de Exploración de Hidrocarburos (Mendoza), Relatorio 1, Mendoza, p. 123–148.

Yuan, X. et al., 2000, Subduction and collision processes in the Central Andes constrained by converted seismic phases: Nature, v. 408, p. 958–961, doi:10.1038/35050073.

Yuan, X., Sobolev, S.., and Kind, R., 2002, Moho topography in the central Andes and its geodynamic implications: Earth and Planetary Science Letters, v. 199, p. 389–402, doi:10.1016/S0012-821X(02)00589-7.

Zimmermann, U., Niemeyer, H., and Meffre, S., 2009, Revealing the continental margin of Gondwana: The Ordovician arc of the Cordón de Lila (northern Chile): International Journal of Earth Sciences, v. 99, p. 39–56, doi:10.1007/s00531-009-0483-8.

Zonenshayn, L., Savostin, L., and Sedov, A., 1984, Global paleogeodynamic reconstructions for the last 160 million years: Geotectonics, v. 18, p. 181–195.

Supplementary Material A.

Gravity data for Chapter 2

Point	UTM X	UTM Y	Z (m)	BS (mgal)	BC (mgal)
P142	550928.4	7492511	3112.05	564.02	565.52
P141	553308.3	7491264	3192.93	563.55	565.06
P140	554701.5	7490529	3242.17	560.41	561.93
P139	556949.1	7489270	3318.05	548.48	550.15
P138	558899.1	7488681	3405.84	540.83	542.91
P137	560817.2	7487540	3451.03	533.2	535.1
P136	562977.2	7481926	3344.57	530.56	533.17
P135	564905.7	7479469	3135.07	529.57	532.21
P134	566967.9	7477265	2960.42	529.13	532.01
P133	569081	7473254	2624.56	512.87	516.35
P132	570807.3	7471057	2491.23	505.97	509.45
P131	573026.8	7468682	2492.32	497.84	500.91
P130	575082.6	7467119	2560.63	494.16	496.97
P129	577169.9	7465893	2646.25	494.95	497.98
P128	578888.7	7465801	2547.51	497.66	501.95
P127	581084.6	7466655	2494.86	497.24	500.7
P126	582966.6	7465842	2460.63	493.8	497.53
P125	585282.4	7465730	2463.08	489.49	493.53
P124	587046	7465553	2484.44	485.83	490.07
P123	588899.2	7465361	2514.76	482.79	487.24
P122	591259.3	7465098	2542.88	478.42	483.3
P121	592985.3	7464843	2569.45	474.57	479.84
P120	595491.1	7464637	2619.84	471.14	477.28
P119	597162	7465053	2716.32	469.18	475.5
P118	599396	7465626	2868.19	464.52	471.15
P117	601423.8	7465980	3028.48	460.92	467.56
P116	603092.4	7466005	3157.05	459.49	466.14
P115	602327.3	7434944	2459	501.47	507.84
P143	602327.3	7434944	2459	501.47	507.84

Gravity and magnetic data for Chapter 3

Point_ID	UTM X	UTM Y	Z (m)	BS (mGal)	BC (mGal)	Z Mag (m)	Mag (nT)
1	515229.3	7430930.71	2927.69	589.34	590.65	3422.97	-53.67
2	515806.86	7431175.96	2934.04	590.39	591.7	3427.09	-38.58
3	516307.42	7431360.28	2940.42	589.45	590.79	3435.72	-27.71
4	516807.18	7431511.64	2950.99	593.19	594.55	3443.78	-18.47
5	517290.86	7431727.1	2960.07	594.64	596	3454.97	-6.65
6	517795.56	7432037.1	2971.76	593.71	595.1	3464.64	11.19
7	518304.31	7431880.48	2971.09	594.13	595.49	3465.87	17.82
8	518801.32	7431817.23	2970.11	593.39	594.75	3465.18	25.00
9	519302.26	7431667.23	2972.33	592.66	594.02	3466.75	29.87
10	519814.53	7431608.36	2975.02	591.72	593.06	3469.09	34.63
11	520298.87	7431613.16	2975.83	590.39	591.75	3469.65	38.01
12	520785.6	7431616.83	2979.3	588.79	590.15	3473.45	38.29
13	521306.28	7431607.28	2981.86	588.04	589.4	3476.22	33.18
14	521801.82	7431610.29	2986.43	587.89	589.25	3480.02	23.89
15	522305.13	7431616.54	2990.46	587.89	589.25	3483.38	15.70
16	522814.64	7431634.95	2994.54	588.13	589.49	3488.81	6.51
17	523309.39	7431641.06	2999.11	587.91	589.3	3492.90	-4.71
18	523809.47	7431689.81	3005.37	586.85	588.24	3498.35	-13.58
19	524308.56	7431814.56	3012.1	585.42	586.84	3505.93	-18.81
20	524799.52	7432080.67	3022.65	584.25	585.69	3516.33	-21.27
21	525305.38	7432216.01	3030.84	582.91	584.38	3526.12	-21.15
22	525810.86	7432147.16	3038.74	580.91	582.38	3533.33	-14.28
23	526309.13	7432090.83	3047.26	578.86	580.36	3540.87	-0.51
24	526774.97	7432024.97	3054.07	577.48	578.98	3547.62	14.80
25	527310.97	7431955.07	3063.54	576.77	578.29	3557.59	32.33
26	527806.15	7431855.56	3073.17	576.29	577.84	3565.76	48.18
27	528316.3	7431819.87	3083.77	575.5	577.08	3575.69	60.84
28	528810.78	7431826.78	3092.85	575.09	576.69	3585.96	65.72
29	529303.52	7431847.24	3101.26	574.27	575.9	3595.77	67.12
30	529815.25	7431631.42	3112.68	572.55	574.21	3605.91	67.90
31	530317.36	7431587.39	3117.62	571.45	573.16	3611.57	66.49
32	530815.25	7431506.47	3126.06	570.46	572.22	3619.48	*
33	531310.76	7431349.29	3135.13	569.08	570.9	3629.42	*
34	531796.79	7431205.95	3141.65	567.49	569.39	3636.57	*
35	532317.48	7431215.94	3151.64	566.43	568.41	3646.07	*
36	533306.51	7431191.37	3167.93	564.76	566.98	3662.63	60.02
37	533813.08	7431195.81	3177.44	564	566.35	3671.97	60.54
38	534305.65	7431419.86	3176.25	563.83	566.29	3673.21	59.99

39	534820.42	7431322.14	3183.29	563.24	565.91	3677.67	62.69
40	535313.45	7431286.53	3192.32	562.11	565.1	3685.02	65.65
41	535798.51	7431329.94	3199.97	560.62	564.04	3693.21	68.13
42	536325.96	7431436.61	3201.04	558.45	562.75	3681.75	*
43	543061.9	7431319.83	2530.92	542.42	545.49	3033.04	-111.37
44	543493.84	7431189.3	2509.6	541.38	544.3	3012.49	-120.22
45	544004.1	7431050.61	2483.45	539.27	542.08	2987.00	-107.90
46	544501.49	7430793.01	2457.31	538.23	540.94	2960.09	-77.21
47	545002	7430568.71	2433.68	537.27	539.9	2937.89	-39.29
48	545494.56	7430449.03	2413.86	536.27	538.84	2917.77	-11.47
49	545999.39	7430308.97	2394.58	534.81	537.32	2899.23	7.78
50	546497.31	7430206.29	2377.76	533.3	535.76	2883.11	18.39
51	547006.01	7430120.8	2365.83	531.79	534.17	2868.15	*
52	547491.51	7429993.8	2359.45	530.65	532.95	2864.08	*
53	548100.52	7429789.79	2358.51	529.18	531.34	2862.82	*
54	548598.88	7429651.13	2359.57	527.92	529.99	2863.69	*
55	549099.07	7429504.57	2358.04	526.24	528.25	2862.74	*
56	549596.14	7429358.3	2357.77	524.69	526.65	2861.50	*
57	550099.61	7429214.03	2357.8	522.98	524.89	2861.78	*
58	550597.16	7429020.04	2358.46	521.45	523.32	2860.33	*
59	551099.66	7428836.5	2357.99	519.92	521.78	2860.62	*
60	551599.38	7428669.72	2357.64	518.43	520.31	2859.68	*
61	552099.36	7428541.03	2361.35	517.19	519.13	2862.00	*
62	552629.04	7428345.69	2371.71	515.73	517.88	2875.49	*
63	560141.86	7427836.34	2381.46	512.02	513.54	2883.70	*
64	560511.28	7427777.43	2370.58	512.9	514.44	2873.43	*
65	561017.28	7427697.17	2363.53	513.44	514.98	2865.82	*
66	561514.59	7427618.06	2356.22	514.03	515.58	2860.15	*
67	562009.09	7427540.45	2353.52	513.99	515.54	2854.19	*
68	562515	7427458.87	2351.24	513.91	515.46	2854.00	*
69	563007.54	7427381.6	2351.14	514.29	515.84	2853.76	*
70	563525.62	7427299.5	2349.41	514.48	516.04	2853.12	*
71	564026.8	7427219.47	2348.29	514.83	516.39	2851.06	*
72	564515.52	7427142.98	2347.11	515.06	516.63	2850.04	*
73	565037.04	7427060.99	2346.39	515.37	516.95	2849.78	*
74	565387.52	7426490.32	2344.84	515.01	516.58	2849.36	*
75	565511.9	7426985.5	2345.36	515.51	517.1	2849.01	*
76	565693.7	7426453.06	2344.27	515.1	516.68	2846.98	*
77	565996.78	7426908.5	2343.86	515.51	517.1	2848.71	*
78	566196.28	7426392.15	2342.88	515.06	516.66	2845.49	*
79	566501.47	7426828.71	2344.17	515.76	517.36	2849.20	*

80	566697.37	7426330.84	2343.51	515.28	516.88	2847.06	*
81	566999.82	7426749.16	2342.98	515.64	517.26	2846.39	*
82	567189.4	7426274.13	2342.42	515.18	516.8	2845.25	*
83	567501.47	7426670.12	2342.97	515.82	517.45	2844.71	*
84	567733.41	7426206.31	2342.08	515.23	516.86	2845.12	*
85	567999.15	7426590.02	2341.84	515.55	517.19	2844.74	*
86	568256.47	7426143.96	2342.33	515.24	516.87	2844.07	*
87	568763.18	7426105.9	2341.92	515.08	516.74	2845.15	*
88	573276.56	7425537.48	2341.4	512.38	514.18	2841.02	*
89	573797.87	7425473.3	2342.26	511.97	513.79	2841.63	*
90	574297.65	7425414.8	2340.65	511.88	513.73	2842.23	*
91	574795.71	7425351.24	2340.89	511.29	513.16	2841.68	*
92	575298.55	7425289.91	2340.59	510.89	512.79	2842.33	*
93	575799.99	7425240.46	2340.59	510.58	512.5	2841.02	*
94	576296.51	7425179.65	2340.17	510.2	512.14	2842.82	*
95	576801.01	7425110.79	2340.2	509.79	511.76	2841.27	*
96	577302.69	7425050.11	2339.99	509.34	511.34	2843.36	*
97	577802.13	7424989.8	2340.14	509.03	511.06	2841.14	*
98	578300.59	7424927.62	2340.54	508.7	510.76	2844.06	*
99	578802.84	7424922.08	2340.61	508.17	510.25	2843.19	*
100	579303.89	7424816.46	2339.46	507.51	509.63	2841.95	*
101	579799.7	7424679.65	2340.92	507.13	509.27	2843.26	*
102	580298.68	7424582.59	2340.23	506.47	508.65	2842.14	*
103	580799.33	7424481.38	2339.68	505.89	508.11	2843.49	*
104	581296.38	7424516.46	2339.93	505.4	507.65	2843.01	*
105	581798.04	7424521.58	2339.55	504.93	507.22	2842.21	*
106	582302.56	7424445.15	2339.64	504.4	506.72	2842.27	*
107	582799.6	7424374.72	2339.62	503.8	506.17	2843.04	*
108	583300.08	7424297.86	2339.15	503.23	505.64	2843.03	*
109	583801.51	7424221.89	2339.89	503.1	505.56	2842.38	367.78
110	584453.69	7424507	2340.04	502.68	505.2	2843.10	409.33
111	585009.27	7424644.2	2340.68	502.5	505.06	2842.56	421.75
112	585510.96	7424661.07	2340.92	502.28	504.89	2843.28	394.15
113	586015.57	7424653.92	2340.93	502.08	504.74	2842.92	242.89
114	586501.14	7424649.37	2341.06	501.75	504.47	2842.97	140.68
115	586997.29	7424652.95	2341.11	501.43	504.21	2843.52	109.72
116	587510.54	7424654.16	2341.97	501.27	504.1	2844.04	73.74
117	587994.83	7424654.43	2342.69	501.08	503.96	2844.70	50.04
118	588481.19	7424656.49	2343.36	500.97	503.91	2845.25	32.79
119	588986.97	7424653.59	2345.3	501	504	2847.05	26.78
120	589473.89	7424655.86	2346.66	500.93	503.98	2848.78	31.08

121	589987.41	7424655.02	2348.07	500.87	504	2849.10	46.52
122	590481.09	7424655.91	2349.73	500.87	504.06	2850.87	64.94
123	590965.37	7424657.31	2351.98	500.91	504.17	2853.33	63.35
124	591426.11	7424657.27	2353.86	500.98	504.3	2855.04	56.97
125	591929.97	7424657.5	2357.17	501.14	504.53	2858.85	51.43
126	592479.31	7424654.48	2361.04	501.46	504.92	2862.16	45.86
127	592974.14	7424654.87	2365.13	501.76	505.3	2866.87	40.54
128	593417.96	7424656.26	2367.17	502.15	505.76	2869.99	35.19
129	593979.87	7424657.84	2371.82	502.61	506.32	2872.32	27.88
130	594488.26	7424318.4	2375.93	503.14	506.92	2877.77	23.45
131	594968.86	7424299.85	2381.16	503.58	507.44	2883.26	18.82
132	595491.32	7424201.61	2387.57	504.28	508.22	2889.01	15.39
133	595984.7	7424120.52	2393.26	505.06	509.09	2894.23	14.13
134	596492.36	7423992.77	2399.39	505.99	510.11	2901.83	11.13
135	596985.08	7423855.87	2405.75	506.61	510.82	2908.11	9.05
136	597514.03	7423735.24	2411.94	507.26	511.57	2914.35	8.08
137	597994.18	7423637.63	2416.83	507.98	512.4	2918.44	7.47
138	598483.11	7423440.38	2420.84	508.65	513.2	2920.76	7.04
139	598997.82	7423137.87	2428.42	509.22	513.88	2930.32	8.87
140	599483.94	7422874.73	2436.02	509.74	514.53	2936.38	11.57
141	599992.46	7422522.17	2444.95	510.04	514.96	2946.73	14.88
142	600497.35	7422231.92	2454.52	510.53	515.59	2955.65	18.85
143	600994.58	7421842.63	2466.38	511.46	516.67	2967.59	24.60
144	601496.01	7421835.28	2477.41	513.02	518.4	2977.96	30.05
145	601907.41	7422682.88	2474.24	515.26	520.96	2978.07	28.68
146	517137.37	7476406.53	2605.12	594.94	596.33	3101.51	60.80
147	519975.79	7476718.31	2630.39	594.89	596.25	3122.93	67.46
148	521954.82	7476923.63	2653.11	588.86	590.19	3148.23	76.40
149	523972.9	7477137.93	2680.92	591.23	592.54	3173.91	82.31
150	525965.65	7476881.47	2709.87	591.63	592.94	3202.57	118.13
151	528002.15	7476214.44	2674.48	592.67	593.98	3235.71	141.78
152	529829.45	7475143.88	2773.17	595.85	597.16	3265.94	160.61
153	532002.31	7473779.36	2824.21	599.25	600.53	3317.04	*
154	533993.93	7472252.89	2853.01	599.5	600.81	3345.58	84.56
155	535994.02	7471398.98	2896.99	598.36	599.69	3391.58	60.43
156	537971.26	7470460.86	2947.45	595.45	596.81	3442.06	63.05
157	539985.64	7469327.52	3006.61	591.88	593.3	3499.34	59.69
158	541978.4	7468003.06	3070.78	585.39	586.89	3564.96	*
159	544197.32	7467054.03	3145.19	580.2	581.88	3637.01	52.62
160	545234.11	7465580.17	3170.61	576.74	578.5	3662.83	36.55
161	546207.29	7464528.1	3200.65	573.31	575.23	3693.90	35.42

162	547167.65	7463934.72	3236.11	570.09	572.25	3727.01	42.06
163	548216.54	7463848.8	3274.74	566.86	569.56	3767.79	50.73
164	549179.6	7463590.1	3211.65	564.88	567.79	3710.40	58.28
165	550173.87	7463238.58	3121.51	561.6	564.38	3610.77	65.23
166	551239.9	7463082.96	3031.6	558.18	560.85	3522.26	70.39
167	552206.85	7461242.52	2899.3	554.04	557.11	3393.75	72.23
168	553099.9	7460947.49	2830.62	549.01	552.08	3334.05	69.31
169	554180.96	7461128.35	2752.07	542.74	545.78	3253.18	69.52
170	555148.68	7461186.76	2714.49	541.27	544.21	3206.63	70.33
171	556204.28	7461528.89	2686.81	540.04	542.87	3180.60	73.94
172	557198.41	7461812.39	2653.23	539.26	542.3	3156.54	78.90
173	558215.11	7461500.54	2612.36	537.93	541	3109.89	79.68
174	559191.03	7461442.94	2574.29	534.7	537.66	3067.84	81.81
175	560195.66	7461671.48	2529.23	532.4	535.39	3023.49	89.60
176	561285.15	7461911.2	2492.96	530.82	533.81	2987.08	98.17
177	562226.37	7462970.4	2480.13	527.28	530.4	2972.46	83.67
178	565523.59	7465041.67	2478.49	520.66	523.7	2970.39	104.89
179	567994.85	7466980.62	2453.05	513.25	516.59	2946.80	85.69
180	570066.18	7468941.91	2473.85	506.57	510.01	2966.02	88.19
181	571380.97	7470328.85	2478.24	502.98	506.58	2973.09	77.63
182	515270.16	7468630.55	2687.13	593.51	594.93	3186.38	18.88
183	520223.78	7493249.18	2806.35	592.11	593.69	3299.14	92.20
184	602327.29	7434943.52	2549.39	501.47	507.84	*	*
185	509755.22	7515378.64	2324.94	581.64	583.58	*	*

Supplementary Material B.

U-Pb detrital zircon tables for Chapters 2 and 4

Sample KST-1

				CORRECTED RATIOS									CORRECTED AGES (Ma)							
	U (ppm)	Th (ppm)	Th/U	$^{207}Pb/^{206}Pb$	±2s abs	$^{207}Pb/^{235}U$	±2s abs	$^{206}Pb/^{238}U$	±2s abs	$^{208}Pb/^{232}Th$	±2s abs	Rho	$^{206}Pb/^{238}U$	±2s	$^{207}Pb/^{235}U$	±2s	$^{207}Pb/^{206}Pb$	±2s	Best age (Ma)	±2s
1	98	67	0.69	0.0509	0.0044	0.2860	0.0240	0.0390	0.0008	0.0126	0.0007	0.03	101.2	1.8	104.3	7.8	130	180	101.2	1.8
2	107	126	1.18	0.0583	0.0040	0.3190	0.0210	0.0395	0.0008	0.0129	0.0007	0.18	169.6	12.0	204.0	28.0	650	300	169.6	12.0
3	148	161	1.09	0.0552	0.0046	0.2970	0.0220	0.0400	0.0008	0.0127	0.0006	-0.09	220.5	3.6	230.7	5.7	355	81	220.5	3.6
4	273	174	0.64	0.0522	0.0027	0.2900	0.0130	0.0398	0.0005	0.0128	0.0006	0.06	224.3	7.7	292.0	25.0	790	200	224.3	7.7
5	243	148	0.61	0.0500	0.0032	0.2810	0.0160	0.0402	0.0008	0.0130	0.0008	-0.11	239.5	3.1	237.9	4.2	245	74	239.5	3.1
6	138	169	1.23	0.0584	0.0037	0.3200	0.0190	0.0392	0.0007	0.0128	0.0005	0.22	242.3	4.1	243.0	12.0	210	130	242.3	4.1
7	171	89	0.52	0.0523	0.0030	0.2840	0.0130	0.0390	0.0007	0.0132	0.0007	0.01	242.6	3.5	257.0	12.0	380	130	242.6	3.5
8	169	65	0.39	0.0521	0.0030	0.2850	0.0150	0.0396	0.0009	0.0126	0.0008	0.02	242.6	4.4	248.0	18.0	280	190	242.6	4.4
9	256	113	0.44	0.0504	0.0026	0.2760	0.0120	0.0391	0.0006	0.0123	0.0007	-0.08	242.8	5.3	252.0	18.0	280	190	242.8	5.3
10	271	203	0.75	0.0519	0.0025	0.2910	0.0120	0.0402	0.0006	0.0129	0.0005	0.29	244.0	3.9	253.0	11.0	300	130	244.0	3.9
11	100	81	0.81	0.0732	0.0051	0.4200	0.0320	0.0424	0.0011	0.0172	0.0009	0.52	244.1	5.3	260.0	16.0	380	150	244.1	5.3
12	63	56	0.88	0.0551	0.0059	0.2930	0.0280	0.0396	0.0011	0.0132	0.0007	-0.15	244.3	4.2	250.0	12.0	290	140	244.3	4.2
13	127	74	0.58	0.0630	0.0063	0.3610	0.0360	0.0416	0.0008	0.0146	0.0010	0.15	245.1	5.1	279.0	17.0	570	170	245.1	5.1
14	115	53	0.46	0.0521	0.0039	0.2940	0.0200	0.0405	0.0007	0.0125	0.0008	0.02	245.3	3.8	248.0	11.0	240	120	245.3	3.8
15	55	52	0.95	0.0676	0.0065	0.3390	0.0330	0.0354	0.0012	0.0113	0.0008	0.17	245.5	4.0	247.7	9.1	252	110	245.5	4.0
16	353	135	0.38	0.0528	0.0023	0.2860	0.0110	0.0391	0.0005	0.0132	0.0006	0.16	246.0	3.3	241.3	8.1	217	110	246.0	3.3
17	71	23	0.32	0.0525	0.0052	0.2910	0.0230	0.0393	0.0011	0.0134	0.0013	-0.12	246.2	3.4	255.2	8.4	346	100	246.2	3.4
18	83	56	0.68	0.0581	0.0044	0.3180	0.0210	0.0388	0.0008	0.0133	0.0008	-0.07	246.3	4.2	257.0	11.0	280	130	246.3	4.2
19	185	119	0.64	0.0517	0.0034	0.2860	0.0170	0.0407	0.0007	0.0135	0.0007	0.01	246.3	3.4	247.8	9.2	272	110	246.3	3.4
20	108	54	0.50	0.0532	0.0048	0.2810	0.0220	0.0384	0.0009	0.0128	0.0008	-0.11	246.3	3.7	235.0	11.0	100	130	246.3	3.7

21	168	128	0.77	0.0591	0.0040	0.3390	0.0220	0.0408	0.0008	0.0138	0.0007	0.16	246.4	4.3	246.8	8.8	260	120	246.4	4.3
22	123	64	0.52	0.0660	0.0130	0.4200	0.1100	0.0403	0.0013	0.0170	0.0036	0.84	246.4	5.3	263.0	22.0	330	200	246.4	5.3
23	323	212	0.66	0.0545	0.0029	0.3000	0.0140	0.0399	0.0006	0.0138	0.0007	0.03	246.5	4.7	256.0	19.0	240	180	246.5	4.7
24	171	155	0.91	0.0487	0.0029	0.2700	0.0140	0.0404	0.0008	0.0126	0.0006	0.14	247.0	4.4	241.0	11.0	230	130	247.0	4.4
25	162	87	0.54	0.0507	0.0037	0.2780	0.0160	0.0406	0.0008	0.0126	0.0007	-0.29	247.1	3.6	247.2	9.6	220	120	247.1	3.6
26	339	148	0.44	0.0515	0.0024	0.2800	0.0100	0.0394	0.0007	0.0127	0.0007	0.11	247.2	3.9	244.0	14.0	200	140	247.2	3.9
27	186	102	0.55	0.0536	0.0033	0.2940	0.0160	0.0396	0.0007	0.0123	0.0007	0.03	247.4	3.0	255.0	8.3	309	100	247.4	3.0
28	214	95	0.45	0.0499	0.0032	0.2730	0.0170	0.0391	0.0006	0.0127	0.0007	0.19	247.4	4.3	248.0	12.0	220	140	247.4	4.3
29	349	209	0.60	0.0523	0.0026	0.2770	0.0120	0.0390	0.0006	0.0130	0.0006	0.19	247.5	4.7	254.0	12.0	290	130	247.5	4.7
30	189	146	0.77	0.0511	0.0031	0.2710	0.0150	0.0383	0.0007	0.0127	0.0007	0.28	247.6	3.4	246.0	11.0	210	120	247.6	3.4
31	170	97	0.57	0.0507	0.0032	0.2750	0.0160	0.0391	0.0007	0.0118	0.0007	-0.03	247.7	4.5	280.0	15.0	530	150	247.7	4.5
32	262	119	0.46	0.0508	0.0031	0.2810	0.0150	0.0392	0.0006	0.0123	0.0007	0.00	248.0	3.6	250.0	12.0	250	130	248.0	3.6
33	190	110	0.58	0.0528	0.0036	0.2930	0.0170	0.0394	0.0007	0.0126	0.0007	-0.06	248.2	3.5	255.0	11.0	286	110	248.2	3.5
34	296	155	0.52	0.0508	0.0029	0.2750	0.0140	0.0392	0.0006	0.0126	0.0006	0.05	248.4	6.9	261.0	18.0	330	190	248.4	6.9
35	271	391	1.44	0.0477	0.0028	0.2610	0.0130	0.0389	0.0006	0.0123	0.0005	0.03	248.9	4.9	250.0	17.0	250	170	248.9	4.9
36	234	122	0.52	0.0529	0.0031	0.2820	0.0140	0.0386	0.0006	0.0129	0.0006	-0.04	248.9	3.5	256.0	10.0	280	120	248.9	3.5
37	192	161	0.84	0.0547	0.0033	0.2860	0.0150	0.0383	0.0006	0.0123	0.0006	0.02	249.0	4.4	260.0	13.0	340	140	249.0	4.4
38	138	92	0.66	0.0530	0.0032	0.2850	0.0150	0.0392	0.0008	0.0124	0.0007	0.14	249.4	4.2	250.5	8.3	297	93	249.4	4.2
39	124	51	0.41	0.0582	0.0050	0.3380	0.0290	0.0415	0.0008	0.0147	0.0010	0.01	249.7	4.9	280.0	16.0	510	160	249.7	4.9
40	333	191	0.57	0.0509	0.0022	0.2810	0.0100	0.0401	0.0005	0.0127	0.0005	0.14	249.7	4.3	253.0	12.0	260	130	249.7	4.3
41	159	250	1.57	0.0543	0.0038	0.3030	0.0200	0.0406	0.0008	0.0132	0.0005	0.22	249.9	3.8	243.0	14.0	150	140	249.9	3.8
42	370	228	0.62	0.0504	0.0022	0.2781	0.0093	0.0401	0.0006	0.0124	0.0006	-0.02	250.1	7.0	258.0	22.0	330	230	250.1	7.0
43	300	127	0.42	0.0520	0.0028	0.2910	0.0150	0.0400	0.0005	0.0132	0.0007	-0.09	250.2	3.7	273.0	13.0	410	130	250.2	3.7
44	141	86	0.61	0.0612	0.0270	0.3380	0.2000	0.0401	0.0019	0.0145	0.0078	-0.19	250.3	5.6	254.0	12.0	260	120	250.3	5.6
45	240	170	0.71	0.0523	0.0030	0.2760	0.0110	0.0390	0.0007	0.0106	0.0005	-0.12	250.5	4.1	260.0	13.0	310	140	250.5	4.1

46	90	54	0.61	0.0510	0.0045	0.2830	0.0240	0.0408	0.0008	0.0130	0.0008	0.11	250.5	4.0	261.0	13.0	320	140	250.5	4.0
47	94	65	0.69	0.0648	0.0050	0.3550	0.0270	0.0397	0.0008	0.0133	0.0010	0.24	250.7	5.0	306.0	20.0	740	160	250.7	5.0
48	91	81	0.90	0.0512	0.0042	0.2860	0.0220	0.0405	0.0008	0.0132	0.0007	-0.03	250.7	3.1	255.8	9.1	262	100	250.7	3.1
49	112	45	0.40	0.0546	0.0036	0.2940	0.0200	0.0386	0.0009	0.0124	0.0010	0.31	250.9	3.2	253.9	7.6	258	96	250.9	3.2
50	135	209	1.55	0.0619	0.0044	0.3630	0.0240	0.0415	0.0009	0.0147	0.0007	0.16	251.1	5.1	249.0	16.0	200	160	251.1	5.1
51	320	158	0.49	0.0510	0.0025	0.2860	0.0130	0.0405	0.0006	0.0126	0.0006	0.20	251.1	3.2	259.5	9.7	310	110	251.1	3.2
52	149	122	0.82	0.0507	0.0038	0.2800	0.0200	0.0397	0.0008	0.0126	0.0007	0.08	251.4	5.2	261.0	14.0	340	140	251.4	5.2
53	330	153	0.46	0.0506	0.0025	0.2670	0.0100	0.0389	0.0005	0.0125	0.0005	-0.17	251.5	4.1	264.0	12.0	330	130	251.5	4.1
54	120	107	0.89	0.0503	0.0040	0.2870	0.0220	0.0403	0.0009	0.0125	0.0008	0.12	252.0	3.4	258.0	10.0	296	110	252.0	3.4
55	420	297	0.71	0.0514	0.0021	0.2846	0.0097	0.0397	0.0005	0.0123	0.0005	0.04	252.3	3.9	265.0	11.0	390	110	252.3	3.9
56	423	188	0.44	0.0528	0.0026	0.2900	0.0120	0.0397	0.0005	0.0127	0.0006	-0.21	252.3	4.2	264.2	9.5	320	120	252.3	4.2
57	281	373	1.33	0.0536	0.0027	0.2920	0.0120	0.0400	0.0006	0.0128	0.0005	0.15	252.4	3.8	251.0	11.0	230	130	252.4	3.8
58	402	455	1.13	0.0520	0.0024	0.2870	0.0120	0.0397	0.0005	0.0126	0.0005	0.16	252.6	5.0	271.0	15.0	400	160	252.6	5.0
59	137	154	1.12	0.0527	0.0034	0.2950	0.0180	0.0398	0.0008	0.0129	0.0005	0.20	252.7	3.1	255.4	9.6	250	110	252.7	3.1
60	126	126	1.00	0.0536	0.0034	0.2930	0.0190	0.0400	0.0008	0.0126	0.0007	0.18	252.7	3.6	259.4	9.4	337	110	252.7	3.6
61	690	1177	1.71	0.0495	0.0019	0.2794	0.0076	0.0407	0.0005	0.0129	0.0004	-0.26	252.7	4.6	245.0	16.0	200	180	252.7	4.6
62	418	186	0.44	0.0535	0.0024	0.2980	0.0110	0.0401	0.0005	0.0130	0.0006	0.28	252.8	4.9	260.0	15.0	330	140	252.8	4.9
63	159	112	0.70	0.0559	0.0030	0.3160	0.0170	0.0415	0.0009	0.0139	0.0007	0.31	253.3	3.2	253.5	8.6	232	99	253.3	3.2
64	244	191	0.78	0.0515	0.0026	0.2860	0.0140	0.0393	0.0006	0.0120	0.0006	0.23	253.3	3.5	248.8	7.4	197	95	253.3	3.5
65	146	90	0.62	0.0514	0.0032	0.2770	0.0140	0.0395	0.0007	0.0130	0.0007	-0.02	253.3	12.0	294.0	100.0	570	380	253.3	12.0
66	98	128	1.31	0.0520	0.0043	0.2780	0.0210	0.0394	0.0008	0.0124	0.0006	0.16	253.6	3.3	264.0	9.0	355	100	253.6	3.3
67	66	58	0.87	0.0524	0.0047	0.2900	0.0250	0.0405	0.0010	0.0137	0.0009	0.17	253.9	4.8	250.0	13.0	180	130	253.9	4.8
68	189	76	0.40	0.0510	0.0030	0.2810	0.0140	0.0399	0.0006	0.0125	0.0008	-0.03	254.0	5.8	271.0	16.0	410	150	254.0	5.8
69	170	114	0.67	0.0523	0.0029	0.2970	0.0160	0.0408	0.0008	0.0115	0.0007	0.40	254.1	3.7	259.0	9.2	304	120	254.1	3.7
70	948	786	0.83	0.0534	0.0019	0.2550	0.0072	0.0348	0.0006	0.0101	0.0004	0.08	254.6	5.7	255.0	18.0	240	170	254.6	5.7

71	173	64	0.37	0.0725	0.0027	1.6100	0.0410	0.1619	0.0020	0.0502	0.0020	0.01	254.8	7.8	329.0	65.0	670	330	254.8	7.8
72	286	381	1.33	0.0497	0.0043	0.1086	0.0085	0.0158	0.0003	0.0050	0.0002	-0.20	255.1	4.4	267.0	17.0	330	170	255.1	4.4
73	23	36	1.56	0.0600	0.0084	0.2310	0.0330	0.0267	0.0020	0.0060	0.0012	0.32	255.2	4.9	246.0	12.0	120	130	255.2	4.9
74	1425	3270	2.29	0.0511	0.0016	0.2642	0.0052	0.0379	0.0005	0.0123	0.0004	0.26	255.4	4.0	262.0	12.0	300	120	255.4	4.0
75	164	91	0.55	0.0594	0.0046	0.3320	0.0240	0.0413	0.0009	0.0127	0.0009	0.02	255.7	4.0	255.0	10.0	234	110	255.7	4.0
76	181	126	0.70	0.0535	0.0031	0.2980	0.0150	0.0398	0.0007	0.0128	0.0006	0.04	255.8	6.1	256.0	20.0	230	190	255.8	6.1
77	203	82	0.40	0.0527	0.0030	0.2930	0.0150	0.0404	0.0007	0.0130	0.0007	0.06	256.1	4.2	262.0	16.0	280	160	256.1	4.2
78	110	82	0.74	0.0501	0.0042	0.2750	0.0210	0.0400	0.0007	0.0121	0.0008	-0.15	256.1	5.0	256.0	16.0	250	170	256.1	5.0
79	70	32	0.45	0.0552	0.0043	0.3040	0.0220	0.0401	0.0010	0.0135	0.0010	0.08	256.1	5.1	262.0	12.0	300	130	256.1	5.1
80	81	41	0.50	0.0557	0.0054	0.3000	0.0280	0.0390	0.0009	0.0129	0.0009	0.12	256.5	4.7	250.0	14.0	210	160	256.5	4.7
81	175	74	0.42	0.0527	0.0032	0.2950	0.0150	0.0405	0.0008	0.0143	0.0009	0.05	256.5	4.8	267.0	16.0	340	150	256.5	4.8
82	223	101	0.45	0.0514	0.0025	0.2770	0.0110	0.0388	0.0006	0.0121	0.0006	0.05	257.4	4.2	256.0	13.0	260	130	257.4	4.2
83	216	144	0.67	0.0527	0.0029	0.2860	0.0130	0.0394	0.0006	0.0122	0.0006	-0.13	257.4	2.9	251.0	6.2	163	87	257.4	2.9
84	172	73	0.42	0.0534	0.0035	0.2950	0.0170	0.0396	0.0007	0.0133	0.0008	-0.02	257.7	4.8	294.0	17.0	530	140	257.7	4.8
85	151	107	0.71	0.0511	0.0031	0.2690	0.0130	0.0391	0.0007	0.0122	0.0006	-0.07	257.8	4.9	251.0	19.0	210	190	257.8	4.9
86	475	199	0.42	0.0540	0.0025	0.2860	0.0110	0.0389	0.0006	0.0128	0.0006	0.19	258.0	4.8	263.0	13.0	290	130	258.0	4.8
87	90	77	0.86	0.0525	0.0037	0.2990	0.0200	0.0404	0.0007	0.0122	0.0007	-0.12	258.2	6.2	272.0	18.0	310	170	258.2	6.2
88	178	148	0.83	0.0500	0.0036	0.2720	0.0170	0.0395	0.0006	0.0123	0.0005	-0.09	260.6	5.4	296.0	18.0	530	170	260.6	5.4
89	185	72	0.39	0.0514	0.0028	0.2770	0.0140	0.0388	0.0006	0.0121	0.0007	0.25	261.9	5.3	312.0	18.0	620	150	261.9	5.3
90	202	88	0.43	0.0531	0.0027	0.2960	0.0130	0.0399	0.0007	0.0130	0.0007	-0.06	262.0	4.7	293.0	22.0	530	200	262.0	4.7
91	165	119	0.72	0.0557	0.0033	0.3090	0.0160	0.0396	0.0006	0.0123	0.0005	0.05	262.1	5.2	278.0	13.0	400	130	262.1	5.2
92	81	37	0.45	0.0543	0.0044	0.3090	0.0230	0.0409	0.0010	0.0138	0.0010	-0.04	262.5	4.9	308.0	26.0	660	210	262.5	4.9
93	160	73	0.46	0.0523	0.0034	0.2790	0.0160	0.0386	0.0007	0.0123	0.0007	-0.13	267.8	6.7	362.0	23.0	1070	150	267.8	6.7
94	112	61	0.55	0.0527	0.0045	0.2800	0.0230	0.0384	0.0007	0.0123	0.0007	-0.07	967.0	11.0	977.0	17.0	1001	76	967.0	11.0

Sample KST-2

				CORRECTED RATIOS												CORRECTED AGES (Ma)				
	U (ppm)	Th (ppm)	Th/U	$^{207}Pb/^{206}Pb$	±2s abs	$^{207}Pb/^{235}U$	±2s abs	$^{206}Pb/^{238}U$	±2s abs	$^{208}Pb/^{232}Th$	±2s abs	Rho	$^{206}Pb/^{238}U$	±2s	$^{207}Pb/^{235}U$	±2s	$^{207}Pb/^{206}Pb$	±2s	Best age (Ma)	±2s
1	67	69	1.04	0.0602	0.0064	0.3230	0.0330	0.0392	0.0009	0.0117	0.0008	0.25	102.2	3.7	100.0	21.0	40	390	102.2	3.7
2	111	156	1.40	0.0670	0.0052	0.3730	0.0290	0.0398	0.0008	0.0136	0.0008	0.08	207.2	3.8	214.0	17.0	300	160	207.2	3.8
3	210	81	0.39	0.0510	0.0031	0.2670	0.0160	0.0386	0.0005	0.0128	0.0008	0.11	236.9	2.9	239.0	11.0	280	120	236.9	2.9
4	162	124	0.77	0.0497	0.0032	0.2700	0.0160	0.0390	0.0006	0.0124	0.0008	0.00	237.4	3.4	237.0	14.0	200	150	237.4	3.4
5	373	197	0.53	0.0520	0.0033	0.2860	0.0200	0.0399	0.0007	0.0132	0.0009	0.16	238.0	3.6	247.2	9.0	313	94	238	3.6
6	226	178	0.79	0.0520	0.0030	0.2670	0.0140	0.0374	0.0005	0.0116	0.0006	0.08	238.9	3.8	254.0	12.0	340	110	239	3.8
7	310	155	0.50	0.0533	0.0023	0.2760	0.0110	0.0376	0.0006	0.0119	0.0007	0.20	240.5	5.3	253.0	15.0	330	160	241	5.3
8	182	94	0.51	0.0555	0.0029	0.2960	0.0140	0.0401	0.0008	0.0129	0.0008	0.13	240.6	4.0	249.0	13.0	300	140	241	4.0
9	108	38	0.35	0.0533	0.0042	0.2890	0.0230	0.0394	0.0007	0.0129	0.0011	0.15	241.5	3.6	242.1	9.6	247	91	242	3.6
10	287	263	0.91	0.0511	0.0024	0.2710	0.0130	0.0391	0.0005	0.0124	0.0006	0.04	241.8	8.1	298.0	26.0	640	240	242	8.1
11	196	249	1.27	0.0575	0.0047	0.3210	0.0280	0.0408	0.0006	0.0131	0.0008	0.55	242.7	4.7	247.0	17.0	230	160	243	4.7
12	136	56	0.41	0.0527	0.0037	0.2790	0.0190	0.0388	0.0008	0.0121	0.0011	0.06	242.8	7.0	270.0	29.0	360	250	243	7.0
13	96	81	0.85	0.0525	0.0043	0.2860	0.0240	0.0398	0.0008	0.0123	0.0008	0.11	242.9	31.0	282.0	190.0	560	470	243	31.0
14	118	45	0.38	0.0515	0.0038	0.2820	0.0200	0.0397	0.0007	0.0137	0.0010	-0.12	243.8	4.2	268.0	19.0	480	160	244	4.2
15	182	163	0.90	0.0507	0.0035	0.2620	0.0170	0.0375	0.0005	0.0096	0.0005	-0.10	244.3	3.3	239.0	13.0	230	130	244	3.3
16	78	76	0.96	0.0540	0.0042	0.2920	0.0230	0.0391	0.0008	0.0122	0.0008	0.27	244.4	3.2	262.0	12.0	390	120	244	3.2
17	94	101	1.08	0.0508	0.0037	0.2780	0.0220	0.0384	0.0008	0.0121	0.0007	0.21	244.7	3.3	243.4	9.4	220	110	245	3.3
18	95	94	0.99	0.0601	0.0043	0.3210	0.0250	0.0389	0.0007	0.0131	0.0007	0.10	245.1	2.4	254.4	7.5	309	86	245	2.4
19	96	54	0.56	0.0575	0.0043	0.3210	0.0230	0.0404	0.0009	0.0134	0.0012	-0.11	245.6	4.8	249.0	16.0	320	160	246	4.8
20	328	171	0.52	0.0515	0.0024	0.2730	0.0130	0.0393	0.0004	0.0119	0.0007	0.27	245.8	3.8	271.0	14.0	460	140	246	3.8

21	132	82	0.62	0.0521	0.0035	0.2790	0.0170	0.0391	0.0006	0.0122	0.0008	-0.15	246.1	2.7	247.0	11.0	240	120	246	2.7
22	194	104	0.54	0.0530	0.0027	0.3050	0.0160	0.0415	0.0006	0.0132	0.0008	0.30	246.2	4.6	283.0	19.0	550	150	246	4.6
23	133	196	1.48	0.0568	0.0045	0.2950	0.0230	0.0393	0.0008	0.0126	0.0007	-0.13	246.2	3.9	238.0	14.0	150	140	246	3.9
24	220	177	0.80	0.0544	0.0027	0.2980	0.0150	0.0394	0.0005	0.0130	0.0007	0.18	246.2	4.0	249.0	12.0	220	120	246	4.0
25	132	123	0.94	0.0538	0.0039	0.2920	0.0190	0.0395	0.0007	0.0127	0.0007	-0.07	246.2	3.9	270.0	13.0	450	120	246	3.9
26	90	82	0.91	0.0532	0.0048	0.2830	0.0250	0.0392	0.0009	0.0124	0.0008	0.17	246.4	3.7	242.0	13.0	220	140	246	3.7
27	114	80	0.70	0.0573	0.0046	0.3010	0.0240	0.0385	0.0007	0.0130	0.0007	0.08	246.4	3.8	253.0	13.0	280	130	246	3.8
28	125	127	1.02	0.0534	0.0039	0.2820	0.0190	0.0380	0.0009	0.0117	0.0006	-0.04	246.5	4.1	289.0	19.0	630	180	247	4.1
29	61	42	0.69	0.0618	0.0049	0.3320	0.0250	0.0390	0.0007	0.0134	0.0010	-0.05	246.5	6.8	275.0	37.0	510	200	247	6.8
30	131	162	1.23	0.0543	0.0038	0.2790	0.0170	0.0380	0.0007	0.0122	0.0006	0.02	246.6	3.0	253.8	9.1	289	100	247	3.0
31	66	43	0.65	0.0524	0.0050	0.2890	0.0270	0.0396	0.0007	0.0134	0.0010	0.02	246.9	3.0	245.0	10.0	220	100	247	3.0
32	217	155	0.71	0.0517	0.0025	0.2870	0.0150	0.0398	0.0005	0.0130	0.0007	0.19	247.0	3.8	246.0	14.0	270	140	247	3.8
33	123	98	0.80	0.0530	0.0032	0.2790	0.0170	0.0391	0.0007	0.0125	0.0008	0.36	247.2	5.1	258.0	18.0	320	170	247	5.1
34	152	60	0.39	0.0527	0.0027	0.2870	0.0150	0.0395	0.0006	0.0121	0.0008	0.23	247.2	4.1	249.0	14.0	310	120	247	4.1
35	87	78	0.91	0.0698	0.0046	0.3900	0.0250	0.0404	0.0008	0.0146	0.0008	0.11	247.2	5.8	272.0	19.0	430	180	247	5.8
36	42	34	0.80	0.0576	0.0068	0.3150	0.0350	0.0395	0.0012	0.0143	0.0012	-0.13	247.5	4.0	249.0	14.0	270	150	248	4.0
37	67	99	1.48	0.0581	0.0047	0.3210	0.0250	0.0394	0.0008	0.0116	0.0007	-0.05	247.8	5.3	257.0	20.0	280	180	248	5.3
38	120	140	1.16	0.0551	0.0041	0.3000	0.0220	0.0398	0.0007	0.0127	0.0007	0.12	247.9	3.8	243.5	8.8	170	98	248	3.8
39	77	55	0.71	0.0515	0.0050	0.2810	0.0260	0.0400	0.0008	0.0131	0.0009	-0.11	247.9	3.7	255.5	9.7	300	110	248	3.7
40	236	129	0.55	0.0505	0.0022	0.2720	0.0140	0.0393	0.0007	0.0119	0.0008	0.46	248.0	5.8	281.0	25.0	560	230	248	5.8
41	232	241	1.04	0.0564	0.0032	0.3270	0.0180	0.0421	0.0006	0.0133	0.0007	0.02	248.1	4.7	267.0	17.0	510	160	248	4.7
42	141	74	0.52	0.0557	0.0034	0.3050	0.0180	0.0389	0.0006	0.0137	0.0011	-0.04	248.3	2.7	245.0	9.7	260	98	248	2.7
43	319	297	0.93	0.0502	0.0025	0.2760	0.0140	0.0389	0.0004	0.0124	0.0006	-0.05	248.3	4.3	244.0	11.0	210	89	248	4.3
44	191	195	1.02	0.0529	0.0043	0.2370	0.0200	0.0327	0.0006	0.0104	0.0007	0.26	248.5	3.2	254.0	12.0	310	130	249	3.2
45	52	45	0.86	0.0558	0.0069	0.3110	0.0380	0.0384	0.0011	0.0130	0.0010	0.00	248.7	4.3	252.0	16.0	280	140	249	4.3

46	128	126	0.99	0.0547	0.0034	0.3010	0.0190	0.0403	0.0008	0.0129	0.0007	-0.06	248.7	5.0	260.0	14.0	370	130	249	5.0
47	446	500	1.12	0.0515	0.0021	0.2700	0.0120	0.0382	0.0006	0.0117	0.0006	-0.04	249.1	4.4	262.0	18.0	350	160	249	4.4
48	181	132	0.73	0.0557	0.0037	0.3010	0.0180	0.0395	0.0006	0.0128	0.0007	0.07	249.1	3.3	264.0	12.0	370	110	249	3.3
49	238	108	0.45	0.0543	0.0028	0.2990	0.0140	0.0400	0.0006	0.0128	0.0008	0.07	249.2	5.0	284.0	18.0	510	180	249	5.0
50	189	113	0.59	0.0497	0.0034	0.2650	0.0170	0.0389	0.0006	0.0112	0.0007	-0.06	249.4	4.1	258.0	15.0	300	150	249	4.1
51	472	348	0.74	0.0524	0.0019	0.2852	0.0095	0.0388	0.0004	0.0121	0.0006	-0.08	249.5	7.4	273.0	27.0	360	250	250	7.4
52	421	415	0.99	0.0526	0.0024	0.2830	0.0110	0.0390	0.0005	0.0124	0.0006	-0.05	249.5	5.2	260.0	19.0	270	170	250	5.2
53	74	66	0.88	0.0522	0.0050	0.2800	0.0280	0.0401	0.0008	0.0123	0.0008	0.21	249.6	3.4	255.0	12.0	320	110	250	3.4
54	79	34	0.43	0.0555	0.0046	0.3060	0.0250	0.0391	0.0009	0.0129	0.0011	0.07	249.9	3.7	266.0	14.0	380	140	250	3.7
55	245	163	0.67	0.0486	0.0028	0.2660	0.0150	0.0397	0.0005	0.0123	0.0008	0.04	249.9	5.5	257.0	19.0	310	170	250	5.5
56	122	110	0.90	0.0523	0.0036	0.2830	0.0200	0.0393	0.0007	0.0124	0.0008	0.11	250.1	4.5	258.0	20.0	280	190	250	4.5
57	42	20	0.48	0.0643	0.0073	0.3470	0.0350	0.0382	0.0013	0.0139	0.0013	0.05	250.1	4.3	257.0	20.0	220	190	250	4.3
58	89	55	0.61	0.0541	0.0033	0.3010	0.0190	0.0401	0.0008	0.0136	0.0008	0.07	250.2	5.8	269.0	26.0	360	240	250	5.8
59	243	99	0.41	0.0524	0.0024	0.2880	0.0130	0.0400	0.0004	0.0128	0.0007	-0.08	250.3	3.2	289.0	11.0	590	110	250	3.2
60	155	98	0.63	0.0597	0.0031	0.3300	0.0140	0.0396	0.0005	0.0133	0.0008	-0.05	250.7	3.2	239.0	12.0	100	120	251	3.2
61	48	38	0.80	0.0559	0.0064	0.3090	0.0340	0.0396	0.0009	0.0125	0.0011	-0.02	251.0	4.1	255.0	16.0	280	160	251	4.1
62	148	102	0.69	0.0512	0.0027	0.2790	0.0150	0.0389	0.0006	0.0131	0.0008	0.21	251.1	5.1	251.0	16.0	240	160	251	5.1
63	72	34	0.47	0.0528	0.0048	0.2900	0.0250	0.0395	0.0008	0.0141	0.0011	-0.10	251.4	4.7	260.0	17.0	330	170	251	4.7
64	528	322	0.61	0.0518	0.0017	0.2883	0.0082	0.0399	0.0004	0.0130	0.0006	0.06	251.5	3.1	255.0	12.0	280	110	252	3.1
65	192	129	0.67	0.0498	0.0022	0.2720	0.0110	0.0392	0.0006	0.0125	0.0008	0.00	251.7	4.9	322.0	22.0	830	170	252	4.9
66	122	91	0.75	0.0536	0.0046	0.2860	0.0230	0.0395	0.0009	0.0122	0.0008	0.14	251.8	5.0	253.0	19.0	270	170	252	5.0
67	189	73	0.38	0.0508	0.0029	0.2840	0.0160	0.0401	0.0006	0.0131	0.0008	0.28	251.8	4.5	265.0	17.0	350	160	252	4.5
68	119	77	0.64	0.0538	0.0039	0.3060	0.0220	0.0407	0.0007	0.0137	0.0008	-0.12	251.8	2.9	259.9	10.0	360	110	252	2.9
69	243	161	0.66	0.0538	0.0027	0.2850	0.0150	0.0378	0.0006	0.0129	0.0008	0.31	252.1	4.1	255.0	16.0	260	130	252	4.1
70	300	218	0.73	0.0566	0.0030	0.3030	0.0170	0.0389	0.0006	0.0132	0.0007	0.29	252.2	2.5	257.0	6.4	285	72	252.2	2.5

71	401	262	0.65	0.0495	0.0020	0.2690	0.0110	0.0400	0.0005	0.0128	0.0007	0.08	252.7	2.7	258.0	9.7	311	93	252.7	2.7
72	478	236	0.49	0.0533	0.0027	0.2920	0.0130	0.0398	0.0005	0.0138	0.0007	-0.13	252.7	4.5	272.0	13.0	470	130	252.7	4.5
73	117	104	0.89	0.0526	0.0049	0.2840	0.0250	0.0396	0.0007	0.0127	0.0008	-0.05	252.8	4.9	250.0	20.0	280	190	252.8	4.9
74	333	320	0.96	0.0545	0.0031	0.2930	0.0150	0.0386	0.0005	0.0127	0.0006	-0.06	253.0	3.7	265.0	11.0	380	120	253.0	3.7
75	103	100	0.97	0.0540	0.0034	0.2900	0.0170	0.0393	0.0008	0.0135	0.0008	0.09	253.1	3.3	243.7	8.6	169	90	253.1	3.3
76	64	61	0.94	0.0579	0.0045	0.3190	0.0230	0.0403	0.0007	0.0127	0.0008	-0.17	253.4	4.7	267.0	11.0	410	110	253.4	4.7
77	117	55	0.47	0.0617	0.0026	0.8310	0.0290	0.0980	0.0012	0.0321	0.0017	-0.06	253.5	3.7	253.0	13.0	240	120	253.5	3.7
78	269	235	0.87	0.0513	0.0026	0.2720	0.0120	0.0387	0.0005	0.0122	0.0006	-0.27	253.6	5.1	266.0	15.0	350	140	253.6	5.1
79	267	161	0.60	0.0520	0.0020	0.2888	0.0100	0.0403	0.0005	0.0125	0.0007	0.06	253.7	5.2	254.0	22.0	280	200	253.7	5.2
80	86	70	0.82	0.0566	0.0034	0.3090	0.0170	0.0400	0.0007	0.0134	0.0008	-0.01	254.2	6.0	279.0	18.0	440	160	254.2	6.0
81	146	60	0.41	0.0578	0.0083	0.3120	0.0550	0.0390	0.0011	0.0150	0.0027	0.09	254.4	4.7	268.0	14.0	370	140	254.4	4.7
82	110	60	0.55	0.0523	0.0031	0.2980	0.0170	0.0412	0.0008	0.0141	0.0009	0.10	254.4	4.4	279.0	18.0	470	180	254.4	4.4
83	443	282	0.64	0.0523	0.0015	0.3260	0.0092	0.0452	0.0006	0.0155	0.0007	0.28	254.6	3.0	257.2	8.2	278	88	254.6	3.0
84	55	27	0.49	0.0480	0.0100	0.1060	0.0230	0.0160	0.0006	0.0058	0.0007	0.07	255.2	5.4	281.0	17.0	430	150	255.2	5.4
85	99	74	0.75	0.0528	0.0044	0.2900	0.0230	0.0398	0.0008	0.0138	0.0008	-0.14	255.2	4.9	332.0	18.0	870	140	255.2	4.9
86	256	235	0.92	0.0523	0.0026	0.2850	0.0120	0.0392	0.0006	0.0123	0.0007	-0.15	256.9	4.4	269.0	17.0	320	160	256.9	4.4
87	197	94	0.48	0.0518	0.0034	0.2760	0.0170	0.0391	0.0006	0.0127	0.0009	0.17	256.9	5.7	258.0	24.0	250	210	256.9	5.7
88	139	76	0.54	0.0599	0.0480	0.3210	0.5200	0.0384	0.0051	0.0124	0.0140	0.59	257.7	3.8	280.0	21.0	430	160	257.7	3.8
89	70	62	0.89	0.0531	0.0056	0.2840	0.0290	0.0405	0.0009	0.0126	0.0009	0.01	260.5	5.1	264.0	13.0	260	130	260.5	5.1
90	213	82	0.39	0.0520	0.0029	0.2850	0.0150	0.0393	0.0005	0.0136	0.0009	0.29	262.1	3.8	271.0	13.0	310	120	262.1	3.8
91	142	132	0.93	0.0517	0.0039	0.2830	0.0200	0.0397	0.0008	0.0132	0.0008	0.05	263.1	4.5	257.0	16.0	180	150	263.1	4.5
92	128	93	0.73	0.0506	0.0036	0.2900	0.0210	0.0417	0.0007	0.0139	0.0009	0.09	265.5	3.9	286.0	13.0	440	120	265.5	3.9
93	203	109	0.54	0.0528	0.0033	0.2850	0.0170	0.0390	0.0006	0.0128	0.0007	-0.18	284.9	3.8	286.4	7.1	302	70	284.9	3.8
94	138	155	1.12	0.0570	0.0041	0.3150	0.0220	0.0402	0.0010	0.0129	0.0008	0.14	602.5	7.2	613.0	16.0	660	90	602.5	7.2

Sample KST-4

				CORRECTED RATIOS									CORRECTED AGES (Ma)							
	U (ppm)	Th (ppm)	Th/U	$^{207}Pb/^{206}Pb$	±2s abs	$^{207}Pb/^{235}U$	±2s abs	$^{206}Pb/^{238}U$	±2s abs	$^{208}Pb/^{232}Th$	±2s abs	Rho	$^{206}Pb/^{238}U$	±2s	$^{207}Pb/^{235}U$	±2s	$^{207}Pb/^{206}Pb$	±2s	Best age (Ma)	±2s
1	160	54	0.34	0.0558	0.0027	0.2390	0.0130	0.0318	0.0008	0.0100	0.0008	0.09	110.0	3.7	127.0	14.0	430	230	110.0	3.7
2	357	355	0.99	0.0494	0.0028	0.1480	0.0085	0.0220	0.0004	0.0067	0.0004	0.02	113.0	4.1	115.0	14.0	120	240	113.0	4.1
3	134	130	0.97	0.0700	0.0051	0.4030	0.0330	0.0415	0.0009	0.0140	0.0010	0.54	113.1	2.2	118.0	8.1	220	160	113.1	2.2
4	340	35	0.10	0.0656	0.0016	1.1440	0.0360	0.1290	0.0036	0.0392	0.0022	0.61	113.1	5.5	128.0	30.0	320	420	113.1	5.5
5	170	114	0.67	0.0590	0.0023	0.6990	0.0270	0.0863	0.0016	0.0257	0.0014	0.12	114.4	6.5	125.0	28.0	140	460	114.4	6.5
6	269	219	0.81	0.0522	0.0024	0.2730	0.0130	0.0383	0.0007	0.0119	0.0006	0.27	131.5	3.2	132.7	8.3	180	120	131.5	3.2
7	198	175	0.88	0.0512	0.0025	0.3300	0.0150	0.0467	0.0008	0.0147	0.0008	-0.08	137.5	4.7	154.0	16.0	420	230	137.5	4.7
8	48	19	0.39	0.0540	0.0081	0.1690	0.0250	0.0230	0.0009	0.0076	0.0011	0.04	140.5	2.6	140.1	7.4	180	110	140.5	2.6
9	232	105	0.45	0.0533	0.0027	0.2820	0.0170	0.0399	0.0011	0.0143	0.0008	0.06	142.4	5.0	154.0	16.0	310	240	142.4	5.0
10	275	121	0.44	0.0488	0.0030	0.1400	0.0093	0.0206	0.0005	0.0064	0.0005	0.21	144.1	3.5	152.0	11.0	220	160	144.1	3.5
11	121	64	0.53	0.0584	0.0036	0.3080	0.0190	0.0387	0.0008	0.0129	0.0008	0.08	144.3	2.7	149.2	9.1	270	140	144.3	2.7
12	298	169	0.57	0.0511	0.0038	0.1237	0.0089	0.0177	0.0004	0.0061	0.0004	0.02	145.0	4.0	160.0	17.0	350	220	145.0	4.0
13	106	69	0.65	0.0576	0.0022	0.6730	0.0300	0.0851	0.0015	0.0256	0.0015	0.26	146.5	5.4	159.0	21.0	270	290	146.5	5.4
14	132	62	0.47	0.0560	0.0042	0.3170	0.0230	0.0419	0.0008	0.0146	0.0011	0.11	146.9	3.9	173.0	13.0	520	170	146.9	3.9
15	190	93	0.49	0.0537	0.0029	0.2830	0.0160	0.0389	0.0008	0.0123	0.0007	0.15	151.0	4.6	160.0	17.0	300	250	151.0	4.6
16	52	31	0.60	0.0488	0.0062	0.1210	0.0150	0.0177	0.0006	0.0054	0.0007	0.22	151.4	5.5	198.0	29.0	720	330	151.4	5.5
17	42	30	0.73	0.0747	0.0086	0.4300	0.0530	0.0405	0.0012	0.0163	0.0013	0.23	151.7	4.0	149.0	16.0	140	220	151.7	4.0
18	66	54	0.82	0.0571	0.0055	0.3190	0.0320	0.0400	0.0009	0.0129	0.0008	0.29	160.2	5.9	210.0	21.0	780	220	160.2	5.9
19	78	53	0.68	0.0558	0.0031	0.6720	0.0410	0.0866	0.0017	0.0262	0.0015	0.01	163.0	6.2	165.0	41.0	110	410	163.0	6.2
20	172	42	0.24	0.0589	0.0022	0.7630	0.0290	0.0928	0.0015	0.0298	0.0016	-0.01	202.1	4.9	217.0	10.0	400	110	202.1	4.9

21	183	86	0.47	0.0496	0.0033	0.2580	0.0170	0.0372	0.0007	0.0120	0.0008	0.03	228.2	4.9	233.0	13.0	300	120	228.2	4.9
22	122	78	0.64	0.0544	0.0041	0.2960	0.0230	0.0386	0.0008	0.0130	0.0009	0.15	234.1	5.2	252.0	18.0	360	150	234.1	5.2
23	174	112	0.65	0.0528	0.0026	0.3150	0.0150	0.0425	0.0008	0.0133	0.0008	-0.04	235.6	4.3	232.0	14.0	180	150	235.6	4.3
24	199	126	0.63	0.0543	0.0035	0.3050	0.0180	0.0397	0.0007	0.0136	0.0008	-0.21	237.0	5.7	253.0	22.0	400	210	237.0	5.7
25	188	140	0.74	0.0521	0.0031	0.2820	0.0170	0.0390	0.0009	0.0120	0.0007	0.22	237.2	4.1	227.0	13.0	200	130	237.2	4.1
26	95	101	1.06	0.0505	0.0052	0.2770	0.0290	0.0393	0.0009	0.0123	0.0007	0.05	237.9	4.7	256.0	18.0	440	180	237.9	4.7
27	137	152	1.11	0.0641	0.0033	0.6650	0.0380	0.0757	0.0015	0.0249	0.0013	0.36	238.1	3.6	239.5	8.8	249	90	238.1	3.6
28	77	39	0.51	0.0541	0.0067	0.1540	0.0190	0.0216	0.0008	0.0080	0.0007	0.10	240.4	4.3	244.4	11.0	258	110	240.4	4.3
29	374	200	0.53	0.0601	0.0017	0.7000	0.0220	0.0841	0.0013	0.0268	0.0013	0.27	242.5	4.4	246.2	11.0	282	100	242.5	4.4
30	343	228	0.66	0.0512	0.0023	0.2730	0.0130	0.0380	0.0007	0.0117	0.0006	0.15	242.8	5.0	280.0	14.0	610	140	242.8	5.0
31	69	59	0.86	0.0650	0.0100	0.2330	0.0260	0.0252	0.0009	0.0096	0.0009	-0.05	243.2	4.4	242.0	12.0	200	120	243.2	4.4
32	232	197	0.85	0.0533	0.0026	0.2820	0.0130	0.0390	0.0008	0.0119	0.0007	0.22	243.7	5.3	254.0	16.0	340	160	243.7	5.3
33	223	299	1.34	0.0744	0.0021	1.9040	0.0620	0.1837	0.0026	0.0553	0.0026	0.17	244.0	4.8	246.0	12.0	280	120	244.0	4.8
34	207	172	0.83	0.0530	0.0032	0.2890	0.0180	0.0401	0.0007	0.0121	0.0007	0.02	244.2	5.1	261.0	18.0	320	160	244.2	5.1
35	133	65	0.49	0.0531	0.0031	0.2890	0.0160	0.0404	0.0009	0.0123	0.0008	0.18	244.5	3.9	252.0	12.0	340	120	244.5	3.9
36	143	57	0.40	0.0546	0.0039	0.2850	0.0200	0.0385	0.0009	0.0126	0.0010	-0.14	244.9	4.2	242.6	11.0	237	110	244.9	4.2
37	78	52	0.66	0.0510	0.0057	0.1730	0.0200	0.0237	0.0007	0.0079	0.0009	-0.25	245.0	5.2	271.0	15.0	510	130	245.0	5.2
38	39	17	0.44	0.0700	0.0110	0.2210	0.0350	0.0238	0.0009	0.0108	0.0014	0.19	245.7	4.9	254.0	13.0	340	120	245.7	4.9
39	315	82	0.26	0.0511	0.0034	0.1571	0.0099	0.0226	0.0004	0.0082	0.0007	0.01	246.5	5.2	251.0	14.0	310	120	246.5	5.2
40	93	62	0.67	0.0550	0.0045	0.2850	0.0230	0.0376	0.0008	0.0128	0.0009	-0.03	246.8	4.9	251.7	11.0	310	110	246.8	4.9
41	57	27	0.48	0.0533	0.0064	0.1660	0.0190	0.0223	0.0008	0.0073	0.0010	0.02	248.6	5.7	248.0	23.0	180	200	248.6	5.7
42	258	87	0.34	0.0723	0.0022	1.4930	0.0650	0.1500	0.0043	0.0503	0.0025	0.76	249.9	4.5	255.0	13.0	280	130	249.9	4.5
43	218	67	0.31	0.0503	0.0031	0.2700	0.0150	0.0385	0.0007	0.0128	0.0009	-0.07	250.0	6.0	285.0	15.0	580	140	250.0	6.0
44	162	128	0.79	0.0565	0.0029	0.5770	0.0300	0.0739	0.0014	0.0230	0.0011	-0.10	250.2	5.2	275.0	14.0	510	120	250.2	5.2
45	112	105	0.94	0.0589	0.0049	0.1830	0.0140	0.0231	0.0006	0.0075	0.0006	-0.01	251.0	4.5	269.0	14.0	350	140	251.0	4.5

46	355	141	0.40	0.1246	0.0025	5.6260	0.1400	0.3265	0.0053	0.0929	0.0044	0.66	251.7	4.6	258.9	9.2	348	90	251.7	4.6
47	248	160	0.65	0.0592	0.0020	0.5970	0.0250	0.0731	0.0017	0.0234	0.0014	0.31	252.2	6.9	255.0	13.0	330	110	252.2	6.9
48	143	129	0.91	0.0625	0.0031	0.6570	0.0330	0.0765	0.0014	0.0250	0.0013	-0.03	252.6	5.8	278.0	25.0	450	210	252.6	5.8
49	176	135	0.77	0.0503	0.0035	0.1620	0.0120	0.0226	0.0006	0.0073	0.0005	0.08	253.4	4.0	257.0	14.0	310	130	253.4	4.0
50	60	51	0.85	0.0916	0.0029	3.3350	0.1200	0.2619	0.0044	0.0777	0.0038	0.53	255.1	5.4	257.0	13.0	290	120	255.1	5.4
51	120	98	0.82	0.0546	0.0038	0.3190	0.0220	0.0417	0.0009	0.0139	0.0008	-0.07	255.2	4.6	251.0	13.0	240	130	255.2	4.6
52	249	125	0.50	0.1019	0.0023	4.0300	0.1300	0.2881	0.0059	0.0845	0.0040	0.87	255.7	7.5	361.0	36.0	980	250	255.7	7.5
53	154	150	0.97	0.0581	0.0026	0.7090	0.0340	0.0885	0.0015	0.0266	0.0014	0.24	259.2	4.0	270.4	10.0	347	95	259.2	4.0
54	254	89	0.35	0.0592	0.0021	0.6240	0.0230	0.0774	0.0013	0.0247	0.0013	0.16	260.5	5.6	289.0	14.0	510	120	260.5	5.6
55	100	65	0.65	0.0487	0.0057	0.1600	0.0190	0.0238	0.0006	0.0073	0.0008	0.10	261.2	7.2	293.0	29.0	510	220	261.2	7.2
56	24	30	1.27	0.0802	0.0041	2.0730	0.0990	0.1910	0.0039	0.0555	0.0032	-0.01	262.0	5.5	344.0	25.0	960	140	262.0	5.5
57	29	10	0.33	0.0550	0.0140	0.1360	0.0320	0.0179	0.0010	0.0064	0.0013	0.03	263.3	5.8	279.0	17.0	430	170	263.3	5.8
58	558	179	0.32	0.0738	0.0017	1.6310	0.0410	0.1637	0.0024	0.0477	0.0023	-0.11	264.6	5.2	278.0	18.0	450	160	264.6	5.2
59	30	35	1.18	0.1047	0.0040	4.0000	0.1500	0.2843	0.0063	0.0836	0.0043	0.13	268.0	6.8	284.0	20.0	420	170	268.0	6.8
60	247	206	0.83	0.0515	0.0032	0.2810	0.0170	0.0404	0.0007	0.0124	0.0007	0.05	268.1	4.7	277.0	12.0	310	110	268.1	4.7
61	34	24	0.71	0.0570	0.0170	0.1320	0.0360	0.0177	0.0009	0.0068	0.0011	-0.20	272.9	4.7	276.0	12.0	280	120	272.9	4.7
62	280	224	0.80	0.0511	0.0024	0.2680	0.0140	0.0387	0.0007	0.0122	0.0007	0.33	283.0	4.5	286.0	13.0	300	110	283.0	4.5
63	291	48	0.16	0.0795	0.0020	1.9870	0.0610	0.1835	0.0039	0.0627	0.0033	0.20	291.8	5.2	287.0	20.0	230	170	291.8	5.2
64	220	131	0.59	0.0531	0.0026	0.3260	0.0170	0.0449	0.0007	0.0139	0.0008	0.25	294.2	5.0	290.0	12.0	250	110	294.2	5.0
65	102	110	1.08	0.0563	0.0052	0.2860	0.0280	0.0375	0.0009	0.0119	0.0007	-0.11	348.2	20.0	384.0	21.0	530	62	348.2	20.0
66	88	51	0.57	0.0558	0.0072	0.1350	0.0160	0.0172	0.0006	0.0067	0.0009	0.10	360.0	15.0	375.0	39.0	470	250	360.0	15.0
67	48	43	0.90	0.0588	0.0066	0.3410	0.0380	0.0414	0.0012	0.0129	0.0010	-0.01	454.6	10.0	475.0	15.0	560	73	454.6	10.0
68	98	52	0.53	0.0543	0.0068	0.1680	0.0170	0.0228	0.0006	0.0077	0.0015	-0.07	459.7	8.3	463.0	20.0	460	120	459.7	8.3
69	246	139	0.56	0.2606	0.0048	21.9300	1.1000	0.6125	0.0300	0.1589	0.0084	0.78	470.3	9.3	519.0	22.0	740	110	470.3	9.3
70	106	101	0.95	0.0607	0.0038	0.3190	0.0180	0.0384	0.0008	0.0124	0.0009	-0.17	475.1	8.3	511.0	20.0	650	110	475.1	8.3

71	412	580	1.41	0.0513	0.0020	0.2651	0.0110	0.0376	0.0006	0.0117	0.0006	0.05	480.4	7.7	492.0	15.0	557	81	480.4	7.7
72	172	251	1.46	0.0587	0.0031	0.3280	0.0180	0.0412	0.0009	0.0135	0.0007	0.06	481.0	7.6	474.1	12.0	446	75	481.0	7.6
73	163	164	1.01	0.0523	0.0030	0.2760	0.0160	0.0386	0.0008	0.0123	0.0007	-0.06	485.8	7.9	501.0	14.0	557	80	485.8	7.9
74	172	55	0.32	0.0917	0.0021	3.0900	0.0820	0.2457	0.0036	0.0711	0.0037	0.10	519.0	11.0	555.0	34.0	740	160	519.0	11.0
75	51	28	0.54	0.0650	0.0055	0.7360	0.0590	0.0838	0.0019	0.0259	0.0025	-0.06	520.7	7.6	540.0	14.0	607	65	520.7	7.6
76	188	61	0.32	0.0583	0.0023	0.6840	0.0280	0.0846	0.0015	0.0266	0.0015	0.21	523.7	8.7	531.0	17.0	558	83	523.7	8.7
77	195	119	0.61	0.0593	0.0021	0.6350	0.0230	0.0783	0.0013	0.0240	0.0013	0.06	526.6	9.1	521.0	18.0	514	94	526.6	9.1
78	32	17	0.52	0.0577	0.0073	0.4560	0.0560	0.0575	0.0025	0.0206	0.0023	0.22	533.7	9.3	539.0	16.0	541	84	533.7	9.3
79	196	198	1.01	0.0523	0.0031	0.2870	0.0170	0.0395	0.0007	0.0120	0.0007	0.00	535.3	9.9	522.0	24.0	420	120	535.3	9.9
80	627	52	0.08	0.0584	0.0016	0.4610	0.0320	0.0555	0.0033	0.0215	0.0032	-0.04	546.5	8.7	542.0	20.0	514	100	546.5	8.7
81	91	78	0.86	0.0554	0.0047	0.3250	0.0270	0.0425	0.0011	0.0138	0.0009	0.02	563.2	9.6	571.0	21.0	620	99	563.2	9.6
82	174	171	0.99	0.0567	0.0032	0.3120	0.0180	0.0396	0.0009	0.0124	0.0007	0.11	572.0	8.6	574.0	17.0	552	81	572.0	8.6
83	243	139	0.57	0.0539	0.0030	0.2830	0.0150	0.0387	0.0006	0.0118	0.0007	0.03	782.0	21.0	777.0	17.0	788	52	782.0	21.0
84	356	184	0.52	0.0533	0.0022	0.2910	0.0120	0.0398	0.0007	0.0124	0.0007	-0.16	901.0	24.0	924.0	27.0	983	62	901.0	24.0
85	114	58	0.51	0.0510	0.0040	0.3290	0.0270	0.0463	0.0009	0.0149	0.0010	0.15	977.4	13.0	984.0	15.0	1040	47	977.4	13.0
86	151	140	0.93	0.0547	0.0040	0.2800	0.0220	0.0370	0.0008	0.0111	0.0007	0.15	1086.0	23.0	1111.0	21.0	1180	49	1086.0	23.0
87	273	312	1.14	0.0519	0.0028	0.3110	0.0160	0.0432	0.0008	0.0134	0.0007	-0.07	1087.0	14.0	1081.0	22.0	1060	58	1087.0	14.0
88	336	180	0.54	0.0540	0.0023	0.3060	0.0130	0.0410	0.0007	0.0132	0.0007	-0.02	1126.0	21.0	1144.0	34.0	1181	100	1126.0	21.0
89	22	9	0.38	0.0570	0.0150	0.1840	0.0500	0.0256	0.0010	0.0081	0.0020	-0.41	1416.0	18.0	1429.0	21.0	1454	43	1454.0	43.0
90	146	77	0.53	0.0528	0.0031	0.2570	0.0170	0.0360	0.0008	0.0112	0.0007	0.31	1499.0	22.0	1486.0	27.0	1465	60	1465.0	60.0
91	294	52	0.18	0.0563	0.0019	0.5960	0.0200	0.0775	0.0013	0.0251	0.0016	-0.11	1635.0	30.0	1640.0	27.0	1656	41	1656.0	41.0
92	177	205	1.16	0.0496	0.0031	0.2520	0.0160	0.0375	0.0007	0.0115	0.0006	0.01	1612.0	32.0	1641.0	30.0	1702	75	1702.0	75.0
93	123	60	0.49	0.0600	0.0026	0.7580	0.0360	0.0913	0.0016	0.0274	0.0016	0.08	1821.0	26.0	1919.0	22.0	2020	36	2020.0	36.0
94	139	72	0.52	0.0600	0.0039	0.3260	0.0200	0.0396	0.0010	0.0147	0.0010	0.40	3080.0	130.0	3180.0	63.0	3250	29	3250.0	29.0

Sample KST-6

				CORRECTED RATIOS									CORRECTED AGES (Ma)							
	U (ppm)	Th (ppm)	Th/U	$^{207}Pb/^{206}Pb$	±2s abs	$^{207}Pb/^{235}U$	±2s abs	$^{206}Pb/^{238}U$	±2s abs	$^{208}Pb/^{232}Th$	±2s abs	Rho	$^{206}Pb/^{238}U$	±2s	$^{207}Pb/^{235}U$	±2s	$^{207}Pb/^{206}Pb$	±2s	Best age (Ma)	±2s
1	215	157	0.73	0.0542	0.0043	0.2310	0.0180	0.0315	0.0005	0.0100	0.0005	-0.14	70.7	1.8	100.4	14.0	990	200	70.7	1.8
2	204	231	1.14	0.0554	0.0056	0.1190	0.0140	0.0158	0.0004	0.0054	0.0003	-0.18	101.0	2.3	114.0	12.0	510	200	101.0	2.3
3	326	337	1.04	0.0579	0.0026	0.4070	0.0200	0.0515	0.0008	0.0151	0.0007	0.06	199.6	3.2	210.0	14.0	410	170	199.6	3.2
4	303	426	1.41	0.0631	0.0048	0.3650	0.0370	0.0429	0.0010	0.0140	0.0008	0.29	231.9	14.0	295.0	16.0	790	110	231.9	14.0
5	136	152	1.12	0.0663	0.0043	0.3460	0.0250	0.0392	0.0009	0.0138	0.0007	0.25	233.2	4.2	239.0	15.0	280	140	233.2	4.2
6	65	20	0.31	0.0689	0.0065	0.3910	0.0420	0.0407	0.0012	0.0192	0.0014	0.06	237.4	4.1	262.0	13.0	480	110	237.4	4.1
7	209	312	1.49	0.0554	0.0035	0.2910	0.0210	0.0385	0.0006	0.0121	0.0006	0.22	240.5	5.7	277.0	27.0	570	170	240.5	5.7
8	415	243	0.59	0.0550	0.0023	0.3380	0.0150	0.0450	0.0007	0.0145	0.0006	-0.32	243.7	3.8	259.0	16.0	470	120	243.7	3.8
9	128	89	0.69	0.0674	0.0029	0.9620	0.0560	0.1034	0.0023	0.0396	0.0018	0.30	245.8	4.0	272.0	18.0	510	150	245.8	4.0
10	174	102	0.58	0.0606	0.0057	0.3200	0.0300	0.0392	0.0008	0.0144	0.0009	0.26	247.5	5.5	301.0	19.0	800	130	247.5	5.5
11	456	51	0.11	0.0730	0.0024	1.6390	0.0650	0.1636	0.0023	0.0534	0.0025	0.21	248.0	5.0	280.0	22.0	670	170	248.0	5.0
12	204	119	0.58	0.1039	0.0033	4.1990	0.1600	0.2951	0.0041	0.0852	0.0036	0.39	248.6	5.1	294.0	21.0	650	180	248.6	5.1
13	223	167	0.75	0.0552	0.0033	0.3130	0.0190	0.0405	0.0008	0.0128	0.0007	0.14	251.8	5.3	291.0	19.0	540	160	251.8	5.3
14	132	92	0.69	0.0709	0.0030	1.0190	0.0820	0.1076	0.0051	0.0323	0.0017	0.13	253.2	5.0	277.0	19.0	510	140	253.2	5.0
15	416	33	0.08	0.0613	0.0023	0.6650	0.0280	0.0796	0.0012	0.0383	0.0031	0.25	253.3	4.1	261.0	13.0	370	110	253.3	4.1
16	335	125	0.37	0.0537	0.0025	0.3390	0.0180	0.0465	0.0007	0.0163	0.0009	0.12	256.1	5.1	276.0	14.0	450	130	256.1	5.1
17	289	104	0.36	0.0717	0.0026	1.6220	0.0660	0.1648	0.0022	0.0482	0.0021	-0.11	256.3	6.0	300.0	23.0	620	180	256.3	6.0
18	137	123	0.89	0.0653	0.0034	0.6820	0.0400	0.0779	0.0014	0.0243	0.0012	0.11	257.3	7.2	333.0	28.0	940	160	257.3	7.2
19	133	23	0.18	0.0755	0.0040	0.9440	0.0480	0.0920	0.0020	0.0545	0.0033	-0.08	262.4	4.6	306.0	15.0	609	110	262.4	4.6
20	397	471	1.19	0.1096	0.0095	4.1800	0.3700	0.2708	0.0210	0.0819	0.0074	-0.04	268.1	6.6	320.0	26.0	700	170	268.1	6.6

21	118	167	1.42	0.0634	0.0060	0.3720	0.0370	0.0425	0.0011	0.0137	0.0008	-0.14	271.0	6.1	321.0	25.0	730	120	271.0	6.1
22	180	127	0.70	0.0712	0.0028	1.1310	0.0520	0.1169	0.0019	0.0381	0.0017	0.32	283.5	4.3	295.0	12.0	390	89	283.5	4.3
23	178	83	0.46	0.0755	0.0026	1.9650	0.0810	0.1870	0.0031	0.0596	0.0027	0.48	283.9	4.2	346.0	15.0	770	97	283.9	4.2
24	252	119	0.47	0.2484	0.0074	14.2400	0.5500	0.4188	0.0071	0.1038	0.0048	0.85	289.0	18.0	396.0	130.0	1000	470	289.0	18.0
25	160	84	0.53	0.1959	0.0059	13.7700	0.5100	0.5115	0.0071	0.1449	0.0060	0.53	292.8	4.3	296.0	13.0	334	100	292.8	4.3
26	141	43	0.31	0.0770	0.0031	1.6320	0.0790	0.1568	0.0033	0.0499	0.0027	0.17	297.6	6.0	398.0	29.0	980	160	297.6	6.0
27	78	75	0.96	0.0609	0.0059	0.3460	0.0320	0.0406	0.0010	0.0143	0.0007	-0.11	307.7	4.9	316.0	14.0	380	94	307.7	4.9
28	384	350	0.91	0.0540	0.0029	0.2940	0.0180	0.0401	0.0007	0.0128	0.0006	0.33	323.9	4.6	346.0	15.0	500	93	323.9	4.6
29	72	72	1.00	0.0745	0.0061	0.4840	0.0420	0.0473	0.0010	0.0171	0.0009	-0.09	329.0	7.0	343.0	25.0	510	150	329.0	7.0
30	89	74	0.83	0.1091	0.0041	4.6500	0.2100	0.3096	0.0042	0.0841	0.0037	0.40	467.0	6.0	468.0	18.0	508	86	467.0	6.0
31	82	36	0.44	0.0831	0.0033	2.0780	0.1000	0.1842	0.0032	0.0590	0.0030	0.20	477.3	6.6	484.0	16.0	516	79	477.3	6.6
32	109	51	0.47	0.0643	0.0036	0.7160	0.0440	0.0823	0.0014	0.0302	0.0018	0.14	483.3	8.1	526.0	23.0	740	110	483.3	8.1
33	140	54	0.38	0.0775	0.0033	1.9290	0.0900	0.1832	0.0029	0.0558	0.0029	-0.08	493.4	7.2	517.0	17.0	677	80	493.4	7.2
34	128	63	0.49	0.0623	0.0052	0.3380	0.0280	0.0393	0.0008	0.0143	0.0010	-0.26	499.8	6.6	502.5	16.0	543	72	499.8	6.6
35	131	95	0.73	0.1167	0.0038	5.4890	0.2100	0.3423	0.0046	0.1001	0.0043	0.13	509.8	8.3	547.0	26.0	730	110	509.8	8.3
36	320	163	0.51	0.0731	0.0350	0.4810	0.1900	0.0459	0.0029	0.0191	0.0099	0.34	567.4	12.0	677.0	24.0	1071	100	567.4	12.0
37	140	167	1.19	0.0637	0.0037	0.8040	0.0550	0.0933	0.0016	0.0295	0.0015	0.22	574.7	9.3	601.0	29.0	700	120	574.7	9.3
38	229	150	0.66	0.0631	0.0100	0.9190	0.1800	0.1063	0.0035	0.0340	0.0026	-0.12	619.1	8.4	646.0	23.0	767	78	619.1	8.4
39	471	160	0.34	0.0966	0.0029	3.4770	0.1300	0.2628	0.0034	0.0760	0.0032	0.08	630.3	9.3	639.0	21.0	683	79	630.3	9.3
40	144	96	0.67	0.1118	0.0036	5.0130	0.2000	0.3277	0.0044	0.0976	0.0042	0.33	632.0	21.0	705.0	32.0	943	76	632.0	21.0
41	313	164	0.52	0.0698	0.0099	0.1040	0.0160	0.0110	0.0003	0.0046	0.0004	0.24	634.5	13.0	694.0	27.0	880	89	634.5	13.0
42	806	635	0.79	0.0585	0.0019	0.6410	0.0260	0.0806	0.0011	0.0247	0.0010	0.41	643.0	9.1	649.0	22.0	702	87	643.0	9.1
43	170	255	1.50	0.0577	0.0044	0.4030	0.0360	0.0524	0.0011	0.0167	0.0009	0.09	651.3	20.0	660.0	67.0	690	170	651.3	20.0
44	160	128	0.80	0.0849	0.0034	2.2730	0.1000	0.1962	0.0036	0.0588	0.0029	0.16	655.4	9.3	674.0	24.0	730	89	655.4	9.3
45	206	166	0.81	0.0604	0.0063	0.3150	0.0380	0.0380	0.0009	0.0129	0.0009	0.18	659.0	29.0	713.0	36.0	940	78	659.0	29.0

46	132	180	1.37	0.0775	0.0030	1.9580	0.0870	0.1845	0.0027	0.0550	0.0023	0.10	670.8	9.1	695.0	20.0	782	65	670.8	9.1
47	318	76	0.24	0.0733	0.0025	1.4900	0.0670	0.1500	0.0028	0.0496	0.0024	0.39	711.6	10.0	719.0	22.0	759	76	711.6	10.0
48	424	90	0.21	0.0620	0.0024	0.8760	0.0390	0.1027	0.0016	0.0341	0.0025	0.46	713.0	11.0	767.0	26.0	955	77	713.0	11.0
49	162	158	0.97	0.0577	0.0045	0.3080	0.0250	0.0401	0.0008	0.0137	0.0006	0.12	848.7	18.0	1025.0	26.0	1424	81	848.7	18.0
50	352	71	0.20	0.0703	0.0028	0.9950	0.0640	0.1031	0.0036	0.0379	0.0022	0.72	901.0	16.0	934.0	27.0	1015	67	901.0	16.0
51	100	46	0.46	0.0964	0.0035	3.2700	0.1500	0.2477	0.0042	0.0825	0.0037	0.31	915.0	14.0	946.0	29.0	1018	77	915.0	14.0
52	240	164	0.68	0.0634	0.0026	0.8970	0.0420	0.1049	0.0016	0.0334	0.0015	0.46	939.0	18.0	990.0	29.0	1107	78	939.0	18.0
53	92	49	0.53	0.1117	0.0037	4.9200	0.1900	0.3180	0.0056	0.0947	0.0045	0.36	976.5	13.0	985.0	25.0	1008	66	976.5	13.0
54	187	53	0.28	0.0783	0.0031	1.9100	0.1100	0.1800	0.0058	0.0572	0.0030	0.62	983.5	12.0	978.0	26.0	977	71	983.5	12.0
55	125	80	0.64	0.0605	0.0044	0.3340	0.0250	0.0398	0.0009	0.0146	0.0008	0.36	1060.8	14.0	1068.0	27.0	1105	69	1060.8	14.0
56	237	109	0.46	0.0843	0.0028	2.5790	0.1100	0.2209	0.0059	0.0674	0.0040	0.07	1067.0	32.0	1083.0	40.0	1144	81	1067.0	32.0
57	166	191	1.15	0.0581	0.0043	0.3090	0.0230	0.0389	0.0007	0.0119	0.0006	-0.02	1068.0	18.0	1061.0	28.0	1032	67	1068.0	18.0
58	225	132	0.58	0.0642	0.0028	0.9450	0.0460	0.1070	0.0016	0.0359	0.0016	-0.22	1084.0	16.0	1089.0	31.0	1120	85	1084.0	16.0
59	268	115	0.43	0.0655	0.0029	0.3330	0.0210	0.0366	0.0024	0.0146	0.0009	0.18	1090.0	17.0	1140.0	34.0	1259	78	1090.0	17.0
60	167	79	0.47	0.0734	0.0030	1.5420	0.0730	0.1525	0.0024	0.0451	0.0025	0.31	1091.6	15.0	1102.0	31.0	1139	82	1091.6	15.0
61	301	306	1.02	0.0526	0.0037	0.2660	0.0190	0.0368	0.0007	0.0113	0.0007	-0.07	1105.0	17.0	1107.0	28.0	1078	68	1105.0	17.0
62	297	298	1.00	0.0652	0.0027	0.8910	0.0440	0.1008	0.0014	0.0313	0.0014	0.45	1148.8	14.0	1150.0	27.0	1169	66	1148.8	14.0
63	295	322	1.09	0.0571	0.0029	0.2940	0.0170	0.0375	0.0007	0.0111	0.0005	0.27	1154.8	20.0	1202.0	33.0	1302	79	1154.8	20.0
64	287	191	0.67	0.0762	0.0026	1.8650	0.0760	0.1789	0.0025	0.0504	0.0023	0.04	1192.0	19.0	1255.0	31.0	1368	65	1192.0	19.0
65	370	65	0.18	0.0644	0.0024	1.0310	0.0440	0.1167	0.0018	0.0376	0.0021	-0.14	1234.0	15.0	1268.0	27.0	1346	61	1234.0	15.0
66	316	391	1.24	0.0603	0.0034	0.3520	0.0200	0.0416	0.0008	0.0132	0.0006	0.26	1286.0	32.0	1294.0	33.0	1307	63	1286.0	32.0
67	570	499	0.87	0.0570	0.0023	0.5870	0.0280	0.0751	0.0010	0.0218	0.0010	-0.03	1426.0	22.0	1480.0	34.0	1548	66	1548.0	66.0
68	247	173	0.70	0.0656	0.0030	0.4010	0.0220	0.0450	0.0007	0.0154	0.0008	0.11	1504.0	17.0	1522.0	29.0	1557	57	1557.0	57.0
69	233	88	0.38	0.0864	0.0027	2.4890	0.0930	0.2109	0.0029	0.0608	0.0027	0.17	1667.0	20.0	1675.0	32.0	1691	58	1691.0	58.0
70	234	123	0.53	0.0733	0.0025	1.8450	0.0760	0.1802	0.0033	0.0501	0.0022	0.50	1545.0	90.0	1666.0	70.0	1783	150	1783.0	150.0

71	647	520	0.80	0.0575	0.0022	0.6110	0.0260	0.0769	0.0011	0.0230	0.0009	-0.40	1738.0	21.0	1764.0	37.0	1792	66	1792.0	66.0
72	456	52	0.11	0.0651	0.0021	0.9830	0.0380	0.1097	0.0016	0.0419	0.0022	0.36	1827.0	22.0	1823.0	33.0	1825	61	1825.0	61.0
73	301	178	0.59	0.0870	0.0030	2.4430	0.1000	0.2031	0.0036	0.0505	0.0022	0.07	1779.0	28.0	1809.0	33.0	1833	60	1833.0	60.0
74	748	354	0.47	0.0539	0.0024	0.3660	0.0200	0.0489	0.0008	0.0151	0.0008	-0.32	1898.0	22.0	1898.0	33.0	1907	57	1907.0	57.0
75	466	198	0.43	0.0787	0.0025	2.1070	0.0820	0.1951	0.0026	0.0563	0.0023	0.27	2668.0	30.0	2733.8	35.0	2793	51	2793.0	51.0
76	657	184	0.28	0.0903	0.0036	1.7470	0.0730	0.1407	0.0032	0.0407	0.0025	-0.19	2258.0	33.0	2767.0	38.0	3173	48	3173.0	48.0

Sample N-3

				CORRECTED RATIOS									CORRECTED AGES (Ma)							
	U (ppm)	Th (ppm)	Th/U	$^{207}Pb/^{206}Pb$	±2s abs	$^{207}Pb/^{235}U$	±2s abs	$^{206}Pb/^{238}U$	±2s abs	$^{208}Pb/^{232}Th$	±2s abs	Rho	$^{206}Pb/^{238}U$	±2s	$^{207}Pb/^{235}U$	±2s	$^{207}Pb/^{206}Pb$	±2s	Best age (Ma)	±2s
1	115	105	0.91	0.0570	0.0067	0.1830	0.0220	0.0236	0.0006	0.0075	0.0005	0.05	68.4	1.8	71.3	6.8	130	210	68.4	1.8
2	760	439	0.58	0.0493	0.0033	0.0760	0.0055	0.0113	0.0002	0.0038	0.0002	-0.17	68.5	1.5	71.7	6.2	280	160	68.5	1.5
3	935	542	0.58	0.0573	0.0033	0.0879	0.0055	0.0111	0.0002	0.0039	0.0003	0.21	68.8	1.9	74.6	9.1	200	180	68.8	1.9
4	76	57	0.75	0.0770	0.0087	0.2280	0.0260	0.0239	0.0007	0.0086	0.0007	0.18	69.0	1.6	70.5	6.5	110	190	69.0	1.6
5	407	234	0.57	0.0681	0.0060	0.1130	0.0100	0.0118	0.0003	0.0049	0.0003	0.04	69.3	1.7	83.1	7.2	400	190	69.3	1.7
6	86	66	0.77	0.0570	0.0054	0.3470	0.0320	0.0457	0.0011	0.0156	0.0009	0.21	69.3	1.7	73.0	9.0	290	210	69.3	1.7
7	38	47	1.24	0.0873	0.0049	2.5400	0.1300	0.2115	0.0041	0.0637	0.0030	0.02	69.9	2.5	91.0	12.0	570	260	69.9	2.5
8	597	335	0.56	0.0510	0.0057	0.0763	0.0099	0.0107	0.0003	0.0037	0.0004	0.17	70.6	1.2	81.6	4.9	410	130	70.6	1.2
9	926	351	0.38	0.0582	0.0019	0.6960	0.0270	0.0864	0.0012	0.0275	0.0012	0.34	71.4	1.2	85.5	5.1	500	120	71.4	1.2
10	52	36	0.69	0.0630	0.0130	0.1080	0.0240	0.0124	0.0006	0.0056	0.0007	0.32	72.0	1.3	84.1	5.2	450	130	72.0	1.3
11	458	293	0.64	0.0517	0.0039	0.0874	0.0067	0.0123	0.0003	0.0041	0.0002	0.00	72.1	2.1	81.9	8.1	320	210	72.1	2.1
12	390	157	0.40	0.0482	0.0050	0.0721	0.0069	0.0108	0.0003	0.0042	0.0003	-0.09	72.1	1.3	74.0	3.8	170	110	72.1	1.3
13	406	180	0.44	0.0488	0.0036	0.0816	0.0062	0.0122	0.0003	0.0041	0.0003	0.13	72.2	2.2	95.0	11.0	620	230	72.2	2.2
14	401	250	0.62	0.0478	0.0054	0.0830	0.0090	0.0120	0.0002	0.0042	0.0002	-0.25	72.2	2.3	90.0	13.0	490	300	72.2	2.3
15	858	658	0.77	0.0553	0.0034	0.0838	0.0052	0.0110	0.0002	0.0037	0.0002	0.04	72.4	1.8	101.2	9.6	910	180	72.4	1.8
16	1080	1310	1.21	0.0502	0.0021	0.1906	0.0087	0.0276	0.0004	0.0089	0.0004	-0.15	72.5	1.2	73.7	3.9	130	110	72.5	1.2
17	702	540	0.77	0.0539	0.0032	0.0905	0.0055	0.0122	0.0002	0.0040	0.0003	0.06	72.6	1.4	74.3	5.2	140	130	72.6	1.4
18	350	139	0.40	0.0550	0.0025	0.3650	0.0180	0.0489	0.0008	0.0163	0.0008	-0.08	72.7	1.3	83.7	5.3	380	140	72.7	1.3
19	146	93	0.64	0.0519	0.0039	0.2860	0.0210	0.0397	0.0009	0.0123	0.0008	-0.01	73.2	1.9	90.0	8.2	590	200	73.2	1.9
20	100	113	1.13	0.0556	0.0037	0.3510	0.0240	0.0467	0.0011	0.0147	0.0007	-0.06	73.7	2.4	98.0	12.0	750	220	73.7	2.4

21	129	77	0.60	0.0508	0.0069	0.0870	0.0110	0.0127	0.0004	0.0041	0.0004	-0.23	74.2	1.5	76.4	5.2	140	140	74.2	1.5
22	196	194	0.99	0.0564	0.0055	0.0914	0.0079	0.0120	0.0003	0.0042	0.0003	-0.10	74.2	1.8	84.1	8.6	460	200	74.2	1.8
23	482	624	1.29	0.0517	0.0044	0.0733	0.0066	0.0107	0.0002	0.0035	0.0002	0.01	74.9	1.5	90.0	6.2	560	150	74.9	1.5
24	647	2510	3.88	0.0510	0.0035	0.0841	0.0061	0.0121	0.0002	0.0037	0.0002	-0.13	75.9	1.6	108.3	9.4	830	170	75.9	1.6
25	210	187	0.89	0.0615	0.0070	0.0960	0.0120	0.0113	0.0003	0.0043	0.0003	-0.10	76.6	1.9	91.0	7.4	540	200	76.6	1.9
26	308	292	0.95	0.0524	0.0049	0.1450	0.0160	0.0204	0.0006	0.0064	0.0007	-0.12	76.7	1.5	80.4	8.3	130	200	76.7	1.5
27	225	126	0.56	0.0497	0.0041	0.1113	0.0093	0.0163	0.0004	0.0054	0.0004	0.13	77.3	1.8	94.4	10.0	530	190	77.3	1.8
28	96	99	1.04	0.0600	0.0090	0.0930	0.0140	0.0113	0.0004	0.0039	0.0003	-0.13	77.4	1.7	83.8	7.0	220	180	77.4	1.7
29	368	365	0.99	0.0581	0.0041	0.0915	0.0067	0.0117	0.0002	0.0040	0.0002	0.09	77.6	1.3	81.9	5.7	270	150	77.6	1.3
30	75	74	0.98	0.0578	0.0063	0.3660	0.0440	0.0475	0.0009	0.0160	0.0010	0.15	77.6	1.6	82.5	5.3	250	130	77.6	1.6
31	463	249	0.54	0.0505	0.0032	0.0848	0.0057	0.0121	0.0003	0.0041	0.0003	-0.03	77.9	1.8	79.5	5.8	100	150	77.9	1.8
32	183	95	0.52	0.1893	0.0058	13.5700	0.5000	0.5244	0.0069	0.1431	0.0061	0.53	78.0	1.2	79.0	4.5	110	120	78.0	1.2
33	350	158	0.45	0.0486	0.0037	0.0855	0.0068	0.0126	0.0003	0.0042	0.0003	0.12	78.1	1.6	80.7	6.3	130	160	78.1	1.6
34	180	128	0.71	0.0515	0.0040	0.2380	0.0190	0.0330	0.0008	0.0108	0.0007	-0.25	78.2	1.4	87.9	5.1	360	120	78.2	1.4
35	853	506	0.59	0.0554	0.0036	0.0861	0.0057	0.0113	0.0002	0.0038	0.0002	-0.06	78.6	2.8	78.0	13.0	110	290	78.6	2.8
36	131	77	0.58	0.0514	0.0049	0.1760	0.0170	0.0244	0.0006	0.0081	0.0005	0.04	78.9	1.7	86.3	6.2	250	160	78.9	1.7
37	1168	1981	1.70	0.0484	0.0027	0.0809	0.0048	0.0122	0.0002	0.0038	0.0002	0.37	79.7	3.9	102.0	21.0	540	370	79.7	3.9
38	298	195	0.65	0.0492	0.0032	0.1940	0.0150	0.0278	0.0006	0.0090	0.0006	0.29	80.7	1.8	83.1	6.3	120	160	80.7	1.8
39	126	75	0.60	0.0530	0.0068	0.1990	0.0260	0.0274	0.0008	0.0096	0.0009	-0.39	81.1	2.6	84.0	10.0	90	260	81.1	2.6
40	165	132	0.80	0.0573	0.0039	0.3660	0.0270	0.0466	0.0009	0.0150	0.0008	-0.09	81.8	1.6	100.8	6.9	530	150	81.8	1.6
41	657	435	0.66	0.0495	0.0034	0.0783	0.0055	0.0116	0.0002	0.0037	0.0002	0.15	88.1	1.7	93.3	7.4	270	180	88.1	1.7
42	108	94	0.87	0.0544	0.0040	0.3390	0.0250	0.0453	0.0010	0.0148	0.0009	0.06	93.6	3.2	133.0	17.0	710	240	93.6	3.2
43	94	56	0.60	0.0709	0.0093	0.1420	0.0190	0.0146	0.0005	0.0054	0.0006	-0.37	104.3	2.4	106.8	8.5	190	170	104.3	2.4
44	155	93	0.60	0.0519	0.0055	0.2100	0.0210	0.0293	0.0007	0.0098	0.0006	-0.16	126.9	2.6	140.0	9.1	340	150	126.9	2.6
45	217	91	0.42	0.0547	0.0054	0.0842	0.0087	0.0112	0.0003	0.0040	0.0004	0.12	129.9	3.8	137.0	14.0	260	180	129.9	3.8

46	164	94	0.57	0.0542	0.0033	0.3520	0.0230	0.0472	0.0009	0.0146	0.0008	0.22	143.2	3.6	162.0	17.0	370	210	143.2	3.6
47	511	407	0.80	0.0528	0.0026	0.1898	0.0098	0.0265	0.0005	0.0083	0.0004	0.01	147.7	3.0	150.3	8.7	170	130	147.7	3.0
48	730	401	0.55	0.0560	0.0035	0.0864	0.0056	0.0112	0.0002	0.0038	0.0002	-0.22	150.5	3.6	169.0	19.0	370	240	150.5	3.6
49	166	95	0.57	0.0630	0.0074	0.1020	0.0130	0.0115	0.0004	0.0042	0.0004	-0.12	152.1	4.4	212.0	22.0	950	240	152.1	4.4
50	745	484	0.65	0.0498	0.0025	0.0757	0.0042	0.0113	0.0002	0.0037	0.0002	-0.02	155.6	3.8	163.0	15.0	270	200	155.6	3.8
51	256	108	0.42	0.0700	0.0068	0.1050	0.0110	0.0113	0.0003	0.0048	0.0005	-0.16	166.9	2.5	170.7	7.8	204	98	166.9	2.5
52	220	90	0.41	0.0576	0.0053	0.0856	0.0077	0.0108	0.0003	0.0042	0.0003	0.02	168.6	2.9	176.3	8.3	320	110	168.6	2.9
53	330	314	0.95	0.0513	0.0048	0.0850	0.0079	0.0121	0.0003	0.0042	0.0002	-0.10	170.7	2.9	170.7	8.3	176	110	170.7	2.9
54	50	45	0.92	0.0585	0.0058	0.3660	0.0370	0.0471	0.0013	0.0154	0.0011	0.10	174.2	5.3	182.0	21.0	200	220	174.2	5.3
55	275	157	0.57	0.0591	0.0057	0.0977	0.0110	0.0121	0.0003	0.0045	0.0003	0.04	175.2	2.7	177.0	7.4	193	94	175.2	2.7
56	230	124	0.54	0.0617	0.0057	0.0929	0.0089	0.0114	0.0003	0.0039	0.0003	-0.26	177.0	3.9	181.0	12.0	170	140	177.0	3.9
57	138	188	1.36	0.0538	0.0063	0.1660	0.0200	0.0225	0.0006	0.0078	0.0005	-0.21	186.2	4.1	199.0	17.0	370	200	186.2	4.1
58	157	195	1.24	0.0524	0.0062	0.2480	0.0290	0.0327	0.0011	0.0106	0.0007	-0.43	202.6	2.7	202.6	7.2	222	76	202.6	2.7
59	127	92	0.72	0.0650	0.0093	0.0950	0.0130	0.0109	0.0004	0.0040	0.0003	0.09	207.3	6.7	224.0	22.0	340	220	207.3	6.7
60	230	82	0.36	0.0490	0.0048	0.0730	0.0071	0.0107	0.0003	0.0037	0.0003	-0.18	209.0	5.1	218.0	15.0	260	150	209.0	5.1
61	368	204	0.56	0.0528	0.0046	0.0953	0.0082	0.0138	0.0003	0.0047	0.0003	0.00	216.6	5.7	225.0	17.0	330	180	216.6	5.7
62	912	551	0.60	0.0488	0.0024	0.0753	0.0041	0.0113	0.0002	0.0036	0.0002	0.08	250.4	6.2	269.0	21.0	490	160	250.4	6.2
63	135	115	0.85	0.0611	0.0038	0.3940	0.0250	0.0462	0.0009	0.0158	0.0008	0.03	250.7	5.8	254.0	17.0	280	150	250.7	5.8
64	227	163	0.72	0.0542	0.0027	0.3480	0.0200	0.0469	0.0008	0.0153	0.0007	-0.10	285.8	5.8	294.0	19.0	370	160	285.8	5.8
65	994	228	0.23	0.0505	0.0022	0.1819	0.0091	0.0262	0.0004	0.0089	0.0004	0.29	287.0	5.4	308.0	19.0	380	160	287.0	5.4
66	357	309	0.87	0.0594	0.0039	0.1045	0.0075	0.0128	0.0003	0.0046	0.0002	-0.01	287.9	7.0	320.0	26.0	470	190	287.9	7.0
67	94	83	0.89	0.0542	0.0048	0.2490	0.0200	0.0342	0.0009	0.0114	0.0007	-0.02	291.0	5.8	336.0	18.0	670	120	291.0	5.8
68	71	53	0.75	0.0519	0.0043	0.3380	0.0260	0.0465	0.0011	0.0153	0.0009	-0.02	292.7	6.7	293.0	20.0	260	160	292.7	6.7
69	66	48	0.73	0.0559	0.0043	0.3060	0.0270	0.0396	0.0010	0.0145	0.0009	0.31	293.6	5.5	315.0	19.0	520	140	293.6	5.5
70	3318	1284	0.39	0.0505	0.0017	0.2209	0.0089	0.0319	0.0004	0.0107	0.0004	0.08	293.6	7.5	291.0	18.0	330	130	293.6	7.5

71	424	164	0.39	0.0544	0.0037	0.1480	0.0100	0.0199	0.0004	0.0066	0.0004	-0.03	294.4	6.6	304.0	18.0	380	140	294.4	6.6
72	104	71	0.69	0.0560	0.0043	0.3490	0.0260	0.0455	0.0009	0.0154	0.0008	-0.23	295.7	4.8	307.0	14.0	357	110	295.7	4.8
73	119	139	1.17	0.0545	0.0035	0.3340	0.0240	0.0466	0.0012	0.0136	0.0007	-0.11	296.8	7.9	322.0	28.0	490	220	296.8	7.9
74	452	427	0.94	0.0494	0.0026	0.1834	0.0097	0.0268	0.0005	0.0085	0.0004	0.01	296.9	5.7	317.0	20.0	450	150	296.9	5.7
75	271	190	0.70	0.0550	0.0056	0.0870	0.0093	0.0116	0.0003	0.0040	0.0003	-0.16	297.1	5.2	305.0	17.0	340	130	297.1	5.2
76	340	213	0.63	0.0524	0.0064	0.0749	0.0096	0.0108	0.0003	0.0037	0.0003	-0.15	298.9	5.8	312.0	31.0	500	190	298.9	5.8
77	304	218	0.72	0.0496	0.0029	0.1599	0.0100	0.0232	0.0005	0.0073	0.0004	0.01	307.9	5.0	317.0	13.0	387	99	307.9	5.0
78	114	113	0.99	0.0477	0.0077	0.0810	0.0140	0.0123	0.0004	0.0037	0.0003	0.31	534.4	7.0	536.1	16.0	542	68	534.4	7.0
79	384	244	0.64	0.0495	0.0040	0.0829	0.0067	0.0122	0.0003	0.0042	0.0003	-0.19	546.0	12.0	600.0	32.0	820	150	546.0	12.0
80	45	52	1.14	0.0668	0.0047	0.7980	0.0560	0.0884	0.0019	0.0291	0.0016	0.05	1237.0	22.0	1279.0	40.0	1340	100	1237.0	22.0
81	165	124	0.75	0.0554	0.0036	0.3600	0.0260	0.0471	0.0009	0.0155	0.0008	-0.16	2717.0	29.0	2720.0	37.0	2734	50	2734.0	50.0

Sample N-1

				CORRECTED RATIOS									CORRECTED AGES (Ma)							
	U (ppm)	Th (ppm)	Th/U	$^{207}Pb/^{206}Pb$	±2s abs	$^{207}Pb/^{235}U$	±2s abs	$^{206}Pb/^{238}U$	±2s abs	$^{208}Pb/^{232}Th$	±2s abs	Rho	$^{206}Pb/^{238}U$	±2s	$^{207}Pb/^{235}U$	±2s	$^{207}Pb/^{206}Pb$	±2s	Best age (Ma)	±2s
1	107	65	0.61	0.0593	0.0055	0.3240	0.0300	0.0396	0.0011	0.0142	0.0009	0.29	66.2	3.1	68.8	9.1	150	180	66.2	3.1
2	140	160	1.14	0.0650	0.0100	0.0940	0.0150	0.0107	0.0004	0.0038	0.0003	-0.08	68.3	2.3	91.0	13.0	640	300	68.3	2.3
3	377	143	0.38	0.0729	0.0023	1.7560	0.0680	0.1755	0.0025	0.0509	0.0022	-0.02	68.6	3.1	87.0	15.0	580	320	68.6	3.1
4	563	405	0.72	0.0510	0.0048	0.0890	0.0081	0.0126	0.0003	0.0043	0.0002	0.11	69.3	3.1	92.0	14.0	590	280	69.3	3.1
5	65	22	0.34	0.0549	0.0072	0.1780	0.0210	0.0237	0.0009	0.0074	0.0008	0.03	69.8	3.6	86.0	18.0	260	430	69.8	3.6
6	170	149	0.88	0.0498	0.0074	0.0790	0.0110	0.0117	0.0003	0.0037	0.0003	-0.17	71.4	1.5	76.8	5.6	190	140	71.4	1.5
7	55	43	0.78	0.0515	0.0059	0.2930	0.0330	0.0409	0.0012	0.0136	0.0009	0.24	71.7	2.2	93.0	9.9	800	220	71.7	2.2
8	1050	1111	1.06	0.0486	0.0033	0.0808	0.0063	0.0123	0.0002	0.0038	0.0002	0.34	72.3	1.2	74.8	5.3	150	150	72.3	1.2
9	102	69	0.68	0.0613	0.0110	0.0900	0.0170	0.0107	0.0005	0.0036	0.0005	0.12	73.0	1.2	74.2	4.3	140	120	73.0	1.2
10	48	39	0.81	0.0600	0.0140	0.0860	0.0200	0.0109	0.0006	0.0039	0.0004	-0.10	73.0	1.5	75.9	5.5	230	140	73.0	1.5
11	129	97	0.75	0.0606	0.0064	0.1000	0.0110	0.0118	0.0004	0.0044	0.0003	0.22	73.1	2.5	84.0	11.0	340	280	73.1	2.5
12	551	1119	2.03	0.0498	0.0024	0.1592	0.0090	0.0231	0.0004	0.0073	0.0003	0.25	73.3	1.8	85.0	7.6	350	190	73.3	1.8
13	395	253	0.64	0.0490	0.0035	0.0830	0.0062	0.0120	0.0003	0.0037	0.0002	0.13	73.6	2.0	99.0	12.0	680	240	73.6	2.0
14	495	600	1.21	0.0497	0.0049	0.0703	0.0099	0.0103	0.0005	0.0032	0.0002	0.29	73.8	1.4	80.9	6.3	290	160	73.8	1.4
15	416	216	0.52	0.0610	0.0042	0.0990	0.0085	0.0123	0.0003	0.0046	0.0003	0.10	74.3	2.2	85.0	9.7	400	220	74.3	2.2
16	117	74	0.63	0.0572	0.0040	0.3330	0.0250	0.0431	0.0009	0.0147	0.0009	-0.12	74.4	1.8	73.3	5.6	110	160	74.4	1.8
17	404	236	0.58	0.0517	0.0039	0.0864	0.0066	0.0122	0.0002	0.0040	0.0003	-0.11	74.5	2.6	99.0	15.0	820	280	74.5	2.6
18	74	54	0.72	0.0555	0.0043	0.3520	0.0280	0.0453	0.0010	0.0150	0.0008	0.12	74.8	1.5	76.0	5.1	110	140	74.8	1.5
19	452	375	0.83	0.0496	0.0036	0.0897	0.0062	0.0132	0.0003	0.0041	0.0003	0.03	75.2	2.0	76.6	10.0	200	260	75.2	2.0
20	212	207	0.98	0.0541	0.0055	0.1050	0.0120	0.0140	0.0003	0.0041	0.0003	0.32	75.2	2.1	78.1	8.7	140	240	75.2	2.1

21	83	29	0.35	0.0600	0.0110	0.1430	0.0250	0.0175	0.0007	0.0061	0.0010	0.01	75.3	2.5	96.0	9.7	650	210	75.3	2.5
22	194	115	0.59	0.0537	0.0070	0.0904	0.0160	0.0121	0.0004	0.0045	0.0004	-0.06	75.8	2.0	79.6	6.2	210	180	75.8	2.0
23	383	205	0.54	0.0607	0.0048	0.1071	0.0079	0.0125	0.0003	0.0048	0.0003	-0.25	76.2	2.2	82.2	8.4	170	210	76.2	2.2
24	210	122	0.58	0.0518	0.0029	0.3270	0.0190	0.0459	0.0009	0.0147	0.0008	-0.12	76.8	2.7	83.0	12.0	140	280	76.8	2.7
25	109	61	0.56	0.0529	0.0055	0.1590	0.0170	0.0225	0.0006	0.0069	0.0006	0.07	77.1	1.6	80.8	6.0	140	140	77.1	1.6
26	232	140	0.60	0.0613	0.0042	0.2670	0.0180	0.0318	0.0006	0.0108	0.0006	0.01	77.4	2.7	87.6	14.0	280	240	77.4	2.7
27	94	102	1.09	0.0536	0.0039	0.3530	0.0240	0.0482	0.0012	0.0150	0.0008	0.06	77.5	1.8	79.0	6.0	230	170	77.5	1.8
28	105	83	0.80	0.0538	0.0077	0.0820	0.0130	0.0114	0.0004	0.0040	0.0004	0.17	77.9	1.4	84.0	6.2	250	160	77.9	1.4
29	174	136	0.78	0.0542	0.0130	0.3510	0.1100	0.0468	0.0014	0.0156	0.0027	0.24	78.1	1.7	77.8	6.8	70	190	78.1	1.7
30	108	84	0.77	0.0530	0.0088	0.0950	0.0150	0.0125	0.0004	0.0042	0.0005	0.12	78.7	1.4	78.9	5.8	120	140	78.7	1.4
31	252	199	0.79	0.0533	0.0050	0.0859	0.0082	0.0114	0.0003	0.0037	0.0003	0.02	78.7	1.6	81.2	5.8	140	150	78.7	1.6
32	272	299	1.10	0.0511	0.0035	0.1790	0.0120	0.0257	0.0005	0.0080	0.0004	-0.03	78.9	1.9	95.7	7.8	580	150	78.9	1.9
33	1211	1192	0.98	0.0486	0.0023	0.0841	0.0045	0.0125	0.0002	0.0040	0.0002	0.17	78.9	1.5	86.9	6.4	310	180	78.9	1.5
34	131	65	0.49	0.0580	0.0033	0.3740	0.0240	0.0472	0.0010	0.0169	0.0008	-0.10	79.2	2.9	88.0	17.0	340	290	79.2	2.9
35	266	232	0.87	0.0504	0.0045	0.1520	0.0140	0.0217	0.0006	0.0073	0.0005	-0.03	79.3	2.4	87.0	11.0	280	240	79.3	2.4
36	247	135	0.55	0.0561	0.0035	0.3070	0.0190	0.0407	0.0008	0.0144	0.0007	-0.12	79.3	1.7	76.8	5.6	-10	150	79.3	1.7
37	646	520	0.80	0.0524	0.0038	0.0886	0.0067	0.0125	0.0002	0.0043	0.0002	0.00	79.6	5.5	85.0	62.0	90	450	79.6	5.5
38	125	105	0.84	0.0551	0.0064	0.0870	0.0110	0.0116	0.0004	0.0045	0.0003	0.04	79.8	1.3	86.1	6.5	290	160	79.8	1.3
39	80	48	0.60	0.0577	0.0042	0.3680	0.0280	0.0488	0.0010	0.0153	0.0011	0.07	79.9	2.5	91.0	14.0	260	320	79.9	2.5
40	156	90	0.58	0.0521	0.0046	0.1680	0.0150	0.0237	0.0005	0.0078	0.0005	-0.14	79.9	1.4	82.5	6.5	170	160	79.9	1.4
41	116	86	0.74	0.0653	0.0084	0.1030	0.0130	0.0115	0.0003	0.0044	0.0004	-0.02	80.2	1.9	103.0	7.3	610	180	80.2	1.9
42	112	61	0.55	0.0639	0.0088	0.1090	0.0150	0.0126	0.0004	0.0054	0.0005	0.07	80.3	1.5	81.9	4.2	118	100	80.3	1.5
43	166	122	0.73	0.0490	0.0057	0.0804	0.0093	0.0117	0.0003	0.0039	0.0003	0.01	80.5	1.6	86.0	7.5	170	190	80.5	1.6
44	421	220	0.52	0.0523	0.0023	0.3460	0.0170	0.0480	0.0007	0.0153	0.0007	0.19	80.6	2.8	104.0	14.0	560	270	80.6	2.8
45	131	135	1.03	0.0604	0.0029	0.8510	0.0450	0.1023	0.0018	0.0314	0.0014	0.15	84.4	1.8	87.2	5.7	190	140	84.4	1.8

46	277	107	0.39	0.0475	0.0043	0.0799	0.0072	0.0122	0.0003	0.0042	0.0003	-0.10	85.0	2.5	116.0	14.0	730	240	85.0	2.5
47	506	344	0.68	0.0523	0.0044	0.0896	0.0069	0.0123	0.0002	0.0040	0.0002	-0.45	86.0	3.2	95.0	19.0	350	360	86.0	3.2
48	481	351	0.73	0.0478	0.0035	0.0750	0.0059	0.0116	0.0003	0.0037	0.0002	0.16	89.7	2.1	101.0	11.0	390	220	89.7	2.1
49	423	348	0.82	0.0488	0.0026	0.1809	0.0100	0.0268	0.0005	0.0085	0.0004	-0.02	89.9	1.7	90.4	4.1	109	92	89.9	1.7
50	174	101	0.58	0.0532	0.0047	0.1910	0.0160	0.0263	0.0006	0.0089	0.0005	-0.10	89.9	2.3	93.5	9.8	190	220	89.9	2.3
51	385	298	0.77	0.0497	0.0039	0.0810	0.0064	0.0121	0.0003	0.0040	0.0002	0.18	91.2	2.6	95.0	14.0	130	290	91.2	2.6
52	93	66	0.71	0.0510	0.0320	0.0880	0.0860	0.0124	0.0009	0.0046	0.0011	0.20	93.8	2.6	97.6	9.2	190	200	93.8	2.6
53	360	134	0.37	0.0575	0.0026	0.6100	0.0280	0.0769	0.0012	0.0290	0.0014	0.06	112.0	4.4	134.0	22.0	450	340	112.0	4.4
54	88	35	0.40	0.0520	0.0110	0.1000	0.0210	0.0134	0.0005	0.0056	0.0006	-0.03	126.4	3.8	135.0	17.0	440	250	126.4	3.8
55	124	94	0.76	0.0492	0.0057	0.0830	0.0094	0.0119	0.0004	0.0040	0.0003	0.20	138.2	3.9	143.0	12.0	160	190	138.2	3.9
56	94	73	0.77	0.0523	0.0065	0.1590	0.0200	0.0219	0.0005	0.0078	0.0006	-0.12	139.5	3.4	157.0	18.0	350	250	139.5	3.4
57	214	45	0.21	0.0583	0.0025	0.6260	0.0290	0.0787	0.0013	0.0283	0.0016	0.00	143.1	3.7	153.0	15.0	290	220	143.1	3.7
58	88	87	0.99	0.0566	0.0042	0.3730	0.0280	0.0488	0.0011	0.0157	0.0010	0.16	146.9	2.3	150.6	8.1	214	110	146.9	2.3
59	463	221	0.48	0.0516	0.0034	0.0777	0.0058	0.0114	0.0002	0.0037	0.0003	0.43	150.8	5.4	168.0	18.0	350	250	150.8	5.4
60	92	82	0.89	0.0689	0.0074	0.3090	0.0340	0.0326	0.0009	0.0122	0.0010	-0.23	150.9	3.4	157.0	13.0	220	170	150.9	3.4
61	91	49	0.53	0.0555	0.0046	0.2360	0.0210	0.0301	0.0009	0.0107	0.0008	0.02	163.5	2.9	166.9	11.0	210	140	163.5	2.9
62	192	109	0.57	0.0658	0.0089	0.1210	0.0150	0.0133	0.0004	0.0054	0.0005	0.08	167.4	3.8	176.0	13.0	300	180	167.4	3.8
63	120	122	1.02	0.0525	0.0036	0.3370	0.0240	0.0465	0.0010	0.0151	0.0008	0.05	170.6	2.9	169.8	8.4	143	110	170.6	2.9
64	1017	614	0.60	0.0485	0.0027	0.0759	0.0046	0.0114	0.0002	0.0035	0.0002	0.08	181.6	6.0	219.0	17.0	650	190	181.6	6.0
65	2190	922	0.42	0.0479	0.0020	0.0932	0.0044	0.0141	0.0003	0.0048	0.0002	0.24	190.9	5.3	217.0	17.0	470	180	190.9	5.3
66	73	38	0.52	0.0534	0.0051	0.2200	0.0220	0.0304	0.0009	0.0104	0.0010	0.20	193.0	5.8	203.0	19.0	320	200	193.0	5.8
67	83	28	0.34	0.0501	0.0080	0.0990	0.0160	0.0143	0.0004	0.0056	0.0007	0.02	201.6	3.9	240.0	14.0	600	140	201.6	3.9
68	418	225	0.54	0.0542	0.0021	0.3650	0.0160	0.0492	0.0008	0.0161	0.0007	0.36	206.9	5.3	271.0	25.0	820	190	206.9	5.3
69	98	61	0.62	0.0596	0.0040	0.3960	0.0270	0.0484	0.0010	0.0158	0.0008	-0.12	250.4	6.9	282.0	23.0	540	190	250.4	6.9
70	1116	461	0.41	0.0559	0.0021	0.5180	0.0210	0.0681	0.0021	0.0213	0.0009	0.52	254.4	5.9	281.0	23.0	490	180	254.4	5.9

71	78	40	0.51	0.0580	0.0052	0.3210	0.0310	0.0403	0.0009	0.0148	0.0010	0.30	257.0	4.8	275.0	15.0	410	130	257.0	4.8
72	177	103	0.59	0.0511	0.0053	0.1013	0.0100	0.0147	0.0004	0.0048	0.0004	-0.10	258.6	7.4	259.0	25.0	200	200	258.6	7.4
73	831	649	0.78	0.0498	0.0036	0.0766	0.0056	0.0113	0.0002	0.0039	0.0002	0.06	265.1	4.2	269.8	16.0	296	120	265.1	4.2
74	106	153	1.44	0.0617	0.0032	0.8250	0.0470	0.0970	0.0017	0.0316	0.0014	0.34	271.7	5.4	293.0	20.0	470	170	271.7	5.4
75	79	45	0.57	0.0617	0.0055	0.2440	0.0210	0.0286	0.0010	0.0107	0.0008	0.15	278.5	4.3	277.0	14.0	280	130	278.5	4.3
76	247	91	0.37	0.0545	0.0026	0.3620	0.0210	0.0479	0.0009	0.0181	0.0009	0.00	285.3	6.3	308.0	21.0	420	160	285.3	6.3
77	829	538	0.65	0.0480	0.0033	0.0778	0.0054	0.0117	0.0002	0.0038	0.0002	0.08	289.3	5.5	287.0	15.0	260	130	289.3	5.5
78	533	354	0.66	0.0497	0.0038	0.0835	0.0062	0.0123	0.0003	0.0041	0.0002	-0.09	290.7	5.2	294.0	15.0	300	130	290.7	5.2
79	213	237	1.11	0.0520	0.0029	0.3140	0.0180	0.0442	0.0007	0.0136	0.0006	0.03	292.9	6.1	296.0	19.0	260	140	292.9	6.1
80	430	202	0.47	0.0497	0.0038	0.0848	0.0068	0.0125	0.0002	0.0043	0.0003	-0.06	294.8	8.4	305.0	62.0	350	230	294.8	8.4
81	449	260	0.58	0.0529	0.0033	0.3050	0.0210	0.0420	0.0007	0.0133	0.0007	0.08	297.5	6.1	322.0	18.0	480	130	297.5	6.1
82	768	467	0.61	0.0504	0.0035	0.0786	0.0060	0.0111	0.0002	0.0038	0.0002	0.01	298.7	5.1	299.0	18.0	260	150	298.7	5.1
83	103	92	0.90	0.0523	0.0100	0.0920	0.0180	0.0124	0.0005	0.0042	0.0004	0.05	301.4	5.4	313.0	15.0	360	99	301.4	5.4
84	108	81	0.75	0.0507	0.0075	0.0830	0.0130	0.0120	0.0004	0.0038	0.0004	0.24	302.2	4.2	301.1	13.0	289	98	302.2	4.2
85	119	117	0.98	0.0623	0.0098	0.0960	0.0160	0.0108	0.0005	0.0039	0.0004	0.16	303.4	7.2	306.0	18.0	350	140	303.4	7.2
86	211	153	0.72	0.0515	0.0057	0.0970	0.0110	0.0141	0.0004	0.0046	0.0003	0.02	304.6	6.3	337.0	19.0	550	150	304.6	6.3
87	124	54	0.44	0.0529	0.0071	0.0900	0.0120	0.0124	0.0004	0.0046	0.0005	0.06	306.9	6.1	317.0	21.0	440	170	306.9	6.1
88	443	267	0.60	0.0450	0.0032	0.0787	0.0060	0.0124	0.0003	0.0042	0.0003	-0.17	307.2	6.8	326.0	22.0	450	160	307.2	6.8
89	768	576	0.75	0.0536	0.0042	0.0831	0.0067	0.0115	0.0002	0.0034	0.0002	-0.23	309.3	4.7	317.0	11.0	395	89	309.3	4.7
90	319	197	0.62	0.0503	0.0042	0.0817	0.0066	0.0118	0.0003	0.0038	0.0003	0.39	424.4	13.0	425.3	15.0	453	79	424.4	13.0
91	178	89	0.50	0.0620	0.0061	0.0970	0.0100	0.0112	0.0003	0.0047	0.0004	0.13	477.8	7.4	483.0	19.0	510	93	477.8	7.4
92	113	78	0.69	0.0650	0.0110	0.1040	0.0170	0.0116	0.0004	0.0045	0.0004	-0.51	488.0	7.5	499.0	18.0	548	91	488.0	7.5
93	104	109	1.05	0.0542	0.0071	0.1440	0.0190	0.0198	0.0006	0.0067	0.0004	0.04	597.0	9.9	608.0	26.0	630	110	597.0	9.9
94	201	143	0.71	0.0527	0.0030	0.3350	0.0200	0.0461	0.0008	0.0151	0.0008	0.01	628.0	11.0	626.0	25.0	614	100	628.0	11.0
95	350	192	0.55	0.0521	0.0036	0.3430	0.0240	0.0474	0.0008	0.0151	0.0009	-0.20	1042.3	13.0	1029.0	25.0	1015	68	1042.3	13.0

Sample SP3-85

				CORRECTED RATIOS									CORRECTED AGES (Ma)							
n°	U (ppm)	Th (ppm)	Th/U	$^{207}Pb/^{206}Pb$	±2s abs	$^{207}Pb/^{235}U$	±2s abs	$^{206}Pb/^{238}U$	±2s abs	$^{208}Pb/^{232}Th$	±2s abs	Rho	$^{206}Pb/^{238}U$	±2s	$^{207}Pb/^{235}U$	±2s	$^{207}Pb/^{206}Pb$	±2s	Best age (Ma)	±2s
1	65	53	0.81	0.072	0.026	0.44	0.1700	0.0455	0.0013	0.0154	0.0010	0.17	286.9	8.3	361	44	790	250	286.9	8
2	95	42	0.44	0.0619	0.0096	0.091	0.0150	0.01065	0.0007	0.00417	0.0006	-0.23	68.3	4.4	88	14	550	300	68.3	4
3	30	21	0.68	0.051	0.026	0.101	0.0530	0.0152	0.0013	0.0058	0.0012	-0.05	97.2	8.2	94	44	60	520	97.2	8
4	105	101	0.96	0.061	0.0047	0.366	0.0330	0.0468	0.0012	0.01461	0.0007	0.17	294.7	7.5	314	23	540	130	294.7	8
5	107	90	0.84	0.057	0.0046	0.349	0.0300	0.0465	0.0014	0.0154	0.0010	-0.09	293	8.8	302	22	440	150	293.0	9
6	132	90	0.68	0.0553	0.0067	0.34	0.0370	0.0464	0.0013	0.0156	0.0014	-0.01	292.6	8.1	295	27	370	180	292.6	8
7	173	103	0.59	0.054	0.0042	0.344	0.0290	0.0482	0.0012	0.01635	0.0007	-0.15	303.5	7.6	304	18	360	140	303.5	8
8	193	93	0.48	0.0514	0.0066	0.098	0.0140	0.0143	0.0018	0.00532	0.0003	-0.03	92	11	94	13	180	230	92.0	11
9	252	157	0.62	0.0536	0.0077	0.328	0.0490	0.0458	0.0014	0.01614	0.0006	0.07	288.9	8.8	287	30	330	120	288.9	9
10	228	116	0.51	0.081	0.048	0.167	0.0500	0.02152	0.0006	0.00738	0.0004	0.02	137.2	3.5	135	11	490	420	137.2	4
11	94	54	0.57	0.0504	0.0069	0.154	0.0210	0.02267	0.0009	0.0092	0.0026	-0.01	144.5	5.3	144	19	140	240	144.5	5
12	184	111	0.60	0.0567	0.0036	0.357	0.0260	0.0464	0.0013	0.01598	0.0007	-0.09	292.5	8.2	308	19	490	120	292.5	8
13	84	69	0.83	0.067	0.024	0.107	0.0400	0.01241	0.0005	0.00435	0.0004	0.02	79.5	3.1	98	30	300	370	79.5	3
14	121	59	0.48	0.0519	0.0096	0.077	0.0140	0.01111	0.0004	0.00375	0.0005	0.17	71.2	2.6	74	13	120	310	71.2	3
15	312	316	1.01	0.052	0.018	0.094	0.0370	0.01326	0.0005	0.0045	0.0020	-0.10	84.9	3.4	91	22	220	260	84.9	3
16	103	52	0.51	0.0614	0.0076	0.185	0.0240	0.02241	0.0006	0.00807	0.0006	0.04	142.9	3.9	170	20	490	220	142.9	4
17	124	87	0.70	0.061	0.012	0.093	0.0160	0.01091	0.0004	0.00466	0.0004	0.01	69.9	2.7	90	15	670	290	69.9	3
18	320	205	0.64	0.0566	0.0075	0.361	0.0550	0.0466	0.0010	0.01493	0.0005	-0.03	293.8	6.3	305	33	280	110	293.8	6
19	186	167	0.90	0.0553	0.0033	0.348	0.0260	0.0475	0.0011	0.01545	0.0010	-0.43	299.1	6.5	305	18	410	120	299.1	7
20	487	521	1.07	0.0536	0.0022	0.319	0.0190	0.04468	0.0010	0.01409	0.0003	0.90	281.8	6	281	15	354	89	281.8	6
21	111	50	0.45	0.052	0.013	0.094	0.0220	0.01378	0.0005	0.00432	0.0005	0.14	88.2	3	90	19	200	310	88.2	3
22	85	51	0.59	0.06	0.045	0.11	0.1000	0.01525	0.0007	0.00567	0.0007	0.10	97.6	4.2	107	33	370	470	97.6	4
23	256	82	0.32	0.054	0.016	0.093	0.0110	0.0138	0.0004	0.00417	0.0003	0.11	88.3	2.6	90	10	290	230	88.3	3

24	120	58	0.48	0.067	0.01	0.11	0.0160	0.01224	0.0005	0.00538	0.0006	-0.19	78.4	3.1	105	14	750	240	78.4	3
25	94	100	1.06	0.045	0.011	0.07	0.0160	0.01079	0.0005	0.00317	0.0003	-0.08	69.2	3.1	67	15	-110	360	69.2	3
26	316	267	0.84	0.0551	0.0032	0.348	0.0250	0.0458	0.0012	0.0144	0.0005	-0.07	288.5	7.1	302	18	390	110	288.5	7
27	219	181	0.83	0.0536	0.0082	0.312	0.0830	0.0424	0.0011	0.0131	0.0007	-0.03	267.5	6.8	275	28	350	110	267.5	7
28	122	78	0.64	0.068	0.012	0.203	0.0370	0.02165	0.0008	0.008	0.0017	0.05	138.1	4.9	183	28	530	240	138.1	5
29	160	180	1.13	0.0538	0.0048	0.334	0.0330	0.0446	0.0011	0.01359	0.0005	0.12	281	6.7	290	24	260	140	281.0	7
30	659	306	0.46	0.0472	0.004	0.0846	0.0088	0.01188	0.0004	0.00388	0.0003	0.30	76.1	2.8	82.2	8.1	80	150	76.1	3
31	111	65	0.59	0.0528	0.0061	0.168	0.0200	0.02218	0.0007	0.0078	0.0008	0.26	141.4	4.5	156	17	250	210	141.4	5
32	108	48	0.45	0.0568	0.0082	0.101	0.0170	0.01413	0.0006	0.00392	0.0005	-0.04	90.5	3.7	97	15	330	240	90.5	4
33	314	396	1.26	0.0523	0.0031	0.352	0.0240	0.0474	0.0014	0.01409	0.0004	-0.07	298.4	8.5	305	18	270	110	298.4	9
34	378	108	0.29	0.0478	0.0035	0.0875	0.0077	0.01284	0.0004	0.00404	0.0003	0.02	82.3	2.4	84.9	7.2	90	140	82.3	2
35	76	41	0.54	0.0511	0.0046	0.359	0.0390	0.0492	0.0015	0.0167	0.0029	-0.10	309.5	9.5	308	29	210	170	309.5	10
36	184	103	0.56	0.0522	0.003	0.333	0.0240	0.0456	0.0011	0.0135	0.0006	0.13	287.4	6.5	290	19	270	120	287.4	7
37	67	27	0.40	0.069	0.018	0.123	0.0310	0.01389	0.0008	0.004	0.0190	-0.16	88.9	5.1	114	27	370	430	88.9	5
38	129	93	0.72	0.0543	0.004	0.346	0.0290	0.0471	0.0012	0.01435	0.0007	0.36	296.5	7.5	300	22	340	150	296.5	8
39	131	154	1.18	0.0572	0.0056	0.363	0.0400	0.0466	0.0015	0.01363	0.0009	0.11	293.3	9.1	311	28	420	170	293.3	9
40	282	173	0.61	0.0541	0.0031	0.344	0.0250	0.0465	0.0011	0.01404	0.0007	0.08	292.7	6.7	300	19	350	120	292.7	7
41	582	520	0.89	0.0506	0.0051	0.142	0.0130	0.02105	0.0005	0.00637	0.0003	-0.46	134.3	3.1	134	11	190	170	134.3	3
42	100	56	0.56	0.058	0.0096	0.112	0.0200	0.01487	0.0006	0.00462	0.0006	0.11	95.1	3.7	106	18	310	280	95.1	4
43	404	178	0.44	0.056	0.016	0.103	0.0320	0.0138	0.0004	0.0056	0.0020	-0.03	88.4	2.7	99	9.8	370	180	88.4	3
44	122	54	0.44	0.052	0.011	0.072	0.0160	0.01064	0.0005	0.00371	0.0005	0.09	68.2	3.1	70	15	130	340	68.2	3
45	18	7	0.37	0.061	0.031	0.136	0.0560	0.0145	0.0014	0.0057	0.0022	-0.15	92.6	8.6	115	48	360	670	92.6	9
46	141	91	0.64	0.0585	0.0033	0.351	0.0250	0.0467	0.0012	0.01664	0.0010	0.04	294.3	7.6	304	19	540	120	294.3	8
47	191	103	0.54	0.054	0.01	0.104	0.0240	0.0146	0.0012	0.0082	0.0015	-0.06	93.6	7.5	100	17	280	290	93.6	8
48	72	34	0.47	0.047	0.013	0.105	0.0270	0.01611	0.0009	0.0057	0.0060	-0.02	103	5.5	105	21	270	340	103.0	6
49	89	45	0.50	0.063	0.047	0.093	0.0600	0.01137	0.0005	0.00582	0.0009	-0.09	72.9	3	89	21	450	390	72.9	3
50	239	172	0.72	0.0537	0.0031	0.319	0.0240	0.0452	0.0011	0.01428	0.0005	0.19	284.9	6.5	280	18	330	120	284.9	7

51	154	119	0.78	0.069	0.011	0.43	0.0900	0.047	0.0014	0.0157	0.0018	0.06	296.3	8.7	361	51	840	200	296.3	9
52	118	108	0.92	0.0543	0.0063	0.355	0.0430	0.0475	0.0013	0.01527	0.0006	0.14	298.9	8.2	296	24	300	160	298.9	8
53	321	179	0.56	0.0518	0.0045	0.0861	0.0090	0.0122	0.0004	0.00401	0.0002	0.03	78.2	2.4	83.5	8.3	240	170	78.2	2
54	183	87	0.47	0.0529	0.0066	0.104	0.0130	0.01457	0.0004	0.00512	0.0004	0.10	93.2	2.8	99	12	230	210	93.2	3
55	546	320	0.59	0.053	0.0037	0.305	0.0270	0.0415	0.0015	0.01311	0.0006	0.10	262.1	9.2	269	17	360	120	262.1	9
56	338	239	0.71	0.0555	0.0052	0.344	0.0450	0.0455	0.0013	0.01509	0.0009	0.38	286.8	8.1	300	30	420	140	286.8	8
57	219	128	0.58	0.0528	0.0036	0.34	0.0270	0.0468	0.0012	0.01509	0.0006	-0.11	294.9	7.5	296	20	280	130	294.9	8
58	267	65	0.24	0.051	0.011	0.108	0.0270	0.01532	0.0007	0.0069	0.0017	0.17	98	4.5	103	22	200	250	98.0	5
59	275	186	0.68	0.0549	0.0032	0.357	0.0250	0.047	0.0013	0.01561	0.0006	0.32	295.9	7.8	309	19	370	120	295.9	8
60	271	206	0.76	0.0575	0.0052	0.47	0.0630	0.0596	0.0019	0.0227	0.0012	0.40	373	12	391	37	490	140	373.0	12
61	320	201	0.63	0.051	0.005	0.329	0.0350	0.0468	0.0013	0.0144	0.0011	-0.02	294.6	7.8	289	25	260	160	294.6	8
62	287	56	0.20	0.068	0.0031	0.898	0.0700	0.0951	0.0024	0.044	0.0085	0.34	585	14	636	30	790	93	585.0	14
63	144	112	0.78	0.053	0.024	0.301	0.0570	0.0438	0.0014	0.0222	0.0047	-0.04	276.6	8.4	273	24	270	250	276.6	8
64	171	180	1.06	0.056	0.011	0.278	0.0410	0.0363	0.0010	0.01106	0.0006	0.97	229.8	6.3	247	30	470	170	229.8	6
65	248	201	0.81	0.0559	0.0036	0.34	0.0260	0.0447	0.0012	0.01511	0.0005	-0.07	282.2	7.4	296	19	410	120	282.2	7
66	143	112	0.78	0.068	0.0059	0.451	0.0440	0.0485	0.0014	0.0187	0.0023	0.08	305.5	8.8	387	28	910	150	305.5	9
67	153	103	0.68	0.0531	0.0033	0.339	0.0250	0.0466	0.0012	0.01488	0.0005	-0.20	293.7	7.5	299	19	320	130	293.7	8
68	101	62	0.62	0.0517	0.008	0.105	0.0160	0.01498	0.0007	0.00538	0.0008	-0.03	95.8	4.3	105	15	300	280	95.8	4
69	160	79	0.49	0.0487	0.0071	0.076	0.0100	0.01084	0.0004	0.00464	0.0006	-0.09	69.5	2.6	76.2	9.8	130	240	69.5	3
70	243	100	0.41	0.0509	0.005	0.0746	0.0082	0.01084	0.0003	0.00367	0.0003	0.22	69.5	2.1	72.7	7.7	190	180	69.5	2
71	64	57	0.89	0.0565	0.0062	0.331	0.0390	0.0436	0.0014	0.01478	0.0007	-0.08	274.9	8.6	286	30	410	220	274.9	9
72	108	53	0.49	0.0634	0.0088	0.084	0.0150	0.01054	0.0005	0.0037	0.0006	-0.10	67.6	3	87	14	470	310	67.6	3
73	179	138	0.77	0.0533	0.0042	0.359	0.0340	0.0497	0.0012	0.01609	0.0007	0.21	312.9	7.4	309	24	250	130	312.9	7
74	96	43	0.45	0.064	0.015	0.083	0.0210	0.0101	0.0029	0.00367	0.0006	0.07	65	18	79	19	490	360	65.0	18
75	51	52	1.02	0.067	0.018	0.093	0.0280	0.01093	0.0008	0.00344	0.0004	0.20	70.1	5.1	94	25	610	440	70.1	5
76	52	29	0.56	0.06	0.015	0.183	0.0400	0.023	0.0013	0.0083	0.0015	-0.13	146.4	8.1	168	31	560	340	146.4	8
77	146	156	1.07	0.086	0.016	0.54	0.1100	0.0458	0.0013	0.0125	0.0006	0.03	288.9	8.1	394	40	930	180	288.9	8

78	261	115	0.44	0.0491	0.0046	0.093	0.0094	0.01391	0.0004	0.0053	0.0011	0.06	89.1	2.6	89.9	8.8	170	160	89.1	3
79	159	102	0.64	0.053	0.026	0.34	0.1700	0.0482	0.0012	0.01514	0.0007	-0.06	303.6	7.4	298	15	280	130	303.6	7
80	182	118	0.65	0.0514	0.0033	0.332	0.0260	0.0472	0.0011	0.01502	0.0007	-0.01	297	7	289	20	220	130	297.0	7
81	130	145	1.12	0.076	0.035	0.18	0.0480	0.02228	0.0008	0.00706	0.0004	-0.03	142	5	160	31	560	460	142.0	5

Sample SP3-86

				CORRECTED RATIOS									CORRECTED AGES (Ma)							
n°	U (ppm)	Th (ppm)	Th/U	$^{207}Pb/^{206}Pb$	±2s abs	$^{207}Pb/^{235}U$	±2s abs	$^{206}Pb/^{238}U$	±2s abs	$^{208}Pb/^{232}Th$	±2s abs	Rho	$^{206}Pb/^{238}U$	±2s	$^{207}Pb/^{235}U$	±2s	$^{207}Pb/^{206}Pb$	±2s	Best age (Ma)	±2s
1	513	171	0.333	0.0477	0.0001	0.0854	0.0028	0.01296	0.0004	0.00367	0.00043	0.75	83	2.8	83.1	2.6	82	4	83.0	2.8
2	91	54	0.589	0.0523	0.0009	0.335	0.014	0.0465	0.0015	0.01290	0.00110	0.85	293.1	9.3	293	11	296	42	293.1	9.3
3	292	199	0.682	0.0521	0.0010	0.325	0.011	0.0455	0.0013	0.01486	0.00072	0.72	287.6	7.9	285.6	8.9	289	47	287.6	7.9
4	415	438	1.055	0.0515	0.0008	0.319	0.011	0.0448	0.0011	0.01385	0.00044	0.61	282.5	6.8	281.2	8.5	262	40	282.5	6.8
5	345	322	0.933	0.0519	0.0009	0.324	0.01	0.0457	0.0011	0.01445	0.00048	0.37	287.8	6.7	284.7	7.9	279	43	287.8	6.7
6	319	238	0.746	0.0514	0.0008	0.328	0.011	0.04613	0.0010	0.01477	0.00035	0.33	290.7	6.1	289.2	8.5	256	38	290.7	6.1
7	398	198	0.497	0.0476	0.0000	0.0824	0.0019	0.01255	0.0003	0.00392	0.00030	0.77	80.4	2.2	80.4	1.8	80	1	80.4	2.2
8	634	415	0.655	0.0517	0.0007	0.3391	0.0089	0.0476	0.0010	0.01506	0.00045	0.45	299.9	6.3	296.3	6.8	273	33	299.9	6.3
9	227	168	0.740	0.0513	0.0006	0.3199	0.0099	0.045	0.0011	0.01389	0.00053	0.62	284	6.7	281.7	7.6	254	30	284.0	6.7
10	209	95	0.452	0.0490	0.0001	0.161	0.0045	0.02361	0.0007	0.00754	0.00067	0.76	150.4	4.7	151.4	4	149	6	150.4	4.7
11	330	244	0.738	0.0519	0.0007	0.3297	0.0083	0.0461	0.0010	0.01416	0.00057	0.66	290.3	6.3	289.3	6.4	282	34	290.3	6.3
12	192	138	0.719	0.0519	0.0006	0.3317	0.0098	0.047	0.0013	0.01359	0.00067	0.77	295.8	7.8	290.6	7.6	280	32	295.8	7.8
13	148	79	0.536	0.0520	0.0008	0.3162	0.008	0.0446	0.0013	0.01260	0.00120	0.73	281.3	7.9	278.8	6.3	287	38	281.3	7.9
14	431	326	0.756	0.0510	0.0008	0.322	0.011	0.0455	0.0011	0.01493	0.00044	0.62	287	6.8	282.9	8.5	240	37	287.0	6.8
15	195	117	0.600	0.0518	0.0007	0.331	0.012	0.0467	0.0014	0.01395	0.00074	0.62	294.2	8.3	291.4	9.5	277	35	294.2	8.3
16	296	290	0.980	0.0512	0.0008	0.3323	0.0094	0.0465	0.0011	0.01453	0.00032	0.66	293.1	7	291.1	7.2	247	37	293.1	7.0
17	305	216	0.708	0.0515	0.0007	0.3003	0.008	0.0424	0.0011	0.01267	0.00045	0.76	267.4	7.1	266.5	6.3	263	34	267.4	7.1
18	262	249	0.951	0.0474	0.0000	0.0672	0.0024	0.01024	0.0004	0.00326	0.00029	0.97	65.7	2.6	66	2.3	67	2	65.7	2.6
19	148	93	0.631	0.0517	0.0007	0.332	0.013	0.0466	0.0012	0.01427	0.00070	0.35	293.7	7.5	291.2	9.7	272	34	293.7	7.5
20	113	127	1.122	0.0518	0.0005	0.3182	0.0094	0.0449	0.0013	0.01361	0.00067	0.66	283.3	7.9	280	7.3	278	23	283.3	7.9
21	260	107	0.413	0.0517	0.0008	0.34	0.01	0.0474	0.0012	0.01506	0.00065	0.76	298.7	7.7	296.6	8.1	270	36	298.7	7.7
22	82	30	0.362	0.0523	0.0008	0.342	0.013	0.0478	0.0015	0.01550	0.00150	0.44	301.2	9	298	10	296	39	301.2	9.0

23	837	706	0.843	0.0515	0.0008	0.3196	0.0081	0.0449	0.0011	0.01291	0.00045	0.80	283.2	6.5	281.5	6.2	263	40	283.2	6.5
24	282	205	0.727	0.0523	0.0008	0.3417	0.0082	0.0475	0.0012	0.01431	0.00077	0.79	299.4	7.2	299.2	6.1	300	39	299.4	7.2
25	584	193	0.330	0.0476	0.0001	0.0813	0.0022	0.01243	0.0004	0.00373	0.00032	0.86	79.6	2.4	79.4	2.1	79	4	79.6	2.4
26	58	72	1.244	0.0488	0.0014	0.07	0.011	0.0094	0.0011	0.00230	0.00110	0.98	60.3	6.8	68	10	92	52	60.3	6.8
27	449	295	0.658	0.0516	0.0008	0.3335	0.0088	0.0466	0.0011	0.01413	0.00048	0.82	293.5	6.7	292.2	6.8	267	39	293.5	6.7
28	144	155	1.076	0.0562	0.0014	0.613	0.023	0.0796	0.0020	0.02516	0.00060	0.65	494	12	485	14	458	61	494.0	12.0
29	239	124	0.517	0.0520	0.0009	0.332	0.01	0.0464	0.0012	0.01339	0.00081	0.81	292.2	7.6	290.7	7.7	284	40	292.2	7.6
30	177	115	0.653	0.0519	0.0009	0.345	0.013	0.0473	0.0016	0.01531	0.00079	0.46	297.8	9.6	300.5	9.5	278	41	297.8	9.6
31	237	147	0.619	0.0518	0.0008	0.329	0.011	0.0462	0.0012	0.01399	0.00065	0.56	291.4	7.4	288.5	8	277	38	291.4	7.4
32	62	46	0.739	0.0473	0.0000	0.067	0.0045	0.0101	0.0006	0.00279	0.00067	0.62	64.8	4	65.7	4.3	65	0	64.8	4.0
33	372	298	0.801	0.0524	0.0008	0.3386	0.0099	0.0472	0.0013	0.01538	0.00055	0.83	297.4	7.9	295.9	7.6	302	36	297.4	7.9
34	117	88	0.754	0.0474	0.0000	0.0691	0.0035	0.01061	0.0005	0.00310	0.00051	0.86	68	3.5	67.8	3.3	67	1	68.0	3.5
35	75	45	0.605	0.0477	0.0000	0.086	0.0049	0.01318	0.0008	0.00430	0.00110	0.96	84.4	5.1	83.7	4.6	85	0	84.4	5.1
36	207	93	0.450	0.0515	0.0008	0.331	0.011	0.0469	0.0012	0.01291	0.00078	0.45	295.2	7.3	290.1	8.7	260	36	295.2	7.3
37	213	211	0.991	0.0521	0.0008	0.3295	0.0091	0.0468	0.0014	0.01343	0.00054	0.87	294.6	8.5	288.9	7.1	288	38	294.6	8.5
38	268	227	0.847	0.0474	0.0000	0.0691	0.0021	0.01061	0.0004	0.00321	0.00033	0.89	68	2.4	67.8	2	68	1	68.0	2.4
39	193	142	0.736	0.0522	0.0008	0.34	0.013	0.0474	0.0016	0.01370	0.00100	0.80	298.7	9.6	297	9.7	295	36	298.7	9.6
40	157	187	1.190	0.0473	0.0000	0.0682	0.0024	0.01027	0.0004	0.00340	0.00031	0.65	65.8	2.4	66.9	2.3	65	1	65.8	2.4
41	136	95	0.699	0.0474	0.0000	0.0656	0.0031	0.00989	0.0005	0.00327	0.00057	0.74	63.4	2.9	64.4	2.9	69	1	63.4	2.9
42	444	281	0.633	0.0521	0.0009	0.3311	0.0092	0.0463	0.0011	0.01417	0.00062	0.71	291.8	6.5	291.3	7.1	290	41	291.8	6.5
43	200	118	0.590	0.0514	0.0007	0.32	0.011	0.0451	0.0012	0.01353	0.00076	0.63	284.5	7.2	281.9	8.5	255	31	284.5	7.2
44	153	118	0.773	0.0473	0.0000	0.0681	0.0026	0.01043	0.0004	0.00313	0.00038	0.89	67.3	2.7	67.3	2.6	67	1	67.3	2.7
45	191	174	0.911	0.0533	0.0009	0.384	0.012	0.0524	0.0017	0.01728	0.00091	0.88	329	10	330	9	339	40	329.0	10.0
46	599	868	1.449	0.0489	0.0003	0.1576	0.0035	0.02356	0.0006	0.00741	0.00016	0.53	150.1	3.6	148.5	3.1	141	16	150.1	3.6
47	307	318	1.036	0.0517	0.0008	0.3291	0.0091	0.047	0.0011	0.01392	0.00044	0.29	296	6.8	288.7	7.3	271	38	296.0	6.8
48	373	274	0.735	0.0517	0.0007	0.33	0.01	0.0465	0.0011	0.01376	0.00051	0.55	293.1	6.8	289.2	7.7	269	33	293.1	6.8
49	287	166	0.578	0.0521	0.0007	0.3363	0.0066	0.047	0.0011	0.01417	0.00077	0.72	296.4	7	294.2	5.1	289	35	296.4	7.0

50	312	224	0.719	0.0521	0.0008	0.334	0.01	0.0468	0.0011	0.01334	0.00053	0.66	294.9	7	292.5	8	288	37	294.9	7.0
51	469	405	0.864	0.0520	0.0007	0.3168	0.0084	0.0449	0.0011	0.01276	0.00048	0.53	283.2	6.9	279.3	6.6	283	36	283.2	6.9
52	444	290	0.653	0.0507	0.0006	0.314	0.011	0.0448	0.0013	0.01441	0.00077	0.52	282.6	8.2	277	8.3	225	31	282.6	8.2
53	287	181	0.629	0.0533	0.0009	0.3303	0.0072	0.0449	0.0010	0.01475	0.00098	0.89	283.1	6	289.6	5.6	340	40	283.1	6.0
54	173	126	0.728	0.0515	0.0007	0.3285	0.0097	0.0455	0.0012	0.01394	0.00075	0.55	286.8	7.5	289.5	7.5	263	34	286.8	7.5
55	125	122	0.976	0.0473	0.0000	0.0685	0.0029	0.01052	0.0005	0.00389	0.00036	0.99	67.5	3.2	67.2	2.7	67	1	67.5	3.2
56	98	56	0.574	0.0510	0.0006	0.3	0.011	0.0432	0.0015	0.01310	0.00110	0.43	272.8	9.3	265.9	9.2	238	28	272.8	9.3
57	287	202	0.704	0.0521	0.0008	0.3298	0.0075	0.046	0.0011	0.01337	0.00072	0.58	289.8	6.9	289.2	5.8	292	36	289.8	6.9
58	430	299	0.695	0.0519	0.0009	0.328	0.01	0.0458	0.0012	0.01396	0.00071	0.77	288.7	7.4	287.9	7.5	282	42	288.7	7.4
59	101	92	0.907	0.0474	0.0000	0.0686	0.0033	0.01044	0.0004	0.00315	0.00047	0.84	67	2.8	67.3	3.1	68	1	67.0	2.8
60	190	165	0.868	0.0535	0.0012	0.358	0.019	0.0479	0.0018	0.01440	0.00130	0.68	301	11	310	14	346	50	301.0	11.0
61	102	78	0.766	0.0474	0.0000	0.0665	0.0032	0.01023	0.0006	0.00283	0.00061	0.89	65.6	3.6	65.3	3	68	0	65.6	3.6
62	268	194	0.725	0.0520	0.0008	0.3297	0.0082	0.046	0.0012	0.01376	0.00060	0.77	290.1	7.3	289.2	6.3	286	37	290.1	7.3
63	85	81	0.950	0.0474	0.0000	0.0691	0.0036	0.01053	0.0006	0.00327	0.00044	0.89	67.5	3.7	67.7	3.5	68	0	67.5	3.7
64	415	387	0.933	0.0512	0.0008	0.3157	0.0089	0.0444	0.0011	0.01403	0.00046	0.33	279.8	6.8	278.3	6.9	247	36	279.8	6.8
65	201	164	0.819	0.0518	0.0007	0.3275	0.0086	0.0462	0.0011	0.01395	0.00059	0.48	291.2	6.6	287.4	6.7	278	33	291.2	6.6
66	166	69	0.414	0.0510	0.0006	0.286	0.01	0.0407	0.0013	0.01230	0.00110	0.76	257.2	7.8	255	8.1	240	29	257.2	7.8
67	374	258	0.690	0.0516	0.0008	0.3313	0.0094	0.0465	0.0011	0.01421	0.00043	0.65	293	6.7	290.3	7.2	265	39	293.0	6.7
68	282	178	0.631	0.0475	0.0003	0.071	0.013	0.0108	0.0017	0.00360	0.00140	0.89	69	11	69	12	75	15	69.0	11.0
69	200	164	0.820	0.0516	0.0007	0.3145	0.0095	0.0444	0.0012	0.01326	0.00054	0.52	280.1	7.3	278.5	7.4	266	35	280.1	7.3
70	356	235	0.660	0.0515	0.0008	0.3211	0.0093	0.0452	0.0011	0.01357	0.00052	0.45	285	6.7	282.5	7.2	262	38	285.0	6.7
71	80	76	0.945	0.0474	0.0000	0.0685	0.0037	0.01048	0.0006	0.00295	0.00042	0.89	67.2	3.6	67.2	3.4	68	2	67.2	3.6
72	109	51	0.469	0.0475	0.0000	0.0726	0.0035	0.01114	0.0006	0.00412	0.00080	0.97	71.4	3.5	71.1	3.3	72	2	71.4	3.5
73	125	144	1.152	0.0474	0.0000	0.0674	0.0031	0.01044	0.0005	0.00348	0.00038	0.86	66.9	3.3	66.2	2.9	67	0	66.9	3.3
74	317	191	0.603	0.0513	0.0006	0.3179	0.0091	0.0449	0.0011	0.01355	0.00055	0.57	282.9	6.6	280.1	7.2	251	31	282.9	6.6
75	463	352	0.760	0.0513	0.0008	0.3268	0.0095	0.046	0.0010	0.01409	0.00041	0.49	290	6.5	287	7.3	252	37	290.0	6.5
76	100	47	0.466	0.0473	0.0000	0.0639	0.0052	0.0097	0.0008	0.00330	0.00130	0.89	62.2	5.4	62.8	4.9	65	0	62.2	5.4

77	241	148	0.614	0.0512	0.0007	0.328	0.011	0.0458	0.0012	0.01481	0.00051	0.63	288.9	7.4	287.4	8.6	249	33	288.9	7.4
78	197	140	0.710	0.0474	0.0000	0.0713	0.0021	0.01091	0.0004	0.00367	0.00035	0.95	69.9	2.3	69.9	2	71	0	69.9	2.3
79	207	131	0.631	0.0518	0.0007	0.315	0.012	0.0442	0.0012	0.01397	0.00073	0.66	279	7.1	277.7	9.2	276	34	279.0	7.1
80	129	97	0.751	0.0474	0.0000	0.0707	0.0033	0.01094	0.0006	0.00375	0.00060	0.90	70.1	3.7	69.3	3.1	71	2	70.1	3.7
81	128	50	0.387	0.0477	0.0000	0.0889	0.0039	0.01349	0.0006	0.00453	0.00088	0.94	86.4	4	86.4	3.6	87	2	86.4	4.0
82	156	75	0.483	0.0474	0.0000	0.069	0.0028	0.01061	0.0004	0.00331	0.00058	0.89	68	2.7	67.7	2.6	69	0	68.0	2.7
83	243	145	0.597	0.0517	0.0007	0.331	0.011	0.0463	0.0011	0.01489	0.00062	0.38	291.7	6.7	289.9	8.5	270	34	291.7	6.7
84	227	128	0.563	0.0500	0.0003	0.2103	0.0077	0.03055	0.0010	0.00875	0.00096	0.88	194	6	193.7	6.5	197	17	194.0	6.0
85	151	100	0.662	0.0501	0.0003	0.2272	0.0072	0.0333	0.0010	0.00946	0.00082	0.59	211	6.4	207.7	6	201	15	211.0	6.4
86	204	130	0.637	0.0515	0.0007	0.32	0.012	0.0447	0.0013	0.01407	0.00073	0.75	281.6	7.8	281.2	9.6	262	33	281.6	7.8
87	297	213	0.717	0.0517	0.0007	0.328	0.009	0.0462	0.0011	0.01364	0.00057	0.42	291.3	7.1	287.9	7	272	32	291.3	7.1
88	451	272	0.604	0.0522	0.0008	0.3333	0.009	0.0465	0.0011	0.01322	0.00063	0.92	293.2	6.7	291.9	7.2	292	39	293.2	6.7
89	320	237	0.741	0.0522	0.0008	0.3324	0.0086	0.0462	0.0012	0.01385	0.00066	0.99	291.1	7.5	291.3	6.6	296	38	291.1	7.5
90	159	117	0.733	0.0474	0.0000	0.0676	0.0034	0.01033	0.0006	0.00291	0.00035	0.92	66.3	3.6	66.4	3.3	68	1	66.3	3.6
91	204	146	0.716	0.0474	0.0000	0.069	0.0024	0.01058	0.0004	0.00355	0.00036	0.98	67.8	2.7	67.7	2.2	68	0	67.8	2.7
92	34	25	0.734	0.0475	0.0000	0.0737	0.0068	0.0109	0.0011	0.00420	0.00120	0.74	70	7	71.8	6.7	75	0	70.0	7.0
93	79	58	0.727	0.0474	0.0000	0.0677	0.0042	0.01052	0.0006	0.00363	0.00064	0.74	67.4	4	66.4	4	68	1	67.4	4.0
94	228	131	0.573	0.0519	0.0007	0.328	0.01	0.0459	0.0011	0.01339	0.00078	0.58	289.4	6.8	288.1	7.8	282	35	289.4	6.8
95	214	144	0.673	0.0522	0.0008	0.332	0.011	0.046	0.0015	0.01352	0.00087	0.81	289.6	9.2	290.9	8.5	292	40	289.6	9
96	310	260	0.839	0.0477	0.0000	0.0789	0.0029	0.012	0.0005	0.00312	0.00044	0.89	76.9	3.3	77.1	2.8	83	1	76.9	3
97	715	449	0.628	0.0517	0.0008	0.3291	0.0086	0.0457	0.0010	0.01418	0.00050	0.60	288.3	6.3	288.7	6.6	272	39	288.3	6
98	42	26	0.630	0.0474	0.0000	0.0721	0.0054	0.01099	0.0009	0.00390	0.00120	0.81	70.4	5.6	70.5	5.1	72	1	70.4	6
99	296	219	0.740	0.0513	0.0008	0.3157	0.0095	0.0449	0.0011	0.01298	0.00065	0.43	283.2	6.9	278.3	7.4	255	40	283.2	7
100	138	120	0.872	0.0475	0.0000	0.0716	0.0032	0.01087	0.0005	0.00343	0.00040	0.76	69.7	3.4	70.1	3.1	73	0	69.7	3

Sample SP3-92

				CORRECTED RATIOS									CORRECTED AGES (Ma)							
n°	U (ppm)	Th (ppm)	Th/U	$^{207}Pb/^{206}Pb$	±2s abs	$^{207}Pb/^{235}U$	±2s abs	$^{206}Pb/^{238}U$	±2s abs	$^{208}Pb/^{232}Th$	±2s abs	Rho	$^{206}Pb/^{238}U$	±2s	$^{207}Pb/^{235}U$	±2s	$^{207}Pb/^{206}Pb$	±2s	Best age (Ma)	±2s
1	433	19	0.045	0.0528	0.0040	0.2240	0.0170	0.0316	0.0012	0.0103	0.0007	0.16	200.4	7.2	204	14	368	82	200.4	7.2
2	397	11	0.028	0.0506	0.0037	0.0773	0.0055	0.0115	0.0003	0.0036	0.0003	-0.02	73.5	1.8	75.4	5.2	372	65	73.5	1.8
3	265	42	0.158	0.0525	0.0014	0.3050	0.0110	0.0432	0.0012	0.0140	0.0011	0.41	272.5	7.2	270.4	8.8	292	39	272.5	7.2
4	452	13	0.029	0.0468	0.0028	0.0769	0.0046	0.0120	0.0003	0.0042	0.0003	0.01	76.6	2.1	75.1	4.3	371	94	76.6	2.1
5	1183	21	0.018	0.0509	0.0021	0.0743	0.0030	0.0108	0.0003	0.0037	0.0003	-0.10	69.4	1.7	72.8	2.8	319	78	69.4	1.7
6	110	2	0.017	0.0480	0.0140	0.0690	0.0200	0.0106	0.0005	0.0034	0.0006	0.19	67.6	3.2	70	18	900	210	67.6	3.2
7	190	10	0.052	0.0533	0.0044	0.3470	0.0290	0.0461	0.0012	0.0161	0.0011	0.14	290.6	7.3	299	22	506	84	290.6	7.3
8	413	11	0.026	0.0537	0.0063	0.0812	0.0087	0.0113	0.0003	0.0040	0.0004	-0.07	72.2	2.1	78.9	8.2	600	110	72.2	2.1
9	141	10	0.068	0.0533	0.0051	0.3440	0.0310	0.0470	0.0013	0.0138	0.0010	-0.11	296.1	7.7	297	24	425	75	296.1	7.7
10	180	2	0.014	0.0480	0.0130	0.0780	0.0210	0.0114	0.0004	0.0032	0.0004	0.09	73.2	2.8	74	20	730	170	73.2	2.8
11	567	12	0.022	0.0527	0.0034	0.0858	0.0057	0.0117	0.0003	0.0039	0.0003	0.16	75.1	1.8	83.4	5.3	441	86	75.1	1.8
12	160	6	0.035	0.0485	0.0057	0.0795	0.0095	0.0117	0.0003	0.0032	0.0005	0.11	74.8	2	77.2	8.9	485	99	74.8	2.0
13	514	8	0.015	0.0490	0.0049	0.0752	0.0071	0.0113	0.0003	0.0035	0.0003	-0.12	72.6	2	73.3	6.7	460	100	72.6	2.0
14	62	1	0.014	0.0660	0.0290	0.1040	0.0520	0.0123	0.0008	0.0050	0.0012	0.04	79	4.9	86	48	1680	450	79.0	4.9
15	310	22	0.070	0.0529	0.0018	0.3380	0.0120	0.0466	0.0011	0.0146	0.0009	0.15	293.4	6.6	295.3	9.1	352	41	293.4	6.6
16	266	6	0.021	0.0522	0.0054	0.0807	0.0081	0.0114	0.0003	0.0037	0.0003	-0.03	73.3	2.1	78.4	7.6	580	110	73.3	2.1
17	159	13	0.081	0.0521	0.0027	0.3300	0.0170	0.0457	0.0012	0.0132	0.0010	-0.10	287.8	7.3	288	13	311	59	287.8	7.3
18	732	10	0.014	0.0553	0.0037	0.0833	0.0055	0.0110	0.0003	0.0035	0.0003	0.09	70.2	1.9	81.2	5.1	389	71	70.2	1.9
19	171	4	0.022	0.0458	0.0076	0.0690	0.0110	0.0111	0.0004	0.0037	0.0004	0.06	71.4	2.5	67	11	630	140	71.4	2.5
20	283	17	0.060	0.0562	0.0031	0.3510	0.0200	0.0459	0.0013	0.0149	0.0010	-0.20	289.1	7.9	304	15	478	71	289.1	7.9
21	1590	48	0.030	0.0476	0.0016	0.0764	0.0027	0.0117	0.0003	0.0038	0.0002	0.11	75.1	1.9	74.7	2.6	213	57	75.1	1.9
22	166	3	0.021	0.0537	0.0080	0.0860	0.0140	0.0114	0.0004	0.0037	0.0004	0.06	73.3	2.8	86	12	690	150	73.3	2.8

23	93	10	0.108	0.0557	0.0037	0.3620	0.0230	0.0486	0.0014	0.0161	0.0013	-0.01	305.8	8.7	318	17	477	58	305.8	8.7
24	178	4	0.021	0.0621	0.0095	0.0930	0.0140	0.0109	0.0005	0.0052	0.0006	0.18	70	2.9	92	12	790	140	70.0	2.9
25	105	7	0.069	0.0552	0.0057	0.2400	0.0240	0.0320	0.0009	0.0102	0.0010	-0.06	202.8	5.8	216	20	509	86	202.8	5.8
26	33	3	0.091	0.0560	0.0100	0.3630	0.0700	0.0454	0.0015	0.0173	0.0023	0.54	286.3	9.6	304	50	790	150	286.3	9.6
27	426	8	0.018	0.0507	0.0044	0.0819	0.0069	0.0116	0.0003	0.0038	0.0003	-0.11	74.2	2.1	79.6	6.5	484	92	74.2	2.1
28	157	5	0.029	0.0496	0.0060	0.0856	0.0087	0.0121	0.0004	0.0036	0.0004	-0.03	77.3	2.5	83	8.2	490	110	77.3	2.5
29	355	23	0.064	0.0541	0.0018	0.3550	0.0130	0.0479	0.0012	0.0154	0.0009	0.13	301.8	7.3	309.9	9.8	381	55	301.8	7.3
30	230	14	0.062	0.0536	0.0036	0.3540	0.0220	0.0487	0.0013	0.0150	0.0010	0.24	307.4	8	306	16	452	82	307.4	8.0
31	584	6	0.011	0.0534	0.0071	0.0850	0.0100	0.0113	0.0003	0.0038	0.0003	-0.12	72.5	2.2	84	9.1	680	140	72.5	2.2
32	525	36	0.068	0.0527	0.0016	0.3187	0.0095	0.0442	0.0010	0.0150	0.0009	-0.05	278.6	6.1	281.7	7	344	48	278.6	6.1
33	436	8	0.019	0.0460	0.0054	0.0721	0.0085	0.0113	0.0003	0.0039	0.0003	0.16	72.2	1.8	70.3	8	430	140	72.2	1.8
34	272	14	0.053	0.0497	0.0030	0.2240	0.0130	0.0322	0.0008	0.0105	0.0007	0.07	204.5	4.9	204	11	350	69	204.5	4.9
35	182	4	0.024	0.0630	0.0110	0.0790	0.0130	0.0091	0.0004	0.0039	0.0006	0.09	58.4	2.3	80	12	770	120	58.4	2.3
36	98	5	0.049	0.0484	0.0065	0.0750	0.0110	0.0111	0.0003	0.0046	0.0006	0.07	70.9	2.1	73.1	9.9	660	160	70.9	2.1
37	552	8	0.015	0.0440	0.0046	0.0661	0.0071	0.0109	0.0003	0.0035	0.0002	0.04	69.8	1.8	64.7	6.7	309	82	69.8	1.8
38	197	11	0.054	0.0518	0.0029	0.3500	0.0210	0.0481	0.0015	0.0160	0.0011	0.20	303	8.9	305	15	436	66	303.0	8.9
39	860	15	0.018	0.0504	0.0034	0.0758	0.0051	0.0111	0.0003	0.0037	0.0002	0.10	71.2	1.9	74.8	4.9	310	67	71.2	1.9
40	388	6	0.017	0.0523	0.0071	0.0830	0.0110	0.0116	0.0004	0.0038	0.0004	0.38	74.3	2.2	80	11	620	180	74.3	2.2
41	126	3	0.022	0.0580	0.0100	0.0860	0.0140	0.0114	0.0005	0.0037	0.0006	-0.04	73	3.1	83	13	760	140	73.0	3.1
42	91	11	0.119	0.0559	0.0040	0.3660	0.0250	0.0489	0.0012	0.0164	0.0012	-0.08	307.9	7.2	314	18	508	81	307.9	7.2
43	440	8	0.019	0.0534	0.0061	0.0816	0.0089	0.0111	0.0003	0.0035	0.0003	0.34	71.2	2.2	79.3	8.4	490	100	71.2	2.2
44	338	18	0.053	0.0536	0.0021	0.3370	0.0130	0.0453	0.0010	0.0142	0.0009	0.15	285.4	6.4	294	10	337	38	285.4	6.4
45	320	6	0.020	0.0540	0.0054	0.0856	0.0082	0.0114	0.0004	0.0040	0.0003	0.18	73	2.6	83.2	7.6	410	110	73.0	2.6
46	113	10	0.091	0.0473	0.0036	0.0906	0.0068	0.0136	0.0004	0.0052	0.0005	0.14	87.3	2.3	87.8	6.3	304	77	87.3	2.3
47	152	11	0.070	0.0559	0.0044	0.3730	0.0260	0.0486	0.0016	0.0161	0.0010	-0.18	306	10	320	19	595	90	306.0	10.0
48	267	10	0.036	0.0550	0.0037	0.3320	0.0250	0.0443	0.0011	0.0149	0.0010	0.21	279.5	6.9	294	18	460	100	279.5	6.9
49	213	4	0.020	0.0499	0.0061	0.0789	0.0094	0.0113	0.0004	0.0038	0.0003	0.18	72.2	2.4	78	9.1	540	110	72.2	2.4

50	205	4	0.019	0.0424	0.0062	0.0690	0.0100	0.0117	0.0004	0.0044	0.0004	0.30	75	2.4	67.1	9.8	460	140	75.0	2.4
51	498	39	0.078	0.0528	0.0016	0.3334	0.0099	0.0459	0.0010	0.0144	0.0008	-0.11	289	6.4	291.9	7.5	304	33	289.0	6.4
52	213	18	0.085	0.0545	0.0036	0.3510	0.0230	0.0468	0.0013	0.0146	0.0010	-0.01	294.9	7.7	305	17	457	73	294.9	7.7
53	211	8	0.036	0.0527	0.0038	0.2340	0.0160	0.0323	0.0008	0.0102	0.0007	-0.02	204.6	5.1	217	13	345	61	204.6	5.1
54	94	8	0.080	0.0538	0.0046	0.2310	0.0200	0.0323	0.0009	0.0107	0.0009	0.11	204.7	5.6	209	17	450	64	204.7	5.6
55	1465	21	0.014	0.0502	0.0020	0.0758	0.0032	0.0112	0.0003	0.0036	0.0002	0.14	71.4	1.7	74.2	3	236	43	71.4	1.7
56	198	2	0.012	0.0620	0.0140	0.0950	0.0210	0.0116	0.0005	0.0042	0.0004	-0.40	74.2	3.3	91	19	1040	210	74.2	3.3
57	541	10	0.018	0.0520	0.0036	0.0799	0.0050	0.0114	0.0003	0.0038	0.0003	-0.14	73.2	2	78	4.7	424	90	73.2	2.0
58	87	2	0.022	0.0560	0.0170	0.0950	0.0270	0.0117	0.0008	0.0037	0.0007	-0.28	75	4.9	95	24	960	290	75.0	4.9
59	132	10	0.079	0.0549	0.0033	0.3640	0.0220	0.0494	0.0012	0.0160	0.0011	0.04	311.1	7.4	313	17	473	67	311.1	7.4
60	114	9	0.083	0.0543	0.0033	0.3560	0.0230	0.0476	0.0011	0.0160	0.0012	0.29	299.5	7.1	308	17	409	56	299.5	7.1
61	112	12	0.110	0.0515	0.0027	0.3390	0.0170	0.0477	0.0013	0.0164	0.0011	0.04	300.4	7.7	298	14	346	68	300.4	7.7
62	412	70	0.170	0.0601	0.0011	0.7760	0.0180	0.0945	0.0020	0.0294	0.0017	0.38	582	12	583	10	611	20	582.0	12.0
63	196	10	0.051	0.0548	0.0040	0.3400	0.0250	0.0452	0.0012	0.0147	0.0010	0.18	284.8	7.2	301	19	492	86	284.8	7.2
64	615	7	0.011	0.0511	0.0048	0.0739	0.0074	0.0107	0.0003	0.0032	0.0002	-0.03	68.6	1.9	72.1	7	270	69	68.6	1.9
65	150	3	0.022	0.0478	0.0069	0.1030	0.0150	0.0158	0.0006	0.0052	0.0005	0.35	101.1	3.7	99	14	590	210	101.1	3.7
66	146	14	0.095	0.0508	0.0025	0.3030	0.0160	0.0425	0.0010	0.0133	0.0009	0.13	268.2	6.4	268	13	357	54	268.2	6.4
67	330	8	0.026	0.0482	0.0037	0.0722	0.0055	0.0109	0.0003	0.0034	0.0003	0.07	69.6	1.7	70.6	5.2	413	94	69.6	1.7
68	84	7	0.088	0.0498	0.0039	0.0890	0.0067	0.0128	0.0003	0.0046	0.0006	-0.04	81.7	1.9	86.4	6.2	450	100	81.7	1.9
69	329	46	0.141	0.0526	0.0025	0.3360	0.0140	0.0461	0.0012	0.0144	0.0009	-0.07	290.6	7.3	297	14	314	34	290.6	7.3
70	292	18	0.060	0.0531	0.0029	0.3370	0.0190	0.0464	0.0011	0.0152	0.0009	-0.02	292.2	6.8	296	14	374	66	292.2	6.8
71	277	6	0.021	0.0501	0.0045	0.0791	0.0070	0.0113	0.0003	0.0037	0.0003	0.29	72.5	1.9	77.1	6.5	506	92	72.5	1.9
72	251	3	0.012	0.0500	0.0077	0.0750	0.0120	0.0109	0.0004	0.0041	0.0004	0.06	69.8	2.7	73	11	570	140	69.8	2.7
73	20	7	0.345	0.0653	0.0059	1.3400	0.1300	0.1447	0.0051	0.0389	0.0036	0.27	871	29	859	55	859	83	871.0	29.0
74	160	8	0.050	0.0508	0.0036	0.2350	0.0170	0.0323	0.0010	0.0102	0.0007	0.19	204.7	5.9	213	14	372	80	204.7	5.9
75	139	10	0.072	0.0530	0.0033	0.3610	0.0200	0.0494	0.0013	0.0160	0.0010	-0.03	310.9	7.8	314	16	377	49	310.9	7.8
76	227	4	0.018	0.0446	0.0062	0.0707	0.0097	0.0112	0.0003	0.0035	0.0003	-0.04	72.1	2.2	68.8	9.1	610	150	72.1	2.2

77	235	19	0.082	0.0551	0.0027	0.3580	0.0170	0.0482	0.0016	0.0156	0.0010	0.05	303.6	9.9	310	13	419	68	303.6	9.9
78	386	6	0.016	0.0501	0.0035	0.0782	0.0052	0.0114	0.0003	0.0040	0.0003	-0.26	73.4	2.1	76.3	4.9	328	84	73.4	2.1
79	235	4	0.019	0.0461	0.0053	0.0728	0.0084	0.0114	0.0004	0.0041	0.0004	0.10	72.7	2.2	71	8	434	91	72.7	2.2
80	103	4	0.036	0.0533	0.0077	0.2610	0.0360	0.0367	0.0013	0.0121	0.0009	-0.39	232.5	8.3	231	29	720	130	232.5	8.3
81	312	14	0.043	0.0525	0.0029	0.3310	0.0190	0.0469	0.0011	0.0148	0.0009	0.14	295.5	6.7	289	14	350	62	295.5	6.7
82	491	20	0.040	0.0549	0.0016	0.3330	0.0110	0.0453	0.0010	0.0144	0.0009	0.18	285.4	6.2	292.6	8.1	402	41	285.4	6.2
83	469	12	0.026	0.0539	0.0032	0.0822	0.0048	0.0115	0.0003	0.0038	0.0003	0.00	73.9	1.9	80.1	4.5	383	65	73.9	1.9
84	960	20	0.020	0.0461	0.0019	0.0734	0.0031	0.0115	0.0003	0.0039	0.0002	0.44	73.9	1.7	71.8	3	223	45	73.9	2
85	256	15	0.059	0.0528	0.0028	0.3400	0.0170	0.0463	0.0011	0.0149	0.0009	-0.05	292	6.9	298	13	355	58	292.0	7
86	319	7	0.021	0.0476	0.0041	0.0756	0.0060	0.0115	0.0003	0.0037	0.0003	-0.29	73.5	2.2	73.8	5.7	427	78	73.5	2
87	885	14	0.016	0.0493	0.0031	0.0760	0.0046	0.0110	0.0003	0.0037	0.0003	-0.04	70.7	1.9	74.3	4.3	373	84	70.7	2
88	190	3	0.017	0.0574	0.0097	0.0900	0.0150	0.0114	0.0005	0.0043	0.0004	0.23	72.8	3.2	87	14	710	180	72.8	3
89	326	6	0.020	0.0509	0.0043	0.0807	0.0064	0.0116	0.0004	0.0041	0.0003	0.07	74.4	2.4	78.7	6	455	84	74.4	2
90	290	5	0.017	0.0646	0.0067	0.1010	0.0110	0.0109	0.0004	0.0042	0.0004	0.23	70	2.4	97	10	970	140	70.0	2
91	78	5	0.068	0.0534	0.0051	0.2460	0.0230	0.0327	0.0010	0.0105	0.0009	0.04	207.1	6.2	221	19	550	120	207.1	6
92	152	8	0.054	0.0520	0.0039	0.2240	0.0140	0.0318	0.0009	0.0110	0.0008	-0.36	201.9	5.5	206	13	380	100	201.9	6
93	408	5	0.011	0.0565	0.0097	0.0860	0.0130	0.0112	0.0004	0.0042	0.0004	-0.39	71.6	2.4	83	12	930	210	71.6	2
94	152	3	0.022	0.0558	0.0074	0.0850	0.0110	0.0115	0.0004	0.0036	0.0004	0.06	73.5	2.6	82	10	760	120	73.5	3

Sample SP3-94

				CORRECTED RATIOS									CORRECTED AGES (Ma)							
n°	U (ppm)	Th (ppm)	Th/U	$^{207}Pb/^{206}Pb$	±2s abs	$^{207}Pb/^{235}U$	±2s abs	$^{206}Pb/^{238}U$	±2s abs	$^{208}Pb/^{232}Th$	±2s abs	Rho	$^{206}Pb/^{238}U$	±2s	$^{207}Pb/^{235}U$	±2s	$^{207}Pb/^{206}Pb$	±2s	Best age (Ma)	±2s
1	843	1178	1.40	0.0525	0.0033	0.337	0.016	0.04641	0.0008	0.0149	0.001	-0.01	292.4	5.1	294	12	313	85	292.4	5
2	344	241	0.70	0.0489	0.0067	0.0795	0.0095	0.01197	0.0003	0.00372	0.00034	-0.38	76.7	2	77.2	8.8	510	140	76.7	2
3	123	75	0.61	0.0621	0.0073	0.629	0.078	0.0743	0.0019	0.0263	0.0025	-0.12	462	11	503	42	730	150	462.0	11
4	117	105	0.90	0.065	0.016	0.086	0.021	0.01059	0.0005	0.00302	0.00052	-0.26	67.9	2.9	87	19	1260	210	67.9	3
5	365	215	0.59	0.0537	0.0036	0.349	0.019	0.04717	0.0010	0.0149	0.0011	0.05	297.1	5.9	303	15	386	88	297.1	6
6	133	114	0.86	0.053	0.01	0.078	0.015	0.01098	0.0004	0.00328	0.00044	0.06	70.4	2.6	75	15	900	150	70.4	3
7	348	225	0.65	0.0497	0.0075	0.072	0.01	0.01042	0.0003	0.00342	0.00033	0.05	66.8	2.1	71.4	9.1	650	140	66.8	2
8	217	160	0.74	0.05	0.012	0.079	0.018	0.01145	0.0004	0.00384	0.00043	0.03	73.4	2.5	76	17	780	210	73.4	3
9	110	89	0.81	0.052	0.016	0.072	0.022	0.0105	0.0006	0.00389	0.00053	0.31	67.3	3.6	71	21	1320	260	67.3	4
10	102	90	0.88	0.052	0.016	0.081	0.023	0.01093	0.0006	0.00327	0.00053	-0.19	70.1	3.8	79	21	1160	230	70.1	4
11	111	85	0.76	0.056	0.015	0.092	0.022	0.01105	0.0005	0.00386	0.00053	0.13	70.8	3.3	86	21	1280	180	70.8	3
12	138	109	0.79	0.062	0.016	0.096	0.022	0.01081	0.0005	0.00394	0.00064	-0.20	69.3	3.4	91	20	1200	230	69.3	3
13	510	149	0.29	0.054	0.0041	0.398	0.028	0.0533	0.0013	0.02	0.0017	0.18	334.7	8	339	20	369	74	334.7	8
14	200	157	0.78	0.058	0.01	0.09	0.015	0.0108	0.0003	0.00339	0.00045	0.25	69.3	2.1	87	13	630	180	69.3	2
15	47	30	0.63	0.092	0.046	0.108	0.059	0.0115	0.0010	0.0047	0.0014	-0.22	73.5	6.4	88	50	2830	230	2830.0	230
16	86	87	1.00	0.07	0.024	0.095	0.036	0.01062	0.0006	0.00405	0.00069	0.09	68.1	4.1	97	33	1500	250	68.1	4
17	144	164	1.13	0.049	0.011	0.071	0.016	0.01072	0.0005	0.00326	0.00033	-0.01	68.7	3.2	71	15	960	160	68.7	3
18	169	118	0.70	0.057	0.011	0.086	0.016	0.0115	0.0005	0.00361	0.00044	0.34	73.7	3.4	83	15	760	160	73.7	3
19	56	40	0.72	0.063	0.033	0.072	0.044	0.01102	0.0008	0.00341	0.00075	-0.11	70.6	5.3	75	41	2020	250	2020.0	250
20	343	231	0.67	0.0507	0.0076	0.072	0.011	0.01055	0.0003	0.00355	0.00036	-0.04	67.7	2.1	70	10	420	150	67.7	2
21	229	138	0.60	0.047	0.011	0.066	0.014	0.01007	0.0004	0.00387	0.00041	0.03	64.6	2.6	65	13	520	210	64.6	3
22	651	672	1.03	0.0521	0.0036	0.27	0.015	0.03691	0.0010	0.01391	0.00098	-0.19	233.6	6.3	242	12	344	74	233.6	6

23	114	86	0.76	0.061	0.017	0.089	0.025	0.01086	0.0006	0.00354	0.00062	-0.03	69.6	3.6	84	22	990	260	69.6	4
24	388	254	0.65	0.0507	0.0061	0.0736	0.008	0.01044	0.0003	0.00328	0.00032	-0.06	67	1.9	71.8	7.5	440	110	67.0	2
25	131	182	1.39	0.054	0.016	0.068	0.022	0.01018	0.0004	0.0035	0.00033	-0.25	65.3	2.6	63	21	1370	140	65.3	3
26	100	58	0.58	0.038	0.013	0.08	0.025	0.0108	0.0006	0.00364	0.00073	0.70	69.3	3.5	74	23	1690	420	69.3	4
27	1057	620	0.59	0.051	0.0032	0.266	0.013	0.0375	0.0011	0.01338	0.00097	0.33	237.3	6.9	239	10	276	85	237.3	7
28	633	422	0.67	0.0471	0.0046	0.076	0.012	0.01137	0.0009	0.00373	0.0006	0.08	72.9	5.6	74	11	270	100	72.9	6
29	576	573	0.99	0.0468	0.0052	0.0705	0.0075	0.01083	0.0003	0.00339	0.00026	0.19	69.4	1.8	69.9	7.1	420	110	69.4	2
30	350	166	0.47	0.0509	0.006	0.077	0.0084	0.01094	0.0004	0.00356	0.0004	0.41	70.1	2.2	74.9	7.9	515	93	70.1	2
31	230	139	0.60	0.0518	0.0096	0.075	0.014	0.01049	0.0004	0.00368	0.00046	0.04	67.3	2.7	75	13	730	160	67.3	3
32	183	110	0.60	0.057	0.013	0.083	0.02	0.0108	0.0005	0.00369	0.00056	0.08	69.2	3	82	18	870	170	69.2	3
33	82	83	1.01	0.054	0.022	0.077	0.029	0.01065	0.0005	0.0039	0.00052	0.34	68.3	3.4	74	29	1390	190	68.3	3
34	175	168	0.96	0.046	0.012	0.075	0.016	0.01061	0.0004	0.0032	0.00041	0.08	68.1	2.6	73	15	630	220	68.1	3
35	196	87	0.44	0.0573	0.0069	0.159	0.035	0.0201	0.0033	0.0083	0.0014	-0.07	128	21	157	29	850	110	128.0	21
36	389	242	0.62	0.0509	0.007	0.0713	0.0081	0.01029	0.0003	0.00336	0.00036	-0.20	66	2	69.6	7.6	570	180	66.0	2
37	145	139	0.96	0.047	0.014	0.075	0.022	0.01113	0.0004	0.00355	0.00044	0.15	71.4	2.8	71	20	870	210	71.4	3
38	330	418	1.27	0.058	0.01	0.087	0.016	0.01077	0.0003	0.0035	0.00043	0.08	69.1	2	84	14	850	180	69.1	2
39	122	75	0.61	0.05	0.017	0.074	0.027	0.0108	0.0005	0.00367	0.00066	0.07	69.3	3	70	25	1190	230	69.3	3
40	142	89	0.62	0.0557	0.007	0.236	0.026	0.03099	0.0009	0.01032	0.00099	0.02	196.7	5.7	222	21	570	140	196.7	6
41	442	226	0.51	0.0485	0.0097	0.074	0.016	0.01108	0.0004	0.00337	0.00043	-0.05	71	2.3	72	13	320	220	71.0	2
42	285	247	0.87	0.051	0.0082	0.072	0.01	0.01044	0.0003	0.00341	0.00031	-0.12	67	2.2	70.5	9.5	500	150	67.0	2
43	702	754	1.07	0.0475	0.0043	0.0696	0.0057	0.01072	0.0003	0.00321	0.00024	0.51	68.7	1.8	68	5.5	372	78	68.7	2
44	67	65	0.98	0.055	0.023	0.081	0.035	0.01081	0.0007	0.00392	0.00058	-0.02	69.3	4.3	78	32	1470	250	69.3	4
45	334	341	1.02	0.0512	0.0077	0.083	0.011	0.01127	0.0003	0.0037	0.00033	0.07	72.3	2	80	11	440	150	72.3	2
46	231	61	0.26	0.065	0.0042	1.163	0.06	0.1283	0.0023	0.0397	0.0035	0.07	778	13	781	28	794	92	778.0	13
47	377	275	0.73	0.05	0.0059	0.0714	0.009	0.01014	0.0004	0.00326	0.00031	0.30	65	2.2	69.7	8.5	490	110	65.0	2
48	242	167	0.69	0.051	0.011	0.076	0.015	0.01013	0.0004	0.00385	0.00045	0.05	65	2.6	73	14	980	190	65.0	3
49	256	291	1.14	0.0481	0.0076	0.079	0.012	0.01142	0.0004	0.00389	0.00037	0.28	73.2	2.8	76	11	660	130	73.2	3

50	136	106	0.78	0.051	0.013	0.073	0.017	0.01043	0.0005	0.00358	0.00047	0.10	66.9	2.9	70	16	900	180	66.9	3
51	392	748	1.91	0.0498	0.0073	0.0702	0.0096	0.01018	0.0003	0.0035	0.00032	-0.17	65.3	2	70.1	8.9	450	170	65.3	2
52	271	145	0.53	0.0471	0.0049	0.147	0.014	0.02223	0.0006	0.00751	0.00069	0.05	141.7	3.8	138	12	389	84	141.7	4
53	129	112	0.86	0.058	0.015	0.09	0.024	0.01123	0.0005	0.00362	0.00046	0.04	72	2.9	88	23	1040	180	72.0	3
54	245	154	0.63	0.0473	0.0076	0.069	0.011	0.01031	0.0004	0.00331	0.00037	-0.13	66.1	2.3	67	11	560	93	66.1	2
55	108	89	0.82	0.066	0.018	0.082	0.024	0.01039	0.0006	0.00277	0.00042	0.18	66.6	3.8	81	22	1270	260	66.6	4
56	56	36	0.65	0.058	0.026	0.088	0.04	0.01097	0.0008	0.0029	0.001	-0.07	70.3	5.2	94	34	1350	250	70.3	5
57	478	115	0.24	0.0519	0.0045	0.3	0.023	0.04116	0.0010	0.0165	0.0013	-0.09	260	6.1	266	17	360	130	260.0	6
58	395	220	0.56	0.0657	0.0075	0.0962	0.0098	0.01054	0.0003	0.00407	0.00042	-0.03	67.6	2.1	92.6	9.1	930	140	67.6	2
59	72	57	0.80	0.053	0.022	0.074	0.031	0.01012	0.0006	0.00346	0.00061	0.11	64.9	3.9	71	28	1370	210	64.9	4
60	181	136	0.75	0.054	0.01	0.078	0.015	0.01081	0.0004	0.00333	0.00038	0.03	69.3	2.7	77	14	890	180	69.3	3
61	178	154	0.87	0.064	0.03	0.091	0.054	0.01125	0.0008	0.0042	0.0012	0.07	72.1	5.1	94	45	920	310	72.1	5
62	182	117	0.64	0.0516	0.0099	0.078	0.014	0.01099	0.0004	0.00348	0.00036	-0.12	70.5	2.4	78	13	870	160	70.5	2
63	416	332	0.80	0.049	0.0069	0.073	0.0091	0.0106	0.0003	0.00364	0.00033	-0.37	68	2	73.4	8.5	570	120	68.0	2
64	128	105	0.82	0.07	0.016	0.108	0.025	0.01148	0.0005	0.00344	0.00068	-0.09	73.6	3.4	101	22	1320	150	73.6	3
65	195	154	0.79	0.0606	0.0093	0.099	0.014	0.01179	0.0004	0.0039	0.00043	0.07	75.5	2.3	98	13	830	140	75.5	2
66	201	203	1.01	0.0568	0.0052	0.375	0.03	0.0479	0.0012	0.0159	0.0012	0.02	301.4	7.1	322	22	510	100	301.4	7
67	211	128	0.60	0.0495	0.0094	0.076	0.013	0.01077	0.0004	0.00383	0.0005	-0.10	69	2.7	76	12	690	140	69.0	3
68	247	156	0.63	0.0523	0.0046	0.303	0.022	0.0429	0.0014	0.0138	0.0011	0.09	270.8	8.6	267	17	357	79	270.8	9
69	257	281	1.09	0.048	0.011	0.075	0.013	0.01049	0.0004	0.00331	0.00034	0.19	67.3	2.3	73	12	800	160	67.3	2
70	187	134	0.72	0.0441	0.0095	0.068	0.014	0.011	0.0004	0.00359	0.00041	0.01	70.5	2.4	69	13	520	150	70.5	2
71	216	132	0.61	0.055	0.013	0.076	0.017	0.01019	0.0004	0.00312	0.00049	-0.04	65.4	2.4	76	16	980	190	65.4	2
72	195	91	0.47	0.0476	0.0087	0.069	0.014	0.01073	0.0004	0.00401	0.00054	0.06	68.8	2.5	67	13	800	220	68.8	3
73	83	86	1.03	0.05	0.021	0.072	0.027	0.01015	0.0006	0.00287	0.00044	-0.04	65.1	4	74	25	1200	240	65.1	4
74	496	303	0.61	0.0583	0.0082	0.085	0.012	0.01083	0.0003	0.00388	0.00047	-0.02	69.5	2.1	82	11	890	160	69.5	2
75	302	376	1.25	0.0516	0.0078	0.077	0.011	0.01062	0.0004	0.0033	0.00027	-0.02	68.1	2.4	76	10	800	180	68.1	2
76	1106	179	0.16	0.0494	0.0053	0.0738	0.0088	0.0107	0.0010	0.00363	0.00071	0.01	68.3	6.6	72.3	8.1	330	160	68.3	7

77	130	99	0.76	0.058	0.011	0.085	0.016	0.01105	0.0004	0.00349	0.00048	-0.18	70.8	2.8	82	15	930	150	70.8	3
78	722	398	0.55	0.0502	0.0042	0.0685	0.005	0.01023	0.0002	0.00325	0.00027	0.13	65.6	1.5	67.2	4.8	356	84	65.6	2
79	407	292	0.72	0.0543	0.0064	0.0776	0.0085	0.01071	0.0003	0.00319	0.0003	-0.08	68.7	2.1	75.4	7.9	590	120	68.7	2

Supplementary Material C

Publications and collaborations within the study area

A brief explanation of each paper and their relationship to the thesis is presented below:

The papers presented by **Martínez et al. (2017, 2018)** study several seismic sections within the Salar de Atacama and Salar de Punta Negra basins, with an emphasis on the influence of inherited early Mesozoic (?) extensional structures and their later reactivation. Both studies show a clear link between the start of compression and the generation of the Preandean Basins, and as such have been cited in the discussion of this thesis.

The study by **Rubilar et al. (2017)** was one of the first performed in the area with a balanced, kinematic reconstruction of the Cordillera de la Sal based on seismic reflection surveys and available field data. It also highlights the role of evaporite tectonics in the formation of the feature. The tectonic setting presented for the Oligocene-Miocene in this work is at odds with that interpreted in this thesis and by later authors, and as such it is an important contribution for the discussion.

The article by **Bascuñán et al. (2016)** comprises the results from the Master's degree thesis, which raised several questions that were approached in this PhD. thesis. It provides the groundwork for most of the geological setting during the Late Cretaceous, the interaction of the different components of the Cretaceous back-arc with the basin, and the ages, provenance and depositional events involved, along with a tentative timing for the beginning and evolution of compression in the Late Cretaceous.

Finally, the article by **Narea et al. (2015)** highlights the presence of tectonic rotations along the Cerros de Tuina and Barros Arana Syncline, and provides a good constraint on the effects (or lack thereof) of different deformational events on the amount of rotation of the Mesozoic units, and the importance of the K-T event in establishing the configuration of the present-day forearc.

Tectonophysics 744 (2018) 333–349

Contents lists available at ScienceDirect

Tectonophysics

journal homepage: www.elsevier.com/locate/tecto

Tectonic interaction between Mesozoic to Cenozoic extensional and contractional structures in the Preandean Depression (23°–25°S): Geologic implications for the Central Andes

F. Martínez[a,*], C. López[a], S. Bascuñan[b], C. Arriagada[c]

[a] Departamento de Ciencias Geológicas, Universidad Católica del Norte, Angamos 0610, Antofagasta, Chile
[b] Departamento de Geología, FCFM, Universidad de Chile, Santiago, Chile
[c] Independent Tectonic Consultant, Chile

ARTICLE INFO

Keywords:
Sedimentary basin
Seismic profile
Contraction
Faults
Tectonic interaction

ABSTRACT

A multidisciplinary study supported by field data and 2-D seismic information was conducted to understand the tectonic interactions between Mesozoic to Cenozoic extensional and contractional structures along the Preandean Depression (23°–25°S) in northern Chile, which have been largely debated. This work gives some new ideas about the control that ancient basement extensional faults exert on the crustal shortening and growth of those orogenic belts located over normal subduction zones similar to the Central Andes. In this work, two sedimentary basins were analyzed: the Salar de Atacama and the Salar de Punta Negra, both of which correspond to intra-montane basins bounded by the Domeyko Cordillera and the current volcanic arc of the Central Andes. The interpretation of a series of west to east-oriented 2-D seismic profiles revealed three types of structural interaction: i) pure positive reactivation; ii) decapitation of previous normal faults by reverse faults; and iii) transport of previous normal faults by thrust ramps. Inversion anticlines and basement-involved contractional structures were the most common observed structures, indicating that the geometry and distribution of inherited normal faults of the Paleozoic and Mesozoic basement played an important role in basin contraction. The different modes of tectonic interaction frequently created variations on the geometry and kinematic of the final structural styles present in the region. Commonly the Upper Cretaceous to Cenozoic synorogenic tectonosequences recorded the ages of contractional deformation that affected the region. Similar to other regions of northern Chile, basin inversion occurred during the Late Cretaceous and subsequent propagation of reverse faults occurred from the upper Late Cretaceous to the present. The basement-involved reverse fault structures usually create the most important positive topographic relief in this part of the western Central Andes. Using as example our study area, we finally conclude that the original position and distribution of ancient basement pre-orogenic normal faults in the orogenic belts condition the final vergence and kinematic of the subsequent thrust systems related to shortening episodes.

1. Introduction

The Preandean Depression in northern Chile (Fig. 1) is one of five tectonic provinces of the forearc of the Central Andes. This province is located between the Domeyko Cordillera (or Chilean Precordillera) and the magmatic arc, and exhibits a significant negative structural relief, evidenced by a series of Cretaceous and Cenozoic NNE-oriented intra-montane basins (Figs. 1 and 2). Along the northern and central part of the depression, the Salar de Atacama and Punta Negra (Figs. 1 and 2) are the main basins, with an approximate area of 21,000 km^2. Both consist of topographic lows occupied by salt flats and mostly sedimentary (Cretaceous)-Tertiary continental deposits. Here, the salt flats and more recent continental deposits mostly prevent observation of their internal structure and complete stratigraphic record.

Regional studies (e.g., Arriagada et al., 2006; Jordan et al., 2002, 2007; Martínez et al., 2017; Muñoz et al., 2002; Pananont et al., 2004) have taken advantage of 2-D seismic information to interpret the structure and deformation history of the Preandean Depression and most major efforts have involved the northern part along the Salar de Atacama Basin as it contains a complete set of geological information that includes oil well data, gravity and seismic profiles (Fig. 3), and some field data from its western section. These studies have attempted

* Corresponding author.
E-mail address: fernando.martinez@ucn.cl (F. Martínez).

https://doi.org/10.1016/j.tecto.2018.07.016
Received 5 March 2018; Received in revised form 20 June 2018; Accepted 24 July 2018
Available online 27 July 2018
0040-1951/

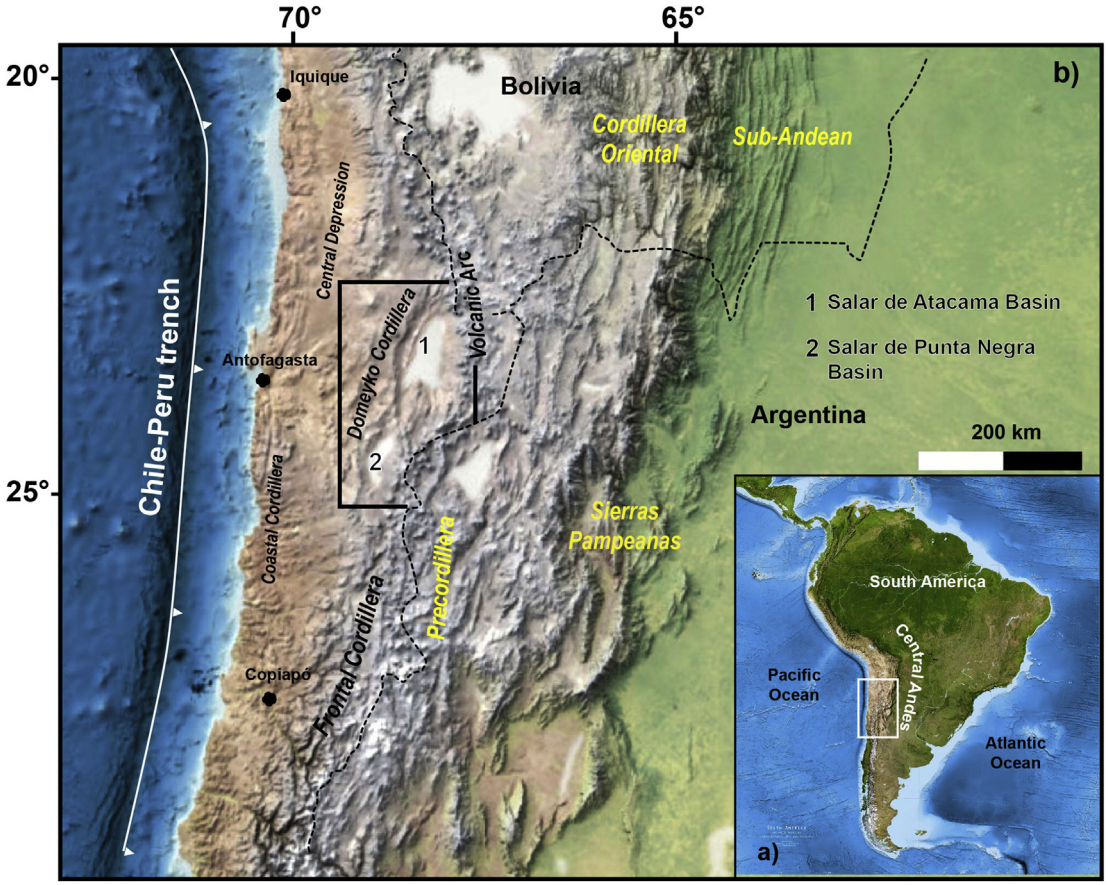

Fig. 1. Location of the Preandean Depression in the Central Andes, northern Chile, and distribution of neighboring tectonic provinces in Chile, Argentina, and Bolivia.

to explain the structure of the region using different tectonic models, which include: a) the Late Cretaceous tectonic inversion of a former Jurassic extensional basin (e.g., Tarapacá Basin; Arriagada et al., 2006; Bascuñán et al., 2016; Mpodozis et al., 2000, 2005; Muñoz et al., 2002; Mpodozis and Ramos, 2008) that extended from northern Perú to northern Chile during Jurassic-Early Cretaceous; b) the creation of a flexural foreland basin during the Late Cretaceous (Flint et al., 1993; Hartley et al., 1992); c) the Cenozoic tectonic collapse of a pre-existing Eocene thrust system, and even Pliocene margin-parallel strike-slip deformation (Kuhn, 2002). More recent works (Martínez et al., 2017) in the Salar de Punta Negra Basin (Fig. 2) have interpreted the structure as the result of different superimposed extensional and contractional episodes active during the Mesozoic (extension) and Cenozoic (contraction).

The existence of different models indicates that the structure of the Preandean Depression is complex and not completely understood. Some works (Muñoz et al., 2002; Mpodozis et al., 2005; Martínez et al., 2017) agree that extensional and contractional structures played an important role during its evolution. Interactions between such structures are commonly observed in many basins of the Central Andes in Chile and Argentina (e.g., Salta Rift, Santa Barbara System, Chañarcillo, and Neuquén basins; Carrera et al., 2006; Giambiagi et al., 2003; Kley et al., 1999; Martínez et al., 2013; Mescua and Giambiagi, 2012) and are frequently associated with the positive and/or negative reactivation of pre-existing basement structures. Although the surface geology of the Preandean Depression has been relatively well studied, the nature of the tectonic interaction between extensional and contractional structures on the subsurface remains a topic of debate. For example, previous studies have proposed different geometries for structures as the Salar Fault and the Barros Arana Syncline in the Salar de Atacama Basin (Fig. 3), thus revealing opposite interpretations to regional structures (Arriagada et al., 2006; Flint et al., 1993; Jordan et al., 2007; Pananont et al., 2004; Rubilar et al., 2017).

To understand the tectonic interactions between the Mesozoic and Cenozoic extensional and contractional structures in the central part of the Preandean Depression and their tectonic implications for the geological evolution of the western Central Andes, we present a new seismic and structural interpretation of 2-D seismic profiles of the Salar de Atacama and Punta Negra basins. In this study, we document the structural styles that result from this interaction and model the geometry of first-order faults considering the deformation style of their hanging wall blocks. We also determine the structural and stratigraphic characteristics of the seismic sequences involved in deformation. We finally documented as the original position and distribution of ancient basement pre-orogenic normal faults in the orogenic belts condition the final vergence and kinematic of the subsequent thrust systems related to Cenozoic shortening episodes. The results obtained here, could be used to compare similar structural relationships observed in other orogenic belts worldwide.

2. Geological setting

The northern and central part of the Preandean Depression in northern Chile (Fig. 2) is formed by two NNE-oriented intra-montane basins: the Salar de Atacama and Salar de Punta Negra basins. They form an area of negative relief between the Domeyko Cordillera and the Western Cordillera and/or magmatic arc (Fig. 2) with elevations between ~3000 and 2300 m.a.s.l. (Gardeweg et al., 1994; Maksaev and Zentilli, 1999; Soto et al., 2005; Arriagada et al., 2006; Reutter et al., 2006; Martínez et al., 2017).

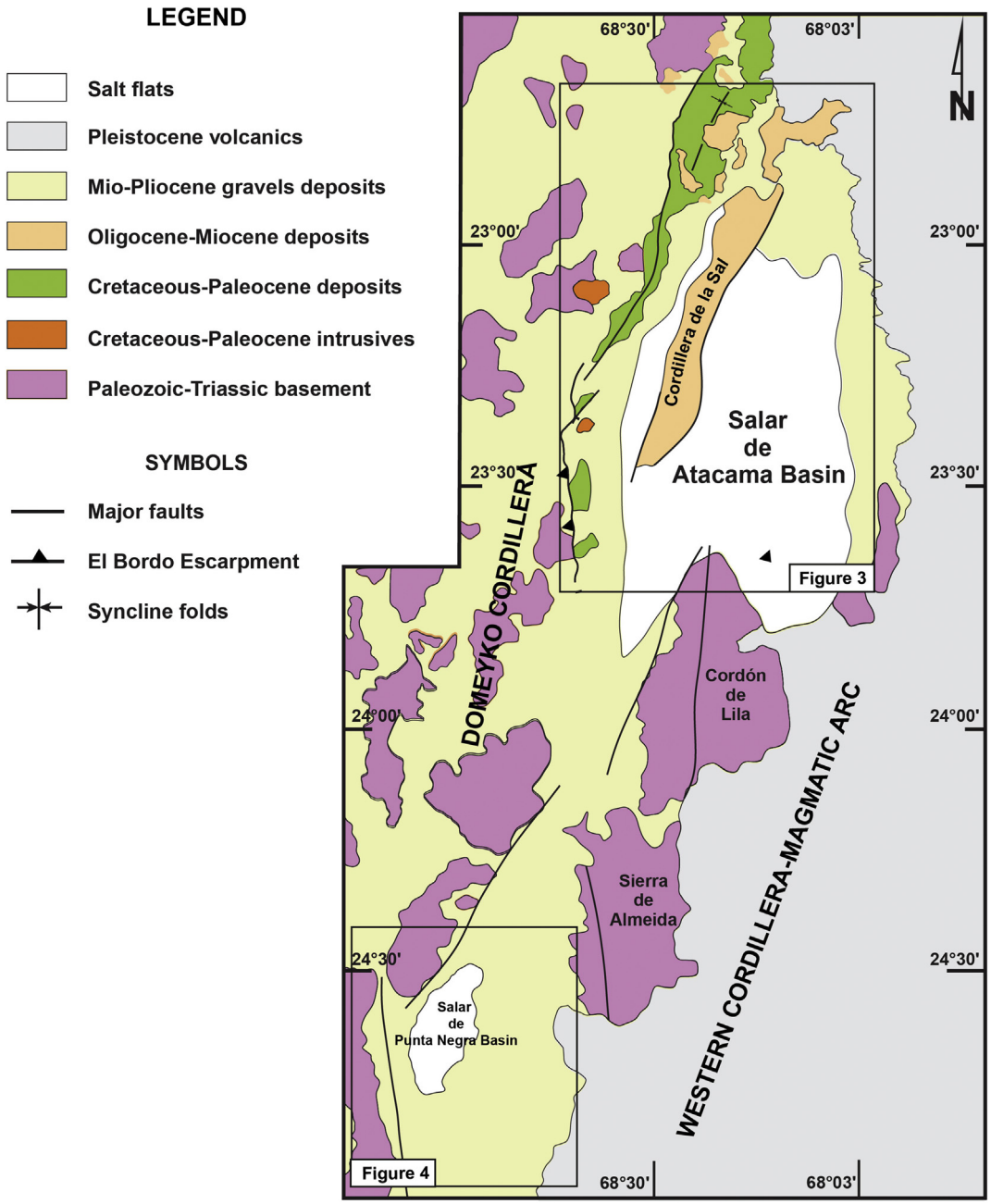

Fig. 2. Simplified geological map showing the plan-view distribution of major tectonic provinces and geological units that form part of the forearc of northern Chile, between 23° and 24°30′ S.

2.1. Salar de Atacama Basin

The Salar de Atacama Basin is the most studied region of the Preandean Depression. The use of field, oil well, and seismic data has revealed the distribution of major volcanic and sedimentary stratigraphic units beneath the basin. The oldest rocks in this region are mainly exposed in the Cordón de Lila along the southern termination of the basin (Figs. 2 and 3) and defined as the Lila Complex (Niemeyer, 1984) These consist of Lower Paleozoic sedimentary and igneous rocks (sandstones with intercalated pillow lavas) and some stratified volcanic and sedimentary deposits of Upper Paleozoic to Triassic age (Niemeyer, 1984; Niemeyer et al., 1997), which are interpreted as the products of a former volcanic arc and shallow marine deposits (Niemeyer, 1989).

On surface, the Mesozoic rocks are mainly represented by stratified Cretaceous successions exposed to the east of the El Bordo Escarpment and along the Barros Arana Syncline on the northwest flank of the basin (Fig. 3). They consist of a thick (almost 4000 m) continental volcanic and sedimentary succession composed of conglomerates, laminated sandstones, gypsum layers, mudstones, and andesites, which form part of the Purilactis Group (Dingman, 1963; Hartley et al., 1992; Charrier and Reutter, 1994; Mpodozis et al., 2005; Bascuñán et al., 2016). This is composed of the Tonel, Purilactis, Barros Arana, and Cerro Totola formations (Fig. 5a) that are commonly associated with fluvial, alluvial, and lacustrine deposits (Dingman, 1963; Bascuñán et al., 2016). Recent U–Pb ages of detrital zircons have reported maximum depositional ages of 149 Ma for the lower section of the Purilactis Group and 73–79 Ma for its upper section exposed in the Barros Arana Syncline (Bascuñán et al., 2016; Fig. 3). Other research has reported K–Ar ages between ~66–40 Ma for the upper section of this succession, as well as some related intrusions (Mpodozis et al., 2005; Fig. 3). The lower

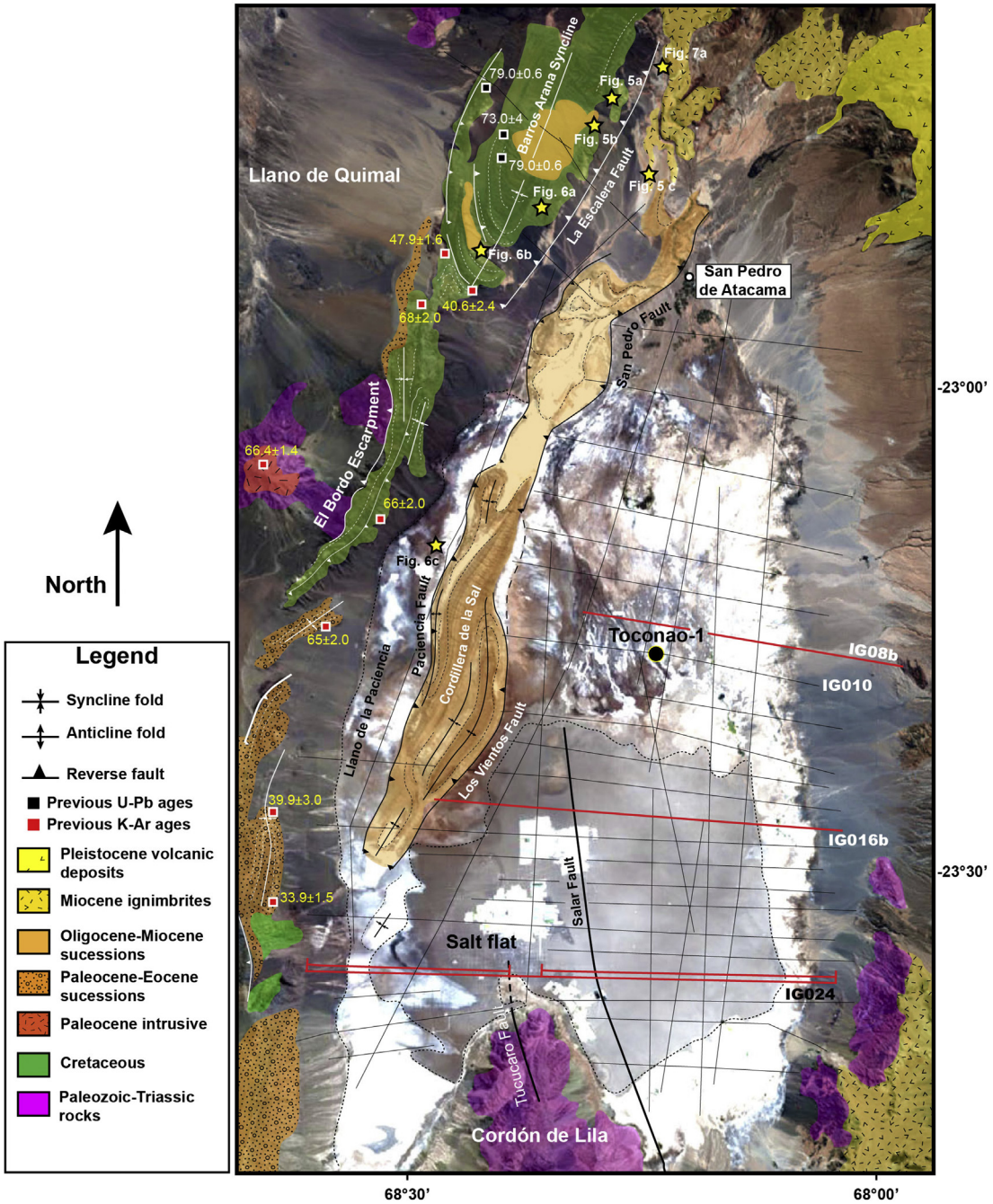

Fig. 3. Simplified geological map over a Landsat 8 image of the Salar de Atacama Basin (modified from Arriagada et al., 2006 and Becerra et al., 2014) and location of the 2-D seismic profiles used in this study (red lines). K–Ar and U–Pb ages were taken from Mpodozis et al. (2005) and Bascuñán et al. (2016). The yellow stars indicate the location of photographs in Fig. 5 and 6. The white dotted lines indicate stratification. Abbreviations: Paleozoic-Triassic rocks: Lila Complex; Cretaceous: Purilactis Group; Paleocene intrusives: Paleocene granitic rocks; Paleocene-Eocene successions: Naranja Formation; Oligocene-Miocene successions: San Pedro and Tambores (Paciencia Group) fms; Miocene ignimbrites; Quaternary volcanic deposits: mainly lavas and ignimbrites. Location of the Toconao-1 oil well is indicated. (For interpretation of the references to colour in this figure legend, the reader is referred to the web version of this article.)

sections of this group (Tonel Formation; Arriagada et al., 2006) frequently exhibit contractional growth strata that provide clear evidence for synorogenic accumulation since at least 149 Ma (Fig. 6a, b).

Such as it has been recognized by Arriagada et al. (2006) (Fig. 2b in this work), along the westernmost part of the basin, the Purilactis Group is unconformably covered by almost 1900 m of folded Paleocene and Eocene sedimentary rocks (Fig. 3), predominantly composed of orange stratified sandstones and gypsum known as the Naranja Formation and volcanic (tuffs) and sedimentary (conglomerates) succession defined as Loma Amarilla Formation (Dingman, 1963; Ramirez and Gardeweg, 1982; Hammerschmidt et al., 1992; Mpodozis et al., 1999; Arriagada et al., 2006). Mpodozis et al. (2005) reported K–Ar and $^{40}Ar–Ar^{39}$ ages of 39.9 ± 3 Ma and 43.8 ± 0.5 Ma, respectively, indicating an Eocene age. Although both formations have been well reported at the surface, they have not been clearly identified under the basin using Toconao-1 oil well data (Muñoz et al., 1997, 2002) so their subsurface interpretation remains highly speculative. Oligocene and Miocene deposits are mostly exposed along the Cordillera de la Sal (Fig. 3), and also along the northern and southeastern edges of the basin (Fig. 3), where they are affected by mesoscale folds and reverse faults

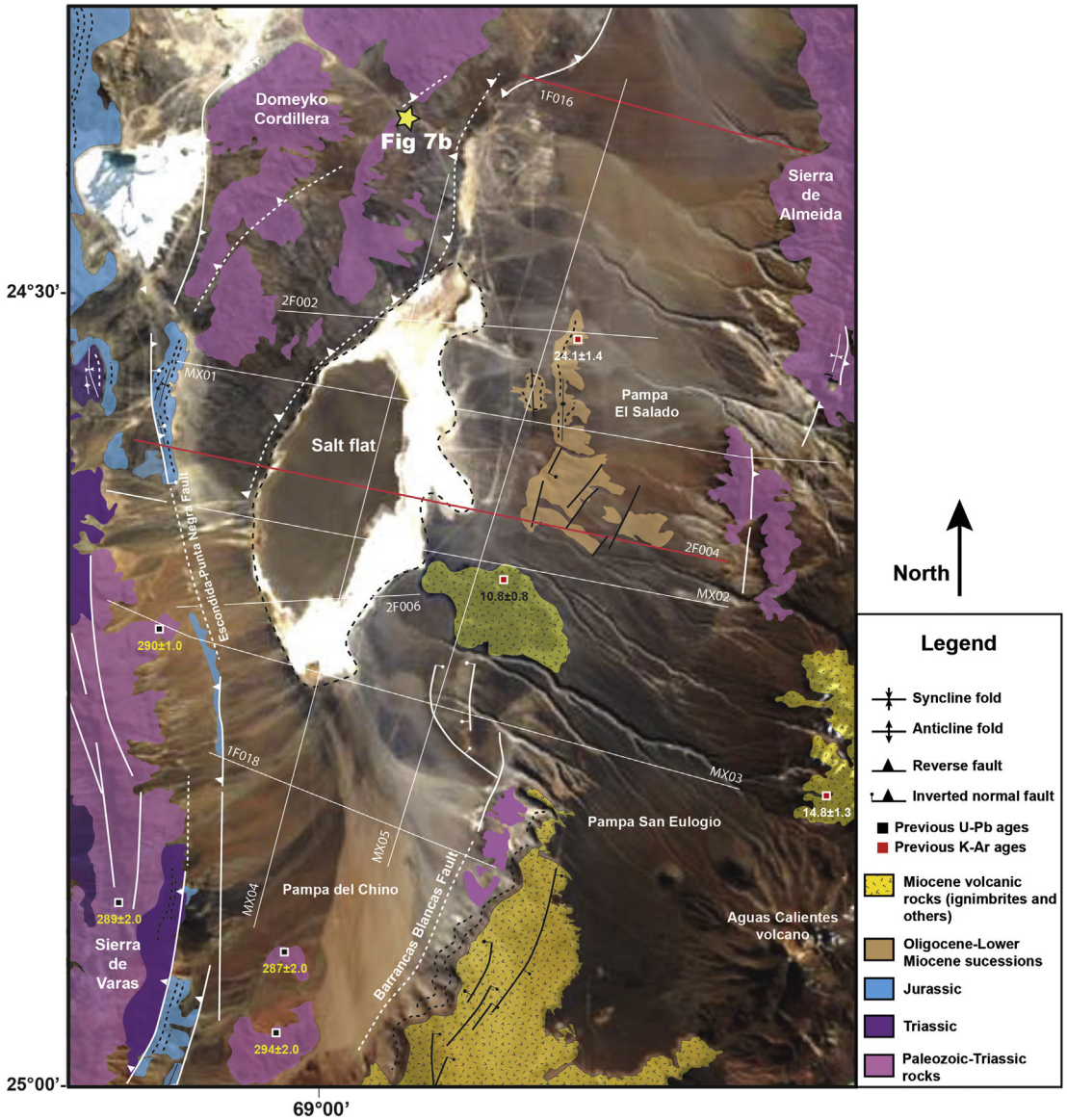

Fig. 4. Simplified geological map over a Landsat 8 image of the Salar de Punta Negra Basin and the eastern part of the Domeyko Cordillera (modified from Gardeweg et al., 1993, 1994 and González et al., 2015) and location of the 2-D seismic profiles used in this study (red lines). The yellow star indicates the location of the photographs in Fig. 7. The white and black dotted lines indicate stratification. Abbreviations: Paleozoic-Triassic rocks: Zorritas and/or La Tabla fms; Triassic: Sierra de Varas Formation; Jurassic: El Profeta Formation; Oligocene-Miocene successions: Pampa de Mulas Formation; Miocene ignimbrites. (For interpretation of the references to colour in this figure legend, the reader is referred to the web version of this article.)

(Fig. 5b,c). The Oligocene section consist of evaporites and siliciclastic rocks (sandstones, conglomerates, and shales) assigned to the Paciencia Group composed of the San Pedro (Fig. 5c) and Tambores formations (Brüggen, 1934; Ramirez and Gardeweg, 1982; Marinovic and Lahsen, 1984; Flint et al., 1993). Both formations are associated with lacustrine and alluvial deposits and have K–Ar ages of approximately 26 Ma (Mpodozis et al., 2000). The Miocene consist of ignimbrites and other more recent volcanic products that lie unconformably over the folded sedimentary rocks of the upper sections of the Purilactis Group (Fig. 5c).

2.2. Salar de Punta Negra Basin

The oldest rocks of this basin are mostly exposed along the eastern Domeyko Cordillera and the eastern flank of the basin along the Sierra de Almeida (Fig. 4). These correspond to thick (> 2000 m) successions of Paleozoic (Devonian to Carboniferous) to Lower Triassic volcanic and sedimentary deposits known as Zorritas and La Tabla formations, which are intruded by some Permian (280–200 Ma) granitoids (Cecioni and Frutos, 1975; Isaacson et al., 1985; Niemeyer et al., 1997; Maksaev and Zentilli, 1999; González et al., 2015; Rubinstein et al., 2016). These have been interpreted as the products of an ancient magmatic arc active during the Paleozoic on the western margin of Gondwana (Breitkreuz and Zeil, 1994; Breitkreuz and Van Schmus, 1996).

The Paleozoic rocks are commonly covered by Lower Mesozoic successions composed of continental and marine Upper Triassic and Jurassic stratified rocks exposed along a narrow N–S deformed belt (Fig. 4) in the western edge of the basin and the easternmost part of the Domeyko Cordillera. The Upper Triassic successions consist of andesitic and siliciclastic rocks made of sandstones, shales assigned to Sierra de Varas Formation (González et al., 2015; Fig. 8). In the eastern Domeyko Cordillera, the Triassic deposits are unconformably covered by marine Jurassic successions (Fig. 4) composed of calcareous sandstones, mudstones, limestones, and black shales defined as the Profeta Formation (Chong, 1973; Ardill et al., 1998). Both Triassic and Jurassic deposits exhibit important changes of thickness and contain intra-formational

normal faults (Amilibia et al., 2008). These characteristics suggest that they are *syn*-rift sequences related to the stratigraphic infill of ancient extensional basins (e.g., the Tarapacá and Profeta basins; Mpodozis and Ramos, 1989, 2008; Mpodozis and Cornejo, 1997; Scheuber and González, 1999; Mpodozis et al., 2005).

Along the central part of the basin to the west of the Pampa del Salado Upper Oligocene-Lower Miocene deposits are exposed (Fig. 4). These consist of almost 1000 m of stratified gravels, sandstones, conglomerates, ignimbrites, and volcanic ash defined as the Pampa de Mulas Formation (Chong, 1973; Gardeweg et al., 1993; Marinovic et al., 1995; Fig. 4). These are traditionally correlated with rocks of the Paciencia Group in the Salar de Atacama Basin. Previous research based on seismic visualization recognized contractional growth strata in the Pampa de Mulas Formation, indicating that this corresponds to a continental synorogenic sequence (Martínez et al., 2017). To the central, east and south part, Mio-Pliocene rocks represent the youngest infill of the basin (Fig. 4). They correspond to sedimentary (mainly sandstones and conglomerates) and other volcanic flows that are preferentially exposed in the Pampa San Eulogio (Fig. 4). Martínez et al. (2017) also used the seismic configuration of these successions to interpret them as synorogenic deposits.

3. Surface structure of the study area

The most prominent structures in the study area are exposed along the western edges of both basins (Figs. 3 and 4). In the Salar de Atacama Basin, the El Bordo Escarpment, the Barros Arana Syncline, and the Cordillera de la Sal (Fig. 3) thin-skinned folded belt represent first-order structures. El Bordo Escarpment is a NNE-striking topographic scarp 900 m high that separates the Domeyko Cordillera and the Salar de Atacama Basin (Arriagada et al., 2006). Along this scarp, Paleozoic and Triassic rocks overlie Cretaceous deposits of the Purilactis Group (Fig. 3), which are frequently folded and faulted.

To the northernmost part of the basin, the NNE-striking Barros Arana Syncline (Fig. 3) is an open syncline that includes the complete succession of the Purilactis Group, and which narrows toward the south (Fig. 3). Along its western limb, the middle section of the Purilactis Group is detached by an east-dipping thrust exposed along the Llano de Quimal (Fig. 3; Arriagada et al., 2006). Its eastern limb is bounded by the NNE-striking La Escalera Fault (Becerra et al., 2014), which consists of a west-dipping reverse fault along which the Purilactis Group overlies Miocene ignimbrites (Fig. 3). Previous analyses of 2-D seismic profiles have interpreted this structure as a syncline that formed over a shallow east-verging ramp (Arriagada et al., 2006).

The Cordillera de la Sal is a NNE-striking thin-skinned folded belt located in the Salar de Atacama Basin between the Llano de la Paciencia and the salt flats (Figs. 3 and 6c). It is composed of a series of narrow and asymmetrical anticlines and synclines that exhibit an en echelon array and that commonly involve Oligocene deposits of the Paciencia Group. They consist of west and east-verging folds with cores of evaporitic rocks, bounded by NNE-striking, west and east-dipping thrusts (Fig. 6c) (Paciencia, Los Vientos and San Pedro faults; Becerra et al., 2014; Rubilar et al., 2017), forming a pop-up structure (Fig. 3). This structural style has frequently been interpreted as a thin-skinned deformation pattern resulting from eastern propagation of the Domeyko Cordillera (Muñoz et al., 2002). Other subsidiary and mesoscale reverse faults have been observed along the northernmost part of the Cordillera de la Sal that mainly affect the Oligocene sedimentary deposits of the San Pedro Formation and Miocene ignimbrites (Figs. 5b, 7a).

In the Salar de Punta Negra Basin, the main structures (Fig. 4) are commonly highly eroded and/or covered by Quaternary gravels that hinder observations. They are related to NE-SW and N-S-striking basement-involved reverse faults that separate basement ridges (e.g., Sierra de Varas; Fig. 4) from narrow belts of folded and faulted *syn*-rifted Mesozoic rocks (predominantly Triassic and Jurassic). Escondida-Punta Negra Fault (Fig. 4) represents the main structure in this sector and consists of a large and NNE-striking fault, which was recently interpreted as the western master fault of the Salar de Punta Negra Basin (Martínez et al., 2017). This is a high-angle fault that joins Paleozoic rocks with Jurassic rocks and Pliocene and recent deposits (Fig. 4). Moreover, the western edge of the Salar de Punta Negra Basin is frequently marked by escarpments associated with west-dipping basement-related reverse faults (Fig. 7b). Different interpretations have suggested that these structures could be kilometric (> 10 km length) basement strike-slip faults associated with transpressive deformation during the Eocene (Maksaev, 1990; Mpodozis et al., 1993; Tomlinson and Blanco, 1997); however, more recent studies supported by balanced cross sections and seismic interpretation along the eastern Domeyko Cordillera and the western site of the Salar de Punta Negra Basin have indicated that it corresponds to a partially inverted Mesozoic normal fault of the former Tarapacá Basin established in the region during Jurassic (Amilibia et al., 2008; Martínez et al., 2017). Along the eastern part of the Salar de Punta Negra Basin, a series of east-dipping, basement-related reverse faults have been recognized to west and south of the Sierra de Almeida. Seismic profiles located near to this area (Pampa El Salado) show as these faults affect the Paleozoic rocks and also Oligocene deposits and Miocene ignimbrites and even the Recent cover of the basin (Martínez et al., 2017).

4. Methodology

In order to understand the interaction between extensional and contractional structures in the central part of the Preandean Depression, we interpreted a series of W-E 2-D seismic profiles distributed along the Salar de Atacama and Punta Negra basins (Figs. 3 and 4). We interpreted those seismic profiles located in the central and southern parts of both basins, because they contain good examples of the tectonic interaction between Mesozoic to Cenozoic extensional and contractional structures. Seismic data were integrated with geological information from previous studies based on mapping at 1:100.000 scale (Padilla, 1985; Gardeweg et al., 1993, 1994; Becerra et al., 2014; González et al., 2015) and other stratigraphic data derived from the Toconao-1 oil well in the central part of the Salar de Atacama Basin. The seismic data consist of a two-dimensional (2-D) seismic survey acquired and facilitated by ENAP-Sipetrol, which was previously used to identify possible oil and gas prospects under the Preandean Depression. Based on the appearance and continuity of the seismic reflectors, we classified the data as of moderate to good quality, and is better quality in the Salar de Atacama Basin.

The seismic profiles were first filtered and then migrated in time so that the vertical scale is in seconds (TWT). The velocity and density information of Toconao-1 required for time-depth conversion of the seismic data was not available for this study. Nevertheless, previous research has already performed this conversion, which is only applicable to the Salar de Atacama Basin (Pananont et al., 2004). In order to document the along-strike variation of structures, we perform seismic and structural interpretation of five seismic profiles: three in the Salar de Atacama Basin and two in the Salar de Punta Negra Basin (Figs. 3 and 4, lines IG024, IG08b, IG016b, 1F016 and 2F004). Before interpreting the seismic data, we made a seismic amplitude model using 2-D Move software (Midland Valley) to obtain a better contrast, in which reflectors with high amplitudes were highlighted. Then, we correlated the main seismic reflectors with geological units exposed along the seismic lines. This approach was mainly applied to the Salar de Punta Negra Basin due to the lack of available oil well data. On the other hand, we used the seismic and well data calibration (Muñoz et al., 2002; Jordan et al., 2007) from Toconao-1 in the Salar de Atacama Basin (Fig. 3) to correlate the first order sequences present under this basin. Considering that this study has a structural approach, we used a grayscale in the seismic profiles because it enables easy identification of faults.

Interpretation of the seismic profiles and modeling of the faults and

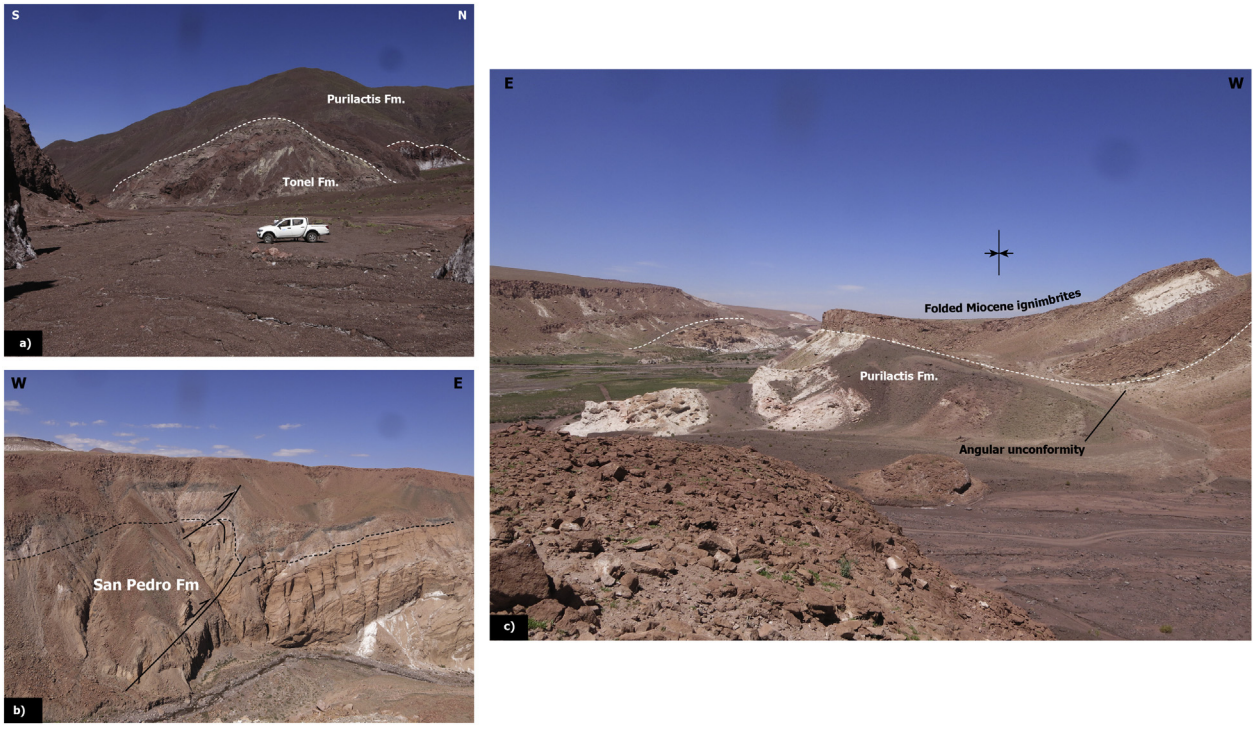

Fig. 5. a) View of the contact relationship between the Tonel and Purilactis formations of the Purilactis Group, b) meso-scale reverse faulting and folding affecting the Oligocene-Miocene deposits of the Paciencia Group (San Pedro Formation), and c) view of the folded unconformity between the Paciencia Group and the deformed Miocene ignimbrites exposed along the Salar de Atacama Basin. See Fig. 3 for location.

folds was performed using the StructureSolver software of Nunns and Rogan Company, which allowed rapid and precise forward modeling of the structures. The structures were interpreted according to the following criteria: a) recognition of reflector cut-off; b) recognition of truncated reflectors related to thrust faults and angular unconformities; c) lateral changes of amplitude to identify faults; and d) changes in

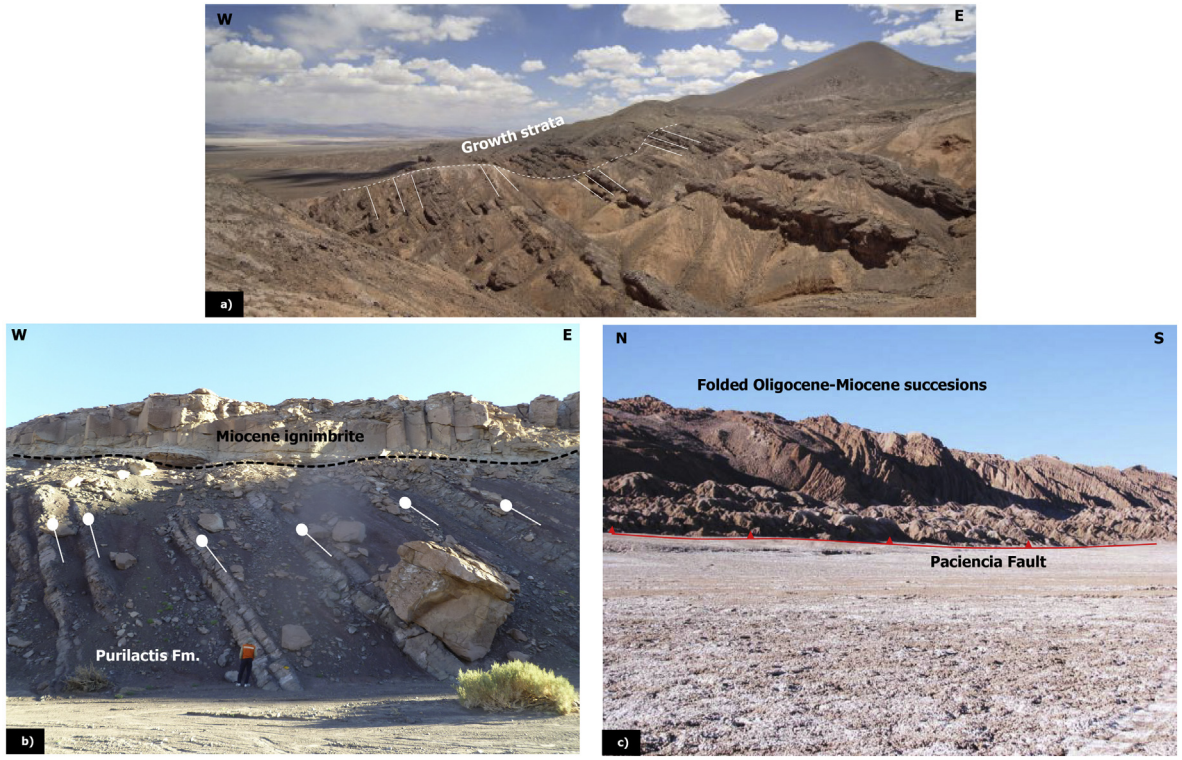

Fig. 6. a) W-E view of the growth strata preserved within synorogenic deposits of the Purilactis Group, b) detail of the angular unconformity between the synorogenic deposits of the upper Purilactis Group and the Miocene ignimbrites exposed along the Barros Arana Syncline, and c) plan-view aspect of the Paciencia Fault bounding the western flank of the Cordillera de la Sal from the Llano de la Paciencia region. See Fig. 3 for location.

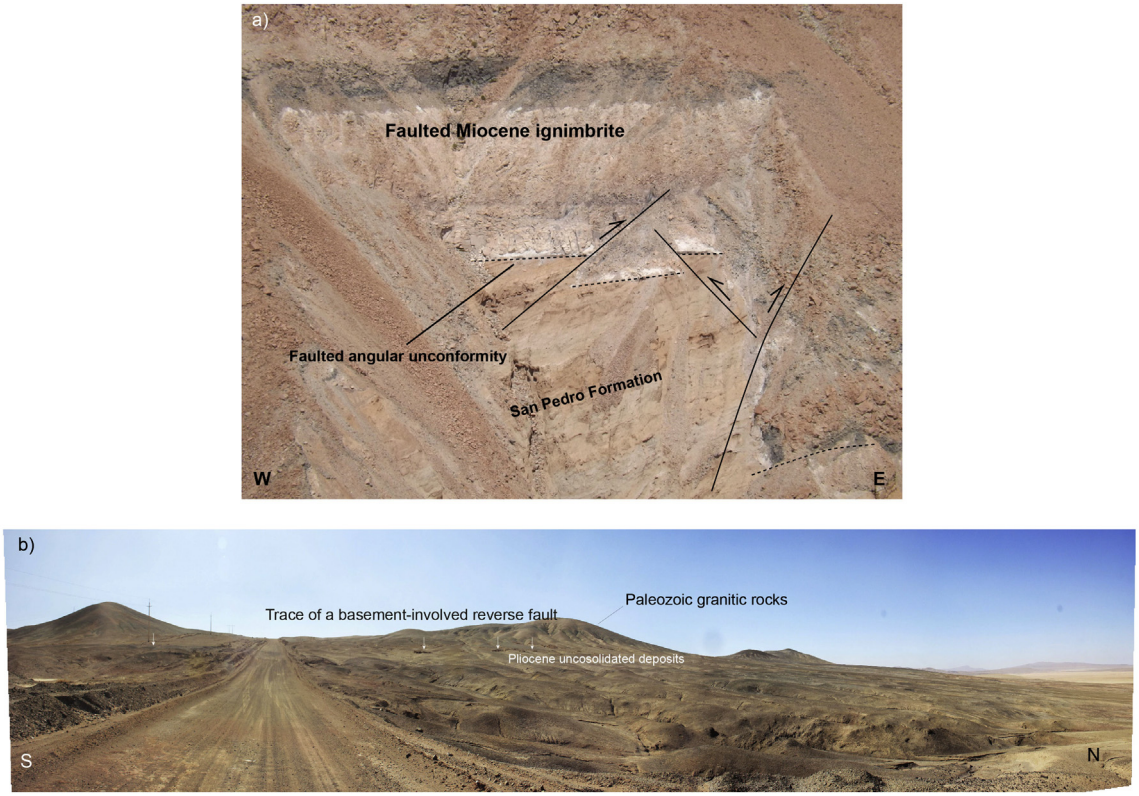

Fig. 7. a) Detail of the folded and faulted angular unconformity between the Oligocene-Miocene synorogenic deposits of the San Pedro Formation and the Miocene ignimbrites along the northern part of the Salar de Atacama Basin, and b) panoramic view showing traces of the basement-involved reverse faults that affect the western edge of the Salar de Punta Negra Basin. See Figs. 3 and 7 for location.

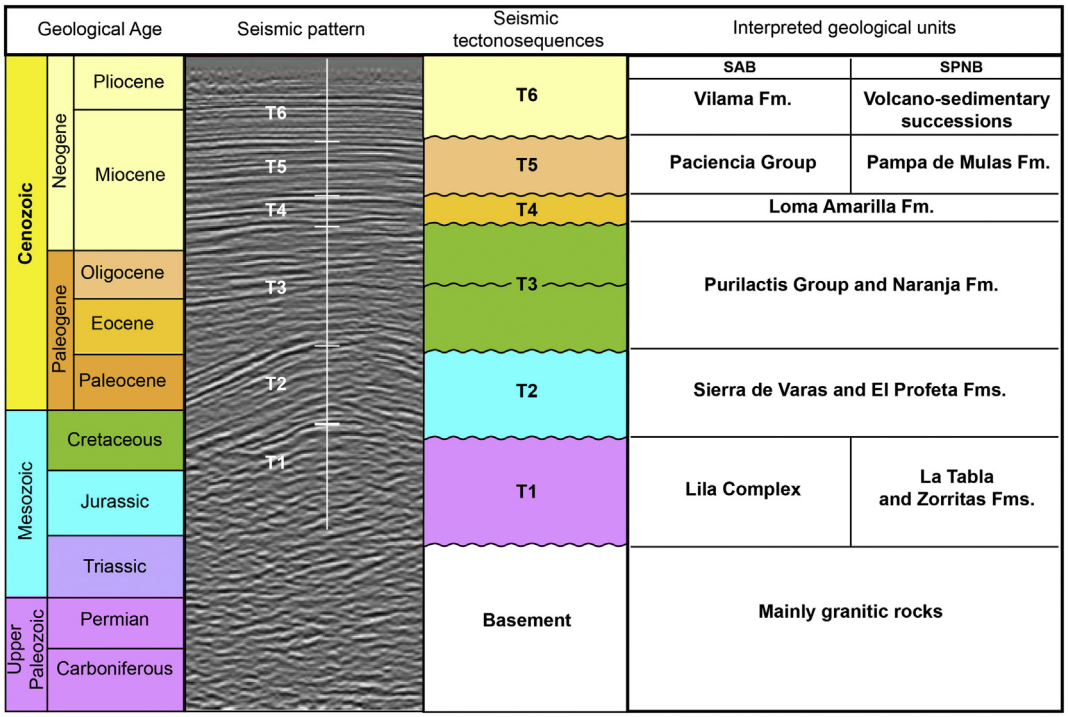

Fig. 8. Stratigraphic template showing the proposed correlation between the tectonosequences interpreted in this work and the geological units exposed along the Salar de Atacama and Salar de Punta Negra basins. The seismic profile corresponds to the central section of line IG010 located along the central part of the Salar de Atacama Basin. The projection of the Toconao-1 oil well is indicated into the seismic data. Abbreviations: SAB: Salar de Atacama Basin, SPNB: Salar de Punta Negra Basin.

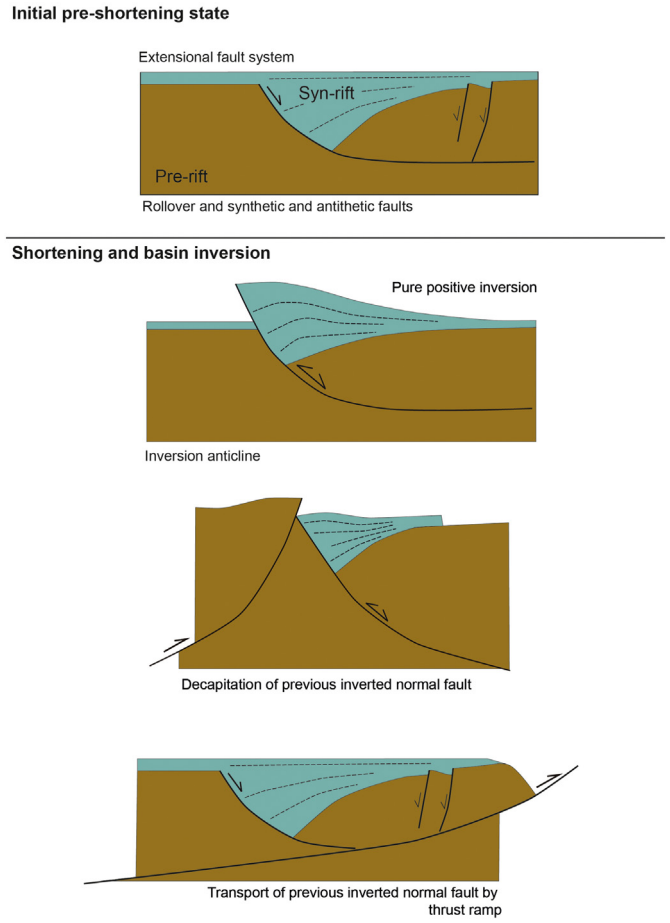

Fig. 9. Cartoon illustrating the main extensional and contractional interaction styles recognized in the Preandean basins.

reflector dip associated with folds and faults. Other criteria included determining the change of thickness of the stratigraphic sequences on each side of the faults in order to interpret structural styles and deposition history.

4.1. Limitations of this study

The main limitations of this work are associated with the quality of some seismic profiles, specifically those in the Salar de Punta Negra Basin (Fig. 4). These are typically of moderate quality in the first two seconds and highlight the stratified geological units very well, further, the deepest parts of the basin and some basement-involved structures are poorly constrained with this data. The absence of borehole information also hinders identification and correlation of geological units present on the subsurface, as well as the time-depth conversion of the seismic profiles. The seismic data in the Salar de Punta Negra Basin is only constrained by correlation with the crystalline basement and stratified rocks exposed along its western and eastern parts.

In the Salar de Atacama Basin, the seismic data does not have a good control on Lower Mesozoic successions and this is better constrained in the Salar de Punta Negra Basin. As 2-D seismic profiles were used in this study, it is difficult to spatially differentiate all the geological formations described in the geological setting; therefore, we only interpret seismic tectonosequences. Considering these limitations, we recommend that this data is used only to understand first-order structures present in the study area.

5. Seismic and stratigraphic tectonosequences

The interpretation of seismic tectonosequences is based on the identification of seismic reflector patterns and angular unconformities from seismic reflector terminations (e.g., on-laps, erosional truncations, top-laps, etc.) and contrasts of seismic amplitude. We associated the acoustic basement with the crystalline basement rocks of the basins, which are mostly composed of Paleozoic granitic rocks (geological setting).

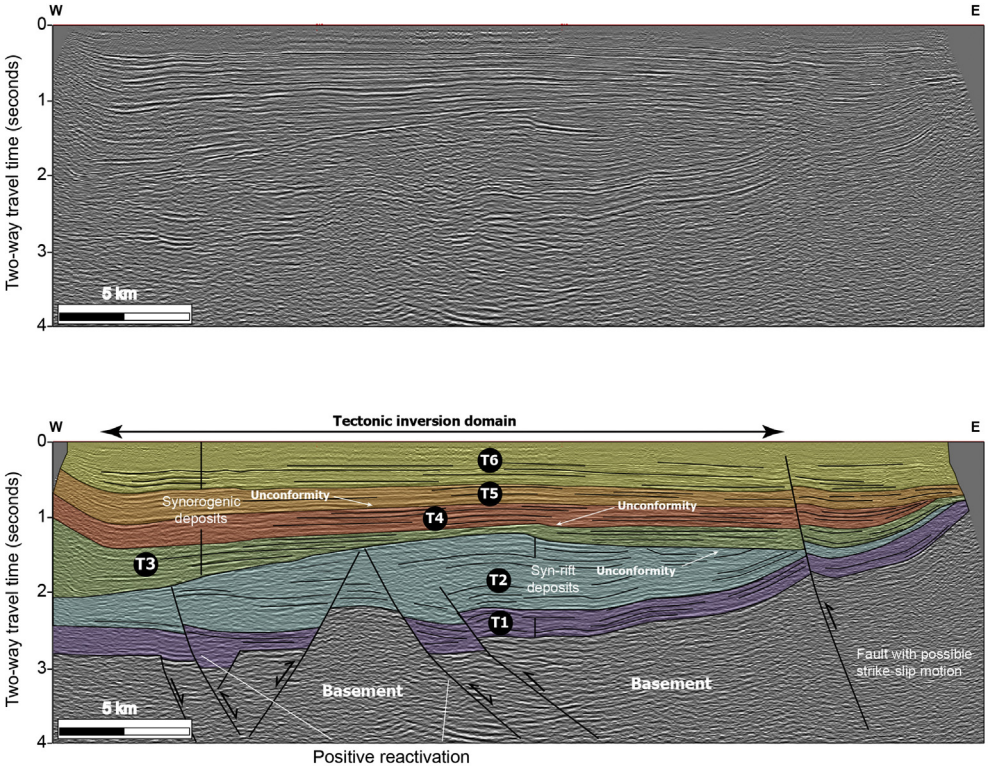

Fig. 10. Uninterpreted and interpreted 2-D seismic profile IG08b, showing a pair of partially inverted half-graben structures along the central section of the Salar de Atacama Basin. See Fig. 3 for location. T1-T2: Upper Paleozoic-Jurassic *syn*-rift tectonosequences; T3: Upper Cretaceous-Paleocene synorogenic tectonosequences; T4: Eocene synorogenic tectonosequences; T5: Oligocene-Miocene synorogenic tectonosequences; T6: Mio-Pliocene synorogenic tectonosequences.

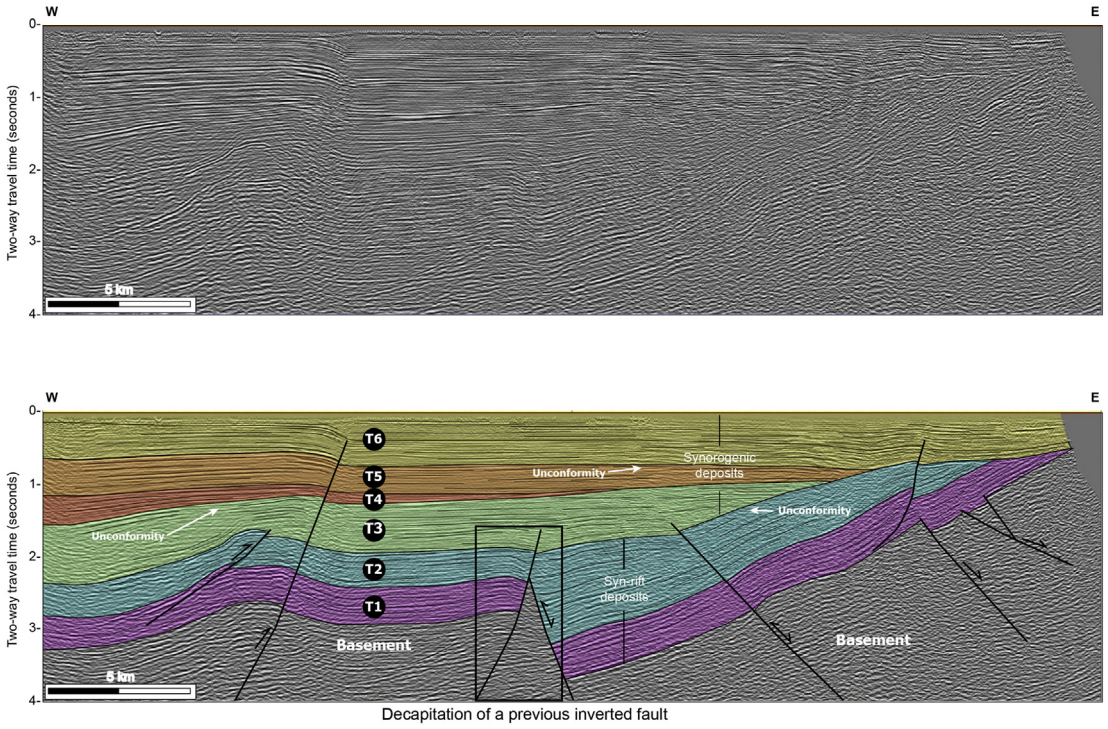

Fig. 11. Uninterpreted and interpreted 2-D seismic profile IG016b, showing the structural interaction between extensional and contractional structures along the south-central section of the Salar de Atacama Basin. The seismic profile shows a good example of decapitation of normal faults by reverse faults. See Fig. 3 for location. T1 to T6 presented as in Fig. 10.

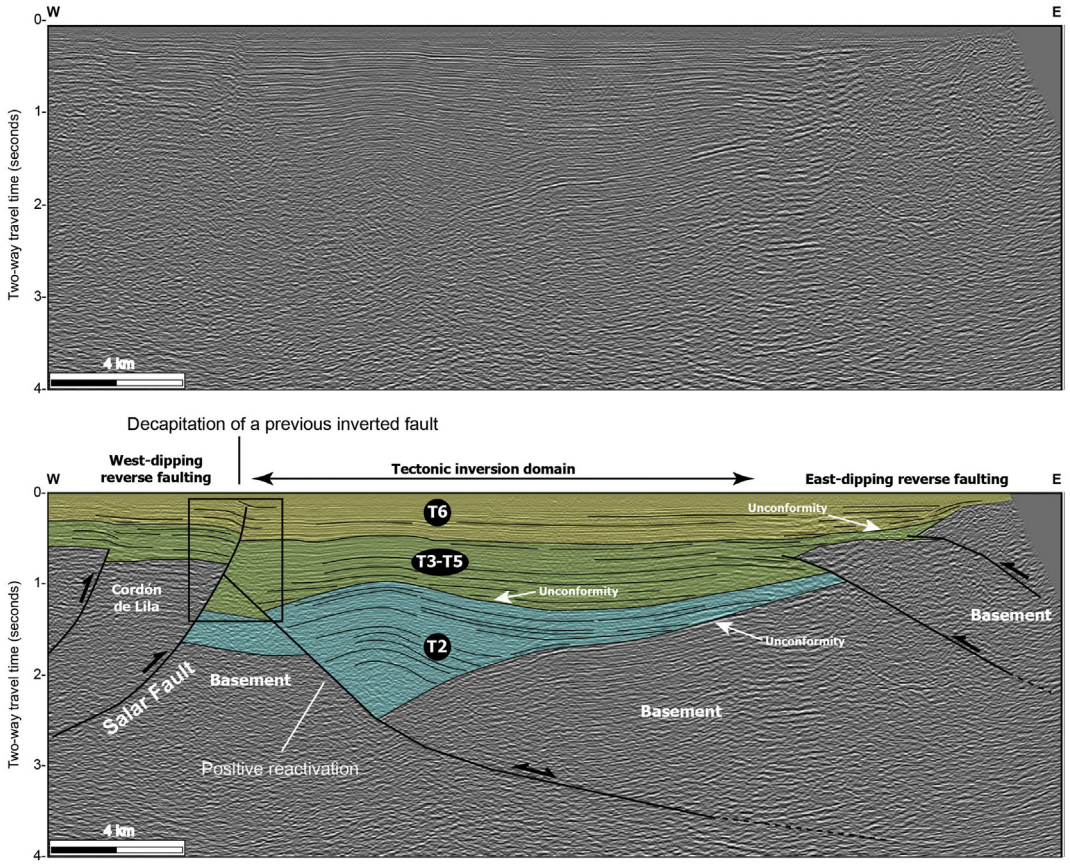

Fig. 12. Uninterpreted and interpreted eastern segment of the 2-D seismic profile IG024. The seismic interpretation shows two types of structural interaction: normal faults by reverse faults and the transport of normal faults by a thrust ramp. See Fig. 3 for location. T1 to T6 presented as in Fig. 10.

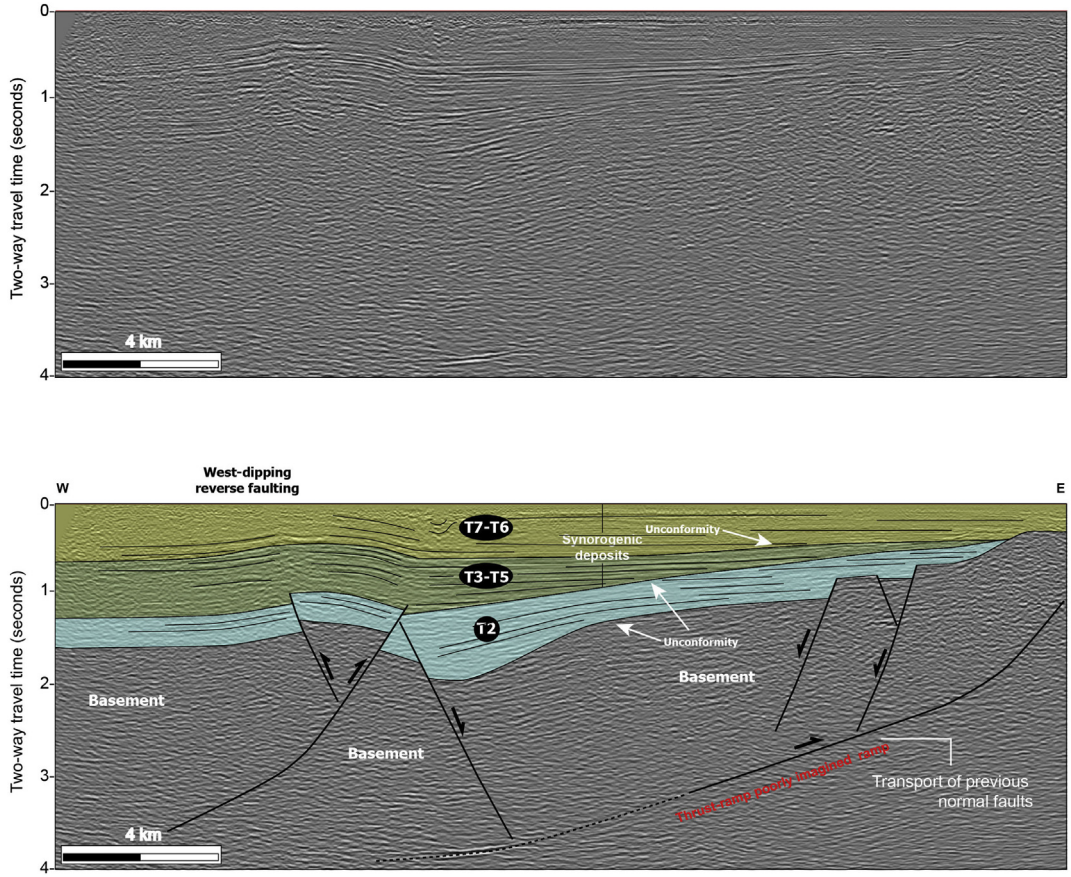

Fig. 13. Uninterpreted and interpreted western segment of the 2-D seismic profile IG024, showing the main structural styles (inversion anticline and basement-involved reverse faults) observed along the south and easternmost part of the Salar de Atacama Basin. See Fig. 3 for location. T1 to T6 presented as in Fig. 10.

These typically exhibit seismic reflectors with chaotic patterns that are very difficult to interpret and correlate. The upper surface is marked by a continuous reflector of high amplitude that represents the regional unconformity between the basement and the stratigraphic cover (Fig. 8). The stratigraphic cover includes the following tectonosequences.

Tectonosequence 1. (T1, Fig. 8) This is composed of low-amplitude and semi-continuous reflectors that usually onlap against the top of the basement. In the Salar de Atacama Basin, it consists of a uniform package of parallel seismic reflectors (Fig. 8), but in the Salar de Punta Negra Basin, it consists of an asymmetric stratigraphic wedge that thickens toward the master faults and shows a geometry similar to that reported by *syn*-rift sequences.

The seismic reflectors of this tectonosequence usually correlate with Upper Paleozoic volcanic and sedimentary successions (rhyolitic volcanic rocks, sandstones, and conglomerates) of La Tabla and/or Zorritas formations (Fig. 8). In the Salar de Atacama Basin, these could correlate with the igneous and sedimentary successions of the Lila Complex (Fig. 8). Although these have been previously considered as basement rocks (geological setting) of the basins, their dominant seismic expression (wedge shapes) observed in the Salar de Punta Negra Basin indicates that they were accumulated under extensional conditions.

Tectonosequence 2. (T2, Fig. 8). This is composed of a series of parallel and variable high and low- amplitude reflectors (Fig. 8) forming a wedge shape that fill some half-graben structures. Its basal section is marked by an angular unconformity defined by the onlap terminations of their basal reflectors against the top of tectonosequence 1 (Fig. 8) and/or the top of the basement. In the Salar de Atacama Basin, this was drilled by the Toconao-1 oil well (Muñoz et al., 2002; Jordan et al., 2007) and consists of sedimentary (sandstones, shales, mudstones) and volcanic rocks (e.g., tuff, lavas) that have been correlated with synorogenic deposits of the Upper Cretaceous-Paleocene Purilactis Group (e.g., Mpodozis et al., 2005; Arriagada et al., 2006; Bascuñán et al., 2016). However; its seismic expression is not geometrically compatible with that reported by synorogenic sequences, because these not shown important variations on thickness over contractional structures. On the contrary, this is mostly associated with a syn-rift sequence. Based on this criteria, we suggest that these rocks could be older than the Purilactis Group and are likely part of the syn-rift Mesozoic successions (e.g., Sierra de Varas, El Profeta formations) identified beneath the Salar de Punta Negra Basin (Fig. 8).

Tectonosequence 3. (T3, Fig. 8) This consists of a thick package of low and high amplitude seismic reflectors that unconformably overlie tectonosequence 2 (Fig. 8). The reflectors frequently show onlap terminations against the top of the underlying tectonosequence 2 (Fig. 8). This also reveals the characteristic change of thickness over contractional structures (inversion anticlines, synclines, thrust faults; Figs. 10, 11 and 12) indicating that its accumulation was controlled by the relief created during contractional deformation. An angular unconformity is commonly recognized in this tectonosequence, which could be interpreted as the limit between Upper Cretaceous and Paleocene deposits, but, this is only identified in the central part to the Salar de Atacama Basin. To the south, this unconformity is not clearly visible. Samples from the Toconao-1 oil well have revealed a volcaniclastic composition (volcaniclastic sandstones, conglomerates, claystones) to this tectonosequence, which has been correlated with the Upper

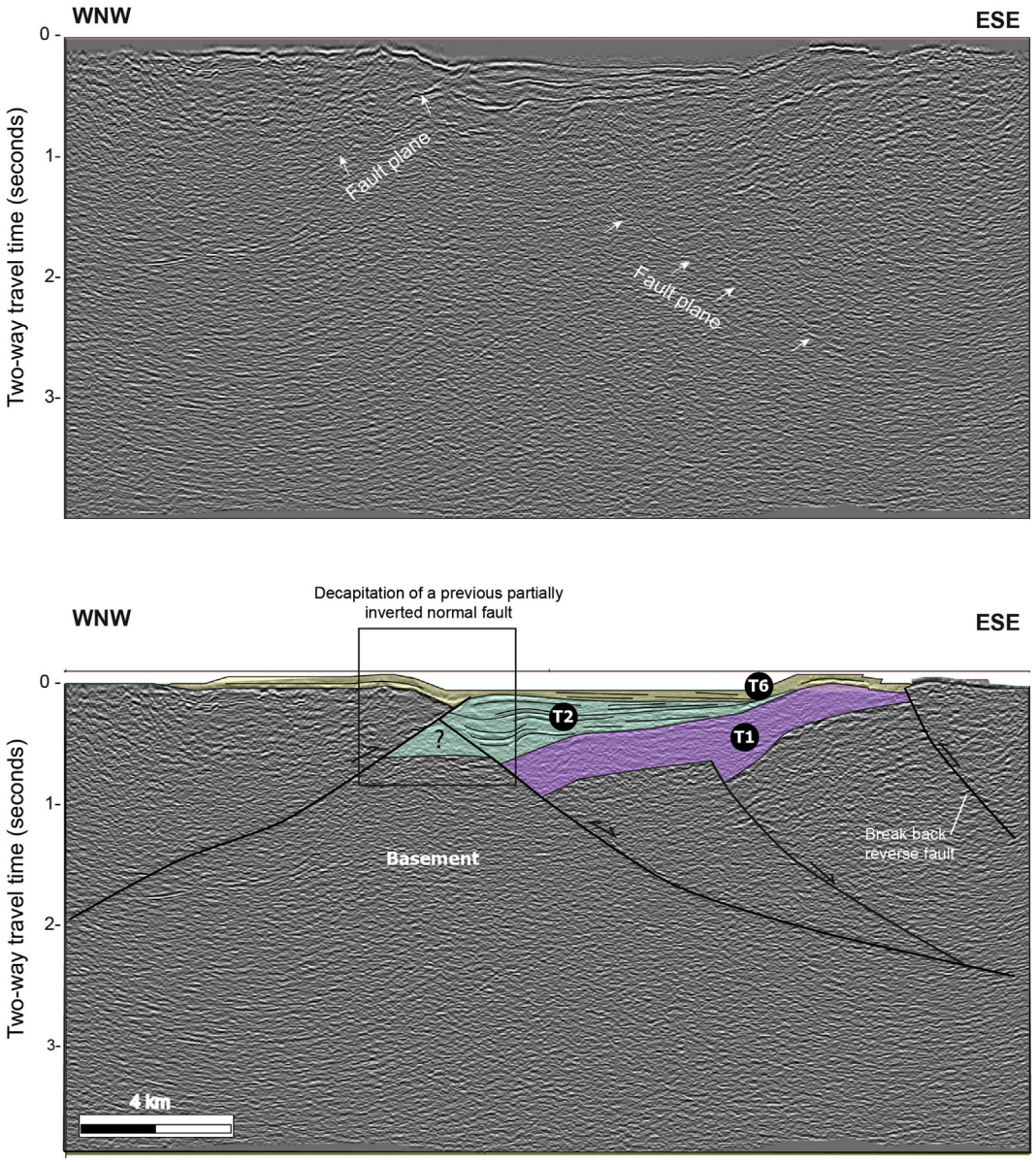

Fig. 14. Uninterpreted and interpreted 2-D seismic profile 1F016, showing decapitation of the upper section of a partially inverted normal fault by basement-involved faults in the northern part of the Salar de Punta Negra Basin (Modified from Martínez et al., 2017). See Fig. 4 for location. T1 to T6 presented as in Fig. 10.

Cretaceous-Paleocene Purilactis Group and part of the Naranja Formation (Muñoz et al., 2002; Arriagada et al., 2006; Fig. 8). Following its seismic expression and previous interpretations, we interpret this complete package of reflectors as an Upper Cretaceous-Paleocene synorogenic sequence.

Tectonosequence 4. (T4, Fig. 8) This consists of intercalated low and high-amplitude reflectors that unconformably overlie tectonosequence 3 (Fig. 8). Similar to tectonosequence 3, this also shows important variations of thickness over contractional folds, characterizing a synorogenic character (Figs. 10 and 11). The basal reflectors of the younger tectonosequence 5 typically truncate its upper section (Fig. 8). Data from the Toconao-1 borehole indicate that this is composed of conglomerates, sandstones, and claystones correlated with the Eocene successions previously dated by Mpodozis et al. (2005) described in the geological setting, even, fission-track ages of sandstone clasts have also indicated an Eocene age for this unit (Muñoz et al., 2002). Following the interpreted stratigraphic record for the Salar de Atacama Basin (Muñoz et al., 2002; Arriagada et al., 2006) and the northern part of the Salar de Punta Negra Basin, we correlated this tectonosequence with Eocene sedimentary deposits (Loma Amarilla Formation; Fig. 8).

Tectonosequence 5. (T5, Fig. 8) This predominantly consists of a series of continuous and parallel high-amplitude seismic reflectors (Fig. 8) that form an extensive cover mostly recognized along the central part of the Salar de Atacama Basin and central and southernmost parts of the Salar de Punta Negra Basin. The basal reflectors frequently onlap again the top of tectonosequence 4; however, these terminations are only observed in some sectors (Figs. 10 and 11). A strong reflector typically marks the top of this tectonosequence. Samples from the Toconao- 1 well and others taken from outcrops indicate that it consists of sedimentary rocks that include interstratified Oligocene-Miocene conglomerates, sandstones, gravels, ignimbrites, and other subordinate volcanic products that have been correlated with the Oligocene-Miocene Paciencia Group and/or Pampa de Mulas Formation (Fig. 8). These frequently thicken toward the frontal and back-limb of folded structures, thereby indicating a synorogenic character.

Tectonosequence 6. (T6, Fig. 8) This is a package of variable

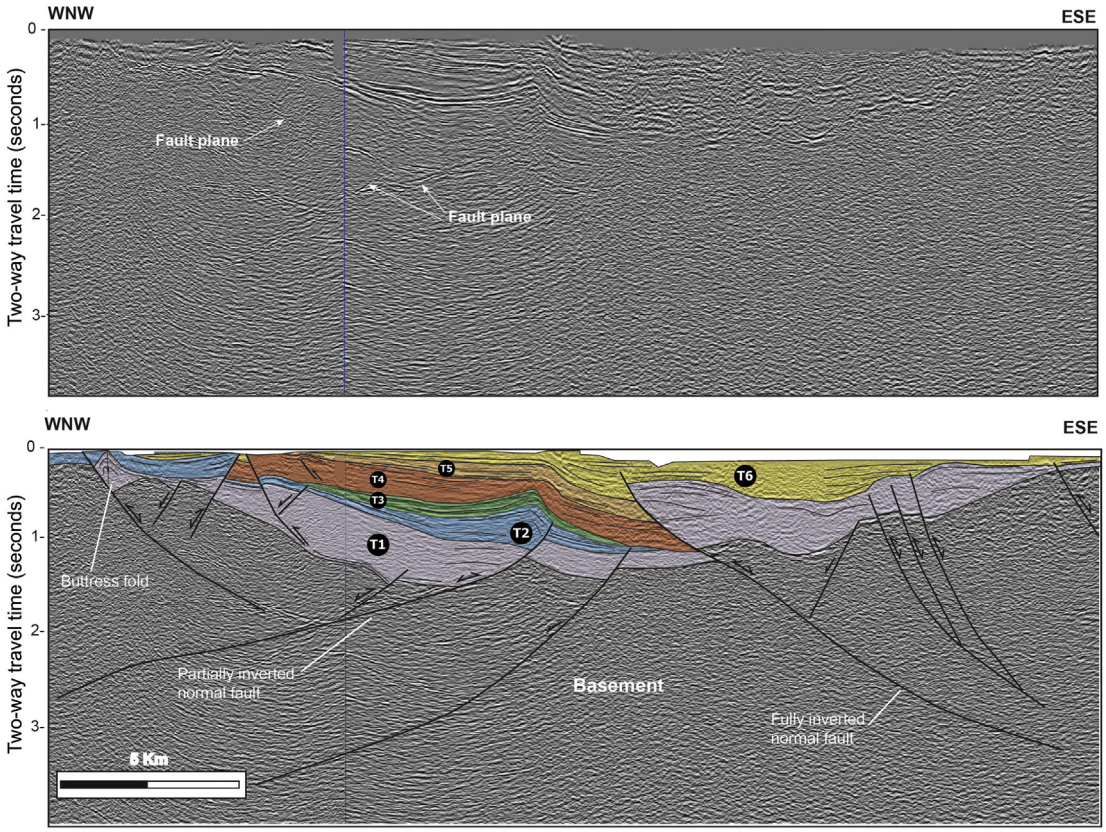

Fig. 15. Uninterpreted and interpreted 2-D seismic profile 2F004, showing a series of doubly-dipping inverted faults and folds, which reveal the positive tectonic inversion of previous normal faults in the north-central part of the Salar de Punta Negra Basin (Modified from Martínez et al., 2017). See Fig. 4 for location. T1 to T6 presented as in Fig. 10.

reflectors of high and low amplitude that overlie tectonosequence 6 (Fig. 8). The base is defined by an angular unconformity over which the basal reflectors commonly onlap against the limbs of contractional folds (Figs. 10 and 11). This is the youngest tectonosequence that infills both basins. Information from subsurface (Toconao-1 well) and surface indicate that this consists of volcanic and sedimentary rocks (sandstones, gravels, evaporites, and ignimbrites) correlated with Mio-Pliocene deposits, some of which show contractional growth strata, indicating a synorogenic nature.

6. Relationship between extensional and contractional structures

Based on our seismic and structural interpretation, interactions between extensional and contractional structures occur in three ways: a) pure positive reactivation of previous normal faults; b) decapitation of previous normal faults by reverse faults; and c) transport of previous normal faults over thrust ramps (Fig. 9).

6.1. Pure positive reactivation

Pure positive reactivation is represented by the tectonic inversion of inherent basement normal faults that form part of asymmetrical half-graben structures and opposite dipping normal faults separated by basement structural highs and/or horst blocks (Fig. 10). Structures related to this tectonic process are usually observed in the central and southern end of the Salar de Atacama Basin (Figs. 10,11,12) and the north and central part of the Salar de Punta Negra Basin (Figs. 14 and 15). The seismic profiles located in both areas have highlighted large asymmetrical and doubly-verging anticlines with arrowhead shapes that involve Upper Paleozoic and Mesozoic stratigraphic wedges (tectonosequences TS1 and TS2; see details in seismic and stratigraphic tectonosequences). The stratigraphic wedges usually thicken toward the fault planes and the anticlines typically have long wavelengths with short, steep frontal limbs and large, sub-horizontal back limbs. This geometry is commonly acquired by the folding of *syn*-rift wedges when the slip of previous normal faults is reversed; therefore, this geometry evidences positive reactivation of previous normal faults (Figs. 10, 12, 14, 15). The anticlines frequently affect the hanging wall of ancient basement normal faults and their current tectonic vergence is strongly conditioned by the initial dip. Some buttress folds preserved under the Salar de Punta Negra Basin (Fig. 15) are narrow with overturned frontal limbs thus indicating that have been shorted and buttressed again the reactivated normal faults. Usually, the reactivated normal faults vary between faults with moderate angle, listric geometry and faults with high-angle, planar geometry. The majority of the normal faults have been partially reactivated; only some were fully reactivated and are mostly observed in the Salar de Punta Negra Basin (Figs. 14 and 15). Some inversion anticlines have been partially eroded and cover by synorogenic deposits related to the tectonosequences 3, 4 and/or 6. This situation is mostly associated with the areal distribution of the synorogenic deposits over the inverted structures. Recent research has interpreted similar partially inverted structures in the northern part of the Salar de Atacama Basin (Rubilar et al., 2017), indicating that structures exposed in this sector resulted from tectonic inversion of inherited basement normal faults.

6.2. Decapitation of previous normal faults by reverse faults

This type of structural interaction is mainly interpreted in the southern end of the Salar de Atacama Basin (Figs. 11, 12 and 13) and the northern region of the Salar de Punta Negra Basin (Fig. 14). It consists of basement-involved reverse faults that typically cut the upper

section of ancient reactivated or non-normal faults (Figs. 11–14). In the Salar de Atacama Basin, the crystalline basement rocks of the Cordon de Lila are uplifted by east-dipping reverse faults (e.g., Salar Fault; Fig. 12); however, the seismic profiles transverse to these faults show preserved inversion anticlines and reactivated normal faults at their footwall blocks, indicating that the reverse faults decapitated part of the upper section of previously reactivated normal faults (Figs. 11, 12). This situation is also observed to the east of the Cordon de Lila (Fig. 12), where characteristic changes of thickness in the *syn*-rift deposits related to the tectonosequence T2 are recognized in the hanging wall and footwall of the basement-involved reverse faults. Commonly these have greater thickness at the footwall block of the reverse faults, which is unusual considering that they were accumulated previous to the contractional deformation (Fig. 12). This structural and stratigraphic relationship indicates that some previous normal faults were decapitated by younger basement-involved reverse faults. Similarly, in the northern region of the Salar de Punta Negra Basin, an east-dipping basement-involved reverse fault placed the Paleozoic basement rocks over a stratigraphic wedge composed of syn-rift tectonosequences 1 and 2 (Fig. 14). The basement rocks form part of the footwall block of a previous normal fault, which is quite similar to those situation observed to the east of the Cordon de Lila; therefore, we interpret that the reverse fault decapitated the upper section of ancient normal faults, even, the seismic profiles of this region have highlighted part of this ancient normal fault (Fig. 14), which is characterized by a high amplitude seismic reflector. Previous research carried out in the Salar de Punta Negra Basin has suggested that some of the normal faults were positively inverted prior to their decapitation (Martínez et al., 2017). The last is confirmed considering the fact that some partially inverted faults in the southern end of the Salar de Atacama have been deformed and cut by basement-involved reverse faults (Figs. 11, 12 and 13). Commonly the upper section of the reverse faults has high angles, which are commonly confused with high angle normal faults (Pananont et al., 2004; Rubilar et al., 2017, among others). This structural relationship suggests that some of the original normal faults helped localize new basement-involved reverse faults. This process occurs when some inverted normal faults acquire a high angle and are locked during the basin contraction thus facilitating that they are cut.

6.3. Transport of previous normal faults by thrust ramps

This structural relationship has mainly been interpreted to the west of the Cordon de Lila in the Salar de Atacama Basin (Fig. 13). Seismic profiles in this region have highlighted a series of west-dipping high angle planar normal faults at the hanging wall block of a large east-dipping basement thrust ramp (Fig. 13), which is related to the westward continuity of the Salar Fault interpreted on the Fig. 12. The lower sections of normal faults are typically truncated along the lower section of the thrust ramp, indicating that they were eastward passively transported through the basement thrust ramp. In contrast to other normal faults, these do not show evidence of positive reactivation and are generally buried by synorogenic deposits related to tectonosequences T3-T6. These faults correspond to antithetic normal faults that affect the hanging wall block of an ancient Mesozoic rollover structure, which is related to an east-dipping Mesozoic basement normal master fault. These antithetic normal faults controlled the accumulation of the *syn*-rift Mesozoic deposits associated with the tectonosequence T2 (Fig. 10). Although their lower sections usually are poorly highlighted by the seismic profile, we interpreted that they have been cut and them passively transported by the basement thrust ramp. The ramp corresponds to a low angle west-dipping high seismic amplitude reflector, which is partially highlighted by the seismic data (Fig. 11). We interpreted that this structure favored the uplift and exposure of the Paleozoic rocks along the Cordon de Lila (Fig. 3). The structure of the footwall of the thrust ramp has not sufficiently been highlighted by the seismic data and therefore is unknown. We suppose that the footwall block also is mainly composed of Paleozoic basement rocks.

Similar situations have been interpreted in other regions of the Central Andes, such as the Chilean Frontal Cordillera (Martínez et al., 2016), the Cuyo Basin in Argentina (Giambiagi et al., 2003) and the Eastern Cordillera of Peru. Usually, this situation occurs when the initial dip angle of the previous normal faults is relatively high ($> 45^{\circ}$), so that they cannot be reactivated and finally are cut and transported by new contractional structures. Is very possible that the new basement thrust ramp have taken advantage of the basal detachment of the previous normal faults, because this has an angle dip favorable to guide the contractional deformation, but, this is an only a hypothesis. Commonly, this structural style is associated with high degrees of crustal shortening. These thrust ramps are considered the most favorable structures to accommodate the Cenozoic crustal shortening interpreted in the region, since they allow to duplicate the original thickness of the upper continental crust and can cause greater subsidence.

7. Discussion

The results obtained from our new seismic and structural interpretations allowed us to document the role of ancient extensional and/or normal faults during progressive deformation of the study Andean region. Many large contractional structures buried beneath the Preandean basins used basement normal faults during their propagation thus indicating that the interaction between normal and contractional structures was an important process during the shortening of this part of the Central Andes. The tectonic interaction between basement normal and reverse/thrust faults is a common process, which generally occurs in the first growth stages of orogenic belts (Scisciani et al., 2002), however; the previous normal faults also could be positively reactivated during different shortening episodes during the evolution of the orogens.

The oldest normal faults in the Preandean Depression are thought to result from earliest Late Paleozoic to Mesozoic extensional deformation episodes, as has been observed in neighboring regions in Chile (e.g., Domeyko Cordillera; Amilibia et al., 2008) and Argentina (e.g., Salta Rift; Kley et al., 2005; Carrera et al., 2006; Monaldi et al., 2008). Nevertheless, the existence of Mesozoic inherited basement normal faults along and under the Preandean basins has always been questioned, because there are few outcrops of Mesozoic (e.g., Jurassic and Lower Cretaceous) *syn*-rift deposits and on the contrary, most of the exposures of these deposits are restricted to the Domeyko Cordillera in Chile and other basins in Argentina. Nevertheless, some interpretations have suggested that contractional structures observed in regions as the Salar de Atacama could have originated from the tectonic inversion of ancient Mesozoic normal faults (Muñoz et al., 2002; Mpodozis et al., 2005) related to the Tarapacá back-arc extensional-related basin.

Some relevant evidence of this tectonic process, such as the occurrence of deformed syn-rift stratigraphic wedges, reactivated normal faults and inversion anticlines, among others, has not commonly been reported to the Preandean basins. Only a recent study in the Salar de Punta Negra demonstrated the existence of inverted Mesozoic half-graben structures under this basin (Martínez et al., 2017), thus supporting the previous structural interpretations of the Salar de Atacama Basin. In the current study, we have interpreted a series of Upper Paleozoic and Mesozoic stratigraphic wedges related to syn-rift deposits in the lower parts of the Preandean basins, which strongly evidence that this study region was tectonically extended prior to crustal shortening experienced during the Andean deformation, however; the magnitude and orientation of this crustal extension is still highly speculative.

In the region, positive reactivation of these normal faults is typically expressed by the presence of inversion anticlines on their hanging wall blocks. Although we have not restored these structures, we supposed that only those preferably oriented perpendicular to the position of the regional contractional stress field and with low and moderate initial dip angles ($\leq 45^{\circ}$) were reactivated, such as has usually been documented

by some experimental models (Bonini et al., 2012 and references herein). In both Salar de Atacama and Salar de Punta Negra basins, many of the inversion anticlines are unconformably covered by Upper Cretaceous synorogenic deposits, indicating that basin inversion was initiated during this time. Others inverted structures are directly covered by synorogenic Oligocene deposits, indicating that some normal faults were later reactivated (Martínez et al., 2017). Similar structural and stratigraphic relationships are interpreted in other basins in northern Chile (e.g., Chañarcillo, Lautaro basins), even in some parts of the Chilean Coastal Cordillera, indicating that initial contraction of Mesozoic back-arc related extensional basins in Chile was common during this time (Late Cretaceous), which is associated with the Peruvian tectonic phase (Jaillard, 1992).

Some inverted and/or normal faults are decapitated and/or transported by basement-related reverse faults and thrust ramps. The reverse faults typically affect the upper segments of the inverted and/or normal faults with opposite dip to these. These situations have been commonly interpreted in other regions of the Central Andes in Chile and Argentina, such as: the Lagunillas Basin (Martínez et al., 2016), Salta Rift (Carrera et al., 2006), El Metán Basin (Iaffa et al., 2011) and the Cuyo basins (Giambiagi et al., 2003), the Eastern Cordillera of Peru and also in other deformed belts around the world, such as the Apennines (Scisciani et al., 2002; Scisciani, 2009), the Alps (Butler, 1989; Butler et al., 2006), the Colombian Andes (Mora et al., 2009, 2010). Usually, this occurs when the initial dip angle of the previous normal faults is relatively high ($> 45°$), so that they cannot be reactivated and finally are cut and transported by new contractional structures. This interplay generally occurs from the steepening of reactivated normal faults, which result in locking and deformation by new reverse faults.

Considering the geometry of synorogenic tectonosequences T3-T6, we interpret that the basement-involved contractional structures are contemporaneous with accumulation of these sequences. Field data (tectonic escarpments) indicate that some may even exhibit recent activity. Previous studies have suggested that evolution of the Preandean Depression was interrupted by an important tectonic collapse during the Oligocene, causing the creation of normal faults (Jordan et al., 2007; Rubilar et al., 2017). We did not identify extensional structures and, in contrast, the tectonosequences associated with the Oligocene succession were mostly accumulated during the propagation of contractional structures.

The interaction between extensional and contractional structures observed in the Preandean Depression is similar to those recognized in other regions of the Central Andes, especially in the Chilean Frontal Cordillera (Martínez et al., 2016). Although tectonic inversion played an important role during initial deformation of the region, the basement-involved reverse faults and thrusts resulted in the most important structures for crustal uplift, such as those identified in other neighboring regions (Domeyko Cordillera; Maksaev and Zentilli, 1999). Previous studies based on apatite fission track analyses have argued that these reverse faults propagated rapidly after the Eocene (Maksaev and Zentilli, 1999). Furthermore, the occurrence of angular unconformities between Cenozoic synorogenic deposits indicate that Andean deformation occurred diachronically in successive pulses (Paleocene, Eocene, Oligocene, Miocene, and even recent times). We suggest that the tectonic evolution of the Preandean basin occurred in three stages: i) Late Paleozoic-Mesozoic crustal extension and creation of half-graben structures; ii) Late Cretaceous tectonic inversion of half-graben structures; and iii) upper Late Cretaceous (?) and Cenozoic crustal shortening and creation of basement-involved reverse faults and thrust ramps.

8. Concluding remarks

A combination of field data and seismic profiles of two Preandean basins (Salar de Atacama and Salar de Punta Negra) was used to identify the presence and influence of pre-orogenic and ancient normal faults over the Andean contractional structures. Our results indicate that:

- Exits a serie of ancient normal faults under the Preandean Depression of the Central Andes, which have been clearly highlighted by the seismic data.
- The structure of this region consists of doubly-vergent inverted and basement-involved contractional structures, which suggest that important tectonic interactions between extensional and contractional structures occurred during its tectonic evolution. Usually, the original distribution of the normal faults, finally condition the final geometry and kinematics of the thrusts and reverse faults. The normal faults can be tectonically reactivated and/or decapitated depending of their initial geometry.
- The selective tectonic inversion of Late Paleozoic and Mesozoic half-graben structures previously established in this part of the Central Andes favored the creation of an initial relief composed of inversion anticlines, along which thick Upper Paleozoic and Mesozoic *syn*-rifted deposits were extruded and partially eroded.
- The seismic data show as the structural vergence of the contractional structures in the region is strongly conditioned by the initial dip of the ancient normal faults. It is a good example of how these are responsible for the along-strike variation of structural styles in orogenic belts established in regions that have been previously extended.
- Upper Cretaceous synorogenic deposits over the inversion anticlines commonly recorded the initial contraction of previous normal faults, while Cenozoic synorogenic deposits were mostly accumulated during propagation of large basement-involved reverse faults. This situation correlates very well with some interpretations made for many inverted basins in South America, which suggest that Paleozoic and Mesozoic half-graben structures were reactivated early during the Late Cretaceous.
- Successive Cenozoic crustal shortening of the region triggered propagation of east and west-vergent basement-involved reverse faults that partially modified the initial geometry of both inverted structures and/or normal faults. These structures appear to be responsible for the crustal uplift of the western and eastern edges of the basins, which represent the most important topographic relief in the region.

Acknowledgments

This work was supported by the Fondecyt project 11170098 "*Structure and tectonic evolution of the Pre-Andean Depression, Central Andes: case study of the Salar de Punta Negra Basin*". We acknowledge Dr. Lisandro Rojas and the ENAP-SIPETROL Company for providing the seismic data, and the Nunns and Rogan Company for providing the academic license of the StructureSolver software used for seismic and structural interpretation. Special thanks are given to Luis Acevedo for Landsat image support and Rodrigo Riquelme for constructive conversations. Finally, we thanks the constructive comments and suggestions from two anonymous reviewers that benefited this work.

References

Amilibia, F. Sabat, K.R. McClay, J.A. Muñoz, E. Roca, G. Chong. 2008. The role of inherited tectono-sedimentary architecture in the development of the central Andean mountain belt: insights from the cordillera de Domeyko, vol. 30, pag., 1520–1539. J. Struct. Geol.

Ardill, J., Flint, S., Chong, G., Wilke, H., 1998. Sequence stratigraphy of the Mesozoic Domeyko basin, northern Chile. J. Geol. Soc. Lond. 155, 71–88.

Arriagada, C., Cobbold, P.R., Roperch, P., 2006. The Salar de Atacama Basin: a record of cretaceous to Paleogene compressional tectonics in the Central Andes. Tectonics 25, TC1008.

Bascuñán, S., Arriagada, C., Le Roux, J., Deckart, K., 2016. Unraveling the Peruvian Phase of the Central Andes: stratigraphy, sedimentology and geochronology of the Salar de Atacama Basin (22°30–23°S), northern Chile. Basin Res. 28, 365–392. https://doi.

org/10.1111/bre.12114.
Becerra, J., Henríquez, S.M., Arriagada, C., 2014. Geología del area Salar de Atacama, región de Antofagasta. Servicio Nacional de Geología y Minería. Carta Geológica de Chile, Serie Geología Básica 166: 111 p., 1 mapa escala 1:100.000. Santiago, Chile.
Bonini, M., Sani, F., Antonielli, B., 2012. Basin inversion and contractional reactivation of inherent normal faults: a review based on previous and new experimental models. Tectonophysics 522, 55–88.
Breitkreuz, C., Van Schmus, W.R., 1996. U-Pb geochronology and significance of late Permian ignimbrites timing of the magmatism of the paleo-pacific border of Gondwana: U-Pb geochronology in northern Chile. J. S. Am. Earth Sci. 9, 281–293.
Breitkreuz, C., Zeil, W., 1994. The late carboniferous to triassic volcanic belt in Northern Chile. In: Reutter, K.J., Scheuber, E., Wigger, P.J. (Eds.), Tectonics of the Southern Andes. Springer, pp. 277–292.
Brüggen, H., 1934. Grundzüge der Geologie und Lagerstättenkunde Chiles. Mathematische-Naturwissenscnafiliche. Klasse, Heidelberger Akademie der Wissenschaften, Tübingen.
Butler, R.W.H., 1989. The influence of pre-existing basin structure on thrust system evolution in the Western Alps. In: Cooper, M.A., Williams, G.D. (Eds.), Inversion Tectonics. Geological Society of London, Special Publication. 44. pp. 105–122.
Butler, R.W.H., Tavarnelli, E., Grasso, M., 2006. Structural inheritance in mountain belts: an Alpine–Apennine perspective. J. Struct. Geol. 28, 1893–1908.
Carrera, N., Muñoz, J.A., Sàbat, F., Roca, E., Mon, R., 2006. The role of inversion tectonics in the structure of the cordillera oriental (NW Argentinean Andes). J. Struct. Geol. 28, 1921–1932.
Cecioni, A., Frutos, J., 1975. Primera noticia sobre el hallazgo de Paleozoico Inferior marino en la Sierra de Almeida, Norte de Chile. Congr. Argent. Paleontol. Bioestratigr. 1 (1), 191–207.
Charrier, R., Reutter, K.-J., 1994. The Purilactis Group of Northern Chile: Boundary between arc and backarc from late Cretaceous to Eocene. In: Reutter, K.-J., Scheuber, E., Wigger, P. (Eds.), Tectonics of the Southern Central Andes. Springer, Heidelberg, pp. 189–202.
Chong, G., 1973. Reconocimiento geológico del área Catalina-Sierra de Varas y estratigrafía del Jurásico del Profeta, provincial de Antofagasta. Memoria de prueba. Departamento de Geología, Universidad de Chile. pp. 284.
Dingman, R. J. 1963. Cuadrángulo Tulor, Provincia de Antofagasta. Instituto de Investigaciones Geológicas, Santiago, Carta Geológica de Chile, 1:50.000, 11.
Flint, S., Turner, P., Jolley, E.J., Hartley, A.J., 1993. Extensional tectonics in convergent margin basins: an example from the Salar de Atacama. Chil. Andes. Geol. Soc. Am. Bull. 105, 603–617.
Gardeweg, M., Ramírez, C.F., Davidson, J., 1993. Mapa Geológico del área Salar de Punta Negra y Volcán Llullaillaco, Región de Antofagasta. Serv. Nac. Geol. Min. Doc. Trab. 5 (1:100.000).
Gardeweg, M., Pino, H., Ramírez, C.F., Davidson, J., 1994. Mapa Geológico del área de Imilac y Sierra Almeida, Región de Antofagasta. Serv. Nac. Geol. Min. Doc. Trab. 7 (1:100.000).
Giambiagi, L., Ramos, V., Godoy, E., Alvarez, P., Orts, D., 2003. Cenozoic deformation and tectonic style of the Andes, between 33 and 34 south latitude. Tectonics. https://doi.org/10.1029/2001TC001354.
González, R., Wilke, G.H., Menzies, A.H., Riquelme, R., Herrera, C., Matthews, S., Espinoza, F., Cornejo, P., 2015. Carta Sierra de Varas, Región de Antofagasta. Servicio Nacional de Geología y Minería, Carta Geológica de Chile. Serie Geología Básica 178, 1 mapa escala 1:100.000.
Hammerschmidt, K., Döbel, R., Friedrichsen, H., 1992. Implication of 40Ar/39Ar dating of tertiary volcanics rocks from the north-Chilean Precordillera. Tectonophysics 202, 55–81.
Hartley, A., Flint, S., Turner, P., Jolley, E.J., 1992. Tectonic controls on the development of a semi-arid alluvial basin as reflected in the stratigraphy of the Purilactis Group (Upper Cretaceous-Eocene) northern Chile. J. S. Am. Earth Sci. 5, 275–296.
Iaffa, D., Sabat, F., Mu~noz, J.A., Mon, R., Gutierrez, A.A., 2011. The role of inherited structures in a foreland basin evolution. The Metan Basin in NW Argentina. J. Struct. Geol. 33, 1816e1828.
Isaacson, P., Fischer, L., Davidson, J., 1985. Devonian and carboniferous stratigraphy of sierra de Almeida, Northern Chile, preliminary results. Rev. Geol. Chile 25 (26), 113–124.
Jaillard, E., 1992. La Fase Peruana (Cretáceo Superior) en la Margen Peruana. Bol. Soc. Geol. Perú 83, 81–87.
Jordan, T., Muñoz, N., Hein, M., Lowenstein, T., Godfrey, L., Yu, J., 2002. Active faulting and folding without topographic expression in an evaporitic basin, Chile. Geol. Soc. Am. Bull. 114 (11), 1406–1421.
Jordan, T.E., Mpodozis, C., Muñoz, N., Blanco, N., Pananont, P., Gardeweg, M., 2007. Cenozoic subsurface stratigraphy and structure of the Salar de Atacama basin, northern Chile. J. S. Am. Earth Sci. 23, 122–146.
Kley, J., Monaldi, C., Salfity, J.A., 1999. Along-strike segmentation of the Andean foreland: causes and consequences. Tectonophysics 301, 75–94.
Kley, J., Rossello, E.A., Monaldi, C.R., Habighorst, B., 2005. Seismic and field evidence for selective inversion of cretaceous normal faults, Salta rift, Northwest Argentina. Tectonophysics 399, 55–172.
Kuhn, D., 2002. Fold and thrust belt structures and strike-slip faulting at the SE margin of the Salar de Atacama basin, Chilean Andes. Tectonics. https://doi.org/10.1029/2001TC901042.
Maksaev, V., 1990. Metallogeny, Geological Evolution and Thermochronology of the Chilean Andes between Latitudes 21 and 26 South, and the Origin of the Major Porphyry Copper Deposits (Tesis doctoral). Dalhousie University, Halifax, pp. 544.
Maksaev, V., Zentilli, M., 1999. Fission track thermochronology of the Domeyko Cordillera, northern Chile: implications for Andean tectonics and porphyry copper metallogenesis. Explor. Min. Geol. 8, 65–89.
Marinovic, N., Lahsen, A. 1984. Hoja Calama. Región de Antofagasta. Servicio Nacional de Geología y Minería, Carta Geológica de Chile, No. 58: 150 p., 1 mapa escala 1:250.000.
Marinovic, N., Smoje, I., Maksaev, V., Hervé, M., Mpodozis, C., 1995. Hoja Aguas Blancas, Región de Antofagasta. Serv. Nac. Geol. Min. Doc. Trab. 70.
Martínez, F., Arriagada, C., Peña, M., Del Real, I., Deckart, K., 2013. The structure of the Chañarcillo Basin: an example of tectonic inversion in the Atacama region, northern Chile. J. S. Am. Earth Sci. 42, 1–16.
Martínez, F., Arriagada, C., Peña, M., Deckart, K., Charrier, R., 2016. Tectonic styles and crustal shortening of the Central Andes "Pampean" flat-slab segment in northern Chile (27°–29°S). Tectonophysics 667, 144–162.
Martínez, F., González, R., Bascuñan, S., Arriagada, C., 2017. Structural styles of the Salar de Punta Negra Basin in the Preandean depression (24°–25°S) of the Central Andes. J. S. Am. Earth Sci. https://doi.org/10.1016/j.jsames.2017.08.004.
Mescua, J., Giambiagi, L., 2012. Fault inversion vs. new thrust generation: a case study in the Malargüe fold-and-thrust belt, Andes of Argentina. J. Struct. Geol. 31, 51e63.
Monaldi, C.R., Salfity, J.A., Kley, J., 2008. Preserved extensional structures in an inverted cretaceous rift basin, northwestern Argentina: outcrop examples and implications for fault reactivation. Tectonics 27. https://doi.org/10.1029/2006TC001993.
Mora, A., Gaona, T., Kley, J., Montoya, D., Parra, M., Quiroz, L.I., Reyes, G., Strecker, M.R., 2009. The role of inherited extensional fault segmentation and linkage in contractional orogenesis: a reconstruction of lower cretaceous inverted rift basins in the eastern cordillera of Colombia. Basin Res. 21, 111–137.
Mora, A., Horton, B.K., Mesa, A., Rubiano, J., Ketcham, R.A., Parra, M., Blanco, V., Garcia, D., Stockli, D.F., 2010. Cenozoic Deformation Patterns in the Eastern Cordillera, Colombia: Inferences from fission track results and structural relationships. Reporte Interno, UTexas-ICP.
Mpodozis, C., Cornejo, P., 1997. El rift Triásico-Sinemuriano de Sierra Exploradora, Cordillera de Domeyko (25 e26S): asociaciones de facies y reconstrucción tectónica. VIII Congreso Geologico Chileno. Antofagasta, Actas I. Sesión Temática 3, 550–554.
Mpodozis, C., Ramos, V.A., 1989. The Andes of Chile and Argentina. In: Ericksen, G.E., Cañas, M.T., Reinemund, J.A. (Eds.), Geology of the Andes and its Relation to Hydrocarbon and Energy Resources. Circum-Pacific Council for Energy and Hydrothermal Resources, American Association of Petroleum Geologists, Houston, Texas, Earth Science Series Vol. 11. pp. 59–90.
Mpodozis, C., Ramos, V., 2008. Tectónica Jurásica en Argentina y Chile: extensión, subducción oblicua, rifting, deriva y colisiones? Rev. Asoc. Geol. Argent. 63 (479–495), 2008.
Mpodozis, C., Marinovic, N., Smoje, I., Cuitiño, L., 1993. Estudio geológico-estructural de la Cordillera de Domeyko entre Cerro Limón Verde y Sierra Mariposas, Región de Antofagasta: Servicio Nacional de Geología y Minería [Chile], Santiago, Informe Registrado IR-93-04. (282 p.).
Mpodozis, C., Arriagada, C., Roperch, P., 1999. Cretaceous to Paleogene Geology of the Salar de Atacama Basin, Northern Chile: A reappraissal of the Purilactis Group Stratigraphy. Proceedings 4th International Symposium on Andean Geodynamics (ISAG), Göttingen, Germany. pp. 523–526.
Mpodozis, C., Blanco, N., Jordan, T., Gardeweg, M.C., 2000. Estratigrafía y deformación del Cenozoico tardio en la región norte de la Cuenca del Salar de Atacama: La zona de Vilama-Pampa Vizcachitas. In: Actas IX Congresso Geológico Chileno, Puerto Varas. 2. pp. 598–603.
Mpodozis, C., Arriagada, C., Basso, M., Roperch, P., Cobbold, P., Reich, M., 2005. Late Mesozoic to Paleogene stratigraphy of the Salar Atacama Basin, Antofagasta, northern Chile: implications for the tectonic evolution of the Central Andes. Tectonophysics 399, 125–154.
Muñoz, N., Charrier, R., Reutter, J.K., 1997. Evolución de la Cuenca del Salar de Atacama: Inversión tectónica y relleno de una cuenca de antepaís de retroarco. In: Proceedings 8th Congreso Geológico Chileno. 1. pp. 195–199.
Muñoz, N., Charrier, R., Jordan, T., 2002. Interactions between basement and cover during the evolution of the Salar de Atacama Basin, Northern Chile. Rev. Geol. Chile 29, 55–80.
Niemeyer, H., 1984. La megafalla Tucúcaro en el extremo sur del Salar de Atacama: Una Antigua zona de cizalle reactivada en el Cenozoico. Departamento de Geología, Universidad de Chile, Santiago, Comunicaciones. 34. pp. 37–45.
Niemeyer, H., 1989. El Complejo Igneo-Sedimentario del Cordón de Lila, Región de Antofagasta: significado tectónico. Rev. Geol. Chile 16 (2), 163–181.
Niemeyer, H., Urzua, F., Rubinstein, C., 1997. Nuevos antecedentes estratigraficos y sedimentologicos de la Formacion Zorritas, Devonico-Carbonifero de Sierra Almeida. Reg. Antofagasta, hile. Rev. Geol. Chile 24 (1), 25–43.
Padilla, H., 1985. Informes de avance, Enero y Febrero, proyecto "Geología regional de enlace entre Quebrada de Vaquillas y Salar de Pedernales". Archivo técnico ENAP-Magallanes.
Pananont, P., Mpodozis, C., Blanco, N., Jordan, T.E., Brown, L.D., 2004. Cenozoic evolution of the northwestern Salar de Atacama Basin, northern Chile. Tectonics 23, TC6007. https://doi.org/10.1029/2003TC001595.
Ramirez, C.; Gardeweg, P., 1982. Hoja Tocona, Región de Antofagasta. Servicio Nacional de Geología y Minería, Carta Geológica de Chile, 58: mapa escala 1:250.000, p. 1-121, Santiago.
Reutter, K.J., Charrier, R., G€otze, H.J., Schurr, B., Wigger, P., Scheuber, E., Giese, P., Reuther, C.D., Schmidt, S., Rietbrock, A., Chong, G., Belmonte-Pool, A., 2006. The Salar de Atacama Basin: a subsiding block within the western edge of the Altiplano-Puna Plateau. In: Oncken, O. (Ed.), The Andes Active Subduction Orogeny. Springer, Berlin Heidelberg, Berlin, pp. 303–325.
Rubilar, J., Martínez, F., Arriagada, C., Becerra, J., 2017. Structure of the Cordillera de la Sal: A key tectonic element for the Oligocene-Neogene evolution of the Salar de Atacama basin, Central Andes, northern Chile. J. S. Am. Earth Sci. https://doi.org/10.1016/j.jsames.2017.11.013.

Rubinstein, C.V., Petus, E., Niemeyer, H., 2016. Palynostratigraphy of the Zorritas formation, Antofagasta region, Chile: insights on the Devonian/Carboniferous boundary in western Gondwana. Geosci. Front. https://doi.org/10.1016/j.gsf.2016.04.005.

Scheuber, E., González, G., 1999. Tectonics of the Jurassic–early cretaceous magmatic arc of the north Chilean Coastal Cordillera (22°–26°S): a story of crustal deformation along a convergent plate boundary. Tectonics 18, 895–910.

Scisciani, V., 2009. Styles of positive inversion tectonics in the central Apennines and in the Adriatic foreland: implications for the evolution of the Apennine chain (Italy). Struct. Geol. https://doi.org/10.1016/j.jsg.2009.02.004.

Scisciani, V., Tavarnelli, E., Calamita, F., 2002. The interaction of extensional and contractional deformations in the outer zones of the central Apennines, Italy. J. Struct. Geol. 24, 1647–1658.

Soto, R., Martinod, J., Riquelme, R., Hérail, G., Audin, L., 2005. Using geomorphological markers to discriminate Neogene tectonic activity of north Chilean forearc (24°–25° S). Tectonophysics 41, 41–55.

Tomlinson, A., Blanco, N., 1997. Structural evolution and displacement history of the West fault System, Precordillera, Chile: Part 1 y 2, synmineral history. In: Proceedings 8th Congreso Geológico Chileno, Antofagasta. 3. pp. 1873–1882.

Journal of South American Earth Sciences 87 (2018) 188–199

Contents lists available at ScienceDirect

Journal of South American Earth Sciences

journal homepage: www.elsevier.com/locate/jsames

Structural styles of the Salar de Punta Negra Basin in the Preandean Depression (24°-25°S) of the Central Andes

Fernando Martínez [a, *], Rodrígo Gonzalez [a], Sebastian Bascuñan [b], César Arriagada [b]

[a] Facultad de Ingeniería y Geología, Departamento de Ciencias Geologicas, U. Católica del Norte, Angamos 0610, Antofagasta, Chile
[b] Departamento de Geología, Universidad de Chile, Santiago, Chile

ARTICLE INFO

Article history:
Received 8 May 2017
Received in revised form
13 July 2017
Accepted 4 August 2017
Available online 19 September 2017

ABSTRACT

We have combined 2D seismic information with field data to interpret the structure underneath the Salar de Punta Negra Basin. The interpretation of NW-SE oriented seismic profiles along the basin shows that its structure consists of a doubly-verging contractional system composed of inverted and basement-involved structures. West-verging inversion anticlines and high-angle reactivated normal faults are preferentially located at the central and eastern parts of the basin. These commonly involve Upper Paleozoic to Mio-Pliocene volcanic and sedimentary stratigraphic wedges, indicating that these resulted from the tectonic inversion of ancient basement structures that acted as normal faults during extensional episodes in the Paleozoic and Mesozoic. East-verging, basement-cored anticlines and reverse faults are located at the western part of the basin and they are generally related to blind ramps, which form part of the eastern termination of the Domeyko Cordillera. The presence of unconformable Tertiary (Eocene, Oligocene and Mio-Pliocene) synorogenic deposits over the contractional structures (basement cored and inversion anticlines) suggest that these could have been developed progressively during this period. Finally, we show here as the shortening of ancient extensional system played a fundamental role in the Andean deformation of the Preandean Depression of northern Chile.

1. Introduction

The western section of the Central Andes in northern Chile between latitudes 23°-25°S is located over a normal subduction segment, where the Pacific oceanic plate is inclined approximately 30° to the east under the continental margin. In this region, the Central Andes correspond to an orogenic belt composed of five large N-S oriented morphological units, which are from west to east: the Coastal Cordillera, the Central Depression, the Chilean Precordillera or also called Domeyko Cordillera, the Preandean Depression and the Western Cordillera or the active volcanic zone (Fig. 1). In this context, the Preandean Depression represents a significant negative structural relief trapped between the Domeyko Cordillera and the active volcanic zone, and its configuration is mostly characterized by a series of saline and narrow Tertiary basins, which include the Salar de Atacama and the Salar de Punta Negra basins (Fig. 1).

For many years, the structural studies carried out along these latitudes (23°-25°S) of the Central Andes have been concentrated in three regions: the Eastern Cordillera and the Sub-Andean Range in Bolivia and Argentina and along the Domeyko Cordillera in Chile. The fundamental reasons are related to the oil and gas exploration in the Sub-Andean Range, which has allowed concentrating great efforts into understanding the structure of this region, and the second is associated with the study of the major porphyry copper deposits located in the Domeyko Cordillera. At least in Chile, this situation implies that other provinces along the region have not been fully studied from a structural point of view. One of these provinces is the Preandean Depression, where only few studies (Gardeweg et al., 1994; Muñoz et al., 2002; Mpodozis et al., 2005; Arriagada et al., 2006; Amilibia et al., 2008; Bascuñan et al., 2015) have paid attention to its structure. However, these works were centered mainly on the Salar de Atacama Basin (Fig. 1).

Different studies focused on the Salar de Atacama Basin (Fig. 1) have proposed that the tectonic evolution of the Preandean Depression is associated with different Late Cretaceous to Cenozoic shortening episodes of a former Cretaceous rift basin (Tarapacá Basin) (Muñoz et al., 2002; Arriagada et al., 2006; Bascuñan et al., 2015; among others). Other works have also

* Corresponding author.
E-mail address: fernando.martinez@ucn.cl (F. Martínez).

http://dx.doi.org/10.1016/j.jsames.2017.08.004
0895-9811/

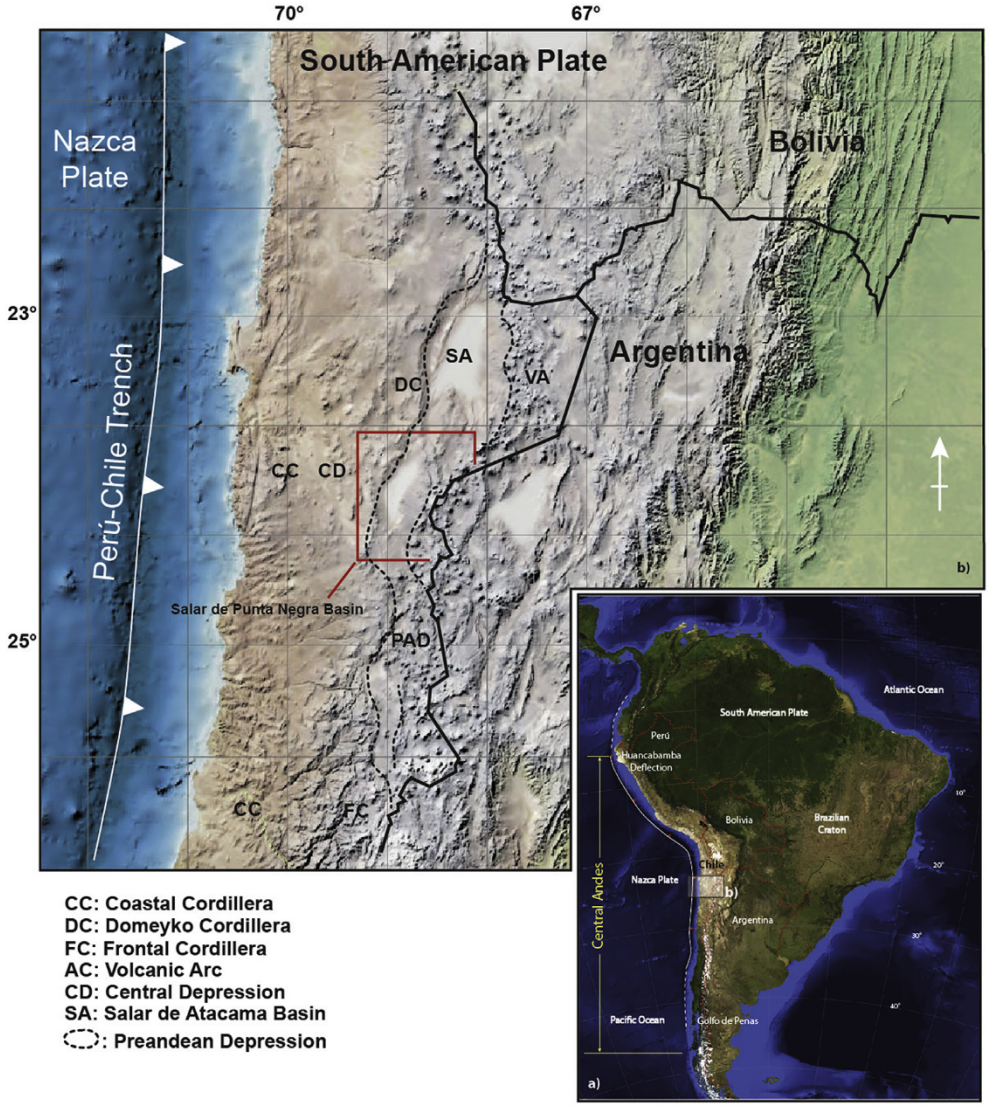

Fig. 1. a) Geographic location of the study region along the Central Andes of South America, and b) Location of the Salar de Punta Negra Basin along the Preandean Depression, and distribution of the main morphotectonic units established in the normal subduction segment of the Central Andes of northern Chile, between 23° and 25°S.

suggested that localized Cenozoic crustal extension also occurred during its evolution (Maceralli et al., 1991; Flint et al., 1993; Pananont et al., 2004). All these studies coincide that at least at the surface, the main structural styles of this region consist of NNE-striking and east-verging faults and folds with variable geometry and kinematics, which affect large basement ridges, as well as syn-rift Mesozoic and Tertiary synorogenic successions (Jordan et al., 2002; Muñoz et al., 2002; Arriagada et al., 2006; Amilibia et al., 2008). Nevertheless, and despite all these efforts, the structure of the central and southern parts of the Preandean Depression is still poorly understood, and therefore considered as an "unexplored region" from an Andean tectonic point of view. Considering this problem, and in order to give ideas about the structural styles of the central part of the Preandean Depression, the main objective of this contribution is present the structural interpretation of the first subsurface images of the Salar de Punta Negra Basin from 2D seismic profiles, which will allow knowing the deformation style in this region. The results obtained here will allow us interpret some tectonic aspects of the geological evolution of this region.

2. Geological setting

The Salar de Punta Negra Basin corresponds to an intramontane basin with dimension of 77 km length and 30 km wide (Fig. 2), located immediately south of the Salar de Atacama Basin (Fig. 1) in the Preandean Depression. This basin is bounded to the west by the Domeyko Cordillera and to the east by the current volcanic zone of the Central Andes (Fig. 2). The stratigraphic record of the basin is best observed along its west and east border, owing to the thick Cenozoic volcanic and sedimentary cover (Fig. 2) which prevents the observation of both older stratigraphic sequences and tectonic structures.

The oldest rocks in the area correspond to Middle Devonian to Early Carboniferous siliciclastic rocks of the Zorritas Formation (Cecioni and Frutos, 1975), a sedimentary and continental sequence of ca. 2.700 m thick, deposited mainly in a marine tidal platform (Niemeyer et al., 1997; Rubinstein et al., 2016, Fig. 2). This formation is unconformably overlain by a volcanic succession composed of pyroclastic acidic rocks described as La Tabla Formation (García, 1967; Cornejo et al., 1993, Fig. 2). Other group of old rocks

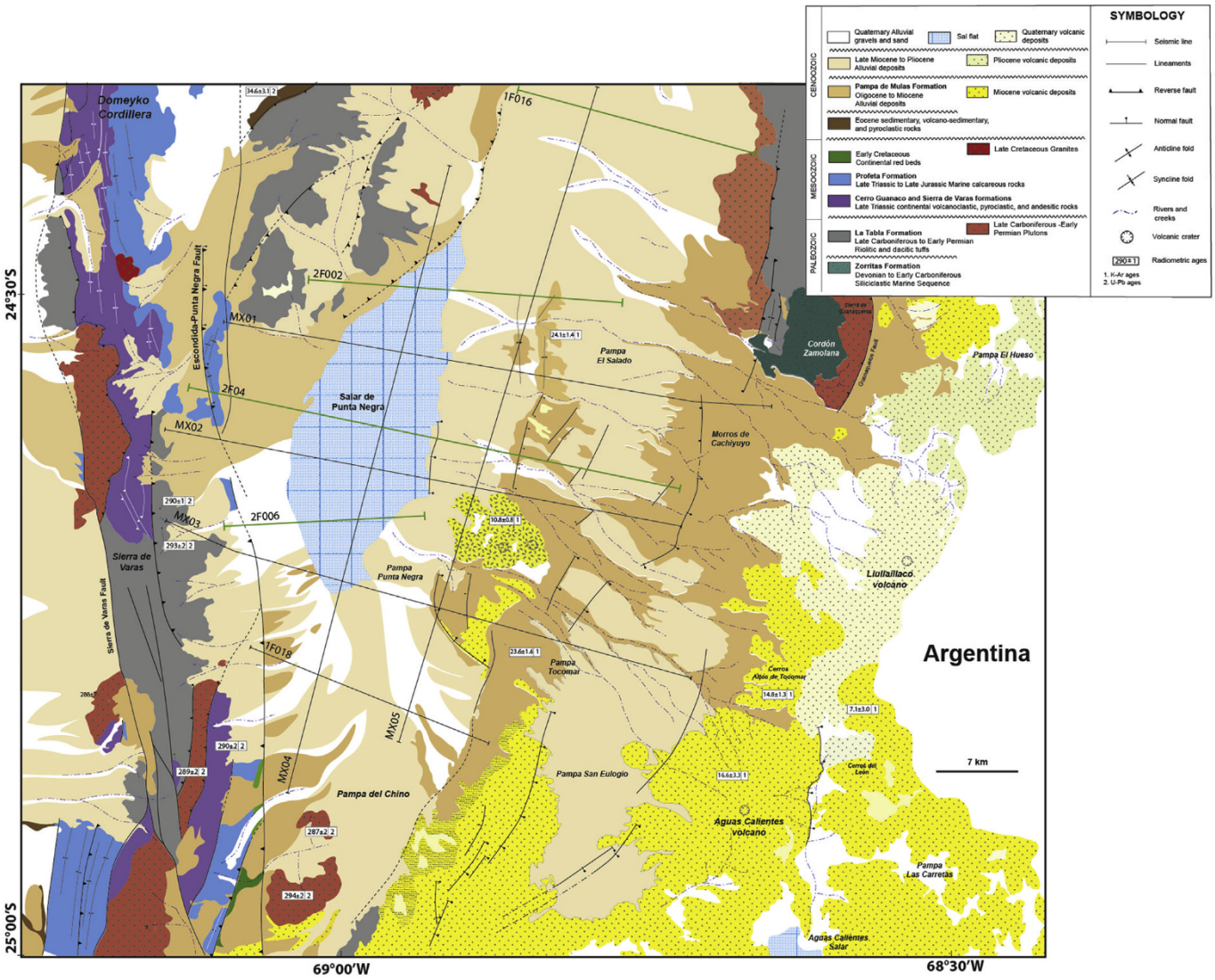

Fig. 2. Simplified geological map of the Salar de Punta Negra Basin and the eastern part of the Cordillera de Domeyko showing the location of the seismic profiles available (Modified from González et al., 2015; Gardeweg et al., 1993, 1994).

includes plutonic (granites, granodiorites and monzogranites) bodies emplaced ca. 300 -280 Ma, which crop out in the form of isolated blocks along the western and eastern parts of the Salar de Punta Negra Basin (e.g., Cordón de Zamolanas, Morros de Cachilluyo, Pampa del Chino, among others; Fig. 2). The latter are frequently associated with the basement of the basin (Fig. 2), and have been related to an ancient magmatic arc possibly active between the Early Pennsylvanian-Early Permian in the western margin of Gondwana (Breitkreuz C Zeil, 1994; Breitkreuz and Van Schmus, 1996).

The Mesozoic successions in the region commonly rest over Paleozoic stratified rocks (Fig. 2). These are composed of the Upper Triassic Sierra Guanaco and Sierra de Varas formations, and the Rhaetian to Jurassic Profeta Formation. The Sierra Guanaco Formation is a volcanic and sedimentary succession composed of interbedded andesitic and siliciclastic rocks (González et al., 2015), while the Sierra de Varas Formation consists of fluvial and lacustrine deposits intercalated with pyroclastic deposits (González et al., 2015). Both formations are covered by the Rhaetian to Jurassic Profeta Formation (Chong, 1973; Ardill et al., 1998; González et al., 2015), a marine calcareous succession composed of conglomerates, sandstones and calcareous sedimentary rocks. All these Mesozoic formations have been traditionally associated with the syn-rift fill of ancient Mesozoic extensional back-arc basins (Tarapacá and Profeta basins), which were developed at these latitudes in response to rollback subduction of the oceanic Nazca plate beneath central South America, due to Gondwana break-up (Mpodozis and Ramos, 1990; Mpodozis and Cornejo, 1997). The Mesozoic record culminates with a Lower Cretaceous succession made of stratified red beds associated with a marine regression event (Naranjo and Puig, 1984; Vicente, 2006; González et al., 2015).

Paleogene and Neogene successions are found in the central part of the basin, and isolated Eocene sedimentary successions have been recognized in the northern part of the basin (Fig. 2), which have been interpreted an stratigraphic equivalent of the Naranja Formation exposed in the Salar de Atacama Basin (Arriagada et al., 2006). The latter consist of pyroclastic and sedimentary continental rocks (González et al., 2015; Astudillo et al., in press) accumulated in a contractional setting resulting from an orogenic event named the “Incaic Orogeny” (Maksaev, 1990). The Upper Oligocene-Lower Miocene deposits consist of interbedded gravels, conglomerates,

sandstones, ignimbrites and volcanic ashes, which were defined as the Pampa de Mulas Formation (Chong, 1973; Marinovic et al., 1995, Fig. 2). These are overlain by unconsolidated Mio-Pliocene continental sediments and volcanic flows, which are frequently present along the Pampa de San Eulogio locality (Fig. 2). Finally, the most recent deposits in the basin are represented by the Pliocene and Quaternary volcanic complexes located along the eastern section of the basin (Gardeweg et al., 1993), and by the saline crust that occupies its central zone (Fig. 2).

3. Methodology

To identify and interpret the structural styles present underneath the Salar de Punta Negra Basin, we have integrated field data and 2D seismic profiles. The geological data used in this study (Fig. 2) correspond to previous 1:100.000 geological maps (Padilla, 1985; Gardeweg et al., 1993, 1994; González et al., 2015), which were elaborated to document the stratigraphic record of the region. The geological information shown in the maps is mainly supported by field observations and radiometric ages (K-Ar and U-Pb ages). The seismic profiles used here are located transversally throughout the basin (Fig. 2). These WNW-ESE oriented seismic profiles correspond to a two-dimensional (2D) seismic survey of approximately 2310 km^2 facilitated by ENAP-Sipetrol, which was acquired during the 1970s to visualize possible structural traps of oil and gas underneath the Preandean Depression.

The seismic data was acquired using Vibroseis, and has moderate quality and resolution. This generally highlights both the stratigraphic units and the basement of the basin. All the seismic profiles used here were filtered and migrated in time and thus show an adequate resolution within the first three seconds (TWT). In this study, we only show the interpretation of four WNW-ESE oriented seismic profiles (lines IF016, 2F04, 2F002, 2F006) distributed north to south (Fig. 2), that allow documenting the variation of the structural styles along the basin. To carry out the structural interpretation, we first projected within the seismic profiles the contacts of the tectonosequences exposed along the trace of the seismic lines, which are mostly located in the west and east extremes of the lines. This process was done in this way, because there is no oil-well information available in the study area to calibrate the seismic data. During this process, we correlated the main seismic reflectors and tectonosequences identified in the seismic data with the geological units exposed along the basin (Fig. 3). To visualize and interpret the seismic data we used the StructureSolver software of Nunns and Rogan Company. To identify geological structures we used the following criteria: a) occurrence of truncated reflectors to identify faults and angular unconformities, b) lateral loss and breakage of reflectors to identify faults, c) progressive and drastic changes in dip of reflectors associated with the occurrence of folds and faults and, d) conical topographic structures to identify paleo-volcanoes, among others.

3.1. Limitations of the data

The limitations of the seismic data used in this work are mainly related to their quality. This data generally show a relative well resolution in the first two seconds, however; the deepest parts are poorly constrained with this data. Large and master faults are commonly well illuminated, however; those located along the easternmost part, as well as the basement structures, are mainly interpreted from the contact relationships observed on the surface. The presence of some igneous bodies also difficult the structural interpretation in the central part of the basin. Another limitation is associated with the absence of borehole information, which is necessary to perform the time-deep conversion of the seismic data and constrain the geological information of the subsurface. The limited expositions of geological units along the basin could be other important limitation in this work, however; some contacts between the stratigraphic cover and the basement of the basin are well exposed in the extremes of the seismic profiles. All these limitations have impeded to distinguish between structures that are more or less well recognized from those more speculative in the seismic profiles.

4. Major tectonosequences underneath the Salar de Punta Negra Basin

We have divided the stratigraphic record of the basin into two major geological units, according to their seismic characteristics (amplitude and reflection patterns): the Paleozoic Basement and the stratigraphic fill, which are shown in a template of correlation between the field data and the seismic facies (Fig. 3). Based on the identification of major angular unconformities, the fill of the basin is subdivided into five (5) main tectonosequences (TS1-TS5; Fig. 3). The lithologic character of these tectonosequences and the position of the unconformities were constrained by previous geological mapping (Gardeweg et al., 1993; González et al., 2015) and by the interpretation of lateral and vertical terminations of reflections (e.g., onlaps, toplaps, and erosional truncations). Each tectonosequence was related to a tectonic event, based on the structural styles identified in the seismic profiles, and the tectonic and stratigraphic relationships observed along neighboring regions (e.g., Domeyko Cordillera; Chong, 1973; Amilibia et al., 2008; González et al., 2015). The Paleozoic Basement and the tectonosequences are described as follows:

a) *Basement:* The basement is represented by the Carboniferous and Permian granitic rocks located on the western and easternmost parts of the basin. In the seismic profiles, they correspond to an acoustic basement with a chaotic appearance (Fig. 3). A high amplitude reflector in the lowest parts of the basin is frequently the marker used to identify the top of the basement. This reflector correlates with the stratigraphic contact between the Upper Paleozoic (Carboniferous-Permian) stratified formations and the Paleozoic granitic rocks that crop out in the eastern and westernmost parts of the basin (Figs. 4–6).
b) *Tectonosequence TS1:* Corresponds to the oldest stratigraphic units of the basin. This tectonosequence has a double wedge shape with a maximum thickness beneath the central part of the basin and that thins both to the west and east parts of the basin (Figs. 4–5). Its basal section onlaps against the top of the basement and correlates with the stratigraphic contact between Paleozoic granites and the Upper Paleozoic volcanic and sedimentary deposits (sandstones and conglomerates) of the Zorritas Formation exposed in the easternmost part of the basin (Figs. 2 and 3). This package of reflectors may possibly contain the La Tabla Formation (rhyolitic and dacitic volcanic rocks), but the seismic resolution did not allow us to separate them.
c) *Tectonosequence TS2:* Consists of a mostly sedimentary (tuff, laves, calcareous sandstones, shale, mudstones, among others) wedge that overlies TS1. They are separated by an angular unconformity, which is recognized by the lateral termination of its basal reflectors that onlap against the top of TS1. Following the stratigraphic record identified along the easternmost part of the Domeyko Cordillera and the westernmost part of the basin (Fig. 2), this tectonosequence could be associated with the Mesozoic deposits of the basin (Figs. 2 and 3). In the seismic data, this tectonosequence has a

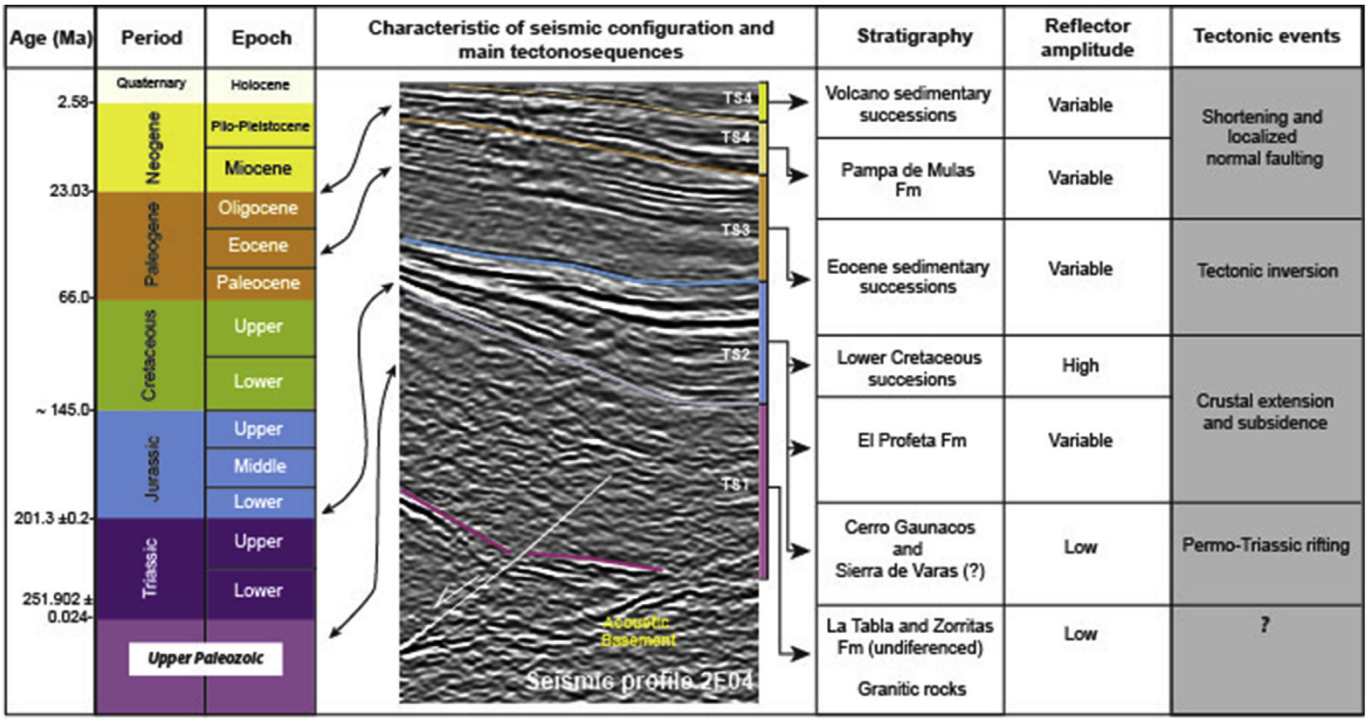

Fig. 3. Correlation template between the geological units recognized on the surface of the Salar de Punta Negra Basin and the main tectonosequences identified from the seismic profiles showed in the central section of the line 2F04.

geometric expression very similar to those reported to syn-rift sequences related to extensional processes and normal faulting. The syn-rift sequences usually thicken toward the fault planes as faults growth and down slip of the hanging wall occur. During this process, they acquire a wedge shape and the younger strata dip less steeply than older strata (Withjack et al., 2002), such as is observed in this tectonosequence (Fig. 4). Within this tectonosequence there are some high amplitude reflectors which could be correlated with the top of the Triassic to Lower Cretaceous deposits (identified at surface, however, the seismic resolution did not allow us to separate them. Based on these points, we have decided to group in this tectonosequence the complete Mesozoic syn-rift fill of the basin (Fig. 3).

d) *Tectonosecuence TS3:* It consists of a stratigraphic section with variable thickness that unconformably overlies TS2. The seismic reflectors of the TS2 commonly are truncated by the basal section of this tectonosequence. This is composed of a series of continuous and parallel reflectors with intercalated high and low amplitude. Different to TS1 and/or TS2, they have not a wedge shape related to syn-rift sequence and contrarily these show a seismic pattern, where its basal reflectors frequently are most inclined that those observed in its upper section forming thus a fan shape similar to the reported by growth strata, which are relatively thicker over the flanks of anticlines folds. This shape could be comparable with the geometry reported by syn-inversion and/or syn-orogenic sequences. We interpreted these reflectors as an Eocene sequence (mainly sandstones and conglomerates) following the stratigraphic record observed on surface, especially in the northeast part of the Domeyko Cordillera, however; its basal section could be oldest (Upper Cretaceous ?). Similar seismic patterns have been observed to the Eocene Naranja Formation under the Salar de Atacama Basin (Arriagada et al., 2006, Fig. 1)

e) *Tectonosequence TS4:* Consist of a thin package of seismic reflectors that unconformably cover the tectonosequence TS3. This is mostly identified in those seismic profiles located at the central and south parts of the basin. This is composed of reflectors with variable amplitude (Fig. 3), which commonly onlap again the oldest deformed tectonosequences. Based on their stratigraphic position, we interpreted that they could correspond to the Oligo-Miocene volcanic and sedimentary Pampa Mulas Formation (Fig. 3). Some internal reports of the ENAP-Sipetrol also have reported this tectonosequence as part of the Pampa de Mulas Formation.

f) *Tectonosequence TS5:* Corresponds to the youngest tectonosequence identified beneath the Salar de Punta Negra Basin. It is separated from TS4 by an angular unconformity (Fig. 3), which correlates with the contact between the Pampa de Mulas Formation and the Mio-Pliocene volcanic and sedimentary (mainly sands, grabels and ignimbrites) deposits that cap the basin. This sequence shows variable reflectors with high and low amplitude, although the basal reflectors that generally onlap against the limbs of contractional folds, indicating that they were accumulated during compressive pulses (Figs. 5–7).

5. Structural styles in the Salar de Punta Negra Basin

The interpretation of seismic profiles has revealed that the structure beneath the Salar de Punta Negra Basin can be divided into two main tectonic domains, composed of inverted structures and basement-involved contractional structures (Figs. 4–7). To better understand their configuration and distribution, we have analyzed the basin structure in three segments (north, central and south), which coincide with the position of the seismic profiles used.

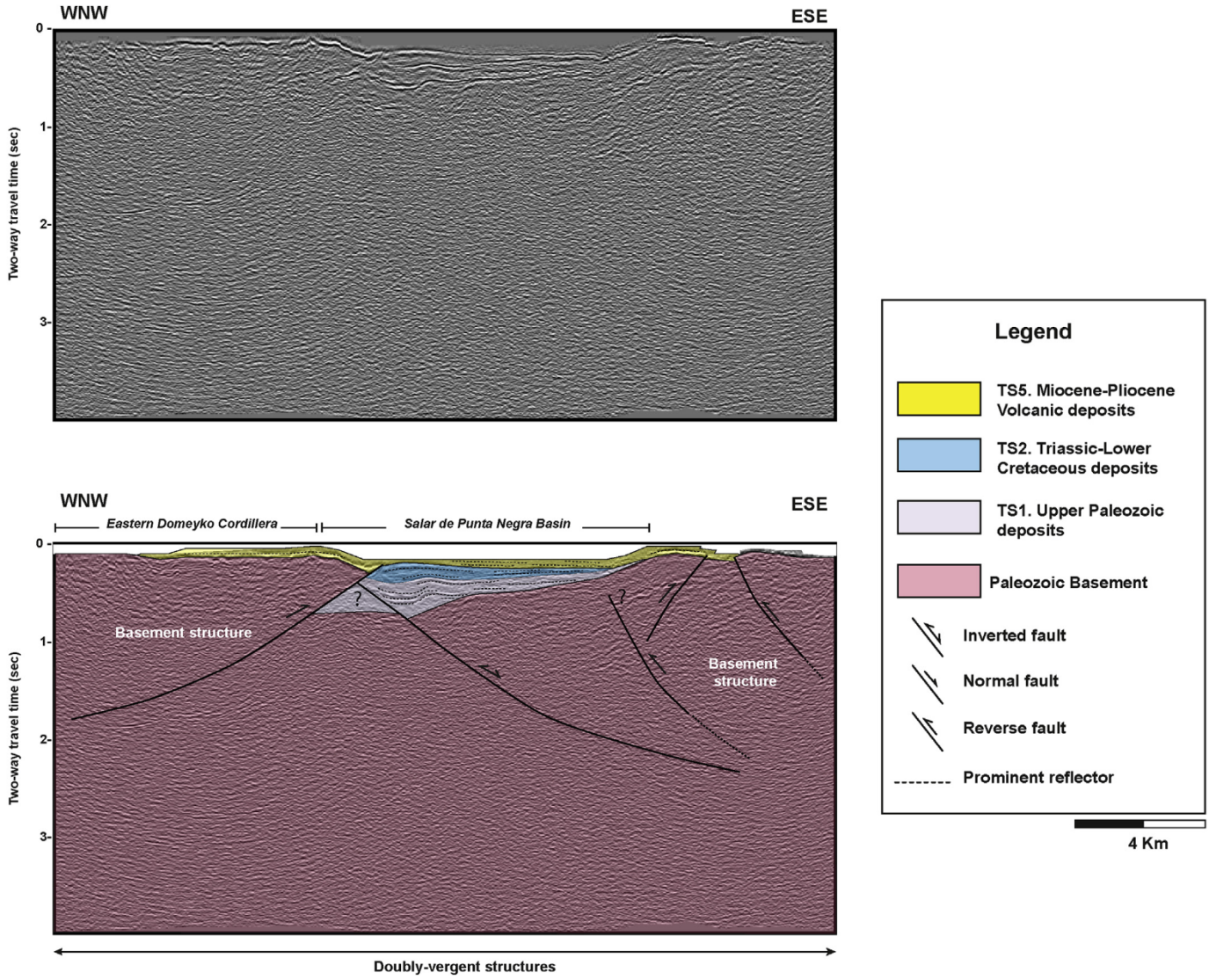

Fig. 4. a) Uninterpreted WNW-ESE seismic profile (Line 1F016) and b) Interpreted seismic profile showing the main structural styles of the northern segment of the Salar de Punta Negra Basin (see location on Fig. 2).

5.1. Northern segment

We used seismic profile 1F016 and 2F002 (Fig. 2) to analyze this segment. Such as illustrated in Figs. 4 and 5, the western part of this segment is characterized by the occurrence of basement-involved contractional structures that coincide with the eastern termination of the Domeyko Cordillera. These structures include basement-cored anticlines and reverse faults (Figs. 4 and 5). The hanging wall of the faults consists of broad and east-verging asymmetrical anticlines that mainly involve the basement of the basin, however; they affect the Mesozoic and Cenozoic infill (tectonosequences TS1-TS5) in some places, such as is observed in Fig. 5. The faults generally have a moderate angle and correspond to west-dipping blind ramps, which usually are poorly illuminated by the seismic data. Their position and dips are commonly determined by the location and vergence of the anticlines (Figs. 4 and 5).

Along the central and eastern part of this segment, two structural styles were recognized. In the northern part of this segment, the structures consist of west-verging basement faults of high angles (Figs. 4 and 5) with reverse motion that forms the western bound of the basin, however; other groups of structures observed in the central and southern part of this segment corresponds to west-verging asymmetrical anticlines and high angle faults (Figs. 4 and 5). These structures mainly involve the basement of the basin, the Paleozoic (TS1), Mesozoic (TS2) (Fig. 4) and Cenozoic tectonosequences TS4-TS5 (Fig. 5). The anticlines are preferentially located in the hanging wall of high angle faults (Figs. 4 and 5), and along these the tectonosequences TS1-TS2 commonly form stratigraphic wedges that thicken toward the fault planes (Figs. 4 and 5), evidencing thus that at least TS1 and TS2 were accumulated during extensional deformation episodes occurred in Upper Paleozoic and Mesozoic times, previous to contractional folding. These anticlines are unconformably covered by the Cenozoic tectonosequences (TS4 and TS5), which usually onlap against the limbs of the anticlines (Figs. 4 and 5) and of some growth synclines (Fig. 5). Based on these structural and stratigraphic relationships, the anticline folds have been interpreted as inversion anticlines linked to the reactivation of previous normal faults (Fig. 4). On the other hand, the Cenozoic tectonosequences TS4 and TS5 that onlap against the limbs of the inversion anticlines suggest that were accumulated contemporaneously to the tectonic inversion process (Figs. 4 and 5).

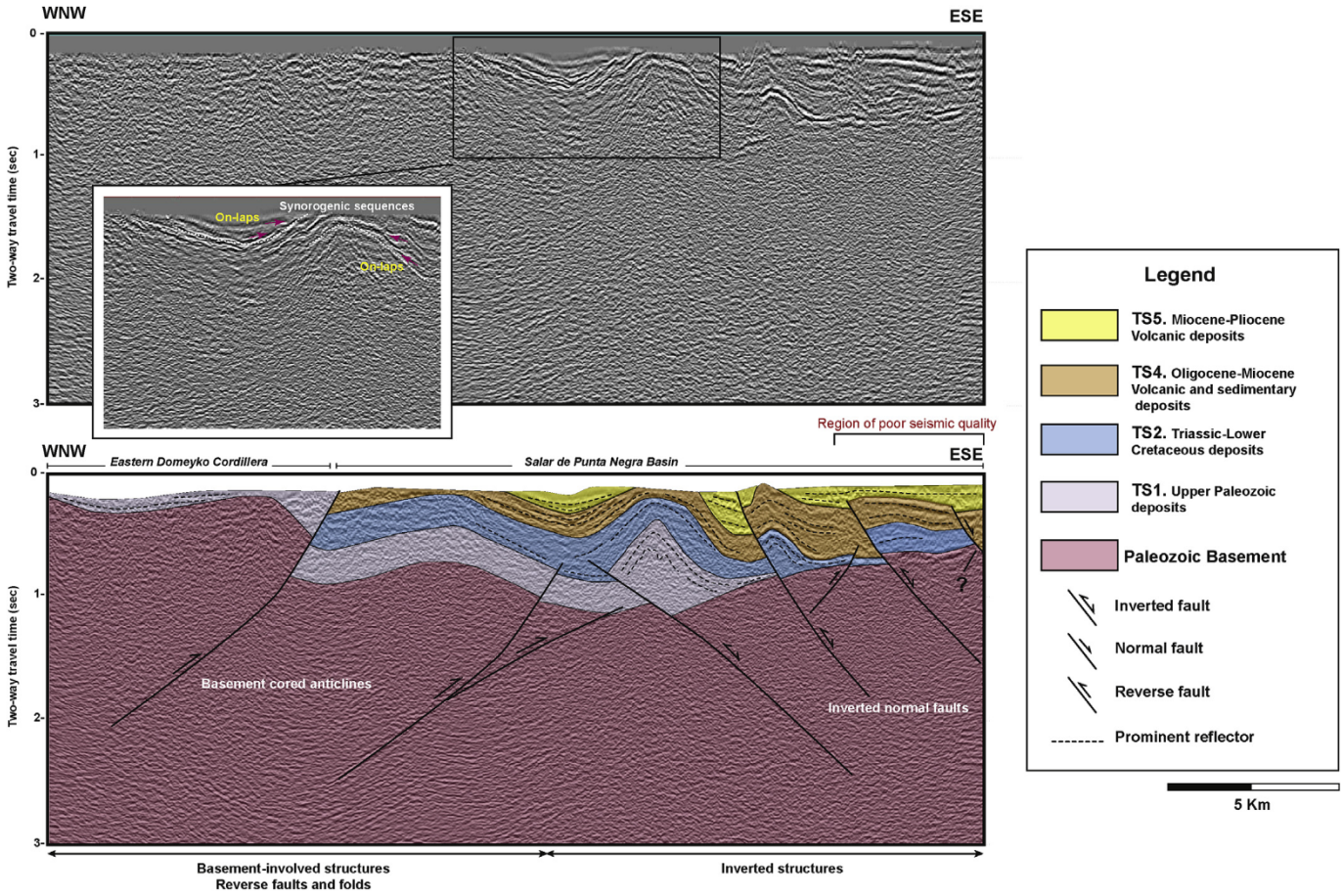

Fig. 5. a) Uninterpreted WNW-ESE seismic profile (Line 2F002) and b) Interpreted seismic profile showing the main structural styles of the northern segment of the Salar de Punta Negra Basin (see location on Fig. 2).

5.2. Central segment

The structure of this segment is illuminated by seismic profile 2F04 (Fig. 2). Along this segment the structural styles consist of doubly-verging (east and west) faults and folds (Fig. 6). The main structures along this segment are is represented by a series of asymmetrical inverted half-grabens, which is bounded by western and eastern master listric and planar faults (Fig. 6). In the western and central part these structures involve the basement of the basin and the Mesozoic and Cenozoic tectonosequences (TS1-TS5) (Fig. 6). Here, the western master fault is represented by the Escondida-Punta Negra Fault that consists of an east-dipping basement fault (Fig. 6). The hanging wall of this fault is composed of an asymmetrical and west-verging anticline that affects the Mesozoic tectonosequence and the Cenozoic tectonosequences (TS3 and TS4). Other master fault is located under the central part of the basin (Fig. 6) and consists of a west-dipping blind fault. Its hanging wall is composed of a thick stratigraphic wedge of Upper Paleozoic to Mesozoic successions related to the tectonosequences TS1 to TS2 (Fig. 6). This wedge generally thickens toward the fault plane, indicating that its accumulation was synchronic with a normal movement of the fault. This stratigraphic wedge is unconformably covered by the Cenozoic tectonosequences TS3-TS5, which also show important variations of thickness and geometries that are mostly associated with synorogenic accumulation (Fig. 6). All these tectonosequences are affected by an east-verging and asymmetrical fold with and arrowhead geometry, which is interpreted as an inversion anticline along which tectonosequences TS1 to TS5 are elevated over the footwall of the fault (Fig. 6).

In the eastern part of this segment the seismic quality is poor and usually this is affected by the presence of volcanic bodies, however; here is possible identify a series of east-dipping planar and semi-planar faults with moderate and high angles that penetrate into the basement of the basin. These faults generally affect the tectonosequences TS1 and TS5 (Fig. 6). In the hanging wall of the faults, the Upper Paleozoic tectonosequence forms stratigraphic wedges (TS1; Fig. 6) similar to those created during contemporaneous normal faulting and sedimentation, which usually thicken toward the faults, however; these stratigraphic wedges are affect by west-verging and asymmetrical anticlines with long and short wavelengths (Fig. 6), associated with the positive tectonic reactivations of ancient normal faults. The younger Mio-Pliocene tectonosequences (TS5) lie unconformably over the frontal and back limbs of the anticlines, and usually form fan geometries associated with synorogenic deposits (Fig. 5).

5.3. Southern segment

The interpretation of this segment was constrained by seismic profile 2F006 (Fig. 7). This profile allowed identifying two different structural styles. The westernmost part consists of an east-verging reverse fault that involves basement rocks and the Mesozoic tectonosequence TS2 (Fig. 7). This fault places the basement and the Mesozoic tectonosequences over Cenozoic tectonosequences

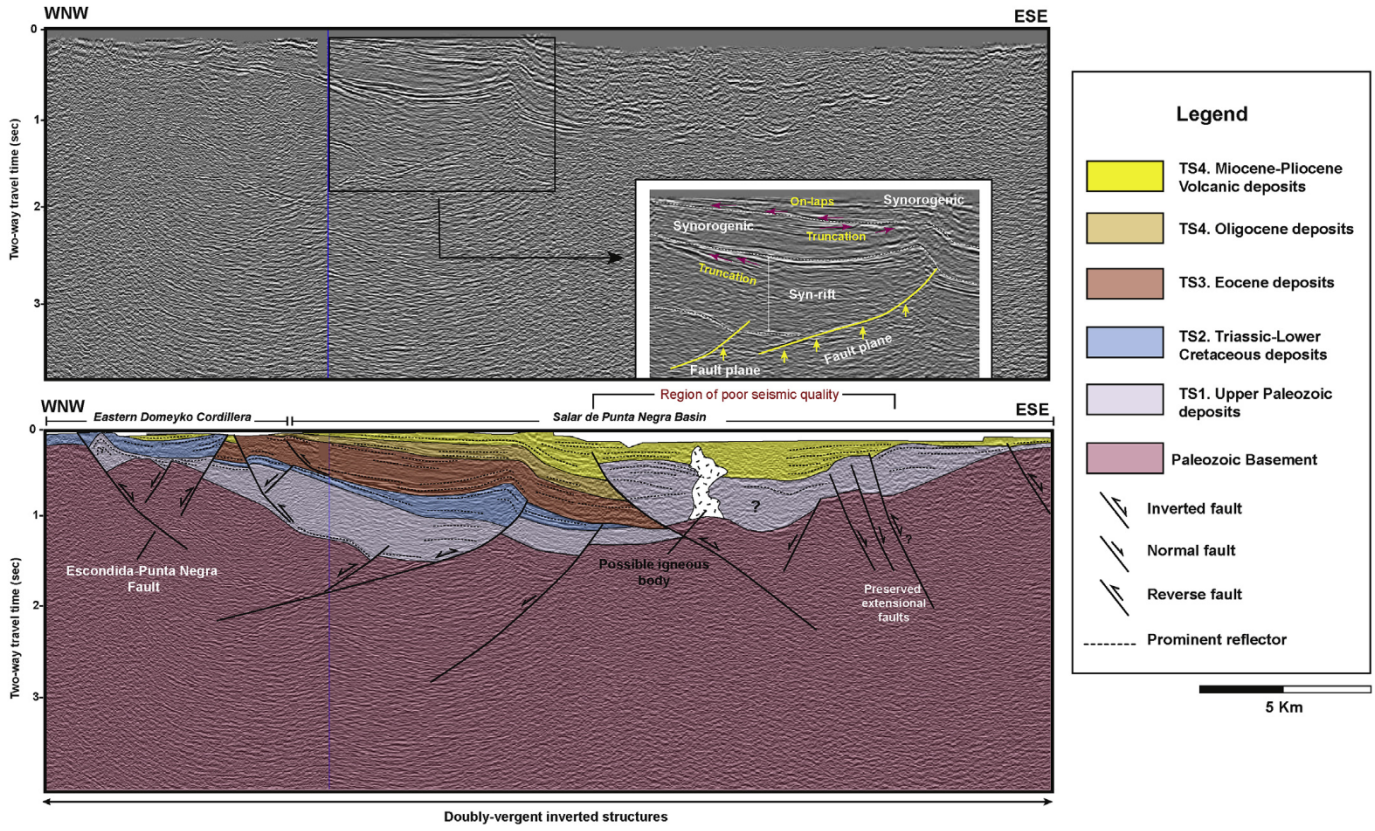

Fig. 6. a) Uninterpreted WNW-ESE seismic profile (Line 2F04) and b) Interpreted seismic profile showing the main structural styles of the central segment of the Salar de Punta Negra Basin (see location on Fig. 2).

(Fig. 7). The hanging wall of the reverse faults is composed by a basement-cored anticline (Fig. 7).

East of this fault, the structural style is characterized by the occurrence of a series of west-dipping, inverted normal faults with listric geometries (Fig. 7). These faults affect both the basement and the Upper Paleozoic-Cenozoic fill (Tectonosequences TS1-TS5) and commonly show strong and middle degrees of positive reactivation. These differences can be related to some factors that include, the original dip of the normal faults, variations of the coefficient of friction, cohesion of the fault plane or even the presence or not of fluid along the fault, however; we believe that the original geometry of the faults is the main factor. The most important of these faults is located at the eastern edge of the basin (Fig. 7). Here, the hanging wall of this fault consists of a thick stratigraphic wedge constituted of tectonosequences TS1 to TS2. This wedge is affected by a large and asymmetrical east-verging anticline with an "arrowhead" geometry (Fig. 7). As in the central segment, the Upper-Paleozoic-Mesozoic stratigraphic wedge is unconformably covered by a series of parallel reflectors packages that thicken toward the back limb of the anticline. These reflectors have been interpreted as Eocene successions, similar to those observed in the seismic line 2F04 (Fig. 6). The Mio-Pliocene tectonosequence TS5 overlies unconformably the top of the inversion anticlines and the tectonosequence TS3. The basal reflector of this tectonosequence usually show onlap terminations again the top of the tectonosequence TS3 indicating that this is mostly associated with synorogenic accumulation during contractional deformation. The hanging wall also is cut and displaced by a series of second-order west-dipping normal faults that only affect the basement and the oldest tectonosequence (TS1) (Fig. 7).

6. Discussion

6.1. Tectonic implications of the architecture of the Preandean Depression

The seismic and structural interpretations shown in this work indicate that the structure of the central part of the Preandean Depression in the Punta Negra Basin is dominated by two main structural styles, represented by reverse and inverted faults. The firsts are related to reverse faults and/or basement-cored anticlines that are mainly confined to the westernmost part of the study area representing the eastern termination of the Domeyko Cordillera. These structures are commonly the responsible for the uplift and exhumation of the oldest rocks in the region. This interpretation coincides with previous observations reported by Amilibia et al. (2008), who argued that the structural configuration of the western Preandean Depression was mostly achieved by the eastward propagation of basement ramps and newly-formed reverse faults (e.g., short-cut structures) created from the tectonic inversion of the Mesozoic Tarapacá Basin, and not by purely strike-slip deformation.

Other studies (Mpodozis et al., 2005; Arriagada et al., 2006) carried out in the Salar de Atamana Basin (Fig. 1) also recognized similar structures and they were interpreted as responsible for the creation of the negative relief of the Preandean Depression from their weight and the lithostatic load. These would have started growing since the Late Cretaceous (Bascuñan et al., 2015), thus allowing for the accumulation of thick synorogenic successions (e.g., Purilactis Group) in the northern part of the region. Although these interpretations have been well supported in the Salar de

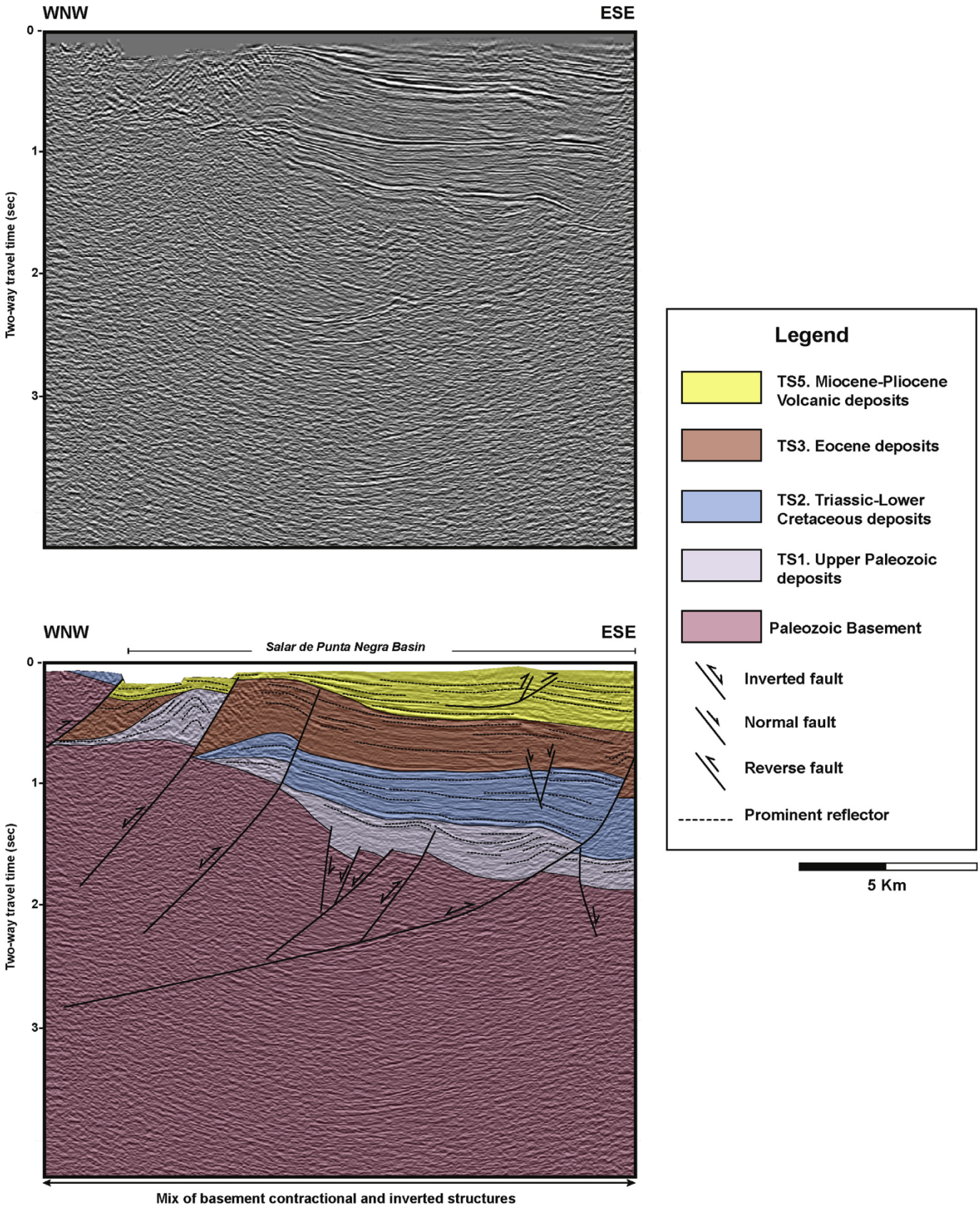

Fig. 7. a) Uninterpreted WNW-ESE seismic profile (Line 2F006) and b) Interpreted seismic profile showing the main structural styles of the southern segment of the Salar de Punta Negra Basin (see location on Fig. 2).

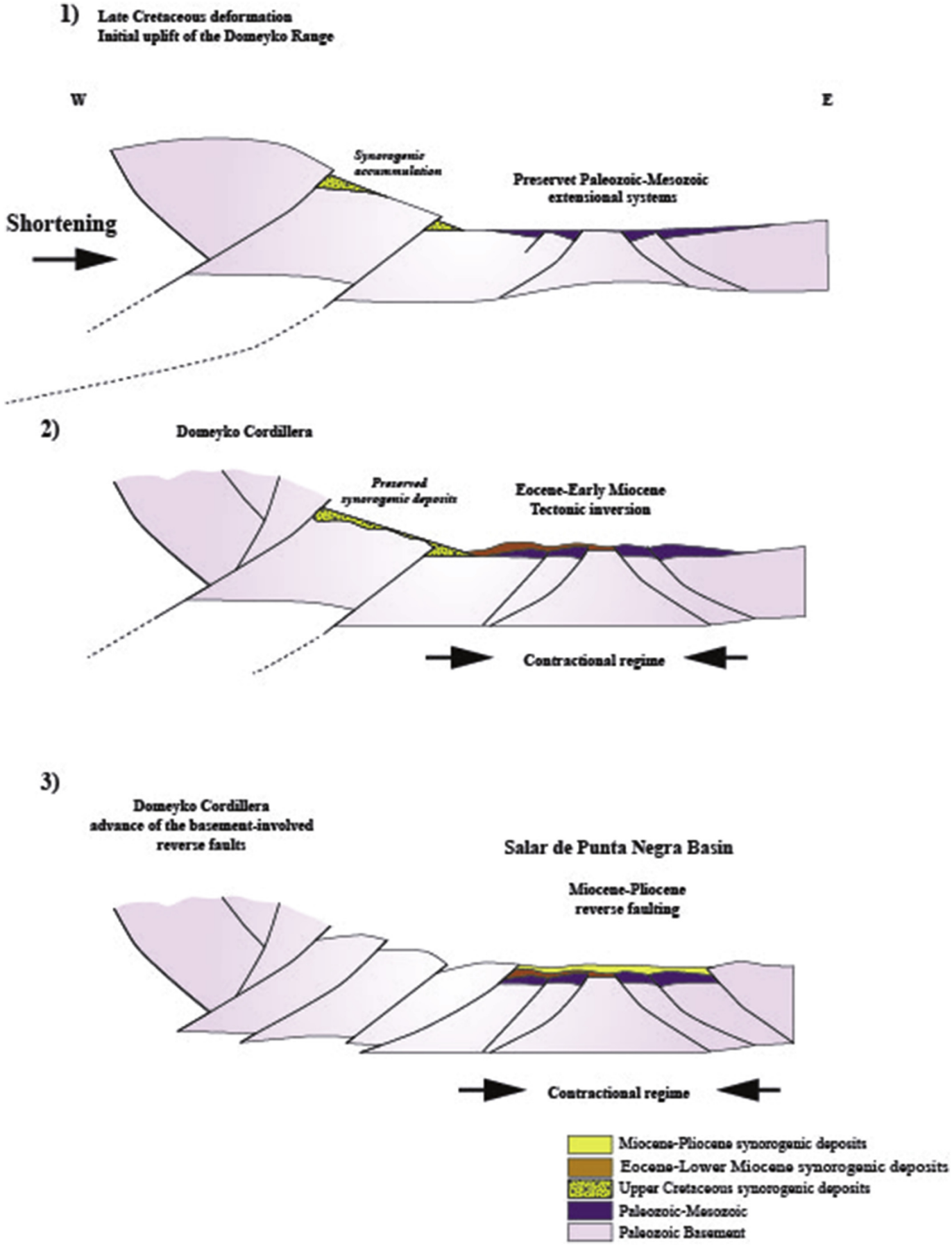

Fig. 8. Cartoon illustrating the hypothetical tectonic evolution of the Salar de Punta Negra since the Late Cretaceous.

Atacama Basin by outcrop and well data, we haven't been able to find stratigraphic or structural evidence to propose a similar interpretation.

The second structural style identified here is related to inverted structures, which are mainly located along the central and eastern part of the Salar de Punta Negra Basin (Fig. 2). These correspond to inversion anticlines related to the positive reactivation of ancient normal faults. Earlier studies (e.g., Gardeweg et al., 1993) have interpreted these structures as normal faults that cut the Oligocene and Miocene successions on surface. Nevertheless, the seismic data show that the hanging walls of these faults involve prominent stratigraphic wedges made of Upper Paleozoic and Mesozoic deposits, with geometries similar to those developed during extensional deformation. This suggests that these inverted structures were controlled by inherited normal faults that evolved during the Paleozoic and Mesozoic times, which are possibly part of the Tarapacá Basin. Although Paleozoic normal faults have not been reported in the region, the correlation between Paleozoic volcanic successions observed at the surface and the seismic data support this idea. On the other hand, we do not rule out the possibility that these structures had an oblique or strike-slip component during the tectonic inversion process, such as it has been observed in previous works (Giambiagi et al., 2016). However, it is difficult to argue with the available data. Similarly to this region, the tectonic inversion of ancient Mesozoic extensional systems also has been well recognized in many regions of the Chilean and Argentinean Central Andes (e.g., Lautaro, Chañarcillo, Tarapacá basins in Chile, Amilibia et al., 2008; Martínez et al., 2012, 2016; Neuquén Basin, Salta Rift in Argentina, Giambiagi et al., 2003; Carrera et al., 2006; Iaffa et al., 2011; Mescua and Giambiagi, 2012, among others). This situation indicate that the tectonic inversion of previous normal faults also was a first-order process during the Andean deformation of the forearc in northern Chile and that a structural inheritance controlled the Cenozoic tectonic evolution of this region, Models from the northern part of the Preandean Depression (Townsend, 1988; Flint et al., 1993; Jordan et al., 2002; Pananont et al., 2004) have argued the presence of large Oligocene and Miocene normal faults created from a Cenozoic extensional collapse, however; these structures have not been clearly observed in the study area and, on the contrary the Miocene successions recognized in the Salar de Punta Negra Basin show evidence of synorogenic deposition. Our interpretations are more associated with the idea that this region has been mostly shortened by the tectonic inversion and thrusting of the Mesozoic extensional systems of the Tarapacá Basin (Muñoz et al., 2002; Mpodozis et al., 2005; Arriagada et al., 2006; Bascuñan et al., 2015). The new seismic interpretations indicate that some of the Oligo-Miocene normal faults previously identified in the eastern part of Salar de Punta Negra by Gardeweg et al. (1993) correspond to Paleozoic and Mesozoic basement-involved reactivated normal faults. These faults have played a fundamental role during the contractional episodes experienced by the region.

Based on the new data presented here, we can only interpret that the architecture of the Preandean Depression resulted from a superposition of contractional to extensional tectonic events, which possibly occurred from the Eocene “Incaic orogeny” (Fig. 8), since the synorogenic tectonosequences interpreted here usually consist of Eocene to Mio-Pliocene deposits, however; we do not rule out that these can be older (Upper Cretaceous ?).

7. Conclusions

Based on the results presented in this work, we conclude that the configuration of the Salar de Punta Negra Basin is the result of the interaction between extensional and contractional events. This intramontane basin is composed of doubly verging structures, consisting in basement-involved contractional and inverted structures, forming the main structural styles. These structural styles were achieved by tectonic inversion of ancient Upper Paleozoic and Mesozoic normal faults and by reverse faulting of Paleozoic and crystalline basement rocks. The inherited normal faults played a fundamental role during the later Cenozoic contractional episodes that led to the shortening and thickening of the forearc of northern Chile. The reactivation of ancient Paleozoic and Mesozoic extensional structures suggest that this region has always been an area of crustal weakness at least from Paleozoic times. The tectonic inversion of normal faults and reverse faulting seems to have happened from the Eocene and this continued during Miocene-Pliocene times, although the determination of the exact age of deformation is difficult due to the absence of updated geochronology. We recommended take care to interpret the normal faults identified on the surface along the central part of the basin, since these can be inverted normal faults. Finally, the subsurface images used here allowed for the first time to determine that the Preandean Depression at this latitude is a morphotectonic feature with a hybrid structural configuration, comprised of a mix of basement and inverted structures, similar to those reported in neighboring regions in Chile and Argentina.

Acknowledgment

The authors are grateful to Lisandro Rojas (ENAP-Sipetrol) by facilitate the seismic data used in this work. On the other hand, we thanks to Nunns and Rogan for provided the software StructureSolver used to the seismic visualization. We also thanks to José Mescua and Guido Gianni for the constructive reviews, which improved strongly this work. Finally we thanks to the researchers of the Paleomagnetism and Andean Tectonic Laboratory of the University of Chile.

References

Amilibia, A., Sàbat, F., McClay, K.R., Muñoz, J.A., Roca, E., Chong, G., 2008. The role of inherited tectono-sedimentary architecture in the development of the central Andean mountain belt: insights from the Cordillera de Domeyko. J. Struct. Geol. 30, 1520–1539.

Ardill, J., Flint, S., Chong, G., Wilke, H., 1998. Sequence stratigraphy of the mesozoic Domeyko basin, northern Chile. J. Geol. Soc. Lond. 155, 71–88.

Arriagada, C., Cobbold, P.R., Roperch, P., 2006. The Salar de Atacama basin: a record of Cretaceous to Paleogene compressional tectonics in the Central Andes. Tectonics 25, TC1008.

Astudillo, N., Ferrando, R., Montecino, D., Espinoza, F., Matthews, S., Cornejo, P., Arévalo, C. (en prep.). Carta Augusta Victoria, Región de Antofagasta. Servicio Nacional de Geología y Minería, Carta Geológica de Chile, Serie Geología Básica, 1 mapa escala 1:100.000.

Bascuñan, S., Arriagada, C., Le Roux, J., Deckart, K., 2015. Unraveling the Peruvian Phase of the Central Andes: stratigraphy, sedimentology and geochronology of the Salar de Atacama Basin (22°30–23°S), northern Chile. Basin Res. https://doi.org/10.1111/bre.12114.

Breitkreuz C Zeil, W., 1994. The late carboniferous to triassic volcanic belt in Northern Chile. In: Reutter, K.J., Scheuber, E., Wigger, P.J. (Eds.), Tectonics of the Southern Andes. Springer, pp. 277–292.

Breitkreuz, C., Van Schmus, W.R., 1996. U-Pb geochronology and significance of Late Permian ignimbrites timing of the magmatism of the paleo-pacific border of Gondwana: U-pb geochronology in Northern Chile. J. S. Am. Earth Sci. 9, 281–293.

Carrera, N., Muñoz, J.A., Sàbat, F., Roca, E., Mon, R., 2006. The role of inversion tectonics in the structure of the Cordillera Oriental (NW Argentinean Andes). J. Struct. Geol. 28, 1921–1932.

Cecioni, A., Frutos, J., 1975. Primera noticia sobre el hallazgo de Paleozoico Inferior marino en la Sierra de Almeida, Norte de Chile. Congr. Argent. Paleontol. Bioestratigr. 1 (1), 191–207.

Chong, G., 1973. Reconocimiento geológico del area Catalina-Sierra de Varas y estratigrafía del Jurásico del Profeta, provincial de Antofagasta. Memoria de prueba. Departamento de Geología, Universidad de Chile, p. 284.

Cornejo, P., Mpodozis, C., Ramirez, C.F., Tomlinson, A.J., 1993. Estudio Geológico de la Región de Potrerillos y El Salvador (26°-27° Lat. S.). Servicio Nacional de Geología y Minería-CODELCO, Informe Registrado, IR-93-01: 258, 12 mapas, escala

1:50.000. Santiago.
Flint, S., Turner, P., Jolley, E.J., Hartley, A.J., 1993. Extensional tectonics in convergent margin basins: an example from the Salar de Atacama. Chil. Andes. Geol. Soc. Am. Bull. 105, 603–617.
García, F., 1967. Geología del Norte Grande de Chile. In: Simposium sobre el Geosinclinal Andino n° 3. Sociedad Geológica de Chile. Empresa Nacional del Petróleo, p. 138.
Gardeweg, M., Ramírez, C.F., Davidson, J., 1993. Mapa Geológico del área Salara de Punta Negra y Volcán Llullaillaco, Región de Antofagasta. Serv. Nac. Geol. Min. Doc. Trab. 5 (1:100.000).
Gardeweg, M., Pino, H., Ramírez, C.F., Davidson, J., 1994. Mapa Geológico del área de Imilac y Sierra Almeida, Región de Antofagasta. Serv. Nac. Geol. Min. Doc. Trab. 7 (1:100.000).
Giambiagi, L., Ramos, V., Godoy, E., Álvarez, P., Orts, D., 2003. Cenozoic deformation and tectonic style of the Andes, between 33° and 34° south latitude. Tectonics. http://dx.doi.org/10.1029/2001TC001354.
Giambiagi, L., Alvarez, P., Spagnotto, S., 2016. Temporal variation of the stress field during the construction of the central Andes: constrains from the volcanic arc region (22–26°S), Western Cordillera, Chile, during the last 20 Ma. Tectonics 35, 2014–2033. http://dx.doi.org/10.1002/2016TC004201.
González, R., Wilke, G.H., Menzies, A.H., Riquelme, R., Herrera, C., Matthews, S., Espinoza, F., Cornejo, P., 2015. Carta Sierra de Varas, Región de Antofagasta. Servicio Nacional de Geología y Minería, Carta Geológica de Chile. Serie Geología Básica 178, 1 mapa escala 1:100.000.
Iaffa, D., Sàbat, F., Muñoz, J.A., Mon, R., Gutierrez, A.A., 2011. The role of inherited structures in a foreland basin evolution. The Metán Basin in NW Argentina. J. Struct. Geol. 33, 1816–1828.
Jordan, T., Muñoz, N., Hein, M., Lowenstein, T., Godfrey, L., Yu, J., 2002. Active faulting and folding without topographic expression in an evaporitic basin, Chile. Geol. Soc. Am. Bull. 114 (11), 1406–1421.
Maceralli, C.E., Su, M., Townsend, F., 1991. Structure and seismic stratigraphy of the Atacama Basin, Northern Chile. Proc. VI Congr. Geol. Chil. 133–137.
Maksaev, V., 1990. Metallogeny, Geological Evolution and Thermochronology of the Chilean Andes between Latitudes 21° and 26° South, and the Origin of the Major Porphyry Copper Deposits. Tesis doctoral. Dalhousie University, Halifax, p. 544.
Marinovic, N., Smoje, I., Maksaev, V., Hervé, M., Mpodozis, C., 1995. Hoja Aguas Blancas, Región de Antofagasta. Serv. Nac. Geol. Min. Doc. Trab. 70.
Martínez, F., Arriagada, C., Mpodozis, C., Peña, M., 2012. The Lautaro Basin: a record of inversion tectonics in northern Chile. Andean Geol. 39 (2), 258–278.
Martínez, F., Arriagada, C., Peña, M., Deckart, K., Charrier, R., 2016. Tectonic styles and crustal shortening of the Central Andes "Pampean" flat-slab segment in northern Chile (27°-29°S). Tectonophysics 667, 144–162.
Mescua, J., Giambiagi, L., 2012. Fault inversion vs. new thrust generation: a case study in the Malargüe fold-and-thrust belt, Andes of Argentina. J. Struct. Geol. 31, 51–63.
Mpodozis, C., Ramos, V.A., 1990. The Andes of Chile and Argentina. In: Ericksen, G.E., Cañas Pinochet, M.T., Reinemud, J.A. (Eds.), Geology of the Andes and its Relation to Hydrocarbon and Mineral Resources, Circumpacific Council for Energy and Mineral Resources, Earth Sciences Series, Houston 11, pp. 59–90.
Mpodozis, C., Cornejo, P., 1997. El rift Triásico-Sinemuriano de Sierra Exploradora, Cordillera de Domeyko (25 –26S): asociaciones de facies y reconstrucción tectónica. VIII Congreso Geológico Chileno. Antofagasta, Actas I. Sesión Temática 3, 550–554.
Mpodozis, C., Arriagada, C., Basso, M., Roperch, P., Cobbold, P., Reich, M., 2005. Late mesozoic to paleogene stratigraphy of the Salar Atacama Basin, antofagasta, Northern Chile: implications for the tectonic evolution of the central Andes. Tectonophysics 399, 125–154.
Muñoz, N., Charrier, R., Jordan, T., 2002. Interactions between basement and cover during the evolution of the Salar de Atacama Basin, Northern Chile. Rev. Geol. Chile 29, 55–80.
Naranjo, J., Puig, A., 1984. Hojas Taltal y Chañaral, Regiones de Antofagasta y Atacama. Serv. Nac. Geol. Minería, Carta Geol. Chile 62-63, 140, 1 mapa escala 1: 250.000.
Niemeyer, H., Urzua, F., Rubinstein, C., 1997. Nuevos antecedentes estratigraficos y sedimentologicos de la Formacion Zorritas, Devonico-Carbonifero de Sierra Almeida. Reg. Antofagasta,hile Rev. Geol. Chile 24 (1), 25–43.
Padilla, H., 1985. Informes de avance, Enero y Febrero, proyecto "Geología regional de enlace entre Quebrada de Vaquillas y Salar de Pedernales". Archivo técnico ENAP-Magallanes.
Pananont, P., Mpodozis, C., Blanco, N., Jordan, T.E., Brown, L.D., 2004. Cenozoic evolution of the northwestern Salar de Atacama Basin, northern Chile. Tectonics 23, TC6007,. http://dx.doi.org/10.1029/2003TC001595.
Rubinstein, C.V., et al., 2016. Palynostratigraphy of the Zorritas Formation, antofagasta region, Chile: insights on the devonian/carboniferous boundary in western Gondwana. Geosci. Front. https://doi.org/10.1016/j.gsf.2016.04.005.
Townsend, G.F., 1988. Exploración petrolera en la cuenca del Salar de Atacama, región de Antofagasta, Chile. Vertiente 4, 45–55.
Vicente, J.C., 2006. Dynamic paleogeography of the Jurassic Andean Basin: pattern of regression and general considerations on main features. Rev. la Asoc. Geol. Argent. 61 (3), 408–437.
Withjack, M., Schlische, R., Olsen, P., 2002. Sedimentation in continental rifts. Soc. Sediment. Geol. Special Publ. 73, 57–81.

Journal of South American Earth Sciences xxx (2017) 1–11

Contents lists available at ScienceDirect

Journal of South American Earth Sciences

journal homepage: www.elsevier.com/locate/jsames

Structure of the Cordillera de la Sal: A key tectonic element for the Oligocene-Neogene evolution of the Salar de Atacama basin, Central Andes, northern Chile

Juan Rubilar [a, *], Fernando Martínez [b], César Arriagada [a], Juan Becerra [a], Sebastián Bascuñán [a]

[a] Departamento de Geología, Facultad de Ciencias Físicas y Matemáticas, Universidad de Chile, Plaza Ercilla 803, Santiago, Chile
[b] Departamento de Geología, Facultad de Ingeniería, Universidad Católica del Norte, Angamos 0610, Antofagasta, Chile

ARTICLE INFO

Article history:
Received 18 July 2017
Received in revised form
16 November 2017
Accepted 17 November 2017
Available online xxx

Keywords:
Salar de Atacama
Cordillera de la sal
San Pedro Formation
Salt tectonics
Inversión tectonics
Oligocene

ABSTRACT

The Salar de Atacama basin is the main topographic low of the Preandean Depression of the Central Andes of northern Chile. Although numerous studies have been carried out in this area, the origin of the depression is still a matter of debate. The integration of seismic reflection and surface structural data along the basin allows the characterization of Oligocene and Neogene tectonic activity of the Salar de Atacama. A key element to unravel the Neogene to recent history of the basin is found along the Cordillera de la Sal, which comprises more than 3000 m of continental sedimentary succession assigned to the San Pedro Formation. Detailed analysis of the seismic data shows that large depocenters involving distal alluvial facies and evaporitic members of the San Pedro Formation accumulated in close relation with Oligocene extension. Extension was controlled by a first order normal fault located along the western flank of the Atacama basin, which appears as a key structural feature of the internal architecture of the Salar de Atacama. The rise of the Cordillera de la Sal ridge during the Neogene involved compression and sinistral strike slip in its southern domain, in combination with salt diapirism in its north domain. This transition is related to the thickness and distribution of the evaporitic lower members of the San Pedro Formation, which also controls the depth of the detachment level beneath the Cordillera de la Sal. Our results show that the current relief of the Salar de Atacama basin is mainly due to Oligocene extension and subsequent Neogene tectonic inversion.

1. Introduction

The Central Andes is the largest active compressional orogenic belt located in the western hemisphere, it is created by the subduction of the Pacific oceanic plate under the continental margin of South America (Fig. 1). This orogenic belt extends nearly 5000 km of length, from the Huancabamba deflection in Perú to the Golfo de Penas in southern Chile and Argentina (Fig. 1). According to the current geometry of the subducted slab beneath the western margin of South America, it has been divided in different segments related to flat, steep or normal subduction zones (Isacks and Barazangi, 1977; Jordan et al., 1983; Cahill and Isacks, 1992). Along the normal subduction zone in northern Chile, between 22° and 24°S, the Central Andes is composed of five N-S oriented morphotectonic units, defined from west to east as: the Coastal Cordillera, the Longitudinal Valley, the Chilean Precordillera (also called Domeyko Cordillera), the Preandean Depression and the current Central Volcanic Zone (Fig. 1).

Previous regional works developed at these latitudes have suggested that the configuration of this region was achieved by crustal thickening and tectonic shortening, which occurred uninterruptedly during Paleogene and Neogene times, and was mostly concentrated in the fold and thrust belts located in the backarc regions of the Central Andes (e.g. Eastern Cordillera and the Subandean ranges; Baby et al., 1997; Lamb and Hoke, 1997; Elger et al., 2005; Carrapa et al., 2011; Eichelberger and McQuarrie, 2015). However, there is evidence which indicates that a moderate shortening has also been accumulated along the forearc regions, at least from the Late Cretaceous onwards (Farias et al., 2005; García and Hérail, 2005; Arriagada et al., 2006; Amilibia et al., 2008;

* Corresponding author.
E-mail address: juanfernandorubilar@gmail.com (J. Rubilar).

https://doi.org/10.1016/j.jsames.2017.11.013
0895-9811/

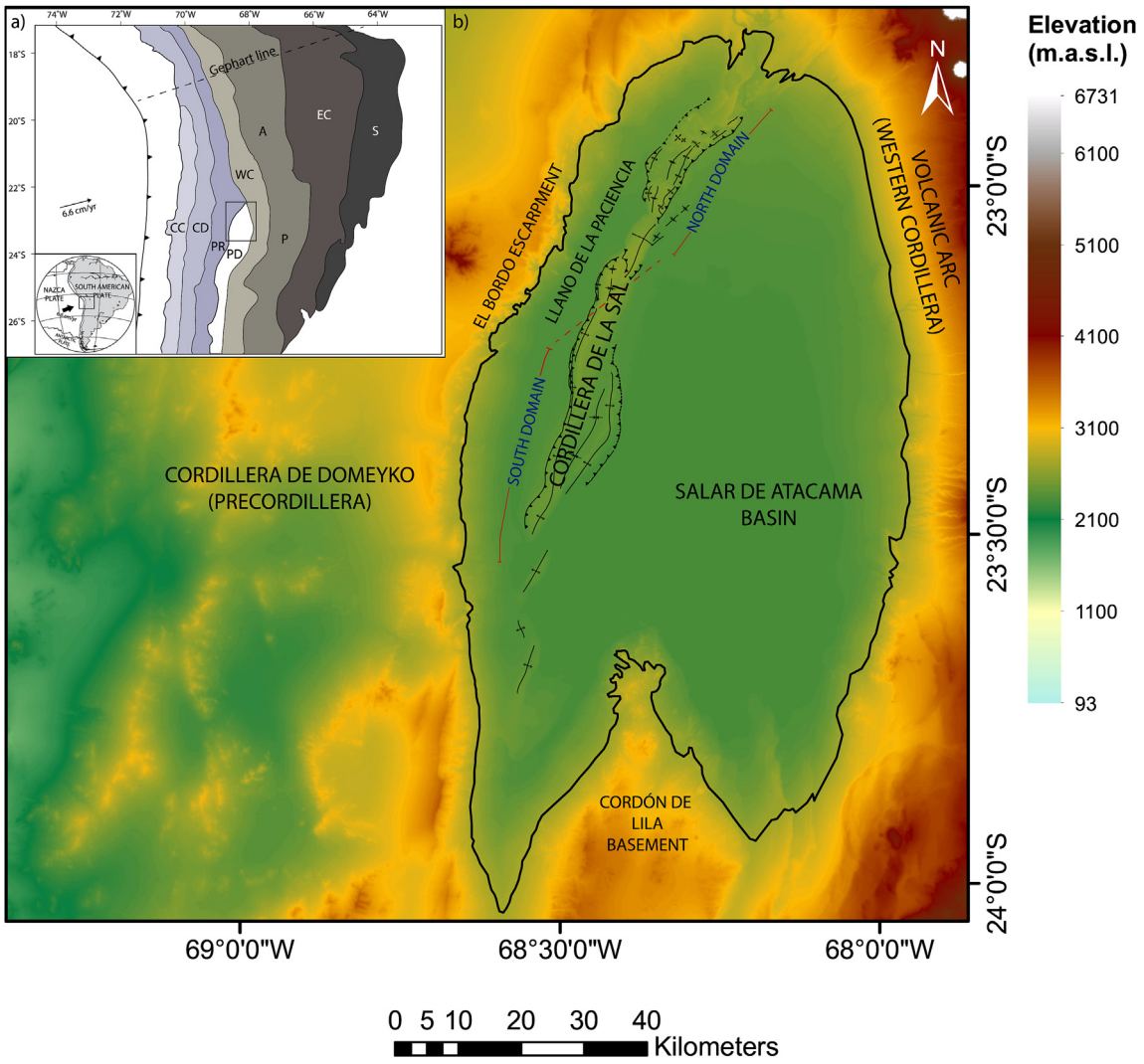

Fig. 1. A) Central Andes between 18° and 26°S showing the main morphostructural units. From west to east; CC: Coastal Cordillera; CD: Central Depression; PR: Precordillera (also called Domeyko Cordillera); PD: Preandean Depression; WC: Western Cordillera (current volcanic arc); A: Altiplano; P: Puna; EC: Eastern Cordillera; S: Subandean range. The study area is marked with a square. B) Elevation model of the Salar de Atacama Basin, showing the structural mapping of the Cordillera de la Sal and the morphostructural units in the basin.

Bascuñan et al., 2015). In addition, other works mainly developed along the Preandean Depression in northern Chile, and especially in the Salar de Atacama Basin (Fig. 1), have proposed that Andean deformation in the forearc was dramatically disrupted during Oligocene times by extensional tectonics (Flint et al., 1993; Pananont et al., 2004; Jordan et al., 2007; among others). These authors also suggest that this extensional stage could represent a first-order geological episode in the Central Andes. This interpretation has been broadly discussed, and still represents a controversial topic regarding the tectonic evolution of the Central Andes of northern Chile, because the structural evidences of extensional deformation reported from field data are scarce and the causes for a Cenozoic extensional tectonic regime in this region are unclear. The main reason for this problem is that the major structural interpretations were based on the visualization of a W-E seismic profile located along the central section of the Salar de Atacama Basin, where the geometry and kinematics of the faults and folds are very speculative. Therefore there are divergent views about how this part of the Central Andes evolved during the Cenozoic.

In the forearc, between 22° and 27° S, the Salar de Atacama Basin constitutes the largest and widest topographic low of the Central Andes (Fig. 1), which is flanked to the east by the current Central Volcanic Zone and to the west by the Chilean Precordillera or Domeyko Cordillera (Fig. 1). Internally, this basin has a NNE-striking and narrow deformed belt defined as the “Cordillera de la Sal”, composed by Oligocene to Neogene folded evaporitic and clastic continental deposits that represent one of the best examples of salt tectonics occurring in convergent zones (Hudec and Jackson, 2007). The oil exploration carried out in this area during the decade of 1970 by ENAP-Sipetrol recorded a valuable set of 2D seismic data with moderate to good quality, which is used to understand the structural anatomy of this basin and, therefore, of the western section of the Central Andes in northern Chile. These profiles show a good image of some features in subsurface that could help to understand the tectonic controls on the Oligocene and Neogene continental deposits in this region. In order to resolve the problem outlined above, we have analyzed the internal structure of the Cordillera de la Sal by the integration of geological data previously published (Becerra et al., 2014) and a new structural interpretation of a series of 2D reflection profiles. We finally show structural

Please cite this article in press as: Rubilar, J., et al., Structure of the Cordillera de la Sal: A key tectonic element for the Oligocene-Neogene evolution of the Salar de Atacama basin, Central Andes, northern Chile, Journal of South American Earth Sciences (2017), https://doi.org/10.1016/j.jsames.2017.11.013

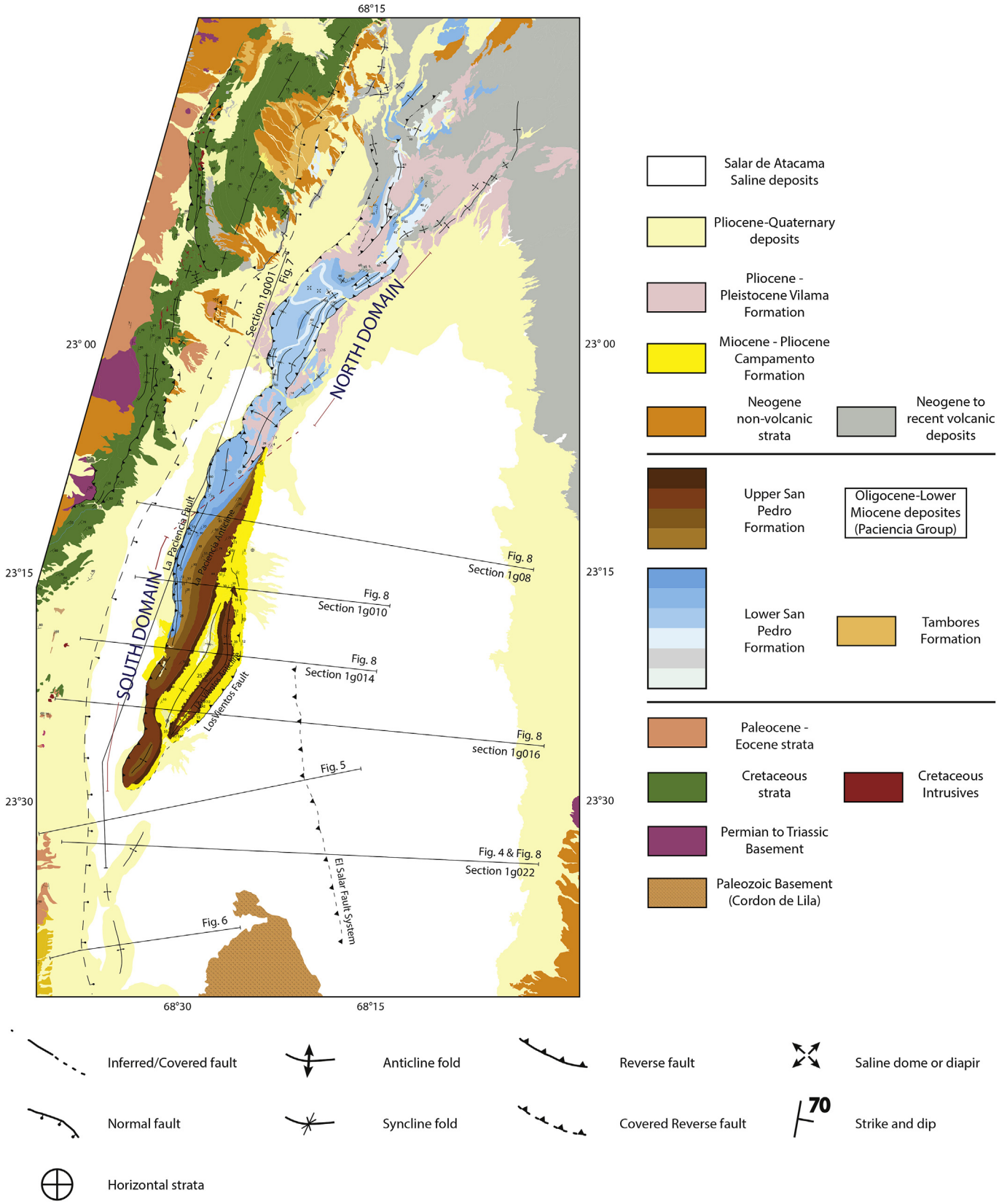

Fig. 2. Geological map of the Salar de Atacama Basin (scale 1:100.000).

Please cite this article in press as: Rubilar, J., et al., Structure of the Cordillera de la Sal: A key tectonic element for the Oligocene-Neogene evolution of the Salar de Atacama basin, Central Andes, northern Chile, Journal of South American Earth Sciences (2017), https://doi.org/10.1016/j.jsames.2017.11.013

model of the Cordillera de la Sal in order to give ideas about the geological evolution of the westernmost part of the Salar de Atacama Basin in the Preandean Depression of northern Chile.

2. Geological framework

The Salar de Atacama Basin is located in the present-day Andean forearc of northern Chile at 23°-24° S. The basin is 150 km long and 80 km wide, has a minimum altitude of about 2300 m.a.s.l. and can be subdivided into four main morphostructural units, which are: El Bordo Escarpment, which represents the structural limit between the Domeyko Cordillera and the western section of the basin; the Llano de la Paciencia, which constitutes a local intramontane depression; the Cordillera de la Sal, and the active Salar de Atacama (salt pan) (*i.e.* Ramírez and Gardeweg, 1982; Mpodozis et al., 2005. Figs. 1b and 2). The El Bordo Escarpment is a 900 m high and 120 km long topographic scarp, developed along the western margin of the Salar de Atacama Basin, where thick successions of stratified Cretaceous deposits lie well-exposed (Mpodozis et al., 2005; Arriagada et al., 2006). These Cretaceous units are generally described in the literature as the "Purilactis Group" and are composed of red sandstones, conglomerates, andesites and rhyolitic rocks (Mpodozis et al., 2005; Arriagada et al., 2006; Bascuñan et al., 2015). Recent works have proposed that facies variations within these units are closely related to Late Cretaceous shortening episodes also known as "Peruvian" tectonic phase (Bascuñan et al., 2015). In the northern El Bordo Escarpment, these rocks are affected by a series of NNE-striking asymmetrical folds and west-verging thrusts (Barros Arana Syncline) that place these Cretaceous successions over Eocene strata (Fig. 2).

Located to the east of the El Bordo Escarpment there is a sub-basin called Llano de la Paciencia that represents a narrow (~8 km wide) intramontane depression (Fig. 2), filled mainly by Quaternary clastic and continental deposits associated with alluvial fans (Marinovic and Lahsen, 1984; Jolley et al., 1990; among others). The Llano de la Paciencia is separated from the folded Cretaceous deposits exposed in the El Bordo Escarpment and the Cordillera de la Sal by a large and continuous NNE inverted normal fault, and by a large and sinuous west-vergent thrust, respectively. The Cordillera de la Sal is a NNE-striking deformed belt composed of evaporites and siliciclastic Oligocene-Miocene rocks (Figs. 2 and 3). Here, the oldest rocks within this Paleogene to Neogene stratigraphic record are represented by the San Pedro and Tambores formations (Paciencia Group, Flint, 1985, Fig. 2), wich consist of nearly 2000 m of continental sedimentary rocks composed of brown sandstones, conglomerates, shales and evaporites, disposed in stratified beds (Fig. 3). These successions have been previously associated with lacustrine and alluvial fan deposits (Brüggen, 1934; Ramírez and Gardeweg, 1982; Marinovic and Lahsen, 1984; Flint et al., 1993). K-Ar ages of 26.6 ± 0.8 Ma and 26.8 ± 1.4 Ma (Travisany, 1979; Mpodozis et al., 2000) reported from tuffs located in the lowermost section of the San Pedro Formation have allowed assigning an upper Oligocene age to these successions. Moreover, previous interpretations of seismic data in this region have indicated that normal faults controlled the deposition of the Paciencia Group (Flint et al., 1993; Pananont et al., 2004; Jordan et al., 2007). The Paciencia Group is unconformably overlain by upper Miocene-Pleistocene and Pliocene-Pleistocene strata defined as the Campamento and Vilama Formations, which crop out along the southern and northern Cordillera de la Sal (Becerra et al., 2014; Henríquez

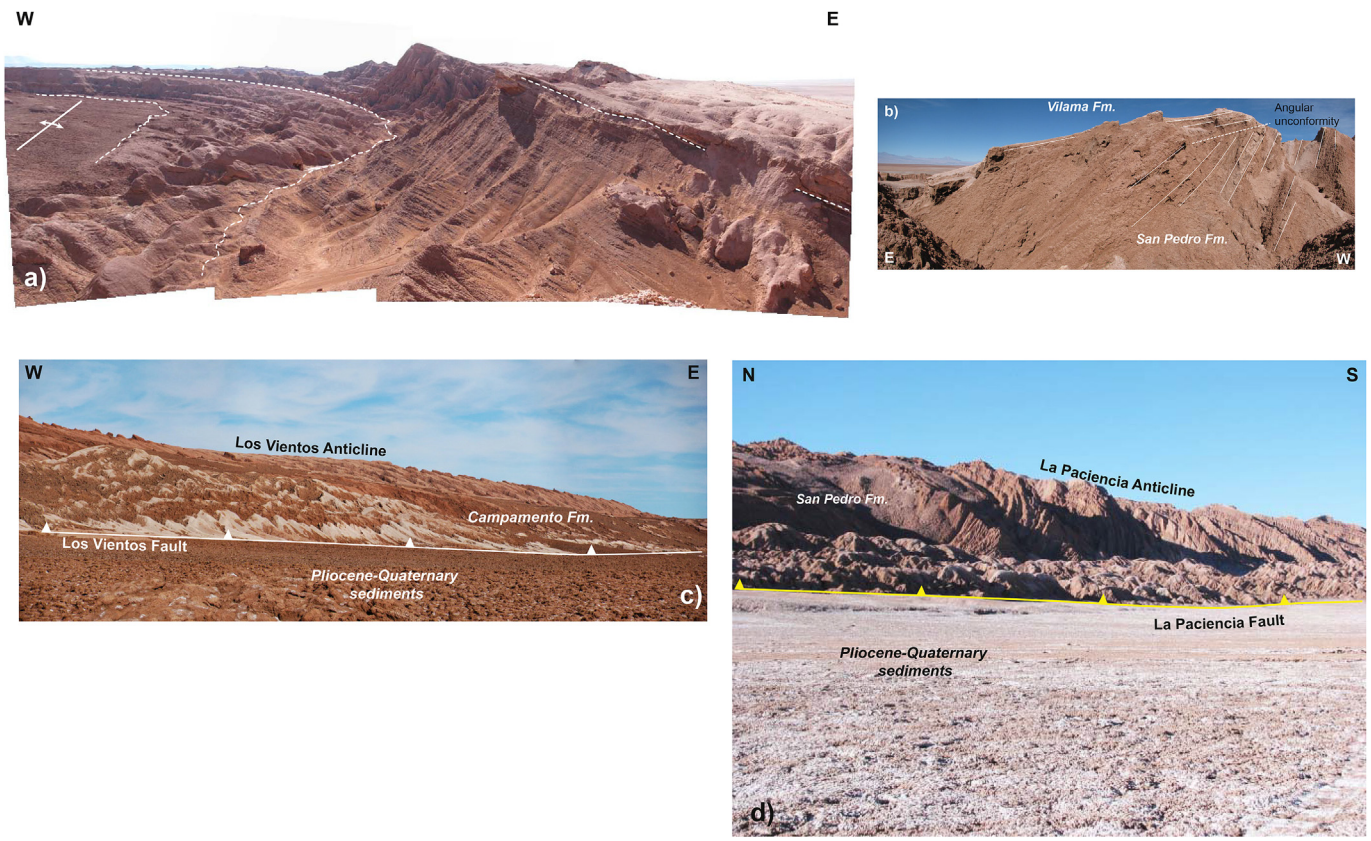

Fig. 3. A) Eastern flank of La Paciencia Anticline. B) Angular unconformity between the folded San Pedro Formation and the Vilama Formation. C) Los Vientos thrust, placing the San Pedro strata over the Pliocene-Quaternary sediments of the Salar de Atacama salt pan. D) La Paciencia thrust, placing the San Pedro strata over the Pliocene-Quaternary sediments of the Llano de la Paciencia.

Please cite this article in press as: Rubilar, J., et al., Structure of the Cordillera de la Sal: A key tectonic element for the Oligocene-Neogene evolution of the Salar de Atacama basin, Central Andes, northern Chile, Journal of South American Earth Sciences (2017), https://doi.org/10.1016/j.jsames.2017.11.013

et al., 2014). These Neogene units include several series of stratified sedimentary evaporitic and terrigenous-siliciclastic rocks (Fig. 3).

3. Data base and methods

To analyze the internal structure of the Cordillera de la Sal, we have integrated geological data from previous studies based on geological mapping (Becerra et al., 2014; Henríquez et al., 2014; scale: 1:100.000) with new interpretations of seismic profiles. Seismic information used in this study corresponds to a 2D seismic survey acquired during the 70s by ENAP-Sipetrol Company. This information has a good to moderate quality, and shows reliable information within the first three seconds TWT, which guarantees a good interpretation. Prior to the interpretation, the seismic information was filtered and migrated. The top and bottom of the seismic sequences associated with stratigraphic formations were taken from previous seismic analyses (Muñoz et al., 2002; Pananont et al., 2004; Arriagada et al., 2006; Jordan et al., 2007), which used the geological information of the Toconao-1 well to interpret the main surfaces observed in the 2D seismic profiles. On the other hand, we also correlated some seismic reflectors with geological units that crop out along the study area; this allowed us to join the surface information with the subsurface information in the Salar de Atacama basin and then to construct a series of balanced cross sections of the Cordillera de la Sal. Some of the most important criteria used for the structural and seismic interpretations were: truncation of seismic reflectors to identify angular unconformities, breaking of continuous reflectors to identify faults, change in dip of reflectors to identify folds and faults, changes in seismic facies to identify salt bodies, among others.

We constructed a structural model of the Cordillera de la Sal with the 2D-modelling software Move (© Midland Valley Exploration Ltd) incorporating structural information along 5 seismic sections; these sections were carried from the Salar de Atacama to the west across the Cordillera de la Sal; stratigraphic interpretations were assured with NS seismic data performed across

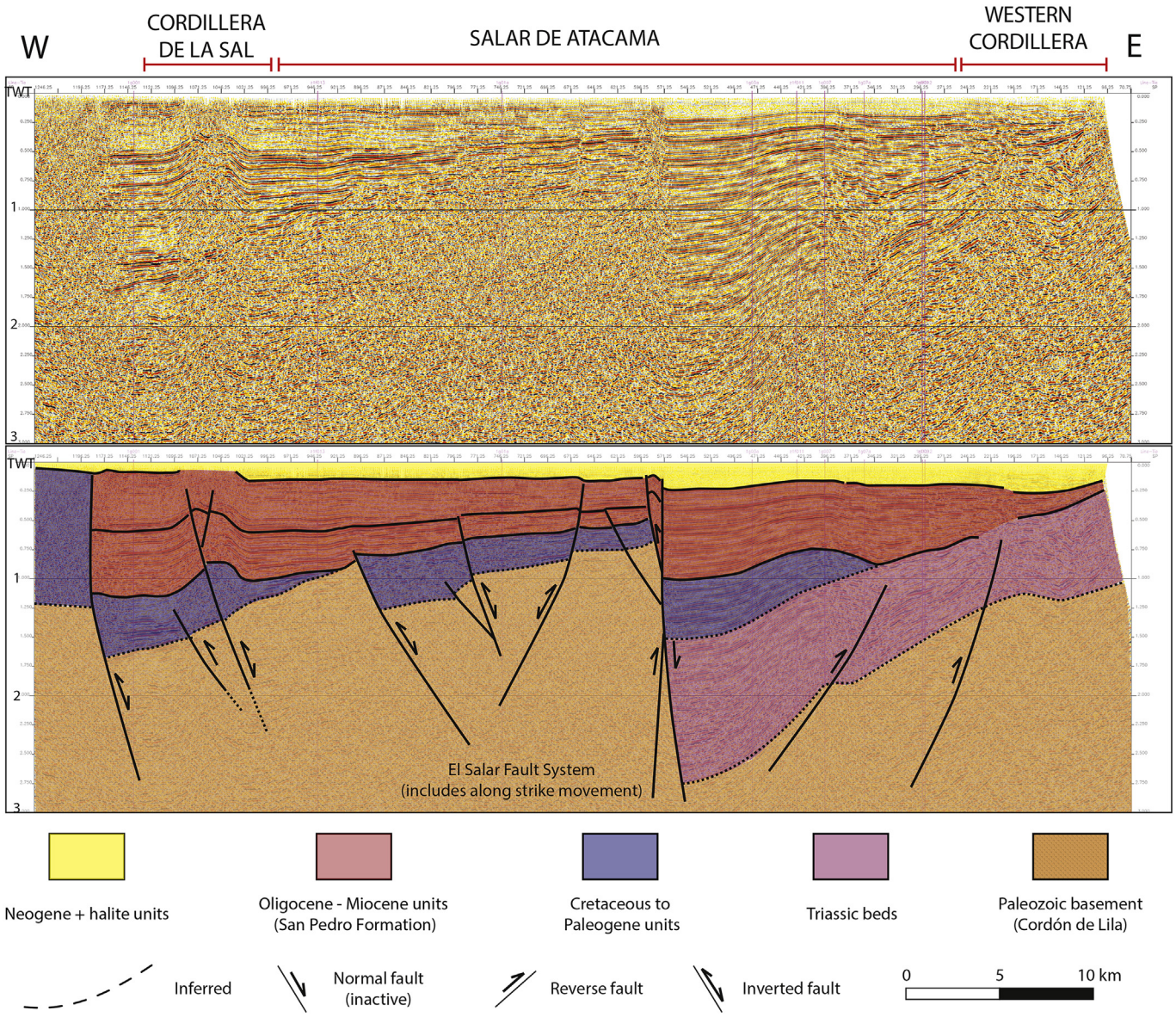

Fig. 4. Seismic section from southern Salar de Atacama Basin (see Fig. 2 for location). Syn-extensional Oligocene units thicken towards the west and show subsequent folding above a main detachment in the Cordillera de la Sal area. On the other hand, these sequences onlap against the Triassic units to the east.

Please cite this article in press as: Rubilar, J., et al., Structure of the Cordillera de la Sal: A key tectonic element for the Oligocene-Neogene evolution of the Salar de Atacama basin, Central Andes, northern Chile, Journal of South American Earth Sciences (2017), https://doi.org/10.1016/j.jsames.2017.11.013

the Llano de la Paciencia (1g001 tie line). Through this methodology we created 5 cross sections, which were constructed through the Southern Domain of the Cordillera de la Sal (see Fig. 2 for location).

4. Results

4.1. Surface structure of the Cordillera de la Sal

The Cordillera de la Sal can be divided into two structural domains, based on the distribution of different structural styles (Fig. 2). The south domain is characterized by an extensive array of NNE-oriented asymmetrical anticlines and synclines, exposed in an *en echelon* arrangement. From west to east, these folds correspond to the La Paciencia Anticline, which consists of an overturned fold that affects the Oligocene sedimentary deposits of the San Pedro Formation (Figs. 2, 3a and 3d). To the southwestern section of the Cordillera de la Sal, this fold is limited by a NNE oriented and west-vergent thrust (La Paciencia Fault), which places the upper section of the San Pedro Formation over Pliocene and Quaternary sediments (Figs. 2 and 3d). To the east of the La Paciencia Anticline is located the Los Vientos Anticline, which consists of a slightly asymmetric fold composed of the San Pedro and Campamento formations and limited by NE-SW striking and east-vergent thrusts (Los Vientos Fault), that place the Campamento Formation over recent saline deposits (Figs. 2 and 3c).

The north domain is formed by a series of NNE-oriented folds that include: a west-overturned anticline, a symmetrical syncline exposing lower evaporitic members of the San Pedro Formation unconformably overlain by the Vilama Formation (Fig. 3b); and a salt dome 10 km long and 4 km wide, elongated in a NE direction (Fig. 2). This contrast in structural styles through the northern sector of the Cordillera de la Sal was previously explained by models that involved transpressive deformation (Wilkes and Görler, 1988, 1994; Macellari et al., 1991), and also as a response to variations in the thickness of the evaporitic members of the San Pedro Formation along strike (Muñoz et al., 2000). The deformation observed in the Cordillera de la Sal has been frequently related to

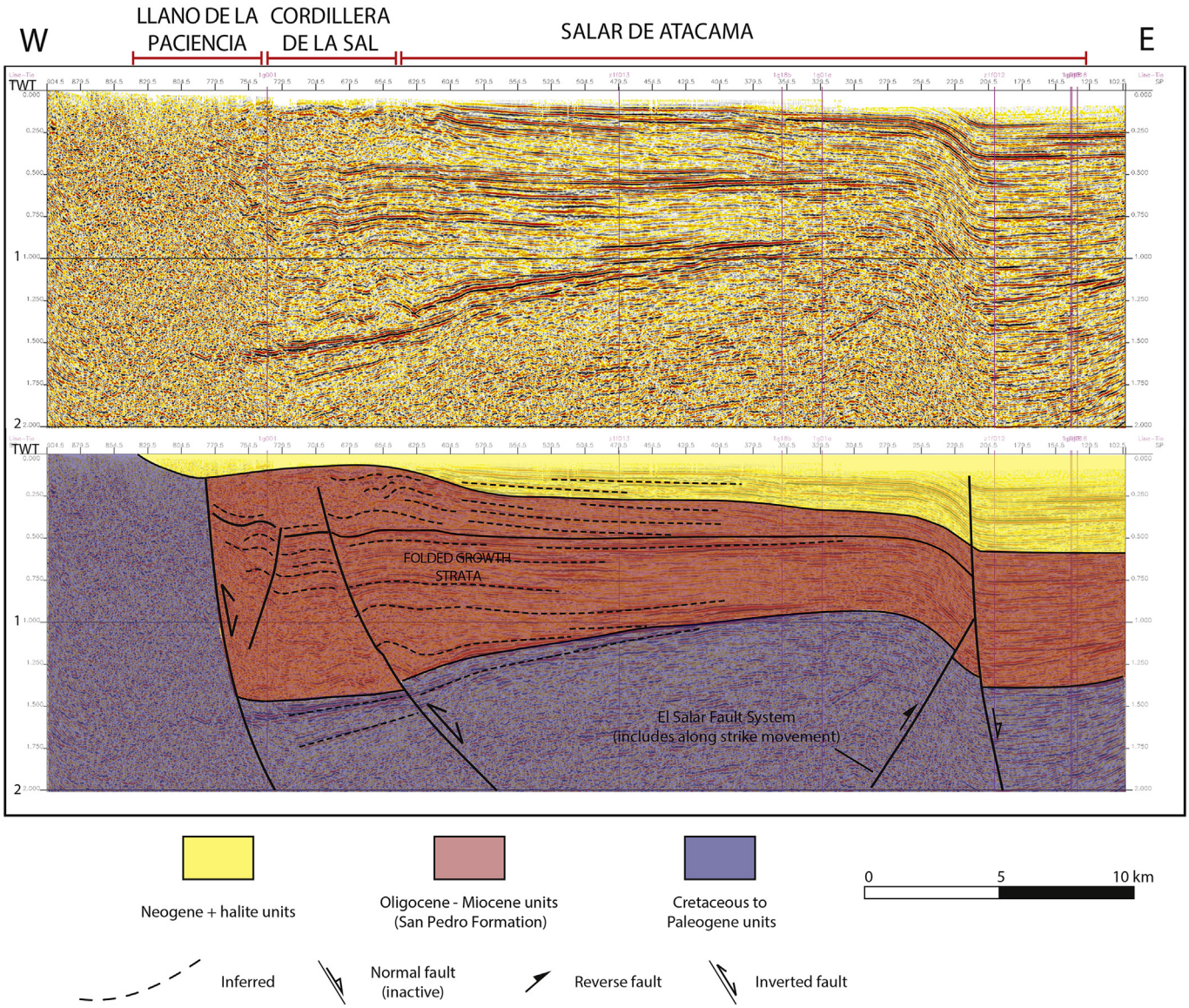

Fig. 5. Seismic section from southern Salar de Atacama basin (see Fig. 2 for location). Syn-extensional Oligocene units thicken towards the west.

Please cite this article in press as: Rubilar, J., et al., Structure of the Cordillera de la Sal: A key tectonic element for the Oligocene-Neogene evolution of the Salar de Atacama basin, Central Andes, northern Chile, Journal of South American Earth Sciences (2017), https://doi.org/10.1016/j.jsames.2017.11.013

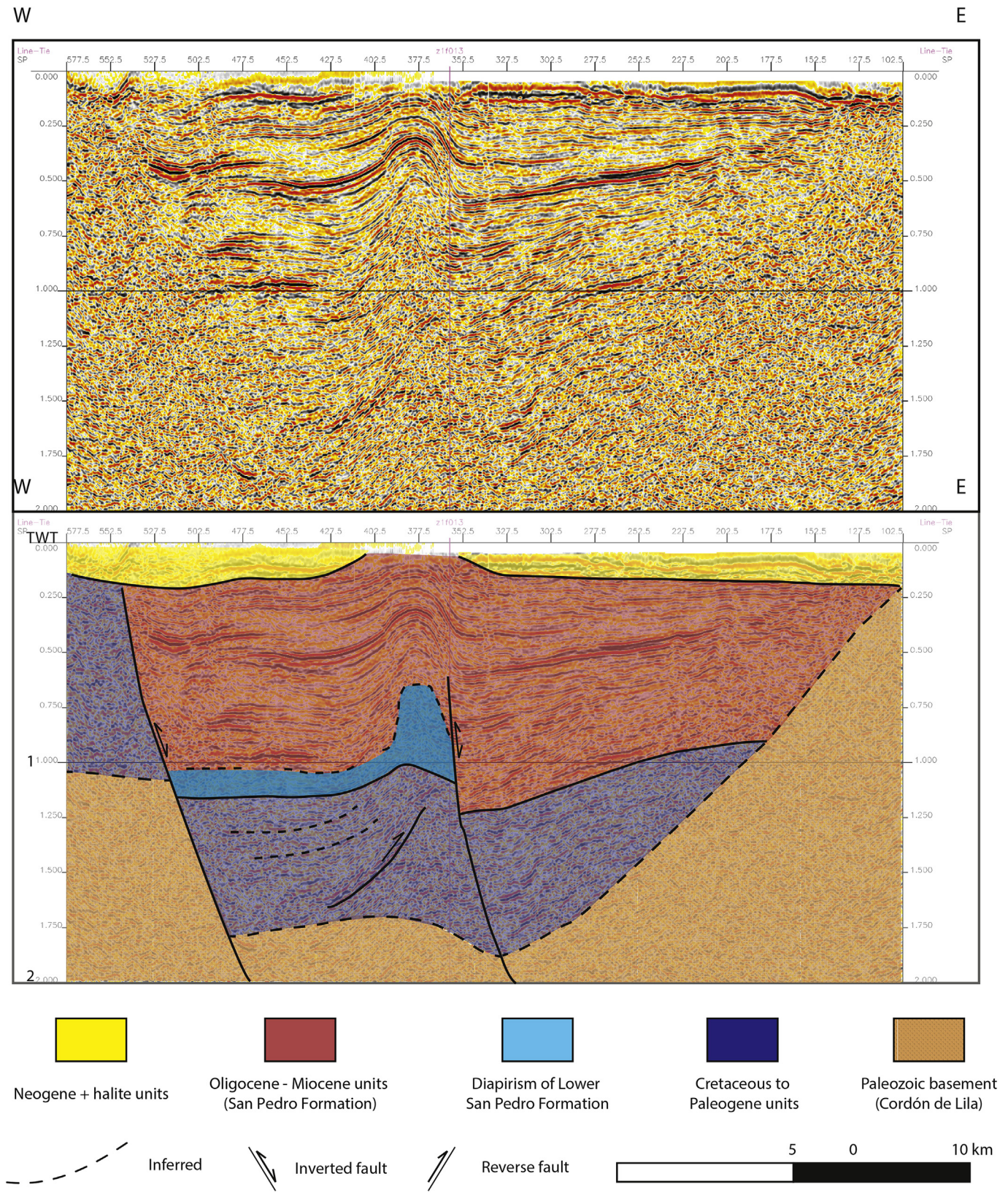

Fig. 6. Seismic section from southern Salar de Atacama basin (see Fig. 2 for location) showing folding and evidences of diapirism. Syn-extensional Oligocene units thicken towards the west.

Please cite this article in press as: Rubilar, J., et al., Structure of the Cordillera de la Sal: A key tectonic element for the Oligocene-Neogene evolution of the Salar de Atacama basin, Central Andes, northern Chile, Journal of South American Earth Sciences (2017), https://doi.org/10.1016/j.jsames.2017.11.013

the eastern propagation of the contractional thick-skinned structures of the Cordillera de Domeyko (Jolley et al., 1990; Muñoz et al., 2002).

4.2. The subsurface structure of the Cordillera de la Sal

The seismic profiles performed across the Cordillera de la Sal are located along its southern part and show a pair of depocenters associated with three intrabasinal extensional basins (Figs. 4 and 5). Both depocenters are tectonically controlled by two high angle (~60°) master faults preferentially inclined to the east. One master fault is located immediately to the west of the Cordillera de la Sal, while the other is located under the central part of the Salar de Atacama Basin (Figs. 4 and 5). These faults affect the basement and the complete stratigraphic record of the study area. Over the hanging wall of these faults, the Oligocene San Pedro Formation presents wedge geometries and thickens towards the fault planes (Figs. 4–6); towards the east these units where deposited in an onlap relation over the basement (Fig. 4). Based on fault position relative to the geometry of these wedges, we interpret that these were accumulated during an Oligocene extensional episode. This interpretation coincides with those made by some authors, who have also interpreted that an extensional deformation episode occurred in the Salar de Atacama basin during the Oligocene, allowing for the accumulation of continental deposits (Flint et al., 1993; Pananont et al., 2004; Jordan et al., 2007).

The review of the seismic profiles also shows the stratified sequences that occupy the hanging wall faults are folded, indicating that at least a shortening episode was superimposed on a previous crustal extension. The folds correspond to asymmetrical and west-verging anticlines, which mainly involve Cenozoic units (Figs. 4–6). The anticlines have "arrowhead" geometries similar to those described for inversion anticlines, as seen in seismic studies and analogue models (Buchanan and McClay, 1991; Pace et al., 2012; Navarrete et al., 2015; Martínez and Cristallini, 2017). These folds are occasionally truncated against the master faults, which tend to increase their dip angles (at least in the upper segments) by effect of positive reactivation. This evidence, and the high angle of the faults, supports the positive tectonic inversion of the master faults (Figs. 4 and 5). According to this, it appears that much of this

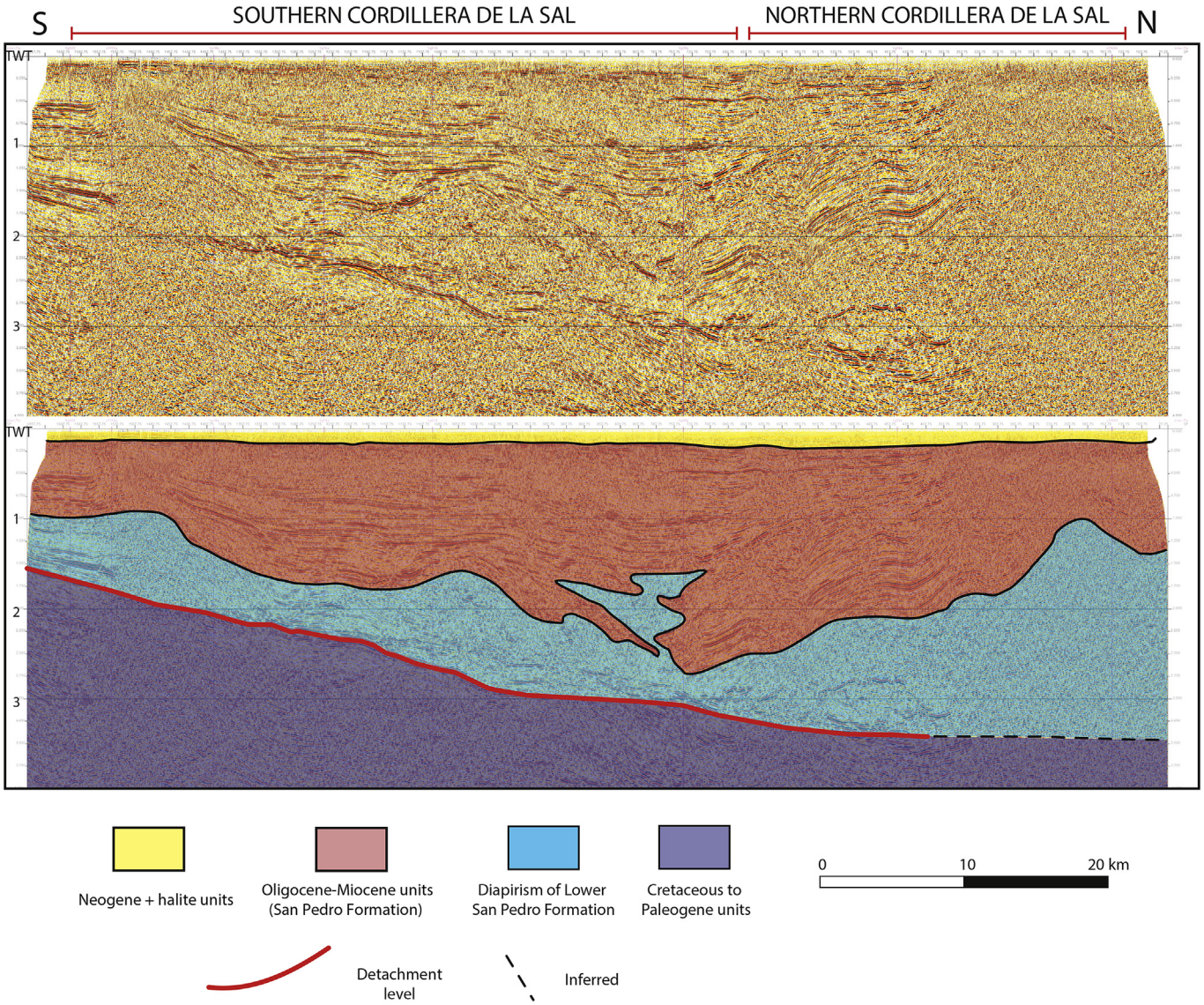

Fig. 7. Seismic section from the Llano de la Paciencia, showing the position of the basal detachment under the Cordillera de la Sal, the northward thickening of the San Pedro Formation and evidences of salt diapirism.

Please cite this article in press as: Rubilar, J., et al., Structure of the Cordillera de la Sal: A key tectonic element for the Oligocene-Neogene evolution of the Salar de Atacama basin, Central Andes, northern Chile, Journal of South American Earth Sciences (2017), https://doi.org/10.1016/j.jsames.2017.11.013

tectonic inversion was mainly accommodated by the Cordillera de la Sal. Here, the salt-cored folding absorbed much of the reverse slip. However, previous studies have also recognized and documented a compressional episode after the accumulation of the Oligocene deposits (Wilkes and Görler, 1994; Mpodozis et al., 2000; Pananont et al., 2004; Reutter et al., 2006; Jordan et al., 2007). Diapirism in the northern Cordillera de la Sal occurred between 17 and 10 Ma, according to seismic and outcrop data (Pananont et al., 2004).

5. Discussion

5.1. Controls on the structural styles of the Cordillera de la Sal

The variations on the structural style of the Cordillera de la Sal are mainly governed by two factors: a) mechanical stratigraphy and b) shortening. The first one affects the transition from the southern to the northern domain of the Cordillera de la Sal due to thickness changes within the San Pedro Formation along the basin, which range from 1000 m beneath the center of the basin to 2000–3000 m in the northern Cordillera de la Sal (Wilkes and Görler, 1994; Jordan et al., 2007). Northward thickening of the ductile layers of the lower San Pedro Formation coincides with the transition from a domain governed by salt-cored folding deformation (southern domain) to a domain characterized by salt diapirism (northern domain). The distribution of ductile beds also coincides with the depth of a detachment level under the Cordillera de la Sal, this feature can be seen on both the structural cross sections from the Cordillera de la Sal (Fig. 8) and on the 1g001 tie line that goes through the Llano de la Paciencia, transversely to the seismic sections presented in this work (Fig. 7). In southern Cordillera de la Sal this detachment is located at a depth of 3000 m (1–2 s TWT), towards the north of the southern domain it reaches depths of almost 6000 m (>3 s TWT). Finally in the northern Cordillera de la Sal there is no detachment level beneath the range, which is coincident with the change in the deformation mechanism. This information allows us to propose that the structural style of the Cordillera de la Sal is controlled by the lithology of the previous basin fill (Muñoz et al., 2000, 2002), as also occurs in other thrust fronts along the world, such as the Pyrenean and the Carpathian belts (Krzywiec and Verges, 2007). Otherwise, differential shortening magnitudes across the range could have influenced in the variations of the geometry of the folds in the Cordillera de la Sal (Fig. 8).

5.2. The Oligocene configuration of the Salar de Atacama basin

Based on the seismic and structural interpretations shown in this work, we propose that an important extensional deformation dominated this part of the Central Andes of northern Chile during

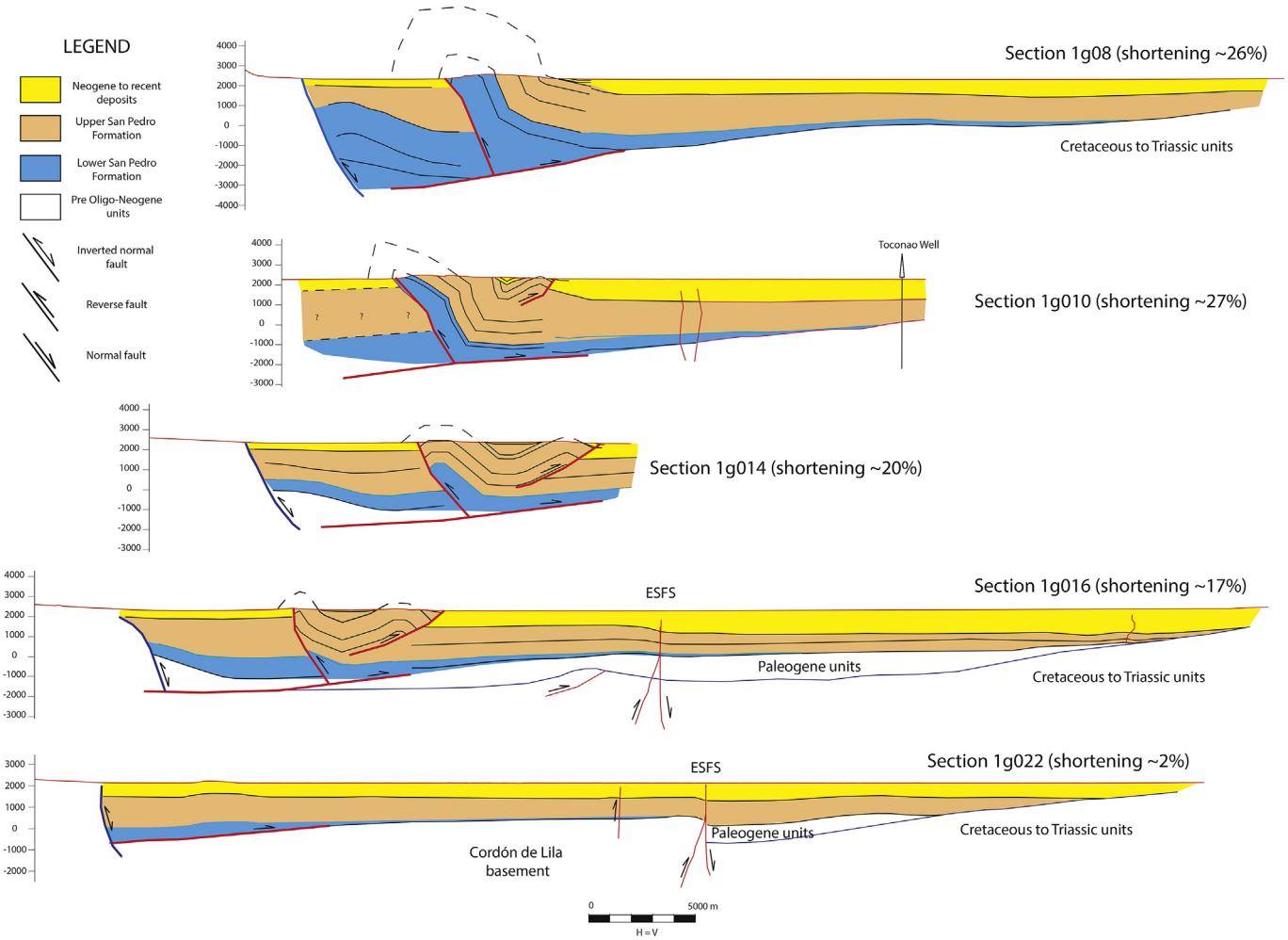

Fig. 8. Structural sections from the Cordillera de la Sal (see Fig. 2 for location).

Please cite this article in press as: Rubilar, J., et al., Structure of the Cordillera de la Sal: A key tectonic element for the Oligocene-Neogene evolution of the Salar de Atacama basin, Central Andes, northern Chile, Journal of South American Earth Sciences (2017), https://doi.org/10.1016/j.jsames.2017.11.013

the Oligocene. The stratigraphic wedges identified in the seismic profiles of the Oligocene successions of the San Pedro Formation can be compared with the classical wedge geometries shown by syn-extensional deposits controlled by normal faults. The examples shown in this work closely match this situation. Such as it has been proposed in previous studies (Pananont et al., 2004; Jordan et al., 2007), we agree that a first-order normal fault array controlled the accumulation of the deposits of the Oligocene San Pedro Formation. These faults formed part of asymmetric half-grabens and intrabasinal depocenters, which were mostly confined to the west of the Salar de Atacama basin. Mechanical subsidence along the master faults created deep spaces in the hanging wall faults, vertical offsets associated to this subsidence range from 2 ± 0.5 km in southwestern Salar de Atacama basin (calculated from 1g022 and z1f12a sections in this work) to 6 ± 1 km in northern Llano de la Paciencia (Pananont et al., 2004); this contrast coincides not only with the variations in the thickness of the Oligocene series accumulated during the subsidence but also with the contrast on the present relief across the western border of the basin. Although many of these faults were later inverted, we suppose that these had initial angles of around 45°. The last interpretation is supported by the wedge shape of the syn-extensional deposits of the Oligocene successions.

Some studies (Wilkes and Görler, 1994; Muñoz et al., 2002; Arriagada et al., 2006), maintain the idea that the complete structure of this part of the Central Andes was developed completely by shortening and crustal thickening. On the other hand, they also indicate that the stratigraphic wedges observed in the Oligocene deposits are a synorogenic component which resulted from Andean deformation. The data shown here indicate that shortening in this region was interrupted after the so-called “Incaic” orogeny (Ramírez and Gardeweg, 1982; Maksaev and Zentilli, 1999), which was followed by an important period of extensional collapse and subsidence. Shortening was resumed during the Neogene whith the rise of the Cordillera de la Sal wich involved salt-cored folding, compression and strike slip in its south domain, and mostly diapirism in its north domain. Our results suggest that inversion tectonics in the Salar de Atacama basin was a first order episode in the evolution of the Central Andes of northern Chile.

6. Conclusions

Tectonic inversion in the Salar de Atacama during the Neogene is described for the first time in this work. Extension was controlled by large normal faults in its western border, while in the eastern border the Tertiary units were deposited in an onlap relation over the basement. The northwards increase in thickness of the Oligocene synextensional evaporites of the lower San Pedro Formation have played a key role in the development and the styles in the deformation of the Neogene Cordillera de la Sal. The southern Cordillera de la Sal changes its deformation mechanism from south to north in response to a deepening of the main detachment; this level is associated with the evaporites of the basin fill. The deformation of this salt-floored basin could be linked to the development of the Preandean Depression, a still controversial morphostructural unit in the Central Andes.

Acknowledgements

The authors gratefully acknowledge the seismic data granted by ENAP Sipetrol, the support of Midland Valley who kindly provided us the Move software license to perform the 2D sections of this study, and SERNAGEOMIN for the field data from the mapping campaign 1:100.000 under the Plan Nacional de Geología project.

References

Amilibia, A., Sàbat, F., McClay, K.R., Muñoz, J.A., Roca, E., Chong, G., 2008. The role of inherited tectono-sedimentary architecture in the development of the central Andean mountain belt: insights from the Cordillera de Domeyko. J. Struct. Geol. 30 (12), 1520–1539.

Arriagada, C., Cobbold, P.R., Roperch, P., 2006. Salar de Atacama basin: a record of compressional tectonics in the central Andes since the mid-Cretaceous. Tectonics 25. https://doi.org/10.1029/2004TC001770.

Baby, P., Rochat, P., Mascle, G., Hérail, G., 1997. Neogene shortening contribution to crustal thickening in the back arc of the central Andes. Geology 25, 883–886.

Bascuñan, S., Arriagada, C., Le Roux, J., Deckart, K., 2015. Unraveling the Peruvian Phase of the Central Andes: stratigraphy, sedimentology and geochronology of the Salar de Atacama Basin (22°30–23°S), northern Chile. Basin Res. 28 (3), 365–392.

Becerra, J., Henríquez, S.M., Arriagada, C., 2014. Geología del área Salar de Atacama, región de Antofagasta. Servicio Nacional de Geología y Minería. Carta Geológica de Chile, Serie Geología Básica 166: 111 p., 1 mapa escala 1:100.000. Santiago, Chile.

Brüggen, J., 1934. Las formaciones de sal y petróleo de la Puna de Atacama. Bol. Min. Petrol., Santiago 32, 105–122.

Buchanan, P.G., McClay, K.R., 1991. Sandbox experiments of inverted listric and planar fault systems. Tectonophysics 188 (1–2), 97–115.

Cahill, T., Isacks, B.L., 1992. Seismicity and shape of the subducted Nazca plate. J. Geophys. Res. Solid Earth 97 (B12), 17503–17529.

Carrapa, B., Trimble, J.D., Stockli, D.F., 2011. Patterns and timing of exhumation and deformation in the Eastern Cordillera of NW Argentina revealed by (U-Th)/He thermochronology. Tectonics 30, TC3003. https://doi.org/10.1029/2010TC002707.

Eichelberger, N., McQuarrie, N., 2015. Kinematic reconstruction of the Bolivian orocline. Geosphere 11 (2), 445–462.

Elger, K., Oncken, O., Glodny, J., 2005. Plateau-style accumulation of deformation: southern Altiplano. Tectonics 24, TC4020. https://doi.org/10.1029/2004TC001675.

Farias, M., Charrier, R., Comte, D., Martinod, J., Herail, G., 2005. Late Cenozoic deformation and uplift of the western flank of the Altiplano: evidence from the depositional, tectonic, and geomorphologic evolution and shallow seismic activity (northern Chile at 19°30′ S). Tectonics 24. https://doi.org/10.1029/2004TC001667.

Flint, S., 1985. Alluvial fan and playa sedimentation in an Andean arid, closed basin: the Paciencia Group (mid Tertiary), Antofagasta, Province, Chile. J. Geol. Soc. Lond. 141, 533–546.

Flint, S., Turner, P., Jolley, E., Hartley, A., 1993. Extensional tectonics in convergent margin basins: an example from the Salar de Atacama, Chilean Andes. Geol. Soc. Am. Bull. 105, 603–617.

García, M., Hérail, G., 2005. Fault-related folding, drainage network evolution and valley incision during the Neogene in the Andean Precordillera of Northern Chile. Geomorphology 65, 279–300.

Henríquez, S.M., Becerra, J., Arriagada, C., 2014. Geología del Área San Pedro de Atacama, Región de Antofagasta. Servicio Nacional de Geología y Minería. Carta Geológica de Chile, Serie Geología Básica, 171: 111 p., 1 mapa escala 1:100.000. Santiago, Chile.

Hudec, M.R., Jackson, M., 2007. Terra infirma: understanding salt tectonics. Earth Sci. Rev. 82 (1), 1–28.

Isacks, B., Barazangi, M., 1977. Island Arcs, Deep Sea Trenches, and Back Arc. Basin. Geometry of Benioff Zones: Lateral Segments and Downgoing Bending of the Subducted Lithosphere, vol. 99, p. 114.

Jolley, E.J., Turner, P., Willians, G.D., Hartley, A.J., Flint, S., 1990. Sedimentological response of an alluvial system to Neogene thrust tectonics, Atacama Desert, northern Chile. J. Geol. Soc. Lond. 147, 769–784.

Jordan, T.E., Isacks, B., Ramos, V.A., Allmendinger, R.W., 1983. Mountain building in the Central Andes. Episodes 3, 20–26.

Jordan, T.E., Mpodozis, C., Muñoz, N., Blanco, N., Pananont, P., Gardeweg, M., 2007. Cenozoic subsurface stratigraphy and structure of the Salar de Atacama Basin, northern Chile. J. S. Am. Earth Sci. 23, 122–146.

Krzywiec, P., Verges, J., 2007. Role of the foredeep evaporites in wedge tectonics and formation of triangle zones: comparison of the Carpathian and Pyrenean thrust fronts. In: Lacombe, O., Lavé, J., Roure, F., Vergés, J. (Eds.), Thrust Belts and Foreland Basins from Fold Kinematics to Hydrocarbon Systems. Frontiers in Earth Sciences Series. Springer, Berlin, pp. 383–394.

Lamb, S., Hoke, L., 1997. Origin of the high plateau in the Central Andes, Bolivia, South America. Tectonics 16 (4), 623–649.

Macellari, C.E., Su, M., Townsend, F., 1991. Structure and seismic stratigraphy of the Atacama Basin, Northern Chile. In: Proc. VI Congr. Geol. Chileno, pp. 133–137.

Maksaev, V., Zentilli, M., 1999. Fission track thermochronology of the Domeyko Cordillera, northern Chile: implications for Andean tectonics and porphyry copper metallogenesis. Explor. Min. Geol. 8, 65–89.

Marinovic, N., Lahsen, A., 1984. Hoja Calama: región de Antofagasta: carta geológica de Chile 1: 250.000 (Servicio Nacional de Geología y Minería).

Martínez, F., Cristallini, E., 2017. The doubly vergent inverted structures in the Mesozoic basins of northern Chile (28°S): a comparative analysis from field data and analogue modeling. J. S. Am. Earth Sci. https://doi.org/10.1016/j.jsames.2017.02.002.

Mpodozis, C., Blanco, N., Jordan, T., Gardeweg, M.C., 2000. Estratigráfia y

Please cite this article in press as: Rubilar, J., et al., Structure of the Cordillera de la Sal: A key tectonic element for the Oligocene-Neogene evolution of the Salar de Atacama basin, Central Andes, northern Chile, Journal of South American Earth Sciences (2017), https://doi.org/10.1016/j.jsames.2017.11.013

deformación del Cenozoico tardio en la región norte de la Cuenca del Salar de Atacama: La zona de Vilama-Pampa Vizcachitas. In: Actas IX Congresso Geológico Chileno, Puerto Varas, vol. 2, pp. 598–603.

Mpodozis, C., Arriagada, C., Basso, M., Roperch, P., Cobbold, P., Reich, M., 2005. Late Mesozoic to Paleogene stratigraphy of the Salar de Atacama Basin, Antofagasta, northern Chile: implications for the tectonic evolution of the Central Andes. Tectonophysics 399, 125–154.

Muñoz, N., Charrier, R., Radic, J.P., 2000. Formación de la Cordillera de la Sal por propagación de fallas y plegamiento por despegue, II Región, Chile. In: Congreso Geológico Chileno, No 9, Actas, vol. 2, pp. 604–608.

Muñoz, N., Charrier, G.R., Jordan, T.E., 2002. Interactions between basement and cover during the evolution of the Salar de Atacama Basin, northern Chile. Rev. Geol. Chile 29, 55–80.

Navarrete, C.R., Gianni, G.M., Folguera, A., 2015. Tectonic inversion events in the western San Jorge Gulf Basin from seismic, borehole and field data. J. S. Am. Earth Sci. 64, 486–497.

Pace, P., Satolli, S., Calamita, F., 2012. The control of mechanical stratigraphy and inversion tectonics on thrust-related folding along the curved Northern Apennines thrust front. Rendiconti della Soc. Geol. Ital. 22, 162–165.

Pananont, P., Mpodozis, C., Blanco, N., Jordan, T.E., Brown, L.D., 2004. Cenozoic Evolution of the Northwestern Salar de Atacama Basin, Northern Chile. Tectonics 23, TC6007. https://doi.org/10.1029/2003TC001595.

Ramírez, C.F., Gardeweg, M., 1982. Hoja Toconao, Región de Antofagasta, Servicio Nacional de Geología y Minería. Carta Geológica de Chile, 54, 1:250,000, 1-122 pp, Santiago, Chile.

Reutter, K.J., Charrier, R., Götze, H.J., Schurr, B., Wigger, P., Scheuber, E., Giese, P., Reuther, C.D., Schmidt, S., Rietbrock, A., Chong, G., Belmonte-Pool, A., 2006. The Salar de Atacama Basin: a subsiding block within the western edge of the Altiplano-Puna Plateau. In: Oncken, O., et al. (Eds.), The Andes Active Subduction Orogeny. Springer Berlin Heidelberg, Berlin, pp. 303–325.

Travisany, A.V., 1979. Consideraciones geneticas sobre el yacimiento estratiforme San Bartolo. In: II Congreso Geológico Chileno, vol. 2, pp. C149–C159.

Wilkes, E., Görler, K., 1988. Sedimentary and structural evolution of the Cordillera de la Sal, II Región, Chile. In: V Congreso Geológico Chileno, Santiago 1, pp. A173–A188.

Wilkes, E., Görler, K., 1994. Sedimentary and Structural Evolution of the Salar de Atacama, Northern Chile. In: Wigger, P., Reutter, K.J. (Eds.), Tectonics of the Southern Central Andes, pp. 171–188.

Please cite this article in press as: Rubilar, J., et al., Structure of the Cordillera de la Sal: A key tectonic element for the Oligocene-Neogene evolution of the Salar de Atacama basin, Central Andes, northern Chile, Journal of South American Earth Sciences (2017), https://doi.org/10.1016/j.jsames.2017.11.013

Basin Research

IAS EAGE

Basin Research (2016) **28**, 365–392, doi: 10.1111/bre.12114

Unraveling the Peruvian Phase of the Central Andes: stratigraphy, sedimentology and geochronology of the Salar de Atacama Basin (22°30–23°S), northern Chile

Sebastián Bascuñán,* César Arriagada,* Jacobus Le Roux*,† and Katja Deckart*

**Departamento de Geología, Universidad de Chile, Santiago, Chile*

†*Centro de Excelencia en Geotermia de los Andes (CEGA), Universidad de Chile, Santiago, Chile*

ABSTRACT

The Salar de Atacama Basin holds important information regarding the tectonic activity, sedimentary environments and their variations in northern Chile during Cretaceous times. About 4000 m of high-resolution stratigraphic columns of the Tonel, Purilactis and Barros Arana Formations reveal braided fluvial and alluvial facies, typical of arid to semi-arid environments, interrupted by scarce intervals with evaporitic, aeolian and lacustrine sedimentation, displaying an overall coarsening-upward trend. Clast-count and point-count data evidence the progressive erosion from Mesozoic volcanic rocks to Palaeozoic basement granitoids and deposits located around the Cordillera de Domeyko area, which is indicative of an unroofing process. The palaeocurrent data show that the source area was located to the west. The U/Pb detrital zircon geochronological data give maximum depositional ages of 149 Ma for the base of the Tonel Formation (Agua Salada Member), and 107 Ma for its middle member (La Escalera Member); 79 Ma for the lower Purilactis Formation (Limón Verde Member), and 73 Ma for the Barros Arana Formation. The sources of these zircons were located mainly to the west, and comprised from the Coastal Cordillera to the Precordillera. The ages and pulses record the tectonic activity during the Peruvian Phase, which can be split into two large events; an early phase, around 107 Ma, showing uplift of the Coastal Cordillera area, and a late phase around 79 Ma indicating an eastward jump of the deformation front to the Cordillera de Domeyko area. The lack of internal deformation and the thicknesses measured suggest that deposition of the units occurred in the foredeep zone of an eastward-verging basin. This sedimentation would have ended with the K-T phase, recognized in most of northern Chile.

INTRODUCTION

The evolution of the Chilean Andes between 22° and 24°S (Fig. 1) has been the focus of diverse studies over the last years, which have characterized the style and timing of the deformation of its different constituents (Ramírez & Gardeweg, 1982; Marinovic & Lahsen, 1984; Charrier & Reutter, 1994; Maksaev & Zentilli, 1999; Mpodozis *et al.*, 2005; Arriagada *et al.*, 2006a; Amilibia *et al.*, 2008; Arriagada *et al.*, 2008). These authors have shown that uplift and shortening were active during the Eocene–Early Oligocene and Neogene, although tenuous evidence of deformation during the mid- to Late Cretaceous has also been recorded. The latter event ('Peruvian Phase'; Steinman, 1929) has been identified along most of the western margin of South America (Cobbold & Rosello, 2003; Jaillard *et al.*, 2005; Jaimes & De Freitas, 2006; Cobbold *et al.*, 2007; Tunik *et al.*, 2010; Martinez *et al.*, 2012; Martínez *et al.*, 2013), although studies concerning its effects and/or timing in the northern Central Andes are scarce.

The Salar de Atacama Basin, located to the east of the Precordillera (known locally as the Cordillera de Domeyko) (Figs 1 and 2), has an important geological record from mid-Cretaceous to present times (Brüggen, 1934, 1942, 1950; Charrier & Muñoz, 1994; Charrier & Reutter, 1990, 1994; Arriagada, 1999; Mpodozis *et al.*, 2005; Arriagada *et al.*, 2006a). Even though much work has been done with regard to its stratigraphy, sedimentology (Brüggen, 1942; Dingman, 1963, 1967; Hartley *et al.*, 1988, 1992) and structure (Macellari *et al.*, 1991; Muñoz *et al.*, 2002; Arriagada, 1999; Pananont *et al.*, 2004; Mpodozis *et al.*, 2005; Arriagada *et al.*, 2006a; Reutter *et al.*, 2006), the Tonel, Purilactis and Barros Arana Formations (which constitute the Purilactis Group *sensu* Mpodozis *et al.*, 2005) still pose important questions about their origin, tectonic setting(s) and, inextricably, about the uplift of the Cordillera de Domeyko during the Late Cretaceous. The lack of fossils, tuff layers or other

Correspondence: Sebastián Bascuñán, Departamento de Geología, Universidad de Chile, Plaza Ercilla 803, 8370450 Santiago, Chile. E-mail: sebascun@ing.uchile.cl

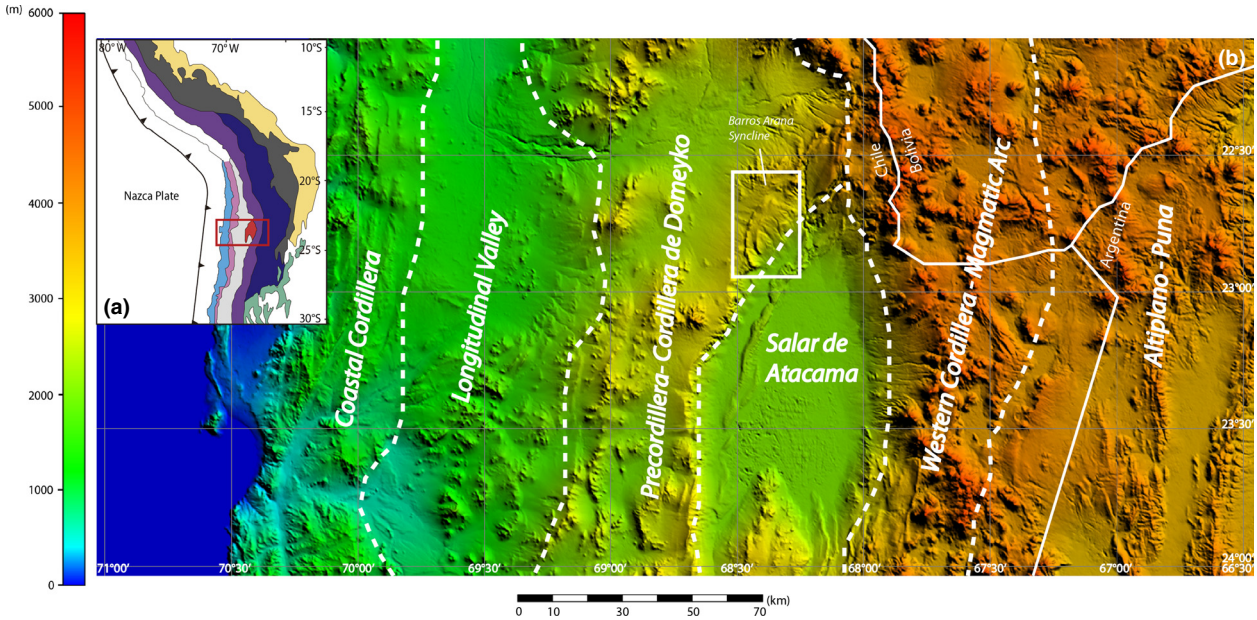

Fig. 1. (a) Map of the western margin of South America showing its main structures. From west to east; light blue: Coastal Cordillera; pink: Longitudinal Valley; grey: Precordillera; red: Salar de Atacama Basin; purple: Western Cordillera; blue: Altiplano–Puna; brown: Eastern Cordillera; yellow: Sub Andean Ranges; green: Santa Barbara and the Sierras Pampeanas. (b) Main tectonic features of the Andes between 22° and 24°S. The study area is inside the white rectangle.

stratigraphic indicators has made dating of these units problematic; the only ages available have been obtained through Ar–Ar analysis of weathered samples (Flint *et al.*, 1989) and in samples south of the Barros Arana Syncline, from Maastrichtian or younger units (Ramírez & Gardeweg, 1982; Hammerschmidt *et al.*, 1992; Charrier & Reutter, 1990, 1994; Arriagada, 1999; Mpodozis *et al.*, 2005); additionally, no dating of samples belonging to the Tonel Formation has been performed. Thus, the time span of these formations remains poorly constrained.

In this contribution, we measured almost 4000 m of high-resolution stratigraphic sections in the Purilactis Group, to establish the relationship between the depositional environments and concomitant tectonic pulses. This, in turn, aids in clarifying the tectonic setting prevalent from Late Cretaceous to Palaeogene times. Additionally, 11 samples were taken for provenance analysis, of which eight were selected for Laser ablation inductively coupled plasma mass spectrometry U–Pb detrital zircon geochronological dating, to better constrain the age and provenance of the Purilactis Group.

GEOLOGICAL SETTING

The Salar de Atacama Basin is one of the most recognizable topographic features in the Chilean Central Andes (Fig. 1) (Isacks, 1988; Allmendinger *et al.*, 1997; Jordan *et al.*, 2002; Götze & Krause, 2002; Yuan *et al.*, 2002; Arriagada *et al.*, 2006a). It is located between 22°30′S and 24°30′S, being a 150-km long (N–S) and 80-km wide (E–W) oriented depression, with its lowest point at 2300 m a.s.l. It lies immediately to the east of the Precordillera and west of the magmatic arc, whose axis shows a 60-km displacement to the east relative to the rest of the arc.

The Precordillera/Cordillera de Domeyko is a well-defined morphostructural unit about 500-km long (N–S), divided into different units formed by a series of basement structures, whose cores are composed of basement rocks bounded by high-angle faults (Amilibia *et al.*, 2008). In the Salar de Atacama area, the Cordillera de Domeyko reaches *ca.* 3000 m a.s.l. and consists of Palaeozoic to Mesozoic ignimbritic and rhyolitic successions associated with basaltic and andesitic rocks, intruded by granitoids with ages spanning between 200 and 300 Ma (Breitkreuz & Van Schmus, 1996; Arriagada *et al.*, 2006a). Evidence of widespread exhumation during the Eocene, possibly related to the Incaic Event, has been previously described (Ramírez & Gardeweg, 1982; Charrier & Reutter, 1994; Maksaev & Zentilli, 1999; Charrier *et al.*, 2009), although syntectonic structures found in Cretaceous successions point to an even earlier event of uplift and erosion (Mpodozis *et al.*, 2005; Arriagada *et al.*, 2006a; Amilibia *et al.*, 2008). The eastern limit of the range coincides with the El Bordo Escarpment (Fig. 2), which exhibits outcrops of Mesozoic and Cenozoic rocks (Charrier & Muñoz, 1994; Arriagada, 1999; Mpodozis *et al.*, 2005; Fig. 2 in Arriagada *et al.*, 2006a). To the NNE, between 22°30′ and 23°S, the Mesozoic formations are folded into the Barros Arana Syncline, which is 80-km long (NE–SW) and 16-km wide (NW–SE) (Hartley *et al.*, 1988, 1992; Arriagada, 1999; Mpodozis *et al.*, 2005; Arriagada *et al.*, 2006a).

East of the El Bordo Escarpment lies the Llano de la Paciencia, a sub-basin 80-km long (N–S) and 8-km wide (E–W), which is filled primarily by Quaternary alluvial

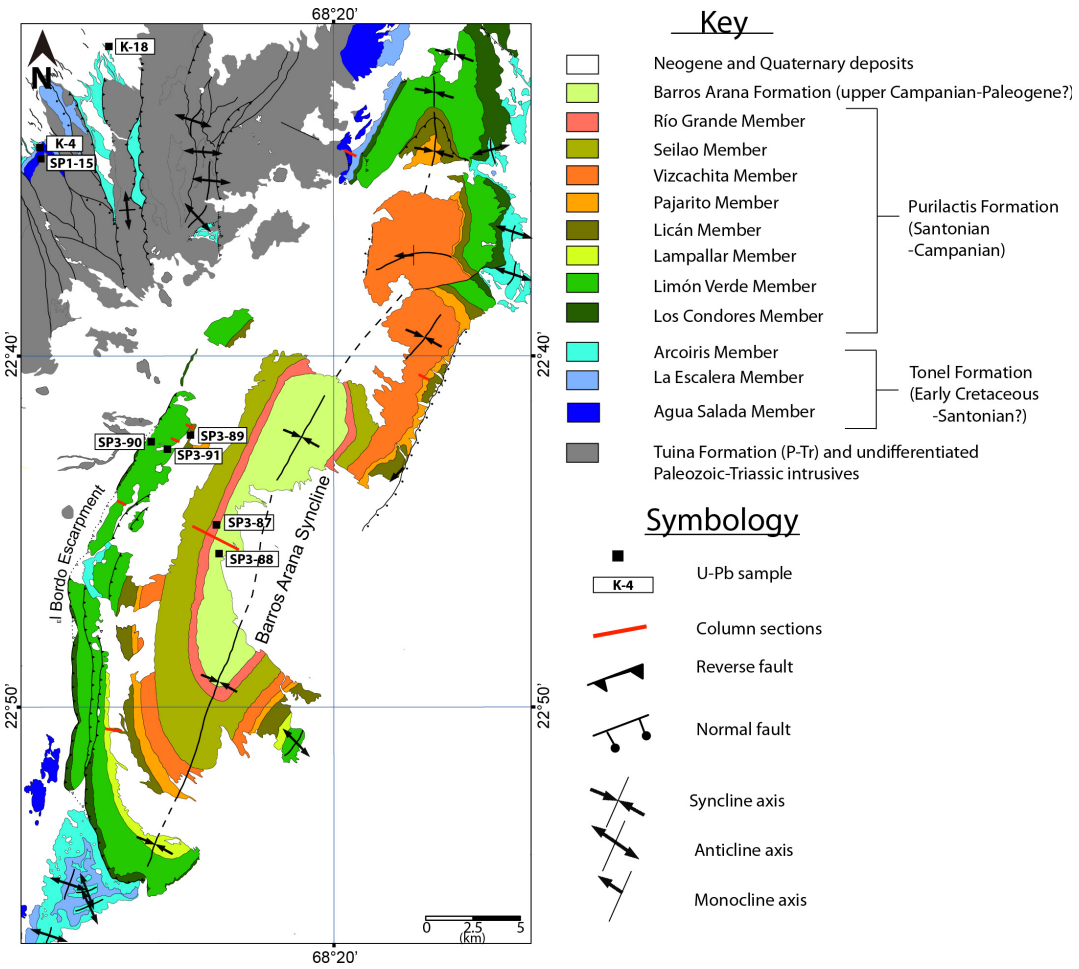

Fig. 2. Geological map of the study area, showing the location of the U/Pb samples and the columns profiled. Modified from Henríquez *et al.* (2014).

fans (Marinovic & Lahsen, 1984; Jolley *et al.*, 1990; Arriagada, 1999; Mpodozis *et al.*, 2005). To the east, the Cordillera de la Sal, a SSW–NNE structure 5–10-km wide, reaches *ca.* 200 m above the basin floor, where Oligocene to Pliocene evaporate-rich sedimentary units are folded (Flint *et al.*, 1993; Jordan *et al.*, 2002; Arriagada *et al.*, 2006a). The present salt pan (salar), formed by a Quaternary alluvial and evaporitic fill, is located east of the Cordillera de la Sal, and overlies Cretaceous to Neogene rocks (Ramírez & Gardeweg, 1982; Marinovic & Lahsen, 1984; Macellari *et al.*, 1991; Muñoz *et al.*, 1997; Jordan *et al.*, 2002; Lowenstein *et al.*, 2003; Arriagada *et al.*, 2006a) .

The basin shows outcrops of ignimbritic successions of Miocene and Pleistocene age towards its eastern border, which corresponds to the current magmatic arc and its deposits (Ramírez & Gardeweg, 1982; Marinovic & Lahsen, 1984). The basin is bounded to the south by the Western Cordillera (Arriagada, 1999; Arriagada *et al.*, 2006a) and the Cordón de Lila Range, composed of igneous and sedimentary rocks of Ordovician–Carboniferous age (Niemeyer, 1989; Coira *et al.*, 2009).

Cretaceous rocks in the Salar de Atacama Basin consist of the Purilactis Group (Figs 3, 4 and 5; Table 1) (*sensu* Mpodozis *et al.*, 2005), which contains the Tonel, Purilactis, Barros Arana and Cerro Totola Formations.

The Tonel Formation is divided into three members (Arriagada, 1999; Mpodozis *et al.*, 2005), starting with *ca.* 60 m of basal breccias and pebble conglomerates with andesitic, rhyolitic and sedimentary clasts (Mpodozis *et al.*, 2005), deposited in the proximal parts of alluvial fans and valley-fills (Hartley *et al.*, 1992). The middle member is composed of 400–1000 m of brown to red, horizontally laminated sandstones, at times alternating with gypsum layers, followed by a top member of unknown thickness containing deformed anhydrite deposits. The last two members display palaeocurrent directions, such as planar cross-bedding in sandstones, indicating a western provenance (Mpodozis *et al.*, 2005), and the depositional setting is interpreted as a playa-lake or continental sabkha environment (Hartley *et al.*, 1992). The contact between the Tonel and Purilactis Formations is frequently faulted (detached) (Fig. 6) (Hartley *et al.*, 1988; Arriagada, 1999; Mpodozis *et al.*, 2005; Arriagada *et al.*, 2006a).

The Purilactis Formation has five members reaching a total thickness of about 3000 m according to Hartley *et al.* (1992) and subsequent researchers (e.g. Arriagada, 1999;

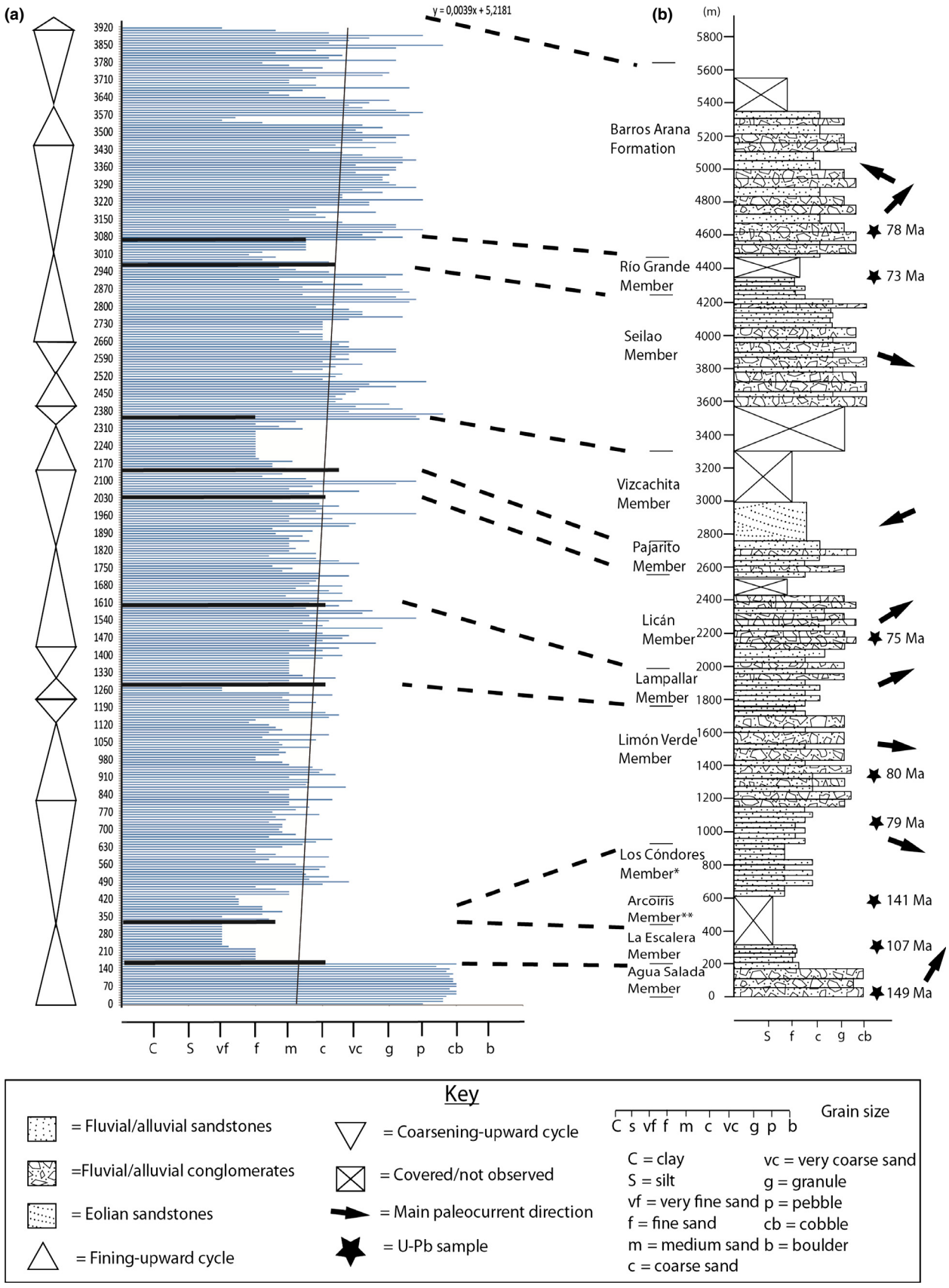

Fig. 3. (a) Measured and (b) compiled stratigraphic column of the Tonel, Purilactis and Barros Arana Formation. Stippled lines indicate parts of the measured column used for the compilation. Tendency line equation shown at the top right corner of (a), showing an overall increase in grain size. Covered areas were estimated with Google Earth. Los Cóndores Member compiled from previous studies (see text). The Arcoiris Member was not measured.

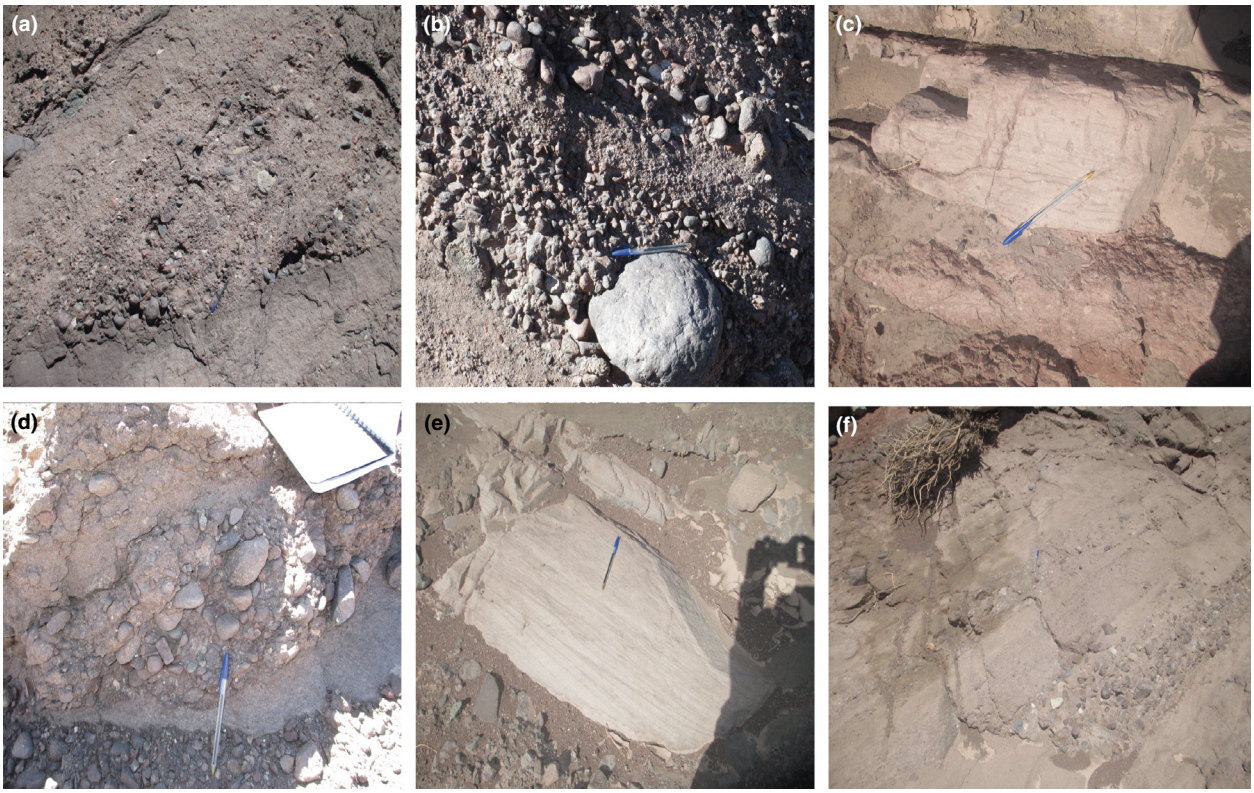

Fig. 4. Facies and outcrops observed in the area: (a) Planar cross-stratified conglomerates (Gpt). (b) Imbricated horizontally stratified conglomerates (Gch). (c) Burrows in laminated sandstones (Sh). (d) Massive, clast-supported conglomerates (Gcm) showing erosional contacts with medium-grained sandstones (Sl). (e) Trough cross-stratified sandstones. (f) Horizontally stratified, clast-supported conglomerates (Gch) intercalated with medium- to coarse-grained sandstones (Sl).

Mpodozis *et al.*, 2005; Arriagada *et al.*, 2006a). The basal portion is represented by the Limón Verde Member, containing 420 m of sandstones and brownish-reddish conglomerates, interpreted as proximal alluvial fan deposits, grading into fine playa-lake deposits towards its upper 40 m, where it shows the transition into the Licán Member (Hartley *et al.*, 1992; Arriagada, 1999; Mpodozis *et al.*, 2005). The latter contains about 700 m of sandstones and red mudstones, interbedded with conglomerates and evaporites, which are interpreted as representing channelized medial to proximal fluvial deposits with distal sheetfloods and playa-lakes (Hartley *et al.*, 1988, 1992; Arriagada, 1999). The Vizcachita Member overlies the Licán Member with a sharp contact, displaying predominantly aeolian facies, with a greater percentage of fluvially reworked deposits in the western outcrops, whereas finer grained aeolian sandsheets and barchans up to 30-m high dominate the eastern deposits. The fluvial sections show a western provenance, whereas the dunes indicate palaeocurrent directions from the south (Hartley *et al.*, 1992; Arriagada, 1999). The change to an aeolian facies may be due to a cessation of tectonic activity, which would have starved the basin of a fluvial input until deposition of the Seilao Member (Hartley *et al.*, 1992). Andesitic flows are found in some locations at the contact between the Vizcachita and Seilao Members (Quebrada Seilao, Hartley *et al.*, 1988, 1992). The Seilao Member shows a return to predominantly alluvial facies, with the presence of poorly confined conglomeratic sheetflood and high-density flood deposits. Some fluvial deposits can be found as small-scale, fining-upward cycles (Hartley *et al.*, 1992; Hartley, 1993), probably representing meandering streams. The Seilao Member fines upward into the 250-m thick Río Grande Member, which contains sandstones, siltstones and varved mudstones, evidencing a possibly permanent, shallow lake subject to alluvial flooding and deposition of distal sheetflood sands (Hartley *et al.*, 1988, 1992; Arriagada, 1999).

The Río Grande Member represents the last unit of the Purilactis Formation, conformably underlying the Barros Arana Formation (Arriagada, 1999). According to Hartley *et al.* (1992), the latter is composed of thick alluvial fan deposits with clasts up to 20 cm in diameter, derived mostly from Palaeozoic granitoids and rhyolites with minor andesites and limestones in the west. The dominant facies are laterally amalgamated, proximal channelized streamflow and sheetflood deposits, together with some high-density flood and debris flow deposits. The large amount of basement-derived clasts, as compared to the Purilactis Formation, suggests deep exhumation of the Cordillera de Domeyko Range during its deposition (Mpodozis *et al.*, 2005).

The Purilactis Group (*sensu* Arriagada, 1999) ends with the Cerro Totola Formation ('Estratos Cerros de Totola'

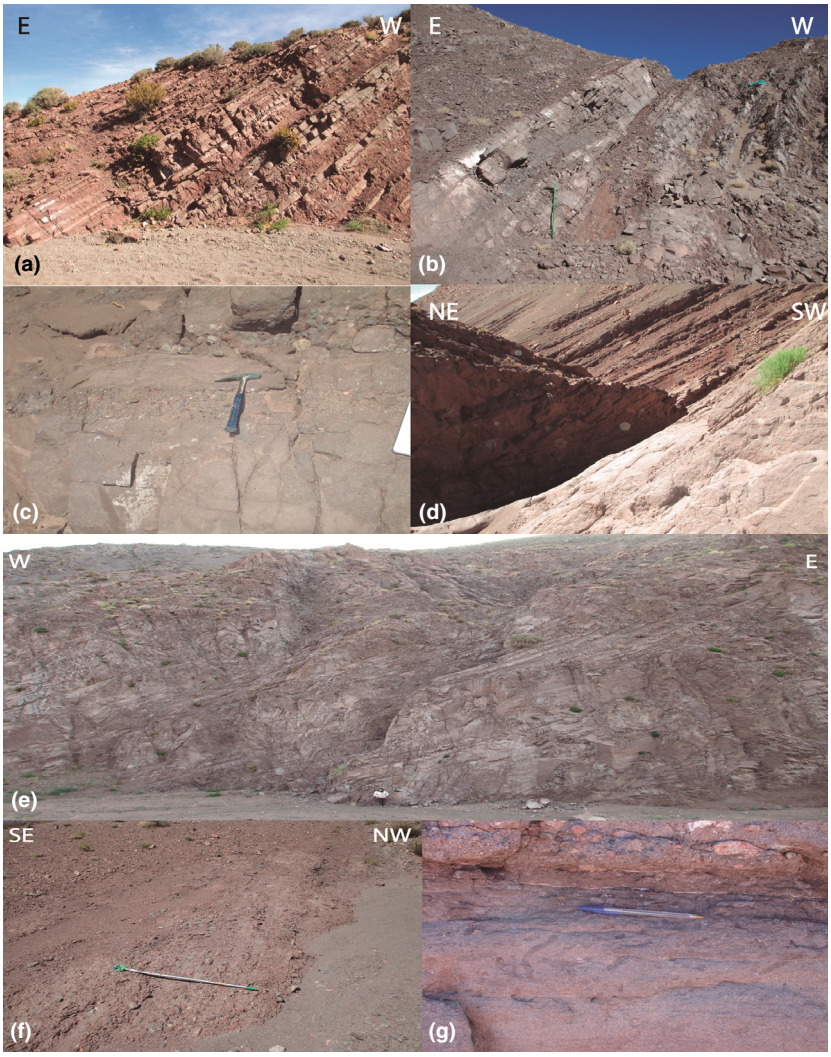

Fig. 5. (a) Laminated, fine- to medium-grained sandstones (Sh) of the Tonel Formation (La Escalera Member). (b) Sandstones and conglomerates of the Limón Verde Member. c) Laminated, fine- to medium-grained sandstones (Sh) interbedded with clast-supported, horizontally stratified conglomerates (Gch), seen in the Lampallar Member. d) Similar deposits of the Licán Member. e) Paleodunes in the Vizcachita Member. f) Typical clast-supported, horizontally laminated conglomerates (Gch) of the Seilao Member. g) Burrows between laminated sandstones and conglomerates of the Barros Arana Formation.

of Arriagada, 1999 and Mpodozis *et al.*, 1999), which is mainly composed of andesites, basaltic andesites and fewer dacites, interbedded with welded rhyolitic tuffs and some sandstones and red volcaniclastic conglomerates (Arriagada, 1999). This unit unconformably overlies deposits of the Tonel Formation and the Licán Member and is currently interpreted as younger than the Barros Arana Formation (Arriagada, 1999; Mpodozis *et al.*, 1999, 2005).

Regarding the age, lavas and related intrusives belonging to the Cerro Totola Formation, which intrude both the Tonel and Purilactis Formations, present K–Ar ages ranging between 70.2 ± 2.0 and 61.0 ± 2.0 Ma, within the Maastrichtian–Danian range, defining a minimum age for the lower terms of the Purilactis Group (Mpodozis *et al.*, 2005). This age is in agreement with a K/Ar age of 63.6 ± 2.8 Ma obtained by Macellari *et al.* (1991) from similar hornblende-rich dykes that intrude the lower Tonel Formation. The maximum age of the group has not been conclusively determined; palaeomagnetic studies of the middle member of the Tonel Formation and the Limón Verde and Licán Members of the Purilactis Formation show that these rocks acquired their magnetization during a period of normal polarity, suggesting deposition during the Cretaceous normal polarity superchron (119–84 Ma) (Arriagada, 1999; Arriagada *et al.*, 2000). In addition, Ramírez & Gardeweg (1982) found reworked limestone clasts in the Purilactis Formation containing pelecypods (*Vaugonia v. l. gottschei* Moericke) and ammonites (*Perisphinctes* sp.,) of Middle Jurassic age, which confirms a post-Jurassic age for the group (Mpodozis *et al.*, 2005).

SEDIMENTOLOGY

Stratigraphic columns, measured on a centimetre to metre scale, and lithological information were collected from different sections throughout the Barros Arana Syncline (Figs 2 and 3). Conglomerate clast counts were performed on at least 100 clasts inside a 50 × 50 cm grid in selected areas, and palaeocurrent directions were measured using palaeochannels, troughs and/or lee side laminae, following method II of DeCelles *et al.* (1983). The clast-count and palaeocurrent information were then compared with data previously published by Hartley *et al.* (1988, 1992).

Table 1. Simplified chronostratigraphic chart

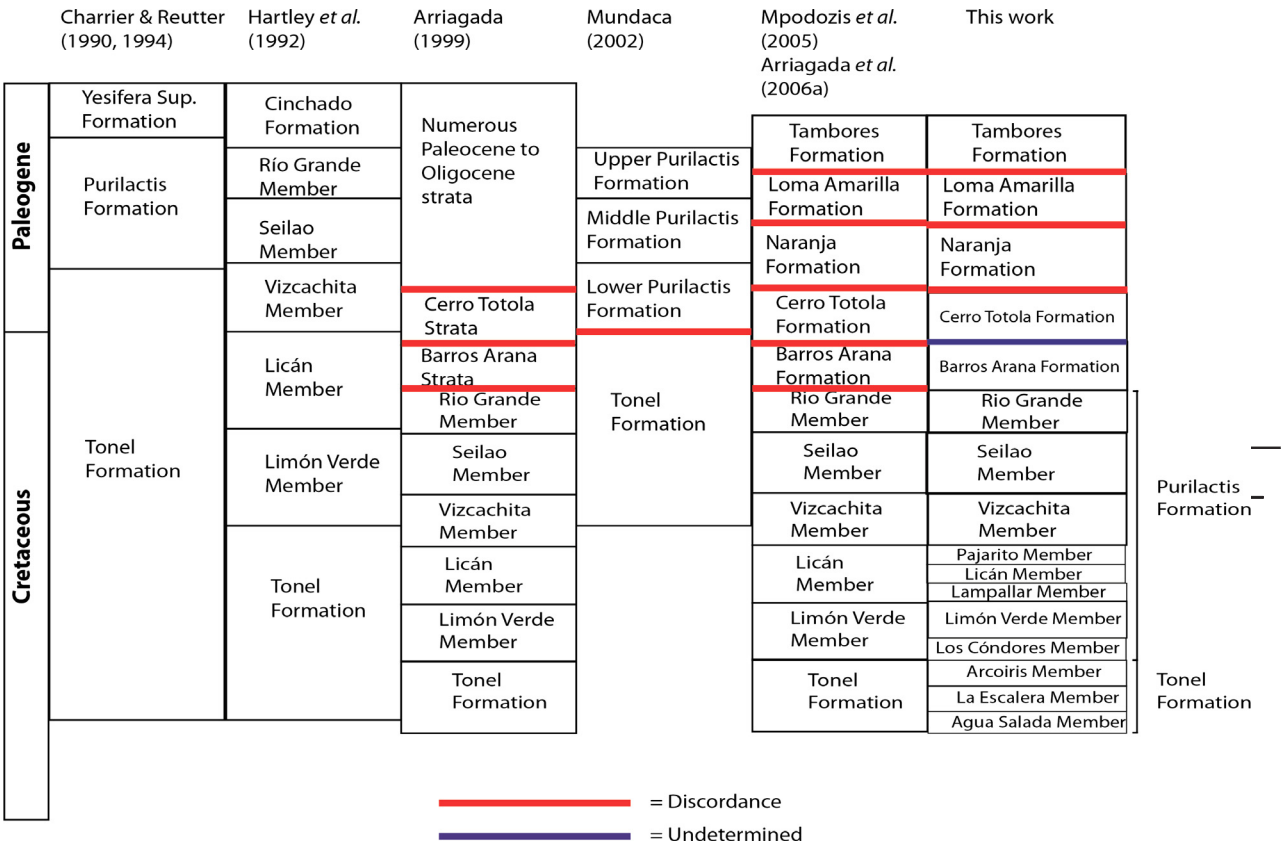

The facies code used here (Table 2; Figs 4 and 5) is partly modified from Miall (1985, 1996), Nalpas *et al.* (2008), Carrapa *et al.* (2012), Siks & Horton (2011) and DeCelles *et al.* (2011). Sedimentological analysis and depositional environment interpretation are based both on the data acquired in this research and that of Hartley *et al.* (1988, 1992), Arriagada (1999) and Mpodozis *et al.* (2005). The more detailed columns can be seen in Appendix A. The subdivisions for the formations proposed by Henríquez *et al.* (2014) are used here.

Lithofacies assemblages

Due to the large amount of columns profiled in this study, and to avoid excessive detail, we describe only the main lithofacies assemblages identified in the Barros Arana Syncline. These correspond to:

(a)Shallow, gravel-bed, braided rivers: This assemblage consists mainly of crudely stratified and/or massive, clast-supported conglomerates (Gch and Gcm, respectively), with clast sizes usually in the granule-pebble range, containing at times isolated clasts of larger sizes (up to 40 cm). The clasts are usually poorly sorted and subrounded to angular in shape, whereas the matrix is composed of a poorly sorted, subangular, coarse- to very coarse-grained sandstone. The most common colours are usually variations of brownish red to brown, and on some occasions grey. Bed thicknesses vary from member to formation, but they are usually between 15 and 1 m, forming compound units 5–15-m thick; the overall low thickness of these beds suggests unchannelized flooding on the lower reaches of alluvial fans (Nemec & Steel, 1984). The individual beds may be hard to identify sometimes, and the contacts between lithosomes are usually slightly erosive, and they may show a fining-upward trend. These conglomerates are generally tabular, though they sometimes show lenses a few cm thick and a metre or so wide, containing matrix-supported conglomerates (either Gmm or Gcm); the tabular character of the beds suggests unconfined or poorly confined flows able to spread laterally while depositing poorly sorted and slightly organized facies ("Sheet Gravels" of Harvey, 1984). This lithofacies is usually intercalated with laminated and horizontally stratified sandstones (Sh and Sl). This pattern of stratified conglomerates interbedded with laminated sandstones is a common sight in braided stream conglomerates, where slight fluctuations in stream velocity may produce this alternation (Nemec & Steel, 1984). Some minor gravity-flow deposits, usually ocurring with this assemblage, have been identified; they are distinguished by a larger presence of massive, matrix- and clast-supported conglomerates (Gmm and Gcm, respectively), which may also show fining- and coarsening-upward trends. Basal contacts are usually sharp and nonerosive, though they might appear irregular when the

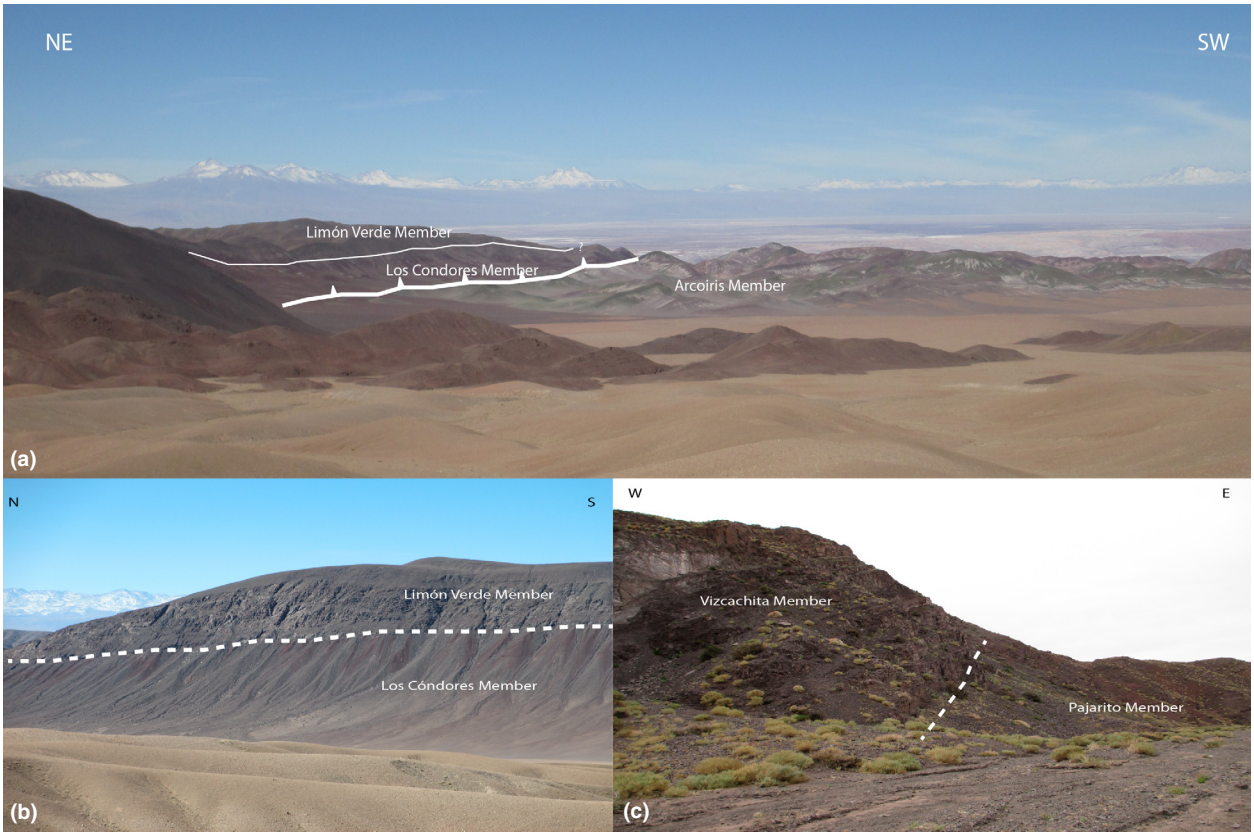

Fig. 6. (a) Sandstones of the Purilactis Formation (Limón Verde and Los Cóndores Members) overlying sandstones and deformed evaporitic deposits of the Tonel Formation (Arcoiris Member), at the southern end of the Barros Arana Syncline. (b) Closer picture of the aforementioned contact. (c) Gradational contact between the Vizachita and Pajarito Members.

sediment is deposited over an eroded surface. The lithosomes may be up to 8-m thick. Even though it is considered part of a different assemblage by Miall (1996), we include it here due to its minor occurrence.

(b)Deep, gravel-bed, braided rivers: This assemblage is recognized by the presence of fining-upward cycles, 6–30-m thick, containing either a stratified or massive basal conglomerate (Gch or Gcm) showing basal scouring,

Table 2. Lithofacies code

Lithofacies	Description	Interpretation
Sh	Medium- to fine-grained sandstones with horizontal lamination	Subcritical to supercritical flow transition
Sp	Fine- to very fine- grained sandstones with planar cross-lamination	2-D dune migration under lower regime conditions
Sl	Medium- to very coarse-grained sandstones with low-angle (<10°) cross-bedding	Deposition over inclined surfaces, or low-angle dune migration
St	Medium- to coarse-grained sandstones with trough cross-bedding	3-D dune migration under lower regime conditions
Gmm	Matrix-supported, massive, structureless conglomerate	Plastic, high-strength debris flow
Gmg	Matrix-supported conglomerate, with inverse or normal grading	Pseudoplastic, low-strength debris flow
Gch	Clast-supported conglomerate with stratification and/or local imbrication	Rapid downstream gravel transport; longitudinal bedforms
Gcm	Clast-supported, massive, structureless conglomerate	Pseudoplastic debris flows; hyper-concentrated flows
Gpt	Clast-supported conglomerates with planar stratification	Slow downstream gravel transport; transverse bedforms
Fm	Mud and silt with desiccation marks and small-scale ripples	Deposition from suspension and/or weak traction currents and dessication

slight channelization, poor to regular sorting and subangular, cobble-to pebble-sized clasts, followed by clast-supported conglomerate bodies around 1-m thick interbedded with medium- to very coarse-grained sandstones. This indicates the development of cycles in channels more than 1-m deep (Miall, 1996). The contacts between these lithosomes are nonerosive and diffuse. The sandstone portion varies from scarce to more than half of an individual cycle. The conglomerates are mostly stratified (Gch), or massive (Gcm) with clast sizes mostly in the granule-pebble range, though they can be cobble-sized locally. The conglomerates can contain boulders up to 40 cm in diameter; this is a common sight in comparison to the previous assemblage. The cycles end with coarse- to medium-grained, laminated sandstones (Sl) containing isolated clasts, with the top usually eroded by the subsequent cycle. Planar, cross-stratified conglomerates (Gpt) may also be found, though not commonly. The colours observed are usually brownish red to different shades of grey.

(c)Distal, sheetflood, sand-bed river: This style of sand-bed rivers is one of the most ubiquitous assemblages identified in the field, together with (a). It is comprised of horizontally laminated sandstones, both very fine- to medium-grained (Sh) and medium- to very coarse-grained (Sl); this lamination may locally become very faint. Sorting varies from good to poor, especially when they are found close to conglomerates or coarser-grained deposits, and roundness is usually subangular to subrounded. The lithosomes may have isolated clasts up to 30 cm in diameter, and may also fine upward; they are, characteristically, tabular in shape, with no apparent channelization. Bed sizes are usually between 15 and 50 cm thick, although coarser grained facies may be thicker on rare occasions (up to 8 m). Contacts are usually sharp and nonerosive. They can also show clast-supported conglomerate lenses with granule- to pebble-sized clasts, presenting basal scouring (either Gcm or Gch). Sandstones with trough cross-bedding (St) may be locally found, as lithosomes are usually thicker than the other sandstone lithofacies (between 1- and 6-m thick). They present the widest variety of colours of all assemblages.

(d)Aeolian deposits: This assemblage comprises homogeneous, grey, medium- to fine-grained sandstones with horizontal lamination (Sh), good sorting and subrounded grains. It shows practically no variations throughout most of the measured section, except for sparse outcrops of poorly sorted, brown, coarse-grained sandstone (Sl) with isolated clasts up to 5 cm in diameter. Lamination is faint in some instances; in higher parts of the column, both horizontal bedding and cross-lamination are clearly developed, showing beds around 30-cm thick. These lithofacies are closely associated with large-scale cross-stratified sandstones (St) (Fig. 5e), which show no evident change in textural maturity or composition. The lithosomes are up to 25-m thick. These deposits have been identified as aeolian deposits (Kocurek, 1981, 1991), consisting of fluvially reworked aeolian sandstones, aeolian dunes and sandsheets. The dunes have been previously identified as barchans by Hartley *et al.* (1988, 1992).

(e)Lacustrine deposits: The abundant occurrence of fine- to very fine-grained sandstones (Sh) and siltstone beds (Fm), usually green or dark brown in colour, marks the presence of this assemblage. The former beds are characteristically either dark green or dark brown, whereas the latter are usually yellowish. Beds are usually <50-cm thick, and may fine upward. They are usually covered or only partially exposed in the sections studied. It is also common to find minor lenses of clast-supported conglomerate lenses (Gcm) and coarse-grained, laminated sandstones (Sl).

Stratigraphic distribution of lithofacies assemblages

The distribution of the assemblages during the Cretaceous is as follows:

Tonel Formation

The lowermost division of the Tonel Formation corresponds to the Agua Salada Member, which was studied in the northwestern part of the Barros Arana Syncline (Fig. 2), where it overlies andesitic and tuffaceous rocks of the Tuina Formation (Raczynski, 1963; Henríquez *et al.*, 2014) with a slight angular unconformity. Here, this member (Fig. 7a and Figure A1) is composed of *ca.* 168 m of light brown deposits of shallow, gravel-bed, braided rivers. A conformable, nonerosive contact with laminated sandstones at *ca.* 168 m of the same section (Fig. 7a and Figure A2) marks the limit with the La Escalera Member, which shows a transition to a more distal environment, with the presence of sheetflood, sand-bed river deposits of a reddish brown colour (Fig. 5a). At *ca.* 230 m, the outcrops are partly covered and darker in colour, representing intervals of the same sand-bed river deposits interbedded with scarce lacustrine assemblages. No outcrops are present above *ca.* 322 m. This member is followed by the Arcoiris Member, which is the top of the Tonel Formation; it was not measured in this study. It lies below the Purilactis Formation (Los Cóndores Member), showing a marked detachment in the southern part of the syncline (Fig. 6a), where it is composed of intercalated siltstones, fine-grained orange sandstones and light-grey evaporites (gypsum and halite) (Hartley *et al.*, 1988, 1992; Arriagada, 1999; Mpodozis *et al.*, 2005; Henríquez *et al.*, 2014). Due to its intensely folded structure, its thickness is hard to determine, though it ranges between 50 and 300 m.

Purilactis Formation

The Los Cóndores Member (Fig. 3), not measured in this study, corresponds to the first member of the Purilactis Formation (basal section of the Limón Verde Member

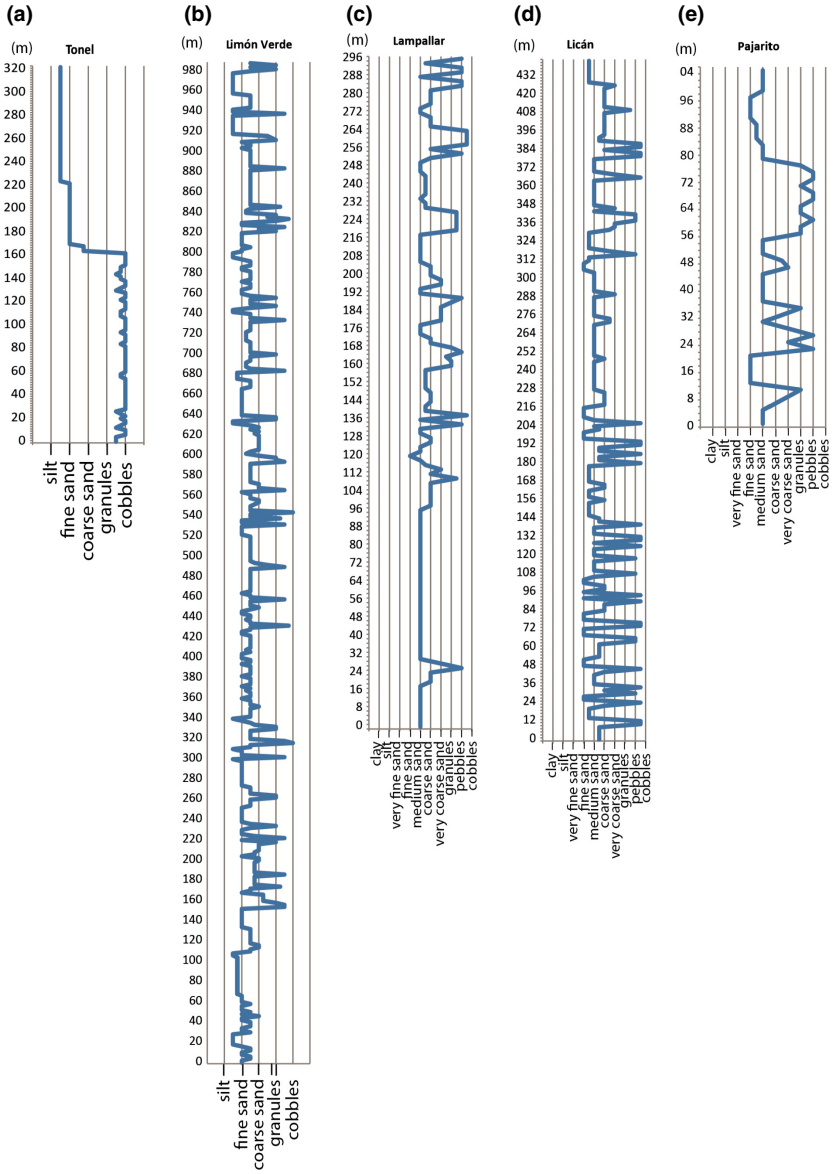

Fig. 7. High-resolution stratigraphic sections of the studied members and formations.

sensu Arriagada, 1999; upper part of the Tonel Formation *sensu* Hartley *et al.*, 1992). The nature of the contact changes throughout the syncline; to the north, the contact is conformable with the Tonel Formation, as clearly seen on satellite images, whereas to the south, it is detached (Fig. 6a). According to Arriagada (1999), it comprises *ca.* 320 m of reddish brown lithofacies belonging to distal, sheetflood, sand-bed rivers with a high braiding index, which is characteristic of distal braid plains. It is overlain in sharp but conformable contact by the Limón Verde Member, showing a sharp contact between them (Fig. 6b), where an important change in colour is observed. The basal section of this member, studied in the western limb of the syncline (Fig. 7b and Figure A3), shows grey to green deposits of distal, sand-bed rivers, which become more reddish towards the top (up to *ca.* 414 m) (Fig. 5b). They also show an overall coarser profile. At *ca.* 414 m, the lithofacies assemblages and the development of different cycles indicate a transition to deep, gravel-bed braided rivers until *ca.* 708 m. From this point onwards, there is a return to sandy, sheetflood assemblages until *ca.* 936 m, where the deposits grade into brownish sandstones and conglomerates of the Lampallar Member. The contact between both units is more clearly appreciated in the field in the southern portions of the syncline, where it rests conformably on the Limón Verde Member (Fig. 2). It is the first of the subdivisions for the Licán Member (*sensu* Hartley *et al.*, 1992) proposed by Henríquez *et al.* (2014). The Lampallar Member (Fig. 7c and Figure A4) shows 250 m of brown to dark brown lithofacies of shallow, gravel braided rivers (Fig. 5c), with scarce gravity-flow intercalations, as shown by the presence of sparse matrix-supported conglomerates. Similar assemblages are found upwards, in the Licán Member, observed in the same flank (Fig. 2). It shows a gradual transition from the previous member (Fig. 7d and Figure A5), where a change to red sandstones marks the difference between both units (Fig. 5d).

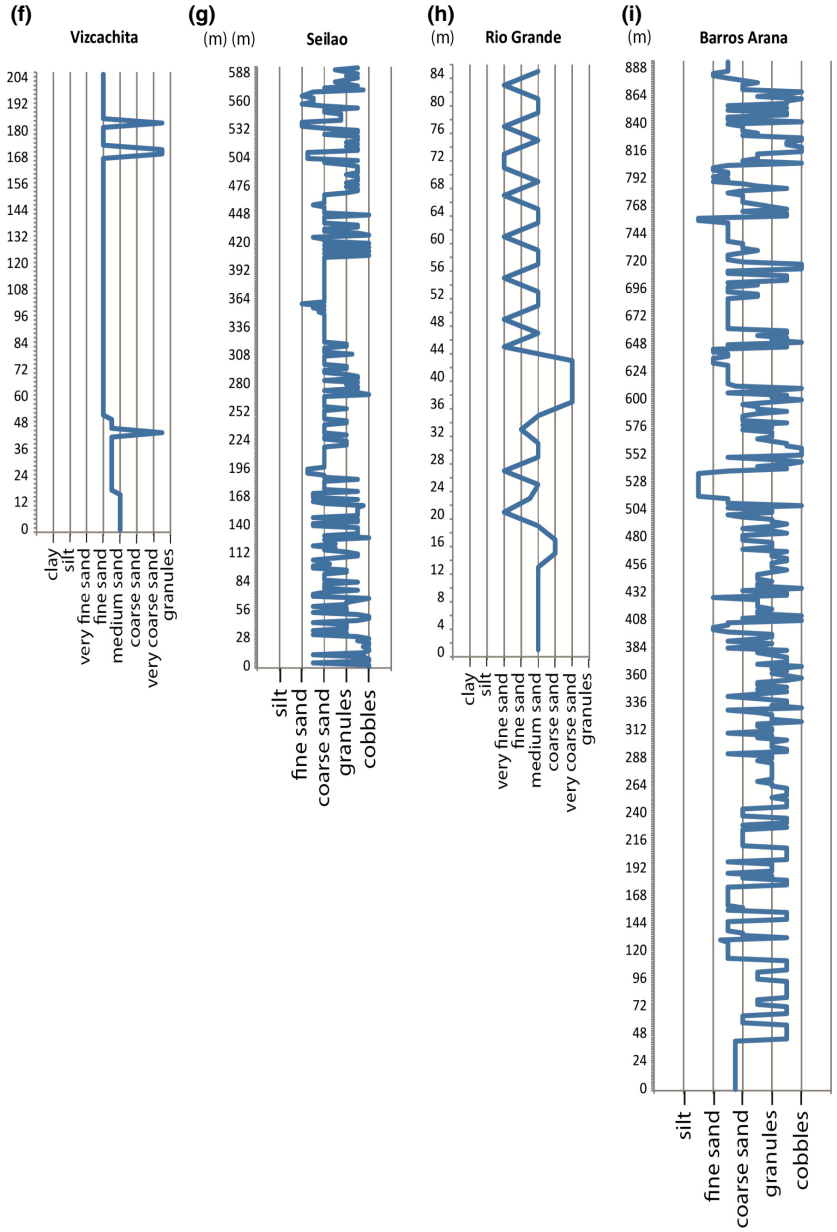

Fig. 7. Continued.

The interpretation for this member is quite similar to the one given for the Lampallar Member, though with a fining-upward trend. More reddish beds could also indicate increased subaerial exposure, which is also reflected by the presence of burrows towards the top of the section. Also, gravity-flow deposits are scarcer than in the previous member. The Licán Member is overlain by the Pajarito Member, observed in the western flank of the syncline, where it conformably underlies the Vizcachita Member (Fig. 6c). The Pajarito Member (Fig. 7e and Figure A6) shows brown to reddish brown sandstones and conglomerates, grading from reddish sandstones of the previous subdivision. The column profiled shows, in its first 78 m, lithofacies belonging to gravel-bed, probably shallow rivers, with a channel depth of *ca.* 1 m, whereas the upper portion (until *ca.* 105 m) signals a change to ephemeral sheetflood, sand-bed rivers.

The Vizcachita Member was partly observed in the northeastern section of the Barros Arana Syncline (Fig. 7f and Figure A7). It shows a transitional contact with the Pajarito Member (Fig. 6c); though the colour clearly changes on satellite images, similar facies are found in both members near their contact. The deposits observed in the *ca.* 205-m column are characteristic of aeolian deposits (Fig. 5e) and ephemeral sand-bed rivers. Hartley *et al.* (1988) suggest a fluvial origin for some of these sandstones, although they also note that this member presents strong lateral variations into aeolian dunes and aeolian sand sheets. They also show that the eastern flank of the syncline presents a more abundant proportion of aeolian sandsheets and dunes than the western flank, which is interpreted to have had a more important fluvial input. This member also presents an andesitic intercalation towards its top, in some places, marking the contact with

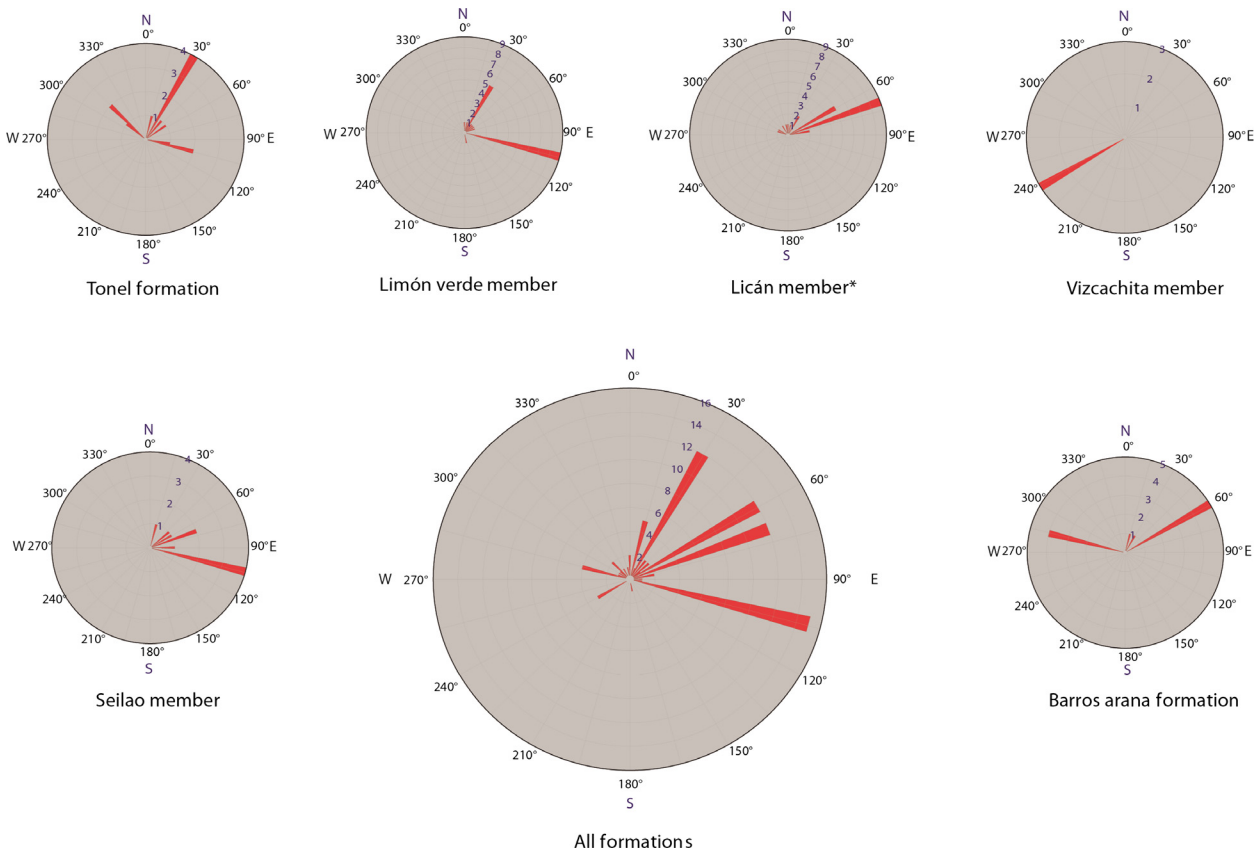

Fig. 8. Palaeocurrent directions obtained in this study. Directions plotted with GEOROSE 0.3.0 software developed by Yong Technology Inc. The Licán Member includes measurements of the Pajarito and Lampallar Members.

the Seilao Member (Hartley *et al.*, 1992; Arriagada, 1999).

The Seilao Member (Fig. 7g and Figure A8), studied on the western flank of the syncline, shows a return to coarser facies, presenting *ca.* 594 m of brown, shallow, gravel-bed braided river deposits, with intervals dominated by ephemeral sheetflood deposits [coarse-grained, laminated sandstones (Sl)] (Fig. 5f). A change to finer grained lithofacies characterizes the deposits of the Río Grande Member, partly observed above the section described for the Seilao Member (Fig. 7h and Figure A9). The contact between members is sharp, conformable and traceable on satellite images (Fig. 2). The section shows *ca.* 85 m of brown to green lithofacies related to ephemeral, poorly confined sand-bed rivers and possibly lacustrine deposits. The outcrops are mostly covered towards the top.

Barros Arana Formation

The Barros Arana Formation was studied in a section directly east of the one described for the Río Grande Member (Fig. 7i and Figure A10) where it forms the core of the Barros Arana Syncline. The section starts with *ca.* 182 m of green to brown deposits resembling both the distal sand-bed river and shallow, braided river assemblages (Fig. 5g), with a slight dominance of the former. At *ca.* 182 m, the column is dominated by assemblages of deep, gravel-bed braided rivers, with lesser intercalations of distal, sheetflood deposits; these deposits are no more than 30-m thick at a time, and usually exhibit a more reddish colour. The column profiled is quite homogeneous until its end at *ca.* 928 m, where it reaches the axis of the syncline.

Palaeocurrent data

Data for palaeocurrent analysis were obtained primarily from palaeochannels and parting lineations found throughout the study area (Figs 3 and 8 and Appendix A in the case of scalars, the direction assumed was the same as that of the closest vectors obtained from other structures, like imbricated clast orientations, planar cross stratification and 3-D expositions of trough cross-strata. These measurements were taken in the Agua Salada and La Escalera Members of the Tonel Formation, the Limón Verde, Lampallar, Licán, Pajarito (the last three grouped together), Vizcachita and Seilao Members of the Purilactis Formation, and the Barros Arana Formation. The data were then tilt-corrected with ROTDIR (Le Roux, 1991) and restored to their original orientation by rotating them 30° counterclockwise, following various palaeomagnetic studies that show such an amount of clockwise rotations in the forearc area during the Tertiary (Arriagada *et al.*, 2000, 2003,

2006b). The corrected data show that the Tonel Formation presents palaeocurrents indicating a predominantly NNE flow, and fewer palaeocurrents in the NW and ESE directions. The Limón Verde Member presents one main palaeocurrent direction showing palaeochannels and parting lineations towards the ESE, and another group of indicators pointing towards the NE. The Lampallar, Licán and Pajarito Members show a dominant transport to the E, recorded in many cross-stratified sandstones, with only a few structures pointing towards the NW. The Vizcachita Member presents large palaeodunes indicating sediment transport to the WSW (Fig. 5e). Data from the Seilao Member show a clear ESE tendency, with some structures pointing to the ENE. The Barros Arana Formation shows a major component to the NE, and a second one to the WNW; the latter component could possibly reflect diagonal and/or point bar migration (Hein, 1984).

This information indicates a general west to east (NE–ESE) transport in most formations and members, with the exception of the mainly aeolian Vizcachita Member showing westerly transport, which is consistent with measurements taken by Hartley *et al.* (1988, 1992). This preferred easterly to southeasterly direction is likely due to uplift of the Cordillera de Domeyko Range (Figs 1 and 2), situated west of the study location, during the sedimentation of the three formations. In this regard, Mpodozis *et al.* (2005) and Arriagada *et al.* (2006a) found growth structures in strata belonging to the Tonel Formation, which indicate a compressional regime during their sedimentation in mid-Cretaceous times; the space available for sediment accumulation and the deformation observed would be partly due to an eastward-verging thrust system related to the Cordillera de Domeyko Range. The directions observed in the Vizcachita Member attest to the main wind direction during its deposition (Kocurek, 1981, 1991). Hartley *et al.* (1992) obtained palaeowind directions to the north; this discrepancy could result from the interpretation of the structures observed in this member (Fig. 5e), where they could be either classified as tangential cross-laminated sets or one flank of a large trough formed by a barchan dune.

PROVENANCE

Conglomerate clast count

Clast counts were performed on the Tonel Formation (Agua Salada Member), the Limón Verde, Pajarito and Seilao Members of the Purilactis Formation and the Barros Arana Formation (Fig. 9). The Agua Salada Member shows a predominance of andesitic and tuffaceous clasts, with only 10% of clasts being of sedimentary rock origin. These are, most likely, a product of erosion within the same formation. The Limón Verde Member presents andesitic clasts as its key component, together with only a minor proportion of sedimentary clasts (15–20%), and even fewer rhyolitic to dacitic tuff clasts (<10%). The observed siltstone and sandstone clasts are similar to the facies described for this member, making them a product of limited erosion or cannibalism. The Lampallar and Licán Members (only qualitatively observed) show clasts of andesitic composition (more than 90%), with few sandstone clasts in the former, whereas the Pajarito Member shows rhyolitic to dacitic tuff clasts (80%) together with andesitic clasts (18%). The Seilao Member shows a prevalence of andesitic clasts, followed by granitic clasts, in a 3 : 1 ratio; this is reversed towards the top of the section. Finally, the Barros Arana Formation shows an increasing proportion of granitic vs. andesitic clasts (around 80% for the former and 20% for the latter), with only minor sandstone and limestone clasts (<5%).

The sections observed document an abundant presence of andesitic clasts, and a gradual increase in granitic, coarse-grained clasts over time; this is most evident in the Barros Arana Formation and Seilao Member sections,

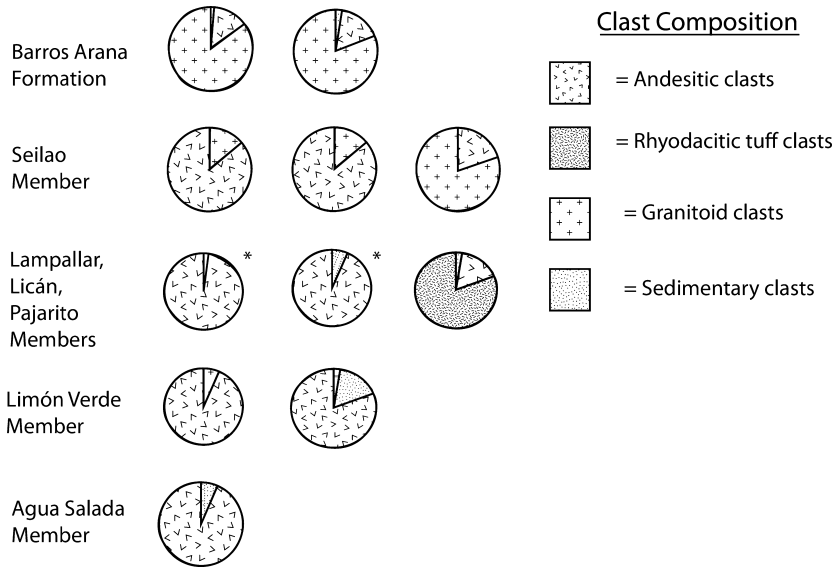

Fig. 9. Conglomerate clast count of the units investigated in this study. Exactly, 100 clasts were counted in each station. The counts marked with an asterisk are qualitative.

where granitic boulders can exceed 30 cm in diameter. These clasts are derived from granitoids probably representing deep exhumation of the Cordillera de Domeyko area (Mpodozis *et al.*, 2005; Basso & Mpodozis, 2012). The source of the andesitic clasts is most likely the Tuina Formation (Raczynski, 1963) and/or exhumed levels of the Late Cretaceous–Eocene Arc (Hartley *et al.*, 1992).

Hartley *et al.* (1988, 1992) obtained similar clast compositions, with a higher percentage of limestone clasts in the Purilactis Formation; this is attributed to uplift of the Triassic–Lower Cretaceous back-arc basin fill, due west of the study area, which is consistent with observed palaeocurrent bearings and growth structures (see above).

Table 3. Parameters for sandstone point counting

Symbol	Description
Qm	Monocrystalline quartz
Qp	Polycrystalline quartz
Qt	Total quartz (Qp + Qm + Ch)
K	Potassium feldspar
P	Plagioclase
(PinLV)	(Plagioclase in volcanic fragments)
Ch	Chert
C	Carbonate
Sm	Sandstone/siltstone fragment
Ls	Total sedimentary fragments (Sm + C)
Lm	Metamorphic fragment
Lv	Volcanic fragment
Lt	Total lithic fragments (Lv + Lt + Lm + Ls)
M	Matrix and cement
D	Iron oxides and accessory minerals
Hb	Hornblende
Ol	Olivine

Sediment provenance

Provenance analyses were performed on 11 medium- to coarse-grained sandstones. Of these, one was taken from the Tonel Formation (La Escalera Member), nine from the Purilactis Formation and one from the Barros Arana Formation. Around 400–500 grains exceeding 0.0625 mm in diameter were counted using a Swift point counter, following the Gazzi-Dickinson method (Dickinson, 1970; Dickinson & Suczek, 1979; Dickinson *et al.*, 1983; Ingersoll *et al.*, 1984; Dickinson, 1985). The parameters and point-counting raw data are listed in Table 3 and Appendix B. The results were plotted on different ternary diagrams, following Dickinson (1985), Weltje (2006) and Ingersoll (2012), and partly using an electronic spreadsheet developed by Zahid & Barbeau (2011) (Fig. 10). The geometric mean was calculated for the Purilactis Formation, following the reasoning provided by Weltje (2002).

The La Escalera Member and the basal Limón Verde Member samples show an important amount of plagioclase, K-feldspar and quartz over lithic fragments; the quartz observed is mostly monocrystalline, whereas lithics are mostly andesitic, microlithic fragments. Samples collected higher in the stratigraphic record (upper Limón Verde Member and samples of the Licán Member *sensu* Hartley *et al.*, 1992) show a more important presence of lithic fragments and plagioclase, occasionally containing red siltstone and minor quartz-feldspathic sandstone fragments. The sandstones of the Vizcachita Member show

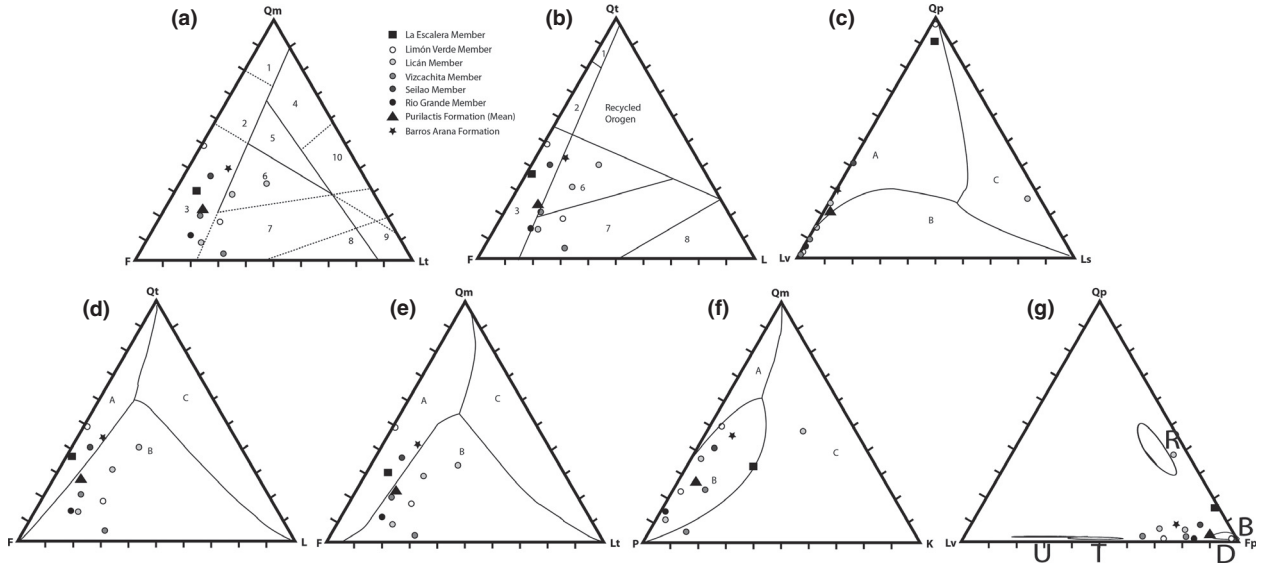

Fig. 10. Sandstone petrographic data: (a) Qm-F-Lt and (b) Qt-F-L diagrams. Fields after Dickinson *et al.* (1983). 1: Craton Interior. 2: Transitional Continental. 3: Basement Uplift. 4: Quartzose Recycled. 5: Mixed. 6: Dissected Arc. 7: Transitional Arc. 8: Undissected Arc. 9: Lithic Recycled. 10: Transitional Recycled. (c) Qp-Lv-Ls, (d) Qt-F-L, (e) Qm-F-Lt and (f) Qm-P-K after Weltje (2006). A: Continental Block Provenance. B: Magmatic Arc Provenance. C: Recycled Orogen Provenance. (g) Qp-Lv-Fp, after Ingersoll (2012). U: Undissected Arc. T: Transitional Arc. R: Recycled Orogen. B: Basement Uplift.

an overall lower percentage of quartz relative to other components, and a relevant presence of andesite fragments; plagioclase and quartz are again important in the Seilao Member, the latter being less abundant in the Río Grande Member. The geometric mean of the Purilactis Formation shows that plagioclase is the most important constituent, followed by monocrystalline quartz, lithic fragments and K-feldspar. Finally, the Barros Arana Formation sample shows monocrystalline quartz and plagioclase as major components. Some accessory minerals found throughout the section comprise iron oxides and micas, hornblende and, in some cases, broken, almost fresh pyroxene, particularly in the samples belonging to the Río Grande and Vizcachita Members.

Most of the sandstones collected plot between the basement uplift and transitional to dissected arc fields, although some samples may show some divergence when different diagrams are used. No clear temporal trend can be observed, although the two upper formations plot closer to the volcanic arc fields, particularly the dissected to transitional arcs in the case of the Barros Arana and Purilactis Formations (Fig. 10a and b). The La Escalera Member plots clearly in the basement uplift field, which is the product of the erosion of uplifted, deeply incised basement; however, Dickinson *et al.* (1983) concede that volcanic arcs can show similar compositions if they are intensively dissected, so that petrographic methods do not help in clarifying the tectonic regime if compositional overlap occurs. In this regard, the petrographic classification must only be seen as a first-order classification.

Weltje (2006) tested the model proposed by the aforementioned authors, and produced modified ternary diagrams by means of statistical analysis. The diagrams are partitioned into three spaces separated by iso-density probability lines, where the grand means of each provenance association and their confidence regions are plotted. The efficiency of the partitioning and the predictive utility of these new diagrams were tested by stochastic simulations. The results show that probabilities of correct inference are: QpLvLs (78%), QFL (76%), QmFLt (74%) and QmPK (64%) (Fig. 10c–f). Also, Ingersoll (2012), who worked on the Sierra Nevada and Southern Cascade Magmatic Arc proposed a QpLvFp diagram (Fig. 10g) based on the discriminant analysis of modern sands shed from the arc. The latter shows a N–S trend, with more exhumation towards its southern end (basement uplift) than the north (undissected arc).

Following these diagrams (Fig. 10c–f), the Tonel Formation falls in the basement uplift and continental block fields, with only one diagram (Fig. 10f) showing a different field. The Purilactis Formation, as a whole, plots in the magmatic arc field, though very close to the continental block field, whereas the Barros Arana Formation plots mostly in the continental block field. On the QpLvFp diagram (Fig. 10g), the sandstones of the Purilactis and Barros Arana Formations are located between the transitional and dissected arc fields, whereas the Tonel Formation is found between the recycled orogen and dissected arc fields.

U–Pb Detrital geochronology

Due to the lack of beds and deposits suitable for more detailed geochronology studies, such as tuffs or other extrusives, U–Pb detrital geochronological analyses by means of laser ablation inductively coupled plasma mass spectrometry were used to constrain the age of these deposits. A total of eight, fine- to coarse-grained samples, encompassing all the formations studied, were chosen for analysis; these were taken from the Tuina area and the Barros Arana Syncline (Fig. 2).

Zircon separation was performed at the Sample Preparation Laboratory (Laboratorio de Preparación de Muestras) of the Universidad de Chile using the Gemeni table, Frantz magnetic separator and heavy liquid procedures. They were then manually separated from other minerals using a binocular microscope. The zircon mineral separates were sent to the Laboratorio de Estudios Isotópicos (LEI), Geoscience Center, Universidad Nacional Autónoma de México (UNAM), Mexico, where around 100 randomly chosen grains were analysed. The analytical work was undertaken by using a *Resonetics Resolution M50* 193 nm laser *Excimer* connected to a *Thermo Xii Series Quadrupole Mass Spectrometer* following analytical procedures and technical details after Solari *et al.* (2010). The employed laser diameter for ablation was 23 μm, and the analysis was performed randomly on the grain surface. The best age was defined using the $^{206}Pb/^{238}U$ and $^{207}Pb/^{206}Pb$ ratios, with an 800 Ma cut-off. Average ages were calculated using *Isoplot v. 3.7* (Ludwig, 2008); they represent the youngest populations ($n \geq 3$) for each of the eight analysed zircon samples. The maximum depositional age for each sample locality is given by this age. Age peaks and populations were also calculated using the Excel spreadsheet Age Pick, provided by the LaserChron Center at the University of Arizona. The Excel spreadsheet Normalized Age Probability Plots, also provided by the University of Arizona, was used to summarize the relative probability plots of the different samples. The results can be seen in Fig. 11. The data tables are shown in Appendix C.

Tonel Formation

Samples from the Tonel Formation (Fig. 11a–c) show contrasting age populations. The basal sample is SP1-15, taken from the Agua Salada Member (Figs 2 and 11a). It presents most of its zircons ($n = 28$) around 247 Ma (Permian–Triassic); other important populations are in the Ordovician ($n = 5$ around 472 Ma and $n = 4$ around 483 Ma), the Permian ($n = 5$ around 279 Ma) and the Permian–Carboniferous ($n = 3$ around 302 Ma). A minor population around 149 Ma ($n = 3$, latest Jurassic) defines the maximum depositional age for the sample. The relative probability plot shows its

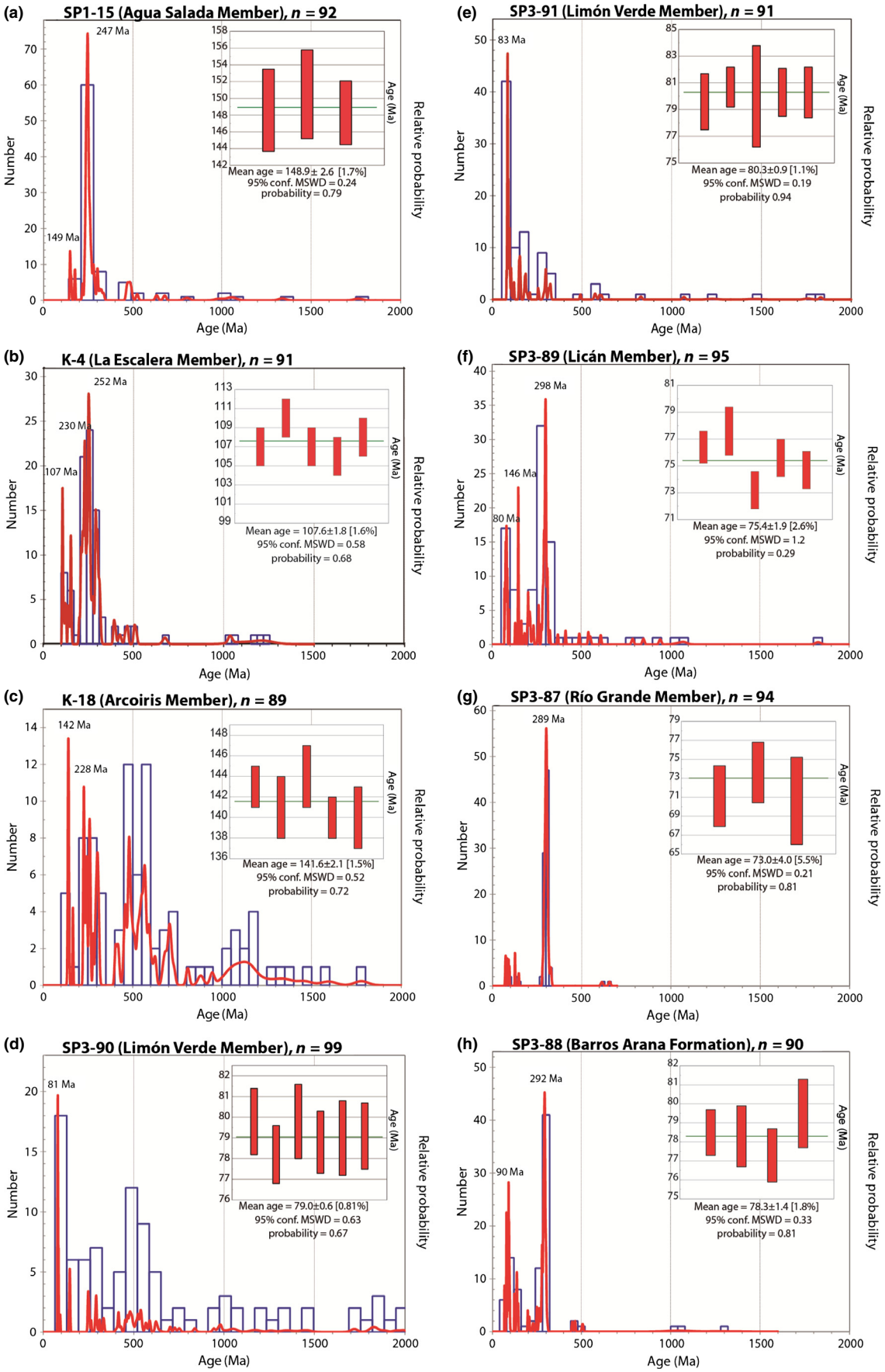

Fig. 11. U/Pb detrital zircon ages for the Tonel (a, b and c), Purilactis (d–f and g) and Barros Arana (h) Formations. Sample locations in Fig. 2.

most important peak at 247 Ma, followed by a minor peak at 149 Ma.

Sample K-4 (Fig. 11b), taken from the La Escalera Member, close to the contact with the Agua Salada Member, presents $n = 24$ zircons in the Triassic, with $n = 5$ zircons around 211 Ma, $n = 7$ around 219 Ma and $n = 12$ around 230 Ma. These are followed by Permian–Triassic (252 Ma, $n = 19$), Permian–Carboniferous ($n = 8$ around 291 Ma and $n = 7$ around 299 Ma), mid- to Early Cretaceous ($n = 5$, around 107 Ma), Jurassic (153 Ma, $n = 4$) and Permian (275 Ma, $n = 3$) populations. The mean age obtained for the youngest population is 107 Ma, which corresponds to the maximum depositional age of the sediment. The relative probability plot shows a high age peak around 252 Ma, followed by 230 Ma and 107 Ma peaks.

Sample K-18, taken from the Arcoiris Member (Fig. 11c) presents a maximum depositional age of 141 Ma. The largest populations found are of Ordovician ($n = 4$ around 459 Ma and $n = 7$ around 480 Ma) and Ediacaran ($n = 6$ around 566 Ma and $n = 4$ around 590 Ma) age. Other noteworthy populations are found (in decreasing order) in the Triassic ($n = 5$ around 228 Ma and $n = 4$ around 243), the Cambrian (566 Ma, $n = 6$), Permian–Carboniferous ($n = 6$ around 303 Ma), the Permian (260 Ma, $n = 5$), and the Early Cretaceous (142 Ma, $n = 5$). It is also worth noting that this sample has zircons in the Meso-Proterozoic (1000–1600 Ma), with $n = 10$ around 1125 Ma. The relative probability plot shows its most prominent peaks around 142 Ma and 228 Ma.

Purilactis Formation

Limón Verde Member. The Limón Verde Member samples, taken near the Cordón de Barros Arana (Fig. 2), show similar ages, but present varying proportions of older zircons. The basal sample (SP3-90, Fig. 11d) presents an important population ($n = 13$) around 81 Ma (Late Cretaceous); the maximum depositional age is 79 Ma. The second most important population is located in the Cambrian ($n = 4$ around 524 Ma and $n = 5$ around 538 Ma), followed by the Ordovician ($n = 3$ around 466 Ma and $n = 5$ around 480 Ma). Permian–Carboniferous zircons ($n = 5$ around 293 Ma) also make an important contribution. Minor zircon populations found are around 146 Ma (Early Cretaceous, $n = 5$); around 248 Ma (Triassic, $n = 4$), around 587 Ma and 621 Ma (Ediacaran, $n = 3$ each), around 981 Ma (Tonian, $n = 4$), around 1050 Ma ($n = 4$, Stenian) and around 1828 Ma (Orosirian, $n = 4$). The relative probability plot shows a prominent peak around 81 Ma.

On the other hand, sample SP3-91 (Fig. 11e), collected higher up in the column, presents most of the zircons between 65 and 100 Ma (Late Cretaceous), concentrated around 83 Ma ($n = 24$) and 93 Ma ($n = 6$) and a mean age for the youngest zircon population of 80 Ma. Other important populations are found around 150 Ma (Jurassic, $n = 9$), around 296 Ma and around 313 Ma (Permian–Carboniferous, $n = 6$ and $n = 3$, respectively). Other important age peaks were obtained for the Early Cretaceous (102 Ma, $n = 3$) and the Carboniferous (321 Ma, $n = 3$). The relative probability has its highest peak around 83 Ma.

Licán Member. The Licán Member (Sample SP3-89; Fig. 11f) presents a maximum depositional age of 75 Ma. Its most important populations are in the Permian–Carboniferous range, with $n = 23$ around 298 Ma, $n = 10$ around 291 Ma and $n = 6$ around 309 Ma; it is followed by a 65–100 Ma (Late Cretaceous, $n = 19$) age peak, with ages grouped around 80 Ma. Minor populations are found around 146 Ma (Early Cretaceous–Late Jurassic, $n = 7$), 202 Ma and 209 Ma (Triassic, $n = 4$ and $n = 3$, respectively). The relative probability plot shows the following age peaks, in decreasing order: 298 Ma, 146 Ma and 80 Ma.

Río Grande Member. The sample obtained from the Río Grande Member (Sample SP3-87; Fig. 11g) shows its largest population in the Permian–Carboniferous ($n = 51$), mainly around 289 Ma. Late Cretaceous zircons ($n = 3$) are also found, grouped around 73 Ma. The maximum depositional age is 73 Ma. The relative probability plot shows a prominent, distinctive age peak at 289 Ma.

Barros Arana Formation

The Barros Arana Formation (Sample SP3-88; Fig. 11h) has a dominant population in the Permian–Carboniferous ($n = 25$), distributed around 292 Ma. It is followed by other Permian populations around 278 Ma ($n = 7$) and 265 Ma ($n = 3$), numerous mid- to Late Cretaceous populations ($n = 4$ around 78 Ma, $n = 4$ around 84 Ma, $n = 9$ around 90 Ma and $n = 3$ around 97 Ma, for a total of $n = 20$) and an Early Cretaceous population around 137 Ma ($n = 5$). The mean age obtained for the youngest population is 78 Ma. The relative probability plot shows age peaks around 292 Ma, 90 Ma and 78 Ma.

With regard to the provenance of the different zircon populations found in these samples, the mid-Cretaceous zircons probably come from the volcanic arc deposits and related intrusives found in the present-day Central Valley, such as the Paradero del Desierto Formation (Cortés, 2000) and the Quebrada Mala Formation (Montaño, 1976; Marinovic & García, 1999). Early Cretaceous to Jurassic zircons were probably derived from the La Negra Arc, which is nowadays exposed in the Coastal Cordillera (Pichowiak *et al.*, 1990; Oliveros *et al.*, 2006). Permian–Triassic ages are found in the Tuina Formation (Fig. 2), observed in the area of the same name (Marinovic & Lahsen, 1984; Henríquez *et al.*, 2014). The El Bordo and Agua Dulce Formations, found to the southwest of the study area, along the El Bordo Escarpment (Ramírez & Gardeweg, 1982; Marinovic & Lahsen, 1984; Basso & Mpodozis, 2012) are also possible sources of Triassic and lower Permian zircons. Other deposits of Permian age

have been recorded at the eastern (Cas Formation; Ramírez & Gardeweg, 1982; Breitkreuz, 1995) and southern edges of the Salar de Atacama (Estratos de Cerro Negro; Zimmermann *et al.*, 2009; Niemeyer, 2013).

The important Late Carboniferous to Permian zircon signal seen from the Licán Member upwards is probably related to the lower sections of the mentioned Permian units and the intrusives seen in Cordillera de Domeyko, which are primarily seen in the Precordillera at this latitude, such as the multiple granodioritic intrusions found in the Sierra de Limón Verde (Complejo Intrusivo Limón Verde Indiferenciado; Marinovic & Lahsen, 1984) and the El Bordo and Agua Dulce Formations (Ramírez & Gardeweg, 1982; Breitkreuz *et al.*, 1992; Basso & Mpodozis, 2012). This provenance is consistent with the conglomerate clast counts and palaeocurrent data, which is also indicative of an unroofing process of the Precordillera.

Early Carboniferous to Silurian zircons are scarcely found in these samples. Ordovician zircons are abundant in samples K-18 and SP3-90 (La Escalera Member and lower Limón Verde Member, respectively); they are probably derived from the Cordón de Lila Complex (Damm *et al.*, 1990; Zimmermann *et al.*, 2009; Niemeyer, 2013), which would have been at least partially exhumed during the sedimentation of the aforementioned units. Similar ages are also found in the Sierra de Moreno Complex, at Quebrada Chojas, the Belén Metamorphic Complex, Aguada de la Perdiz Formation and in northwestern Argentina; they probably represent equivalents to the Ordovician Ocloyic/Famatinian arc seen in northwestern Argentina (Charrier *et al.*, 2007; Hervé *et al.*, 2007; Sola *et al.*, 2013).

The Cambrian–Neoproterozoic populations seen in samples from the Tonel Formation and lower Limón Verde Member may represent the Pampean arc of which the only close representatives found in Chile are a cordierite-bearing gneiss in the Sierra Limón Verde of 777 ± 36 Ma (Damm *et al.*, 1990), and migmatites and schists of the same area (Skarmeta, 1983; *in* Hervé *et al.*, 2007); they could also represent recycled sources. Similar ages are found further to the SE, in Argentina, in the Puncoviscana Formation (Lucassen *et al.*, 2000).

The zircon populations observed between 1000 and 1200 Ma can be related to the Grenvillian Event (Ramos, 2008, 2010). Rocks with these ages have been found in the Choja Metamorphic Complex (Damm *et al.*, 1990), as part of the Antofalla Basement (Ramos, 2008, 2010). The diamictites of the Sierra Limón Verde also present detrital zircons of this age (Morandé *et al.*, 2012), as well as rocks of the El Toco Formation (Bahlburg *et al.*, 2009), which could indicate some form of recycling. Ages similar to the oldest ones found in the Tonel Formation and Limón Verde Member samples (Fig. 11b, c and d) have only been found far north, in the Belén Metamorphic Complex; they may correspond to the protolith of the Antofalla Basement (Ramos, 2008).

DISCUSSION

The high-resolution stratigraphic columns obtained (Figs 3 and 7) together with the palaeocurrents (Fig. 8), clast counts (Fig. 9), petrographic information (Fig. 10) and detrital zircon U–Pb geochronological data (Fig. 11) allow the elaboration of an integrated sedimentary and tectonic evolution model of the basin (Fig. 12). The Tonel Formation (Fig. 12a) presents a fining-upward trend, with the deposition of shallow, gravel- to sand-bed, braided rivers and evaporitic deposits, with an overall NNE-trending flow and andesitic clasts derived from Jurassic–Lower Cretaceous and Permian–Triassic rocks as shown by the detrital zircon data; the maximum depositional ages indicate that this sedimentation could have started around the Jurassic–Cretaceous limit for the lower member (*ca.* 149 Ma), and the mid-Cretaceous (*ca.*107 Ma) for the middle member. The basal to middle Purilactis Formation (Los Cóndores, Limón Verde, Lampallar, Licán and Pajarito Members) begins with mostly shallow, sand- to gravel-bed, braided river deposits, with a W-trending flow (Fig. 12b). The detrital zircon populations show the presence of an Upper Cretaceous component, which also sets the maximum depositional age for this part (*ca.*79–75 Ma), and the clasts found are mostly andesites. An important Permian–Carboniferous zircon population becomes evident from the Licán Member onwards, up to the Barros Arana Formation. The Vizcachita Member (Fig. 12c) shows palaeocurrents opposite to those described before and facies akin to aeolian deposits and fluvial intercalations, indicating an arid to semi-arid environment. The upper part of the Purilactis Formation (Fig. 12d, e) contains assemblages of shallow, gravel-bed, braided rivers (Seilao Member) and shallow, sand-bed rivers and lacustrine deposits (Río Grande Member). The palaeocurrent directions are similar to those of the basal to middle Purilactis Formation, and the maximum depositional ages are also Late Cretaceous (*ca.*73 Ma); the most important population is Permian–Carboniferous in age, and the clast counts show the progressive increase in crystalline, coarse-grained plutonic fragments compared to andesitic, volcanic fragments, indicating unroofing processes. These clasts become predominant in the Barros Arana Formation, which shows similar detrital zircon patterns, and facies of deep, gravel-bed braided rivers, with a clearer development of cycles and channelization (Fig. 12f). Overall, the point-counting data (Fig. 10) indicate erosion of a transitional to dissected magmatic arc and an uplifted crystalline basement, though with no clear temporary trend.

This information evidences the increased progradation over time of alluvial fans or proximal braided rivers into the Salar de Atacama Basin and gradual encroaching of the source region, owing to different tectonic pulses. The lack of obvious regional or local unconformities, or progressive deformation, with the exception of those found in the middle member of the Tonel Formation (see

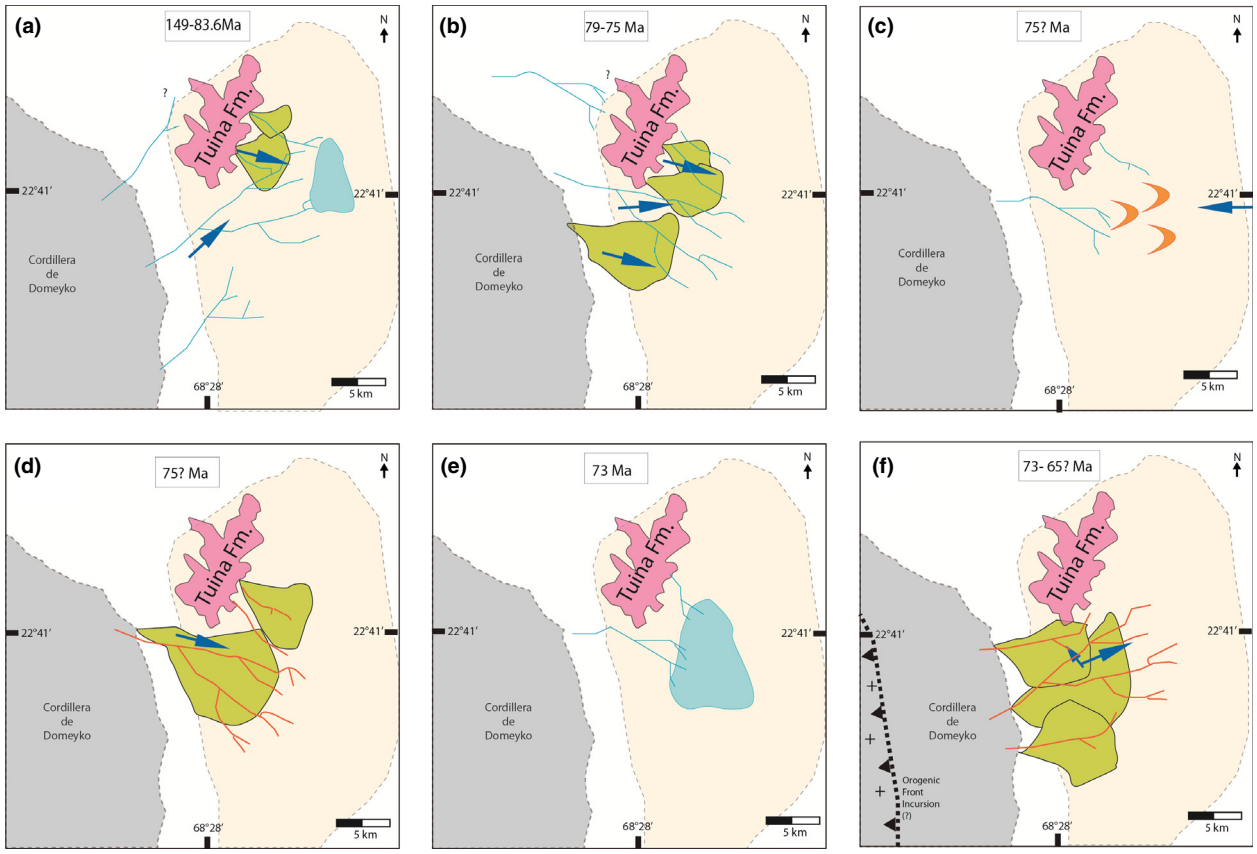

Fig. 12. Facies evolution of the Salar de Atacama Basin during the mid-Cretaceous to Palaeogene. (a) Basal gravel- to mostly sand braided river and lacustrine deposits of the Tonel Formation and part of the Los Cóndores Member. (b) Mainly sand braided rivers and distal alluvial fans of the Limón Verde, Lampallar, Licán and Pajarito Members. (c) Eolian dunes representing the Vizcachita Member. (d) Shallow, gravel braided rivers and alluvial fans of the Seilao Member. (e) Fluvial and lacustrine deposits of the Río Grande Member. (f) Deep, gravel braided rivers and alluvial fans of the Barros Arana Formation. Blue arrows indicate major palaeocurrent directions. The Tuina area (in pink) has been rotated 30° counterclockwise. Light-grey area indicates the present-day western Cordillera de Domeyko outcrop limit. Light-stippled line shows the hypothetical foredeep section of the basin. Crosses indicate positive relief.

above), indicates that the formations were deposited in the (proximal?) foredeep zone of a foreland basin system (DeCelles & Gilles, 1996), possibly following mechanisms such as those proposed by Yang & Miall (2010) and Yang (2011). This lack of deformation between members, though more crude, is also seen in seismic sections (Figs 14 and 15 of Arriagada *et al.*, 2006a).

Many discrepancies have arisen over the years concerning the tectonic setting and precise age of the Mesozoic outcrops in the El Bordo Escarpment. Despite being one of the most studied sectors of the Andes, the lack of robust age data, partly due to the lack of fossils, tuffs or other volcanic units, has led to different models for the basin during the Cretaceous–Palaeogene (See above). Most of the 1990′s tectonic models regarding the Salar de Atacama Basin were influenced by extensional models, where the Barros Arana Syncline was associated with an inverted graben geometry (Macellari *et al.*, 1991). In this model, the Tonel and Purilactis Formations would have been deposited during the latest Cretaceous–Eocene (Charrier & Reutter, 1990, 1994; Reutter *et al.*, 2006), synchronously with the rift units of the Salta Group in NW Argentina (Salfity *et al.*, 1985; Salfity & Marquillas, 1999; Monaldi *et al.*, 2008). These interpretations, along with those of Hartley *et al.* (1992) and Flint *et al.* (1993) were either based on lithological affinities or the seismic lines obtained by ENAP (Empresa Nacional del Petróleo).

Although the basal part of the Tonel Formation west of the Cerros de Tuina area could have accumulated in the Jurassic–Early Cretaceous, the palaeomagnetic data, the ages obtained for the dykes and sills intruding the Tonel and lower Purilactis Formations (Mpodozis *et al.*, 2005), and our U–Pb detrital zircon ages account for a mid- to Late Cretaceous age for the middle Tonel and Purilactis Formations. Also, recent regional mapping carried out along the El Bordo Escarpment, south of the study area, has shown that the Barros Arana Syncline can be understood as a footwall growth syncline developed east of a fault propagation anticline rooted in the Cordillera de Domeyko (Arriagada *et al.*, 2006a). Thus, the western margin of the Salar de Atacama Basin yields evidence for a compressive tectonic setting during, at least, the Late Cretaceous (*ca*. 107 Ma).

Most studies are in agreement concerning the compressive tectonics that occurred during the Palaeogene, which are well documented both along the western edge of the basin and within its centre (Muñoz *et al.*, 2002; Pananont *et al.*, 2004; Arriagada *et al.*, 2006a; Jordan *et al.*, 2007). An important extension event affected this area during the Oligocene, in which the eastern side of the Barros Arana Syncline developed a major normal fault, allowing the accumulation of *ca*. 4000 m of the Oligocene San Pedro Formation, representing most of the current infill (Pananont *et al.*, 2004; Jordan *et al.*, 2007). The recent tectonic history shows clear evidence of compression and active faulting within the modern salar (Jordan *et al.*, 2002; Lowenstein *et al.*, 2003; González *et al.*, 2009).

The major differences associated with the various tectonic models proposed can be found in the centre of the basin, where all studies are based on the aforementioned seismic lines. Here, the attempts to correlate the outcrops in the El Bordo Escarpment with the units drilled in the Toconao X1 well have been hampered by the high structural style variability observed along the different lines, the poor quality of the seismic lines below 2–3 s TWT and the lack of certainty regarding the presence of deposits belonging to the Purilactis Group in the well. A direct consequence of this is the proliferation of the different, at times contradicting, chronostratigraphic proposals for the basin (Macellari *et al.*, 1991; Flint *et al.*, 1993; Muñoz *et al.*, 1997, 2002; Pananont *et al.*, 2004; Arriagada *et al.*, 2006a; Reutter *et al.*, 2006; Jordan *et al.*, 2007). In summary, the Salar de Atacama Basin possesses different, complex events of compressive and extensional deformation, tectonic block rotations and strike-slip deformation imposed over one another that must be carefully approached to fully unravel its internal structure; however, this matter is beyond the scope of this paper.

The U–Pb geochronological data obtained (Fig. 11) yield new evidence about the age of the former Purilactis Group. Although the ages obtained for the formations are consistent with the chronostratigraphic chart presented by Mpodozis *et al.* (2005) and Arriagada *et al.* (2006a), several assumptions must be contended; for instance, the accumulation of the lower Purilactis Formation could not take place entirely during the Late Cretaceous normal polarity superchron (119–83.6 Ma), owing to the presence of zircons younger than 85 Ma. The K/Ar ages obtained by Mpodozis *et al.* (2005) in dykes and intrusions in the lower Purilactis and Tonel Formations, together with the data presented here, show that sedimentation of the La Escalera Member might have begun near 107 Ma (Albian) and continued until around 83.6 Ma (Santonian); this coincides with the strong normal polarity displayed (Arriagada, 1999; Arriagada *et al.*, 2000). The interpretation of the Agua Salada Member data is more complex; although its deposition might have started at 149 Ma, the lack of discordances between members might be more indicative of continuous sedimentation throughout the history of the Tonel Formation since the inception of the foreland basin, or the existence of a paraconformity. No data exist for the Los Cóndores Member, which could have been deposited in the same age range as the La Escalera and Arcoiris Members. Thus, the nature of the time gap between the Tonel and Purilactis Formations cannot be elicited. Sedimentation of the Limón Verde Member could have begun at 79 Ma (Campanian) and continued until no longer than 75 Ma, which is the maximum depositional age obtained for the Licán Member. For the same reasons, the Vizcachita Member cannot represent the magnetic reversal that ended the Late Cretaceous normal polarity superchron (Mpodozis *et al.*, 2005); it might record one of the various events that occurred afterwards.

The age limit of the upper Purilactis (Seilao and Río Grande Members) and Barros Arana Formations is not clear; they are bound by the youngest mean zircon age found in the Río Grande Member (see above), which limits its maximum depositional age to the upper Campanian. The only clear geological constraint on the upper limit for the Barros Arana Formation is the presence of the unconformable Oligocene–Miocene Tambores Formation (Flint *et al.*, 1993; Naranjo *et al.*, 1994). A case could be made for their equivalence to the Naranja and/or Loma Amarilla Formations (Mpodozis *et al.*, 2005; Arriagada *et al.*, 2006a), as their northern continuation; however, the age of the youngest population analysed is older than the ages recorded for both the Cerro Totola and Naranja Formations (Mpodozis *et al.*, 2005). Thus, it can be assumed that the Barros Arana Formation might be, at least, older than 58.0 $\pm$ 3 Ma (Naranja Formation), and possibly older than the Cerro Totola Formation, as envisioned by Mpodozis *et al.* (2005) and Arriagada *et al.* (2006a).

The provenance information suggests that the Salar de Atacama Basin was receiving sediments from sources even farther to the west than the Cordillera de Domeyko, which also appears to have been uplifted, at least partly, earlier than Eocene–Oligocene times, as previously proposed (Maksaev & Zentilli, 1999); its western border was probably being uplifted during and after the mid-Cretaceous (Figs 13 and 14), whereas the eastern border, near the southern end of the basin, was subject to tectonism during the K-T and Incaic events (Arriagada *et al.*, 2006a). The multiple-source provenance is confirmed by the important variations seen in the Tonel Formation and Limón Verde Member samples, which may reflect influx from different tributaries to the system and/or catchment area variations.

The cycles observed in the sedimentary succession and the ages obtained show that the mid-Cretaceous compressive phase was not one event, but rather a long period formed by recurring compressive pulses, similar to the evolution proposed by Noblet *et al.* (1996) for the Central and Northern Andes, particularly for the Quechua and Incaic periods. Interestingly enough, the ages obtained so far are very similar to the ages of the compressive events identified at the Peruvian margin according to Jaillard (1992, 1993). The beginning of sedimentation of the La

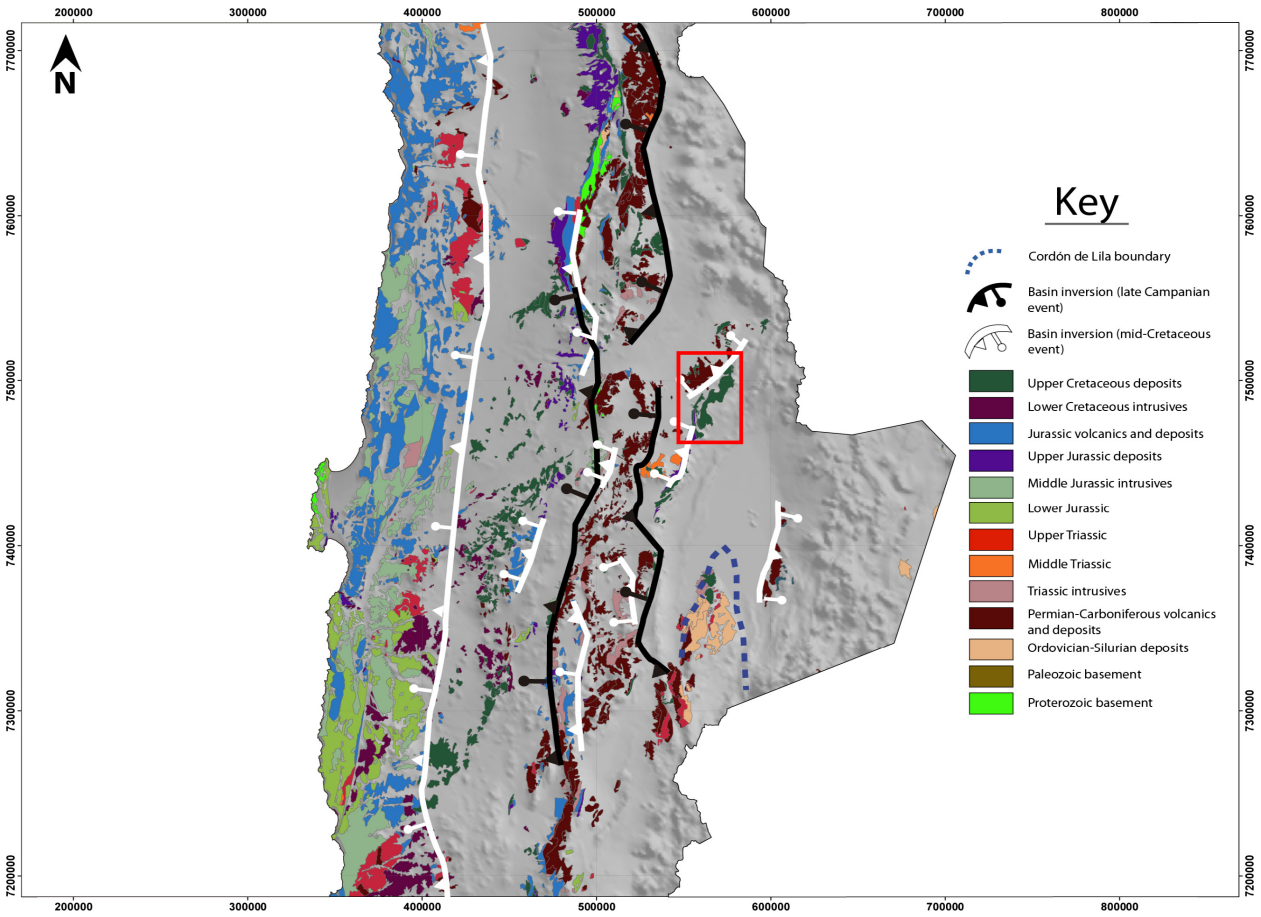

Fig. 13. Basin exhumation and compression in northern Chile. Modified from Servicio Nacional de Geología y Minería (2003).

Escalera Member can be related to the Cenomanian–Albian, Turonian–early Coniacian or late Coniacian–Santonian events; more detailed sampling is required to properly define it. The Limón Verde and Licán Members could be related to the late Campanian event (77–75 Ma), which, according to Jaillard (1992, 1993), is the largest compressive event observed during the Peruvian Phase. Under this scheme, more than 3600 m of sediment accumulated as a result of the latter event, yielding a sedimentation rate of 0.36 mm Ma^{-1} for the Purilactis and Barros Arana Formations (not including the Los Cóndores Member). Though deposition of the Barros Arana Formation could have occurred as a product of the K-T event (Cornejo *et al.*, 1997, 2003), the presence of a well-identified K-T unconformity to the west of Calama (Somoza *et al.*, 2012), which is not found in the study area, points to the contrary. Also, the ages obtained are older than the fission track ages found around Cerro Quimal, due southwest of the study area, by Andriessen & Reutter (1994), which shows slight uplift of the Cerro Quimal area.

Combining the U–Pb geochronological data with the regional geological information, a model can be proposed where the detrital sources are the product of the exhumation of earlier basins (Figs 13 and 14). The first of these exhumations would have affected parts of the Jurassic–Lower Cretaceous magmatic roots found in the present-day coastal area (Pichowiak *et al.*, 1990; Oliveros *et al.*, 2006), which would explain the Early Cretaceous and Jurassic zircons found in the studied formations (particularly in the Tonel Formation, the Limón Verde and the Licán Members). This event would have also exposed and eroded the Permian–Triassic formations. The next exhumation event would have deformed the mid-Cretaceous deposits of the Central Valley and the successions exposed at the western edge of the Cordillera de Domeyko; this signal is observed from the Limón Verde Member upwards. This exhumation would have also uplifted basement units in the Cordillera de Domeyko area, which is reflected in the abundant Carboniferous–Permian zircons observed from the Licán Member upwards. This process is similar to what has been recorded, though with different timings, in the Chañarcillo and Lautaro Basins due south in the Atacama Region (27°–28°S), over the flat-slab region (Martinez *et al.*, 2012; Martínez *et al.*, 2013).

These two steps effectively separate the Peruvian or mid-Cretaceous compressional phase into two different stages; the "early" Peruvian Phase (probably the same as the "Mochica" phase proposed by Mégard, 1984) involved strong compression and uplift of the present Coastal Cordillera area and had minor effects on other sectors close to the actual Salar de Atacama area, between 107 Ma and 83.6 Ma. This is reflected in the facies

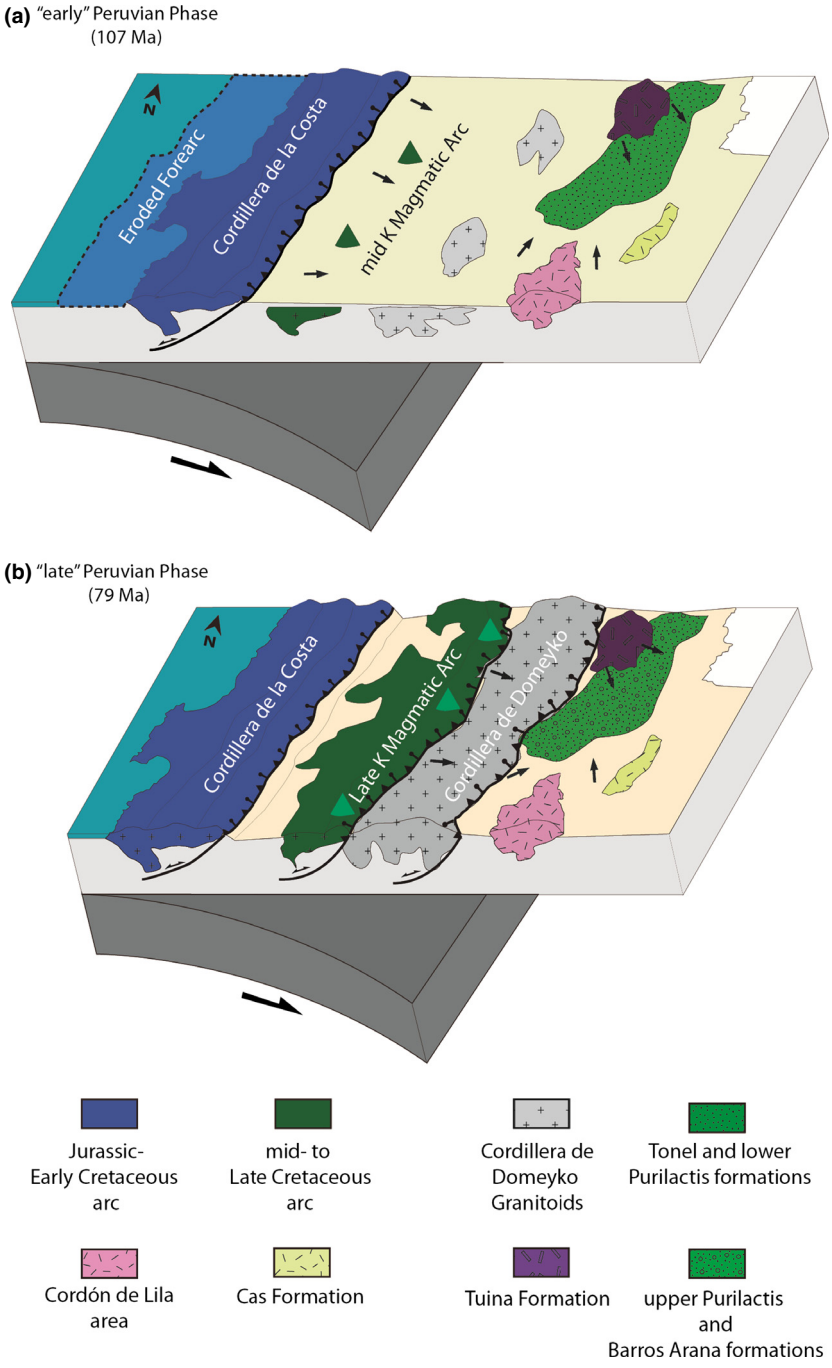

Fig. 14. Schematic cross-section of northern Chile between 22°–23°S, showing basin and orogenic wedge evolution. The figure also shows a hypothetical, eroded forearc.

belonging to the mid- to upper-Tonel Formation, which are less thick and finer grained than the Purilactis and Barros Arana Formations, probably reflecting a more distal deposition. On the other hand, the "late" Peruvian Phase shows an eastward jump of the main deformation area, strongly involving the mid-Cretaceous arc units (see above) and the Cordillera de Domeyko area, reflected in the deposition of the Purilactis and Barros Arana Formations, from 79 to 65 Ma. Sedimentation of the Barros Arana Formation is ended by the K-T event, shown by the deposition of the Cerro Totola Formation, the Naranja Formation, and then the Loma Amarilla Formation during the Incaic Event during the Late Eocene–Early Oligocene (Arriagada, 1999; Mpodozis *et al.*, 2005; Arriagada *et al.*, 2006a).

It can be seen then that the Salar de Atacama Basin does not behave like a classic foreland basin system *sensu* DeCelles & Gilles (1996); instead of progressing continuously to the east, the orogenic wedge appears to have been broken several times during the Late Cretaceous. Though one could still consider all basement blocks west of the basin as part of the orogenic front, its internal structure is far more complicated. The Tolar and Tambillo Basins (Tomlinson *et al.*, 2001), found to the northwest of the study area, could be considered as intra-montane (piggy-back?) basins, and part of the system as a whole.

More evidence for early uplift in this sector during mid-Cretaceous times has been found as far east as the Puna of NW Argentina, where apatite fission track (AFT) dating performed on the Eocene Geste Formation found AFT cooling ages between 88 and 112 Ma, which are explained as a distant signal coming from the Cordillera de Domeyko area (Carrapa & DeCelles, 2008). It is possible then that some formations interpreted to have been deposited in extensional basins, could in fact be compressive in nature; in the case of the Quebrada Mala Formation, the kinematics of the Sierra del Buitre Fault, which controls the deposition of the formation (Marinovic & García, 1999) are not distinctively clear. Andriessen & Reutter (1994) also pointed to the intrusion of the 80 Ma San Cristóbal Pluton in folded Jurassic–Lower Cretaceous deposits as evidence of deformation in the Santonian. They also showed concordant fission track ages of 72 Ma obtained from granitic stocks in Sierra de Navidad, which may indicate a tectonic event around that age; however, the results were not conclusive. In the case of the Cerrillos Formation, interpreted by Martínez *et al.* (2013) as a post-rift succession, Maksaev *et al.* (2009) concluded that its coarse conglomeratic facies provide evidence of tectonic uplift during the middle to late Aptian. Close to this area, around 28°30′S, Merino *et al.* (2013) suggested tectonic unroofing of Lower Cretaceous units in the Coastal Cordillera between 90 and 85 Ma, reflected in the deposition of the Quebrada Seca Formation. It is interesting to note that the Tonel Formation is a time-equivalent of the Quebrada Seca and Cerrillos Formations, whereas the Hornitos Formation (Martínez *et al.*, 2013) seems to be related to the Purilactis and Barros Arana Formations. Similar ages for the beginning of compression have been obtained for the Coastal Range of Central Chile, in the Caleu Pluton and the Las Chilcas Formation (Parada *et al.*, 2005); thus, a broader picture can be conceived where the entire western margin was undergoing compression from mid-Cretaceous times onward.

CONCLUSIONS

The Tonel, Purilactis and Barros Arana Formations show a diverse range of facies, accounting for more than 4000 m of sedimentation since the mid-Cretaceous, during the entire Peruvian Phase. The Tonel Formation shows shallow, gravel-bed, braided river facies (Agua Salada Member), which gradually change upward into fine-grained facies representing a transition to a more distal, possibly lacustrine or overbank environment (La Escalera and Arcoiris Members). The Los Cóndores Member shows sheetflood sandstones belonging to distal braid plains and sand-bed rivers. The Limón Verde Member presents distal, braided, sand-dominated river deposits, or ephemeral sheetflood sediments in mostly arid regions with shallow channel depths, with an upward manifestation of deeper, gravel-bed, braided river deposits. The Lampallar, Licán and Pajarito Members show laminated sandstones, related to slightly channelized, ephemeral, sand-bed rivers, and mostly clast-supported, stratified conglomerates probably deposited in shallow, gravel-bed braided rivers with scarce gravity-flow deposits. It grades into the Vizcachita Member, dominated by aeolian deposits. The Seilao Member shows a return to coarse facies, interpreted as shallow, gravel-bed braided rivers, with intervals dominated by ephemeral sheetflood deposits which grade into the Río Grande Member, showing an abundance of lithofacies related to ephemeral, poorly confined sand-bed rivers and lacustrine deposits. Finally, the Barros Arana Formation exhibits facies typical of deep, gravel-bed braided rivers and flash-flood deposits. Provenance data, conglomerate clast counts and the U–Pb detrital zircon geochronology show that the source of sediments was extremely diverse, reflecting the entire uplift of the arc and back-arc deposits. Sediment transport followed mainly a northeast-eastward direction. The age of these deposits ranges from 149 Ma (Tithonian) to 107 Ma (Albian) for the Agua Salada Member, 107–83.6 Ma (Santonian) for the La Escalera Member, the Arcoiris Member and, possibly, the Los Cóndores Member, and 79 Ma (Campanian) to 65 Ma (Palaeocene) for the rest of the Purilactis and Barros Arana Formations.

The facies variations are intimately associated with the development of the Peruvian Phase; the "early" Peruvian Phase (around 107–83.6 Ma) encompassed deposition of the La Escalera Member, the Arcoiris and the Los Cóndores Members, whereas the "later" Peruvian Phase (79–65 Ma) witnessed deposition of most of the Purilactis and Barros Arana Formations. Although the former event shows deformation and uplift of the Cordillera de la Costa area, the latter presents an eastward jump of the orogenic front to the present Cordillera de Domeyko area. The units were most likely deposited in a foredeep setting, with an increasing proximity to the orogenic front; the front itself is partly a result of the exhumation and cannibalization of previous basins. The different events clearly broke the orogenic wedge into different sections, allowing the appearance of different sources reflected in the stratigraphic record.

In a regional context, these results are in accordance with the age of compression seen elsewhere in north-central Chile and the western margin of South America, and provide new information for the Mesozoic to Cenozoic evolution of the northern Central Andes.

ACKNOWLEDGEMENTS

The authors thank and acknowledge the contributions and funding by the SERNAGEOMIN 1:100.000 National Mapping Project. Sergio Villagrán, Marco Vaccaris, Katherine Narea, Iván Gómez, Susana Henríquez, Juan Becerra and the Laboratorio de Tectónica y Palaeomagnetismo of the Universidad de Chile are thanked for

their field support and work. The authors declare that they have read the "Conflict of Interest" statement by Basin Research, and that they have no conflict of interest to report. We are grateful to Basin Research Editor Sébastien Castelltort, Andrés Folguera, Alberto Resentini and Peter DeCelles for their suggestions on how to improve the manuscript.

SUPPORTING INFORMATION

Additional Supporting Information may be found in the online version of this article:

Figure A1. Measured section of the Agua Salada Member.

Figure A2. Measured section of the La Escalera Member.

Figure A3. Measured section of the Limón Verde Member.

Figure A4. Measured section of the Lampallar Member.

Figure A5. Measured section of the Licán Member.

Figure A6. Measured section of the Pajarito Member.

Figure A7. Measured section of the Vizcachita Member.

Figure A8. Measured section of the Seilao Member.

Figure A9. Measured section of the Río Grande Member.

Figure A10. Measured section of the Barros Arana Formation.

Appendix A. Detailed stratigraphic sections profiled in this study.

Appendix B. Provenance (point-counting) raw data.

Appendix C. Detrital zircon data.

REFERENCES

Allmendinger, R.W., Jordan, T.E., Kay, S.M. & Isacks, B.I. (1997) The evolution of the Altiplano-Puna Plateau of the Central Andes. *Annu. Rev. Earth Planet. Sci. Lett.*, **25**, 139–174.

Amilibia, A., Sábat, F., McClay, K.R., Muñoz, J.A., Roca, E. & Chong, G. (2008) The role of inherited tectono-sedimentary architecture in the development of the central Andean mountain belt: insights from the Cordillera de Domeyko. *J. Struct. Geol.*, **30**(12), 1520–1539.

Andriessen, P.A.M. & Reutter, K.J. (1994) K-Ar and fission track mineral age determination of igneous rocks related to multiple magmatic arc systems along the 23°S latitude of Chile and NW Argentina. In: *Tectonics of the Southern Central Andes: Structure and Evolution of an Active Continental Margin* (Ed. by K.J. Reutter, E. Scheuber & P. Wigger), pp. 141–154. Springer, New York.

Arriagada, C. (1999) Geología y Paleomagnetismo del Borde Oriental de la Cordillera de Domeyko entre los 22°45′ y 23°30′ latitud Sur. II Región, Chile. MSc Thesis, Universidad de Chile, Santiago, (unpublished).

Arriagada, C., Roperch, P. & Mpodozis, C. (2000) Clockwise block rotations along the eastern border of the Cordillera de Domeyko, northern Chile (22°45′–23°30′S). *Tectonophysics*, **326**, 153–171.

Arriagada, C., Roperch, P., Mpodozis, C., Dupont-Nivet, G., Cobbold, P.R., Chauvin, A. & Cortés, J. (2003) Paleogene clockwise tectonic rotations in the forearc of central Andes, Antofagasta region, northern Chile. *J. Geophys. Res.*, **18**(B1), 2032.

Arriagada, C., Cobbold, P.R. & Roperch, P. (2006a) The Salar de Atacama basin: a record of Cretaceous to Paleogene compressional tectonics in the Central Andes. *Tectonics*, **25**, TC1008.

Arriagada, C., Roperch, P., Mpodozis, C. & Fernandez, R. (2006b) Paleomagnetism and tectonics of the southern Atacama Desert (25–28°S), northern Chile. *Tectonics*, **25**, TC4001.

Arriagada, C., Roperch, P., Mpodozis, C. & Cobbold, P.R. (2008) Paleogene building of the Bolivian Orocline: Tectonic restoration of the central Andes in 2-D map view. *Tectonics*, **27**, TC6014.

Bahlburg, H., Vervoort, J.D., Du Frane, S.A., Bock, B., Augustsson, C. & Reimann, C. (2009) Timing of crust formation and recycling in accretionary orogens: insights learned from the western margin of South America. *Earth Sci. Rev.*, **97**, 215–241.

Basso, M. & Mpodozis, C. (2012) Carta Cerro Quimal, Región de Antofagasta. Servicio Nacional de Geología y Minería, *Carta Geológica de Chile, Serie Geología Básica*, **143**, 1–46. 1 Mapa escala 1:100,000. Santiago, Chile.

Breitkreuz, C. (1995) The Late Permian Peine and Cas Formations at the eastern margin of the Salar de Atacama, Northern Chile: stratigraphy, volcanic facies, and tectonics. *Rev. Geol. Chile.*, **22**, 3–23.

Breitkreuz, C. & Van Schmus, W.R. (1996) U-Pb geochronology and significance of Late Permian ignimbrites in Northern Chile. *J. S. Am. Earth Sci.*, **9**(5/6), 281–293.

Breitkreuz, C., Helmdach, F.F., Kohring, R. & Mosbrugger, V. (1992) Late Carboniferous Intra-arc sediments in the north Chilean Andes: stratrigraphy, paleogeograhpy and paleoclimate. *Facies*, **26**, 67–80.

Brüggen, J. (1934) Las Formaciones de Sal y Petróleo de la Puna de Atacama. *Boll. Min. Petról.*, **32**, 105–122. Santiago, Chile.

Brüggen, J. (1942) Geología de la Puna de San Pedro de Atacama y sus formaciones areniscas y arcillas rojas. In: *Congreso Panamericano de Ingeniería de Minas y Geológica, Actas, 2*, 342–467. Imprenta Universo, Santiago, Chile.

Brüggen, J. (1950) *Fundamentos de la Geología de Chile*. pp. 1–374. Instituto Geográfico Militar, Santiago, Chile.

Carrapa, B. & DeCelles, P.G. (2008) Eocene exhumation and basin development in the Puna of northwestern Argentina. *Tectonics*, **27**, TC1015.

Carrapa, B., Bywater-Reyes, S., DeCelles, P.G., Mortimer, E. & Gehrels, G.E. (2012) Late Eocene-Pliocene basin evolution in the Eastern Cordillera of northwestern Argentina (25°–26°S): regional implications for Andean orogenic wedge development. *Basin Res.*, **24**, 249–268.

Charrier, R. & Muñoz, N. (1994) Jurassic-Cretaceous Paleogeographic evolution of the Chilean Andes at 23°–24°S.L. and 34°–35°S.L.: a comparative analysis. In: *Tectonics of the Southern Central Andes: Structure and Evolution of an Active Continental Margin* (Ed. by K.J. Reutter, E. Scheuber & P. Wigger), pp. 233–242. Springer, New York.

Charrier, R. & Reutter, K.J. (1990) The Purilactis group of Northern Chile: link between arc and backarc during Late Cretaceous and Paleogene. In: *Proceedings I ORSTOM-ISAG*, 249–252. ORSTOM Editions, Grenoble, France.

Charrier, R. & Reutter, K.J. (1994) The Purilactis group of northern Chile: boundary between arc and backarc from Late Cretaceous to Eocene. In: *Tectonics of the Southern Central Andes: Structure and Evolution of an Active Continental Margin* (Ed. by K.J. Reutter, E. Scheuber & P. Wigger), pp. 189–202. Springer, New York.

Charrier, R., Pinto, L. & Rodríguez, M.P. (2007) Tectonostratigraphic evolution of the Andean Orogen in Chile. In: *The Geology of Chile* (Ed. by T. Moreno & W. Gibbons), pp. 21–114. The Geological Society, London.

Charrier, R., Farías, M. & Maksaev, V. (2009) Evolución tectónica, paleogeográfica y metalogénica durante el Cenozoico en los Andes de Chile norte y central e implicaciones para las regiones adyacentes de Bolivia y Argentina. *Rev. Asoc. Geol. Argent.*, **65**(1), 5–35.

Cobbold, P.R. & Rosello, E.A. (2003) Aptian to recent compressional deformation, foothills of the Neuquén Basin, Argentina. *Mar. Pet. Geol.*, **20**, 429–443.

Cobbold, P.R., Rosello, E.A., Roperch, P., Arriagada, C., Gómez, L.A. & Lima, C. (2007) Distribution and timing of Andean deformation across South America. In: *Global Tectonic Processes: The Legacy of Mike Coward* (Ed. by A. Ries, R.H. Graham & R.W. Butler), Geological Society Special Publications, London.

Coira, B., Koukharsky, M., Ribeiro Guevara, S. & Cisterna, C.E. (2009) Puna (Argentina) and northern Chile Ordovician Basic Magmatism: a contribution to the tectonic setting. *J. S. Am. Earth Sci.*, **27**, 24–35.

Cornejo, P., Tosdal, R.M., Mpodozis, C., Tomlinson, A.J., Rivera, O. & Fanning, M. (1997) El Salvador, Chile porphyry copper deposit revisited: geologic and geochronologic framework. *Int. Geol. Rev.*, **39**, 22–54.

Cornejo, P., Matthews, S. & Pérez, C. (2003) The "K-T" compressive deformation event in northern Chile (24°–27°S). In: *Proceedings 10th Congreso Geológico Chileno*. Universidad de Concepción, Concepción, Chile.

Cortés, J. (2000) Hoja Palestina, Región de Antofagasta. Servicio Nacional de Geología y Minería, *Mapas Geológicos*, 19. 1 Mapa escala 1:100,000. Santiago, Chile.

Damm, K.W., Pichowiak, S., Harmon, R.S., Todt, W., Kelley, R., Omarini, R. & Niemeyer, H. (1990) Pre-Mesozoic evolution of the central Andes: the basement revisited. *Geol. Soc. Am. Spec. Pap.*, **241**, 101–126.

DeCelles, P.G. & Gilles, K.A. (1996) Foreland basin systems. *Basin Res.*, **8**, 105–123.

DeCelles, P.G., Langford, R.P. & Schwartz, R.K. (1983) Two new methods of paleocurrent determination from trough cross-stratification. *J. Sediment. Petrol.*, **53**, 629–642.

DeCelles, P.G., Carrapa, B., Horton, B.K. & Gehrels, G.E. (2011) Cenozoic foreland basin system in the central Andes of northwestern Argentina: implications for Andean geodynamics and modes of deformation. *Tectonics*, **30**, TC6013.

Dickinson, W.R. (1970) Interpreting detrital modes of greywacke and arkose. *J. Sediment. Petrol.*, **40**, 695–707.

Dickinson, W.R. (1985) Interpreting provenance relation from detrital modes of sandstones. In: *Provenance of Arenites* (Ed. by G.G. Zuffa), pp. 333–363. D. Reidel, Dordrecht, the Netherlands.

Dickinson, W.R. & Suczek, C.A. (1979) Plate tectonics and sandstone composition. *Am. Assoc. Pet. Geol. Bull.*, **63**, 2164–2182.

Dickinson, W.R., Beard, L.S., Brakenridge, G.R., Erjavec, J.L., Ferguson, R.C., Inman, K.F., Knepp, R.A., Lindberg, A. & Ryberg, P.T. (1983) Provenance of North American Phanerozoic sandstones in relation to tectonic. *Geol. Soc. Am. Bull.*, **94**, 222–235.

Dingman, R.J. (1963) Cuadrángulo Tulor. Instituto de Investigaciones Geológicas, *Carta Geológica de Chile*, **11**, 1–35. 1 Mapa escala 1:50,000. Santiago, Chile.

Dingman, R.J. (1967) Geology and Groundwater Resources of the Northern part of the Salar de Atacama, Antofagasta Province, Chile. *U.S. Geol. Surv. Bull.*, **1219**, 1–49.

Flint, S., Hartley, A., Rex, D., Guise, P. & Turner, P. (1989) Geochronology of the Purilactis Formation, Northern Chile: an insight into late cretaceous/early tertiary basin dynamics of the Central Andes. *Rev. Geol. Chile.*, **16**, 241–246.

Flint, S., Turner, P., Jolley, E.J. & Hartley, A.J. (1993) Extensional tectonics in convergent margin basins: an example from the Salar de Atacama, Chilean Andes. *Geol. Soc. Am. Bull.*, **105**, 603–617.

González, G., Cembrano, J., Aron, F., Veloso, E.E. & Shyu, J.B.H. (2009) Coeval compressional deformation and volcanism in the central Andes, case studies from northern Chile (23°S–24°S). *Tectonics*, **28**, TC6003.

Götze, H.J. & Krause, S. (2002) The central Andean gravity high, a relic of an old subduction complex? *J. S. Am. Earth Sci.*, **14**, 799–811.

Hammerschmidt, K., Döbel, R. & Friedrichsen, H. (1992) Implication of $^{40}Ar/^{39}Ar$ dating of Early Tertiary volcanic rocks from the north-Chilean Precordillera. *Tectonophysics*, **202**, 55–81.

Hartley, A.J. (1993) Sedimentological response of an alluvial system to source area tectonism: the Seilao Member of the Late Cretaceous to Eocene Purilactis Formation of northern Chile. In: *Alluvial Sedimentation: International Association of Sedimentologists Special Publication 17* (Ed. by M. Marzo & C. Puigdefabregas), pp. 489–500. Blackwell Publishing Ltd., Oxford, London.

Hartley, A., Flint, S. & Turner, P. (1988) A proposed lithostratigraphy for the Cretaceous Purilactis Formation, Antofagasta Province, northern Chile. In: *Congreso Geológico Chileno No. 5 Actas, 3*, H83–H99. Departamento de Geología y Geofísica de la Universidad de Chile, Santiago.

Hartley, A.J., Flint, S., Turner, P. & Jolley, E.J. (1992) Tectonic controls on the development of a semiarid, alluvial basin as reflected in the stratigraphy of the Purilactis Group (upper Cretaceous-Eocene), northern Chile. *J. S. Am. Earth Sci.*, **5**, 275–296.

Harvey, A.M. (1984) Debris flows and fluvial deposits in Spanish Quaternary alluvial fans: implications for fan morphology. In: *Sedimentology of Gravels and Conglomerates, Memoir 10* (Ed. by E.H. Koster & R.J. Steel), pp. 123–132. Canadian Society of Petroleum Geologists, Calgary, Alberta, Canada.

Hein, F.J. (1984) Deep-sea and fluvial braided channel conglomerates: a comparison of two case studies. In: *Sedimentology of Gravels and Conglomerates, Memoir 10* (Ed. by E.H. Koster & R.J. Steel), pp. 33–49. Canadian Society of Petroleum Geologists, Calgary, Alberta, Canada.

Henríquez, S.M., Becerra, J. & Arriagada, C. (2014) Geología del área San Pedro de Atacama, Región de Antofagasta. Servicio Nacional de Geología y Minería. *Carta Geológica de Chile,*

Serie Geología Básica. 1 Mapa escala 1:100,000. Santiago, Chile.

Hervé, F., Faundez, V., Calderón, M., Massone, H.J. & Willner, A.P. (2007) Metamorphic and plutonic basement complexes. In: *The Geology of Chile* (Ed. by T. Moreno & W. Gibbons), pp. 5–20. The Geological Society, London.

Ingersoll, R.V. (2012) Composition of modern sand and Cretaceous sandstone derived from the Sierra Nevada, California, USA, with implications for Cenozoic and Mesozoic uplift and dissection. *Sed. Geol.*, **280**, 195–207.

Ingersoll, R.V., Bullard, T.F., Ford, R.L., Grimm, J.P., Pickle, J.D. & Sares, S.W. (1984) The effect of grain size on detrital modes: a test of the Gazzi-Dickinson point-counting method. *J. Sediment. Res.*, **54**, 103–116.

Isacks, B.L. (1988) Uplift of the central Andean plateau and bending of the Bolivian orocline. *J. Geophys. Res.*, **93**, 3211–3231.

Jaillard, E. (1992) La Fase Peruana (Cretáceo Superior) en la Margen Peruana. *Bol. Soc. Geol. Perú*, **83**, 81–87.

Jaillard, E. (1993) L'évolution tectonique de la marge péruvienne au Sénonien et Paléocene et ses relations avec la geodynamique. *Bull. Soc. Géolog. France*, **164**(6), 819–830.

Jaillard, E., Bengtson, P. & Dhondt, A.V. (2005) Late Cretaceous marine transgressions in Ecuador and northern Peru: a refined stratigraphic framework. *J. S. Am. Earth Sci.*, **19**, 307–323.

Jaimes, E. & De Freitas, M. (2006) An Albian-Cenomanian unconformity in the northern Andes: evidence and tectonic significance. *J. S. Am. Earth Sci.*, **21**, 466–492.

Jolley, E.J., Turner, P., Williams, G.D., Hartley, A.J. & Flint, S. (1990) Sedimentological response of an alluvial system to Neogene thrust tectonics, Atacama Desert, northern Chile. *J. Geol. Soc. London*, **147**, 769–784.

Jordan, T.E., Muñoz, N., Hein, M., Lowenstein, T., Godfrey, L. & Yu, J. (2002) Active faulting and folding without topographic expression in an evaporite basin, Chile. *Geol. Soc. Am. Bull.*, **114**, 1406–1421.

Jordan, T.E., Mpodozis, C., Muñoz, N., Blanco, N., Pananont, P. & Gardeweg, M. (2007) Cenozoic subsurface stratigraphy and structure of the Salar de Atacama Basin, northern Chile. *J. S. Am. Earth Sci.*, **23**, 122–146.

Kocurek, G. (1981) Significance of interdune deposits and bounding surfaces in aeolian dune sands. *Sedimentology*, **28**, 753–780.

Kocurek, G. (1991) Interpretation of ancient eolian sand dunes. *Annu. Rev. Earth Planet. Sci. Lett.*, **19**, 43–75.

Le Roux, J.P. (1991) Paleocurrent analysis using Lotus 1-2-3. *Comput. Geosci.*, **17**(10), 1465–1468.

Lowenstein, T.K., Hein, M.C., Bobst, A.L., Jordan, T.E., Ku, T. & Luo, S. (2003) An assessment of stratigraphic completeness in climate-sensitive closed-basin lake sediments: Salar de Atacama, Chile. *J. Sediment. Res.*, **73**, 91–104.

Lucassen, F., Becchio, R., Wilke, H.G., Franz, G., Thirlwall, M.F., Viramonte, J. & Wemmer, K. (2000) Proterozoic-Paleozoic development of the basement of the Central Andes (18-26°S) – a mobile belt of the South American craton. *J. S. Am. Earth Sci.*, **13**, 697–715.

Ludwig, K.R. (2008) Isoplot 3.6. *Berkeley Geochron. Ctr. Spec. Pub*, **4**, 1–77.

Macellari, C.E., Su, M.J. & Townsend, F. (1991) Structure and seismic stratigraphy of the Atacama Basin (northern Chile). In: *Congreso Geológico Chileno No. 6 Actas, 1*, 133–137. Servicio Nacional de Geología y Minería, Viña del Mar, Chile.

Maksaev, V. & Zentilli, M. (1999) Fission track thermochronology of the Domeyko Cordillera, northern Chile: implications for Andean tectonics and porphyry copper metallogenesis. *Explor. Min. Geol.*, **8**, 65–89.

Maksaev, V., Munizaga, F., Valencia, V. & Barra, F. (2009) LA-ICP-MS zircon U-Pb geochronology to constrain the age of post-Neocomian continental deposits of the Cerrillos Formation, Atacama Region, northern Chile: tectonic and metallogenic implications. *Andean Geol.*, **36**(2), 264–287.

Marinovic, N. & García, M. (1999) Hoja Pampa Unión. Región de Antofagasta. Servicio Nacional de Geología y Minería, *Mapas Geológicos*, 9. 1 Mapa escala 1:100,000. Santiago, Chile.

Marinovic, N. & Lahsen, A. (1984) Hoja Calama. Servicio Nacional de Geología y Minería, *Carta Geológica de Chile*, **58**, 1–140. 1 Mapa escala 1:250,000. Santiago, Chile.

Martinez, F., Arriagada, C., Mpodozis, C. & Peña, M. (2012) The Lautaro Basin: a record of inversión tectonics in nothern Chile. *Andean Geol.*, **39**(2), 258–278.

Martínez, F., Arriagada, C., Peña, M., Del Real, I. & Deckart, K. (2013) The structure of the Chañarcillo Basin: an example of tectonic inversion in the Atacama region, northern Chile. *J. S. Am. Earth Sci.*, **42**, 1–16.

Mégard, F. (1984) The Andean orogenic period and its major structures in central and northern Peru. *J. Geol. Soc. London*, **141**, 893–900.

Merino, R., Salazar, E., Mora-Franco, C., Creixell, C., Coloma, F. & Oliveros, V. (2013) Fluvial deposition and retroarc volcanism in a Late Cretaceous foreland basin and the unroofing of the Early Cretaceous arc in the chilean Frontal Cordillera at 28°30′S, Atacama Region. *Boll. Geof. Teor. Appl.*, **54**(Suppl. 2), 237–238.

Miall, A.D. (1985) Architectural element analysis: a new method of facies analysis applied to fluvial deposits. *Earth-Sci. Rev.*, **22**, 261–308.

Miall, A.D. (1996) *The Geology of Fluvial Deposits. Sedimentary Facies, Basin Analysis and Petroleum Geology*. Springer-Verlag, New York.

Monaldi, C.R., Salfity, J.A. & Kley, J. (2008) Preserved extensional structures in an inverted Cretaceous rift basin, northwestern Argentina: outcrop examples and implications for fault reactivation. *Tectonics*, **27**, TC1011.

Montaño, J.M. (1976) Estudio geológico de la zona de Caracoles y áreas vecinas, con énfasis en el Sistema Jurásico, Provincia de Antofagasta, II Región, Chile. Bsc Thesis, Universidad de Chile, Santiago, (unpublished).

Morandé, J., Mpodozis, C., Valencia, V., Arriagada, C. & Marquardt, C. (2012) Las Diamictitas de Sierra Limón Verde, Antofagasta: evidencias de Glaciación Neoproterozoica en el Norte de Chile?. In: *Congreso Geológico Chileno XIII Actas, T2*, 271–273. Universidad Católica del Norte, Antofagasta, Chile.

Mpodozis, C., Arriagada, C. & Roperch, P. (1999) Cretaceous to Paleogene geology of the Salar de Atacama basin, northern Chile: a reappraisal of the Purilactis Group stratigraphy. In: *Proceedings IV IRD-ISAG*, pp. 523–526. IRD Editions, Göttingen.

Mpodozis, C., Arriagada, C., Basso, M., Roperch, P., Cobbold, P. & Reich, M. (2005) Late Mesozoic to Paleogene stratigraphy of the Salar de Atacama basin, Antofagasta, northern

Chile: implications for the tectonic evolution of the central Andes. *Tectonophysics*, **399**, 125–154.

Mundaca, P. (2002) Geología de los Cuadrángulos Aguada de la Teca y Barros Arana, II Región, Antofagasta. BSc Thesis, Universidad de Chile.

Muñoz, N., Charrier, R. & Reutter, K. (1997) Evolución de la Cuenca Salar de Atacama: inversión tectónica y relleno de una Cuenca de antepaís de retroarco. In: *Congreso Geológico Chileno No. 8 Actas, 1*, 195–199. Universidad Católica del Norte, Antofagasta.

Muñoz, N., Jordan, T.E. & Charrier, R. (2002) Interactions between basement and cover during the evolution of the Salar de Atacama basin, northern Chile. *Rev. Geol. Chile.*, **29**, 3–29.

Nalpas, T., Dabard, M.P., Ruffet, G., Vernon, A., Mpodozis, C., Loi, A. & Hérail, G. (2008) Sedimentation and preservation of the Miocene Atacama Gravels in the Pedernales Chañaral area, Northern Chile: climatic or tectonic control? *Tectonophysics*, **459**, 161–173.

Naranjo, J.A., Ramírez, C.F. & Paskoff, R. (1994) Morphostratigraphic evolution of the northwestern margin of the Salar de Atacama basin (23°S–68°W). *Rev. Geol. Chile.*, **21**, 91–103.

Nemec, W. & Steel, R.J. (1984) Alluvial and coastal conglomerates: their significant features and some comments on gravelly mass-flow deposits. In: *Sedimentology of Gravels and Conglomerates* (Ed. by E.H., Koster & R.J., Steel). *Can. Soc. Petrol. Geol. Mem.*, **10**, 1–31.

Niemeyer, R.H. (1989) El Complejo Ígneo-Sedimentario del Cordón de Lila, Región de Antofagasta: significado tectónico. *Rev. Geol. Chile.*, **16**(2), 163–181.

Niemeyer, H. (2013) Geología del área Cerro Lila-Peine, Región de Antofagasta. Servicio Nacional de Geología y Mineria. *Carta Geológica de Chile, Serie Geología Básica*, 147. 1 Mapa escala 1:100,000. Santiago, Chile.

Noblet, C., Lavenu, A. & Marocco, R. (1996) Concept of continuum as opposed to periodic tectonism in the Andes. *Tectonophysics*, **255**, 65–78.

Oliveros, V., Féraud, G., Aguirre, L., Fornari, M. & Morata, D. (2006) The Early Andean Magmatic Province (EAMP): $^{40}Ar/^{39}Ar$ dating on Mesozoic volcanic and plutonic rocks from the Coastal Cordillera, northern Chile. *J. Volcanol. Geoth. Res.*, **157**, 311–330.

Pananont, P., Mpodozis, C., Blanco, N., Jordan, T.E. & Brown, L.D. (2004) Cenozoic evolution of the northwestern Salar de Atacama Basin, northern Chile. *Tectonics*, **23**, TC6007.

Parada, M.A., Féraud, G., Fuentes, F., Aguirre, L., Morata, D. & Larrondo, P. (2005) Ages and cooling history of the Early Cretaceous Caleu pluton: testimony of a switch from a rifted to a compressional continental margin in central Chile. *J. Geol. Soc. London*, **162**, 273–287.

Pichowiak, S., Buchelt, M. & Damm, K.W. (1990) Magmatic activity and tectonic setting of the early stages of the Andean cycle in northern Chile. *Geol. Soc. Am. Spec. Pap.*, **241**, 127–144.

Raczynski, A. (1963) Geología del distrito minero de Tuina. BSc Thesis, Universidad de Chile, Santiago, Chile (unpublished).

Ramírez, C.F. & Gardeweg, M. (1982) Hoja Toconao, *Carta Geológica de Chile*, **54**, 1–122. 1 Mapa escala 1:250,000. Santiago, Chile.

Ramos, V.A. (2008) The basement of the Central Andes: The Arequipa and related terranes. *Annu. Rev. Earth Planet. Sci.*, **36**, 289–324.

Ramos, V.A. (2010) The tectonic regime along the Andes: present-day and Mesozoic regimes. *Geol. J.*, **45**, 2–25.

Reutter, K.J., Charrier, R., Götze, H.J., Schurr, B., Wigger, P., Scheuber, E., Giese, P., Reuther, C.D., Schmidt, S., Rietbrock, A., Chong, G. & Belmonte-Pool, A. (2006) The Salar de Atacama Basin: a Subsiding Block within the Western Edge of the Altiplano-Puna Plateau. In: *The Andes Active Subduction Orogeny* (Ed. by O. Oncken), pp. 303–325. Springer, Berlin.

Salfity, J.A. & Marquillas, R.A. (1999) La Cuenca Cretácica-terciaria del Norte Argentino. In: *Geología Argentina, Servicio Geológico Minero, Anales 29* (Ed. by R. Caminos), pp. 613–626. Acadamic Press, Buenos Aires.

Salfity, J.A., Marquillas, R.A., Gardeweg, M.C., Ramírez, C.F. & Davidson, J. (1985) Correlaciones en el Cretácico superior del norte de la Argentina y Chile. In: *Congreso Geológico Chileno No. 4 Actas, 1*, 654–667. Universidad del Norte, Antofagasta.

Servicio Nacional de Geología y Minería. (2003) Mapa Geológico de Chile. 1 Mapa escala 1:1,000,000. Santiago, Chile.

Siks, B. & Horton, B.K. (2011) Growth and fragmentation of the Andean foreland basin during eastward advance of fold-thrust deformation, Puna plateau and Eastern Cordillera, northern Argentina. *Tectonics*, **30**, DOI:10.1029/2011TC002944.

Skarmeta, J. (1983) The structural geology of the Sierra de Moreno, northern Chile. Thesis, University of London, London (unpublished).

Sola, A.M., Becchio, R.A. & Pimentel, M.M. (2013) Petrogenesis of migmatites and leucogranites from Sierra de Molinos, Salta, Northwest Argentina: a petrologic and geochemical study. *Lithos*, **177**, 470–491.

Solari, L.A., Gómez-Tuena, A., Bernal, J.P., Pérez-Arvizu, O. & Tanner, M. (2010) U-Pb zircon geochronology by an integrated LA-ICPMS microanalytical workstation: achievements in precision and accuracy. *Geostand. Geoanal. Res.*, **34–1**, 5–18.

Somoza, R., Tomlinson, A.J., Caffe, P.J. & Vilas, J.F. (2012) Paleomagnetic evidence of earliest Paleocene deformation in Calama (~22°S), northern Chile: andean-type or ridge-collision tectonics? *J. S. Am. Earth Sci.*, **37**, 208–213.

Steinman, G. (1929) *Geologie von Peru*, pp. 448. Karl Winters Universitats-Buchhandlung, Heidelberg.

Tomlinson, A.J., Blanco, N., Maksaev, V., Dilles, J., Grunder, A.L. & Ladino, M. (2001) Geología de la Precordillera Andina de Quebrada Blanca-Chuquicamata, Regiones I y II (20°30′–22°30′S). In: *Servicio Nacional de Geología y Minería, Informe Registrado, IR-01-20*, pp. 1–444. Servicio Nacional de Geología y Minería, Santiago, Chile.

Tunik, M., Folguera, A., Naipauer, M., Pimentel, M. & Ramos, V.A. (2010) Early uplift and orogenic deformation in the Neuquén Basin: constraints on the Andean uplift from U-Pb and Hf isotopic data of detrital zircons. *Tectonophysics*, **489**, 258–273.

Weltje, G.J. (2002) Quantitative analysis of detrital modes: statistically rigorous confidence regions in ternary diagrams and their use in sedimentary petrology. *Earth Sci. Rev.*, **57**, 211–253.

Weltje, G.J. (2006) Ternary sandstone composition and provenance: an evaluation of the 'Dickinson model'. *Geol. Soc. Spec. Publ.*, **264**, 79–99.

Yang, Y. (2011) Tectonically-driven underfilled-overfilled cycles, the middle Cretaceous in the northern Cordilleran foreland basin. *Sed. Geol.*, **233**, 15–27.

Yang, Y. & Miall, A.D. (2010) Migration and stratigraphic fill of an underfilled foreland basin: Middle-Late Cenomanian Belle Fourche Formation in southern Alberta. *Sed. Geol.*, **227**, 51–64.

Yuan, X., Sobolev, S. & Kind, R. (2002) Moho topography in the central Andes and its geodynamic implications. *Earth Planet. Sci. Lett.*, **199**, 389–402.

Zahid, K.M. & Barbeau, D.L. (2011) Constructing sandstone provenance and classification ternary diagrams using electronic spreadsheet. *J. Sediment. Res.*, **81**, 702–707.

Zimmermann, U., Niemeyer, H. & Meffre, S. (2009) Revealing the continental margin of Gondwana: the Ordovician arc of the Cordón de Lila (northern Chile). *Int. J. Earth Sci.*, DOI: 10.1007/s00531-009-0483-811.

Manuscript received 12 August 2014; In revised form 18 December 2014; Manuscript accepted 27 December 2014.

Journal of South American Earth Sciences 64 (2015) 261–272

Contents lists available at ScienceDirect

Journal of South American Earth Sciences

journal homepage: www.elsevier.com/locate/jsames

Paleomagnetism of Permo-Triassic and Cretaceous rocks from the Antofagasta region, northern Chile

K. Narea [a], M. Peña [a], S. Bascuñán [a], J. Becerra [a], I. Gómez [a], K. Deckart [a], F. Munizaga [a], V. Maksaev [a], C. Arriagada [a, *], P. Roperch [b]

[a] Departamento de Geología, Facultad de Ciencias Físicas y Matemáticas, Universidad de Chile, Chile
[b] Géosciences Rennes, Université de Rennes 1, CNRS, Rennes, France

ARTICLE INFO

Article history:
Received 28 April 2015
Received in revised form
8 September 2015
Accepted 10 September 2015
Available online 25 September 2015

Keywords:
Paleomagnetism
Central Andes
Northern Chile
Tectonics
Permo-Triassic
Antofagasta region

ABSTRACT

New paleomagnetic data from Permo-Triassic and Late Cretaceous rocks yield a consistent trend of vertical-axis-tectonic-rotations which are consistent with the Central Andean Rotation Pattern (CARP). However, three sites in the Tuina Formation and one site in the Purilactis Group record large rotations (80°). These mayor rotations are probably due to dextral-transpressive deformation occurring in close relation with the Incaic tectonic phase. Consequently, it is possible to infer that previous tectonic phases Peruvian and K-T would not have produced significant tectonic rotations in the area.

1. Introduction

The central Andes, a noncollisional orogeny, are a prime example of oroclinal bending (Isacks, 1988), the idea that mountain ranges form initially in a linear geometry and then are bent into their more highly curved configuration (Carey, 1955). The "Bolivian Orocline" is the change in trend of the Andes from NW to N near 18°S. The origin of the Bolivian Orocline has traditionally been studied with paleomagnetic data (e.g., Arriagada et al., 2003, 2006a, 2008; Beck, 1987; Coutand et al., 1999; Lamb, 2001; McFadden, 1990; Roperch and Carlier, 1992; Scanlan and Turner, 1992; Somoza and Tomlinson, 2002). Counterclockwise rotations with respect to stable South America are found along the Peruvian margin (Heki et al., 1984, 1985; May and Butler, 1985; Roperch and Carlier, 1992; Roperch et al., 2011) while clockwise rotations characterize the Chilean margin (Forsythe et al., 1987; Hartley et al., 1992a; Riley et al., 1993; Roperch et al., 1997). This pattern of tectonic rotations is usually called Central Andean Rotation Pattern (CARP) (Beck, 2004; Taylor et al., 2005; Roperch et al., 2006; Arriagada et al., 2008).

Mountain building in the Central Andes occurred mainly during the Cenozoic and this is the reason why paleomagnetic studies along the margin of northern Chile and Peru have been focused on essentially Jurassic, Cretaceous and Tertiary units (Fig. 1). While there are numerous paleomagnetic studies in Paleozoic rocks of the Argentinan Andes (Geuna and Ecosteguy, 2004), few studies have been reported for the Paleozoic-Triassic basement in the Andes of Northern Chile (Jesinkey et al., 1987). However, in the study of Jesinkey et al. (1987) there is no paleomagnetic data on Tertiary rocks to test the rotation history of this area.

In the present contribution, we will present paleomagnetic results from the Permo-Triassic Tuina Formation in an area where Cretaceous and Tertiary red beds have already been studied (Hartley et al., 1992a; Arriagada et al., 2000; Somoza and Tomlinson, 2002; Arriagada et al., 2003).

2. Tectonic setting

The oldest rocks found here correspond to a succession of andesitic lavas, tuffs and sandstones (Tuina Formation) deposited in a continental, volcanic environment (Mundaca, 1982). Continental sedimentary rocks of Albian to Maastrichtian-Danian age (Tonel,

* Corresponding author. Departamento de Geología, Facultad de Ciencias Físicas y Matemáticas, Universidad de Chile, Santiago, Chile.
E-mail address: cearriag@cec.uchile.cl (C. Arriagada).

http://dx.doi.org/10.1016/j.jsames.2015.09.008
0895-9811/

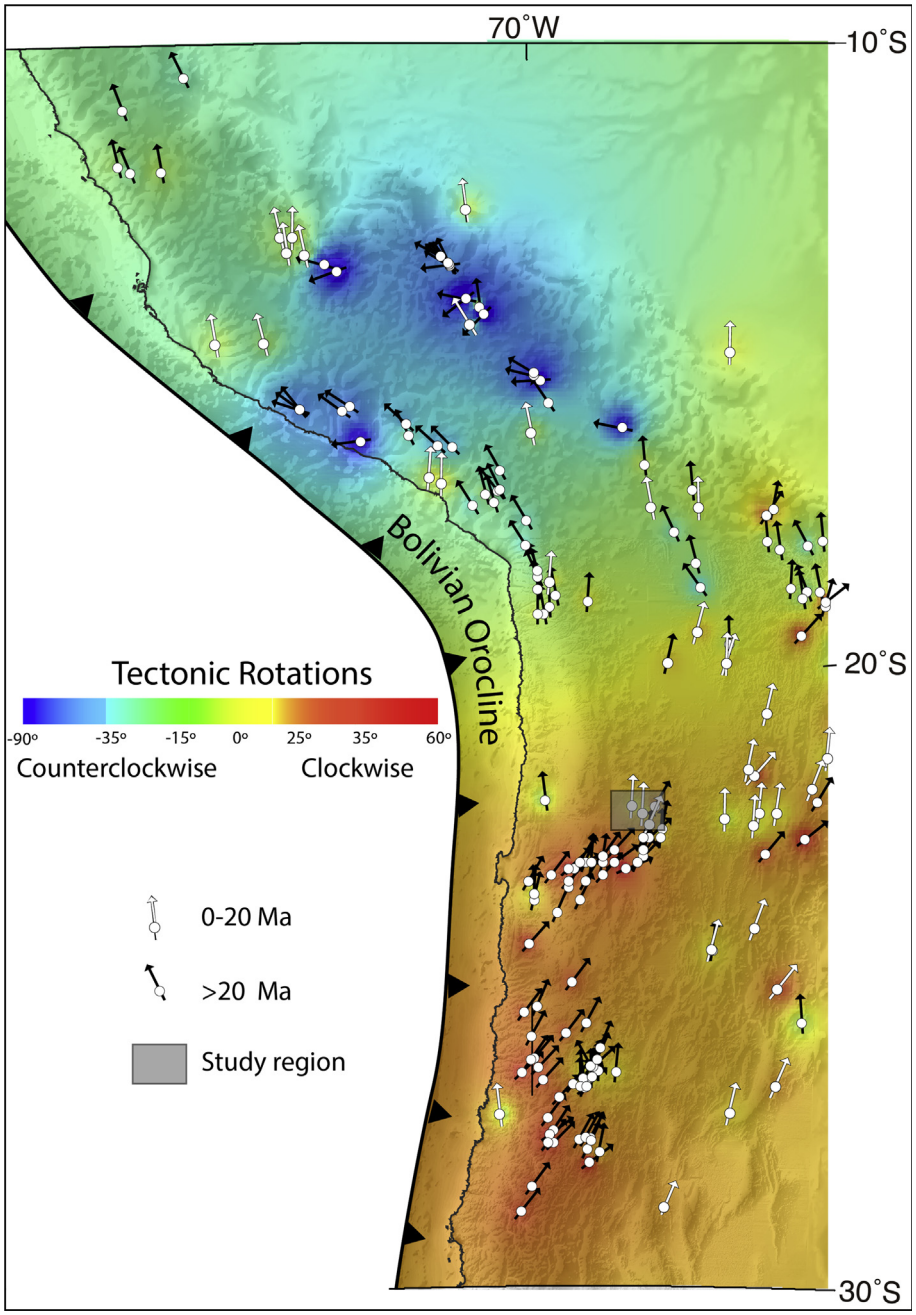

Fig. 1. Tectonic rotations in the central Andes. A raster surface based on the magnitude of rotations has been created by using the inverse distance weighting interpolation method. Paleomagnetically determined block rotations about vertical axes are shown as white arrows for rocks younger than 20 Ma and black arrows for rocks older than 20 Ma. Clockwise (counterclockwise) rotations are shown in warm colors (cool colors). The paleomagnetic database of the central Andes was obtained from Roperch et al. (2006) (see auxiliary material, available at ftp://ftp.agu.org/apend/tc/2005tc001882) and the database of the southern central Andes from Arriagada et al. (2006) (see auxiliary material, available at ftp://ftp.agu.org/apend/tc/2005tc001923).

Purilactis and Barros Arana Formations) lie on top of the former, in slight angular unconformity. A proximal, alluvial sedimentary environment is registered from the Late Oligocene onwards (Tambores Formation), which was deposited in angular unconformity over the Cretaceous and Paleogene units. The paleomagnetic sampling made for this study was performed on two first order morphostructural units: the Cordillera de Domeyko (Fig. 2), in the Cerros de Tuina Area, and the Barros Arana Syncline (Fig. 2), at the western border of the Salar de Atacama Basin.

The Cordillera de Domeyko of northern Chile, is a narrow, N–S oriented mountain chain situated in the Andean forearc. It is located between the Preandean Depression, which borders the Salar de Atacama to the east and the Central Depression to the west (Fig. 2). It has an average height of 3.000 m above sea level, and comprises successions of Paleozoic to Triassic volcano-sedimentary rocks, intruded by Carboniferous to Permian granitoids (Ramírez and Gardeweg, 1982). The volcano-sedimentary units found, whose bases are not exposed, are the Tuina Formation (Late Permian-Middle Triassic) (Raczynnski, 1963; Marinovic and Lahsen, 1984; Mundaca, 2002), the El Bordo Beds (Permian–Triassic) (Ramírez and Gardeweg, 1982), the Peine Group (Bahlburg and Breitkreuz, 1991), and the Cas Formation and its equivalents

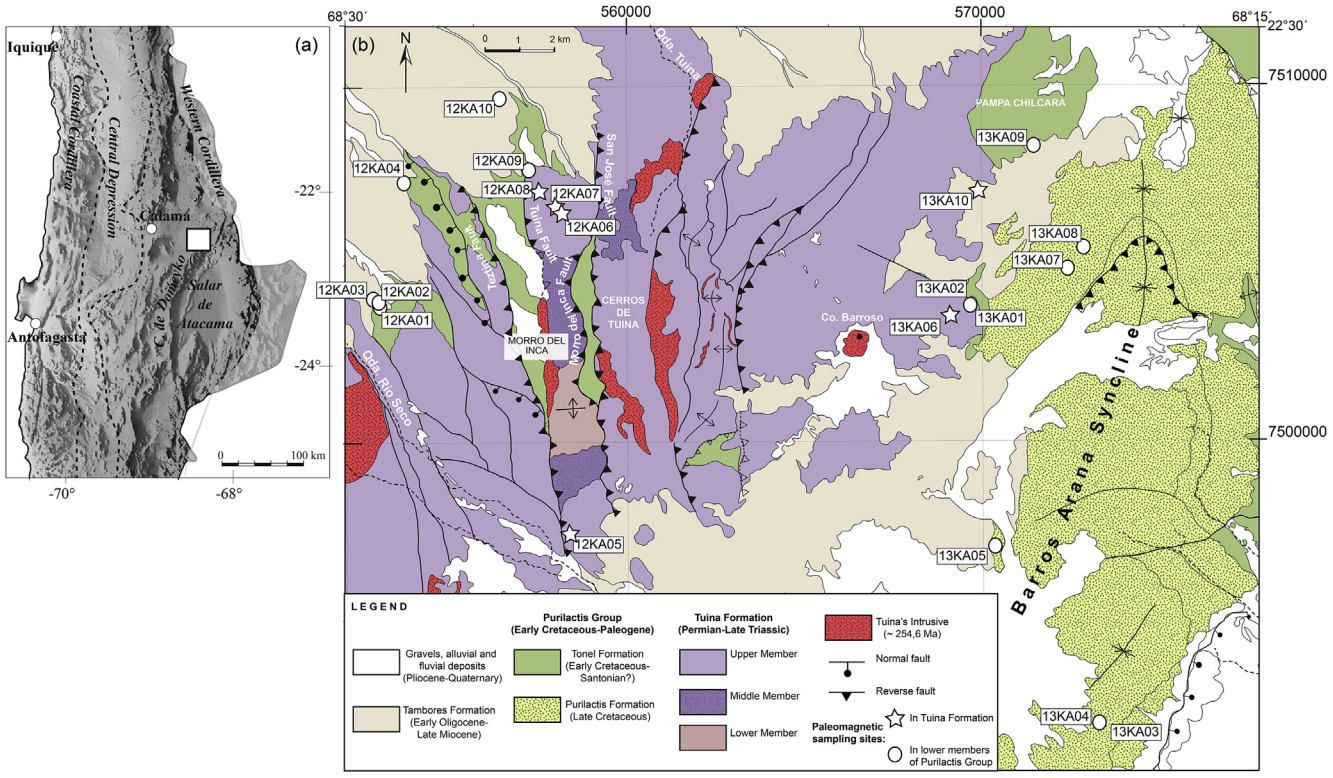

Fig. 2. (a) Location of study region (inside the white quadrate) within a schematic morphostructural map of northern Chile. (b) Simplified geologic map of the study region, showing the location of the paleomagnetic sites.

(Ramírez and Gardeweg, 1982). These last units are related to the Permian–Triassic rifting episode found along Chile and part of Argentina, which was characterized by the development of extended depocenters (Charrier et al., 2007). The Upper Paleozoic to Triassic volcano–plutonic complexes constitute the main pre-Jurassic outcrops found in northern Chile (Breitkreuz and Zeil, 1994).

Between the Late Cretaceous and the Early Oligocene, the Cordillera de Domeyko was the center of subduction-related magmatism, thus representing the magmatic arc at that time

Table 1
Location of the paleomagnetic sampling and magnetic properties.

Sites	Lithology	Latitude	Longitude	NRM (A m^{-1})	K (SI)	Strike	Dip
Barros Arana Syncline: basal sedimentary units of the Purilactis Group (Late Cretaceous)							
Vizcachita member							
13KA03	Sandstone red-brown	22°40.555′	68°17.314′	0.0087	0.00115	199.72	29.18
13KA04	Sandstone red-brown	22°40.534′	68°17.366′	0.0082	0.00230	199.72	29.18
Licán member							
13KA05	Red sandstone	22°37.881′	68°19.152′	0.0043	0.000264	45.6	36
13KA07	Red sandstone	22°33.674′	68°17.840′	0.0079	0.000147	36.4	21.8
13KA08	Red sandstone	22°33.354′	68°17.596′	0.0104	0.000193	47.1	29
Tonel formation							
12KA01	Red sandstone	22°34.225′	68°29.124′	0.0133	0.000160	240	57
12KA02	Red sandstone	22°34.239′	68°29.154′	0.0227	0.000233	248.7	58
12KA03	Sandstone red-brown	22°34.173′	68°29.192′	0.0345	0.000171	246.7	51.6
12KA04	Sandstone red-brown	22°32.407′	68°28.667′	0.0717	0.000282	330	15
12KA09	Red Sandstone	22°32.177′	68°26.663′	0.0235	0.000277	294.5	46.6
12KA10	Orange Sandstone	22°31.094′	68°27.124′	0.0142	0.000115	317.4	21.6
13KA01	Red sandstone	22°34.231′	68°19.450′	0.0172	0.000180	32.31	39.54
13KA02	Red sandstone	22°34.231′	68°19.450′	0.0371	0.000107	32.31	39.54
13KA09	Red sandstone	22°31.801′	68°18.433′	0.0191	0.000181	21.2	47.6
Cordillera de Domeyko: volcanic and sediments units of Tuina Formation							
(Permian–Middle Triassic)							
12KA05	Red sandstone	22°37.695′	68°25.996′	0.0171	0.000242	85.2	26.7
12KA06	Gray Ignimbrite	22°32.827′	68°26.145′	0.0990	0.00105	275.3	45.4
12KA07	Gray ignimbrite	22°32.746′	68°26.220′	0.423	0.000021	280.6	47.3
12KA08	Dacitic Lava	22°32.533′	68°26.465′	0.274	0.000262	287.1	39.2
13KA06	Gray ignimbrite	22°34.381′	68°19.785′	0.0199	0.000179	35.5	25.9
13KA10	Ignimbrite	22°32.502′	68°19.319′	0.0414	0.000140	22.75	25.625

NRM is geometric mean intensity of magnetization in Am^{-1}; K is geometric mean susceptibility (SI), strike and dip are bedding corrections.

(Mpodozis and Ramos, 1990; Scheuber and Reutter, 1992; Reutter et al., 1996). Around the same time, the volcanoclastic, clastic and evaporitic successions of the Purilactis Group (Charrier and Reutter, 1990, 1994; Hartley et al., 1992b) were being deposited east of the magmatic arc, in a foreland basin setting (Mpodozis et al., 2005; Arriagada et al., 2006b; Bascuñán et al., 2015). A first important episode of compressive deformation known as the Peruvian Orogenic Phase (Steinmann, 1929) occured during the Late Cretaceous along the Cordillera de Domeyko (Mpodozis et al., 2005; Arriagada et al., 2006b; Bascuñán et al., 2015). Another deformation episode occurred around the Cretaceous-Cenozoic boundary (K-T event; Cornejo et al., 2003; Somoza et al., 2012). Through the Middle Eocene, the Incaic Orogenic Phase, affected northern Chile especially along the Cordillera de Domeyko and the western border of the Salar de Atacama Basin (Mpodozis et al., 1993; Reutter et al., 1996; Tomlinson and Blanco, 1997; Maksaev and Zentilli, 1999; Mpodozis et al., 2005; Arriagada et al., 2006b). During the Oligocene, the western border of the Salar de Atacama Basin would have been affected by extension, as shown by the accumulation of the continental San Pedro and Tambores Formations (Jordan et al., 2007). The volcanic arc, which was more or less around the same position, shifts to the east in the Miocene (Charrier et al., 2009). The compressive deformation from the Miocene onwards is mainly focused at the borders of the Salar de Atacama Basin and in its central area, along the Cordillera de la Sal (Ramírez and Gardeweg, 1982; Marinovic and Lahsen, 1984). This deformation could be affecting the Pleistocene volcanic units (González et al., 2009). The eastern border of the Cordillera de Domeyko is a 900 m high scarp (the El Bordo Scarp, found south of the study area), which runs for over 120 km along the western margin of the Salar de Atacama Basin. Along this scarp, the Paleozoic basement (the Tuina Formation and the El Bordo Beds in the northern and central segment, respectively) is either detached or overlain by approximately 6.000 m of fine sandstone and conglomerate successions accumulated during the Late Cretaceous (Purilactis Group, Charrier and Reutter, 1994; Arriagada et al., 2000, 2006b; Mpodozis et al., 2005). These successions are part of the lower sedimentary infill of the Salar de Atacama Basin (Macellari et al., 1991; Muñoz et al., 1997).

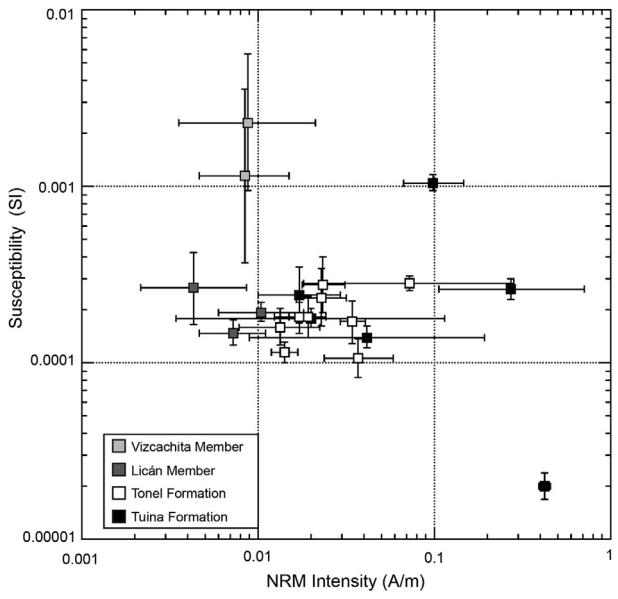

Fig. 3. Geometric site-mean intensity of Natural Remanent Magnetization (A/m) versus magnetic susceptibility (SI). The NRM intensity is usually <0.43 A/m.

3. Paleomagnetic sampling

A total of 181 paleomagnetic samples were drilled at 20 sites in the volcano-sedimentary Tuina Formation and the sedimentary units belonging to the lower members of the Purilactis Group (Table 1, Fig. 2). Unfortunately, only 16 sites gave good results.

Six sites were drilled in the Tuina Formation, four of which were performed in the Cerros de Tuina area. Three of these (12KA06, 12KA07 and 12KA08) are volcanic rocks found NW of Quebrada Tuina and north of Morro del Inca, and belong to outcrops of the Upper Member of the Tuina Formation. The only site with sedimentary rocks (12KA05) of this formation is located immediately east of Quebrada Río Seco. The last two sites (13KA06 and 13KA10) were drilled in the volcanic outcrops east of Cerros de Tuina and

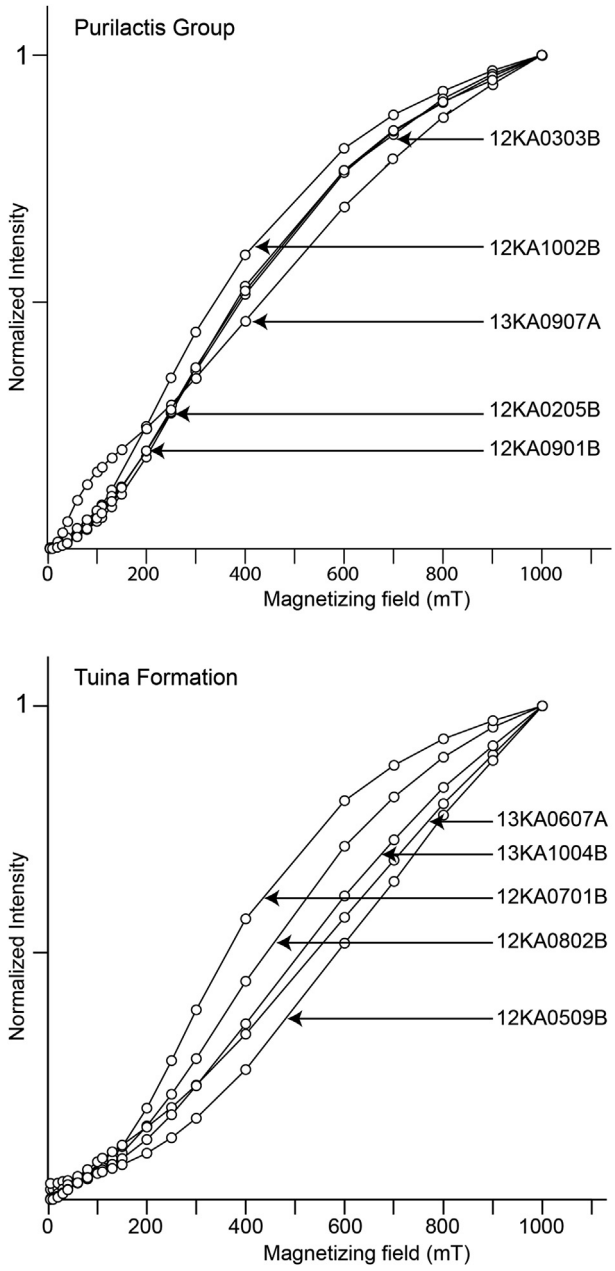

Fig. 4. Isothermal remanent magnetization (IRM) acquisition in five different samples of both the Tuina Formation and the basal members of the Purilactis Group. This analyses show the presence of hematite and scarce magnetite for all samples.

south of Pampa Chilcara, near the western limb of the Barros Arana Syncline (Fig. 2). The remaining 14 sites were obtained in the sedimentary successions of the Tonel and Purilactis Formations. Sites labeled 12KA were drilled in creeks found at the westernmost part of the Cerros de Tuina area, in successions lying directly on top of the Tuina Formation. Sites labeled 13KA were obtained in different points of the western limb of the Barros Arana Syncline. It is important to mention that sites 13KA03 and 13KA04 were the only ones drilled in the eastern limb of the aforementioned syncline (Fig. 2).

Sites in volcanic rocks include only samples from a single flow. Secular variation was thus not averaged at these single bed sites. In contrast, in sedimentary rocks, sampling included different beds along several meters of stratigraphic section. In such cases, mean-site paleomagnetic results should average the secular variation and provide a good estimate of tectonic rotations at the site. Bedding corrections were applied to all sedimentary and volcanic sites (Table 1).

4. Paleomagnetic techniques and magnetic properties

Remanent magnetism was measured with Molspin or Agico JR5A spinner magnetometers at the Universidad de Chile. Magnetic Susceptibility was measured with a Bartington susceptibilimeter. Magnetic susceptibility was also measured after each thermal demagnetization step in order to check magnetic mineralogical changes upon heating. To better constrain the magnetic mineralogy, isothermal remanent magnetism (IRM) acquisition and variation of the susceptibility during heating (K-T) was performed for 10 samples. IRM were obtained with a pulse electro-magnet and

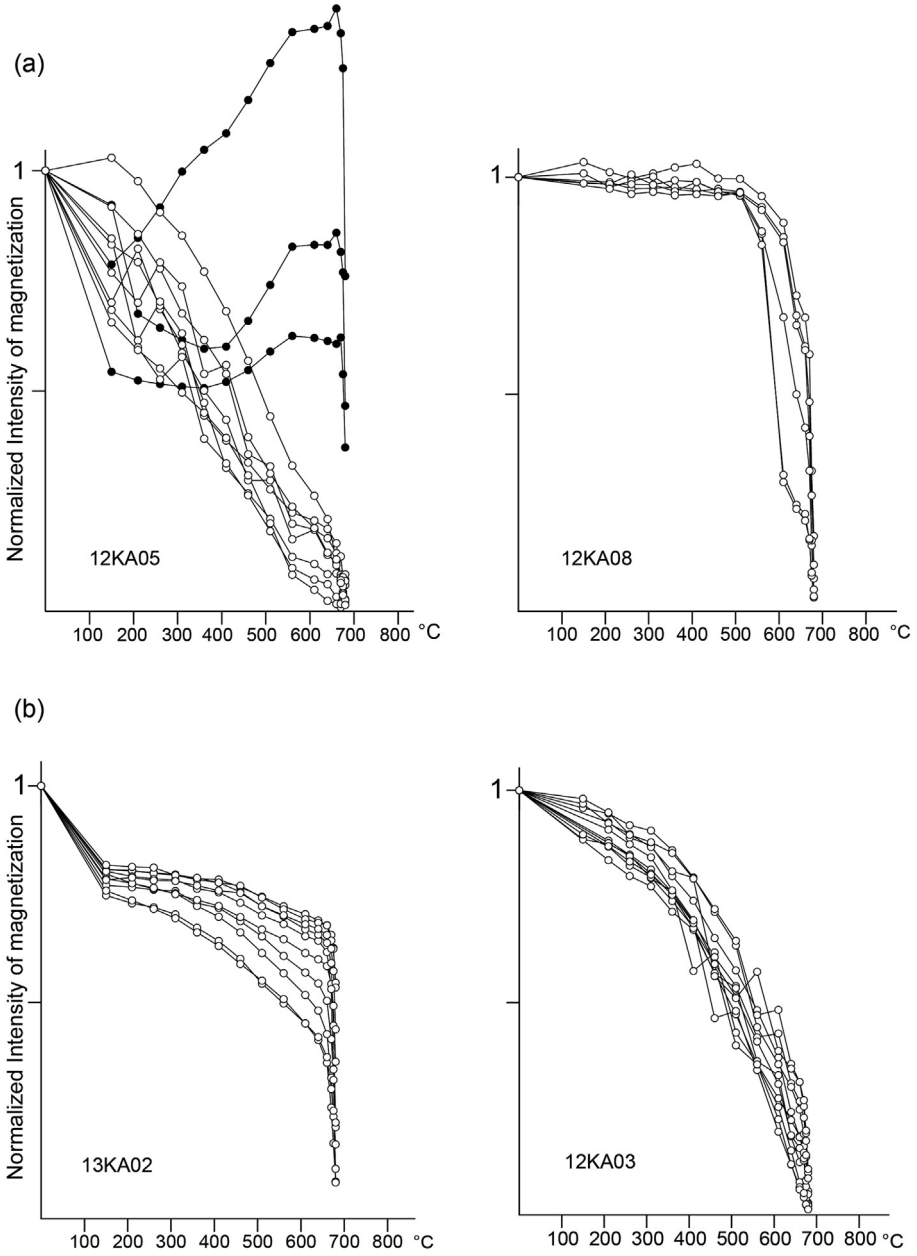

Fig. 5. Variation in the intensity of the remanent magnetization during thermal demagnetization. The demagnetization had to be done at high temperatures, near the Curie temperature for hematite (670–680 °C). (a) Samples from the Tuina Formation. Black circles correspond to three samples with reversed polarity. (b) Samples from the Purilactis Group.

K-T experiments were done with the AGICO KLY3-CS3 instrument.

For all samples, one specimen per mini core was subjected to stepwise thermal demagnetization (12–15 steps) in an ASC Scientific, TD-48 model oven.

A total of 34 samples were subjected to Alternating-Field demagnetization (12–15 steps), but it was not enough to unravel the whole magnetic record (the direction of the characteristic remanent magnetism did not reach the origin).

Demagnetization data were plotted on orthogonal diagrams (Zijderveld, 1967) (Figs. 6 and 7). Principal component analysis (Kirschvink, 1980) was applied to determine sample characteristic remanent magnetism (ChRM) directions. Evidence of secondary overprint was found at a few sites. In these cases, the site-mean characteristic direction including planes and lines was calculated using the procedure described by McFadden and McElhinny (1988). The expected direction and tectonic rotations at a paleomagnetic sites were calculated using the appropriate age reference paleomagnetic pole for South America. We use the Besse and Courtillot (2002) APWP for the Mesozoic units and the reference pole at 250Ma provided by Torsvik et al. (2012) for the Amazonia block (Table 2).

The average magnetic susceptibility and remanent natural magnetization intensity values obtained in the different sites show some variation according to the sampled lithology (Table 1, Fig. 3). The highest NRM values obtained in volcanic rocks was found in site 12KA07, which is also the site with the lowest magnetic susceptibility (Tuina Formation). The highest magnetic susceptibilities obtained in sedimentary rocks were found in the Vizcachita Member samples, belonging to the Purilactis Formation (sites 13KA03 and 13KA04). The sedimentary rock samples of the Tonel Formation (12KA10 and 13KA02) show the lowest magnetic susceptibility. The variation of the magnetic susceptibilities seen in the samples of the Licán and Vizcachita Members may suggest that both units had different sedimentary sources. Overall, the IRM analyses show hematite as the main magnetic carrier (Butler, 1992) with scarce magnetite for all the studied samples (Fig. 4). Consistently, the demagnetization had to be done at high temperatures, near the Curie temperature for hematite (670–680 °C) (Figs. 5–7).

5. Characteristic directions

The analysis of the characteristic directions was straightforward, given the presence of stable magnetizations that point towards the origin (sites 13KA01, 13KA02 and all sites labeled 12KA except 12KA05 and 12KA10). However, some sites also showed unstable magnetizations (sites 13KA08 and 13KA09). In these cases, the method developed by McFadden and McElhinny (1988) was used to find the characteristic directions. In general, the characteristic directions of the Tuina Formation are obtained at 410–680 °C (Figs. 5 and 6). For the Purilactis Formation samples, the characteristic directions are obtained at 560–680 °C (primary directions) and at 345–660 °C (secondary directions) (Figs. 5 and 7).

Site 12KA05 represents a particular case, due to the fact that three of its samples have a magnetization of reversed polarity at high temperature while the other samples present a normal polarity magnetization (Fig. 6). As such, two characteristic directions were calculated using the aforementioned methods (McFadden and McElhinny, 1988; Kirschvink, 1980) (Table 2).

6. Paleomagnetic results

In general, the scatter between sites diminishes after applying tilt correction to the samples (Fig. 8, TC stereonet), either for the Tuina Formation or the Purilactis Group. Normal and reversed polarities directions are obtained for the Tuina Formation. Site 12KA05, drilled in sedimentary rocks, shows both polarities. The

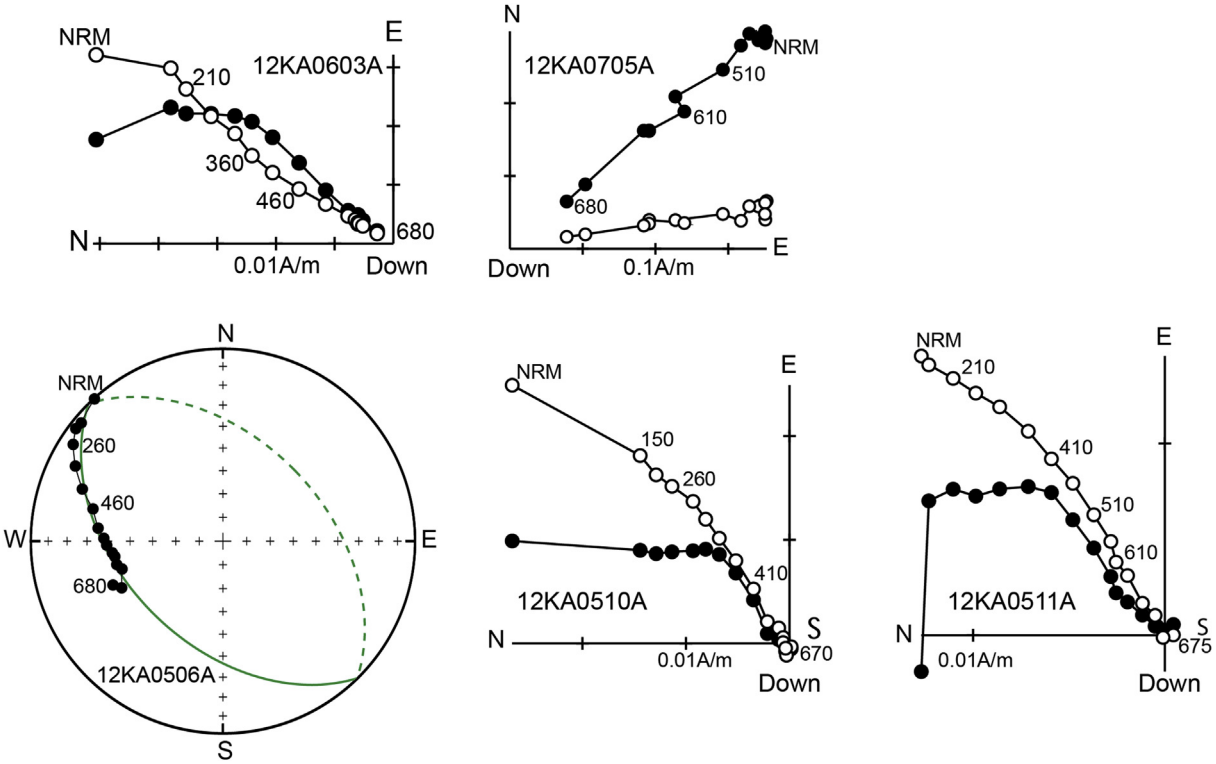

Fig. 6. Selected orthogonal stepwise demagnetization diagrams for sedimentary (sample 12KA05) and volcanic samples belonging to the Tuina Formation (in in situ coordinates). Open circles are projection in the vertical plane, while black circles correspond to the horizontal plane. Numbers indicate temperature steps in °C.

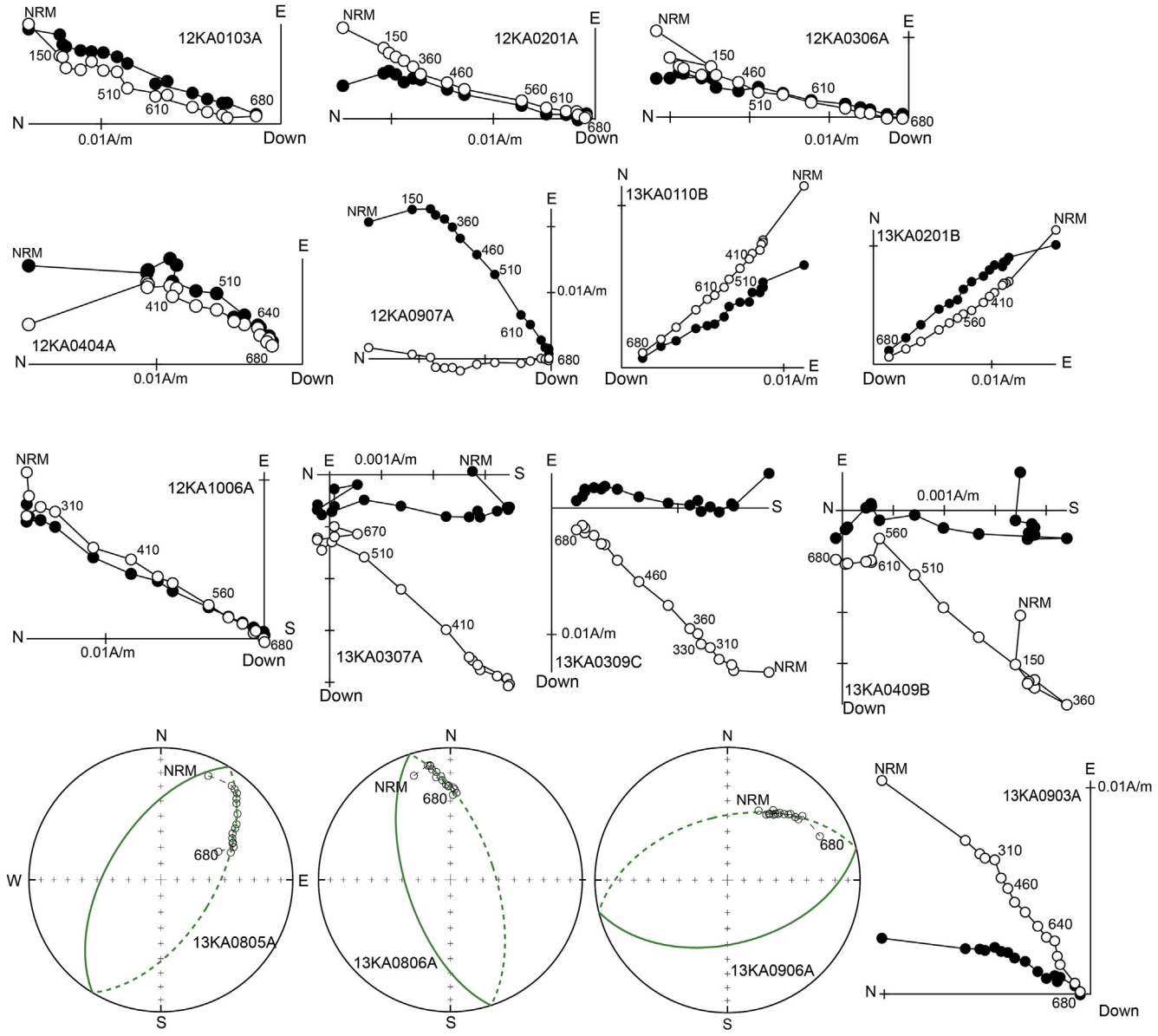

Fig. 7. Selected orthogonal stepwise demagnetization diagrams for sedimentary samples belonging to the basal members of the Purilactis Group (in in situ coordinates). In some cases a soft viscous overprint is removed during the first step of thermal demagnetization.

reversed polarity direction is antipodal, or about 180° away from normal polarity directions. The decrease in scatter, together with the antipodal character of the directions, indicates that the magnetization obtained in the Tuina Formation sites is primary and acquired previous to tilting. The low magnetic susceptibility as well as the highly stable and relatively strong remanent magnetization recorded at site 12KA07 are magnetic characteristics often observed in recent ignimbrites (Paquereau-Lebti et al., 2008), thus supporting the interpretation of a primary magnetization in the Tuina volcanics.

A similar pattern as that described previously by Hartley et al. (1992a), Arriagada et al. (2000) and Somoza and Tomlinson (2002) has been identified for the Purilactis Group (Table 2, Fig. 10). The magnetic inclination after tilt correction shows a better grouping both in the Tuina Formation and in the Purilactis Group. However, the declinations present some scatter. This suggests that, though clockwise rotation is evident, the magnitude of it might be variable and controlled partially by local deformation.

Table 2 shows the calculated tectonic rotation per site, and the inclination difference (flattening) from the expected inclination. The Tuina Formation sites yield fairly high rotation magnitudes between 38 and 79° clockwise (Fig. 9). The Purilactis Group sites shows rotations between 7 and 64° clockwise (Fig. 9). Sites 13KA05, 13KA06, 13KA07 and 13KA10 could not be included in the final results due to the complex and erratic magnetic behavior shown by the samples during demagnetization process. In in situ coordinates, the mean characteristic direction obtained in site 13KA09 is comparable to the mean characteristic direction observed in the other sites belonging to the Tonel Formation after tilt correction suggesting a post-folding magnetization (Table 2).

7. Discussion

7.1. Age of magnetization

Four of the sites obtained in the Tuina Formation show stable

Table 2
Paleomagnetic results.

Site	l	p	t	In situ				Tilt corrected		VGP			Rotation	Inclination	Age
				D (°)	I(°)	α_{95}	k	D(°)	I(°)	Lat(°)	Long(°)	P95	(°)	Error (°)	(Ma)
Barros Arana Syncline: basal sedimentary units of the Purilactis Group (Late Cretaceous)															
Vizcachita member															
13KA03	9	0	9	193.2	40.7	8.3	39.9	216.4	35.4	82.3	228.4	6.9	43.7 ± 10.0	0.8 ± 10.7	80
13KA04	10	0	10	190.3	43.5	6.2	62.4	216.4	39	82.3	228.4	6.9	43.7 ± 8.7	4.4 ± 9.7	80
Licán member															
13KA08	3	6	9	32.6	−45	14.4	15	9.6	−34.2	82.3	228.4	6.9	16.9 ± 15.2	0.3 ± 14.2	80
Tonel formation															
12KA01	5	0	5	14.4	−9.3	10.6	53.5	39.2	−39.1	87.8	29.2	11.5	36.8 ± 14.8	−1 ± 15.2	100
12KA02	5	0	5	13.7	−11.3	5.1	222.2	43.6	−48.1	87.8	29.2	11.5	41.2 ± 11.7	8 ± 13.3	100
12KA03	11	0	11	10.6	−9.4	4.9	88.7	32.3	−45	87.8	29.2	11.5	29.9 ± 11.4	4.9 ± 13.3	100
12KA04	4	1	5	40.2	−37.5	9.4	77.2	35.8	−51.9	87.8	29.2	11.5	33.4 ± 15.8	11.8 ± 14.7	100
12KA09	9	0	9	56	−0.5	4.1	157.1	67	−36.4	87.8	29.2	11.5	64.6 ± 10.8	−3.7 ± 13.1	100
12KA10	10	0	10	22.4	−25.1	4.9	99.5	16.4	−45	87.8	29.2	11.5	14 ± 11.4	5 ± 13.3	100
13KA01	9	0	9	47	−28.8	7.9	43.5	21.9	−33.9	87.8	29.2	11.5	19.5 ± 12.6	−6.2 ± 14.2	100
13KA02	10	0	10	55.5	−29.2	5.0	93.3	27.9	−39.6	87.8	29.2	11.5	25.5 ± 11.3	−0.5 ± 13.3	100
13KA09	10	0	10	20.4	−46.5	2.9	271	340.0	−31.7						
Cordillera de Domeyko: volcanic and sediments of Tuina Formation (Permian-Late Triassic)															
12KA05	1	2	3	231.1	48	9.4	473.1	213.1	31.1	74.1	160.2	3.6	47.1 ± 9.4	−20.8 ± 8.1	250
12KA05	8	0	8	46.9	−44.1	4.7	142.3	32.3	−26.3	74.1	160.2	3.6	46.4 ± 5.4	−25.6 ± 4.9	250
12KA06	4	0	4	43.4	−23.1	3.8	574.4	73.3	−49.1	74.1	160.2	3.6	87.4 ± 5.8	−2.7 ± 4.3	250
12KA07	6	0	6	49.4	−6	3.2	427.6	64.9	−36.9	74.1	160.2	3.6	79 ± 4.7	−14.9 ± 4.0	250
12KA08	6	0	6	44.3	0.4	1.0	4450.7	50.9	−32.1	74.1	160.2	3.6	65 ± 3.5	−19.7 ± 3.2	250

The l and p are numbers of lines and planes used to calculate the mean ChRM direction. t = l + p; D. I. α_{95}. and k. the declination. inclination. angle of confidence at 95% and Fisher parameter k. respectively; Latitude and Longitude are the virtual geomagnetic pole (VGP). P95 is the angle of confidence at 95% for the VGP. Age. estimated age of the magnetization and of the reference pole after Besse and Courtillot (2002) for the Mesozoic units and Torsvik et al. (2012) for the Tuina Formation used to calculate the rotation.

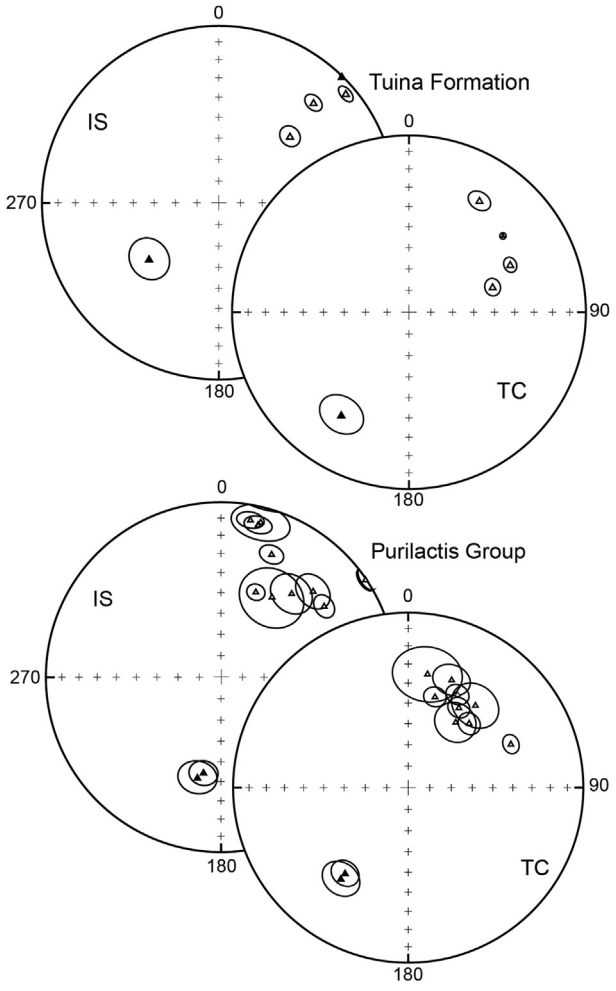

Fig. 8. Simplified geological map showing variation in the magnitude of tectonic rotations. The largest rotations observed are in an area bounded by two reverse faults of opposite vergence (Tuina and Morro del Inca faults).

magnetization. Marinovic and Lahsen (1984) assigned a Permian age to this unit. Recent studies (Henríquez et al., 2014), based on five new U–Pb zircon ages obtained from samples belonging to the Middle and Upper Members of the formation, allow to place it in the Late Permian (Lopingian)-Middle Triassic age. These analyses, together with the primary magnetization data acquired, suggest that the age of magnetization of the four sites would be close to 236–253 Ma.

Regarding the units overlying the Tuina Formation, Bascuñán et al. (2015) estimate that the Tonel Formation would have been deposited between the Albian-Santonian (113–84 Ma), while the Purilactis Formation would have been deposited between the Campanian-Danian (84–61 Ma). These ages are consistent with other paleomagnetic studies that place the Tonel Formation and the basal units of the Purilactis Formation in the "middle" Cretaceous normal polarity superchron (119-84 Ma; Arriagada el al., 2000). The characteristic directions of the primary magnetizations obtained in this study for the Tonel Formation and the basal units of the Purilactis Formation show, preponderantly, normal polarity.

Based on these results, it is possible to conclude that the age of magnetization of the sites belonging to the Tonel and Purilactis Formations range between 110 and 80 Ma.

7.2. Origin of the rotations

The data obtained in the study area show that the Permian–Triassic (Middle Member of the Tuina Formation) and Cretaceous (Purilactis Group) units possess the same rotation pattern (30–40° clockwise), which matches the pattern yielded previously in earlier work (Hartley et al., 1992a; Arriagada et al., 2000; Somoza and Tomlinson, 2002) (Figs. 8–10). This suggests that its origin could be closely associated with the Incaic Orogenic Phase and the building of the Bolivian Orocline (Isacks, 1988; Roperch and Carlier, 1992; McFadden et al., 1995).

Additional tectonic rotations of 57–79,4° clockwise were obtained in the Upper Member of the Tuina Formation (sites 12KA06, 12KA07 and 12KA08) and in a site belonging to the Tonel Formation (12KA09). All these sites overlie the ones belonging to the Tuina

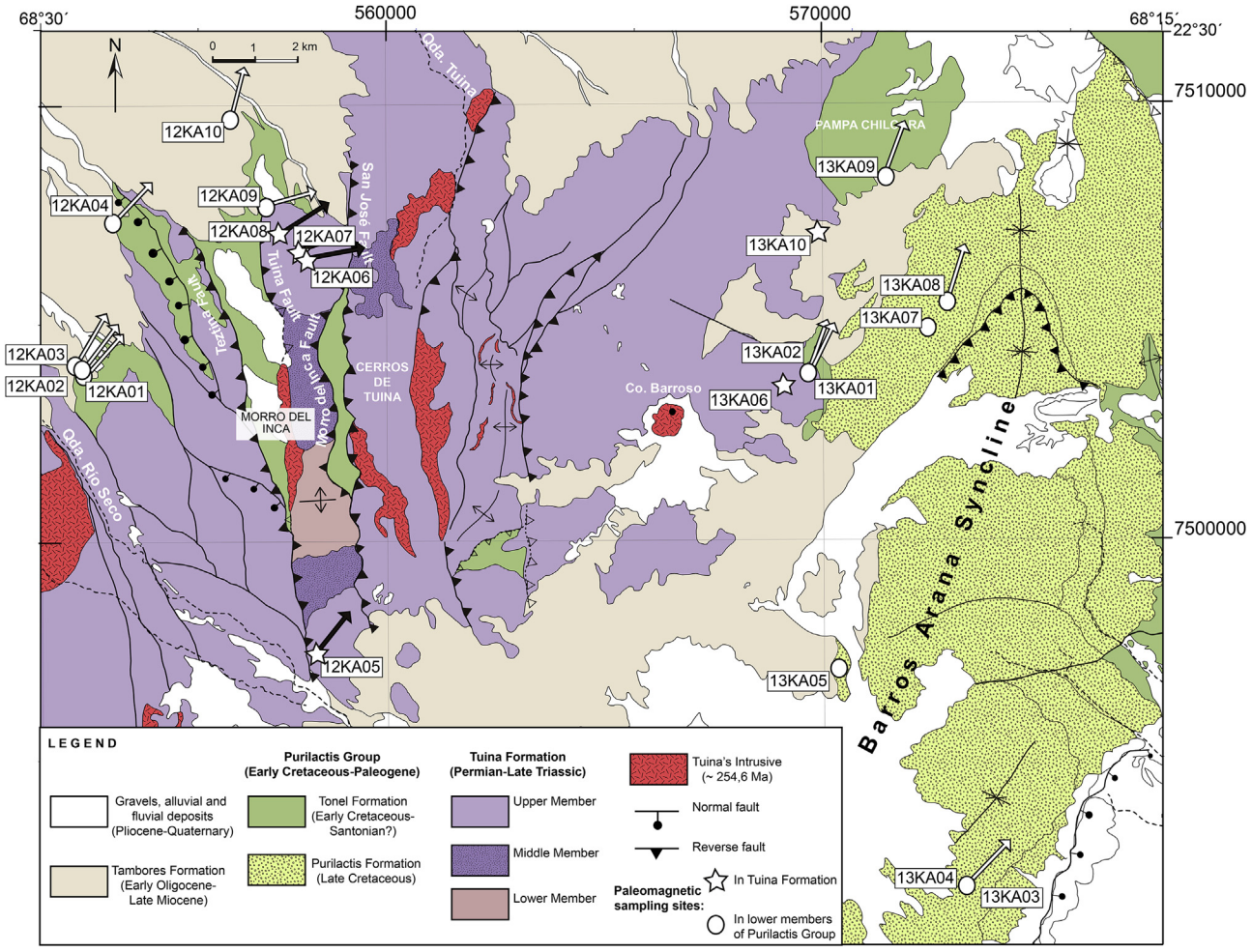

Fig. 9. Equal-area plot of the characteristic directions of the Tuina Formation and the Purilactis Group. IS, in situ. TC, tilt corrected. Upon tilt corrected, there is a significant decrease in the dispersion of the directions.

Formation. The complex structural pattern of this zone may suggest a domain with a higher degree of rotation. The "excess" clockwise rotation could be explained, given the fault geometry (Figs. 8–10), by local, dextral transpressive tectonics. This dextral shear would affect a block bounded by the Tuina, Morro del Inca and San José blocks, effectively increasing the average clockwise rotation locally.

Randall et al. (2001) and Astudillo et al. (2008), who studied structural subdomains of the Domeyko Fault System north and south of the study area, document the presence of anomalous rotations, attributed to the complex kinematic history of the fault system. The magnitude and, at times, sense variation cannot be explained merely by a first order rotation process, as would be expected of an oroclinal bending (Randall et al., 2001).

8. Conclusions

In regard to the magnetic properties, it is possible to conclude that:

- Considering the high temperatures reached during demagnetization (670–680 °C) and the IRM results, it is safe to conclude that the mineral carrying the magnetization is mainly hematite, with a small presence of magnetite in some cases. The magnetic directions observed in the Zijderveld diagrams correspond to univectorial magnetizations pointing towards the origin. We interpret the magnetic vectors as primary magnetizations acquired during the emplacement and the cooling of the volcanic rocks belonging to the Tuina Formation. In the case of the Purilactis Group and site 12KA05 of the Tuina Formation, the magnetization could be associated with either diagenesis, due to the presence of hematite cement, and/or detrital magnetization during sedimentation of these successions.
- The presence of primary magnetizations showing normal and reversed polarities within the Tuina Formation allows discarding a middle Permian age (Kiaman Reversed Polarity Chron) for the studied samples of the Middle and Upper Members. These paleomagnetic results are consistent with a U–Pb age of 236,3 ± 2,5 Ma (Late Triassic) obtained in tuffs belonging to the Upper Member of this formation.
- The Purilactis Group shows normal polarity magnetizations, except for sites 13KA03 and 13KA04, which belong to the Vizcachita Member and show reversed polarities.

It has been possible, for the first time in this area, to obtain favorable measurements in the units belonging to the basement of the Cordillera de Domeyko (Tuina Formation). It is possible to recognize, both in samples belonging to the Tuina Formation as well as the Purilactis Group, the clockwise rotation pattern described previously in this area (Hartley et al., 1992a; Arriagada et al., 2000; Somoza and Tomlinson, 2002). The results obtained point to the existence of 30–40° clockwise tectonic rotations. Some

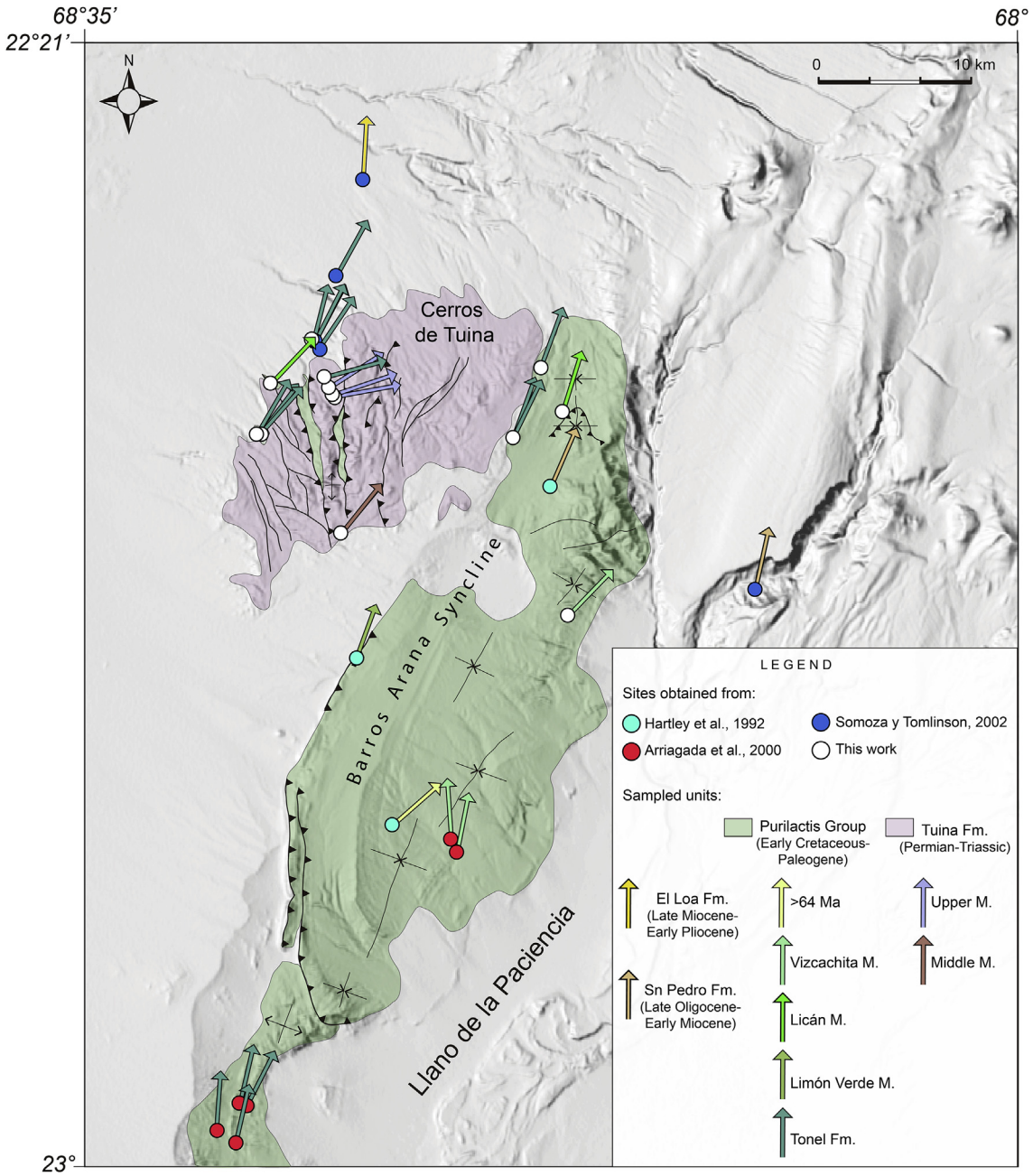

Fig. 10. Compilation of tectonic rotations in the northern part of the Atacama basin. It is possible to recognize, both in samples belonging to the Tuina Formation as well as the Purilactis Group, the clockwise rotation pattern described previously in this area.

sites record even larger clockwise rotations but they are limited to a structural domain bounded by reverse faults of opposite vergence. This domain is probably controlled by a local, dextral transpressive tectonic regime, highlighting the complex kinematic history of this region. Additionally, we conclude that there is not enough evidence of significant rotations in this area, neither in the Permo-Triassic unit (Tuina Formation), nor in the lower members of the Purilactis Group, previous to the rotations which formed the Bolivian Orocline. It is possible to assert that the Peruvian and K-T tectonic phases did not generate significant tectonics rotations in the area.

Acknowledgments

The authors would like to thank Fondecyt-Chile (grant No.1110093, (V. Maksaev, project's leader)). We also appreciated the help of Susana Henríquez for sharing her knowledge of the area; Sergio Villagran and Marco Vaccaris for their collaboration in field. S. Geuna and R. Somoza provided constructive comments on this manuscript.

References

Arriagada, C., Roperch, P., Mpodozis, C., 2000. Clockwise block rotations along the eastern border of the Cordillera de Domeyko, northern Chile (22°45′–23°30′S). Tectonophysics 326, 153–171.

Arriagada, C., Roperch, P., Mpodozis, C., Dupont-Nivet, G., Cobbold, P.R., Chauvin, A., Cortés, J., 2003. Paleogene clockwise tectonic rotations in the forearc of central Andes, Antofagasta region, northern Chile. J. Geophys. Res. 108 (B1), 2032. http://dx.doi.org/10.1029/2001JB001598.

Arriagada, C., Roperch, P., Mpodozis, C., Fernández, R., 2006a. Paleomagnetism and

tectonics of the southern Atacama Desert (25°–28°S) northern Chile. Tectonics 25, TC4001. http://dx.doi.org/10.1029/2005TC001923.
Arriagada, C., Cobbold, P.R., Roperch, P., 2006b. Salar de Atacama basin: a record of compressional tectonics in the central Andes since the mid-Cretaceous. Tectonics 25, TC1008. http://dx.doi.org/10.1029/2004TC001770.
Arriagada, C., Roperch, P., Mpodozis, C., Cobbold, P.R., 2008. Paleogene building of the Bolivian Orocline: tectonic restoration of the central Andes in 2-D map view. Tectonics 27, TC6014. http://dx.doi.org/10.1029/2008TC002269.
Astudillo, N., Roperch, P., Townley, B., Arriagada, C., Maksaev, V., 2008. Importance of small-block rotations in damage zones along transcurrent faults. Evidence from the Chuquicamata open pit, Northern Chile. Tectonophysics 450, 1–20.
Bahlburg, H., Breitkreuz, C., 1991. Paleozoic evolution of active margin basins in the southern Central Andes (northwestern Argentina and northern Chile). J. S. Am. Earth Sci. 4, 171–188.
Bascuñán, S., Arriagada, C., Le Roux, J., Deckart, K., 2015. Unraveling the Peruvian phase of the central Andes: stratigraphy, sedimentology and geochronology of the Salar de Atacama Basin (22°30–23°S), northern Chile. Basin Res. 1365–2117. http://dx.doi.org/10.1111/bre.12114.
Beck, M.E., 1987. Tectonic rotations on the leading edge of south America: the Bolivian orocline revisited. Geology 15 (No. 9), 806–808.
Beck, M.E., 2004. The central Andean rotation pattern: another look. Geophys. J. Int. 157, 1348–1358. http://dx.doi.org/10.1111/j.1365-246X.2004.02266.x.
Besse, J., Courtillot, V., 2002. Apparent and true polar wander and the geometry of the geomagnetic field over the last 200 Myr. J. Geophys. Res. 107, 2300. http://dx.doi.org/10.1029/2000JB00.
Breitkreuz, C., Zeil, W., 1994. The late carboniferous to Triassic volcanic belt in northern Chile. In: Reutter, K., et al. (Eds.), Tectonics of the Southern Central Andes. Springer-Verlag, Berlin, pp. 277–292.
Butler, R., 1992. Palaeomagnetism: Magnetic Domains to Geological Terranes. Blackwell Scientific Publications, Oxford, p. 319.
Carey, S.W., 1955. The orocline concept in geotectonics. Proc. R. Soc. Tasman. 89, 255–258.
Charrier, R., Reutter, K.J., 1990. The Purilactis group of northern Chile: link between arc and backarc during Late Cretaceous and Paleogene. In: Proc. I ORSTOM-isag, Grenoble, pp. 249–252.
Charrier, R., Reutter, K.J., 1994. The Purilactis Group of Northern Chile: Boundary between Arc and Back Arc from Late Cretaceous to Eocene. Tectonics of the Southern Central Andes. Springer-Verlag, Berlin, pp. 189–202.
Charrier, R., Pinto, L., Rodríguez, P., 2007. Tectonostratographic Evolution of the Andean Orogen in Chile. The Geology of Chile. The Geological Society, London, pp. 1–114.
Charrier, R., Farías, M., Maksaev, V., 2009. Evolución tectónica, paleogeográfica y metalogénica durante el Cenozoico en los Andes de Chile norte y central e implicaciones para las regiones adyacentes de Bolivia y Argentina. Rev. la Asoc. Geol. Argent. 65 (1), 5–35.
Cornejo, P., Matthews, S., Pérez de Arce, C., 2003. The KT compressive deformation event in northern Chile (24°27′S). In: X Congreso Geológico Chileno. Extended Abstracts Volume (CD), Concepción.
Coutand, I., Roperch, P., Chauvin, A., Cobold, P.R., Gautier, P., 1999. Vertical axis rotations across the Puna plateau (northwestern Argentina) from paleomagnetic analysis of Cretaceous and Cenozoic rocks. J. Geophys. Res. 104, 22965–22984.
Forsythe, R.D., Kent, D.V., Mpodozis, C., Davidson, J., 1987. Paleomagnetism of permian and triassic rocks, Central chilean Andes. In: McKenzie, G.A. (Ed.), Structure, Tectonics and Geophysics, Geophysical Monograph, 40. .American Geophysical Union, pp. 241–251.
Geuna, S.E., Escosteguy, L.D., 2004. Palaeomagnetism of the upper carboniferous-lower permian transition from Paganzo basin, Argentina. Geophys. J. Int. 157, 1071–1089. http://dx.doi.org/10.1111/j.1365-246X.2004.02229.x.
González, G., Cembrano, J., Aron, F., Veloso, E.E., Shyu, J.B.H., 2009. Coeval compressional deformation and volcanism in the central Andes, case studies from northern Chile (23°S–24°S). Tectonics 28 (6), TC6003.
Hartley, A., Jolley, E.J., Turner, P., 1992a. Paleomagnetic evidence for rotation in the precodillera of northern Chile: structural constraints and implications for the evolution of the Andean forearc. Tectonophysics 205, 49–64.
Hartley, A., Flint, S., Turner, P., Jolley, E.J., 1992b. Tectonic controls on the development of a semi-arid, alluvial basin as reflected in the stratigraphy of the Purilactis group (Upper Cretaceous-Eocene), northern Chile. J. South Am. Earth Sci. 5 (3/4), 275–296.
Heki, K., Hamano, Y., Kinoshita, H., Taira, A., Kono, M., 1984. Paleomagnetic study of Cretaceous rocks of Peru, south America: evidence for rotation of the Andes. Tectonophysics 108, 267–281.
Heki, K., Hamano, Y., Kono, M., 1985. Paleomagnetism of the Neogene Ocros dyke swarm, the Peruvian Andes: impli- cations for the Bolivian orocline. Geophys. J. R. Astron. Soc. 80, 527–534.
Henríquez, S.M., Becerra, J., Arriagada, C., 2014. Geología del área San Pedro de Atacama, Región de Antofagasta. Servicio Nacional de Geología y Minería. Carta Geológica de Chile, Santiago, Chile. Serie Geología Básica. 1 mapa escala 1: 100.000.
Isacks, B.L., 1988. Uplift of the central Andean plateau and bending of the Bolivian orocline. J. Geophys. Res. 93, 3211–3231.
Jesinkey, C., Forsythe, R.D., Mpodozis, C., Davidson, J., 1987. Concordant late Paleozoic paleomagnetizations from the Atacama Desert: implications for tectonic models of the Chilean Andes. Earth Planet. Sci. Lett. 85, 461–472. http://dx.doi.org/10.1016/0012-821X(87)90141-5.
Jordan, T.E., Mpodozis, C., Muñoz, N., Blanco, P., Pananont, M., Gardeweg, M., 2007. Cenozoic subsurface stratigraphy and structure of the Salar de Atacama basin, northern Chile. J. S. Am. Earth Sci. 23, 122–146.
Kirschvink, J.L., 1980. The least-squares line and plane and the analysis of paleomagnetic data. Geophys. J. R. Astron. Soc. 62, 699–718.
Lamb, S., 2001. Vertical axis rotation in the Bolivian orocline, south America. 1. Paleomagnetic analysis of Cretaceous and Cenozoic rocks. J. Geophys. Res. 106, 26–605-26-632.
Macellari, C.E., Su, M., Townsend, F., 1991. Structure and seismic stratigraphy of the Atacama Basin, northern Chile. In: Proc. VI Congr. Geol. Chileno, pp. 133–137.
Maksaev, V., Zentilli, M., 1999. Fission track thermochronology of the Domeyko Cordillera, northern Chile; implications for Andean tectonics and porphyry copper metallogenesis. Explor. Min. Geol. 8, 65–89.
Marinovic, N., Lahsen, A., 1984. Hoja Calama. Servicio Nacional de Geología y Minería, Carta Geológica de Chile, Santiago. No., 140 pp., escala 1:250.000.
May, S.R., Butler, R.F., 1985. Paleomagnetism of the Puente Piedra formation, Central Peru. Earth Planet. Sci. Lett. 72, 205–218.
McFadden, P.L., 1990. A new fold test for paleomagnetic studies. Geophys. J. Int. 103, 163–169.
McFadden, P.L., McElhinny, M.W., 1988. The combined analysis of remagnetization circles and direct observations in paleomagnetism. Earth Planet. Sci. Lett. 87, 161–172.
McFadden, B.J., Anaya, F., Swisher, C.C., 1995. Neogene paleomagnetism and oroclinal bending of the central Andes of Bolivia. J. Geophys. Res. 100, 8153–8167.
Mpodozis, C., Ramos, V., 1990. The Andes of Chile and Argentina. In: Eriksen, G., et al. (Eds.), Geology of the Central Andes and its Relation to Hydrocarbon and Mineral Resources, Earth. Sci. Ser., Circum-pac. Counc. For Energy and Min. Resources, Houston, Tex., 11, pp. 59–90.
Mpodozis, C., Marinovic, N., Smoje, I., 1993. Eocene left lateral strike slip faulting and clockwise block rotations in the Cordillera de Domeyko, west of the Salar de Atacama, northern Chile. In: ORSTOM (Ed.), Second International Symposium of Andean Geodynamics, Paris, pp. 225–228.
Mpodozis, C., Arriagada, C., Basso, M., Roperch, P., Cobbold, R., Reich, M., 2005. Late Mesozoic to Paleogene stratigraphy of the Salar de Atacama Basin, Antofagasta, northern Chile: implications for the tectonic evolution of the central Andes. Tectonophysics 399, 125–154. http://dx.doi.org/10.1016/j.tecto.2004.12.019.
Mundaca, P., 1982. Estratigrafía de los Cuadrángulos Aguada de la Teca y Barros Arana, Provincia El Loa, II Región. Taller de Título II. Univ. Chile, Dpto. Geol. Y Geofís. (Inédito), Santiago, p. 87.
Mundaca, P., 2002. Geología de los Cuadrángulos Aguada de la Teca y Barros Arana, II Región, Antofagasta. Memoria de Título. Departamento de Geología, Universidad de Chile, Santiago.
Muñoz, N., Charrier, R., Reutter, K.J., 1997. Evolución de la Cuenca del Salar de Atacama: Inversión tectónica y relleno de una cuenca de antepaís de retro-arco. Proc. VIII Congr. Geol. Chil. 1, 5–199.
Paquereau-Lebti, P., Fornari, M., Roperch, P., Thouret, J.-C., Macedo, O., 2008. Paleomagnetism, magnetic fabric, and 40Ar/39Ar dating of Pliocene and quaternary ignimbrites in the Arequipa area, southern Peru. Bull. Volcanol. 70, 977–997. http://dx.doi.org/10.1007/s00445-007-0181-y.
Raczynnski, A., 1963. Geología del distrito minero de Tuina. Memoria de Título. Univ. Chile, Depto. Geología, Santiago, p. 117.
Ramírez, C.F., Gardeweg, M.C., 1982. Hoja Toconao, Región de Antofagasta. Serv. Nac. Geol. Min. Carta Geol. Chile 54, 1–122 (1:250.000).
Randall, D., Tomlinson, A., Taylor, G., 2001. Paleomagnetically defined rotations from the Precordillera of northern Chile: evidence of localized in situ fault-controlled rotations. Tectonics 20, 235–254.
Reutter, K., Scheuber, E., Helmcke, D., 1996. The Precordillera fault system of Chuquicamata, northern Chile: evidence for reversals along arc parallel strike-slip faults. Tectonophysics 259, 213–228.
Riley, P.D., Beck, M.E., Burmester, R.F., 1993. Paleomagnetic evidence of vertical axis blocks rotations from the Mesozoic of northern Chile. J. Geophys. Res. 98, 8321–8333.
Roperch, P., Carlier, G., 1992. Paleomagnetism of Mesozoic rocks from the central Andes of southern Peru: importance of rotations in the development of the Bolivian orocline. J. Geophys. Res. 97, 17.233-17.249.
Roperch, P., Dupont-Nivet, G., Pinto, L., 1997. Rotaciones Tectónicas en el Norte de Chile. Proc. VIII Cong. Geol. Chil. 1, 241–245.
Roperch, P., Sempere, T., Macedo, O., Arriagada, C., Fornari, M., Tapia, C., García, M., Laj, C., 2006. Counterclockwise rotation of late Eocene-Oligocene fore-arc deposits in southern Peru and its significance for oroclinal bending in the central Andes. Tectonics 25, TC3010. http://dx.doi.org/10.1029/2005TC001882.
Roperch, P., Carlotto, V., Ruffet, G., Fornari, M., 2011. Tectonic rotations and transcurrent deformation south of the Abancay deflection in the Andes of southern Peru. Tectonics 30, TC2010. http://dx.doi.org/10.1029/2010TC002725.
Scanlan, P.M., Turner, P., 1992. Structural constraints on paleomagnetic rotations south of the Arica bend, northern Chile: implications for the Bolivian orocline. Tectonophysics 205, 141–154. http://dx.doi.org/10.1016/0040-1951(92)90423-4.
Scheuber, E., Reutter, K., 1992. Magmatic arc tectonics in the Central Andes between 21° and 25°S. Tectonophysics 25, 127–140.
Somoza, R., Tomlinson, A., 2002. Paleomagnetism in the Precordillera of northern Chile (22°30′S): implications for the history of tectonic rotations in the Central Andes. Earth Planet. Sci. Lett. 194, 369–381.
Somoza, R., Tomlinson, A.J., Caffe, P.J., Vilas, J.F., 2012. Paleomagnetic evidence of earliest Paleocene deformation in Calama (22°S), northern Chile: Andean-type or ridge-collision tectonics? J. S. Am. Earth Sci. 37, 208–213.

Steinmann, G., 1929. Geologie von Peru. Karl Winter, Heidelberg, Germany, p. 448.
Taylor, G.K., Dashwood, B., Grocott, J., 2005. Central Andean rotation pattern: evidence from paleomagnetic rotations of an anomalous domain in the fore-arc of northern Chile. Geology 33, 777–780. http://dx.doi.org/10.1130/G21876.1.
Tomlinson, A., Blanco, N., 1997. Structural evolution and displacement history of the west fault system, Precordillera, Chile: part 1, synmineral history. Actas VIII Congr. Geol. Chile 3, 1873–1877.
Torsvik, T.H., Van der Voo, R., Preeden, U., Mac Niocaill, C., Steinberger, B., Doubrovine, P.V., van Hinsbergen, D.J.J., Domeier, M., Gaina, C., Tohver, E., Meert, J.G., McCausland, P.J.A., Cocks, L.R.M., 2012. Phanerozoic polar wander, palaeogeography and dynamics. Earth-Sci. Rev. 114, 325–368. http://dx.doi.org/10.1016/j.earscirev.2012.06.007.
Zijderveld, J.D.A., 1967. A.C. Demagnetization of rocks: analysis of results. In: Collinson, D.W., Creer, K.M., Runcorn, S.K. (Eds.), Methods in Palaeomagnetism. Elsevier, pp. 254–286.

Supplementary Material D

List of additional collaborations and presentations

Bascuñán, S., Becerra, J., Rubilar, J.F., Maksymowicz, A., Gómez, I., Martínez, F., Arriagada, C., Le Roux, J.P., Deckart, K., Peña, M., Araya, J., 2016a. Tectonic Evolution of the Central Andes of northern Chile, and its record within the Salar de Atacama Basin (22°-24°S), in: I Simposio de Tectónica Sudamericana-ATECSUD. Santiago, Chile.

Bascuñán, S., Becerra, J., Rubillar, J.F., Gómez, I., Narea, K., Martínez, F., Arriagada, C., Le Roux, J.P., Deckart, K., 2015. Tectonic Evolution of the Central Andes during Mesozoic-Cenozoic times: Insights from the Salar de Atacama Basin, in: AGU Fall Meeting 2015. San Francisco, USA.

Bascuñán, S., Maksymowicz, A., Martínez, F., Becerra, J., Arriagada, C., Peña, M., Gómez, I., 2018. Structure, gravimetry and tectonic analysis of the Preandean Depression-Cordillera de Domeyko border (22°38'-23°15'S), in: AGU Fall Meeting 2018. Washington D.C., USA.

Bascuñán, S., Maksymowicz, A., Martínez, F., Becerra, J., Rubillar, J.F., Arriagada, C., Peña, M., Gómez, I., 2016b. Weighing the Oligocene extensional event in the Salar de Atacama Basin by analysis of depth-converted sections and geophysical data, in: AGU Fall Meeting 2016. San Francisco, USA.

Becerra, J., Arriagada, C., Contreras-Reyes, E., **Bascuñan, S.**, De Pascale, G.P., Reichert, C., Díaz-Naveas, J., Cornejo, N., 2017. Gravitational deformation and inherited structural control on slope morphology in the subduction zone of north-central Chile (ca . 29-33°S). Basin Res. 29, 798–815. https://doi.org/10.1111/bre.12205

Becerra, J., Arriagada, C., Contreras-Reyes, E., Peña, M., Manríquez, P.M., Gómez, I., **Bascuñán, S.**, 2015. Gravitational deformation and inherited structural control on slope morphology, north-central Chile (29-33°S), in: AGU Fall Meeting 2015. San Francisco, USA.

Fuentes, G., Martínez, F., **Bascuñan, S.**, Arriagada, C., Muñoz, R., 2018. Tectonic architecture of the Tarapacá Basin in the northern Central Andes: New constraints from field and 2D seismic data. Geosphere 14, 2430–2446. https://doi.org/10.1130/GES01697.1

Maksymowicz, A., Ruiz, J., Vera, E., Contreras-Reyes, E., Ruiz, S., Arriagada, C., Bonvalot, S., **Bascuñán, S**., 2018. Heterogeneous structure of the Northern Chile marine forearc and its implications for megathrust earthquakes. Geophys. J. Int. 215, 1080–1097. https://doi.org/10.1093/GJI/GGY325

Martínez, F., Arriagada, César, **Bascuñán, S.**, 2018. Mechanisms and Episodes of Deformation Along the Chilean–Pampean Flat-Slab Subduction Segment of the Central Andes in Northern Chile, in: Folguera, A., Contreras-Reyes, E., Heredia, N., Encinas, A., Ianelli, S.B., Oliveros, V., Dávila, F.M., Collo, G., Giambiagi, L.B., Maksymowicz, A., Iglesia Llanos, M.P., Turienzo, M., Naipauer, M., Orts, D., Litvak, V.D., Álvarez, O., Arriagada, C. (Eds.), The Evolution of the Chilean-Argentinean Andes. Springer International Publishing, pp. 273–290. https://doi.org/10.1007/978-3-319-67774-3_11

Martínez, F., Fuentes, G., Perroud, S., **Bascuñan, S**., 2021. Buried thrust belt front of the western Central Andes of northern Chile: Style, age, and relationship with basement heterogeneities. J. Struct. Geol. 147. https://doi.org/10.1016/j.jsg.2021.104337

Martínez, F., Parra, M., Arriagada, C., Mora, A., **Bascuñan, S**., Peña, M., 2017. Late Cretaceous to

Cenozoic deformation and exhumation of the Chilean Frontal Cordillera (28°–29°S), Central Andes. J. Geodyn. 111, 31–42. https://doi.org/10.1016/j.jog.2017.08.004